NOTE TO USERS

Page(s) not included in the original manuscript and are unavailable from the author or university. The manuscript was scanned as received.

missing pages 107 & 322

This reproduction is the best copy available.

UMI®

Theoretical and Experimental Investigations of Photoresponsive and Biomimetic Supramolecular Materials

by

Felaniaina Rakotondradany

A thesis submitted to the Faculty of Graduate Studies and Research of McGill University in partial fulfillment of the requirements of the degree of Doctor of Philosophy

January 2004

Department of Chemistry, McGill University
Montréal, Québec, Canada

© Felaniaina Rakotondradany, 2004

Library and Archives Canada

Published Heritage Branch

395 Wellington Street
Ottawa ON K1A 0N4
Canada

Bibliothèque et Archives Canada

Direction du Patrimoine de l'édition

395, rue Wellington
Ottawa ON K1A 0N4
Canada

Your file Votre référence
ISBN: 0-612-98356-0
Our file Notre référence
ISBN: 0-612-98356-0

NOTICE:
The author has granted a non-exclusive license allowing Library and Archives Canada to reproduce, publish, archive, preserve, conserve, communicate to the public by telecommunication or on the Internet, loan, distribute and sell theses worldwide, for commercial or non-commercial purposes, in microform, paper, electronic and/or any other formats.

The author retains copyright ownership and moral rights in this thesis. Neither the thesis nor substantial extracts from it may be printed or otherwise reproduced without the author's permission.

AVIS:
L'auteur a accordé une licence non exclusive permettant à la Bibliothèque et Archives Canada de reproduire, publier, archiver, sauvegarder, conserver, transmettre au public par télécommunication ou par l'Internet, prêter, distribuer et vendre des thèses partout dans le monde, à des fins commerciales ou autres, sur support microforme, papier, électronique et/ou autres formats.

L'auteur conserve la propriété du droit d'auteur et des droits moraux qui protège cette thèse. Ni la thèse ni des extraits substantiels de celle-ci ne doivent être imprimés ou autrement reproduits sans son autorisation.

In compliance with the Canadian Privacy Act some supporting forms may have been removed from this thesis.

While these forms may be included in the document page count, their removal does not represent any loss of content from the thesis.

Conformément à la loi canadienne sur la protection de la vie privée, quelques formulaires secondaires ont été enlevés de cette thèse.

Bien que ces formulaires aient inclus dans la pagination, il n'y aura aucun contenu manquant.

Canada

A ma famille

Acknowledgements

I would like to thank my thesis supervisors Dr. Hanadi F. Sleiman and Dr. M. A. Whitehead for their enthusiasm for scientific research and their mentorship.

I also would like to gratefully acknowledge the assistance provided by:

- Dr. Anne – Marie Lebuis for single crystal X-Ray analysis and structure solution and refinement for the *trans*-azodibenzoic acid monomer
- Dr. G. Bazuin, Université Laval, for the loan of the Model 233 tonometer and Ms. R. Plésu Université Laval,for technical assistance for the use of the tonometer
- Mr. Michel Preda, Université de Québec à Montréal, Département des Sciences de la Terre et de l'Atmosphère, for XRD analysis
- Dr. Stephanie Warner and Dr. Ian S. Butler, Department of Chemistry, McGill University, for use of the infrared spectrometer and HPLC.
- Mr. Nadim Saadeh, Department of Chemistry, McGill University, for mass spectral analysis and training
- Dr. A. D. Chapman, Concordia University, for the loan of the Vapro 5520-model vapor pressure osmometer
- Dr. P. J. Wright, Concordia University, and D. Dennie, McGill University, for the acquisition of the electrospray ionisation mass spectra.
- Dr. R. St-J. Manley for loan of UV photoreactor
- Mr. Nicolas Bélanger and Dr. M. Andrews for use of the Hg lamp
- Dr. Antisar Hlil and Dr. Alan S. Hay, Department of Chemistry, McGill University, for MALDI-TOF analysis
- Dr. Ignacio Vargas-Baca for his valuable experimental advice
- Mr. Roger Gaudreault and Cascades Inc. for purchase of computational software
- Ms. Cecile Malardier-Jugroot for proof-reading the thesis, and valuable theoretical advice
- Dr. Adam J. Dickie for proof-reading the thesis, theoretical and experimental advice, and, his patience and encouragement
- Sigma Xi for a Grant-in-Aid of Research, McGill University for a teaching assistantship under the supervision of Dr. Grazyna Wilczek

- I would like to thank my colleagues and friends in the Sleiman and Whitehead group especially Cecile, Adam, Roger, Debbie, Kim, Faisal, Hassan, Mohammed, and Bing.
- I would also thank Alessandra, Michel, Muriel and Neil for their support

Abstract

A new approach for design and fabrication of new photoresponsive and biomimetic materials is described using theoretical predictions and experimental characterisations. Novel discrete hydrogen-bonded aggregates are formed from photoresponsive azodibenzoic acid building blocks, which can undergo a reversible *cis-trans* photoisomerisation. In *trans –p*-azodibenzoic acid, the two carboxylic groups are aligned parallel to each other while, in the *cis* isomer, they are almost perpendicular. This structural difference between the two isomers leads to different hydrogen-bonded geometries: the *trans* isomer aggregates linearly whereas its *cis* counterpart forms cyclic tetramers. Molecular and bulk material characterisation are used to identify a higher-order self-organisation from the *cis*-isomers, which results in long, unidimensional rod-like structures.

A new understanding of hydrogen-bonded aggregates is developed, where the thermodynamics of azodibenzoic acid self-assembly are identified using vibrational properties, molecular orbital wavefunctions, and density matrix analysis. Quantum mechanical properties of hydrogen-bonded azodibenzoic acids establish the relative stabilities of the self-assembly products, validating the formation of *trans*- linear tapes and *cis*-cyclic tetramers.

A molecular modelling strategy is implemented to provide detailed information on packing within *cis*-azodibenzoic acid rod-like nanostructures. Energy scans determine face-packing as the preferred macrocycle arrangement. Quantum mechanical optimisation of this face-packed structure shows little deviation from predicted molecular

models, highlighting the strength of this modelling technique. Electronic properties exhibit significant π-electron delocalisation throughout the entire arrays, along with a HOMO-LUMO band gap narrowing towards values typical of non-doped, organic semi-conducting materials.

Dicyano-, ditriazene- and diureido- azobenzene derivatives are introduced to design tightly bound supramolecular structures by multiple hydrogen-bonding and metal-coordination. Using geometric arguments, the conservation of recognition site orientations and electronic properties upon substitution allows the use of the *trans*- and *cis*-azodibenzoic acids as model monomers for the prediction of self-assembly for these new photoresponsive units.

Finally, new triaminopyrimidine nucleosides are synthesised to generate hydrogen-bonded supramolecular structures from DNA-base analogues. Experimental characterisation shows that hydrogen-bonding of the triaminopyrimidine monomer with barbiturates leads to oligomeric species. Using sterically encumbered cyanuric acid nucleosides dramatically alters the hydrogen-bond self-assembly of these molecules, giving rise to discrete hexameric macrocycles which further associate to form elongated nanostructures.

Résumé

Une nouvelle approche pour la conception et la fabrication de nouveaux matériaux photoresponsifs et biomimétiques est décrite par des prédictions théoriques et des caractérisations expérimentales. De nouveaux aggregates discrets liés par ponts hydrogène sont formés à partir de modules photoresponsifs d'acide azodibenzoique qui peuvent subir une photoisomérisation *cis-trans* reversible. Dans l'acide *trans*-azodibenzoique, les deux groupements carboxyliques sont alignés l'un par rapport à l'autre alors que, dans l'isomère *cis*, ils sont presque perpendiculaires. Cette difference structurelle entre les deux isomères mène à différentes geometries liées par ponts hydrogène: l'isomère *trans* s'aggrège de façon linéaire tandis que son homologue *cis* forme des tétramères cycliques. Les techniques de caractérisation de molécules et des matériaux sont utilisées pour identifier un degré supplémentaire d'auto-organisation des isomères *cis*, qui résulte en longs bâtonnets unidimensionels.

Une nouvelle comprehension des aggregates liés par ponts hydrogène est développée, où la thermodynamique de l'auto-assemblage d'acide azodibenzoiques est identifiée en utilisant les propriétés vibrationelles, les functions d'ondes des orbitales moléculaires, et l'analyse de la matrice de densité. Les propriétés quantiques des acides azodibenzoiques établissent la stabilité relative des produits de l'auto-assemblage, tout en validant la formation de rubans linéaires *trans* et de tetramères cycliques *cis*.

Une stratégie basée sur la modélisation moléculaire est mise en oeuvre pour fournir des informations détaillées à propos du packing au sein des nanostructures en bâtonnets d'acide azodibenzoique. Des scans en énergie determine la configuration en

face-à-face comme l'arrangement préféré de ces macrocycles. L'optimisation de cette structure en face-à-face montre peu de deviation par rapport au modèle moléculaire prédit, soulignant la force de cette technique de modélisation. Les propriétés électroniques montrent une délocalisation significative des electron π sur la totalité des Series, avec une diminution de l'espace de bande HOMO-LUMO vers des valeurs typiques de semi-conducteurs organiques non-dopés.

Des dérivés dicyano, ditriazine, et diureido de l'acide azodibenzoique sont introduits pour concevoir des structures supramoléculaires stables par ponts hydrogène multiples et par coordination à des métaux. Usant d'un argument géométrique, la conservation de l'orientation des sites de reconnaissance et des propriétés électroniques lors de l'addition de substituants permet d'utiliser les acides azodibenzoiques *cis* et *trans* comme des modèles pour la prediction de l'autoassemblage de ces nouvelles unités photoresponsives.

Enfin, de nouveaux nucleosides contenant la triaminopyrimidine sont synthétisés pour générer des structures supramoléculaires liées par ponts hydrogène partir d'analogues de base d'ADN. La caractérisation expérimentale montre que la liaison par ponts hydrogène du monomer de triaminopyrimidine avec des barbiturates conduit à des espèces oligomériques. L'utilisation de nucleosides d'acide cyanurique stériquement encombrés change l'auto-assemblage par ponts hydrogène de ces molecules, donnant des macrocycles hexamériques discrets qui s'associent pour former des nanostructures allongées.

Table of Contents

Preface

Dedication ..... *ii*
Acknowledgements ..... *iii*
Abstract ..... *v*
Résumé ..... *vii*
Table of Contents ..... *ix*
List of Figures ..... *xv*
List of Tables ..... *xxvi*
List of Abbreviations and Symbols ..... *xxvii*

Chapter 1: Introduction **1**
1.1. Supramolecular chemistry: Origins and Principles 2
1.1.1. Definition *2*
1.1.2. Principles *3*
1.1.2.1. Covalent vs. Non-Covalent Interactions 3
1.1.2.2. Non-Covalent Interactions 4
1.1.2.2.1. Electrostatic Interactions 5
1.1.2.2.2. Hydrogen Bonds 5
1.1.2.2.3. π-π Interactions and Van der Waals Forces 11
1.1.2.2.4. Charge-Transfer Interactions 14
1.1.2.2.5. Hydrophobic Interactions 14
1.2. Supramolecular chemistry: From Host-Guest Chemistry to Non-Covalent Synthesis 16
1.2.1. Synthesis of New Supermolecules *16*
1.2.1.1. Low-Dimensional Objects 16
1.2.1.1.1. Supramolecular Dimers 16
1.2.1.1.2. Multi-component Self-Assembly of One-Dimensional Structures 24
1.2.1.2. Two-Dimensional Objects 30
1.2.1.3. Three-Dimensional Objects 40
1.2.1.3.1. Self-Assembled Cages, Spheres, and Cylinders 41
1.2.1.3.2. Self-Assembled Platonic and Archimedean solids 44
1.2.2. Biological Supramolecular Chemistry *51*
1.2.2.1. Tobacco Mosaic Virus (TMV) 51
1.2.2.2. Self-Assembling Oligonucleotides 52
1.2.2.2.1. Double-Helical Deoxyribonucleic Acid (DNA) 52
1.2.2.2.2. Higher-Order Olibonucleotides Assemblies 54
a. Oligonucleotide Triple Helices 54
b. Oligonucleotide Quadruplexes and Pentaplexes 56
1.2.3. Synthesis of New Materials and Devices *58*
1.2.3.1. Supramolecular Chirality 58
1.2.3.2. Supramolecular Catalysis and Self-Replicating Systems 62

1.2.3.3. Supramolecular Photochemical and Electrochemical Devices66
1.2.3.3.1. Photo- and Electrochemical Metal-Coordinated Systems.... 67
1.2.3.3.2. Photochromic Systems 69
1.2.3.4. Supramolecular Transmembrane Channels and Charge Carriers..... 76
1.3. Scope of the Thesis 79
1.4. References and Notes: 81

Chapter 2: Theoretical Methods and Experimental Techniques 108
2.1. Theoretical Methods..... 109
2.1.1. Molecular Mechanics Methods 110
2.1.1.1. Molecular Mechanics Bonding Potentials 110
2.1.1.2. Molecular Mechanics Non-Bonding Potentials 112
2.1.2. Quantum Mechanical Methods 112
2.1.2.1. The molecular orbital approach 114
2.1.2.2. Hartree-Fock self-consistent field (HF-SCF) methods..... 117
2.1.2.3. Ab initio Calculation Methods 120
2.1.2.4. Semi-Empirical Calculation Methods 121
2.1.3. Theoretical Determination of Thermodynamic Properties..... 124
2.2. Experimental Methods..... 128
2.2.1. Electrospray Ionisation Mass Spectrometry (ESI-MS)..... 128
2.2.2. Fluorescence Spectroscopy 130
2.2.3. X-ray Diffraction (XRD)..... 132
2.2.4. Transmission Electron Microscopy (TEM) 133
2.2.5. Dynamic Light Scattering (DLS) 136
2.3. References and Notes..... 138

Chapter 3: Photoresponsive Supramolecular Systems: Self-Assembly of Azodibenzoic acid Linear Tapes and Cyclic Tetramers..... 141
3.1. Introduction..... 142
3.2. Results and Discussion 144
3.2.1. Theoretical Calculations 144
3.2.2. Synthesis and Self-Assembly of trans-Azodibenzoic Acid 1..... 147
3.2.3. Reversible Photoisomerization of trans-Azodibenzoic Acid 1 to the cis-Form 2..... 150
3.2.4. Self-Assembly of cis-Azodibenzoic Acid 2..... 152
3.2.5. Transmission Electron Microscopy and Dynamic Light Scattering Studies..... 155
3.3. Conclusion..... 159
3.4. Experimental Section..... 160
3.5. References and Notes:..... 169

Chapter 4: Photoresponsive Supramolecular Systems: Theoretical Study of Self-Assembled Azodibenzoic Acid Tapes and Rosettes 175
4.1. Introduction 176
4.2. Theoretical Procedures 180
4.3. Results and Discussion 181
4.3.1. Trans-1 and cis-2 p-Azodibenzoic Acid Monomers 181
4.3.2. Nomenclature of the hydrogen-bonded aggregates 182
4.3.3. PM3 Optimized Hydrogen-bond Geometries and Enthalpies 183
4.3.4. PM3 Enthalpies and Free Energies of the Optimized Hydrogen-bonded Structures 187
4.3.5. PM3 Vibrational Properties of the Optimized Hydrogen-bonded Structures 190
4.3.6. Electronic Population Analysis of the PM3 Optimized Hydrogen-bonded Structures 195
4.4. Conclusion 204
4.5. References and Notes 204

Chapter 5: Photoresponsive Supramolecular Systems: Packing in Self-Assembled Azodibenzoic Acid Cyclic Tetramers **211**
5.1. Introduction 212
5.2. Theoretical Methods 217
5.2.1. Initial Geometry of Monomers and Tetramers Through Quantum Mechanical Calculations 217
5.2.2. Scanning of Packing Structures Through Empirical Force Fields 217
5.2.3. Optimisation of Stacked Tetramers Through Quantum Mechanical Calculations 218
5.3. Results and Discussion 219
5.3.1. Quantum Mechanics Calculations of cis-Azodibenzoic Acid Cyclic Tetramers 219
5.3.2. Evaluation of Packing in cis-Azodibenzoic Acid Cyclic Tetramers 223
5.3.2.1. Face-to-Face Packing Arrangement of Hydrogen-Bonded Cyclic Tetramers 226
5.3.2.2. Herringbone Packing Arrangement of Hydrogen-Bonded Cyclic Tetramers 240
5.3.3. Quantum Mechanical Study of Packing in cis-Azodibenzoic Acid Cyclic Tetramers 248
5.3.3.1. Geometry Optimisation of Close-Packed Hydrogen-Bonded Cyclic Tetramers 248
5.3.3.2. Electronic Properties of Close-Packed Hydrogen-Bonded Cyclic Tetramers 253
5.4. Conclusion 263

5.5. References and Notes 264

Chapter 6: New Photoresponsive Supramolecular Systems Using Metal Coordination and Multiple Hydrogen-Bonding 267

6.1. Introduction 268
6.2. Results and discussion 272
6.2.1. Theoretical Evaluation of Monomer Geometries 272
6.2.2. Synthesis of trans-Azobisbenzonitrile 7 276
6.2.3. Reversible Photoisomerization of trans-Azobisbenzonitrile 7 to the cis-Form 8 277
6.2.4. Self-Assembly of trans- 7 and cis- Azobisbenzonitrile 8 280
6.2.5. Transmission Electron Microscopy of trans- 7 and cis-Azobisbenzonitrile 8 in presence of Ag(I) 286
6.2.6. Synthesis of trans-Azobisbenzodiaminotriazine 9 288
6.2.7. Self-Assembly of trans-9 and cis-Azobisbenzodiaminotriazine 10 289
6.2.7.1. Design of Theoretical Models for the Self-Assembly of *trans*-**9** and *cis*-Azobisbenzodiaminotriazine **10** 289
6.2.7.2. Theoretical Evaluation of the Self-Assembly of *trans*-**9** and *cis*-Azobisbenzodiaminotriazine **10** 297
6.2.8. Self-Assembly of trans-11 and cis-Azobisbenzoureidotriazine 12 310
6.3. Conclusion 313
6.4. Experimental and Theoretical Methods 315
6.3. Generalities 315
6.4. Synthesis and Experimental Characterisation 315
6.5. Theoretical calculations 318
6.5. References and Notes 319

Chapter 7: Hydrogen-Bond Self-Assembly of DNA-Base Analogues: Theory and Experiment 322

7.1. Introduction 323
7.2. Results and discussion 326
7.2.1. Theoretical Predictions 326
7.2.1.1. Theoretical Calculations of Hydrogen-bond Geometries 326
7.2.1.2. Theoretical Evaluation of Hydrogen-bond Geometry 329
7.2.1.3. Molecular Modelling of Hydrogen-bonded Aggregates 329
7.2.1.4. Electronic Population Analysis of the PM3 Optimized Hydrogen-bonded Structures 334
7.2.2. Synthesis of DNA-base Analogues 15 and 16 338
7.2.2.1. Synthesis of Triaminopyrimidine DNA-base Analogue **15** 338
7.2.2.2. Synthesis of Cyanuric Acid DNA-base Analogue **16** 341
7.2.3. Self-Assembly of Triaminopyrimidine 15 with Diethylbarbituric Acid 14 342

7.2.3.1. ^{1}H NMR Titration of DNA-base Analogue **15** by Diethylbarbituric Acid **14**..... 342
7.2.3.2. Electrospray Ionisation Mass Spectrometry of DNA-base Analogue **15** and Diethylbarbituric Acid **14** Mixture 345
7.2.4. Self-Assembly of Triaminopyrimidine 15 with DNA-base Analogue 16 346
7.2.4.1. ^{1}H NMR Titration of DNA-base Analogue **15** by Cyanuric Acid **16** 346
7.2.4.2. Electrospray Ionisation Mass Spectrometry of DNA-base Analogue **15** and Cyanuric Acid **16** Mixtures 350
7.2.5. Absorbance and Fluorescence Properties of DNA-base Analogue 15 351
7.2.6. Transmission Electron Microscopy and Dynamic Light Scattering Studies of Triaminopyrimidine 15/ Diethylbarbituric acid 14 and Triaminopyrimidine 15 / Cyanuric Acid 16 Mixtures 353
7.2.7. Theoretical Evaluation of the Packing Properties 357
7.3. Conclusion 360
7.4. Experimental section 361
7.4.1. Generalities 361
7.4.2. Synthesis 362
7.4.3. Characterisation of the Self-Assembly of Nucleoside 15 with Barbituric Acid 14 and Cyanuric Acid 16 370
7.4.4. Theoretical Calculations 371
7.5. References and Notes 372

Chapter 8: Conclusions, Contributions to Original Knowledge, and Suggestions for Future Work 380
8.1. Conclusions 381
8.1.1. Theoretical and Experimental Investigations of Self-Assembled Photoresponsive Materials 381
8.1.2. Theoretical and Experimental Investigations of Self-assembled Biomimetic Materials 384
8.2. Contributions to Original Knowledge 385
8.2.1. An Integrated Theoretical and Experimental Approach 385
8.2.2. Self-Assembly of Reversibly Photoswitched Supramolecular Structures 386
8.2.3. Self-Assembly of Artificial DNA-Bases into Hexameric Rosettes and Triple Helices 387
8.2.4. Quantum Mechanical Investigations of Thermodynamic Properties in Supramolecular Structures 388
8.2.5. Vibrational Analysis of Hydrogen-Bonded Supramolecular Aggregates 389
8.2.6. Density Matrix Analysis of Hydrogen-Bonded Supramolecular Structures 389

8.2.7. Directed Energy Scan of Close-Packed Supramolecular Macrocycles *390*
8.2.8. Molecular Orbital Analysis of Close-Packed Supramolecular Macrocycles *391*
8.3. Suggestions for Future Work 392
8.3.1. Characterisation of Metal-Coordinated and Multiply Hydrogen-Bonded Photoresponsive Structures *392*
8.3.2. Theoretical Investigations of Self-Assembly in Solvated Environments *393*
8.3.3. Theoretical Investigation of Macrocycle Networks *394*
8.3.4. Incorporation of Triaminopyrimidine Nucleosides into DNA *395*
8.3.5. Improvements of Triaminopyrimidine/Cyanuric Acid DNA-Rosettes 395

List of Figures

Figure 1. 1. Common one- and multi-centred hydrogen bond configurations. The simple hydrogen bond is usually bent in the crystal. 6
Figure 1. 2. Intramolecular bifurcated hydrogen bonds in tricarboxylate 1. 8
Figure 1. 3. Self-assembly of the polymolecular structure 2 from the 2,6-diaminopyridine P and the uracil U derivatives of tartaric acid using hydrogen bonds. R = $C_{12}H_{25}$ 9
Figure 1. 4. Weak D-H···π and C-H···π hydrogen bonding interactions. (a) and (c) T-shaped interaction. (b) Offset stacking. 11
Figure 1. 5. Purine-selective aromatic receptor forming complex 3 with propyladenine. 12
Figure 1. 6. 1,4-disubstituted benzene-cyclophane complexes 4a-f. 16
Figure 1. 7. Metal cation binding macrobicyclic cryptands 5a-5d 17
Figure 1. 8. Ammonium cation binding macrocyclic polyethers 6a-d 18
Figure 1. 9. Stable hydrogen-bonded complex 8 formed between a 2,6-pyridinediamide-based host and a barbiturate guest 19
Figure 1. 10. Dimer formation between urea and thiourea derivatives and glutamic dicarboxylate. 20
Figure 1. 11. Representation of a rotaxane and a catenane. 20
Figure 1. 12. Rotaxanes formed between bipyridinium derivative and *bis- p*-phenylene-34-crown-10. 21
Figure 1. 13. Formation of rotaxane 11 by threading then stoppering 22
Figure 1. 14. Self-assembly of catenane 12 from five components. 23
Figure 1. 15. Metal-mediated self-assembly of catenane 13 by coordination of copper(I) with two 2,9-substituted 1,10-phenanthroline ring derivatives. 24
Figure 1. 16. Schematic representation of one-dimensional supramolecular structures. 25
Figure 1. 17. Self-assembly of hydrogen-bonded tapes 14 and 15 from dicarboxylic acid derivatives and ribbon 16 from dipyridone. 26
Figure 1. 18. Self-assembly of tapes 17 through multiple hydrogen bonds between melamine M and barbituric acid BAR derivatives 27
Figure 1. 19. Self-assembly of hydrogen-bonded helix 18 from a bispyridine substituted isophthalic acid and heptanedioic acid 28
Figure 1. 20. Double-helicate 19 obtained by metal coordination of oligo-bipyridyl ligands. 29
Figure 1. 21. Double-helical $[M_3L_2]^{6+}$ complexes 20 and 21 incorporating segmented tris-terpyridyl ligands. 30
Figure 1. 22. Representation of some finite two-dimensional systems. 31
Figure 1. 23. Organic 22 and metal coordinated 23 molecular ladders. 32
Figure 1. 24. Self-assembled structure of 3x3 molecular grid 24 formed by coordination of silver(I) ions. 33
Figure 1. 25. Schematic representation of two-dimensional supramolecular polygons. 34
Figure 1. 26. Hydrogen bonded cyclic trimer 25 obtained from quinoline derivatives. 35
Figure 1. 27. Cyclic trimers 26 and 27 formed by metal coordination. 36
Figure 1. 28. Cyclic tetramer 28 formed by metal coordination. 37
Figure 1. 29. Cyclic tetramer formed by self-complementary hydrogen bonds between porphyrins derivatives. 38
Figure 1. 30. Hydrogen bonding self-assembly of cyclic hexamers 30 and 31. 39

Figure 1. 31. Hydrogen bonding self-assembly of pre-organized cyclic hexamers.....40
Figure 1. 32. Hydrogen bonding self-assembly of a porphyrin-containing molecular cage. 42
Figure 1. 33. Hydrogen bond self-assembly of 'tennis ball' dimer 34 43
Figure 1. 34. Multicomponent self-assembly of cylinder 35 through metal coordination.44
Figure 1. 35. Platonic and Archimedean solids. 45
Figure 1. 36. Metal-mediated self-assembly of molecular tetrahedral 36 and 37.....47
Figure 1. 37. Metal-mediated self-assembly of molecular cube 38. 48
Figure 1. 38. Metal-mediated self-assembly of supramolecular truncated tetrahedron 39.49
Figure 1. 39. Metal-mediated self-assembly of a molecular cuboctahedron 40. 49
Figure 1. 40. Metal-mediated self-assembly of truncated trigonal bipyramid 41.....50
Figure 1. 41. Metal-mediated self-assembly of a small molecular rhombihexahedron. R = phenyl.....51
Figure 1. 42. Self-assembly of the tobacco mosaic virus from 2130 protein monomers and one single RNA strand. 52
Figure 1. 43. Self-assembly of complementary DNA single strands into a double-helix..53
Figure 1. 44. Specific Watson-Crick base-pairing of adenine and thymine (A T), and guanine and cytosine (G C) in the DNA double-helix.....53
Figure 1. 45. Watson-Crick and Hoogsteen base-pairing in TAT, AAT, C^+GC, GGC triple helices. 55
Figure 1. 46. Self-assembly of self-complementary guanosine strands into G-quartets. ($M^+ = K^+$) 57
Figure 1. 47. Self-assembly of self-complementary isoguanosine strands into *i*G-quintets. ($M^+ = Cs^+$).....58
Figure 1. 48. Diastereoselective hydrogen-bonding self-assembly of enantio-pure calix[4]arene dimelamines and 5,5-diethylbarbituric acid. The assignment of the *M*/*P*-configuration is based on a clockwise (*P*) or anticlockwise (*M*) orientation of the two melamine units in the assembly. 60
Figure 1. 49. . Supramolecular helices formed from bifunctional ureidotriazine derivatives. 61
Figure 1. 50. Autocatalytic (a) and cross-catalytic (b) self-replicating systems.....63
Figure 1. 51. Artificial self-replicating system involving a self-complementary adenine receptor. 64
Figure 1. 52. Template-directed self-replication of guanine (G)- and cytosine (C)-containing hexadeoxynucleotides. 66
Figure 1. 53. Self-assembled redox active rotaxane 55 from two different transition metals. Inset: Redox potential plot of 55 by cyclovoltammetry. 68
Figure 1. 54. Self-assembly of 2+2 Ru(II)-Zn(II) metallacycles into molecular wire 56. 69
Figure 1. 55. Typical photochromic molecules. 70
Figure 1. 56. Photoregulation of cavity size using diarylethenes. 72
Figure 1. 57. Photoresponsive molecules incorporated in liquid-crystalline polymers. ...74
Figure 1. 58. Hydrogen-bond self-assembly of azobenzene cyclopeptides. 75
Figure 1. 59. Photoregulation of DNA using azobenzene. 76
Figure 1. 60. Hydrogen-bond self-assembly of peptide nanotube 62. 77
Figure 1. 61. Carpet-like cell membrane permeation mechanism. 77

Figure 1. 62. Self-assembled linear porphyrinic tapes.....78
Figure 1. 63. Representation of a functional device from self-assembling porphyrin tapes self-organised into bilayers. The electron donor, D, is $K_4Fe(CN)_6$ and the acceptor, A, is anthraquinonesulfate (AQS).....79
Figure 2. 1. Schematic radial distribution functions for a H 3*s* wavefunction, a Slater-type orbital, and a Gaussian-type orbital.....116
Figure 2. 2. Schematic representation of an electrospray ionisation source using a skimmer for ion focalisation and a N_2 heated flow for desolvation.....129
Figure 2. 3. Schematic representation of the various processes involved in the decay of excited systems.....131
Figure 2. 4 Crystallographic unit cell with side lengths *a*, *b*, and *c*, and angles α (between *b* and *c*), β (between *c* and *a*), and γ (between *a* and *b*).....133
Figure 2. 5. Schematic representation of a transmission electron microscope. Inset: Electron source.....135
Figure 3. 1. PM3 optimized geometry of a linear hexameric tape formed from *trans* azodibenzoic acid.....145
Figure 3. 2. PM3 optimized geometry of the square formed from *cis*-azodibenzoic acid.145
Figure 3. 3. (a) X-ray single crystal data showing the hydrogen-bonded tapes formed by *trans*-1.....148
Figure 3. 4. UV-visible absorption spectrum recorded during the UV irradiation (λ> 300 nm) of a $3.44x10^{-5}$ M solution of *trans*-1 in methanol.....150
Figure 3. 5. Kinetics of the thermal cis-trans reisomerization monitored by ^{1}H-NMR in $CDCl_3$. At 45°C, the concentration of *trans*-1 increased stepwise as shown by the dash-dot-dot line.....151
Figure 3. 6. (a) X-ray diffraction (XRD) pattern for *trans*-1. (b) XRD pattern for *cis*-2. The asterisks mark the presence of *trans*-1 impurities.....154
Figure 3. 7. TEM of a replica for *trans*-1.....156
Figure 3. 8. (a) TEM of directly deposited films of *cis*-2. (b), (c) and (d) TEM of replicas of *cis*-2. (e) and (f) Representations of possible packing modes (alkyl chains are omitted for clarity).....158
Figure 4. 1. Hydrogen-bonded *cis*-azodibenzoic acid pentameric tape $c-\mathbf{T}_5^3$ which contains 3 N=N kinks. (Each N=N kink is indicated by a dark circle.) The dashed line represents an additional, weak N···H hydrogen-bond (3.12 – 3.25 Å), between the *cis*-azobenzene nitrogen and the terminal carboxylic acid group.....183
Figure 4. 2. Enthalpies of formation for two hydrogen-bonds HB_1 and HB_2 (inset) in the *cis*-azodibenzoic acid aggregates as a function of the number of monomers. (a) 0 K. (b) 298 K, 1 atm.....186
Figure 4. 3. (a) Enthalpies at 298 K for the hydrogen-bond self-assembly of *cis*-azodibenzoic acid as a function of the number of monomers. (b) Gibbs free energies at 298 K for the hydrogen-bond self-assembly of *cis*-azodibenzoic acid as a function of the number of monomers. (The geometry of the tetrameric $c-\mathbf{T}_n^3$ and $c-\mathbf{T}_n^4$ tapes are similar.).....188
Figure 4. 4. Normal-mode frequencies for the *cis*-tape $c-\mathbf{T}_6^0$ and hexameric rosette $c-\mathbf{R}_6$. (a) Full spectrum. (b) 1000 – 2000 cm^{-1} region showing $\nu_{N=N}$ (1940 cm^{-1})

stretching, $\nu_{C=O}$ (1790 cm^{-1}) stretching, and $\delta_{C\text{-}O\text{-}H}$ (1100 cm^{-1}) in-plane bending frequencies. (c) 3000 – 3075 cm^{-1} region showing the aromatic $\nu_{sC\text{-}H}$ (3050 cm^{-1}) and $\nu_{asC\text{-}H}$ (3060 cm^{-1}) stretching frequencies. (d) 3760 – 3775 cm^{-1} region showing the bound and unbound $\nu_{O\text{-}H}$ stretching frequencies. 192

Figure 4. 5. Normal-mode frequencies for the tetrameric $c-\mathbf{R_4}$, pentameric $c-\mathbf{R_5}$ and hexameric *cis*-rosette $c-\mathbf{R_6}$. (a) Full spectrum. (b) 1500 – 2000 cm^{-1} region showing $\nu_{N=N}$ (1620 cm^{-1}) stretching, $\nu_{C=O}$ (1940 cm^{-1}) stretching, and $\delta_{C\text{-}O\text{-}H}$ (1795 cm^{-1}) in-plane bending frequencies. (c) 3000 – 3100 cm^{-1} region showing the aromatic $\nu_{sC\text{-}H}$ (3050 cm^{-1}) and $\nu_{asC\text{-}H}$ (3060 cm^{-1}) stretching frequencies. (d) 3760 – 3775 cm^{-1} region showing the bound $\nu_{O\text{-}H}$ (3766 cm^{-1}) and unbound $\nu_{O\text{-}H}$ (3769 cm^{-1}) stretching frequencies. 194

Figure 4. 6. Frontier molecular orbitals for the *cis*-**2** monomer and tetrameric structures. (a) Highest occupied (HOMO) and (b) lowest unoccupied (LUMO) molecular orbitals of *cis*-**2** monomer. (c) HOMO and (d) LUMO for macrocycle $c-\mathbf{R_4}$. (e) HOMO and (f) LUMO for tetrameric tape $c-\mathbf{T_4^0}$. 196

Figure 4. 7. Delocalized molecular orbitals of *cis*-2 macrocycles showing a π-type overlap across the hydrogen-bonds. (a) Tetramer $c-\mathbf{R_4}$. (b) Pentamer $c-\mathbf{R_5}$. (c) Hexamer $c-\mathbf{R_6}$. 197

Figure 4. 8. Density matrix contour of the *trans*-azodibenzoic acid tetrameric tape $t-\mathbf{T_4}$. Bound and unbound carboxylic acid densities are highlighted using □. (Only the first two monomers M1 and M2 are shown for clarity) 200

Figure 4. 9. Density matrix contour of the *cis*-azodibenzoic acid crinkled tetrameric tape $c-\mathbf{T_4^0}$. Bound and unbound carboxylic acid densities are highlighted using □. (Only the first two monomers M1 and M2 are shown for clarity) 202

Figure 4. 10. Density matrix contour of the cis-azodibenzoic acid square $c-\mathbf{R_4}$. Bound and unbound carboxylic acid densities are highlighted using □. (Only the first two monomers M1 and M2 are shown for clarity) 203

Figure 5. 1. Representation of α, the orientation of the aromatic rings relative to the z-axis, $d_{\pi\text{-}\pi}$, the interplanar distance along the z-axis, $o_{\pi\text{-}\pi}$, the horizontal offset, and β, the relative twist, between stacked tetrameric macrocycles. 217

Figure 5. 2. (a) Representations of the possible packing mode between stacked tetrameric macrocycles according to the first model. (b) Representations of possible packing mode between stacked tetrameric macrocycles according to the second model. ... 225

Figure 5. 3. (a) Representation of face-packed cyclic tetramers. (b) Representation of herringbone-packed cyclic tetramers. 226

Figure 5. 4. Total energy plots as a function of interplanar distance $d_{\pi\text{-}\pi}$ for the unsubstituted *cis*-azobenzene derivatives. (a) For $0° < \alpha < 40°$ (b) $40° < \alpha < 90°$. 229

Figure 5. 5. Total energy plots as a function of interplanar distance $d_{\pi\text{-}\pi}$ for the methoxy-disubstituted *cis*-azobenzene derivatives. (a) For $0° < \alpha < 40°$ (b) $40° < \alpha < 90°$. 230

Figure 5. 6. PM3 optimised cyclic tetramers stacked at $d_{\pi\text{-}\pi}$ = 3.5 Å, $\alpha = 0°$, $o_{\pi\text{-}\pi}$ = 0.0 Å, $\beta = 0°$ 231

Figure 5. 7. Cyclic tetramers stacked at $d_{\pi\text{-}\pi}$= 3.5 Å, α = 70°, $o_{\pi\text{-}\pi}$= 0.0 Å, β = 0°. 233
Figure 5. 8. Total energy plots as a function of horizontal offset $o_{\pi\text{-}\pi}$ for the unsubstituted *cis*-azobenzene derivatives. (a) For 0° < α < 40°. (b) 40° < α < 90° 234
Figure 5. 9. Total energy plots as a function of horizontal offset $o_{\pi\text{-}\pi}$ for the methoxy-disubstituted *cis*-azobenzene derivatives. (a) For 0° < α < 40°. (b) 40° < α < 90°. 235
Figure 5. 10. Total energy plots as a function of macrocycle twist β for the unsubstituted *cis*-azobenzene derivatives. (a) For 0° < α < 40°. (b) 40° < α < 90°. 237
Figure 5. 11. Total energy plots as a function of macrocycle twist β for the methoxy-disubstituted *cis*-azobenzene derivatives. (a) For 0° < α < 40°. (b) 40° < α < 90°. 238
Figure 5. 12. PM3 optimised cyclic tetramers stacked at $d_{\pi\text{-}\pi}$= 3.5 Å, α = 0°, $o_{\pi\text{-}\pi}$= 0.0 Å, β = 20°. (a) Top view. (b) Side view. 239
Figure 5. 13. Total energy plots as a function of interplanar distance $d_{\pi\text{-}\pi}$ for the unsubstituted *cis*-azobenzene derivatives. 242
Figure 5. 14. Total energy plots as a function of interplanar distance $d_{\pi\text{-}\pi}$ for the methoxy-disubstituted *cis*-azobenzene derivatives. (a) For 0° < α < 40°. (b) 40° < α < 90°. 243
Figure 5. 15. Total energy plots as a function of horizontal offset $o_{\pi\text{-}\pi}$ for the unsubstituted *cis*-azobenzene derivatives. (a) For 0° < α < 40°. (b) 40° < α < 90°. 246
Figure 5. 16. Total energy plots as a function of horizontal offset $o_{\pi\text{-}\pi}$ for the methoxy-disubstituted *cis*-azobenzene derivatives. (a) For 0° < α < 40°. (b) 40° < α < 90°. 247
Figure 5. 17. Comparison of the molecular orbital diagrams of *cis*-azodibenzoic acid macrocycles alone (1x1), in a 1x3- and 1x5- face-packed arrays. (a) Unsubstituted *cis*-2 systems. (b) Methoxy-substituted *cis*-2 systems. 262
Figure 6. 1. Newly designed *trans*- and *cis*-azobenzene monomers for hydrogen-bonding and metal coordination 270
Figure 6. 2. UV-Vis spectrum of the photoirradiation of *trans*-7 azobisbenzonitrile derivative in CH_2Cl_2 (λ > 300 nm). 277
Figure 6. 3. (a) PM3 energy scan of ω, corresponding to the dihedral angle C-NN-C, in the 2,2'-dimethoxy-azobisbenzonitrile (inset). (b) PM3 energy scan of ω, corresponding to the dihedral angle C-NN-C, in the 2,2'-dimethoxy-azodibenzoic acid (inset). 280
Figure 6. 4. ^{1}H NMR titration of equimolar mixture of *trans*-7/*cis*-8 azobisbenzonitrile using AgOTf. (a) Before titration. (b) After adding 0.5 eq of AgOTf. (c) After adding 1.0 eq. of AgOTf. (d) After adding 2.0 eq. of AgOTf. 284
Figure 6. 5. Representation of peripheral coordination of silver(I) ions to the ether oxygen atoms and the nitrogen atoms of *cis*-8. 285
Figure 6. 6. (a) UV-Vis titration of the equimolar *trans*-7/*cis*-8 mixture by AgOTf. (b) Absorbance of the equimolar *trans*-7/*cis*-8 mixture by AgOTf at λ = 500 nm. 286
Figure 6. 7. (a) Electron micrograph of the equimolar mixture of *trans*-7/*cis*-8/AgOTf . (b) Profile analysis of electron micrograph (a). 287
Figure 6. 8. (a) Representation of hydrogen-bonded linear tapes from *trans*-azobisbenzodiaminotriazine with diethylbarbituric acid. (b) Representation of

hydrogen-bonded cyclic dodecamers from *trans*-azobisbenzodiaminotriazine with diethylbarbituric acid. 298
Figure 6. 9. (a) Representation of hydrogen-bonded helical octamers from *cis*-azobisbenzodiaminotriazine with diethylbarbituric acid. (b) and (c) Representation of hydrogen-bonded boat-like octamers from *cis*-azobisbenzodiaminotriazine with diethylbarbituric acid. (b) Top view. (c) Side view. 300
Figure 6. 10. (a) Representation of hydrogen-bonded helical octamers from *cis*-azodibenzoic acid with isophthalic acid. (b) and (c) Representation of hydrogen-bonded cyclic octamers from *cis*-azodibenzoic acid with isophthalic acid. (b) Top view. (c) Side view. 301
Figure 6. 11. Electron density contour map of the hydrogen-bonded helical octamer formed by *cis*-azodibenzoic acid/isophthalic acid. 308
Figure 6. 12. Electron density contour map of the hydrogen-bonded cyclic octamer formed by *cis*-azodibenzoic acid/isophthalic acid. 309
Figure 6. 13. PM3 optimised geometry of *cis*-azobisbenzoureidotriazine 311
Figure 6. 14. Electron density contour map of the hydrogen-bonded cyclic tetramer formed by *cis*-azobisbenzoureidotriazine 313
Figure 7. 1. Diethylbarbituric acid 14, and triaminopyridine 15 and cyanuric acid nucleosides 16 325
Figure 7. 2. Overlay of triaminopyrimidine 15/ diethylbarbituric acid 14 (black) and triaminopyrimidine 15/ and cyanuric acid 16 linear tapes. (a) Top view. (b) Side view. 333
Figure 7. 3. Density matrix of the triaminopyrimidine 15/diethylbarbituric acid 14 linear tape. The substituents were omitted for clarity. 336
Figure 7. 4. Density matrix representation of the triaminopyrimidine 15/diethylbarbituric acid 14 rosette. The substituents were omitted for clarity. 336
Figure 7. 5. Density matrix of the triaminopyrimidine 15/cyanuric acid 16 linear tape. The substituents were omitted for clarity 337
Figure 7. 6. Density matrix of the triaminopyrimidine 15/cyanuric acid 16 rosette. The substituents were omitted for clarity. 338
Figure 7. 7. ^{1}H NMR titration of DNA-base analogue 15 using diethylbarbituric acid 14 in CD_2Cl_2. (a) Before titration. (b) After adding 0.5 eq of diethylbarbituric acid 14. (c) After adding 1.0 eq. of diethylbarbituric acid 14. 344
Figure 7. 8. Electrospray ionisation mass spectrum of equimolar triaminopyrimidine nucleoside 15 and diethylbarbituric acid 14 mixture. 345
Figure 7. 9. (a) ^{1}H NMR spectrum of DNA-base analogue 15 in MeOD. (b) ^{1}H NMR spectrum of DNA-base analogue 16 in $CDCl_3$. 348
Figure 7. 10. ^{1}H NMR titration of DNA-base analogue 15 using cyanuric acid 16 in CD_2Cl_2. (a) Before titration. (b) After adding 0. 5 eq. of cyanuric acid 16. (c)After adding 1.0 eq. of cyanuric acid 16. 349
Figure 7. 11. Electrospray ionisation mass spectrum of equimolar triaminopyrimidine 15 and cyanuric acid 16 mixture. 350
Figure 7. 12. UV-Vis absorbance spectra of triaminopyrimidine 15 alone and in equimolar mixtures of cyanuric acid 16 352

Figure 7. 13. Steady-state emission fluorescence spectra of triaminopyrimidine 15 alone and in equimolar mixtures of cyanuric acid 16 at λ_{exc} = 365 nm..... 353
Figure 7. 14. Electron micrographs prepared from deposited solutions of triaminopyrimidine 15/diethylbarbituric acid 14. 354
Figure 7. 15. (a) and (b) Electron micrographs prepared from deposited solutions of triaminopyrimidine 15/ cyanuric acid 16 using uranyl acetate as a staining agent. (c) and (d) Profile analysis of the TEM images. Insets: magnified profile analysis to single rod-like structures (see text). 356
Figure 7. 16. PM3 optimised geometry for the triaminopyrimidine/thymine dinucleotide triplex. (a) Top view. (b) Side view. 358
Figure 7. 17. Proposed model for the stacking geometry of the triaminopyrimidine 15/ cyanuric acid 16 hexameric rosette, generated from the MM^+ optimised macrocycles fitted on top of each other. Top view. 360

List of Tables

Table 3. 1. PM3 standard enthalpies and Gibbs free energy of the self-assembly as a function of the hydrogen-bonded aggregate formed with the *trans-* and the *cis-* azodibenzoic acids at 298 K. These energies were obtained by substracting the cumulated energies of the n monomers involved in the self-asssembly of the compound from the energy of the formed complex 146
Table 4. 1. PM3 optimized hydrogen-bonded linear, folded, or closed structures formed from *trans*-1 and *cis*-2 azodibenzoic acids 185
Table 5. 1 . PM3 optimised alkoxy-substituted *cis-p*-azodibenzoic acid monomer geometries.....220
Table 5. 2. PM3 optimised alkoxy-substituted *cis-p*-azodibenzoic acid macrocycle geometries.....222
Table 5. 3. Macrocycle PM3 total enthalpies and hydrogen-bond enthalpies 223
Table 5. 4. PM3 optimised geometries of stacked unsubstituted *cis-p*-azodibenzoic acid macrocycles.....251
Table 5. 5. PM3 optimised geometries of stacked methoxy-substituted *cis-p*-azodibenzoic acid macrocycles.....252
Table 5. 6. Interaction energies for the face-packed cyclic tetramers.....253
Table 5. 7. PM3 Molecular orbital diagrams of 1x3 stacked unsubstituted *cis*-azobenzene tetramers.....256
Table 5. 8. PM3 Molecular orbital diagrams of 1x5 stacked unsubstituted *cis*-azobenzene tetramers.....257
Table 5. 9. PM3 Molecular orbital diagrams of 1x3 stacked methoxy-substituted *cis*-azobenzene tetramers.....259
Table 5. 10. PM3 Molecular orbital diagrams of 1x5 stacked methoxy-substituted *cis*-azobenzene tetramers.....260
Table 6. 1. *Trans-* and *cis*-azobenzene model monomers optimised using semi-empirical PM3 calculations. 275
Table 6. 2. *Trans*-azobisbenzotriazine/diethylbarbituric acid model dimers optimised using semi-empirical PM3 calculations, along with their frontier and hydrogen-bonding molecular orbitals.....292
Table 6. 3. *Trans*-azodibenzoic acid/isophthalic acid model dimers optimised using semi-empirical PM3 calculations, along with their frontier and hydrogen-bonding molecular orbitals.....293
Table 6. 4. *Cis*-azobisbenzotriazine/diethylbarbituric acid model dimers optimised using semi-empirical PM3 calculations, along with their frontier molecular orbitals. 295
Table 6. 5. *Cis*-azodibenzoic acid/isophthalic acid model dimers optimised using semi-empirical PM3 calculations, along with their frontier and hydrogen-bonding molecular orbitals.....296

Table 6. 6. Frontier and hydrogen-bonding molecular orbitals calculated for the *cis*-azodibenzoic acid/isophthalic acid helix using semi-empirical PM3 calculations.....305
Table 6. 7. Frontier and hydrogen-bonding molecular orbitals calculated for the *cis*-azodibenzoic acid/isophthalic acid macrocycle using semi-empirical PM3 calculations. 306

Table 7. 1. Theoretical monomer structures determined using MM^+ and PM3 geometry optimisations.....328

Table 7. 2. Theoretical hydrogen-bonded 14 + 15 complexes determined using MM^+ geometry optimisations.....330
Table 7. 3. Theoretical hydrogen-bonded 15 + 16 complexes determined using MM^+ geometry optimisations.....331
Table 7. 4. MO diagram of hydrogen-bonded T + 15 complexes determined using PM3 geometry optimisations.....360

List of Abbreviations and Symbols

*	First polarization function	4
**	First and second polarization functions	4
3-21G	Split-valence basis set with linear combinations of (i) 3 inner shell GTO, and (ii) 2 / 1 double zeta valence GTO	4
α	Crystallographic unit cell angle	2 , 3
A	Acceptor	1,3-7
A	Arrhenius pre-exponential factor	1
a	Crystallographic unit cell length	4 – 6
β	Crystallographic unit cell angle	4 – 6
β_{ijk}	First molecular hyperpolarizability	1
b	Crystallographic unit cell length	4 – 6
C_6, C_{12}	Van der Waals coefficients	1
C_{ads}	Adsorbate concentration	1
C_n	Fourier expansion coefficient	2
$\mathbf{c_i}$	Coefficient column vector	2
c	Speed of light	2
c	Crystallographic unit cell length	4 – 6
c^i_μ	Atomic orbital coefficient	2
$\Delta_{ads}H$	Enthalpy of adsorption	1
∇^2	Laplacian operator	2
δ_{ij}	Kronecker delta	2
D	Donor	1
D	Diffusion coefficient	2
D_o	Diffusion pre-factor	2
d	NMR doublet	6
d	Atomic orbitals with $l = 2$	2

$d\tau$	Volume element for the electron	2
det	Determinant	2
di	Digonal, *sp* hybridization	3
ε_{bond}	Bond energy	1
ε_i	Orbital energy	2
E	Total electronic energy	2
E	Electric field	2
E_o	Incident electric field	2
E_1, E_2, E_3, E_4	Molecular orbital energy levels	1
E_{ads}	Adsorption activation energy	1
E_{bond}	Combined energies of MM bonding terms	5
E_C	Conduction band-edge	1
E^{calc}	Calculated energy	2
$E_{cross\text{-}term}$	MM Coupled stretch/angle valence energies	2
E_{des}	Desorption activation energy	1
E_{dif}	Diffusion activation energy	1
E_{elstat}	MM Electrostatic energy	2, 5
$E_{inversion}$	MM Inversion energy	2
E_j, E_k, E_l	Electric field vectors	1
$E_N(A,B)$	Core-core repulsion energy	2
$E_{nonbond}$	MM Non-bonding energies	2
E_{ox}	Oxidation energy	1
E_s	Parallel component of electric field	2
E_p	Perpendicular component of electric field	2
E_{total}	MM Total energy	2, 5
E^{true}	True energy	2
E_V	Valence band-edge	1
E_{Vac}	Vacuum energy	1
$E_{valence}$	MM energies for bound atoms	2

E_{vdW}	Van der Waals energy	2, 4, 5
e	Electron charge	2
ESI	Electrospray Ionization	6
Et	Ethyl, $-CH_2CH_3$	1, 3, 6
eV	Electron Volt	1, 3, 4
$\mathbf{F}$	Fock matrix	2
$\mathbf{F}(i)$	Fock one-electron operators	2
FTIR	Fourier-Transform Infrared	1 – 4, 6, 7
γ	Crystallographic unit cell angle	4 – 6
γ_{ijkl}	Second molecular hyperpolarizability	1
G	Gaseous LB phase	1
$g_v(i,j)$	Two-electron operators	2
GIXD	Grazing Incidence X-Ray Diffraction	1, 2
$\mathbf{H}$	Hamiltonian operator	2
$\mathbf{H}^{core}$	One-electron Hamiltonian, with fixed nuclei	2
$\mathbf{H}^{el}$	Electronic Hamiltonian	2
$\mathbf{H}^{total}$	Full many-particle Hamiltonian operator	2
$H_{\mu\mu}$	One-centre, one-electron integrals	2
$H_{\mu\nu}$	Two-centre, one-electron core resonance integrals	2
$\hbar$	Planck's constant / 2π	2
h	XRD Miller index	2, 6
$h_v(i)$	One-electron operators	2
hν	Energy of one photon	5
HOMO	Highest Occupied Molecular Orbital	4-7
IR	Infrared	2, 6
$\mathbf{J}_j$	Coulomb operator	2
$\mathbf{K}_j$	Exchange operator	2
K	Degrees Kelvin	1

K_ϑ	MM Angle bend constant	2
K_r	MM Bond stretch constant	2
k	Boltzmann constant	1
k	XRD Miller index	2
k_{ads}	Rate of adsorption	1
k_{des}	Rate of desorption	1
kcal	kilocalorie	3 – 5
λ	Wavelength	2
$\boldsymbol{l}$	Azimuthal aquantum number	2
l	XRD Miller index	2, 6
LC	Liquid crystal	1
LB	Langmuir-Blodgett	1
LC	Liquid condensed LB phase	1
LCAO	Linear Combination of Atomic Orbitals	2
LE	Liquid expanded LB phase	1
LMO	Localized Molecular Orbital	3
LOMO	Lowest Occupied Molecular Orbital	4-7
LUMO	Lowest Unoccupied Molecular Orbital	4-7
$\boldsymbol{m}$	Magnetic quantum number	2
m	NMR multiplet	6
m_α	Nuclear mass	2
m_i , m_j	Electron mass	2
Me	Methyl, -CH_3	6
MM	Molecular Mechanics	2, 3, 7
MM^+	Hyperchem Molecular Mechanics force field	2 – 5
MO	Molecular Orbital	1 – 4, 7
MS	Mass Spectrometry	6
ν	Frequency, IR mode	2, 6
ν_{as}	Asymmetric IR stretch	3, 6

ν_a	Symmetric IR stretch	3, 6
$\boldsymbol{n}$	Principal quantum number	2
$\boldsymbol{n}^*$	Effective principal quantum number	2
N	Complex film refractive index	2
n_1, n_2, n_3	Ambient, thin film, and solid n_f	2
n_f	Refractive index	2, 6
NLO	Non-Linear Optical	1
NMR	Nuclear Magnetic Resonance	3,6,7
NDDO	Neglect of Diatomic Differential Overlap	2
ϕ	Work function	1
ϕ_m	Work function of a metal	1
ϕ_s	Work function of a semiconductor	1
ϕ_μ	Atomic wavefunctions	2
Ψ	Total electronic wavefunction	2
Ψ^*	Complex conjugate of the wavefunction	2
ψ	x-Axis angle of tilt	4, 5
ψ_i	One-electron wavefunction	2
π	MO with two lobes of opposite sign, separated by a node	1, 3, 4
$\mathbf{P}$	Density matrix	2
P	Electron population	1
p	Atomic orbital with one angular node	2, 4
p-	Perpendicular component of polarization	2
PM3	Parametric Method 3	2 – 4, 7
p-type (p-band)	Positive charge carrier semiconductivity	1
Q_Λ	Coulombic point charge	2
q_{ads}	Thermodynamic heat of adsorption	1
q_c	Heat of compression	1
q_{st}	Isosteric heat of adsorption	1

ρ	Complex amplitude reflection ratio	2
$\mathbf{r}_{AB}$	Distance vector	2
R	Gas constant	1
R_{AB}	Core-core separation	2
$R_{nl}(r)$	Radial component of atomic orbital basis set	2
r	Intermolecular separation	1
$r_{\alpha\beta}$	Nuclear-nuclear separation	2
$r_{\alpha i}$	Nuclear-electron separation	2
r_{ij}	Electron-electron separation	2
r_{on}	Initial distance for smoothing out E_{nonbond}	2
r_{off}	Final distance for smoothing out E_{nonbond}	2
r_p , r_s	Complex amplitude reflection coefficients	2
RMS	Root Mean Square	4
σ	MO with cylindrical symmetry	1
S	Overlap matrix	2
$S_{\mu\nu}$	Overlap integral of atomic orbitals	2
S_{ij}	Overlap integral	2
$S(r)$	Cubic spline switching function,	2
s	NMR singlet	6
s	Screening constant for orbital exponents	2
s	Spherically symmetric atomic orbital	2, 4
s-	Parallel component of polarization	2
SA	Self-Assembly	6
STO-3G	Minimal basis set with STO approximated by linear combinations of 3 GTO	2, 4
θ	XRD angle of reflection	6
θ	Angle of beam incidence	2
θ_1, θ_2	z-Axis angles of rotation	4, 5
θ_s	Surface coverage	1

$\mathbf{T}$	Kinetic energy operator	2
T	Temperature	1
t	NMR triplet	6
THF	Tetrahydrofuran	6
tr	Trigonal, sp^2 hybridization	3
$U_{\mu\mu}$	One-electron energy	2
UHV	Ultra High Vacuum	1
UV	Ultra Violet	5
V	Volts	1
$\mathbf{V}$	Potential energy operator	2
$\mathbf{V}(p)$	One-electron potential functional	2
V_{AB}	Semi-empirical core-electron integral	2
V_n	MM n-fold torsional potential	2
V_{vdW}	Van der Waals potential	1
XRD	X-Ray Diffraction	2, 3
$Y_{lm}(\theta, \varphi)$	Angular component of atomic orbital basis set	2
ζ	Orbital exponent for $R_{nl}(r)$ function	2
Ze	Nuclear charge	2

List of Publications Originated from Research at McGill University

The Faculty of Graduate Studies and Research allows, as an alternative to the traditional thesis format, a manuscript-based thesis where the text of one or more published papers, or papers to be submitted, are included as part of the thesis. The thesis must be more than a collection of manuscripts, and connecting texts must provide continuity between the manuscripts to provide continuity to the thesis.

Chapter 3 is a published manuscript used in the preparation of this thesis. Chapters 4 and 7 have been submitted for publication. Chapter 5 is a manuscript in preparation. Extensive connections between the manuscripts have been incorporated into the thesis. The citations are as follows:

Chapter 3: F. Rakotondradany, M. A. Whitehead, A.-M. Lebuis, H. F. Sleiman. "Photoresponsive Supramolecular Systems: Self-Assembly of Azodibenzoic acid Linear Tapes and Cyclic Tetramers," *Chem. Eur. J.*, **2003,** *9*, 4771.

Chapter 4: F. Rakotondradany, M. A. Whitehead, H. F. Sleiman. "Photoresponsive Supramolecular Systems: Theoretical Study of Self-Assembled Azodibenzoic Acid Tapes and Rosettes, " *J. Am. Chem. Soc.*, **2003**, submitted.

Chapter 5: F. Rakotondradany, M. A. Whitehead, H. F. Sleiman. "Theoretical Evaluation of Packing in Self-Assembled Azodibenzoic Acid Tapes and Rosettes." In preparation.

Chapter 7: F. Rakotondradany, M. A. Whitehead, H. F. Sleiman "Hydrogen-Bond Self-Assembly of DNA-Base Analogues into Hexameric Rosettes", *Angew. Chem. Intl. Ed. Engl.*, **2004**, submitted.

The single crystal X-ray data in Chapter 3 was provided by Dr. A. –M. Lebuis, but the author performed the majority of the theoretical and experimental work in all the manuscripts.

The manuscripts Chapters 3 to 5, and 7 are all co-authored by the research directors, Dr. Hanadi F. Sleiman and Dr. M. A. Whitehead who provided advice and guidance, all work in the thesis was performed by the author

Chapter 1.

Introduction

1.1. Supramolecular chemistry: Origins and Principles

1.1.1. Definition

This thesis describes the introduction of new functional groups into supramolecular systems, initiated by theoretical predictions and illustrated by experimental characterisation.

Supramolecular chemistry has successfully relied on molecular self-assembly principles to create one-, two- and three-dimensional functional materials,[1] using non-covalent interactions like hydrogen-bonds and electrostatic interactions, but also van der Waals, hydrophobic and hydrophilic forces. These non-covalent interactions, in conjunction with covalent forces, have been instrumental in determining structure and function in biological systems.[2] For example, protein function arises from the hydrogen-bonding of amino acids into α-helices and β-sheets combined with van der Waals, hydrophilic and hydrophobic interactions to generate a globular, tertiary structure. In chemical systems, non-covalent interactions are responsible for the spontaneous assembly of lipids bilayers,[3] liquid crystals,[4] and self-assembled monolayers.[5]

To gain understanding of molecular recognition and function, supramolecular chemists first focused on the creation and study of abiotic, artificial analogues of molecular receptors using non-covalent intermolecular forces.[6] Subsequently, a better knowledge about these non-covalent interactions not only contributed to the fabrication of more selective and efficient, artificial receptors,[6, 7] but also led to the creative design and synthesis of increasingly sophisticated, structurally well-defined, supramolecular

architectures. These supramolecular systems built from covalently synthesised low-molecular weight units, which are programmed to self-organise spontaneously, have found a wide range of potential applications in materials chemistry, electronics, biology, sensing systems, and nanotechnology.[1] The increasing degree of sophistication and programmability of these supramolecular systems has allowed dynamic combinatorial libraries of non-covalently bound structures to be built, where self-organised architectures capable of self-selection and self-replication coexist. In the field of nanoscience, such considerable progress allows one to envision the design of complex, self-sufficient systems which can perform multiple tasks, both in sequence and in parallel.[1g,l]

1.1.2. Principles

1.1.2.1. Covalent vs. Non-Covalent Interactions

Unlike covalent synthesis, which requires harsh experimental conditions, supramolecular synthesis consists of the spontaneous, mild assembly of various molecular components into well-defined, nanometer-scale structures.[1] Classical synthetic chemistry makes use of covalent interactions to build new molecules. In such compounds, the formed bonds are characterised by high enthalpy of formation (25-200 kcal/mol) and are therefore kinetically stable. Supramolecular chemistry differs from this traditional approach by relying on non-covalent interactions such as electrostatic interactions, hydrogen-bonding and van der Waals forces to create new molecular entities. Non-covalent intermolecular interactions are significantly weaker (0.1-5 kcal/mol) than covalent forces, and consequently kinetically more labile, which enables a dynamic error-checking mechanism to occur during assembly. As a result of these weak enthalpic

contributions, entropic contributions start playing an essential role in controlling the self-assembly process which quantitatively leads to the thermodynamically most stable aggregate through an economical, multi-component synthesis.

A few general rules emerged from early thermodynamic studies on host-guest complexes.[1a, 1c, 7] The conditions of the self-assembly should be carefully considered because solvents and salts, as well as temperature, can inhibit or favour molecular recognition. Supramolecular stability can be enhanced by using simultaneous, multiple binding interactions to effect strong, specific molecular recognition events from these weak, non-covalent forces. According to the 'lock and key' principle, these multi-site interactions can only be efficiently achieved when electronic and geometric complementarity is adequate between host and guest molecules. Consequently, a careful design of the geometries of host and guest molecules, along with their electron properties, are required to optimise molecular recognition and to generate a stable, well-defined, final supramolecular product.

1.1.2.2. Non-Covalent Interactions[8]

The properties and structural interplays of non-covalent intermolecular interactions are necessary to design and investigate supramolecular systems.[1h-j] Intermolecular forces can be organised into two main groups: medium-range anisotropic forces, such as electrostatic interactions, hydrogen-bonding, direct close-contact between various complementary species; long-range isotropic forces, such as attractive or repulsive interactions like hydrophilic/ hydrophobic, van der Waals and π-π forces.

1.1.2.2.1. *Electrostatic Interactions*

Electrostatic interactions, which can be repulsive or attractive, arise from static molecular charges,[8] and play an important role in natural and artificial molecular recognition.[9] These forces include ion-ion and ion-dipole interactions which are involved in metal coordinating systems.[1h] The relative strength and directionality of these non-covalent interactions is usually described by spherical point charges, which form close or loose contact ion pairs depending on interatomic distance. Based on the Debye-Hückel theory,[10] these additive intermolecular forces have been demonstrated to be proportional to $\frac{1}{r}$ at small interatomic distances r, and $\frac{1}{r^2}$ at large interatomic distances. These electrostatic interactions depend on the polarity of the medium, as increased binding constants can be measured for ionic pairs in solvents with decreased dielectric constant ε.[10a] This solvent-dependence is described by the binding constant K in:

$$K = \kappa (z_A z_B / \varepsilon)^3 Q(b) \quad \text{with} \qquad \textbf{(Eq. 1. 1)}$$

where $b = z_A z_B / \varepsilon a$, z_A and z_B are the charges on atoms A and B, a is the minimum interatomic distance, and κ is a constant.

1.1.2.2.2. *Hydrogen Bonds*

Hydrogen bonds are cohesive electrostatic interactions, which occur between a partially negative proton donor D and a partially or fully negative proton acceptor A, through a bridging hydrogen atom H.[11] Because of their directionality and strength, simple D-H···A interactions are the most reliable, hence the most encountered interactions in crystal engineering and molecular recognition.[1, 12] (Figure 1. 1) Conventional strong

hydrogen bonds (20-60 kJ/mol), involving highly electronegative heteroatom O, N, and F as proton donor D or/and proton acceptor A, have been extensively studied. Upon hydrogen-bond formation, the electron density on H is decreased and a Coulombic interaction is established between H and the electronegative acceptor A. Unconventional weaker hydrogen bonds (2-20 kJ/mol), involving C as proton donor and π-bonds as proton acceptor, have also been investigated more recently.

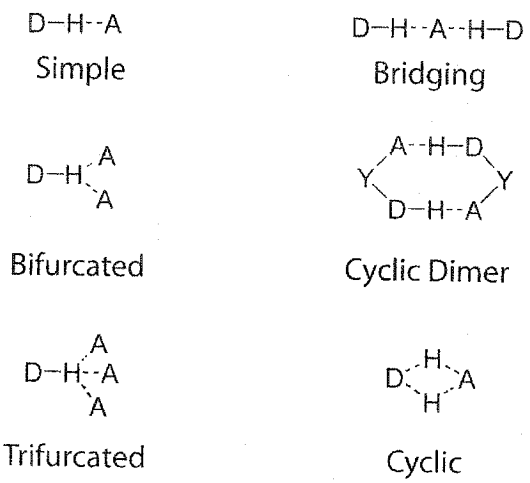
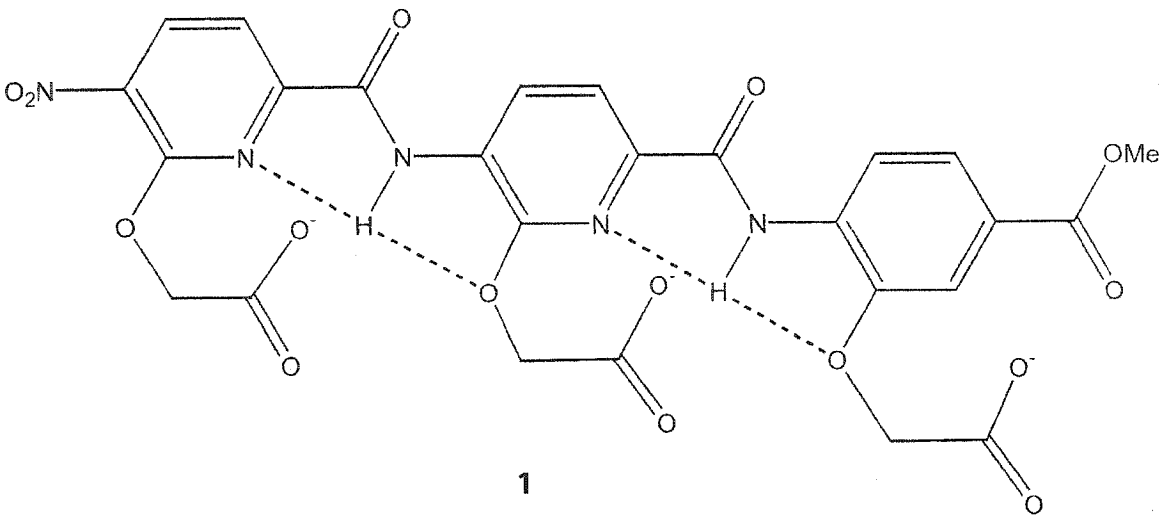


Figure 1. 1. Common one- and multi-centred hydrogen bond configurations. The simple hydrogen bond is usually bent in the crystal.

Hydrogen-bonding is usually described in geometrical features, specifically the bond lengths D···A and H···A, the D-H···A bond angle, θ, and the H···A-Y bond angle, ϕ, which determine the planarity of the D-H···A-Y torsion angle with respect to vicinal atoms Y. For hydrogen bonds using N and O as donors and/or acceptors, the D···A and H···A bond lengths range from 2.50-3.00 Å and 1.40-2.20 Å respectively, while the D-H···A interaction is usually quasi linear (θ ~ 160-180°) and the bond angle ϕ ranges within 120-130°.

Hydrogen bonds can adopt several configurations, as shown in Figure 1. 1. Besides the simple hydrogen bond, the cyclic hydrogen bond, or the cyclic dimer, where the electron density of H is shared between a single proton acceptor A and a single proton donor, multi-centered hydrogen bond arrangements have also been observed. If the hydrogen atom H is approached by a second acceptor A, a bifurcated-donor hydrogen bond is formed, and if the hydrogen atom H is approached by three acceptors, a trifurcated-donor hydrogen bond. Bifurcated-donor interactions are mostly found in acceptor-rich organic structures, bifurcated-acceptor interactions in donor-rich systems.[13] For example, three-centre interactions have been characterised for hydrogen-bonded systems which involve electron-rich metals,[13a] or in oligomers like **1**.[13b] The crystal structure of the tricarboxylic acid derivative, **1**, showed the formation of two intramolecular bifurcated hydrogen bonds between the amide NHs and their neighboring pyridine N and alkoxy O groups (N···N and N···O, 2.6-2.7 Å) (Figure 1. 2). These hydrogen-bonds stabilised the planar conformation of the oligomer. This planar conformation orients the three carboxylate groups in the same direction at regular intervals of ~5 Å, to favour the ionic interactions between the carboxylate groups and Ca^{2+} ions on calcite surfaces.



1

Figure 1. 2. Intramolecular bifurcated hydrogen bonds in tricarboxylate **1**.

Because of their directionality, conventional hydrogen-bonds have been widely used for synthesis of supramolecular dimers, trimers, chains, and infinite as well as discrete one-, two-, and three-dimensional structures.[1, 12] Supramolecular polymer **2** (Figure 1. 3) results from the association of complementary L-, D- or M(*meso*)- tartaric acid derivatives bearing either two 2,6-diaminopyridine groups **P** or two uracil groups **U** at their extremities. In this supramolecular structure, each ditopic component DAD or ADA can form three hydrogen bonds with its partner to give infinite helical polymeric chain.[14] This helical association is responsible for the formation of filaments and fibers from these liquid crystalline compounds.

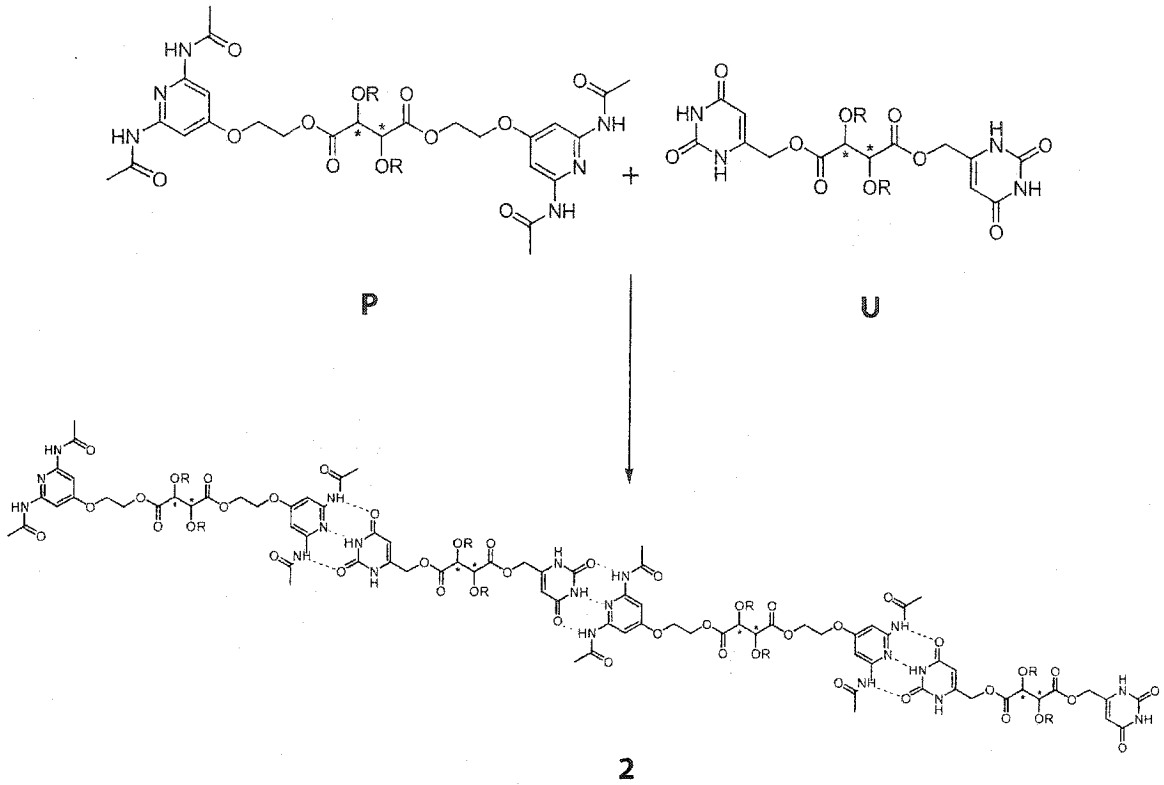


Figure 1. 3. Self-assembly of the polymolecular structure **2** from the 2,6-diaminopyridine **P** and the uracil **U** derivatives of tartaric acid using hydrogen bonds. R = $C_{12}H_{25}$.

Although conventional, strong hydrogen-bonds dominate in the supramolecular synthesis of organic systems, weak hydrogen-bonds have been observed in self-assembled systems in the solid state.[12,15] Owing to the presence of other packing forces, these weak hydrogen-bonds can adopt bent, straightened, compressed or expanded configurations in the crystal, consistent with their low directionality. The most common weak hydrogen bond C-H···A (A = F, O, N, Cl, Br) plays a substantial role in determining crystal packing. In particular, the C-H···O bond is a largely electrostatic hydrogen-bond, which is promoted by the acidity of the hydrogen atom H but quickly weakens at large interatomic distances. As a result, C···O and H···O bond lengths range within 3.00-4.00 Å

and 2.20-3.00 Å respectively, exceeding the van der Waals radii, with shorter C···O bonds in systems containing acidic hydrogen atom. The D-H···A and H···A-Y bond angles, θ and ϕ, are independent of the bond lengths in weak hydrogen bonds, suggesting that the hydrogen atom H orients itself before nucleation and crystallisation. However, linear geometries have been observed in hydrogen-bonds involving weakly charged acceptors, suggesting reduced electrostatic repulsions between donor and acceptor atoms in these weakly charged systems.

D-H···π and C-H···π interactions, shown in Figure 1. 4, are rare and weaker than C-H···A hydrogen-bonds (A = F, O, N, Cl, Br) because the carbon atom is not only less electronegative but also less accessible than the heteroatoms.[16] Although weaker than C-H···A hydrogen-bonds, these weak hydrogen bonds play an important stabilising role in crystals which involve alkynes, alkenes, and aromatic compounds, and can also be classified as π-π interactions (see Section 1.1.2.2.3 below). Their stabilising effect is usually more pronounced in systems containing electron-rich donors, suggesting the presence of attractive electrostatic interactions between the hydrogen atom and the π-electron cloud in favour of hydrogen-bond formation in such systems. For example, in 2,4,6-tris(4-methylphenoxy)-1,3,5-triazine, the methyl group can form C-H···π interactions (D = 3.60 Å; d = 2.77 Å; θ =133°) to induce a noncentrosymmetric packing of the molecule, which leads to NLO properties in the crystal.[17]

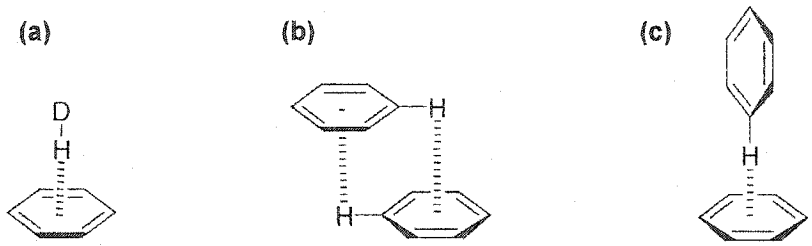


Figure 1. 4. Weak D-H···π and C-H···π hydrogen bonding interactions. (a) and (c) T-shaped interaction. (b) Offset stacking.

1.1.2.2.3. π-π Interactions and Van der Waals Forces

While hydrogen-bonds and others electrostatic forces are responsible for directional, specific binding, π-π interactions are weaker, dispersive forces which act at distances exceeding the electron cloud. π-π interactions have been extensively used in the design of supramolecular systems containing aromatic building blocks.[1, 12, 14, 16, 18] For example, polyaromatic bisanthracene derivative and propyladenine use strong intermolecular hydrogen-bonding interactions to generate host-guest complex **3** (Figure 1. 5).[19] In this complex, relatively strong π-stacking interactions hold the purine in the molecular tweezer formed by the two anthracene extremities of the host, strengthening the effect of the hydrogen-bond.

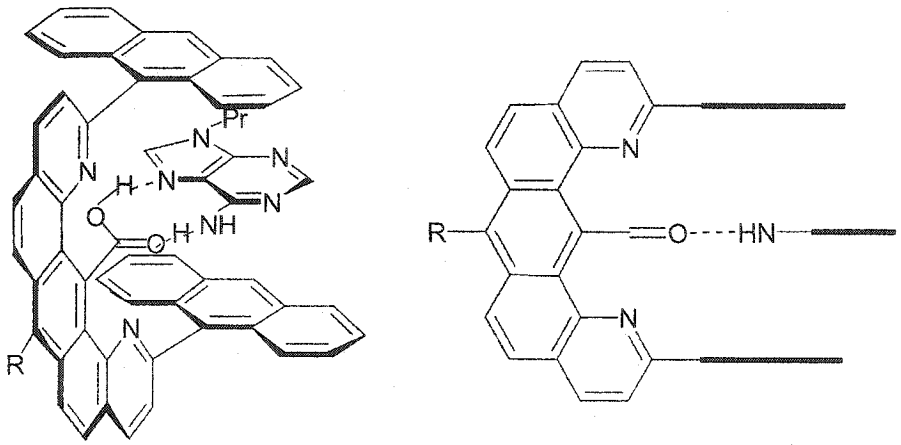


Figure 1. 5. Purine-selective aromatic receptor forming complex **3** with propyladenine

In these supramolecular systems, π-stacking forces give rise to three types of geometrical arrangements planar aromatic molecules, depending on the carbon-hydrogen ratio in the aromatic species. In general, carbon-rich aromatic molecules give stacking and offset-stacking, graphite-like structures (Figure 1. 4b) whereas hydrogen-rich aromatic molecules inclined or T-shape, herringbone geometries (Figure 1. 4c). Stacking consists of a face-to-face overlap between the two rings, to maximise both C···C intermolecular contacts and Van der Waals energy. Offset π-stacking is a shifted overlap between the aromatic rings (Figure 1. 4b), to compensate for strong electrostatic repulsions between the negatively charged π-electron clouds hindering a face-to-face overlap. Herringbone packing consist of a T-shape, or edge-to-face, interaction which favours attractive, electrostatic C-H···π interactions between the perpendicular aromatic rings (Figure 1. 4b, see Section 1. 1. 2. 2. 2).

Solvophobic,[20] electron donor-acceptor,[17b-d,21] and atomic charge models[22] have been proposed to describe π-π interactions. The solvophobic model[19] considers entropic contribution to π-stacking forces, but overlooks the cases of self-assembling aromatic

species in organic solvents and ignores offset π-stacked geometries (Figure 1. 4b). The electron donor-acceptor model[20] addresses π-π^* and charge-transfer interactions (see Section 1. 1. 2. 2. 4) which are limited to attractive forces relative to the excited state. The atomic charge model takes into account variations in the charge distribution of π-systems, but does not differentiate the relative orientations of aromatic species. A simple model, which combines both electrostatic and van der Waals contributions (see below)[16] has more been successful to describe π-π interactions. In this model, the σ-bond framework and the π-electron cloud are considered separately so that an overall attractive π-π interaction results from favourable σ-π electrostatic interactions between aromatic species in addition to van der Waals contributions.

Although weakest of all non-covalent forces, van der Waals forces use their ability to combine their individual contributions to effectively favour the formation of supramolecular systems. Van der Waals interactions are long-range, inductive and dispersive forces which account for diffuse, delocalised intermolecular binding.[8,23] In particular, inductive van der Waals interactions are responsible for isotropic, attractive forces which arise mainly from interactions between permanent dipoles, induced dipoles and from mixed permanent dipole-induced dipole interactions. Similar to inductive interactions, London forces are dispersive van der Waals interactions which arise from fluctuations in the total electron density of the system. The potential energies of these weak forces, V_{vdW}, depend on attractive forces at $\frac{1}{r^6}$ and hard-sphere repulsions at $\frac{1}{r^{12}}$ as shown in Equation 1. 2.

$$V_{vdW} = \frac{C_{12}}{r^{12}} - \frac{C_6}{r^6} \qquad \textbf{(Eq. 1. 2)}$$

where C_{12} and C_6 are molecule-specific coefficients. Because of their $\frac{1}{r^6}$ dependence, these intermolecular forces require the interacting species to be positioned at a close proximity. As a result, van der Waals forces are prevalent in hydrocarbon C···C, C···H, and H···H interactions, and participate in the close-packing of aliphatic side chains.

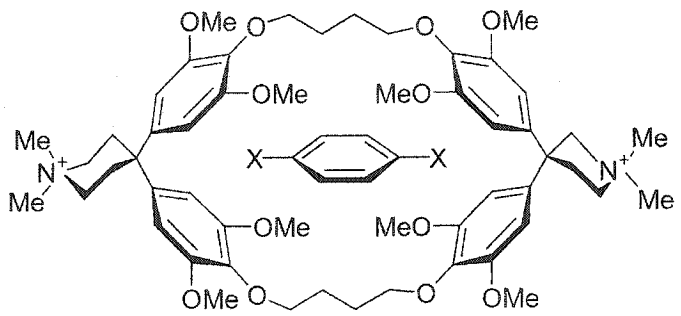
1.1.2.2.4. Charge-Transfer Interactions

Charge transfer (CT) or electron donor-acceptor (EDA) interactions are very weak intermolecular forces which arise from mixed ground AD and excited charge-separated A^+D^- states.[20,24] Charge-transfer complexes are formed favourably by close-contact attractive forces which involve a good electron donor D and a good electron acceptor A. In such complexes, an electron is transferred from the highest occupied molecular orbital of the electron-rich species D and the lowest unoccupied molecular orbital of the electron-poor species A, to give rise to distinct bands observable in the UV-Vis region. For example, fullerenes are electron-deficient molecules that can form stable charge-transfer complexes with electron donors like calixarenes, giving rise to a CT band around 440 nm.[25] The favourable formation of these complexes has strong potential to develop extraction methods for fullerenes.[24c]

1.1.2.2.5. Hydrophobic Interactions

Hydrophobic or solvophobic interactions arise from repulsive forces between water or polar solvents and non-polar molecules, causing these molecules to associate in aqueous or protic environments.[19, 22, 26] Solvent-solute interactions, which consist of solvent-host and solvent-guest interactions, strongly affect complex formation. As a result, these solvent-solute interactions must be outweighed by host-guest and solvent-solvent interactions to induce a partial or full desolvation of both host and guest, and to generate the desired complex. In the case of hydrophobic interactions,[22, 27] van der Waals forces between non-polar molecules and water are counterbalanced by strong hydrogen-bonding interactions between water molecules as well as attractive van der Waals forces between the polar molecules, to favour complexation.

Solvophobic interactions are ill-defined because the nature of the solvent dictates the type of non-covalent interaction. However, hydrophobic interactions play a major role in supramolecular chemistry, controlling many processes such as the aggregation of surfactants into micelles and bilayers,[1,3,4] the folding of protein as well as protein-protein and protein-ligand association.[2] The contribution of hydrophobic interactions has been quantified for the complexation of a series of 1,4-disubstituted benzene derivatives in cyclophane cavities (Figure 1. 6).[28] In these systems, host-guest complexes are more stable in water when hydrophobic methyl- or methoxy- substituents X were used.



4a X = CO_2Me
4b X = MeO
4c X = Me
4d X = CN
4e X = NO_2
4f X = OH

Figure 1. 6. 1,4-disubstituted benzene-cyclophane complexes **4a-f**.

1.2. Supramolecular chemistry: From Host-Guest Chemistry to Non-Covalent Synthesis

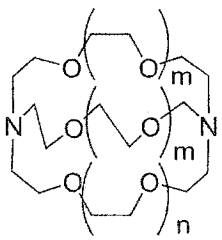
1.2.1. Synthesis of New Supermolecules

1.2.1.1. Low-Dimensional Objects

1.2.1.1.1. Supramolecular Dimers

Supramolecular dimers are the simplest self-assembled systems and result from the stoichiometric mixture of a single host with a single guest. [1a, 6, 7, 29-42] These dimers were the principal motif that supramolecular chemists initially used in the design of artificial

receptors, [1a, 6, 7] to efficiently and selectively mimic enzyme-substrate or antigen-antibody interaction, and other biochemical functions in solution.[1a] In the late 1960s, macrocyclic molecules such as crown ethers, cryptands (Figure 1. 7), and spherands, which could selectively bind ions or small organic molecules within their cavity using non-covalent interactions, were synthesized.[1a, 6, 7] Initial studies of the selective molecular recognition of alkali cations as cryptates have paved the way to a plethora of two-dimensional, macrocyclic holes and three-dimensional, macrobicyclic spheroids as hosts for alkaline-earth and lanthanide cations as well as negative halide cations. Among these hosts, macrobicyclic hosts **5a-5d** (Figure 1. 7) showed significant size-specific selectivity towards alkali cations. When the size of the spherical cavity was increased, the binding affinity was most favourable with the larger K^+ cation than with Li^+ or Na^+.

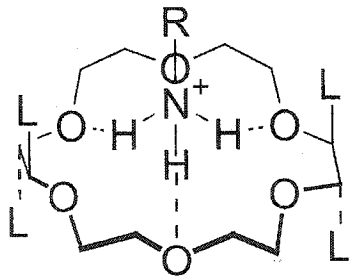


5a m = n = 0
5b m = 0, n = 1
5c m = 1, n = 0
5d m = n = 1

Figure 1. 7. Metal cation binding macrobicyclic cryptands **5a-5d**.

Molecular receptors have also been developed to recognize substituted ammonium ions using polar $^+$N-H···X hydrogen bond interactions. Several macrocyclic polyethers have been shown to bind ammonium cations with both structural and chiral selectivity. In macrocyclic receptor **6** (Figure 1. 8), the side groups L can be altered to tailor the stability and the selectivity of the complex.[30] In the optically active tartaric acid derivative **5b** for

which the crown ether ring serves as the main binding site, strong additional electrostatic interactions assist the formation of the polyether-ammonium complex. This macrocycle has also shown a preference towards primary over secondary and tertiary ammonium cations. More importantly, it has exhibited higher selectivity for the biologically active noradrenalin and norephedrine ions than for adrenalin and ephedrine.



6a L = H

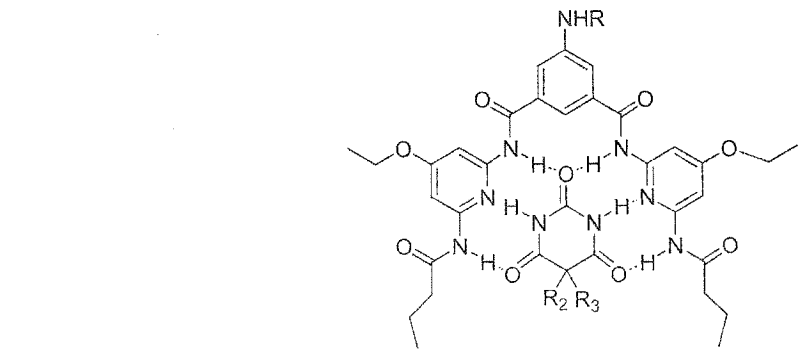
6b L = CO_2^-

6c L = CONYY'

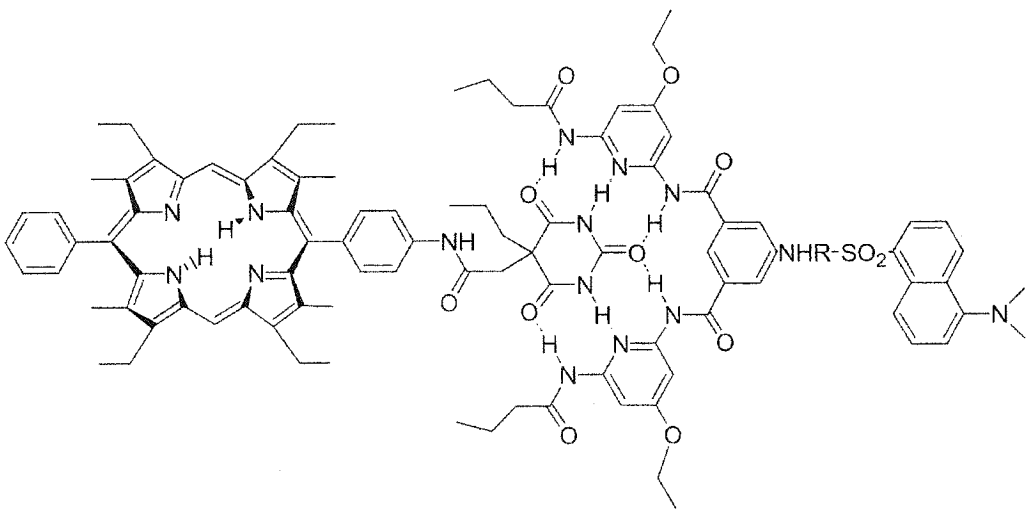
6d L = (L)-CH(CH_2SH)-CO_2Me

Figure 1. 8. Ammonium cation binding macrocyclic polyethers **6a-d**.

Electrostatic, donor-acceptor and especially multiple hydrogen-bonding interactions have also been used to bind neutral molecules, and to maintain host and guest in close contact. [1a, 6, 7, 30] The dimerisation usually occurs in non-polar, aprotic solvents because of the weakness of these intermolecular forces. [6, 7] For example, in complexes like **7** and **8**, the host consisted of two 2,6-pyridinediamide groups joined by an isophthalic acid linker, the guest a barbituric acid derivative (Figure 1. 9).[31] The formation of six strong intermolecular hydrogen-bonds was observed from a stoichiometric mixture of both components, to generate a tightly bound dimeric complex.



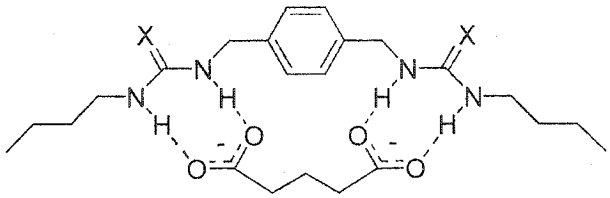
7



8

Figure 1. 9. Stable hydrogen-bonded complexes **7** and **8** formed between a 2,6-pyridinediamide-based host and a barbiturate guest .

Stronger, ionic hydrogen-bonding interactions can lead to supramolecular structures which are stable even in highly polar solvent like dimethylsulfoxide. In the case of dimer **9**,[32] the molecular receptor is composed of two urea or thiourea groups which provide four hydrogen bond donors to the host[33] (Figure 1. 10). The charged dicarboxylate derivative of glutamic acid is used as the guest molecule.[32] The formation of stable 1:1 complexes **9a** and **9b** could be detected by NMR studies in deuterated dimethylsulfoxide.



9a X = O
9b X = S

Figure 1. 10. Dimer formation between urea and thiourea derivatives and glutamic dicarboxylate.

Another family of simple supramolecular dimers are rotaxanes and catenanes[34] (Figure 1. 11). A rotaxane consists of a linear molecule which is mechanically threaded through one cyclic molecule.[33a] The presence of two bulky groups at each extremity of the linear component prevents its unthreading by acting as stoppers. A catenane results from the mechanical interlocking of two cyclic subunits.[33b,c] The coupling of addressable electronic, and optoelectronic properties with mechanical features of these interlocked dimers have been widely investigated and have shown great potential in the development of molecular computing devices.[35-37]

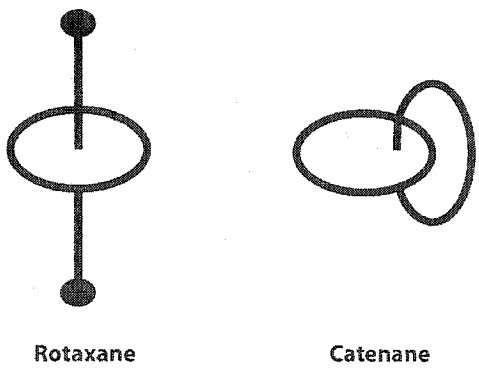
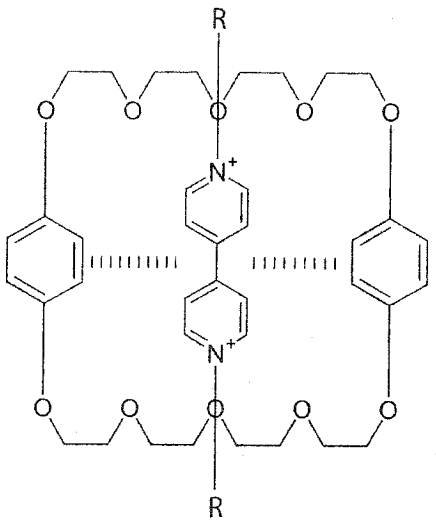


Figure 1. 11. Representation of a rotaxane and a catenane.

If affinity between host and guest is weak, statistical formation of rotaxanes and catenanes usually results in low yields of the product.[35] However, a directed template synthesis, using attractive intermolecular forces between the components to assist the

interlocking process, leads to improved predictability and better yields.[36,36] This type of synthesis uses π-π interactions between aromatic molecules to give supramolecular structures like **10a-d**.[37] (Figure 1. 12) Dications **10** are held in the cavity of the crown macrocycle by favourable, attractive interactions between the π-electron rich hydroquinone derivative and the π-electron deficient dicationic bipyridinium rings. Additional, weak C-H···O hydrogen bonds between the hydrogen atoms α to the nitrogen of the bipyridinium guest and the ether oxygen atoms of the macrocyclic host further stabilize the supramolecular structure.



10a R = H
10b R = CH_3
10c R = $(CH_2)_2OH$
10d R = $(CH_2)_2O(CH_2)_2OH$

Figure 1. 12. Rotaxanes formed between bipyridinium derivative and *bis*- *p*-phenylene-34-crown-10.

The rotaxane **11** shown in Figure 1. 13, is formed from a macrocyclic electron-deficient host, which consists of two bipyridinium dications, and a linear polyether containing an electron-rich 1,4-phenylenediamine.[38] Two bulky tri-isopropylsilyl stoppers are added to the extremities of the polyether after threading.

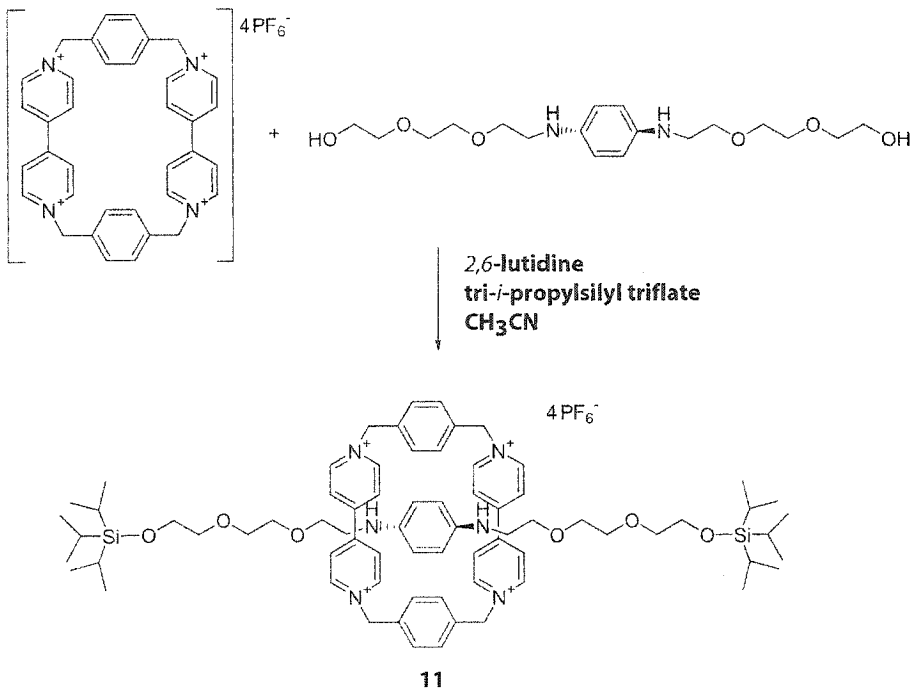
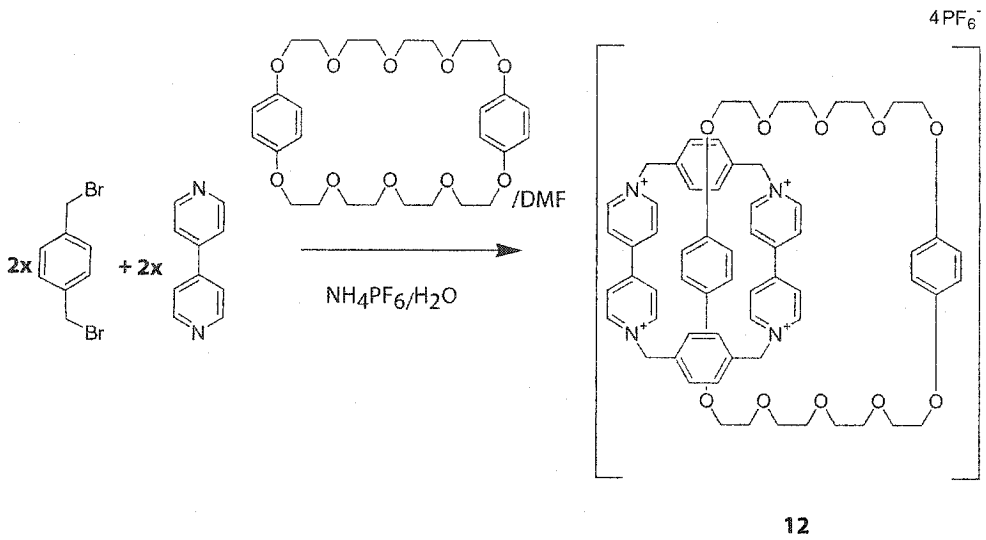


Figure 1. 13. Formation of rotaxane **11** by threading then stoppering.

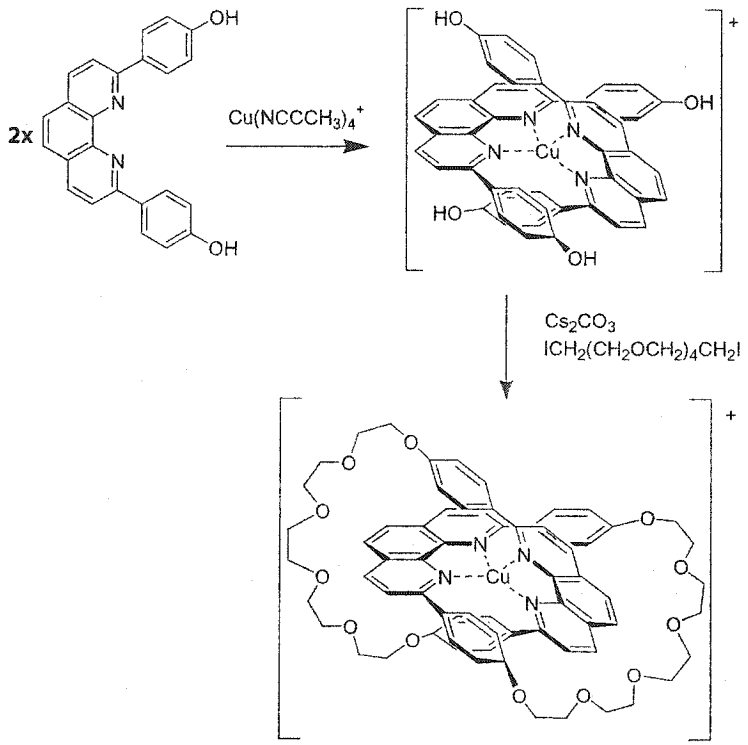
As shown in Figure 1. 14, catenane **12** is formed from a directed template synthesis[35,36] which involves an electron-rich macrocyclic polyether, two 2,2'-bipyridines, and two *p*-dibromoxylene. The bipyridines and the dibromoxylene units serve as precursors for the formation of an electron-deficient bipyridinium macrocycle.[12] During this five-component synthesis, favourable π-π interactions attract the π-electron rich hydroquinone derivative towards the π-electron deficient dicationic bipyridinium rings, to promote the interlocking process.



12

Figure 1. 14. Self-assembly of catenane **12** from five components.

Metal coordination has been used to direct the synthesis of supramolecular catenanes[39,40] and rotaxanes.[41] The metal-containing catenane **13** results from the coordination of a copper(I) ion with two rigid 1,10-phenanthroline derivatives, followed by a ring-closure upon addition of 1,4-diiodo-3,6,9,12-tetraoxatetradecane, as shown in Figure 1. 15.[39] The cationic catenane resisted to electrochemical reduction, proving the existence of a stable, interlocked structure in solution. The formation of the tetrahedral intermediate complex, caused by the symmetrical d^{10} electronic configuration of copper(I), is essential to the geometry and the stability of **13**.



13

Figure 1. 15. Metal-mediated self-assembly of catenane **13** by coordination of copper(I) with two 2,9-substituted 1,10-phenanthroline ring derivatives.

1.2.1.1.2. Multi-component Self-Assembly of One-Dimensional Structures

Numerous infinite one-dimensional structures such as tapes and ribbons[1, 42-45] have been generated from the non-covalent interactions of ditopic molecules, which are units containing two recognition sites (Figure 1. 16). A 120° or 180° orientation of the binding groups leads to the growth of a linear or zigzag chain, resulting into the formation of tapes. Different orientations of the interacting groups within the same supramolecular structure give molecular ribbons.

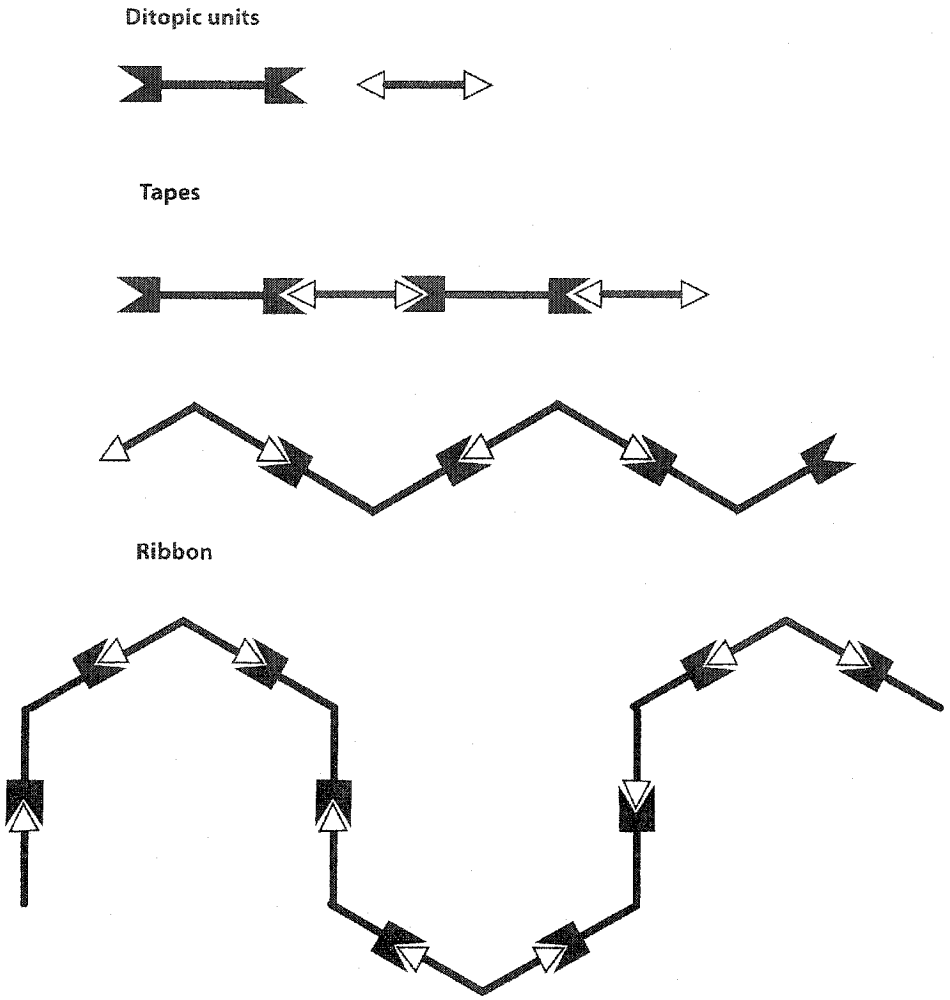


Figure 1. 16. Schematic representation of one-dimensional supramolecular structures.

Simple dicarboxylic acid building blocks such as terephthalic acid and isophthalic acid give one-dimensional tapes **14**[43] and **15**,[44] as shown in Figure 1. 17. In these structures, the self-assembled structures result from the formation of cyclic hydrogen bond dimers (Figure 1. 1) between the individual units. In terephthalic acid, the carboxylic acid groups are antiparallel with respect to each other, leading to a linear tapes while their relative orientation is 120° in isophthalic acid, giving crinkled tapes. Supramolecular ribbons such as **16** are obtained from hydrogen bonding interactions of symmetric dipyridone derivatives which incorporate a rigid acetylene linker.[45] In this

dipyridone-based system, the perpendicular orientation of the amide groups determines the geometry of the one-dimensional structure.

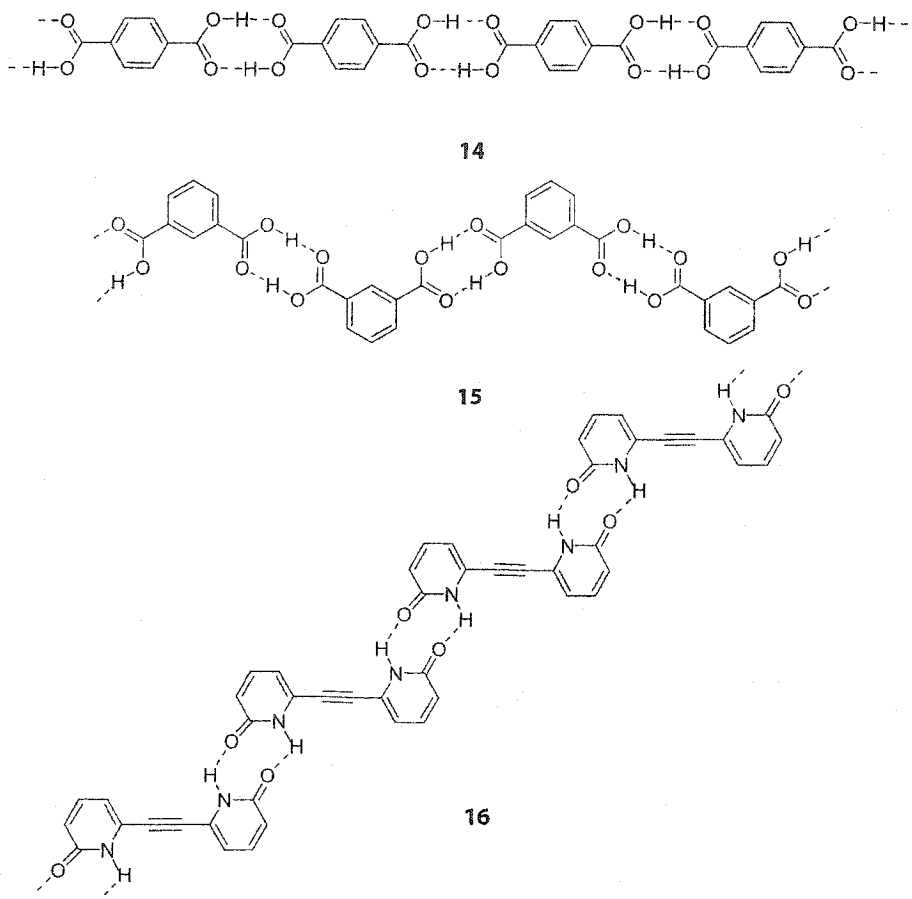


Figure 1. 17. Self-assembly of hydrogen-bonded tapes **14** and **15** from dicarboxylic acid derivatives and ribbon **16** from dipyridone.

Multiple hydrogen bond interactions have also been used to consolidate one-dimensional architectures.[1a-c, 46] In tape **17** shown in Figure 1. 18, three complementary ADA·DAD hydrogen bonds are formed between the melamine **M** and barbituric acid **BAR** derivatives instead of two hydrogen bonds in tapes **14** through **16**, providing more stability to the supramolecular assembly.

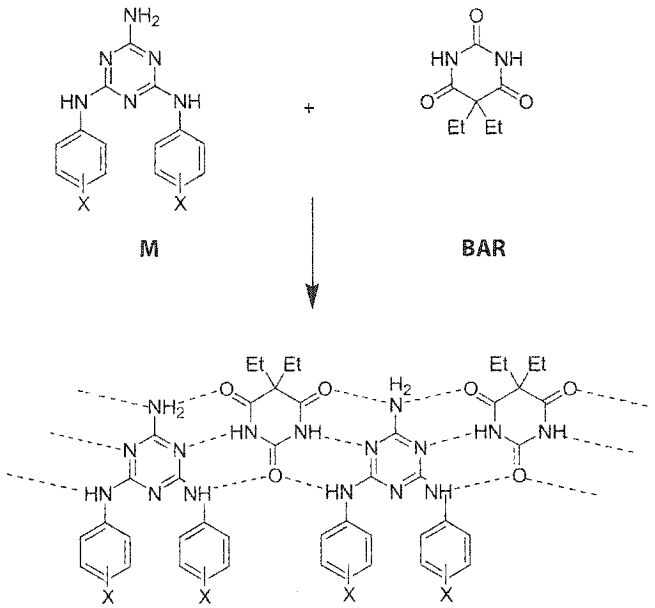
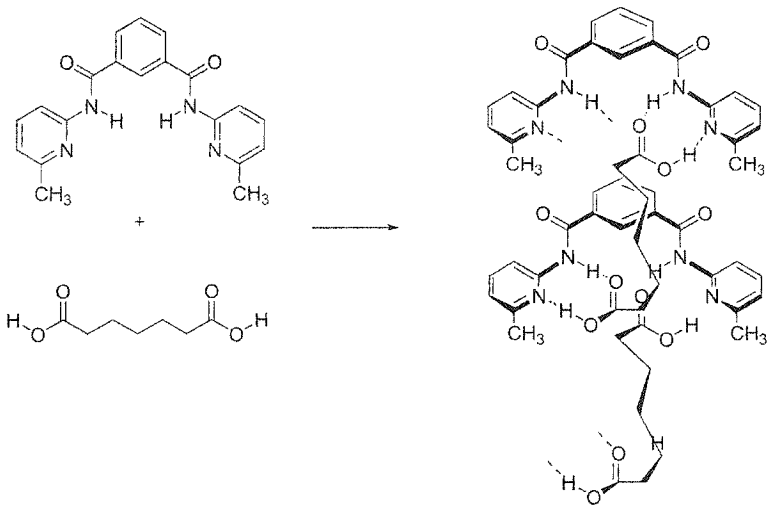


Figure 1. 18. Self-assembly of tapes **17** through multiple hydrogen bonds between melamine **M** and barbituric acid **BAR** derivatives.

These melamine and barbituric acid derivatives form cyclic hexamers, instead of hydrogen-bonded tapes, when large, sterically hindered substituents, *t*-butyl, decyl, etc are at the periphery. To relieve steric hindrance, the crinkled tape is forced to curve towards the cyclic rosette.[1b]

Several self-assembly strategies inspired by the DNA double helix have been explored to generate totally synthetic helical structures in a spontaneous fashion.[1, 13, 47-51] In particular, hydrogen-bonding interactions have been used to synthesize supramolecular helices **1**[13] (Figure 1. 3), and **18**[48] (Figure 1. 19). In the case of **1**, the helicity is induced by the presence of the optically active tartaric acid in the polymer backbone. While L-tartaric acid-based monomers give right-handed helices, D-tartaric acid-based units left-handed ones and M-tartaric acid-based units achiral supramolecules. Assembly **18** is helical because the two aminopyridine substituents are not coplanar, which enables

hydrogen bonding to occur above and below the plane defined by the isophthalic acid ring.

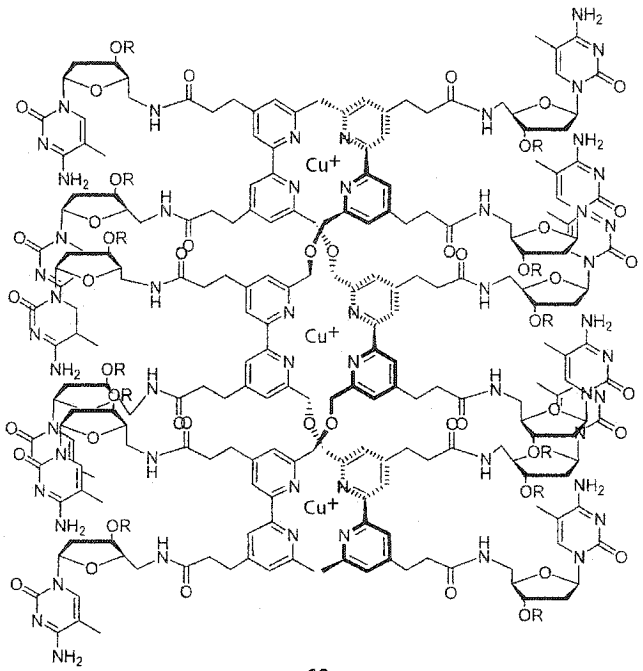


18

Figure 1. 19. Self-assembly of hydrogen-bonded helix **18** from a bispyridine substituted isophthalic acid and heptanedioic acid.

A significant number of double-stranded helicates have been synthesized using metal coordination.[1a, 1d, 49-51] In these supramolecular systems, the metal ions form the helical axis and bind to semi-rigid polydentate oligomers which correspond to the helical strands. Double-helical complexes of stoichiometry $[M_2L_2]^{n+}$ can usually be obtained from the interaction of a tetrahedral metal ion with a bis-bidentate ligand.

Deoxyribonucleo-functionalised 2,2'-bipyridyl trimers interact with copper(I) ions to give a trinuclear double-helicate complex **19** shown in Figure 1. 20.[50] In this type of complex, the helicate formation is driven by successive metal binding, showing the cooperativity of the self-assembly process. Contrary to DNA, the double helical structure is positively charged and the nucleic acid bases are exposed to the surface. Consequently, double-helicate **19** can serve as a receptor for a complementary DNA strand.



19

Figure 1. 20. Double-helicate **19** obtained by metal coordination of oligo-bipyridyl ligands.

Double-helical complexes **20**[51] and **21**[52] result from the coordination of metal cations to segmented tris-terpyridyl ligands (Figure 1. 21). Metal ions such as iron(II) and nickel(II) which favour hexa-coordination require the use of two trimeric ligands, leading to the formation of helical $[M_3L_2]^{6+}$ complex **20**. On the other hand, a mixed-strand double helicate **21** is obtained from the penta-coordination of copper(II) ions with one tris-bipyridyl strand and one tris-terpyridyl strand. The linear trinuclear complex adopts binding geometries in which the central copper (II) ion is trigonal bipyramidal while both peripheral copper(II) ions square pyramidal. When a mixture of the copper(II) and nickel(II) ions is exposed to both tris-bipyridyl and tris-terpyridyl strands, the resulting helicates corresponded to complexes **20** and **21**, suggesting that the coordination of tris-bipyridyl and tris-terpyridyl strands is metal-selective.

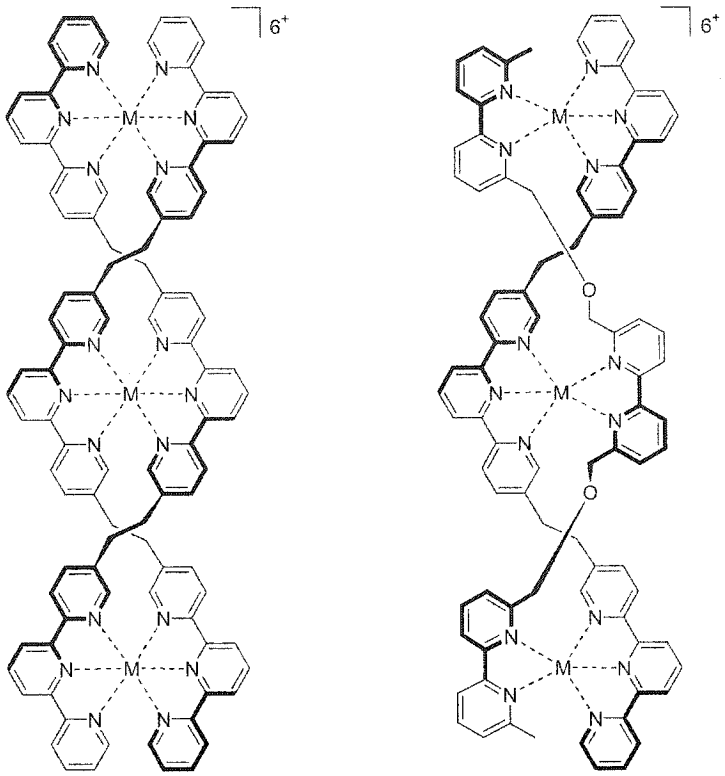


Figure 1. 21. Double-helical $[M_3L_2]^{6+}$ complexes **20** and **21** incorporating segmented tris-terpyridyl ligands.

1.2.1.2. Two-Dimensional Objects

1.2.1.2.1. Molecular Racks, Ladders, and Grids

Supramolecular chemistry has been successful in the creation of two dimensional objects. Both infinite sheets[1,12] and finite two-dimensional systems[1,52-55] such as molecular racks,[53] ladders, [54] and grids[55] have been synthesized. (Figure 1. 22) These structures can arise from oligomers which allow binding perpendicular to the main-chain or the use of T-shaped complementary subunits. In the case of molecular racks, a rigid polydentate oligomer acts as a host for monotopic guests. In ladders, two rigid oligomeric chains are joined by ditopic subunits (Figure 1. 16). In molecular grids, the

oligomer has two recognition units which are antiparallel to each other, thus allowing binding of ditopic hosts on both sides of the chain.

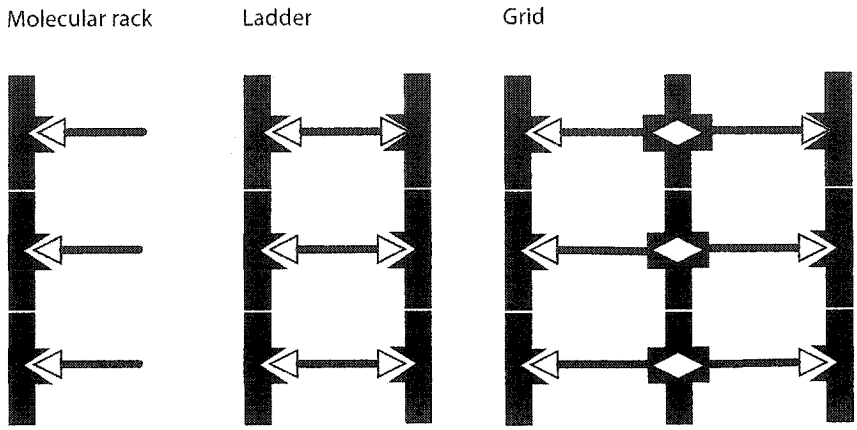
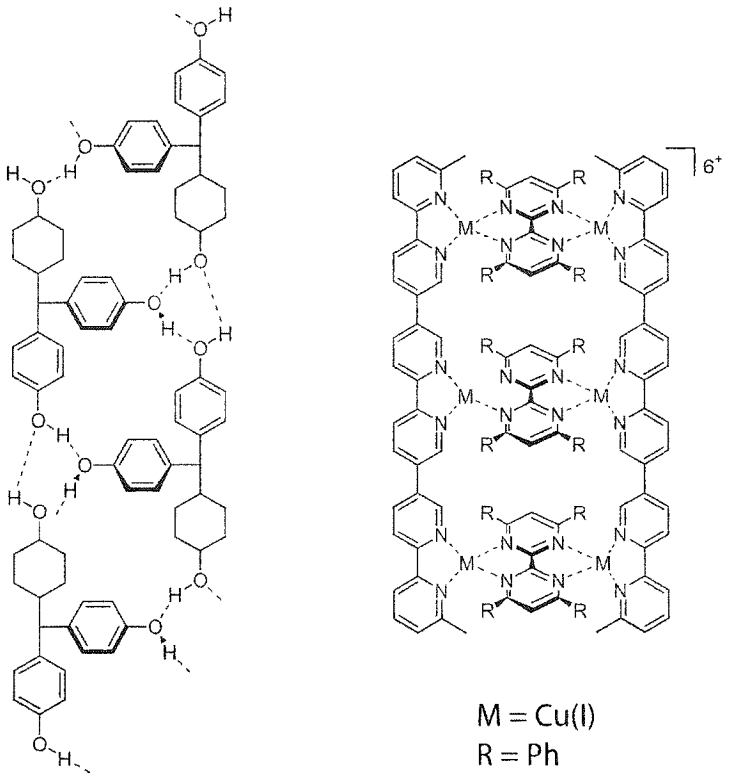


Figure 1. 22. Representation of some finite two-dimensional systems.

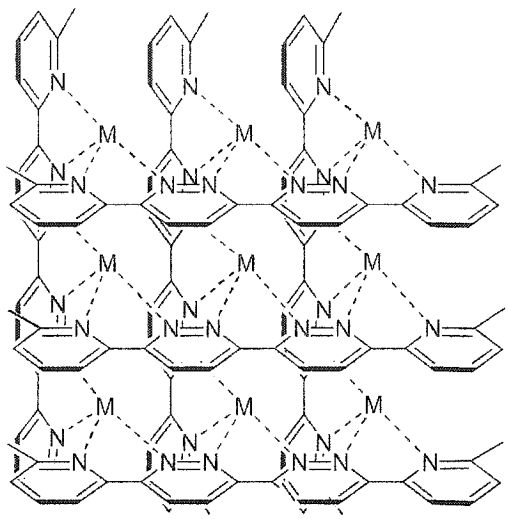
Molecular ladders have been obtained using hydrogen bonds between organic species[54a] and metal coordination.[54b] (Figure 1. 23) Infinite organic ladder **22** is formed by hydrogen bonding interactions between 4,4'-bis(4'-hydroxyphenyl)-1-cyclohexanol molecules. Each monomeric unit has three hydroxyl groups oriented in a T-shaped fashion, allowing the formation of cyclic hydrogen bonds. Metal-coordinated ladder **23** results from the association of two rigid tris-bipyridyl ligands with bipyrimidine and tetrahedral copper(I) ions.[54b]



22 **23**

Figure 1. 23. Organic **22** and metal coordinated **23** molecular ladders.

Oligomeric bipyridyl ligands have been used for the synthesis of 2x2, 3x3, and 4x4 molecular grids.[56] The coordination of six tris-bipyridyl subunits, for which the recognition sites point towards the same direction, with nine tetrahedral silver(I) ions lead to the formation of a discrete 3x3 grid like **24** (Figure 1. 24).[56a]



24

Figure 1. 24. Self-assembled structure of 3x3 molecular grid **24** formed by coordination of silver(I) ions.

1.2.1.2.2. Self-Assembled Macrocyclic Aggregates

The synthesis of macrocyclic aggregates from the non-covalent assembly of three and more components has attracted considerable interest, originating from the desire to form new hosts.[1,57-64] As depicted in Figure 1. 25, the formation of such macrocyclic structures results from the combination of ditopic monomers in which the two recognition units are oriented at specific angle. Specifically, a planar triangle should be obtained from the combination of 60°-angles or 60°- and 180°-angles between the recognition units; lozenge 120°- and 60°-orientation; squares 90°-angles or 90°- and 180°-angles; pentagons 109.5°-orientation; hexagons 120°-angles.

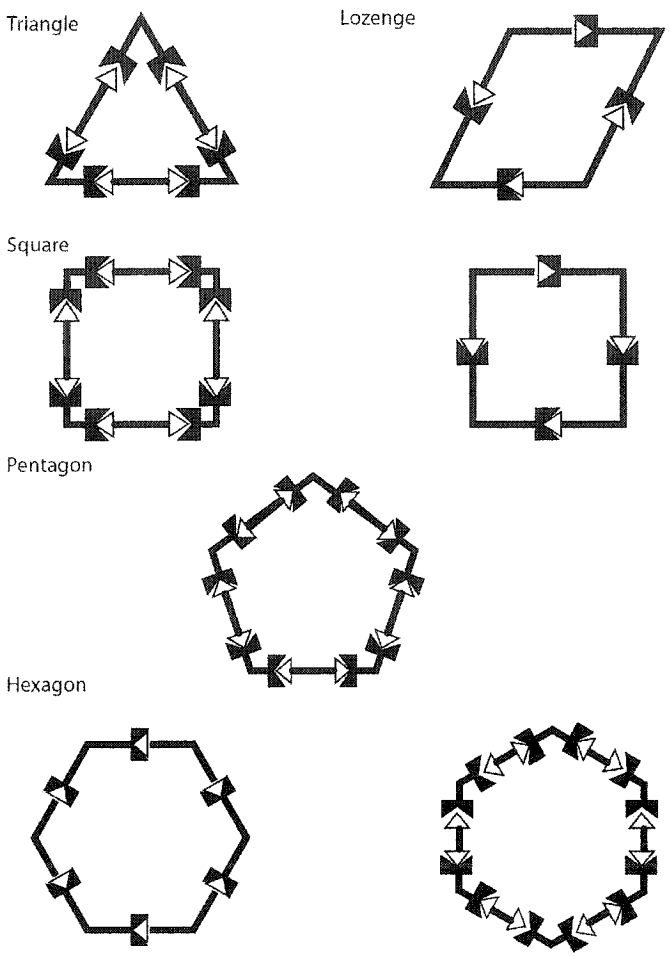
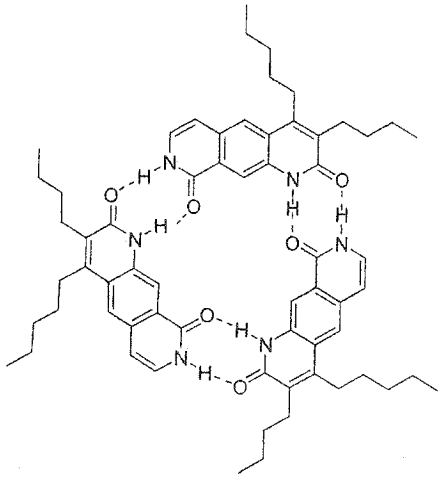


Figure 1. 25. Schematic representation of two-dimensional supramolecular polygons.

a. Self-Assembled Cyclic Trimers

Hydrogen bonding interactions involving cyanuric acid-melamine pairs, 2-aminopyridine-carboxylic acid pairs, and carboxylic acid or pyridone pairs have widely been used in the formation of cyclic assemblies.[1] Cyclic trimer **25**[57a] has been formed by hydrogen bonding interactions between the amide groups of quinoline derivatives, which have a 60°-orientation. (Figure 1. 26) The structure of this discrete structure has been assessed by vapour pressure osmometry and by ^{1}H-NMR titration.



25

Figure 1. 26. Hydrogen bonded cyclic trimer **25** obtained from quinoline derivatives.

Cyclic trimers such as **26** and **27** have been obtained by metal coordination methods.[57] (Figure 1. 27) Metallomacrocycle **26** results from the self-assembly of three platinum(II) ions with benzimidazole bridging ligands.[58a] The triangular shape of the complex is based on the square planar metal vertices combined with the nonlinear 150° angle between the two benzimidazole nitrogens. On the other hand, metallomacrocycle **27** originates from the coordination of iron(II) ions with phenanthroline-linked terpyridyl ligands.[59] In contrast with **26**, the geometry of the supramolecular structure is determined by the 60° orientation of the phenanthroline subunits which are *trans*-coordinated to the iron(II) through the terpyridines.

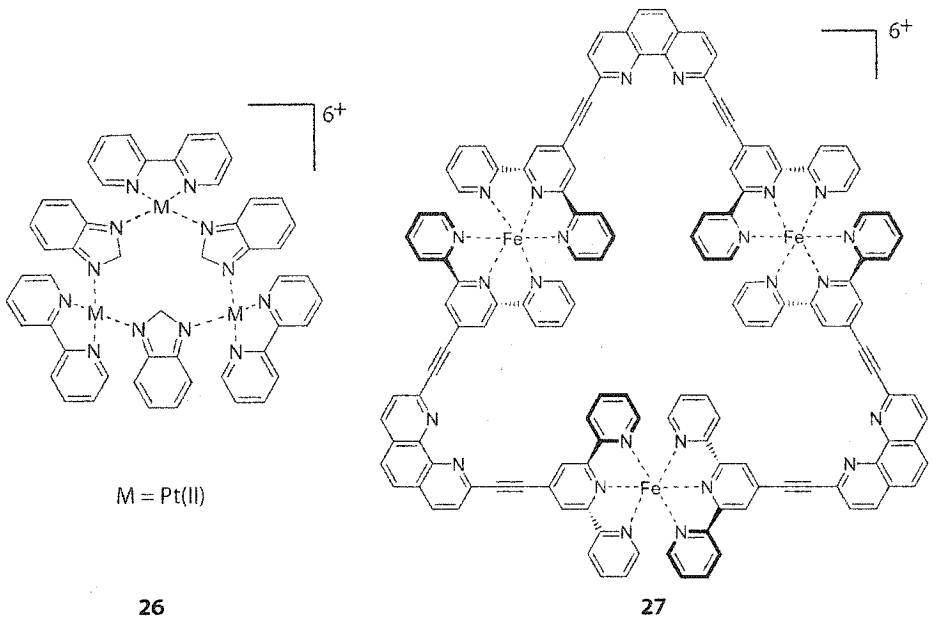
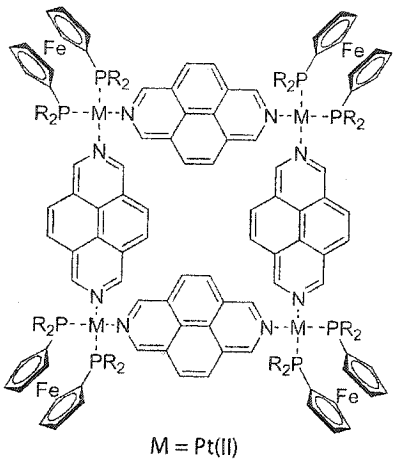


Figure 1. 27. Cyclic trimers **26** and **27** formed by metal coordination.

b. Self-Assembled Cyclic Tetramers

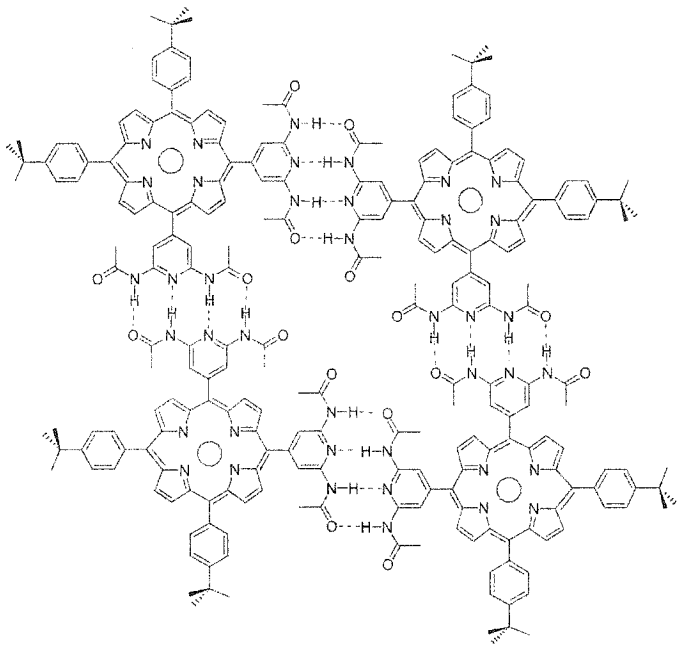
Several different approaches have been exploited in the synthesis of molecular squares.[1, 59, 60] Any square planar, trigonal bipyramidal, or octahedral transition-metal ions which have two *cis*-coordination sites available for binding can be used as vertices for the metal-assisted assembly of squares.[1f, 59] In particular, the ditopic 2,7-diazapyrene ligand forms a heterobimetallic supramolecular square **28** with the ferrocenyl palladium(II) and platinum(II) (Figure 1. 28).[60a]



28

Figure 1. 28. Cyclic tetramer **28** formed by metal coordination.

Complementary hydrogen bonding interactions have also been used to synthesize square tetramers. In cyclic tetramer **29**, four porphyrin derivatives are functionalized with diacetamidopyridyl recognition groups.[61a] (Figure 1. 29) The perpendicular orientation of these recognition units determines the square geometry of the assembly.



29

Figure 1. 29. Cyclic tetramer formed by self-complementary hydrogen bonds between porphyrins derivatives.

c. Self-Assembled Cyclic Hexamers

Various cyclic hexameric aggregates or rosettes held together by hydrogen bonding interactions and metal-coordinated have been reported.[1, 61,62] Simple functionalized isophthalic acid derivatives have been shown to form self-assembled hexameric structure **30** using hydrogen-bonds (Figure 1. 30).[62a] In such hydrogen-bonded assembly, the bulky substituent steric effects favours ring closing over oligomerisation leading to the desired macrocycle. Self-complementary DDA and AAD hydrogen bonding motifs have been used to synthesize the strongly bound hexameric rosette **31** from naphthyridine derivatives.[63]

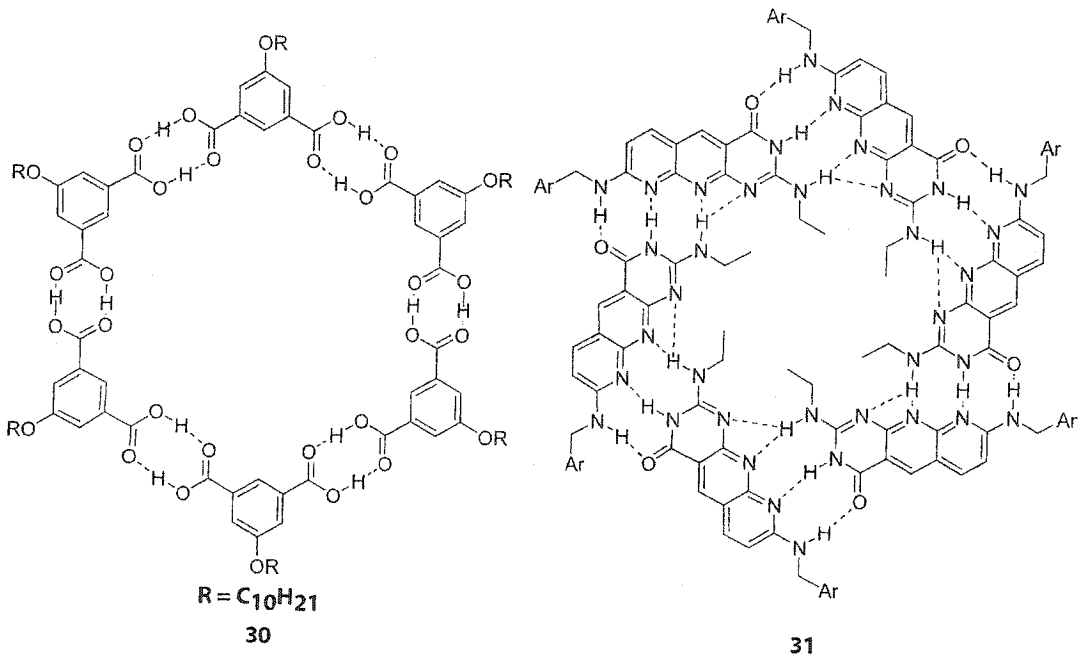
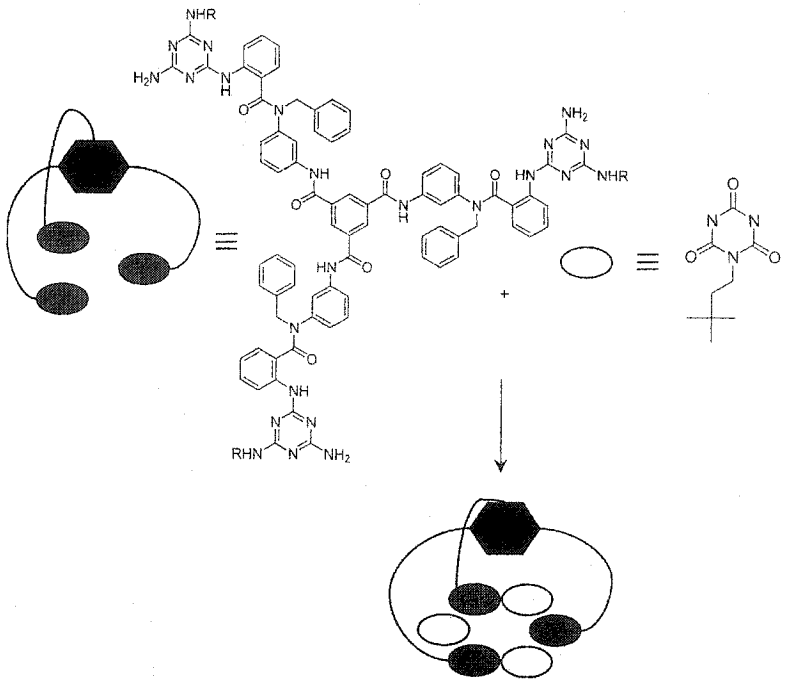


Figure 1. 30. Hydrogen bonding self-assembly of cyclic hexamers **30** and **31.**

Hydrogen bonded supramolecular structures like **32** in which flexible and rigid linkers serve as pre-organising features have been reported.[1b,64] (Figure 1. 31) In this structure, three melamine derivatives are connected to a trimesic acid core by rigid arms. Each melamine forms three hydrogen bonding interactions with a cyanuric acid derivative. The linkers have been incorporated in this melamine - cyanuric acid rosette motif to reduce the entropy-related translational and rotational motions, which disfavor multicomponent self-assembly. Only four molecular subunits are used for the synthesis instead of six. Further pre-organization has been obtained by linking the cyanuric acid monomers to an additional core.



32

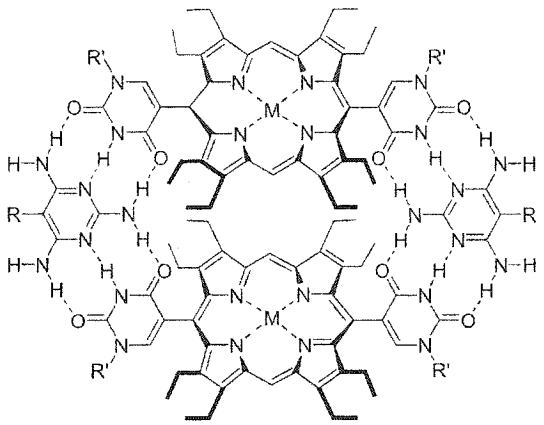
Figure 1. 31. Hydrogen bonding self-assembly of pre-organized cyclic hexamers.

1.2.1.3. Three-Dimensional Objects

Several three-dimensional cages[65-69] and polyhedra[1f, 1h-k, 69-76] have been created using supramolecular chemistry,[1a,b] stimulated by the difficulties of synthesising carbon-based systems like cubane, adamantane, dodecahedrane, norbornanes, and fullerenes. Specifically, the functionalisation of these particularly inert molecules requires extreme experimental conditions. The increasing coordination numbers of these organic compounds also reduces the accessibility of the reactive sites, limiting the efficient use of classical organic chemistry. On the other hand, supramolecular synthesis can generate highly functionalised, multicomponent three dimensional objects in one step. Also, the possible incorporation of metal ions into three dimensional objects broadens the range of valence numbers, and consequently, accessible supramolecular geometries.

1.2.1.3.1. Self-Assembled Cages, Spheres, and Cylinders

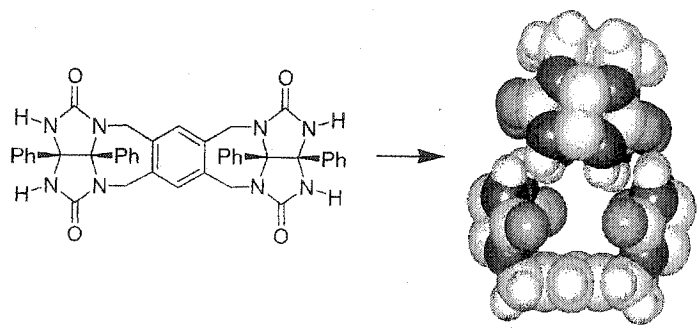
Hydrogen bonding interactions have been used to generate the bis-porphyrin supramolecular cage **33**.[66] (Figure 1. 32) Each porphyrin ring is directly linked to two uracil groups substituted by solubilising decyl groups. Complementary alkyl substituted triaminopyrimidine molecules join the two porphyrin derivatives through a DAD·ADA hydrogen bond motif in dichloromethane. Sterically hindering ethyl substituents on the pyrroles prevents the uracil free rotation relative to the porpyhrin, thus limiting the orientation of the two uracil groups to *syn* and *anti*. In the *anti* rotamer, the uracil binding units are pointing in opposite direction to give hydrogen-bonded ribbons, while they are on the same side in the *cis* rotamer to enable ring-closure. ^{1}H NMR monitoring of the hydrogen bond self-assembly first showed a mixture of *syn* and *anti* rotamers in solution, leading to the formation of oligomeric species upon addition of the pyrimidine. After a few days, the supramolecular ribbons formed from the *anti* rotamer disappeared while the three-dimensional structure **33** remained in solution, suggesting a shift of the *syn/trans* equilibrium towards the *syn* form to favour cage formation.



33

Figure 1. 32. Hydrogen bonding self-assembly of a porphyrin-containing molecular cage.

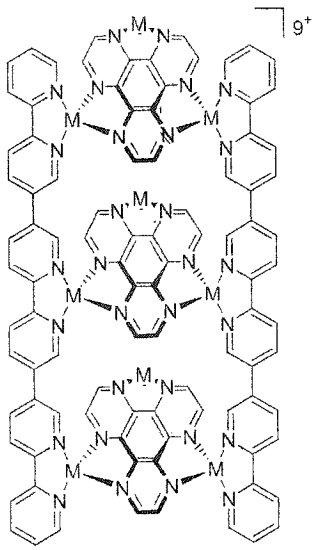
Pseudo-spherical structures have also been created from the dimerisation of crescent-shape small molecules through hydrogen bonding interactions.[66,67] Molecular spheres such as the 'tennis ball' **34**,[67] shown in Figure 1.33, have been designed to selectively encapsulate guest molecules, according to their size and their electronic properties. The tennis ball **34** results from the formation of eight hydrogen bonds between two tetra-urea derivatives and has successfully been used to encapsulate small molecules like methane, ethane, and ethylene within its cavity. Extension of the tetra-urea monomers has led to larger supramolecular capsules, with increased cavity sizes.[68]



34

Figure 1. 33. Hydrogen bond self-assembly of 'tennis ball' dimer **34** .

The multiligand, multimetal self-assembly of two types of ligands and Cu(I) ions results in the formation of cylindrical supramolecular structure **35**.[69] (Figure 1. 34) In this structure, three 5,5'-linked *tris*-bipyridines ligands act as 'pillars' while three hexa-azatriphenylene ligands lie flat, almost on top of each other. Two of the hexa-azatriphenylene ligands form the top and bottom lids of the cylindrical cage, and the third one divides the cage into two compartments of *ca.* 5.4 Å in radius. Distorsions of the tetrahedral coordination to the nine Cu(I) metal ions leads to helical twist in the overall supramolecular conformation.



35

Figure 1. 34. Multicomponent self-assembly of cylinder **35** through metal coordination. The tris-bipyridyl ligand at the back has been omitted for clarity.

1.2.1.3.2. Self-Assembled Platonic and Archimedean solids

The synthesis of Platonic and Archimedean solids has also been achieved using self-assembly. (Figure 1. 35) The faces of Platonic solids consist of identical regular polygons such as equilateral triangles, squares, pentagons, and hexagons leading to tetrahedra, cubes, octahedra, icosahedra, and dodecahedra. In contrast, the regular faces of the thirteen Archimedean solids combine different types of polygons, giving rise to truncated tetrahedra, cuboctahedra, truncated cubes, or rhombicuboctahedra.

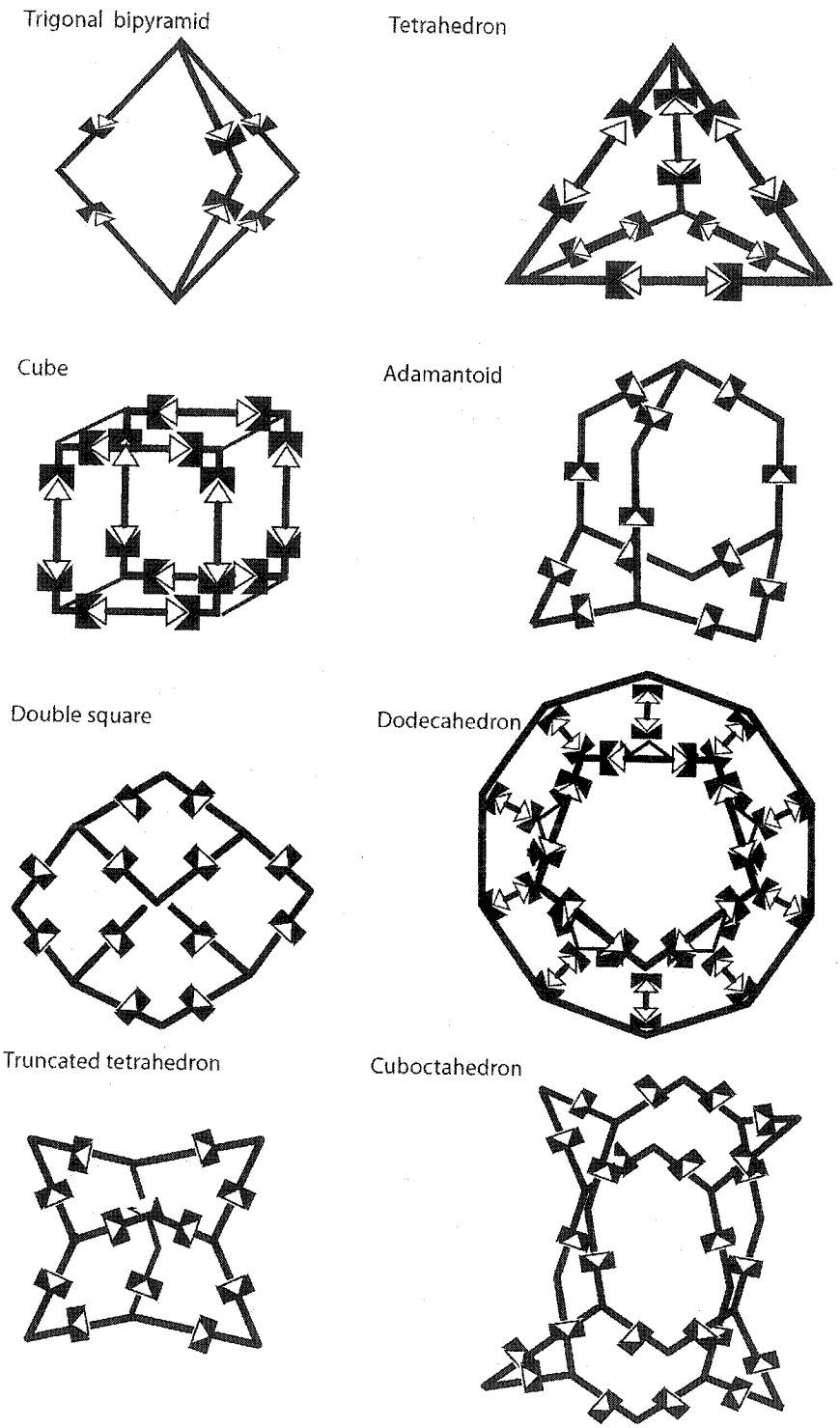


Figure 1. 35. Platonic and Archimedean solids.

a. Supramolecular Tedrahedra and Cubes

The simplest Platonic solid, the tetrahedron, has been synthesised from the self-assembly of four angular tritopic, *i.e.* trifunctionalised, units with six linear ditopic, *i.e.* bifunctionalised units (Figure 1. 35) or from the coordination of six bischelating ligands with four octahedral metal ions.[1f, 1h-k, 70-71] Six flexible pyrazolylpyridine-based multidentate ligands are coordinated to four Co(II) metal ions to generate supramolecular tetrahedron **36**.[71] (Figure 1. 36) Each cobalt cation occupies the vertex of this Platonic solid, while the ligands span over the edges of the tetrahedron. An adamantane-like topology is observed because of the bent structure of the *o*-xylyl linker. Pseudo-octahedral metal vertices can also be combined with trigonal trisbidentate ligands for the triangular faces to give supramolecular tetrahedra. Such a face-directed self-assembly has resulted in the formation of tetrahedron **37** (Figure 1. 35), in which four C_3-symmetrical ligands are coordinated to four Ti(IV) metal ion.[72] This thermodynamically stable M_4L_4 complex has been characterised as a racemic mixture of *T*-symmetrical homochiral compounds.

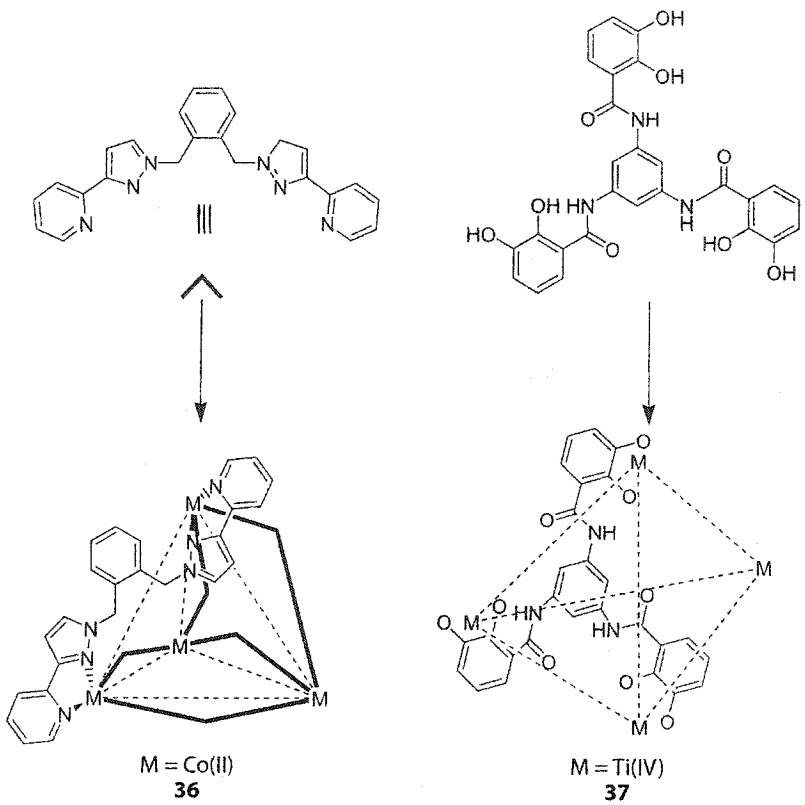
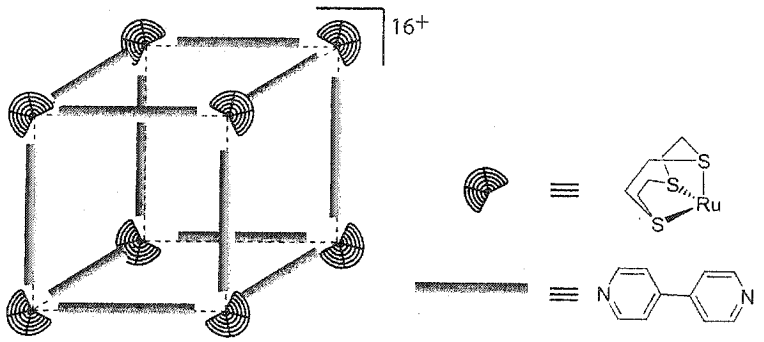


Figure 1. 36. Metal-mediated self-assembly of molecular tetrahedral **36** and **37**.

Although many cubic systems have been synthesised, only a few self-assembled cubes have been reported. Eight octahedral Ru(II) metal corners have been linked to twelve linear 4,4'-bipyridyl bridging units to give cube **38**.[73] (Figure 1. 37) This cube has been isolated from the four-week reaction of the ([9]aneS_3)Ru(DMSO)Cl_2 complex with 4,4'-bipyridine in presence of silver triflate in nitromethane. The X-ray structure of one tris(bipyridyl) ruthenium corner complex, obtained in presence of excess bipyridine, showed the perpendicular relative orientation of the ligands, supporting the cubic arrangement of **38**.



38

Figure 1. 37. Metal-mediated self-assembly of molecular cube **38**.

b. Supramolecular Archimedean Solids

The smallest Archimedean solid, the truncated tetrahedron, is obtained by capping the four tetradron corners.[1f,1g-k,73] Each vertex delimits two hexagons and one equilateral triangle. (Figure 1. 38) Several truncated tetrahedra have been generated from the combination of bis(triflato) palladium(II) or platinum(II) derivatives with tritopic aromatic ligands.[74] In particular, supramolecular structure **39**[73c] has been created from bis(triflato) palladium(II) or platinum(II) derivatives of chiral 2,2'-bis(diphenylphosphino)-1,1'-binaphthyl ligands, leading to optically active supramolecular systems.

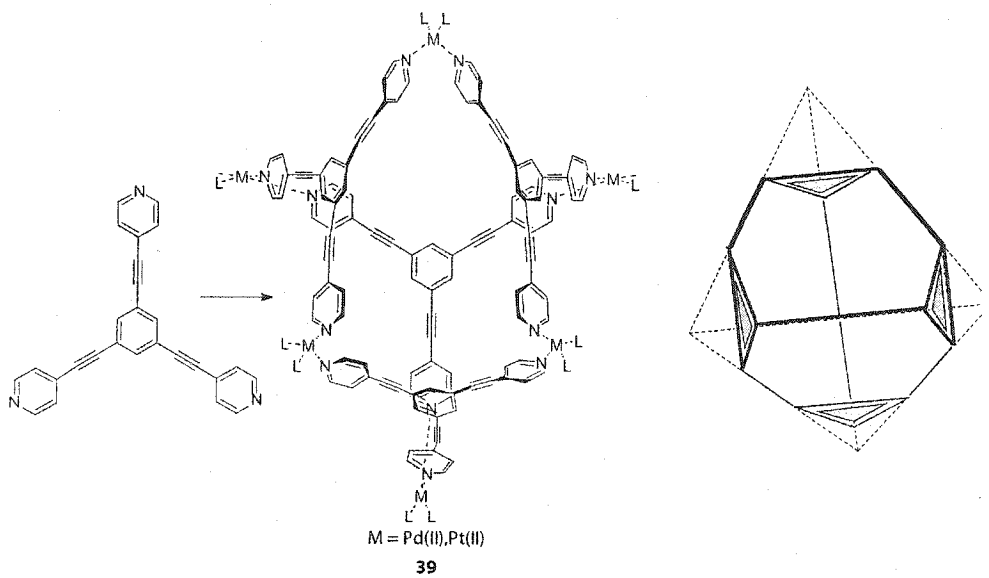


Figure 1. 38. Metal-mediated self-assembly of supramolecular truncated tetrahedron **39**.

The non-covalent synthesis of cuboctahedra, truncated Archimedean solids composed of square and triangular faces, has been achieved from the self-assembly of eight planar tritopic ligands with twelve 108°-ditopic subunits.[75] The tritopic 1,3,5-tris(4-bipyridyl-ethynyl)benzene ligand has been combined with the complementary bis(triflato) platinum(II) metal ion in a 2:3 ratio to form cuboctahedron **40** (Figure 1. 39).

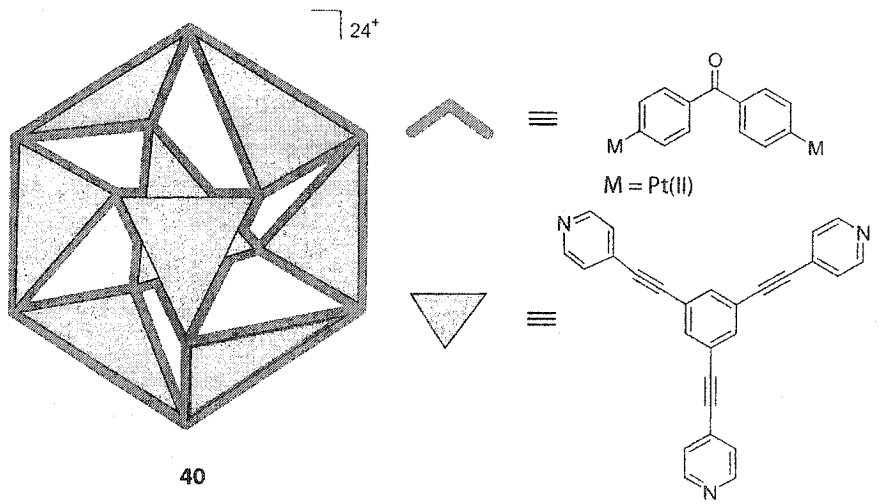


Figure 1. 39. Metal-mediated self-assembly of a molecular cuboctahedron **40**.

Truncated trigonal bipyramid **41**,[76] shown in Figure 1. 40, results from the 1:3 association of hexatopic triangular ligand, 1,3,5-tris(5'-pyrimidyl)benzene with ethylenediamine palladium(II) dinitrate. The 3 x 2.5 x 2.5 nm hexahedron consists of three equatorial, cyclic tetranuclear [Pd(II)-pyrimidyl]$_4$ corners and two apical, trinuclear [Pd(II)-pyrimidyl]$_3$ corners.

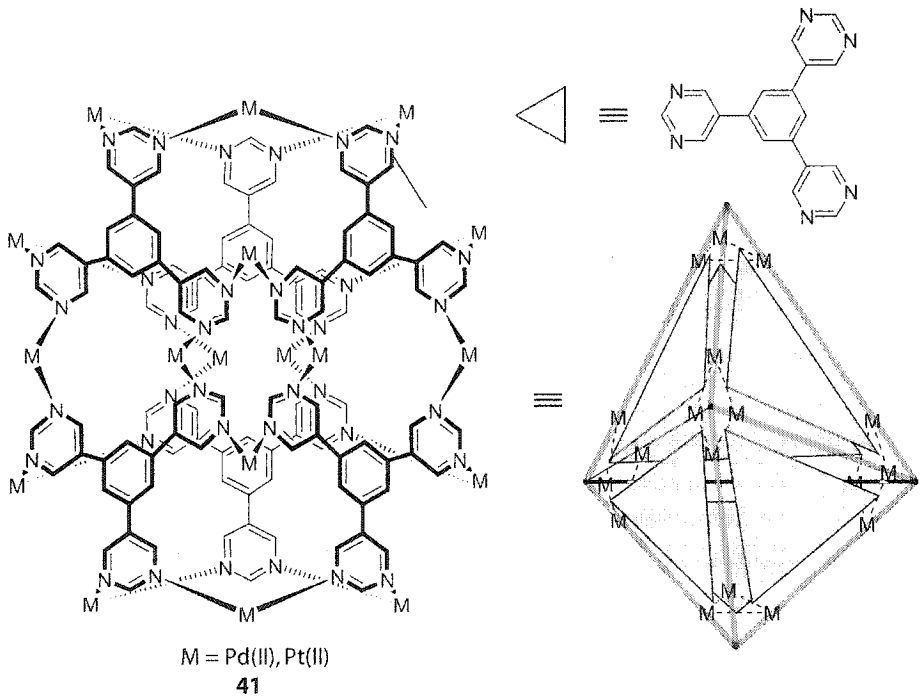
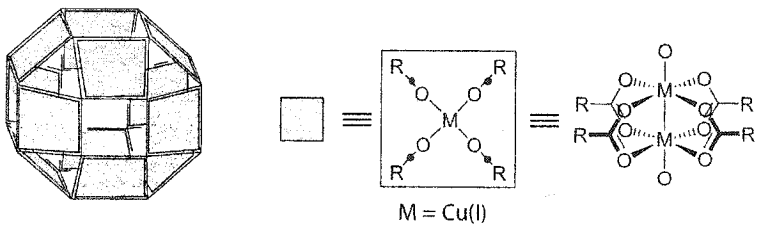


Figure 1. 40. Metal-mediated self-assembly of truncated trigonal bipyramid **41**.

Faceted polyhedra, which are closely related to Platonic and Archimedean solids, are constructed from regular polygons with linked vertices and contain both open (concave) and closed (convex) faces.[77] The small molecular rhombihexahedron **42** shown in Figure 1. 40 has been synthesized by linking the vertices of square metal-organic subunits, $Cu_2(RCO_2)_4A$, to 120°-spacers.[77b] The vertex-linked [(L)(S)Cu_2(benzene-1,3-

dicarboxylate)$_2$]$_{12}$ (L = pyridine, S = methanol), molecular squares self-assemble into *small rhombihexahedra*. [(L)(S)Cu$_2$(benzene-1,3-dicarboxylate)$_2$]$_{12}$, contains pyridine ligands that are axially bonded to the metal ions at the exterior surface, and MeOH ligands lying at the interior surface.



42

Figure 1. 41. Metal-mediated self-assembly of a small molecular rhombihexahedron. R = phenyl

1.2.2. Biological Supramolecular Chemistry

The remarkable specificity, architectural control and efficiency of non-covalent intermolecular forces are omnipresent in Nature. [1c,2] In such biological systems, the thermodynamically controlled self-assembly process follows nucleation-growth sequence, where one initial self-assembled structure forms higher-ordered structures. [1c]

1.2.2.1. Tobacco Mosaic Virus (TMV)

Tobacco mosaic virus (TMV)[78] (Figure 1. 42) is the best understood biological self-assembled structure. [1c,77-84] This helical virus results from the association of 2130 identical protein monomers[79] around a 6400-nucleotide single RNA strand. [80, 81] Virus formation occurs spontaneously using reversible, non-covalent interactions in a crystallisation-like process, which involves a nucleation step followed by a growth step.

During the nucleation step, the protein subunits self-organise around the circumference[82] of a circle delineated by the viral RNA to form a disc.[4, 83, 84] Multiple discs can then be stacked on top of one another to form a cylinder, with the virus genome contained in the hollow centre of the cylinder, coated by the protein shell. It is the conjunction of RNA with the proteins which determines the final structure of the virus. [85] The growth of the helical structure, consequently the length of the virus (3000 Å), is defined by the geometry of the helical RNA strand. The helicity of the assembly, for which the diameter amounts to 180 Å, is determined by the protein subunits.

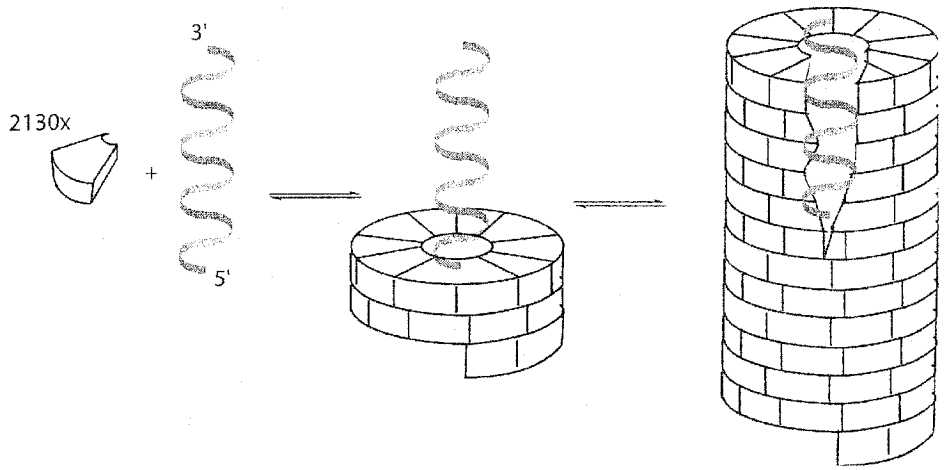


Figure 1. 42. Self-assembly of the tobacco mosaic virus from 2130 protein monomers and one single RNA strand.

1.2.2.2. Self-Assembling Oligonucleotides

1.2.2.2.1. Double-Helical Deoxyribonucleic Acid (DNA)

Deoxyribonucleic acid (DNA)[1, 2, 86-87] best exemplifies the essential role of non-covalent interactions in the determination of biological structure[87] and function.[88] In this biological system, nucleic acids containing purines (adenine (A), guanine (G)) and pyrimidines (thymine (T), cytosine (C)) as aromatic bases, are connected through

phosphodiester linkages, and undergo a highly specific, non-covalent recognition event to form a double-helical structure (Figure 1. 43). [1, 2, 85-86]

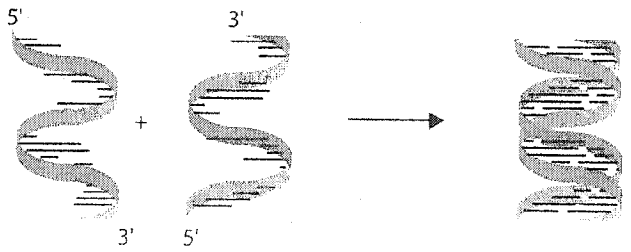


Figure 1. 43. Self-assembly of complementary DNA single strands into a double-helix.

Selective, complementary hydrogen-bonding interactions take place between the individual aromatic bases which compose the two oligonucleotide single strands, to give rise to a double helical structure. The base-pairing between purines and pyrimidines is predetermined by the configuration of the hydrogen-bond acceptors and donors within the aromatic bases, resulting in specific A - T and C - G hydrogen-bonded dimers during this molecular recognition event (Figure 1. 44).[86]

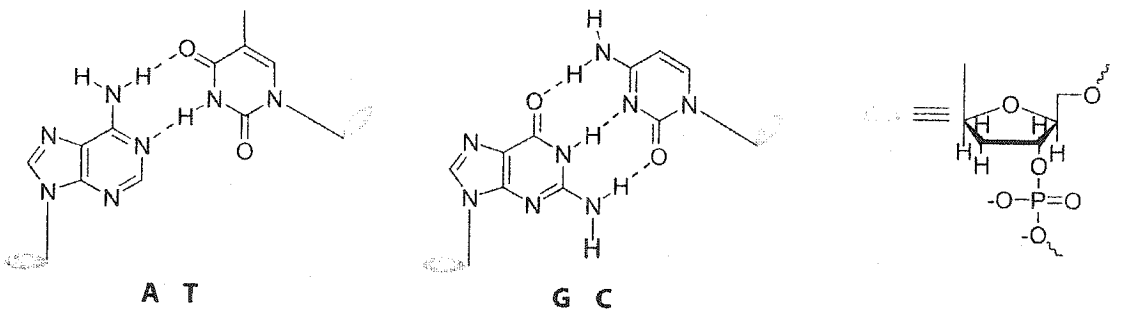


Figure 1. 44. Specific Watson-Crick base-pairing of adenine and thymine (**A T**), and guanine and cytosine (**G C**) in the DNA double-helix.

The aromaticity of the aromatic bases significantly contributes to the interstrand hydrogen-bonding, through significant stabilising van der Waals and π-π forces within the double-stranded structure. [87] The competing effects of electrostatic repulsions and van

der Waals attractions, inherent to π-π interactions (see Section 1. 1. 2. 2. 3),[19-22] inducing an offset stacking arrangement of the DNA bases, which displaces the polyphosphate backbone from linearity and gives rise to the helicity of the double strand. As in most biological systems,[1c,2] the DNA single strands undergo self-assembly into two thermodynamically controlled steps, where nucleation occurs as 3-4 base pairs initiate duplex formation and induces growth assisted by positive cooperative effects.

1.2.2.2.2. Higher-Order Olibonucleotides Assemblies

a. Oligonucleotide Triple Helices

Although usually described as a double-helix, DNA is a polymorphic biological system which not only can adopt bent or coiled conformations,[2a,2d] but also can closely interact with oligonucleotides to form higher-order aggregates.[89-121] The ability of DNA to form higher-order structures was first reported in 1957 with the discovery of triple helices,[90] resulting from the weak but sequence-specific binding of a third oligonucleotide strand into DNA double-helix.[91] In these triple helical structures, the third DNA or RNA strand is incorporated into the major groove of the DNA duplexes where it forms complementary Hoogsteen hydrogen-bonds with purine bases of the Watson-Crick base-pairs (Figure 1. 45). Similar to DNA-duplexes, favourable van der Waals and π-π forces within the double-stranded structure maintain the aromatic base-stacking of the triple helix.

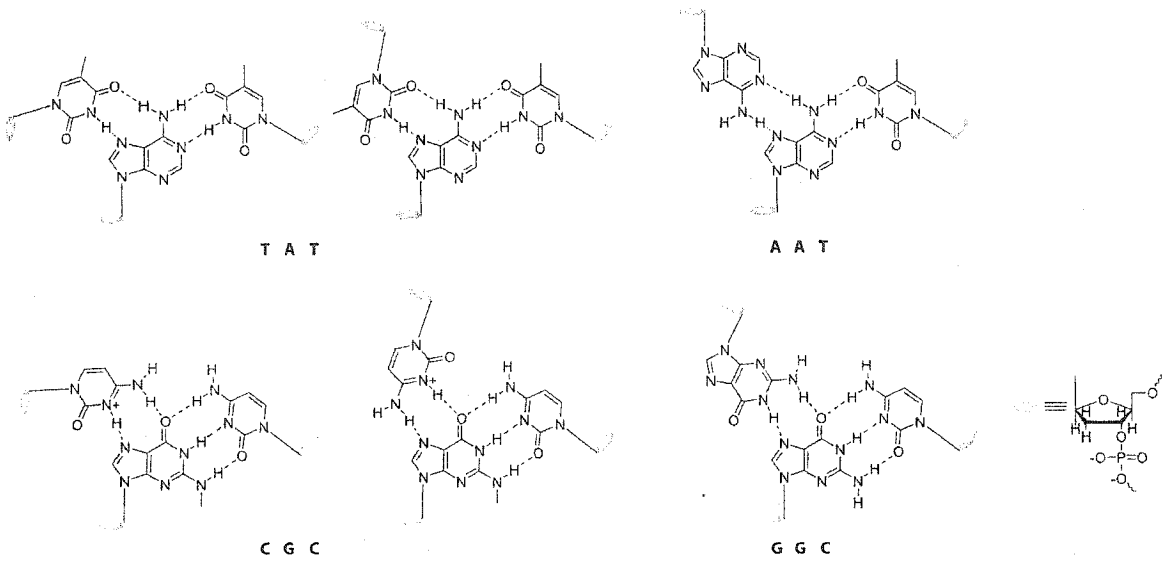


Figure 1. 45. Watson-Crick and Hoogsteen base-pairing in **TAT**, **AAT**, **C^+GC**, **GGC** triple helices.

Because of their sequence-specificity, triple helices are especially attractive for their potential therapeutic use in anti-gene strategies.[89-104] DNA triple helices, or triplexes, have been shown to inhibit initiation[92] and polymerisation processes[93] which occur during gene replication and transcription. Triplex formation also has been shown to interfere with protein-oligonucleotide interactions like DNA transcription, replication, repair, and recombination, which involve helicases and topoisomerases.[94] Single DNA and RNA strands can also undergo triple helix formation with TFO to give rise to secondary structures such as clamps and circular oligonucleotides, that can be used to extract, purify, and to investigate nucleic structures.[95] In addition, clamp oligonucleotides have been shown to inhibit replication and translation processes *in vivo*.[104, 96]

Several challenges, relative to triple helix stability and DNA target accessibility, need to be addressed to effectively implement such strategy for anti-gene therapy.[97] First, triplex formation only occurs through the binding of purine bases, *i.e.* A and G, limiting the repertoire of potential targets for the incoming strand. Second, the weakening of the

Hoogsteen hydrogen-bond in protic solvents tends to destabilise the three-stranded structure.[98] A third triplex stablity problem arises from competition with other sequence-specific self-association (see below). As a result, tremendous effort has been devoted to the development and investigation of natural and artificial triplex forming oligonucleotides (TFO)[89] through the synthesis of nucleotide analogues with modified base, sugar,[91b, 99] or backbone,[100] or the attachment of an intercalating agent.[101] The competitive effects of other self-associated structures can be minimised by changing the experimental conditions[102] or by conjugating the TFO with a secondary structure.[103] The triple helix can also be stabilised with molecules that can irreversibly cross-link or cleave the DNA backbone upon triplex formation.[99h, 104]

Accessibility of nuclear DNA targets is essential for the successful development of anti-gene therapy. Typical methods to effectively introduce the TFO in the nucleus consist in associating the oligonucleotide to with lipophilic groups[105] or increasing the cell permeability. Except for covalently linked oligonucleotides, triple helix formation and activity is difficult to probe *in vitro*. For example, an oligonucleotide-psoralen conjugate was properly incorporated into HIV-1 infected cells to undergo triple helix formation with the viral DNA.[99h] However, much work is still needed to design artificial TFOs with abilities to bind pyrimidine bases,[106] decreased pH dependence, and greater binding affinities to DNA double helices, which will effectively penetrate into the nuclear environment.

b. Oligonucleotide Quadruplexes and Pentaplexes

Besides the triple helix, tetrameric[107-115] structures have also been detected from oligonucleotides. The propensity of guanine(G)-rich oligonucleotides to generate higher-

order self-assembled structures was reported in 1962,[106] but did not attract much attention until experimental evidence for its biological importance. Four coplanar guanine-bases self-associate by hydrogen-bonding interaction following the Hoogsteen base-pairing motif to generate a G-quartet.[108,109] (Figure 1. 46) The formed G-quartet, which can consist of one, two, or four oligonucleotide strands, includes potassium ions within its cavity, which serves as a stabilising agent for the assembly.[107]

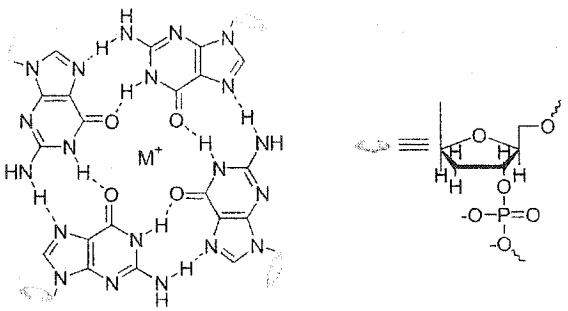


Figure 1. 46. Self-assembly of self-complementary guanosine strands into G-quartets. ($M^+ = K^+$)

G-rich oligonucleotides reside in DNA telomeres, which constitute the end of chromoses and are involved in the replication and stability of DNA,[110] gene promoter regions,[111] and sequences associated with human disease,[112] have been shown to form quadruplex structures *in vitro*. Certain proteins[113] which interact with G-quartets, as well as many potentially therapeutic G-rich oligonucleotide secondary structures,[114] have also been shown to promote quadruplex formation.[113,115] Several small molecules which interact with DNA quadruplexes, have also exhibited selective telomerase inhibition, thereby making G-quartets potential targets for anti-cancer therapy.[116]

One example in which oligonucleotides associate into a DNA pentaplex has been reported recently.[117] In this structure, five self-complementary 2'-deoxy-*iso*-guanine (*i*G) bases self-assemble using hydrogen-bonding to yield a pentameric motif. (Figure 1. 47)

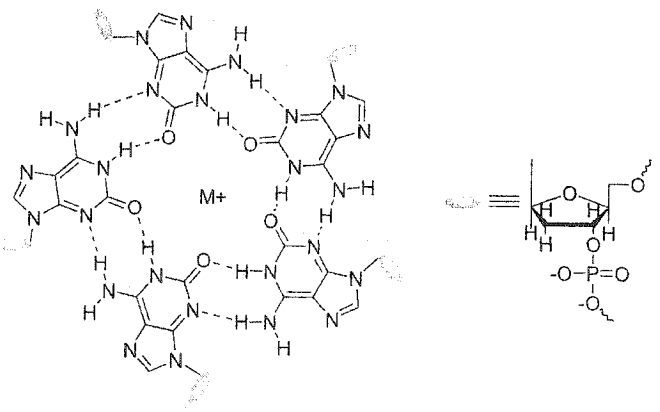


Figure 1. 47. Self-assembly of self-complementary isoguanosine strands into *i*G-quintets. ($M^+ = Cs^+$)

Similar to G-quartets which are stabilised by potassium ions, this *i*G-quintet[118] requires the presence of cesium ions to form. *i*G-oligonucleotides are natural DNA oligomers[119] which result from reactions of DNA with HCN,[120] and have been used to encode genetic information during ribosomal translation *in vitro*.[121] They may also have been involved in early biopolymer evolution.[122]

1.2.3. Synthesis of New Materials and Devices

1.2.3.1. Supramolecular Chirality

Biochemical synthesis involves highly stereoselective transformations which yield one stereoisomer only.[2,77-123] Classical, covalent, chemical synthesis has achieved stereocontrol over covalent bond formation comparable to biochemistry. Although the use of non-covalent and dynamic bonds is more problematic, supramolecular chirality has been successfully introduced in several synthetic systems.[124-127] Non-symmetric arrangement of the individual components in supramolecular structures has been obtained in organic hydrogen-bonded systems as well as in metal-coordinated assemblies.

[125,126] The diastereoselective assembly of enantio-pure calix[4]arene dimelamines and 5,5-diethylbarbituric acid has produced chiral hydrogen-bonded structures **43** (Figure 1. 48).[127] In these multicomponent systems, the chirality is controlled by the use of peripheral chiral substituents on the monomers. A racemic mixture of *M*- and *P*-enantiomers, which have an anticlockwise (*M*) or an clockwise (*P*) orientation with respect to the melamines in the assembly, has been detected for self-assembled structure **43a** in the absence of chiral substituents. The introduction of chiral (*R*,*R*) or (*S*,*S*) substituents in the dimelamine or in the barbituric acid derivative leads to the formation of diastereomeric assembly **43b** (*M*- or *P*- enantiomers). Once formed, enantiomers *M* and *P* remain optically active upon substitution of one of the diastereomeric components by achiral molecules **43c**. The chirality of hydrogen-bonded assembly **43d** is preserved despite the replacement of *both* diastereomeric molecules by achiral barbituric acid, suggesting a memory effect in the assembly.

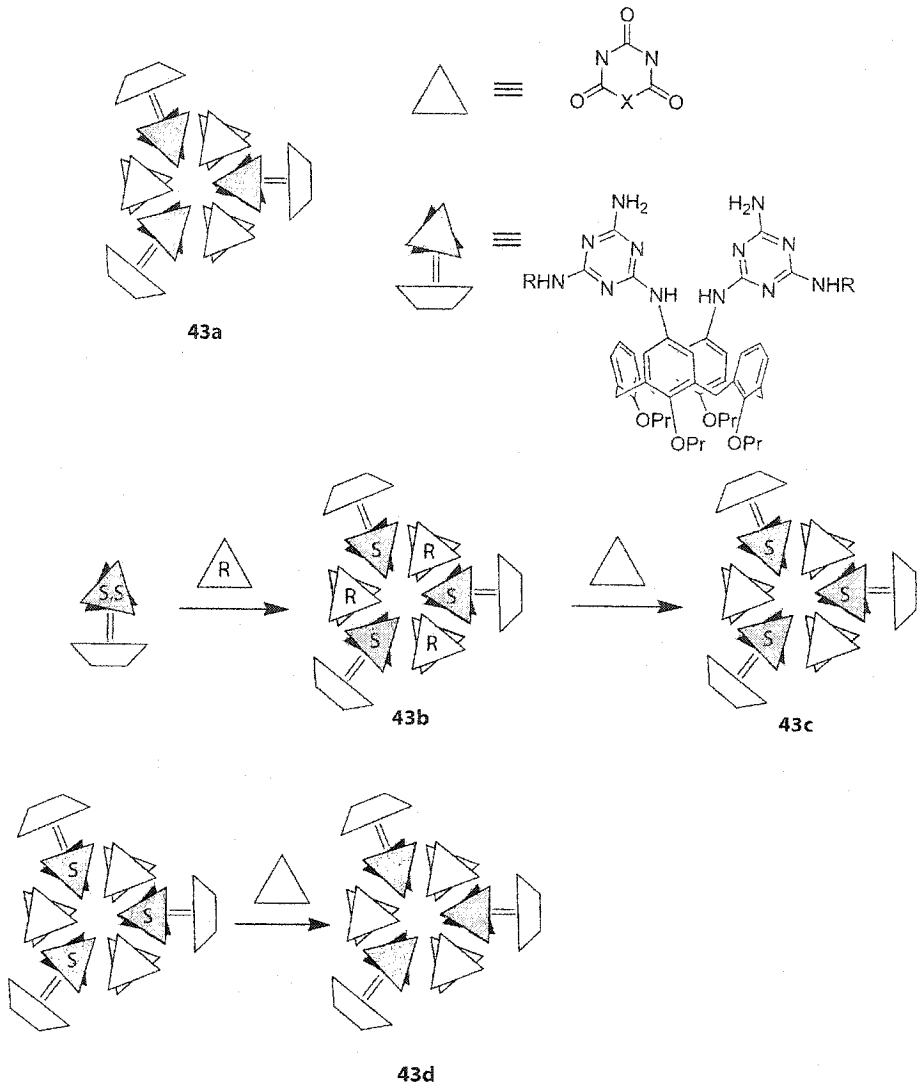


Figure 1. 48. Diastereoselective hydrogen-bonding self-assembly of enantio-pure calix[4]arene dimelamines and 5,5-diethylbarbituric acid. The assignment of the *M*/*P*-configuration is based on a clockwise (*P*) or anticlockwise (*M*) orientation of the two melamine units in the assembly.

A similar control of supramolecular chirality has been obtained in self-assembled helices **44a**,[128] using both hydrophobic and hydrophilic peripheral chiral centres (Figure 1. 49). These supramolecular helices are formed from bifunctional ureidotriazine derivatives which combine π-π stacking interactions and strong quadruple hydrogen-bonds in dodecane and in water. The helicity arises from a temperature-dependent,

cooperative and reversible self-assembly process comparable with DNA helix formation. Progressive addition of hydrogen-bonded chiral ureidotriazine dimers **44b**, which can dissociate to compete with the hydrogen-bonded components of the helix, shortens the helical structures **44c** by capping the extremities of the assembly, but maintain the helicity of **44c**. A chiral memory effect is also observed upon complete replacement of the chiral dimers **44b** by achiral structures **44a**, similar to the melamine-barbituric acid system, **43d**.

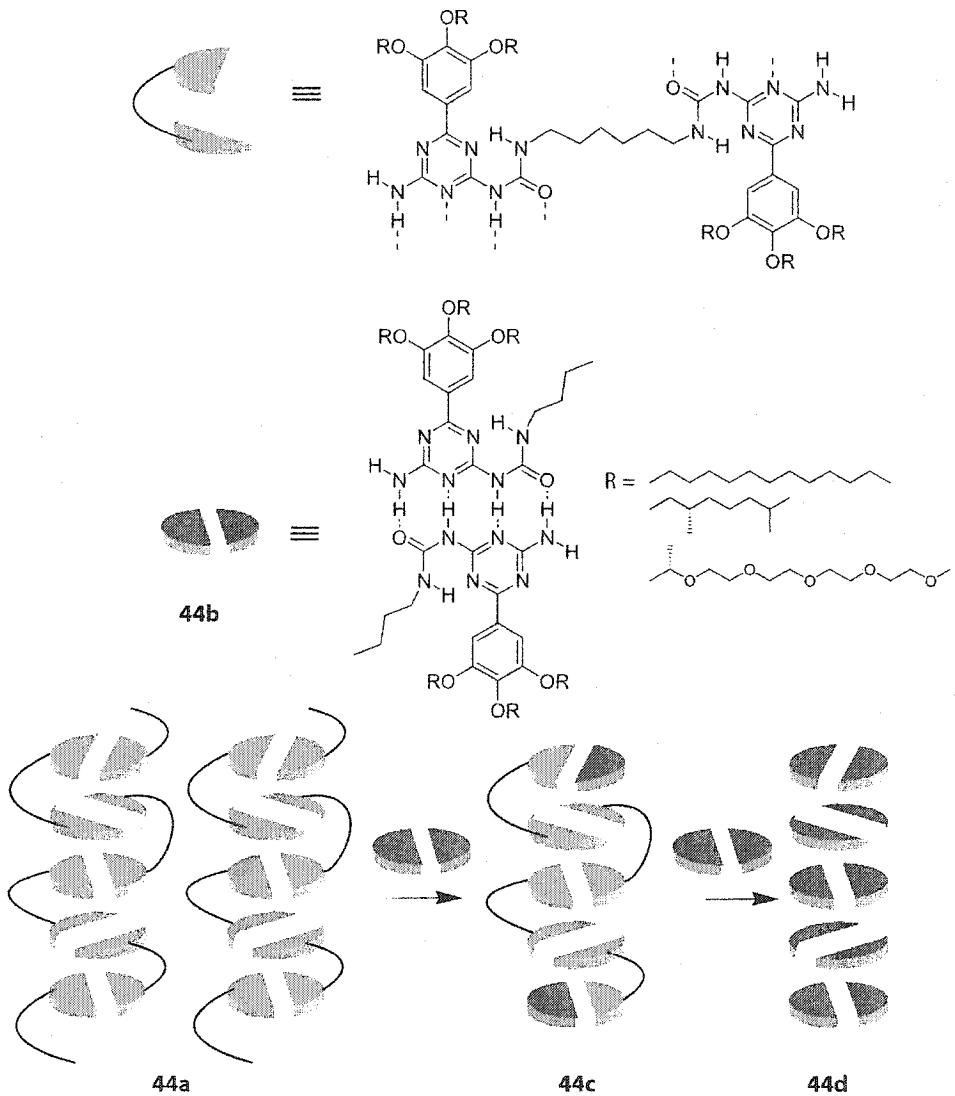


Figure 1. 49. . Supramolecular helices formed from bifunctional ureidotriazine derivatives.

1.2.3.2. Supramolecular Catalysis and Self-Replicating Systems

In natural systems, RNA molecules, viruses and antibodies optimise and amplify their functions upon guest recognition and binding.[2] This environmentally induced evolution implicitly requires the ability of these systems to reproduce themselves under specific conditions. To mimic evolution, a few unnatural, self-replicating supramolecular systems involving nucleic acids,[129] peptides,[130] and simple synthetic molecules have been investigated. These self-replicating systems should also find potential use in the construction of dynamic combinatorial libraries of non-covalently bound structures. Most of these self-replicating systems use self-complementary templates AB' and BA' which are generated autocatalytically (Figure 1. 50a).[131,132] In autocatalytic processes, molecular guests A, B', B, and A' bind onto the molecular templates AB' and BA' to form the termolecular species A-B'-AB' and B-A'-BA'. Ligation between A and A' as well as B and B' gives two AB'and BA' strands, which then serve as templates for another set of A, B', B, and A' molecules. Cross-catalytic systems have also been implemented based on the natural self-replication of nucleic acids (see below), which involves two complementary strands instead of a unique self-complementary strand (Figure 1. 50b). In cross-catalytic processes, molecular guests A, A', B, and B' bind onto the molecular templates AA' and BB' to form the termolecular species A-A'-BB' and B-B'-AA'. Ligation between A and A' as well as B and B' gives two AA'and BB' strands, which then serve as templates for another set of A, A', B, and B' molecules.

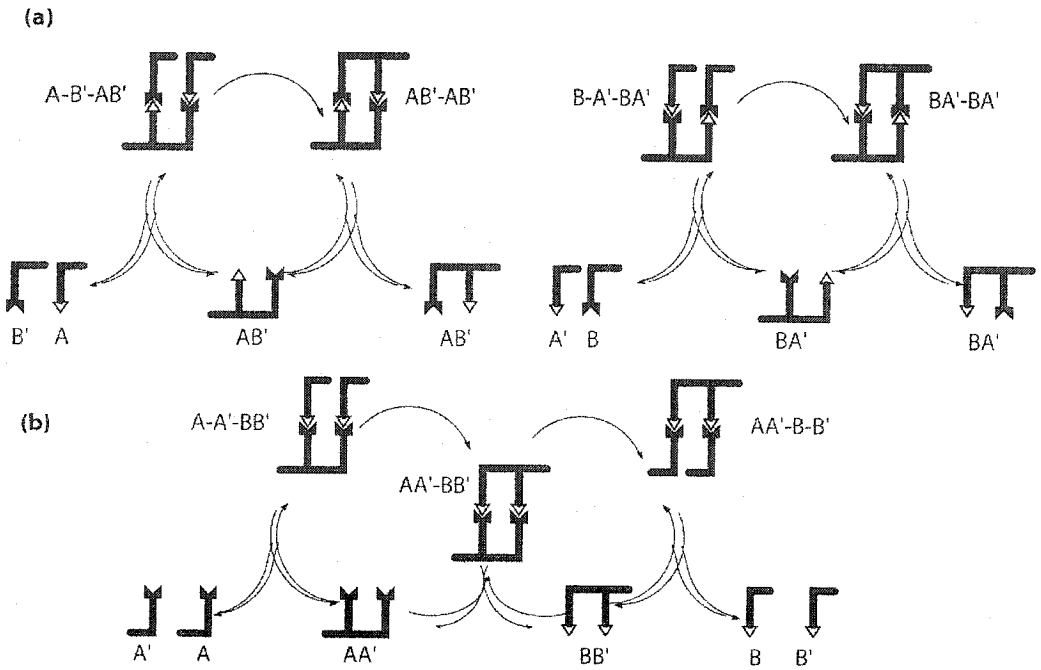


Figure 1. 50. Autocatalytic (a) and cross-catalytic (b) self-replicating systems.

The artificial self-replicating system **45+46** involves the key synthesis of a self-complementary adenine receptor **47** which consists of an amide bond formation between 5'-amino adenine **46** and pentafluorophenyl ester **44**.[133] (Figure 1. 51) The crescent-shape amide **47** uses adenine-phthalimide AD hydrogen bonds and adenine-naphthyl stacking forces to attract and bind both monomers **45** and **46**, creating a microenvironment favourable to autocatalytic reproduction.

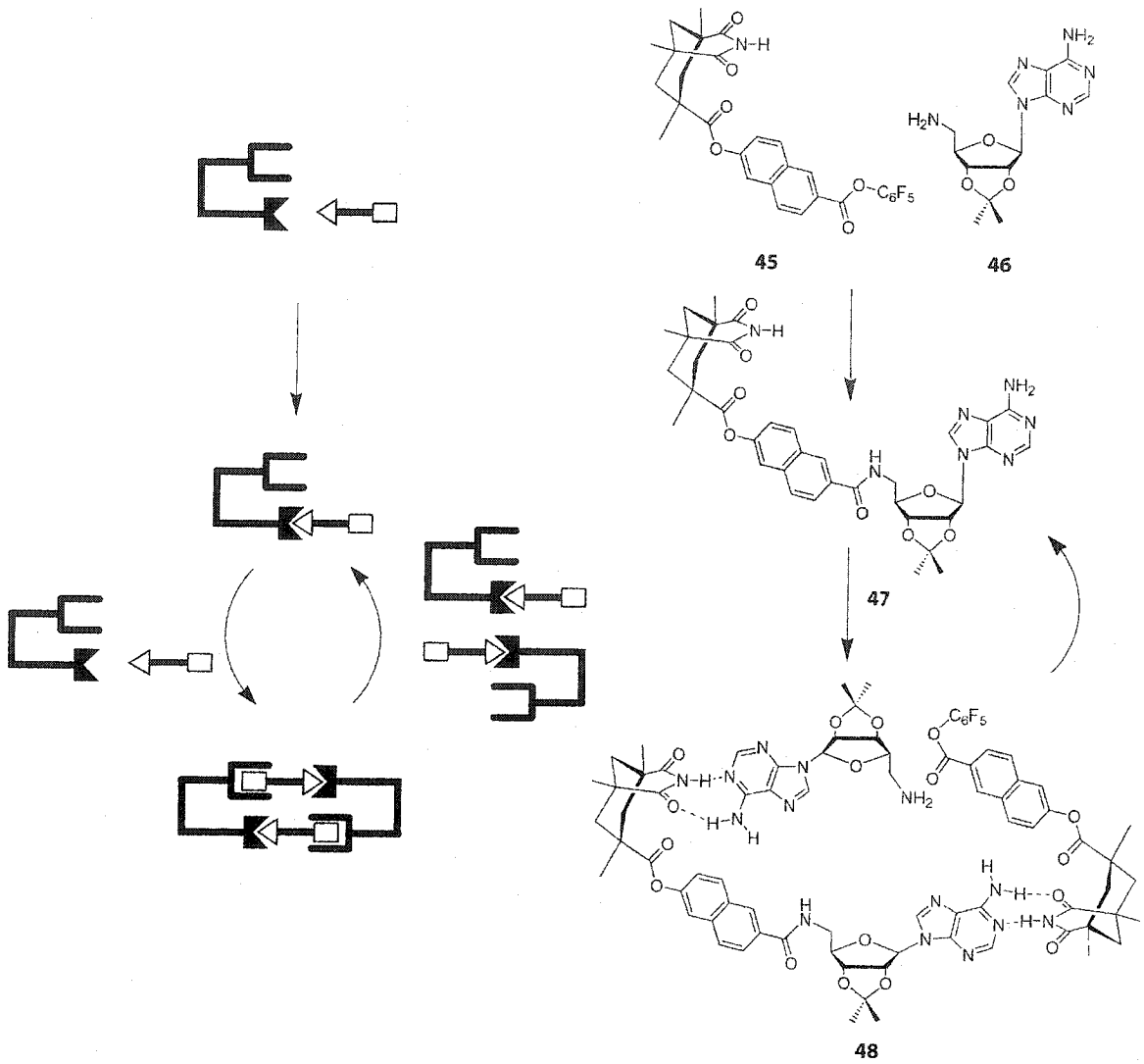


Figure 1. 51. Artificial self-replicating system involving a self-complementary adenine receptor.

Cross-catalytic systems have also been implemented based on the natural self-replication of nucleic acids, which involves two complementary strands instead of a unique self-complementary strand. These cross-catalytic processes generally occur in parallel with autocatalytic processes leading to the formation of four oligomeric strands. The system shown in Figure 1. 52 has been investigated for the template-directed self-replication of guanine (G)- and cytosine (C)-containing hexadeoxynucleotides **54**.[134]

First, a series of monoterminal protected trideoxynucleotides CCGp or CGGp **49** are reacted with water-soluble 1-(3-dimethylaminopropyl-)3-ethylcarbodiimide **50**. The activated residues CCGp or CGGp **51** are condensed with 5'-amino trideoxynucleotides nCCG or nCGG **52** to give four phosphoramidates **54**, *i.e.* two complementary strands CCGpnCCG and CGGpnCGG as well as two self-complementary strands CGGpnCCG and CCGpnCGG. In these condensation reactions, the stacking of the ligated nucleotide bases CG controls the effect of the hexanucleotide template. The template-directed formation of single hexadeoxynucleotide strands predominantly leads to self-complementary products, characteristic of autocatalytic processes. On the other hand, the combinatorial formation of these hexamers gives similar amounts of self-complementary and complementary strands, consistent with the cross-catalysis between complementary strands. These self-replicating systems should find potential use in the construction of dynamic combinatorial libraries of non-covalently bound structures.

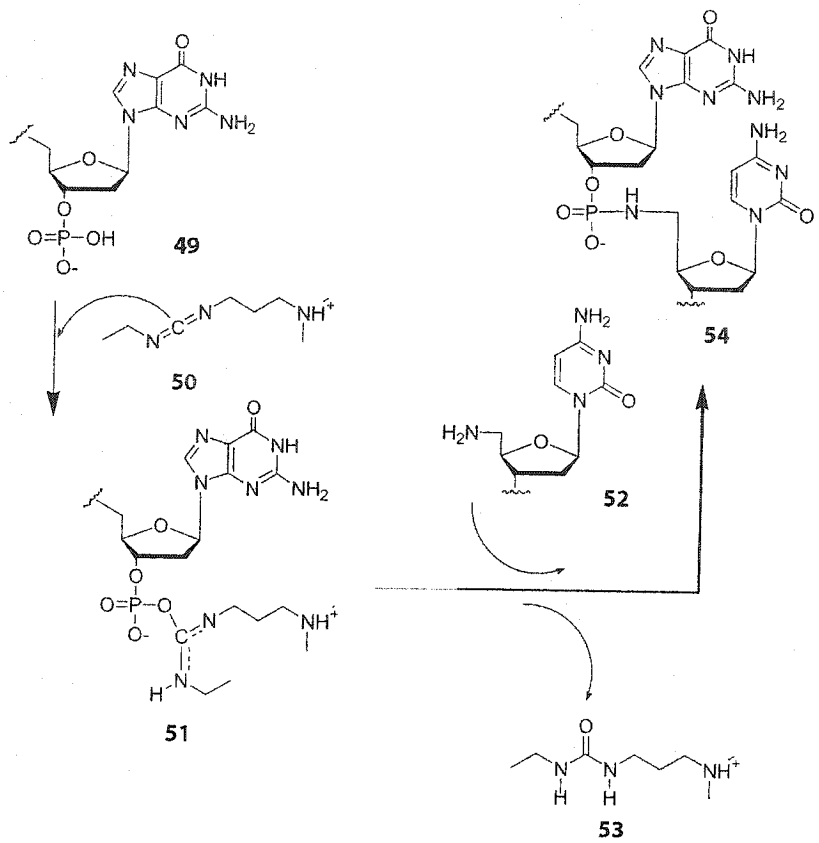


Figure 1. 52. Template-directed self-replication of guanine (G)- and cytosine (C)-containing hexadeoxynucleotides.

1.2.3.3. Supramolecular Photochemical and Electrochemical Devices

Photochemically active species have also been incorporated into supramolecular structures. This is because light-induced phenomena are involved in important biochemical devices such as in natural photosynthetic membranes.[135] Readily available chromophores, for which photochemical properties can be synthetically altered and tailored, can be used for light-induced charge separation, catalysis, or switching.[136] Once introduced into supramolecular systems, such photoactive molecules are expected to

display a photochemical response that differs from the photochemical behaviour of the individual chromophores.

1.2.3.3.1. Photo- and Electrochemical Metal-Coordinated Systems

Transition metal chromophores are attractive for the implementation of photo- and electrochemical devices like catenane **13**[14] (Figure 1. 13) and rotaxane **55** (Figure 1. 53).[137] Redox active rotaxane **55** has been synthesized from two different types of transition metal ions with two different metal-coordination modes. The copper(I) metal ion first forms a tetrahedral complex between one diphenylphenanthroline string and one diphenylphenanthroline macrocycle. The threaded complex which contains terpyridyl units at each extremity is then added to $[Ru(terpy)(acetone)_3]^{2+}$, giving the stoppered catenane **55**. Cyclovoltammograms of the resulting structure showed three distincts transitions, characteristic of the Ru(III)/Ru(II), Ru(II)/Ru(I), and Cu(II)/Cu(I) redox couples, confirming the presence of the two metal ions and, at the same time, showing the electroactive properties of catenane **55**.

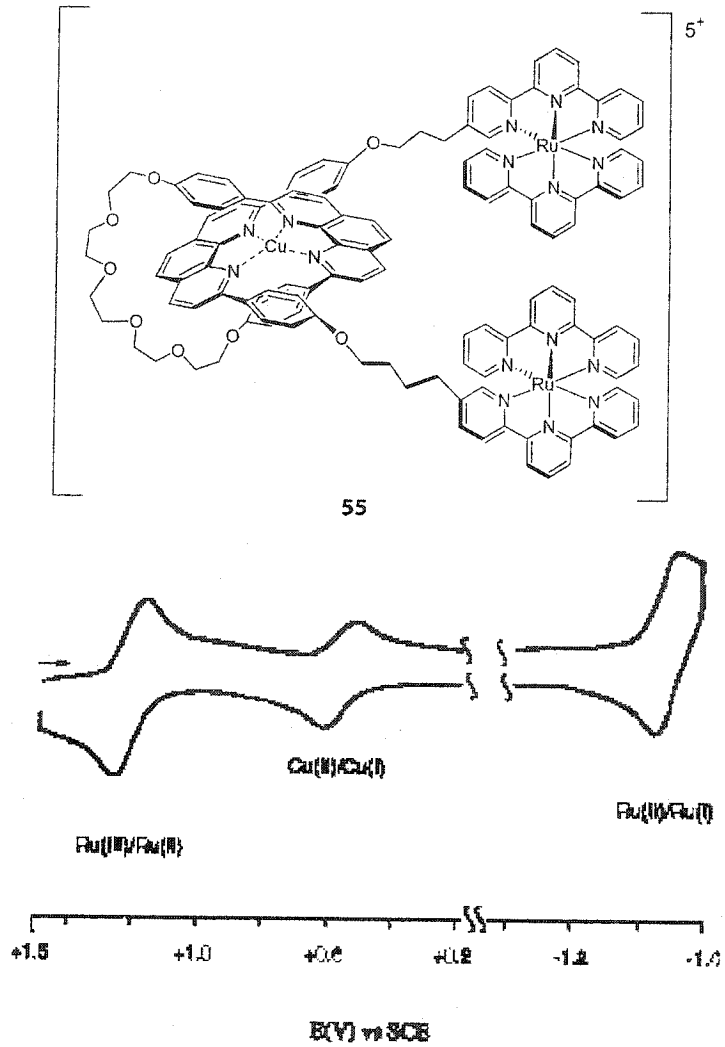
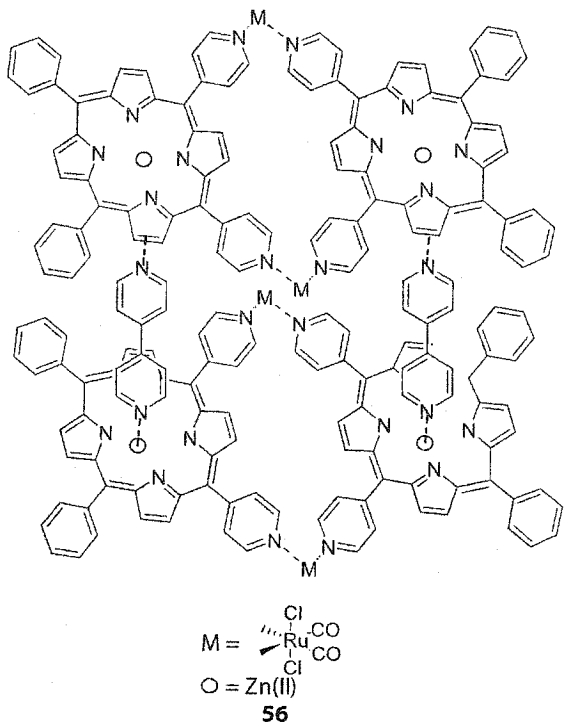


Figure 1. 53. Self-assembled redox active rotaxane **55** from two different transition metals. Inset: Redox potential plot of **55** by cyclovoltammetry.

The photochemical and redox properties of porphyrins[138] and, in particular, oligomeric and polymeric assemblies of metalloporphyrins like **56**,[139] have attracted significant attention for the design of molecular electronic and optical devices or sensors (Figure 1. 54) . Polymeric structure **56** results from the hierarchical self-assembly of 2+2 Ru(II)-Zn(II) metallacycles, during which the Ru(II) metal ion is first coordinated with pyridine-disubstituted Zn-porphyrins to form squares which then react with 4,4'-bipyridine bridging ligands. Strong Ru(II)-pyridine interactions and favourable π-π

stacking interactions between the 2+2 macrocyclic planes contribute to the thermodynamic stability the resulting molecular wire.



56

Figure 1. 54. Self-assembly of 2+2 Ru(II)-Zn(II) metallacycles into molecular wire **56.**

1.2.3.3.2. Photochromic Systems

Photochromic molecules,[140] which can exist in two structurally different equilibrium states A and B at two different wavelength ranges, have been widely incorporated in photoresponsive devices and materials.[139e,f] In such systems, the photoactive species is more stable in state A and can be irradiated using λ_1 to reach state B (Figure 1. 54). Another wavelength λ_2 is used to revert to the initial state A.

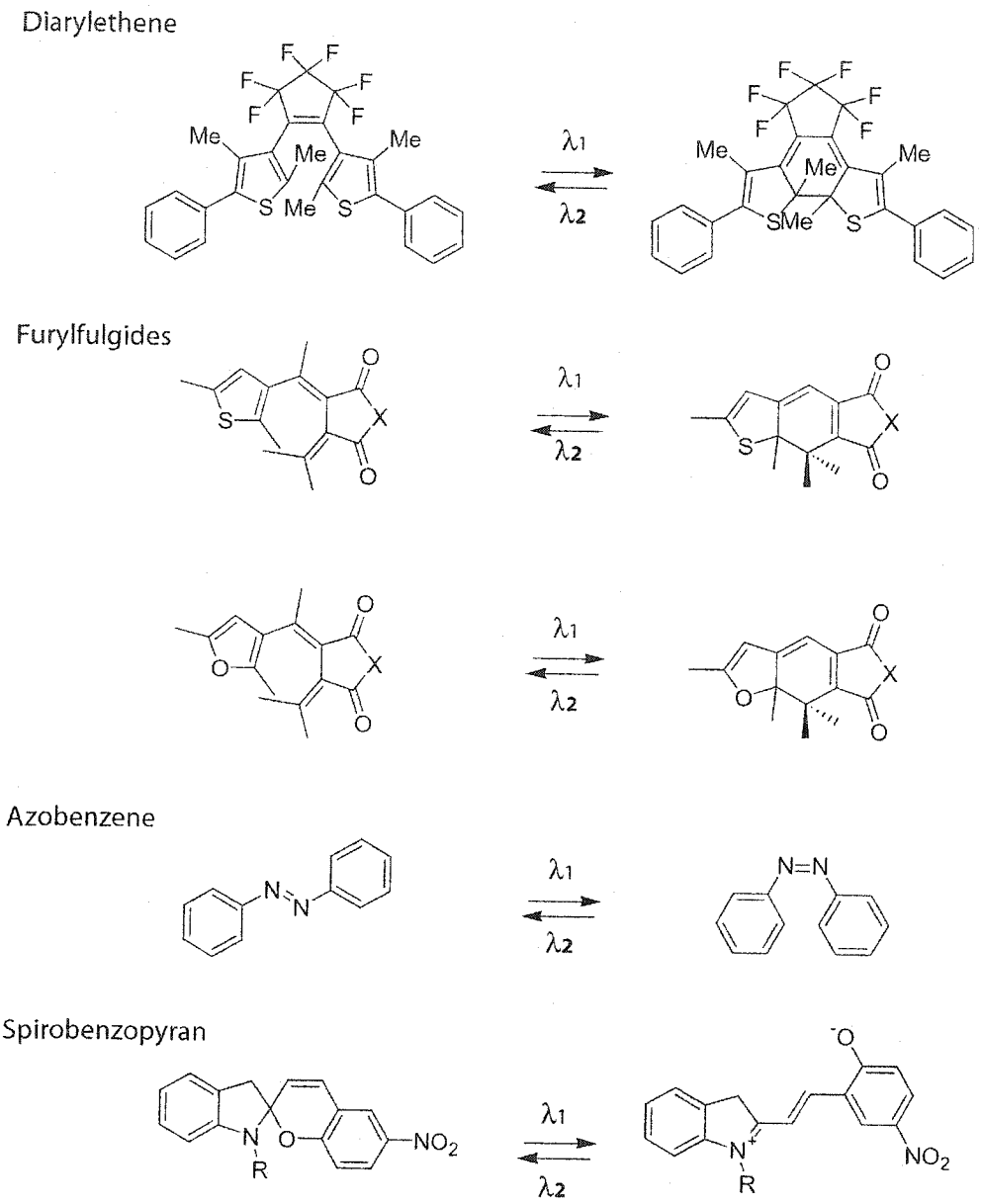


Figure 1. 55. Typical photochromic molecules.

Among these compounds, spirobenzopyrans[141, 144-152] and azobenzenes[142] undergo thermally reversible photochromic reactions, meaning that the photoisomers are thermally unstable and return to their stable form when heated. Photogenerated diarylethene[143, 153-163] and furylfulgide isomers[144, 164] exhibit thermally irreversible photochromism.

Photochromic spirobenzopyran are initially closed molecules, which open upon photoirradiation to give the merocyanine isomer.[140] The photoisomerisation of spirobenzopyrans is accompanied by a dramatic colour change, which can find potential applications in self-developing photography, ophthalmic lenses, or filters.[139e,f] The photochromic behaviour of spirobenzopyrans has been covalently bound to polysiloxanes[145] and calixarenes[146] to reduce the thermal reversibility of the isomerisation. These molecules have also been tethered to fluorescent dyes[147] to photo-modulate energy transfer processes, or attached to crown ethers[148] and chelating agents[149] to produce photoresponsive guests for metal ions. Spirobenzopyrans have been incorporated into glass surfaces,[150] polymers,[151] Langmuir monolayers,[152] Langmuir-Blodgett (LB) films,[148] liquid crystals (LC)[153] to control the physico-chemical properties of these materials using light.

Diarylethenes are especially attractive for their thermal stability. Initial open forms of diarylethenes undergo ring-closure upon photoirradiation (λ = 313 nm), which produces thermally stable, polycyclic compounds.[142] Thermal and photoreversibility can be suppressed or favoured via functionalisation,[154] providing interesting applications in image recording.[136e,f] Photoinduced ring-opening/ring-closing reactions can be used to regulate π-conjugation in thiophene-functionalised,[155] as well as ethylene-[156] or *p*-phenylene vinylene-[157] bridged diarylarenes. Thermally stable diarylethenes have been incorporated in-between β-cyclodextrins to create cavities **57a** and **57b** with photocontrolled sizes, hence tailored binding affinities,(Figure 1. 56) and to generate drug delivery systems with photocontrolled release.[158]

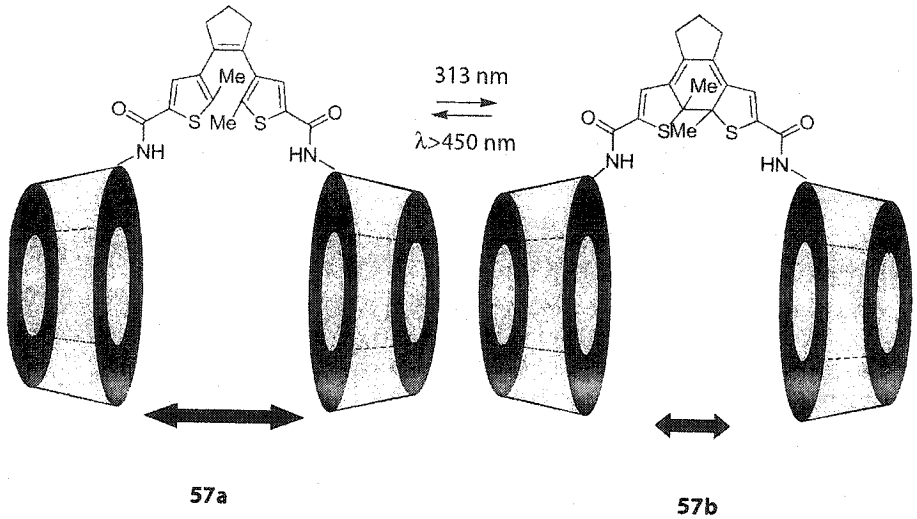


Figure 1. 56. Photoregulation of cavity size using diarylethenes.

Light can be used to switch photoinduced electron transfer in diarylethene-containing dithienylethene-porphyrin-fullerene triads[159] or to affect energy transfer processes in fluorescent dyes.[160] Diarylethenes have also been used to control the magnetic properties of radical functional groups.[161] Similar to spirobenzopyrans, photochromic diaryethenes have incorporated in materials to affect their amorphous,[162] crystalline[163] and liquid crystalline behaviour.[164]

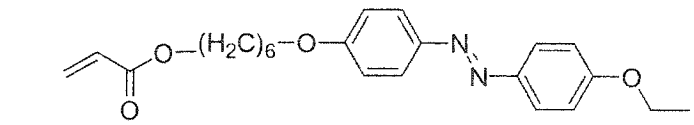
Like the open diarylethene, the open fulgide isomer closes when irradiated with UV light to give a thermally stable, fused ring system. The photoisomerisation of fulgides has been exploited to create devices and materials with interesting optoelectronic properties.[140] For example, incorporation of fulgides in fluorescing polymers have resulted in enhanced fluorescent quantum yields for the closed photoisomers compared to the individual monomers in solution.[165]

Azobenzene photochromic properties have been well exploited despite the thermal reversibility of this molecule.[166] *Trans*-azobenzene is the more stable isomer and can be

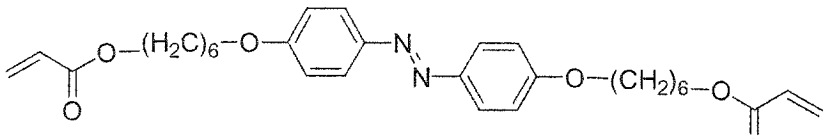
irradiated with UV light (λ = 313 nm) to form *cis*-azobenzene. Heating or irradiation with visible light (λ = 365 nm) favours the recovery of the *trans*-isomer.

Photoresponsive azobenzene have been introduced in a variety of systems ranging from individual molecules to polymers and supramolecular structures. These photoswitchable units have been incorporated in a variety of supramolecular systems such as peptides,[167] DNA,[168] dendrimers,[169], molecular hosts[170] as well as macromolecular and liquid crystalline structures.

The reversible photoisomerisation of azobenzene has been largely used to effect motions in polymer or liquid crystal (LC) matrices. These photoinduced motions can be localised to the direct neighbouring molecular species, but can also be amplified to the entire polymeric or liquid crystalline matrix. Localised motions have been used to cause phase transition in small LC[171] molecules or in polymeric LC[172] using light. For example, the photomechanical properties of azobenzene have been used in crosslinked liquid crystals **58** and **59**.[173] Photoirradiation of a polymer film containing these photoresponsive molecules caused the film to bend, amplifying the effect of light. The choice of the direction of the incident polarised beam on these polymers has observed to precisely determine the direction of the bending motion. This precise photoinduced motion can find potential applications in light-sensitive micro-machines and nanomachines.



58



59

Figure 1. 57. Photoresponsive molecules incorporated in liquid-crystalline polymers.

Numerous azobenzene-containing polymers, liquid crystals, and supramolecular systems like **60** (Figure 1. 58) have been synthesised to implement potential read-write-erase optical data storage devices. Supramolecular structures **60a** and **60b** result from the hydrogen-bond self-assembly of cyclopeptide-disubstituted azobenzene derivatives.[167] The relative orientation of the self-complementary cyclic peptides, para to the N=N linkage of the azobenzene monomers, changes during photoisomerization, thus affecting the supramolecular geometries. As a result, the *trans*-isomer forms polymeric, tape-like structures **60a**, while the peptidic extremities are brought to close proximity in the *cis*-isomer favouring intramolecular hydrogen-bonding interactions.

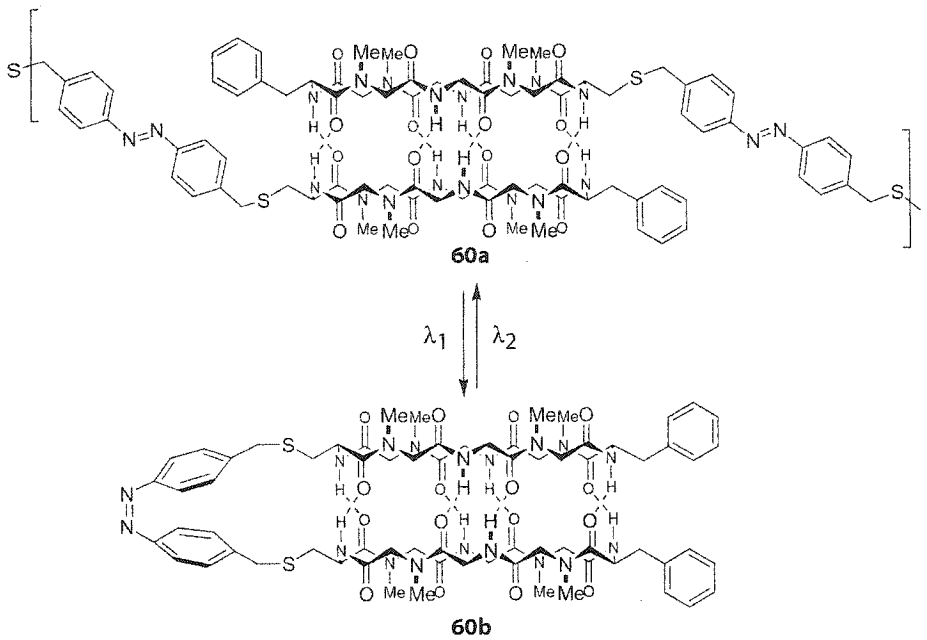
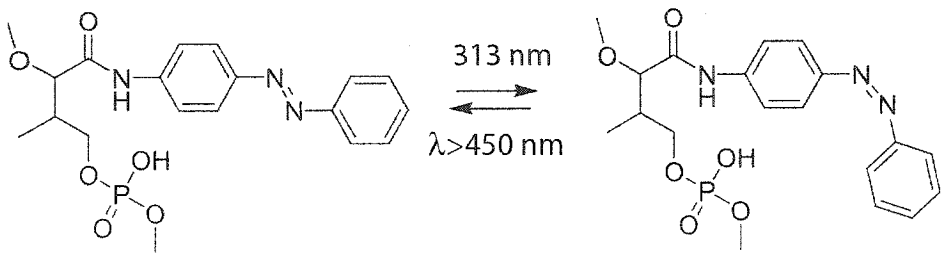


Figure 1. 58. Hydrogen-bond self-assembly of azobenzene cyclopeptides.

Amido-azobenzene units have been introduced in DNA strands **61** to regulate the formation and the dissociation of DNA triple helices.[168] In this system, the *trans*-azobenzene isomers have been shown to favour triplex formation, while the *cis*- isomer destabilised the triple helical structure upon UV light irradiation. ($300 < \lambda < 400$ nm). The dependence of triplex formation on azobenzene conformation suggested that the *trans*-azobenzene tethered DNA strand is brought to close proximity to the DNA target whereas the *cis*-azobenzene isomer displace the DNA strand away from the double helix. These results were consistent with the intercalation of the trans-azobenzene between the base pairs in the target duplex, which stabilises the triplex by stacking interactions. Destabilisation was observed in the case of the *cis*-isomer because of steric hindrance between the photogernerated species and the adjacent base.

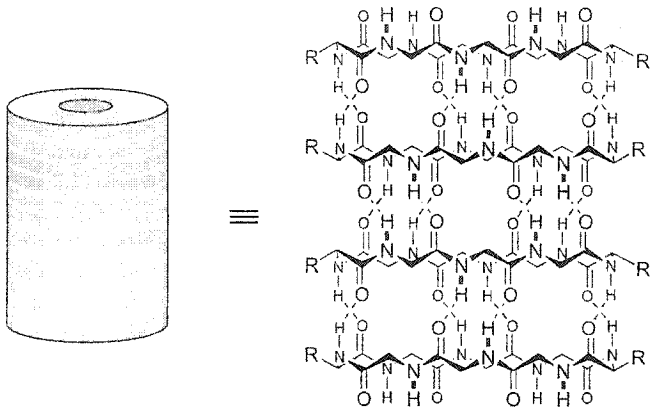


61

Figure 1. 59. Photoregulation of DNA using azobenzene.

1.2.3.4. Supramolecular Transmembrane Channels and Charge Carriers

The design and implementation of tubular supramolecular assemblies has motivated considerable interest due to the potential biological impact of these hollow nanostructures, which can serve as selective transmembrane ion channels, reaction vessels, or nanoscale transport systems.[174] Nanotube **62** arises from the hydrogen-bonding of self-complementary cyclic D,L-alternated peptides (Figure 1. 60).[174a] The properties of **62**, in particular the affinity with phospholipid membranes, can be tuned by varying the nature of the peripheral substituents. The presence of protonated glutamic acid residues in the cyclic peptides at neutral pH was found to be critical for nanotube formation, by inducing hydrogen-bonding between the stacked macrocycles.



62

Figure 1. 60. Hydrogen-bond self-assembly of peptide nanotube **62**.

More recently, similar peptide nanotubes demonstrated efficient, selective and specific antibacterial activity, by permeating cell membranes.[174b] Cyclic peptides containing hydrophilic side chains were found to give the greatest biological activities to the nanotubes. Membrane permeation measurements in oriented phospholipid multilayers showed a 70°-orientation of the peptide nanotubes, exposing most of the hydrophilic side chains to the outer interfaces, consistent with a carpet-like mechanism where repulsive hydrophobic interactions between the nanotube side chains and the membrane enables the peptides to penetrate the multilayers (Figure 1. 61).

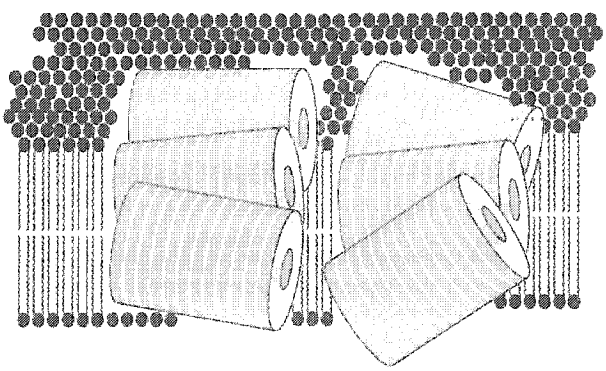
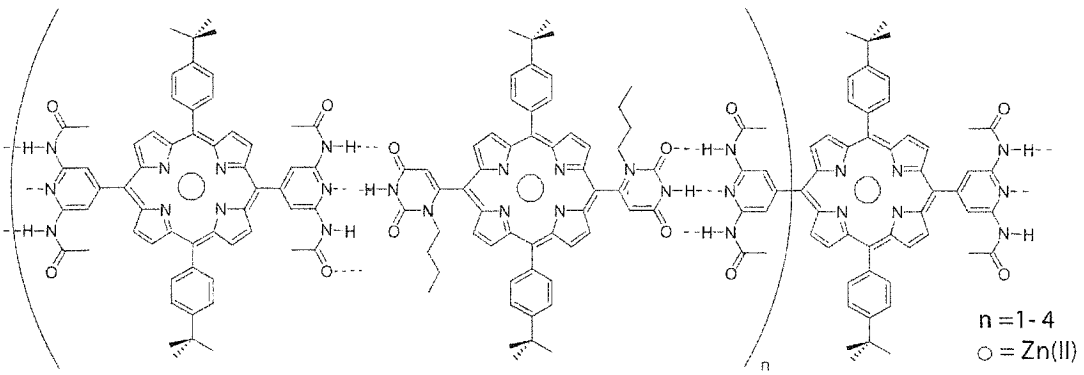


Figure 1. 61. Carpet-like cell membrane permeation mechanism.

Linear tape **63**[175] has been obtained from three DAD·ADA hydrogen-bonding interactions between complementary Zn-porphyrin metallacycles, directly linked to two uracil or two diacetylaminopyridine substituents (Figure 1. 62). Investigations on the incorporation of such self-assembled arrays into lipid membranes not only showed the conservation of the structural integrity of these supramolecular structures but also their ability to adjust their own length to the membrane thickness in aqueous media.



63

Figure 1. 62. Self-assembled linear porphyrinic tapes.

The potential use of self-assembled linear tape **63**[175] as a photogated molecular electronic conductor was investigated in lipid membranes. Transmembrane electron-transfer experiments were carried out for such hydrogen-bonded multiporphyrin assemblies, during which the photocurrent between electron acceptor A and electron B are placed at the inner and outer interfaces was measured (Figure 1. 63). These experiments showed significant photocurrent between electron acceptor A and electron donor B upon irradiation with white light, while the individual monomeric species did not respond to photolysis.

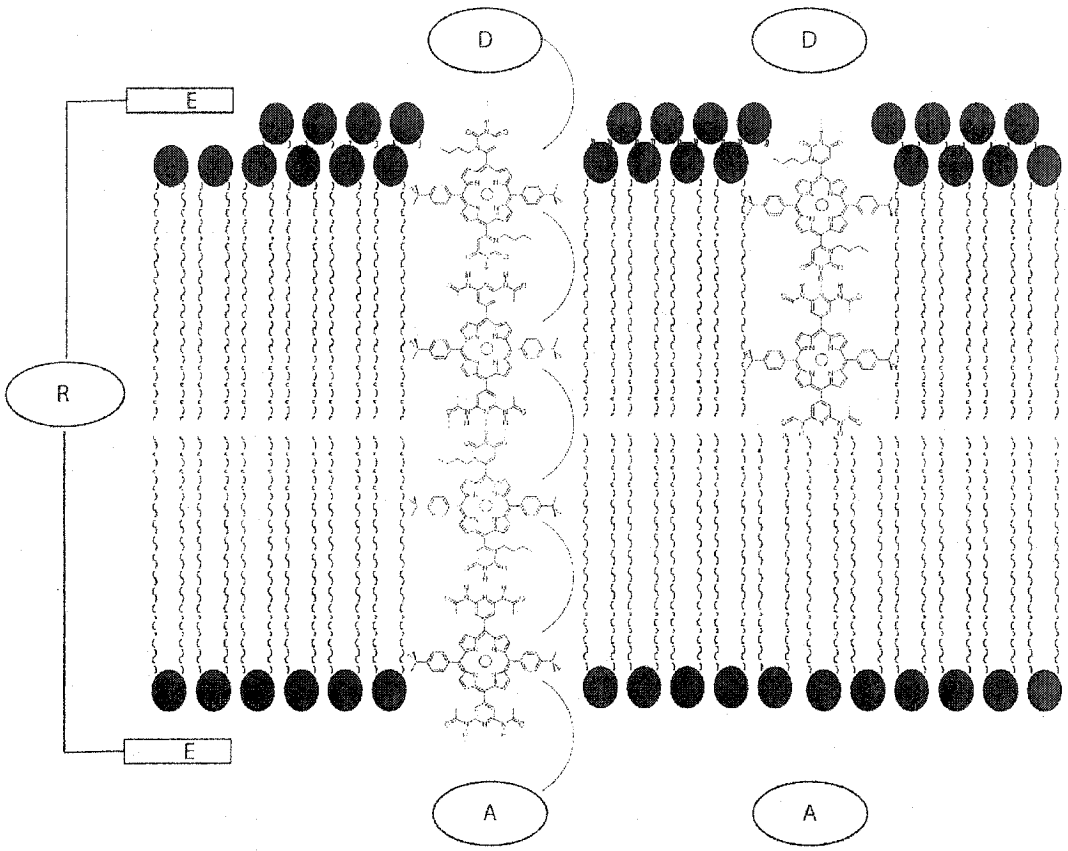


Figure 1. 63. Representation of a functional device from self-assembling porphyrin tapes self-organised into bilayers. The electron donor, D, is $K_4Fe(CN)_6$ and the acceptor, A, is anthraquinonesulfate (AQS).

1.3. Scope of the Thesis

Supramolecular chemistry has been able to build geometrically well-defined, architectures using non-covalent intermolecular interactions between preorganised low-molecular weight building blocks, and, at the same time, introduce interesting physico-chemical functionality into these self-assembled structures.

In this thesis, new functional building blocks are designed and synthesised to control supramolecular geometries. Experimental techniques and theoretical methods are

closely combined to investigate and to characterize the self-assembly processes and products.

Chapter 2 of the thesis describes the tools used to characterise the self-assembled structures. Quantum mechanical and molecular modelling methods are explained and the experimental techniques are developed.

Chapter 3 describes the synthesis of *trans*- and *cis*- azodibenzoic acid derivatives and the characterisation of their hydrogen-bonded self-assembly. An exhaustive experimental description of monomeric and oligomeric structures, supported by theoretical evidence, reveals the formation of infinite, linear tapes from the *trans*-isomer and macrocyclic tetramers from the *cis*-isomer.

Chapter 4 contains the theoretical investigation of hydrogen-bonded azodibenzoic acids using quantum mechanical methods. A new strategy is used to explain the formation of linear and macrocyclic aggregates, in which the calculated Gibbs free energies of formation are supported by the computed vibrational spectra and electron density maps.

Chapter 5 describes the implementation of theoretical methods to investigate the packing properties of macrocyclic supramolecular structures. Geometric scans using molecular mechanics methods are complemented by semi-empirical, quantum mechanical geometry optimisation to determine the spatial arrangement of these structures.

Chapter 6 expands the experimental investigation of photoresponsive supramolecular systems. Metal-coordinated or multiply hydrogen-bonded systems are introduced to improve intermolecular cohesion between the azobenzene monomers. The synthesis of azobisbenzonitrile derivative and its association with silver ions is described. Azobisbenzotriazine derivatives are synthesised and their hydrogen-bonded assembly is

predicted. The introduction of quadruple hydrogen-bonding in azobenzene-containing monomers is also explored using bis-ureidotriazine.

Chapter 7 explores the introduction of DNA-analogues in hydrogen-bonded macrocycles. The synthesis and characterisation of two complementary artificial DNA bases and their hydrogen-bonded assemblies is described both theoretically and experimentally. Theoretical calculations are also performed to predict their incorporation into DNA triple helices.

1.4. References and Notes:

---

[1] (a) J. -M. Lehn, *Supramolecular Chemistry: Concepts and Perspectives*, VCH: Weinheim, 1995. (b) G. M. Whitesides, E. E. Simanek, J. P. Mathias, C. T. Seto, D. N. Chin, M. Mammen, D. M. Gordon, *Acc. Chem. Res.*, **1995**, *28*, 37. (c) J. S. Lindsey, *New J. Chem.*, **1991**, *15*, 153. (d) D. S. Lawrence, T. Jiang, M. Levett, *Chem. Rev.*, **1995**, *95*, 2229. (e) R. E. Meléndez, A. D. Hamilton, *Top. Curr. Chem.*, **1998**, *198*, 97. (f) S. Leininger, B. Olenyuk, P. J. Stang, *Chem. Rev.*, **2000**, *100*, 853. (g) D. N. Reinhoudt, M. Crego-Calama, *Nature*, **2002**, *295*, 2403. (h) J. W. Steed, J. L. Atwood, *Supramolecular Chemistry*, John Wiley & Sons: Chicester, 2000. (i) H. –J. Schneider, A. Yatsimirsky, *Principles and Methods in Supramolecular Chemistry*, John Wiley & Sons: Chicester, 2000. (j) L. F. Lindoy, I. M. Atkinson, *Self-Assembly in Supramolecular Systems*, RSC: Cambridge, 2000. (k) V. Balzani, L. De Cola (Eds.), *Supramolecular Chemistry*, Kluwer: Dordrecht, 1992. (l) J. -M. Lehn, *Proc. Natl. Acad. Sci. USA*, **2002**, *99*, 4763.

[2] (a) A. L. Lehninger, *Biochemistry*, Worth Publishers: New York, 1976. (b) R. E. Dickerson, I. Geis, *Hemoglobin: Structure, Function, Evolution, and Pathology*, Benjamin Cummins Publishing Co.: Reading, 1983. (c) P. Dustin, *Microtubules*, 2nd ed., Springer-Verlag: New York, 1984. (d) G. M. Blackburn, M. J. Gait (Eds.), *Nucleic Acids in Chemistry and Biology*, Oxford University Press: New York, 1990.

[3] P. F. Knowles, P. G. Stockley, *Chem. Br.*, **1995**, 27.

[4] (a) P. Espinet, M. A. Esteruelas, L. A. Oro, J. L. Serrano, E. Sola, *Coord. Chem. Rev.*, **1992**, *117*, 215. (b) R. Bissell, N. Boden, *Chem. Br.*, **1995**, 38.

[5] C. D. Bain, S. D. Evans, *Chem. Br.*, **1995**, 46.

[6] (a) T. Sano, C. R. Cantor, *Proc. Natl. Acad. Sci. USA*, **1995**, *92*, 3180. (b) V. Hedge, C. –Y. Hung, P. Madhukar, R. Cummingham, T. Höpfner, R. P. Thummel, *J. Am. Chem. Soc.*, **1993**, *115*, 872. (c) M. W. Hosseini, J. –M. Lehn, *Helv. Chim. Acta*, **1987**, *70*, 1312. (d) D. G. Lonergan, G. Deslongchamps, S. Tòmas, *Tetrahedron Lett.*, **1998**, *39*, 7861. (e) D. A. Dougherty, *Science*, **1996**, *271*, 163. (f) J. –M. Lehn, R. Meric, J. –P. Vigneron, M. Cesario, J. Guilhem, C. Pascard, Z. Asfari, J. Vicens, *Supramol. Chem.*, **1995**, *5*, 97. (g) H. –J. Schneider, D. Güttes, U. Schneider, *J. Am. Chem. Soc.*, **1988**, *110*, 6449. (h) Y. Inoue, G. W. Gokel (Eds.), *Cation Binding by Macrocycles*, Marcel Dekker: New York, **1990**.

[7] (a) C. J. Pedersen, *Angew. Chem., Int. Ed. Engl.*, **1988**, *27*, 1021. (b) J. –M. Lehn, *Angew. Chem., Int. Ed. Engl.*, **1988**, *27*, 89. (c) D. J. Cram, *Angew. Chem., Int. Ed. Engl.*, **1988**, *27*, 1009.

[8] P. W. Atkins, *Physical Chemistry*, 5th ed., W. H. Freeman and Company: New York, 1994.

[9] (a) H. –J. Schneider, T. Schiestel, P. Zimmerman, *J. Am. Chem. Soc.*, **1992**, *114*, 7698. (b) A. D. Pethybridge, D. J. Spiers, *J. Chem. Soc., Farad. Trans.1*, **1976**, *9*, 64. (c) K. A. Dill, *Biochemistry*, **1990**, *29*, 7133.

[10] (a) R. A. Robinson, R. H. Stokes, *Electrolyte Solutions*, Butterworths: London, 1968. (b) J. O' M. Bockris, A. K. N. Reddy, *Modern Electrochemistry*, Plenum: New York, 1970. (c) B. E. Conway, J. O' M. Bockis, E. Yeager (Eds.), *Comprehensive Treatise on Electrochemistry, Vol. 5*, Plenum Press: New York, 1983.

[11] L. C. Pauling, *The Nature of the Hydrogen-Bond*, 3rd ed, Cornell University Press: Ithaca, 1960.

[12] (a) G. R. Desiraju, C. V. K. Sharma, *The Crystal as a Supramolecular Entity: Perspectives in Supramolecular Chemistry, Vol. 2,* John Wiley & Sons, Chicester, 1996. (b) C. B. Aakeröy, S. K. Seddon, *Chem. Soc. Rev.* **1993**, *22*, 397.

[13] (a) D. Braga, F. Grepioni, P. Sabatino, G. R. Desiraju, *Organometallics*, **1994**, *13*, 3532. (b) L. A. Estroff, C. D. Incarvito, A.D. Hamilton, *J. Am. Chem. Soc.*, **2004**, *126*, 2. (c) F. Lortie, S. Boileau, L. Bouteiller, *Chem. Eur. J.*, **2003**, *9*, 3008.

[14] T. Gulik-Krzywicki, C. Fouquey, J. -M. Lehn, *Proc. Natl. Acad. Sci. USA*, **1993**, *90*, 163.

[15] (a) G. R. Desiraju, *Acc. Chem. Res.*, **1991**, *24*, 290. (b) G. R. Desiraju, *Acc. Chem. Res.*, **1996**, *29*, 441. (c) G. R. Desiraju, *Acc. Chem. Res.*, **2002**, *35*, 565.

[16] (a) H. Adams, F. J. Carver, C. A. Hunter, N. J. Osborne, *Chem. Commun.*, **1996**, 2529. (b) H. Adams, K. D. M. Harris, G. A. Hembury, C. A. Hunter, D. Livingstone, J. F. McCabe, *Chem. Commun.*, **1996**, 2531. (c) C. A. Hunter, J. K. M. Sanders, *J. Am.. Chem. Soc.*, **1990**, *112*, 5525. (d) C. A. Hunter, *Chem. Soc. Rev.*, **1994**, *23*, 101.

[17] K. Biradha, M. J. Zaworotko, *J. Am. Chem. Soc.*, **1998**, *120*, 6431.

[18] (a) G. R. Desiraju, A. J. Gavezzotti, *J. Chem. Soc., Chem. Commun.*, **1989**, 621. (b) B. Askew, P. Ballester, C. Buhr, K. S. Jeong, S. Jones, K. Parris, K. Williams, J. Rebek Jr., *J. Am. Chem. Soc.*, **1989**, *111*, 1082. (c) J. Jazwinski, A. J. Blacker, J. –M. Lehn, M. Cesario, J. Guilhem, C. Pascard, *Tetrahedron Lett.*, **1987**, *28*, 6057. (d) J. –M. Ortholand, A. M. Slawin, N. Spencer, J. F. Stoddart, D. J. Williams, *Angew. Chem., Int. Ed. Engl.*, **1989**, 1394. (e) M. S. Vollmer, T. D. Clark, C. Steinem, M. R. Ghadiri, *Angew. Chem., Int. Ed. Engl.* **1999**, *38*, 1598. (f) D. T. Bong, T. D. Clark, J. R. Ganja, M. R. Ghadiri, *Angew. Chem., Int. Ed. Engl.*, **2001**, *40*, 988. (g) A. S. Shetty, J. Zhang, J. S. Moore, *J. Am. Chem. Soc.*, **1996**, *118*, 1019.

[19] S. C. Zimmerman, W. Wu, Z. Zeng, *J. Am. Chem. Soc.* **1991**, *113*, 196.

[20] (a) H. –J. Schneider, K. Philippi, J. Pöhlman, *Angew. Chem., Int. Ed. Engl.*, **1984**, *23*, 908. (b) J. Canceill, L. Lacombe, A. J. Collet, *J. Chem. Soc., Chem. Commun.*, **1987**, 219. (c) A. R. Fersht, *Enzyme Structure and Mechanism*, Freeman: New York, 1985.

[21] (a) K. Morokuma, *Acc. Chem. Res.*, **1977**, *10*, 294. (b) R. L. Strong, *Intermolecular Forces*, B. L. Pullman (Ed.), Reidel: Dordrecht, 1981, pp 217-232.

[22] A. V. Muehldorf, D. Van Engen, J. C. Warner, A. D. Hamilton, *J. Am. Chem. Soc.*, **1988**, *110*, 6561.

[23] A. Ben-Naim, *Hydrophobic Interactions*, Plenum Press: New York, 1980.

[24] (a) R. Foster, *Organic Charge-Transfer Complexes*, Academic: New York, 1969. (b) R. S. Mulliken, W. B. Person, *Molecular Complexes – A Lecture and Reprint Volume*, Wiley Interscience, 1969.

[25] (a) J. Vicent, V. Böhmer (Eds.), *Calixarenes*, Kluwer: Dordrecht, 1990. (b) R. M. Williams, J. M. Zwier, J. W. Verhoeven, *J. Am. Chem. Soc.*, **1994**, *116*, 6965. (c) J. L. Atwood, G. A. Koutsantonis, C. L. Raston, *Nature*, **1994**, *368*, 229.

[26] H. –J. Schneider, R. Kramer, S. Simova, U. Schneider, *J. Am. Chem. Soc.*, **1988**, *110*, 6442.

[27] (a) C. Tanford, *The Hydrophobic Effect*, 2nd ed., Wiley: New York, 1980. (b) H. S. Frank, M. W. Evans, *J. Chem. Phys.*, **1945**, *13*, 191.

[28] (a) D. B. Smithrud, T. B. Wyman, F. Diederich, *J. Am. Chem. Soc.* **1991**, *113*, 5420. (b) D. B. Smithrud, F. Diederich, *J. Am. Chem. Soc.* **1990**, *112*, 339. (c) F. Diederich, *Angew. Chem., Int. Ed. Engl.*, **1988**, *27*, 362. (d) F. N. Diederich, *Supramolecular Chemistry*, V. Balzani, L. De Cola (Eds.), Kluwer: Dordrecht, 1992, pp 119-136.

[29] (a) J. Rebek, Jr., *Acc. Chem. Res.*, **1990**, *23*, 399. (b) Y. Tobe, S. Sasaki, M. Mizuno, K. Hirose, K. Naemura, *J. Org. Chem.*, **1998**, *63*, 7481. (c) D. H. Williams, J. P. L. Cox, A. J. Doig, M. Gardner, U. Gerhard, P. T. Kaye, A. R. Lal, I. A. Nicholls, C. J. Salter, R. C. Mitchell, *J. Am. Chem. Soc.*, **1991**, *113*, 7020.

[30] (a) J.-P. Behr, J.-M. Lehn, P. Vierling, *J. Chem. Soc. Chem. Commun.* **1976**, 621. (b) J.-P. Behr, J.-M. Lehn, P. Vierling, *Helv. Chim. Acta* **1982**, *65*, 1853. (c) J.-P. Behr, J.-M. Lehn, *Helv. Chim. Acta* **1980**, *63*, 2112.

[31] P. Tecilla, R. P. Dixon, G. Slobodkin, D. S. Alavi, D. H. Waldeck, A. D. Hamilton, *J. Am. Chem. Soc.*, **1990**, *112*, 9408.

[32] (a) W. L. Jorgensen, J. Pranata, *J. Am. Chem. Soc.*, **1990**, *112*, 2008. (b) T. J. Murray, S. C. Zimmerman, *J. Am. Chem. Soc.*, **1992**, *114*, 4010. (c) E. Fan, S.A. Van Arman, S. Kincaid, A. D. Hamilton, *J. Am. Chem. Soc.*, **1993**, *115*, 369.

[33] F. Garcia-Tellado, S. Goswami, S. K. Chang, S. Geib, A. D. Hamilton, *J. Am. Chem. Soc.*, **1990**, *112*, 7393.

[34] (a) H. L. Frisch, E. Wasserman, *J. Am. Chem. Soc.*, **1961**, *83*, 3789. (b) I. T. Harrison, S. Harrison, *J. Am. Chem. Soc.*, **1967**, *89*, 5723. (c) G. Schill, C. Zürcher, W. Vetter, *Chem. Ber.*, **1973**, *106*, 228. (d) G. Schill, *Catenanes, Rotaxanes and Knots*, Academic Press: New York, 1971.

[35] (a) I. T. Harrison, *J. Chem. Soc., Perkin Trans. 1*, **1974**, 301. (b) G. Schill, W. Beckmann, N. Schweickert, H. Fritz, *Chem. Ber.*, **1986**, *119*, 2647.

[36] (a) J. F. Stoddart, *Pure Appl. Chem.*, **1988**, *60*, 467. (b) D. M. Amabilino, J. F. Stoddart, *New Scientist*, **1994**, 25. (c) D. M. Amabilino, J. F. Stoddart, D. J. Williams, *Chem. Mater.*, **1994**, *6*, 1159. (d) S. J. Stoddart, S. J. Langford, J. F. Stoddart, *Pure Appl. Chem.*, **1996**, *68*, 1255. (e) D. Philp, J. F. Stoddart, *Angew. Chem., Int. Ed. Engl.*, **1996**, *35*, 1155. (f) P. T. Glink, J. F. Stoddart, *Pure Appl. Chem.*, **1998**, *70*, 419. (g) J. F. Stoddart, *Proc. Natl. Acad. Sci.*, **2002**, *99*, 4797.

[37] (a) P. L. Anelli, P. R. Ashton, R. Ballardini, V. Balzani, M. Delgado, M. T. Gandolfi, T. T. Goodnow, A. E. Kaifer, D. Philp, M. Pietraskiewicz, L. Prodi, M. V. Reddington, A. M. Z. Slawin, N. Spencer, J. F. Stoddart, C. Vicent, D. J. Williams, *J. Am. Chem. Soc.*,

1992, *114*, 193. (b) P. R. Ashton, D. Philp, M. V. Reddington, A. M. Z. Slawin, N. Spencer, J. F. Stoddart, D. J. Williams, *J. Chem. Soc., Chem. Commun.*, **1991**, 1680.

[38] E. Córdova, R. A. Bissell, A. E. Kaifer, *J. Org. Chem.*, **1995**, *60*, 1033.

[39] (a) J. –M. Kern, J. –P. Sauvage, J. –L. Weidmann, N. Armaroli, L. Flamigni, P. Ceroni, V. Balzani, *Inorg. Chem.*, **1997**, *36*, 5329. (b) B. Mohr, M. Weck, J. –P. Sauvage, R. H. Grubbs, *Angew. Chem., Int. Ed. Engl.*, **1997**, *36*, 1308. (c) C. Pascard, J. Guilhem, S. Chardon-Noblat, J. –P. Sauvage, *New J. Chem.*, **1993**, *17*, 331. (d) D. B. Amabilino, J. –P. Sauvage, *Chem. Commun.*, **1996**, 2441. (e) M. Fujita, F. Ibukuro, H. Hagihara, K. Ogura, *Nature*, **1994**, *367*, 720. (f) M. Fujita, F. Ibukuro, K. Yamaguchi, K. Ogura, *J. Am. Chem. Soc.*, **1995**, *117*, 4175.

[40] C. O. Dietrich-Buchecker, J. – P. Sauvage, J. –M. Kern, *J. Am. Chem. Soc.*, **1984**, *106*, 3043.

[41] (a) J. –C. Chambron, V. Heitz, J. –P. Sauvage, *J. Am. Chem. Soc.*, **1993**, *115*, 12378. (b) M. Linke, J. –C. Chambron, V. Heitz, J. –P. Sauvage, *J. Am. Chem. Soc.*, **1997**, *119*, 11329. (c) S. S. Zhu, P. J. Carroll, T. M. Swager, *J. Am. Chem. Soc.*, **1996**, *118*, 8713. (d) P. N. W. Baxter, H. Sleiman, J. –M. Lehn, K. Rissanen, *Angew. Chem., Int. Ed. Engl.*, **1997**, *36*, 1294. (e) H. Sleiman, P. N. W. Baxter, J. –M. Lehn, K. Airola, K. Rissanen, *Inorg. Chem.*, **1997**, 4734.

[42] M. –J. Brienne, J. Gabard, M. Leclerq, J. –M. Lehn, M. Cesario, C. Pascard, M. Cheve, G. Dutruc-Rosset, *Tetrahedron Lett.*, **1994**, *35*, 8157.

[43] M. Bailey, C. J. Brown, *Acta Crystallogr*, **1967**, *22*, 387.

[44] R. Alcala, S. Martínez-Carrera, *Acta Crystallogr*, **1972**, *B28*, 1671.

[45] Y. Ducharme, J. D. Wuest, *J. Org. Chem.*, **1988**, *53*, 5787.

[46] (a) J. -M. Lehn, M. Mascal, A. DeCian, J. Fischer, *J. Chem. Soc., Chem. Commun.*, **1990**, 479. (b) J. A. Zerkowski, C. T. Seto, D. A. Wierda, G. M. Whitesides, *J. Am. Chem. Soc.*, **1990**, *112*, 9025. (c) J. A. Zerkowski, J. C. McDonald,C. T. Seto, D. A. Wierda, G. M. Whitesides, *J. Am. Chem. Soc.*, **1994**, *116*, 2382. (d) J. A. Zerkowski, G. M. Whitesides, *J. Am. Chem. Soc.*, **1994**, *116*, 4298. (e) J. A. Zerkowski, J. P. Mathias, G. M. Whitesides, *J. Am. Chem. Soc.*, **1994**, *116*, 4305. (f) G. Gotarelli, S. Masiero, E. Mezzina, S. Pieraccini, J. P. Rabe, P. Samori, G. P. Spada, *Chem. Eur. J.*, **2000**, *6*, 3242. (g) T. Kato, *Science*, **2002**, *295*, 2414.s

[47] (a) S. Hanessian, A. Gomtsyan, M. Simard, S. Roelens, *J. Am. Chem. Soc.*, **1994**, *116*, 4495. (b) T. Giorgi, S. Lena, P. Mariani, M. A. Cremoni, S. Masiero, S. Pieraccini, J. P. Rabe, P. Samori, G. Piero, G. P. Spada, G. Gottarelli, *J. Am. Chem. Soc.*, **2003**, *125*, 14741. (c) S. L. Forman, J. C. Fettinger, S. Pieraccini, G. Gottarelli, J. T. Davis, *J. Am. Chem. Soc.*, **2000**, *122*, 406.

[48] J. S. Geib, C. Vincent, E. Fan, A. D. Hamilton, *Angew. Chem., Int. Ed. Engl.*, **1993**, *32*, 119.

[49] (a) J. –M. Lehn, J. –P. Sauvage, J. Simon, R. Ziessel, C. P. Leopardi, G. Germain, J. –P. Declercq, M. Van Meersche, *New J. Chem.* , **1983**, *7*, 413. (b) A. F. Williams, *Pure Appl. Chem.*, **1996**, *68*, 1285. (c) J. –M. Lehn, A. Rigault, J. Siegel, J. Harrowfield, B. Chevrier, D. Moras, *Proc. Natl. Acad. Sci. USA*, **1987**, *84*, 2565. (d) J. –M. Lehn, A. Rigault, *Angew. Chem., Int. Ed. Engl.*, **1988**, *27*, 1095. (e) R. Krämer, J. –M. Lehn, A. Marquis-Rigaud, *Proc. Natl. Acad. Sci. USA*, **1993**, *90*, 5394. (f) E. C. Constable, M. G.

B. Drew, M. D. Ward, *J. Chem. Soc., Chem. Commun.*, **1987**, 1600. (g) E. C. Constable, A. J. Edwards, R. Martinez-Mánez, P. R. Raithby, *J. Chem. Soc., Dalton Trans.*, **1995**, 3253.

[50] U. Koert, M. M. Harding, J. –M. Lehn, *Nature*, **1990**, *346*, 339.

[51] B. Hasenknopf, J. –M. Lehn, *Helv. Chim. Acta*, **1996**, *79*, 1643.

[52] B. Hasenknopf, J. –M. Lehn, G. Baum, D. Fenske, *Proc. Natl. Acad. Sci. USA*, **1996**, *93*, 1397.

[53] (a) G. S. Hanan, C. R. Arana, J. –M. Lehn, G. Baum, D. Fenske, *Chem. Eur. J.*, **1996**, *2*, 1292. (b) G. S. Hanan, C. R. Arana, J. –M. Lehn, D. Fenske, *Angew. Chem., Int. Ed. Engl.*, **1995**, *34*, 1122.

[54] (a) S. Aitipamula, P. K. Thallapally, R. Thaimattam, M. Jaskólski, G. R. Desiraju, *Org. Lett.*, **2002**, *4*, 921. (b) P. N. W. Baxter, G. S. Hanan, J. -M. Lehn, *Chem. Commun.*, **1996**, 2019.

[55] D. M. Bassani, J. –M. Lehn, K. Fromm, D. Fenske, *Angew. Chem., Int. Ed. Engl.*, **1998**, *37*, 2364.

[56] (a) P. N. W. Baxter, J. -M. Lehn, J. Fischer, M. -T. Youinou, *Angew, Chem. Int. Ed. Engl.*, **1994**, *33*, 2284. (b) P. N. W. Baxter, J. -M. Lehn, B. O. Kneisel, D. Fenske, *Chem. Commun.*, **1997**, 2231. (c) P. N. W. Baxter, J. -M. Lehn, B. O. Kneisel, D. Fenske, *Angew. Chem., Int. Ed. Engl.*, **1997**, *36*, 1978.

[57] (a) S. C. Zimmerman, B. F. Duerr, *J. Org. Chem.*, **1992**, *57*, 2215. (b) S. Tirumala, J. T. Davis, *J. Am. Chem. Soc.* **1997**, *119*, 2769. (c) J. L. Sessler, J. Jayawickramarajah, M. Sathiosatham, C. L. Sherman, J. S. Brodbelt, *Org. Lett.*, **2003**, *5*, 2627.

[58] (a) S. -W. Lai, M. C. -W. Chan, S. -M. Peng, C. –M. Che, *Angew. Chem., Int. Ed. Engl.*, **1999**, *38*, 669. (b) J. R. Hall, S. J. Loeb, G. K. H. Shimizu, G. P. A. Yap, *Angew. Chem., Int. Ed. Engl.*, **1998**, *37*, 121.

[59] F. M. Romero, R. Ziessel, A. Dupont-Gervais, A. van Dorsselaer, *J. Chem. Soc., Chem. Commun.*, **1996**, 551.

[60] (a) P. J. Stang, B. Olenyuk, J. Fan, A. M. Arif, *Organometallics*, **1996**, *15*, 904. (b) M. Fujita, J. Yazaki, K. Ogura, *J. Am. Chem. Soc.*, **1990**, *112*, 5645. (c) M. Fujita, J. Yazaki, K. Ogura, *Chem. Lett.*, **1991**, 1031. (d) P. J. Stang, D. H. Cao, *J. Am. Chem. Soc.*, **1994**, *116*, 4981. (d) M. Fujita, Y. J. Kwon, S. Washizu, K. Ogura, *J. Am. Chem. Soc.*, **1994**, *116*, 1151. (e) H. Rauter, E. C. Hillgeris, A. Erxleben, B. Lippert, *J. Am. Chem. Soc.*, **1994**, *116*, 616.

[61] (a) C. M. Drain, X. Shi, T. Milic, F. Nifiatis, *Chem. Commun.*, **2001**, 287. (b) J. Yang, E. Fan, S. J. Geib, A. D. Hamilton, *J. Am. Chem. Soc.*, **1993**, *115*, 5314.

[62](a) For dicarboxylic acids: J. Yang, J. -L. Marendaz, S. J. Geib, A. D. Hamilton, *Tetrahedron Lett.*, **1994**, *35*, 3665. (b) A. Zafar, J. Yang, S. J. Geib, A. D. Hamilton, *Tetrahedron Lett.*, **1996**, *37*, 2327. (c) S. C. Zimmerman, F. Zeng, D. E. C. Reichert, S. V. Kolotuchin, *Science*, **1996**, *271*, 1095 (d) P. Thiyagarajan, F. Zeng, C. Y. Ku, S. C. Zimmerman, *J. Mater. Chem.*, **1997**, *7*, 1221. (e) F. Zeng, S. C. Zimmerman, S. V. Kolotuchin, D. E. C. Reichert, Y. Ma, *Tetrahedron*, **2002**, *58*, 825. (f) For on cyanuric acid-melamine systems: refs 1, M. Mammen, E. E. Simanek, G. M. Whitesides, *J. Am. Chem. Soc.*, **1996**, *118*, 12614. (g) For hexamers using the DDA·AAD hydrogen-bonding motif: M. Mascal, N. M. Hext, R. Warmuth, J. R. Arnall-Culliford, M. H. Moore, J. P.

Turkenburg, *J. Org. Chem.*, **1999**, *64*, 8479. (h) H. Fenniri, P. Mathivanan, K. L. Vidale, D. M. Sherman, K. Hallenga, K. V. Wood, J. G. Stockwell, *J. Am. Chem. Soc.*, **2001**, *123*, 3854. (i) H. Fenniri, B. Deng, A. E. Ribbe, *J. Am. Chem. Soc.*, **2002**, *124*, 11064. (j) A. Marsh, M. Silvestri, J. -M. Lehn, *Chem. Commun.*, **1996**, 1527.

[63] (a) S. V. Kolotuchin, S. C. Zimmerman, *J. Am. Chem. Soc.*, **1998**, *120*, 9092.

[64] (a) C. T. Seto, G. M. Whitesides, *J. Am. Chem. Soc.*, **1990**, *112*, 6409. (b) C. T. Seto, G. M. Whitesides, *J. Am. Chem. Soc.*, **1991**, *113*, 712. (c) C. T. Seto, J. P. Mathias, G. M. Whitesides, *J. Am. Chem. Soc.*, **1993**, *115*, 1321. (d) C. T. Seto, G. M. Whitesides, *J. Am. Chem. Soc.*, **1993**, *115*, 1330. (e) D. N. Chin, D. M. Gordon, G. M. Whitesides, *J. Am. Chem. Soc.*, **1994**, *116*, 12033.

[65] (a) O. F. Schall, G. W. Gokel, *J. Am. Chem. Soc.*, **1994**, *116*, 6089. (b) M. S. Kim, G. W. Gokel, *J. Chem. Soc., Chem. Commun.*, **1987**, 1686. (c) C. A. Hunter, L. D. Sarson, *Angew. Chem., Int. Ed. Engl.*, **1994**, *33*, 2313. (d) T. Kusukawa, M. Fujita, *J. Am. Chem. Soc.* **1999**, *121*, 1397.

[66] C. M. Drain, R. Fischer, E. G. Nolen, J. –M. Lehn, *J. Chem. Soc., Chem. Commun.*, **1993**

[67] (a) R. Wyler, J. de Mendoza, J. Rebek, *Angew. Chem., Int. Ed. Engl.*, **1993**, *32*, 1699. (b) N. Branda, R. Wyler, J. Rebek, *Science*, **1994**, *263*, 1267.

[68] (a) S. Mecozzi, J. Rebek, Jr., *Chem. Eur. J.*, **1998**, *4*, 1016. (b) C. Valdés, U. P. Spitz, S. W. Kubik, J. Rebek, *Angew. Chem., Int. Ed. Engl.*, **1995**, *34*, 1885. (c) R. S. Meissner, J. Rebek, Jr., J. De Mendoza, *Science*, **1995**, *270*, 1485. (d) J. M. Rivera, T. Martin, J. Rebek, *J. Am. Chem. Soc.*, **1998**, *120*, 819.

[69] (a) P. Baxter, J. –M. Lehn, A. De Cian, J. Fisher, *Angew. Chem., Int. Ed. Engl.*, **1993**, *32*, 69. (b) A. Marquis-Rigaud, A. Dupont-Gervais, P. N. W. Baxter, A. Van Dorsselaer, J.-M. Lehn, *Inorg. Chem.*, **1996**, *35*, 2307.

[70] (a) M. Fujita, S. –Y. Yu, T. Kusukawa, H. Funaki, K. Ogura, K. Yamaguchi, *Angew. Chem., Int. Ed. Engl.*, **1998**, *37*, 2082. (b) S. Mann, G. Huttner, L. Zsolnai, K. Heinze, *Angew. Chem., Int. Ed. Engl.*, **1996**, *35*, 2082.

[71] J. S. Fleming, K. L. V. Mann, C. –A. Carrez, E. Psillakis, J. C. Jeffrey, J. A. McCleverty, M. D. Ward, *Angew. Chem. Int. Ed.*, **1998**, *37*, 1279.

[72] C. Bruckner, R. E. Powers, K. N. Raymond, *Angew. Chem., Int. Ed. Engl.*, **1998**, *37*, 1837.

[73] S. Roche, C. Haslam, H. Adams, S. L. Heath, J. A. Thomas, *J. Chem. Soc., Chem. Commun.*, **1998**, 1681.

[74] (a) M. Fujita, D. Oguro, M. Miyazawa, H. Oka, K. Yamaguchi, K. Ogura, *Nature*, **1995**, *378*, 469. (b) F. Ibukuro, T. Kusuwaka, M. Fujita, *J. Am. Chem. Soc.*, **1998**, *120*, 8561. (c) P. J. Stang, B. Olenyuk, D.C. Muddiman, R. D. Smith, *Organometallics*, **1997**, *16*, 3094.

[75] B. Olenyuk, J. A. Whiteford, A. Fechtenkötter, P. J. Stang, *Nature*, **1999**, *398*, 796.

[76] N. Takeda, K. Umemoto, K. Yamaguchi, M. Fujita, *Nature*, **1999**, *398*, 794.

[77] (a) H. Abourahma, A. W. Coleman, B. Moulton, B. Rather, P. Shahgaldian, M. J. Zaworotko, *Chem. Commun.*, 2001, 2380. (b) B. Moulton, J. Lu, A. Mondal, M. J. Zaworotko, *Chem. Commun.*, 2001, 863.

[78] (a) H. Fraenkel-Conrat, R. C. Williams, *Proc. Natl. Acad. Sci. USA*, **1955**, *41*, 690. (b) H. Fraenkel-Conrat, *J. Am. Chem. Soc.*, **1956**, *78*, 882. (c) M.H.V. Van Regenmortel and H. Fraenkel-Conrat (eds.), *Plant Viruses, Vol. 2, The Rod-Shaped Plant Viruses*, New York: Plenum Press, 1986.

[79] (a) W. M. Stanley, *Science*, **1935**, *81*, 644. (b) M. A. Lauffer, A. T. Ansevin, T. E. Cartwright, C. C. Brinton, Nature, **1958**, *181*, 1338. (c) A. Tsugita, D. T. Gish, J. Young, H. Fraenkel-Conrat, C. A. Knight, W. M. Stanley, *Proc. Natl. Acad. Sci. USA*, **1960**, *46*, 1463. (d) F. A. Anderer, H. Uhlig, E. Weber, G. Schramm, *Nature*, **1960**, *186*, 922.

[80] (a) P. Goelet, G. P. Lomonossoff, P. J. G. Butler, M. E. Akam, M. J. Gait, J. Karn, *Proc. Natl. Acad. Sci. USA*, **1982**, *79*, 5818. (b) I. Solis, F. Cercia-Arenal, *Virology*, **1990**, *177*, 553.

[81] (a) G. Stubbs, S. Warren, K. C. Holmes, *Nature*, 1977, **267**, 216. (b) G. Stubbs, C. Stauffacher, *J. Mol. Biol.*, **1981**, *152,* 387. (c) K. Namba, G. Stubbs, *Acta Cryst.*, **1985**, ***A41***, 252. (d) K. Namba, G. Stubbs, *Science*, **1986**, ***231***, 1401. (d) K. Namba, R. Pattanayek, G. Stubbs, *J. Mol. Biol.*, **1989**, *208*, 307.

[82] D. L. D. Caspar, *Nature*, **1956**, *177*, 928.

[83] (a) J. D.Watson, *Biochim. Biophys. Acta*, **1954**, 13, 10. (b) R. E. Franklin, *Nature*, **1955**, *175*, 379. (c) R. E. Franklin, *Nature*, **1956**, *177*, 928. (d) R. E. Franklin, *Acta Cryst.*, **1958**, 11, 213.

[84] A. C. Bloomer, J. N. Champness, G. Bricogne, R. Staden, A. Klug, A. *Nature*,**1978**, *276*, 362.

[85] (a) R. E. Franklin, D. L. D.Caspar, A. Klug, in *Plant Pathology: Problems and Progress, 1908-1958*, C.S. Holton, et al. (eds.), University of Wisconsin Press: Madison, 1959, pp. 447-461. (b) R. E. Franklin, J. D. Bernal, **1958**, *182*, 154.

[86] R. E. Franklin, R.G. Gossling, *Nature*, **1953**,*172*, 156.

[87] (a) R. E. Franklin, R. G. Gossling, *Nature*, **1953**, *171*, 740. (b) J. D. Watson, F. H. C. Crick, *Nature*, **1953**, *171*, *737*.

[88] J. D. Watson, F. H. C. Crick, *Nature*, **1953**, *171*, 964.

[89] (a) T. A. Winters , *Curr. Opin. Mol. Ther.*, **2000**, *6*, 670. (b) D. E. Gilbert, J. Feigon, *Curr. Opin. Struc. Biol.*, **1999**, *9*, 305.

[90] G. Felsenfeld, D. R. Davies, A. Rich, *J. Am. Chem. Soc.*, **1957**, *79*, 2023.

[91] Triplexes: (a) C. Giovannangeli, C. Hélène, *Curr. Opin. Mol. Ther.*, **2000**, *2*, 288. (b) D. Praseuth, A. L. Guieysse, C. Hélène, *Biochim. Biophys. Acta.*, **1999,** *1489*, 181. (c) K. M. Vasquez, J. H. Wilson, *Trends Biochem. Sci.*, **1998**, *23*, 4. (d) M. P. Knauert, P. M. Glazer, *Hum. Mol. Genet.*, **2001**, *10*, 2243. (e) R. V. Guntaka, B. R. Varma, K. T. Weber, *Int. J. Biochem. Cell. Biol.*, **2003**, *35*, 22.

[92] (a) L. Westin, P. Blomquist, J. F. Milligan, Ö. Wrange, *Nucleic Acids Res.*, **1995**, *23*, 2184. (b) G. Duval-Valentin, N. T. Thuong, C. Hélène, *Proc. Natl. Acad. Sci. USA*, **1992**, *89*, 504.

[93] (a) S.L. Young, S.H. Krawczik, M.D. Matteucci, J.J. Toole, *Proc. Natl. Acad. Sci. USA*, **1991**, *88*, 10023. (b) J. U. Skoog, L. J. Maher, III, *Nucleic Acids Res.*, **1993**, *21*, 4055. (c) Z. Wang, T. Rana, *Proc. Natl. Acad. Sci. USA*, **1997**, *94*, 6688. (d) J. C. Hanvey, N. J.

Peffer, J. Bisi, S. A. Thomson, R. Cadilla, J. A. Josey, D. J. Ricca, C. F. Hassman, M. A. Bonham, K. G. Au, *Science*, **1992**, *258*, 1481.

[94] (a) J. R. Spitzner, I. K. Chung, M. T. Muller, *J. Biol. Chem.*, **1995**, *270*, 5932. (b) V. Kopel, A. Pozner, N. Baran, H. Manor, *Nucleic Acids Res.*, **1996**, *24*, 330. (c) N. Mollegaard, O. Buchardt, M. Egholm, P. Nielsen, *Proc. Natl. Acad. Sci. USA*, **1994**, *91*, 3892.

[95] (a) J. C. François, C. Hélène, *Biochemistry*, **1995**, *34*, 65. (b) M. A. Reynolds, L. J. Arnold, M. T. Almazan, T. A. Beck, R. I. Hogrefe, M. D. Metzler, S. R. Stoughton, B. Y. Tseng, T. L. Trapane, P. O. P. Tso, T. M. Woolf, *Proc. Natl. Acad. Sci. USA*, **1994**, *91*, 12433.

[96] H. Orum, P. Nielsen, M. Egholm, R. Berg, O. Buchardt, C. Stanley, *Nucleic Acids Res.* **1993**, *21*, 5332.

[97] (a) J. Sun, T. Garestier, C. Hélène, *Curr. Opin. Struct. Biol.*, **1996**, *6*, 327. (b) N. T. Thong, C. Hélène, *Angew. Chem. Intl. Ed. Engl.*, **1993**, *32*, 666.

[98] N. T. Thong, C. Hélène, *Angew. Chem. Intl. Ed. Engl.*, **1993**, *32*, 697.

[99] (a) S. B. Noonberg, J. C. Francois, D. Praseuth, A. L. Guieysse-Peugeot, J. Lacoste, T. Garestier, C. Hélène, *Nucleic Acids Res.*, **1995**, *23*, 4042. (b) C. Gotfredsen, P. Schultze, J. Feigon, *J. Am. Chem. Soc.*, **1998**, *120*, 4281. (c) J. Liquier, E. Taillandier, R. Klinck, E. Guittet, C. Gouyette, T. Huynh-Dinh, *Nucleic Acids Res.* , **1995**, *23*, 1722. (d) D. Pei, H. Ulrich, P. Schultz, *Science,* **1991**, *253*, 1408.

[100] (a) J. G. Hacia, B. J. Wold, P. B. Dervan, *Biochemistry*, **1994**, *33*, 5367. (b) J. Joseph, J. Kandala, D. Veerapanane, K. Weber, R. Guntaka, *Nucleic Acids Res.*, **1997**, *25*, 2182.

(c) F. Svinarchuk, A. Debin, J. R. Bertrand, C. Malvy, *Nucleic Acids Res.*, **1996**, *24*, 295. (d) P. E. Nielsen, *Perspect. Drug Discov. Design*, **1996**, *4*, 76. (e) H. J. Larsen, P. E. Nielsen, *Nucleic Acids Res.*, **1996**, *24*, 458. (f) T. L. Trapane, R. I. Hogrefe, M. A. Reynolds, L. S. Kan, P. O. P. Tso, *Biochemistry*, **1996**, *35*, 5495. (g) C. Giovannangeli, S. Diviacco, V. Labrousse, S. Gryaznov, P. Charneau, C. Hélène, *Proc. Natl. Acad. Sci. USA*, **1997**, *94*, 79. (h) C. Escudé, C. Giovannangeli, J. S. Sun, D.C. Lloyd, S.M. Gryaznov, T. Garestier, C. Hélène, *Proc. Natl. Acad. Sci. USA*, **1996**, *93*, 4365.

[101] (a) D. S. Pilch, K. J. Breslauer, *Proc. Natl. Acad. Sci. USA*, **1994**, *91*, 9332. (b) I. Haq, J. Ladbury, B. Showdhry, T. Jenkins, *J. Am. Chem. Soc.*, **1996**, *118*, 10693. (c) K. R. Fox, P. Polucci, T. C. Jenkins, S. Neidle, *Proc. Natl. Acad. Sci. USA*, **1995**, *92*, 7887. (d) J. L. Mergny, G. Duval-Valentin, C. H. Nguyen, L. Perrouault, B. Faucon, M. Rougée, T. Montenay-Garestier, E. Bisagni, C. Hélène, *Science*, **1992**, *256*, 1681.

[102] (a) S.B. Noonberg, J.-C. François, T. Garestier, C. Hélène, *Nucleic Acids Res.*, **1995**, *23*, 1956. (b) L. Lacroix, J. Mergny, J. Leroy, C. Hélène, *Biochemistry*, **1996**, *35*, 8715.

[103] (a) T. Vo, S. Wang, E. T. Kool, *Nucleic Acids Res.*, **1995**, *23*, 2937. (b) F. Svinarchuk, I. Nagibneva, D. Chern, S. AitSiAli, L. L. Pritchard, P. Robin, C. Malvy, A. Harel-Bellan, *Nucleic Acids Res.*, **1997**, *25*, 3459.

[104] (a) M. Grigoriev, D. Praseuth, A.L. Guieysse, P. Robin, N.T. Thuong, C. Hélène, A. Harel-Bellan, *Proc. Natl. Acad. Sci. USA*, **1993**, *90*, 3501. (b) P.A. Havre, E.J. Gunther, F.P. Gasparro, P.M. Glazer, *Proc. Natl. Acad. Sci. USA*, **1993**, *90*, 7879. (c) Z. Sandor, A. Bredberg, *Nucleic Acids Res.*, 1994, *22*, 2051.

[105] (a) O. Boussif, F. Lezoualc'h, M. A. Zanta, M. D. Mergny, D. Scherman, B. Demeneix, J. P. Behr, *Proc. Natl. Acad. Sci. USA*, **1995**, *92*, 7297. (b) N. H. Ing, J. M. Beekman, D. J. Kessler, M. Murphy, K. Jayaraman, J. G. Zendegui, M. E. Hogan, B. W. O'Malley, M. J. Tsai, *Nucleic Acids Res.*, **1993**, *21*, 2789. (c) M. A. Bonham, S. Brown, A. L. Boyd, P. H. Brown, D. A. Bruckenstein, J. C. Hanvey, S. A. Thomson, A. Pipe, F. Hassman, J. E. Bisi, B. C. Froehler, M. D. Matteucci, R. W. Wagner, S. A. Noble, L. E. Babiss, *Nucleic Acids Res.*, **1995**, *23*, 1197.

[106] P. A. Beal, P. B. Dervan, *Science*, **1991**, *251*, 1360.

[107] M. Gellert, M. N. Lipsett, D. R. Davies, *Proc. Natl. Acad. Sci. USA*, **1962**, *48*, 2013.

[108] (a) M. A. Keniry, *Biopolymers*, **2001**, *56*, 123. (b) D. Rhodes, R. Giraldo, *Curr. Opin. Struct. Biol.*, **1995**, *5*, 311. (c) D. S. Pilch, G. E. Plum, K. J. Breslauer, *Curr. Opin. Struct. Biol.*, **1995**, *5*, 334. (d) J. Feigon, K. M. Koshlap, F. W. Smith, *Methods Enzymol.*, **1995**, *261*, 225. (e) J. R. Williamson, *Annu. Rev. Biophys. Biomol. Struct.*, **1994**, *23*, 703.

[109] (a) G. Laughlan, A. I. Murchie, D. G. Norman, M. H. Moore, P. C. Moody, D. M. Lilley, B. Luisi , *Science*, **1994**, *265*, 520. (b) K. Phillips, Z. Dauter, A. I. Murchie, D. M. Lilley, B. Luisi , *J. Mol. Biol.*, **1997**, *273*, 171. (c) J. Deng, Y. Xiong, M. Sundaralingam , *Proc. Natl. Acad. Sci. USA.*, **2001**, *98*, 13660. (d) J. Chen, L.R. Zhang, J.M. Min and L.H. Zhang , *Nucleic Acids Res.*, **2002**, *30*, 3005.

[110] (a) E. H. Blackburn, *Cell*, **1994**, *77*, 621. (b) D. Sen, W. Gilbert, *Nature*, **1988**, *334*, 364. (c) W. I. Sundquist, A. Klug, *Nature*, **1989**, *342*, 825. (c) J. R. Williamson, M. K. Raghuraman, T. R. Cech, *Cell*, **1989**, *59*, 871. (d) S. Neidle, G. Parkinson, *Nat. Rev. Drug. Res.*, **2002**, *1*, 383.

[111] (a) T. Evans, E. Schon, G. Gora-Maslak, J. Patterson, A. Efstratiadis, *Nucleic Acids Res.*, **1984**, *12*, 8043. (b) M. W. Kilpatrick, A. Torri, D. S. Kang, J. A. Engler, R. D. Wells, *J. Biol. Chem.*, **1986**, *261*, 11350.

[112] M. Fry, L. A. Loeb, *Proc. Natl. Acad. Sci. USA*, **1994**, *91*, 4950.

[113] (a) R. Giraldo, M. Suzuki, L. Chapman, D. Rhodes, *Proc. Natl. Acad. Sci. USA*, **1994**, *91*, 7658. (b) G. Fang, T. R. Cech, *Cell*, **1993**, *74*, 875. (c) G. Sarig, *J. Biol. Chem.*, **1997**, *272*, 4474.

[114] (a) A. Mazumder, N. Neamati, J. O. Ojwang, S. Sunder, R. F. Rando, Y. Pommier, *Biochemistry*, **1996**, *35*, 13762. (b) L. C. Bock, L. C. Griffin, J. A. Latham, E. H. Vermaas, J. J. Toole, *Nature*, **1992**, *355*, 564.

[115] G. Fang, T. R. Cech, *Biochemistry*, **1993**, *32*, 11646.

[116] (a) L. H. Hurley, R. T. Wheelhouse, D. Sun, S. M. Kerwin, M. Salazar, O. Y. Fedoroff, F. X. Han, H. Y. Han, E. Izbicka, D. D. Von Hoff, *Pharmacol. Ther.*, **2000**, *85*, 141. (b) S. L. Young, S. H. Krawczyk, M. D. Matteucci, J. J. Toole, *Proc. Natl. Acad. Sci. USA*, **1991**, *88*, 10023.

[117] J. C. Chaput, C. Switzer, *Proc. Natl. Acad. Sci.*, **1999**, *96*, 10614.

[118] (a) C. Roberts, J. C. Chaput, C. Switzer, *Chem. Biol.*, **1997**, *4*, 899. (b) S. Tirumala, J. T. Davis, *J. Am. Chem. Soc.*, **1997**, *119*, 2769. (c) F. Seela, C. F. Wei, *Chem. Commun.*, **1997**, 1869.

[119] E. Cherbuliez, K. Bernhard, *Helv. Chim. Acta*, **1932**, *15*, 978.

[120] A. Eschenmoser, B. Loewenthal, *Chem. Soc. Rev.*, **1992**, *21*, 1.

[121] J. D. Bain, C. Switzer, A. R. Chamberlin, S. A. Benner, *Nature*, **1992**, *356*, 537.

[122] A. Rich, in *Horizons in Biochemistry*, M. Kasha, B. Pullman (eds.), Academic: New York, 1962, p. 103.

[123] Examples of chiral biological systems: (a) E. Havinga, *Biochim. Biophys. Acta*, **1954**, *13*, 171. (b) K. Okuyama, S. Arnott, M. Takanyanagi, M. Kakudo, *J. Mol. Biol.*, **1981**, *152*, 427. (c) H. M. Warrick, J. A. Spudich, *Annu. Rev. Cell Biol.*, **1987**, *3*, 379.

[124] (a) M. R. Ghadiri, J. R. Granja, R. A. Milligan, D. E. McRee, N. Khazanovich, *Nature*, **1993**, *366*, 324. (b) M. M. Conn, J. Rebek, Jr ., *Chem. Rev.*, **1997**, *97*, 1647.

[125] (a) M. Saurez, N. Branda, J. –M. Lehn, A. De Cian, J. Fisher, *Helv. Chim. Acta*, **1998**, *81*, 1. (b) J. L. Atwood, L. R. MacGillivray, *Nature*, **1997**, *389*, 469. (c) A. E. Rowan, R. J. M. Nolte, *Angew. Chem., Int. Ed. Engl.*, **1998**, *37*, 63. (d) A. R. A. Palmans, J. A. J. M. Vekermans, E. E. Havinga, E. W. Meijer, *Angew. Chem., Int. Ed. Engl.*, **1997**, *36*, 2648.

[126] (a) W. Zarges, J. Hall, J. –M. Lehn, C. Bolm, *Helv. Chim. Acta*, **1991**, *74*, 1843. (b) C. R. Woods, M. Benaglia, F. Cozzi, J. S. Siegel, *Angew. Chem., Int. Ed. Engl.*, **1996**, *35*, 1830. (c) O. Mamula, A. Von Zelewsky, G. Bernadinelli, *Angew. Chem., Int. Ed. Engl.*, **1998**, *37*, 289. (d) R. K. Castellano, B. H. Kim, J. Rebek, Jr., *J. Am. Chem. Soc.*, **1997**, *119*, 12671.

[127] (a) L. J. Prins, J. Huskens, F. de Jong, P. Timmerman, D. N. Reinhoudt, *Nature*, **1999**, *398*, 498. (b) L. J. Prins, F. de Jong, P. Timmerman, D. N. Reinhoudt, *Nature*, **2000**, *408*, 181. (c) L. J. Prins, P. Timmerman, D. N. Reinhoudt, *J. Am. Chem. Soc*, **2001**, *123*, 10153.

[128] J. H. K. K. Hirschberg, L. Brunsveld, A. Ramzi, J. A. J. M. Vekemans, R. P. Sijbesma, E. W. Meijer, *Nature*, **2000**, *407*, 167.

[129] L. E. Orgel, *Acc. Chem. Res.*, **1995**, *28*, 109.

[130] A. Saghatelian, Y. Yokobayashi, K. Soltani, M. R. Ghadiri, *Nature*, **2001**, *409*, 797.

[131] (a) G. Von Kiedrowski, *Angew. Chem. Int. Ed. Engl.*, **1986**, *25*, 932. (b) G. Von Kiedrowski, B. Wlotzka, J. Helbing, *Angew. Chem. Int. Ed. Engl.*, **1989**, *28*, 1235. (c) T. Achilles, G. Von Kiedrowski, *Angew. Chem. Int. Ed. Engl.*, **1993**, *32*, 1198. (d) D. Sievers, G. Von Kiedrowski, *Nature*, **1994**, *369*, 221.

[132] (a) A. Tetfort, G. Von Kiedrowski, *Angew. Chem. Int. Ed. Engl.*, **1992**, *31*, 654. (b) T. Li, K. C. Nicolaou, *Nature*, **1994**, *369*, 218.

[133] (a) T. Tjivikua, P. Ballester, J. Rebek Jr., *J. Am. Chem. Soc.*, **1990**, *112*, 1249. (b) J. S. Nowick, Q. Feng, T. Tjivikua, P. Ballester, J. Rebek Jr., *J. Am. Chem. Soc.*, **1991**, *113*, 8831. (c) V. Rotello, J. – I. Hong, J. Rebek, Jr., *J. Am. Chem. Soc.*, **1991**, *113*, 9422. (d) J. – I. Hong, Q. Feng, V. Rotello, J. Rebek, Jr., *Science*, **1992**, *255*, 848. (e) Q. Feng, T. K. Park, J. Rebek, Jr., *Science*, **1992**, *256*, 1180.

[134] D. Sievers, G. von Kiedrowski, *Chem. Eur. J.*, **1998**, *4*, 629.

[135] H. Curtis, *Biology*, Worth Publishers Inc: New York, 4th ed., 1986.

[136] V. Balzani (Ed.), *Supramolecular Photochemistry*, Reidel: Dordrecht, 1987.

[137] D. J. Càrdenas, P. Gaviña, J. -P. Sauvage, *J. Am. Chem. Soc.*, **1997**, *119*, 2656.

[138] (a) Y. Kobuke, K. Ogawa, Kazuya, *Bull. Chem. Soc. Jpn*, **2003**, *76*, 689. (b) L. H. Anderson, *Chem. Commun.*, **1999**, *23*, 2323.

[139] E. Iengo, E. Zangrando, R. Minatel, E. Alessio, *J. Am. Chem. Soc.*, **2002**, *124*, 1003.

[140] (a) S. Kobatake, M. Irie, *Annu. Rep. Prog. Chem., Sect. C*, **2003**, *99*, 277. (b) A. Nathanson, P. Rochon, *Chem. Rev.*, **2002**, *102*, 4139. (c) S. Kawata, Y. Kawata, *Chem.*

Rev., **2000**, *100*, 1777. (d) A. Nathanson, P. Rochon, *Can. J. Chem.*, **2001**, *79*, 1093. (e) *Holographic Data Storage*, H. J. Coufal, D. Psaltis, G. T. Sincerbox (Eds.), Springer-Verlag: Berlin, Heidelberg, 2000. (f) H. Dürr, H. B. Laurent, *Photochromism: Molecules and Systems*, Elsevier, Amsterdam, The Netherlands, 1990.

[141] C. Lenoble, R. S. Becker, *J. Phys. Chem.*, **1986**, *90*, 62.

[142] (a) N. K.Viswanathan, D. Y. Kim, S. Bian, J. Williams, W. Liu, L. Li, L. Samuelson, J. Kumar, S. Tripathy, *J. Mater. Chem.*, **1999**, *9*, 1941. (b) K. Ichimura, *Chem. Rev.*, **2000**, *100*, 1847. (c) M. Dumont, A. E. Osman, *Chem. Phys.*, **1999**, *245*, 437. (d) S. Hvilsted, P. S. Ramanujam, *Monatsh., Chem.* **2001**, *132*, 43. (e) J. A. Delaire, K. Nakatani, *Chem. Rev.*, **2000**, *100*, 1817. (f) D. M. Burland, R. D. Miller, C. A. Walsh, *Chem. Rev.*, **1994**, *94*, 31.

[143] (a) M. Irie, K. Uchida, *Bull. Chem. Soc. Jpn.*, **1998**, *71*, 985. (b) M. Irie, *Chem. Rev.*, **2000**, *100*, 1685. (c) A. J. Myles, N. R. Branda, *Adv. Funct. Mater.*, **2002**, *12*, 167.

[144] Y. Yokoyama, *Chem. Rev.*, **2000**, *100*, 1717.

[145] (a) R. Nakao, N. Ueda, Y. Abe, T. Horii, H. Inoue, *Polym. Adv. Technol.*, **1994**, *5*, 240. (b) R. Nakao, N. Ueda, Y. Abe, T. Horii and H. Inoue, *Polym. Adv. Technol.*, **1995**, *6*, 243. (c) R. Nakao, N. Ueda, Y. Abe, T. Horii and H. Inoue, *Polym. Adv. Technol.*, **1995**, *6*, 243. (d) R. Nakao, N. Ueda, Y. Abe, T. Horii and H. Inoue, *Polym. Adv. Technol.*, **1996**, *7*, 863.

[146] K. Tsubaki, K. Mukoyoshi, H. Morikawa, T. Kinoshita, K. Fuji, *Chirality*, **2002**, *14*, 713.

[147] L. Song, E. A. Jares-Erijman, T. M. Jovin, *J. Photochem. Photobiol. A: Chem.*, 2002, **150**, 177 (b) M. Bletz, U. Pfeifer-Fukumura, U. Kolb and W. Baumann, *J. Phys. Chem. A*, **2002**, *106*, 2232. (c) J. Hobley, U. Pfeifer-Fukumura, M. Bletz, T. Asahi, H. Masuhara and H. Fukumura, *J. Phys. Chem. A*, **2002**, *106*, 2265.

[148] (a) M. Tanaka, T. Ikeda, Q. Xu, H. Ando, Y. Shibutani, M. Nakamura, H. Sakamoto, S. Yajima, K. Kimura, *J. Org. Chem.*, **2002**, *67*, 2223. (b) A. M. A. Salhin, M. Tanaka, K. Kamada, H. Ando, T. Ikeda, Y. Shibutani, S. Yajima, M. Nakamura, K. Kimura, *Eur. J. Org. Chem.*, **2002**, 655.

[149] T. Deligeorgiev, S. Minkovska, B. Jejiazkova, S. Rakovsky, *Dyes Pigm.*, **2002**, *53*, 101

[150] (a) R. Rosario, D. Gust, M. Hayes, F. Jahnke, J. Springer, A. A. Garcia, *Langmuir*, **2002**, *18*, 8062. (b) M. Matsumoto, T. Nakazawa, R. Azumi, H. Tachibana, Y. Yamanaka, H. Sakai, M. Abe, *J. Phys. Chem. B*, **2002**, *106*, 11487.

[151] (a) A. E. Ivanov, N. L. Eremeev, P.-O. Wahlund, I. Y. Galaev, B. Mattiasson, *Polymer*, **2002**, *43*, 3819. (b) H. Hirano, K. Osakada, H. Nohira, A. Miyashita, *J. Org. Chem.*, **2002**, *67*, 533.

[152] H. Tachibana, Y. Yamanaka, M. Matsumoto, *J. Mater. Chem.*, **2002**, *12*, 938.

[153] H. Hirano, K. Osakada, H. Nohira, A. Miyashita, *J. Org. Chem.*, **2002**, *67*, 533.

[154] (a) K. Shibata, S. Kobatake, M. Irie, *Chem. Lett.*, **2001**, 618. (b) K. Morimitsu, K. Shibata, S. Kobatake, M. Irie, *Chem. Lett.*, **2002**, 572. (c) K. Morimitsu, K. Shibata, S. Kobatake, M. Irie, *J. Org. Chem.*, **2002**, *67*, 4574. (d) S. Takami, T. Kawai, M. Irie, *Eur. J. Org. Chem.*, **2002**, 3796. (e) D. Guillaumont, T. Kobayashi, K. Kanda, H. Miyasaka,

K. Uchida, S. Kobatake, K. Shibata, S. Nakamura, M. Irie, *J. Phys. Chem. A*, **2002**, *106*, 7222. (f) N. Tanaka, C. Okabe, K. Sakota, T. Fukaminato, T. Kawai, M. Irie, A. Goldberg, S. Nakamura, H. Sekiya, *J. Mol. Struct.*, **2002**, *616*, 113. (g) H. Miyasaka, T. Nobuto, M. Murakami, A. Itaya, N. Tamai, M. Irie, *J. Phys. Chem. A*, **2002**, *106*, 8096. (h) J. Ern, A. T. Bens, H.-D. Martin, K. Kuldova, H. P. Trommsdorff, C. Kryschi, *J. Phys. Chem. A*, **2002**, *106*, 1654.

[155] A. Peters, R. McDonald, N. R. Branda, *Chem. Commun.*, **2002**, 2274.

[156] T. Kaieda, S. Kobatake, H. Miyasaka, M. Murakami, N. Iwai, Y. Nagata, A. Itaya, M. Irie, *J. Am. Chem. Soc.*, **2002**, *124*, 2015.

[157] H. Cho, E. Kim, *Macromolecules*, **2002**, *35*, 8684.

[158] A. Mulder, A. Jukovic, L. N. Lucas, J. van Esch, B. L. Feringa, J. Huskens, D. N. Reinhoudt, *Chem. Commun.*, **2002**, 2734.

[159] P. A. Liddell, G. Kodis, A. L. Moore, T. A. Moore, D. Gust, *J. Am. Chem. Soc.*, **2002**, *124*, 7668.

[160] L. Giordano, T. M. Jovin, M. Irie, E. A. Jares-Erijman, *J. Am Chem. Soc.*, **2002**, *124*, 7481.

[161] (a) K. Matsuda, M. Irie, *J. Am. Chem. Soc.*, **2000**, *122*, 8309. (b) K. Matsuda, M. Irie, *Chem. Eur. J.*, **2001**, *7*, 3466. (c) K. Matsuda, M. Irie, *J. Am. Chem. Soc.*, **2001**, *123*, 9896. (d) K. Matsuda, M. Matsuo, S. Mizoguti, K. Higashiguchi, M. Irie, *J. Phys. Chem. B*, **2002**, *106*, 11218.

[162] (a) M. Fukudome, K. Kamiyama, T. Kawai, M. Irie, *Chem. Lett.*, **2001**, 70. (b) H. Utsumi, D. Nagahama, H. Nakano, Y. Shirota, *J. Mater. Chem.*, **2000**, *10*, 2436. (c) T.

Kawai, N. Fukuda, D. Groschl, S. Kobatake, M. Irie, *Jpn. J. Appl. Phys.*, **1999**, *38(Part 2)*, L1194. (d) J. Chauvin, T. Kawai, M. Irie, *Jpn. J. Appl. Phys.*, **2001**, *40(Part 1)*, 2518. (e) M.-S. Kim, T. Kawai, M. Irie, *Chem. Lett.*, **2000**, 1188. (f) M.-S. Kim, T. Kawai, M. Irie, *Chem. Lett.*, **2001**, 702.

[163] (a) S. Kobatake, T. Yamada, K. Uchida, N. Kato, M. Irie, *J. Am. Chem. Soc.*, **1999**, *121*, 2380. (b) S. Kobatake, M. Yamada, T. Yamada, M. Irie, *J. Am. Chem. Soc.*, **1999**, *121*, 8450. (c) S. Kobatake, K. Shibata, K. Uchida, M. Irie, *J. Am. Chem. Soc.*, **2000**, *122*, 12135. (d) M. Irie, T. Lifka, S. Kobatake, N. Kato, *J. Am. Chem. Soc.*, **2000**, *122*, 4871. (e) K. Shibata, K. Muto, S. Kobatake, M. Irie, *J. Phys. Chem. A*, **2002**, *106*, 209. (f) T. Yamada, K. Muto, S. Kobatake, M. Irie, *J. Org. Chem.*, **2001**, *66*, 6164. (g) S. Kobatake, K. Uchida, E. Tsuchida, M. Irie, *Chem. Commun.*, **2002**, 2804. (h) T. Yamada, S. Kobatake, M. Irie, *Bull. Chem. Soc. Jpn.*, **2002**, *75*, 167. (i) M. Morimoto, S. Kobatake, M. Irie, *Adv. Mater.*, **2002**, *14*, 1027. (j) S. Kobatake, M. Morimoto, Y. Asano, A. Murakami, S. Nakamura, M. Irie, *Chem. Lett.*, **2002**, 1224. (k) S. Irie, T. Yamaguchi, H. Nakazumi, S. Kobatake, M. Irie, *Bull. Chem. Soc. Jpn.*, **1999**, *72*, 1139. (l) S. Irie, M. Irie, *Bull. Chem. Soc. Jpn.*, **2000**, *73*, 2385. (m) S. Irie, M. Irie, *Bull. Chem. Soc. Jpn.*, **2002**, *75*, 2071.

[164] K. E. Maly, M. D. Wand, R. P. Lemieux, *J. Am. Chem. Soc.*, **2002**, *124*, 7898.

[165] Y. Liang, A. S. Dvornikov, P. M. Rentzepis, *Macromolecules*, **2002**, *35*, 9377.

[166] G. S. Hartley, *J. Chem. Soc.*, **1938**, 633.

[167] (a) R. H. Berg, S. Hvilsted, P. S. Ramanujam, *Nature*, **1996**, *383*, 505. (b) P. H. Rasmussen, P. S. Ramanujam, S. Hvilsted, R. H. Berg, *J. Am. Chem. Soc.*, **1999**, *121*,

4738. (c) M. S. Vollmer, T. D. Clark, C. Steinem, M. R. Ghadiri, *Angew. Chem. Int. Ed. Engl.* **1999**, *38*, 1598. (d) D. T. Bong, T. D. Clark, J. R. Ganja, M. R. Ghadiri, *Angew. Chem. Int. Ed. Engl.* **2001**, *40*, 988.

[168] H. Asanuma, T. Ito, T. Yoshida, X. Liang, M. Komiyama, *Angew. Chem. Int. Ed. Engl.*, **1999**, *38*, 2393. (b) X. Liang, H. Asanuma, M. Komiyama, *J. Am. Chem. Soc.*,**2002**, *124*, 1877.

[169] (a) A. Archut, G. C. Azzellini, V. Balzani, L. D. Cola, F. Vogtle, *J. Am. Chem. Soc.*, **1998**, *120*, 12187. (b) A. Archut, F. Vogtle, L. D. Cola, G. C. Azzellini, V. Balzani, P. S. Ramanujam, R. Berg, *Chem. Eur. J.*, **1998**, *4*, 699. (c) A. P. H. J. Schenning, C. Elissen-Roman, J. –W. Weener, M. W. P. L. Baars, S. J. V. D. Gaast, E. W. Meijer, *J. Am. Chem. Soc.*, **1998**, *120*, 8199. (d) K. Tsuda, G. C. Dol, T. Gensch, J. Hofkens, L. Latterini, J. W. Weener, E. W. Meijer, F. C. DeSchryver, *J. Am. Chem. Soc.*, **2000**, *122*, 3445. (e) A. Sidorenko, C. Houphouet-Boigny, O. Villavicencio, M. Hashemzadeh, D. V. McGrath, V. V. Tsukruk, *Langmuir*, **2000**, *16*, 10569. (d) D. M. Junge, D. V. McGrath, *Chem. Commun.*, **1997**, 857. (f) D. L. Jiang, T. Aida, *Nature*, **1997**, *388*, 454. (g) S. Ghosh, A. K. Banthia, *Tetrahedron Lett.*, **2001**, *42*, 501. (h) D. M. Junge, D. V. McGrath, *J. Am. Chem. Soc.*, **1999**, *121*, 4912. (j) S. Yokoyama, T. Nakahama, A. Otomo, S. Mashiko, *J. Am. Chem. Soc.*, **2000**, *122*, 3174. (k) Y. Okuno, S. Yokoyama, S. Mashiko, *J. Phys. Chem. B*, **2001**, *105*, 2163.

[170] S. Shinkai, *Top. Curr. Chem.*, **1984**,

[171] (a) T. Ikeda, T. Miyamoto, S. Kurihara, M. Tsukada, S. Tazuke, *Mol. Cryst. Liq. Cryst.*, **1990**, *182 B*, 373. (b) S. Kurihara, T. Ikeda, T. Sasaki, H. –B. Kim, S. Tazuke, *J. Chem. Soc., Chem. Commun.*, **1990**, 1751.

[172] (a) T. Ikeda, S. Horiuchi, D. Karanjit, S. Kurihara, S. Tazuke, *Macromolecules*, **1990**, *23*, 36. (b) T. Ikeda, S. Horiuchi, D. Karanjit, S. Kurihara, S. Tazuke, *Macromolecules*, **1990**, *23*, 42.

[173] Y. Yu, M. Nakano, T. Ikeda, *Nature*, **2003**, *425*, 145.

[174] (a) D. T. Bong, T. D. Clark, J. R. Ganja, M. R. Ghadiri, *Angew. Chem. Int. Ed. Engl.* **2001**, *40*, 988. (b) S. Fernandez-Lopez, H. –S. Kim, E. C. Choi, M. Delgado, J. R. Granja, A. Khasanov, K. Kraehenbuehl, G. Long, D. A. Weinberger, K. M. Wilcoxen, M. R. Ghadiri, *Nature*, **2001**, *412*, 452.

[175] (a) C. M. Drain, *Proc. Natl. Acad. Sci. USA*, **2002**, *99*, 5178. (b) D. Mauzerall, C. M. Drain, *Biophys. J.*, **1992**, *63*, 1544.

Chapter 2.

Theoretical Methods and Experimental Techniques

2.1. Theoretical Methods

Computational methods are especially attractive, because of their ability to fully describe chemical systems mathematically.[1] Classical, molecular mechanics (MM), which are based on classical physics principles, can be used to solve chemical problems, but extensive parameterisation from empirical data is required to obtain meaningful, predictive results from these classical methods and they have poor accuracy compared with molecular orbital (MO) calculations.[2] However, MM calculations are extremely fast and, consequently, can conveniently solve extremely large, computationally demanding biological and materials model systems involving oligonucleotides, proteins, and polymers.[3] The accurately predicted MM geometries provide a theoretical visualisation of molecular materials.

Approximate molecular orbital (MO) methods consisting of *ab initio*, density functional, and semi-empirical calculation methods have successfully provided interpretations of chemical structure and reactivity, along with accurate predictions of molecular properties. These approximations to the Schrödinger equation have been able to produce new equilibrium and transition state structures, as well as thermodynamic properties, and electronic wavefunctions.

The supramolecular structures described in this thesis were theoretically studied using both classical MM methods and approximate MO calculations, to determine their geometries and energies which could not be provided through experimental techniques.

This Chapter will introduce the principles which govern these computational methods, bringing a better appreciation of these theoretical geometry and energy results.

2.1.1. Molecular Mechanics Methods

Molecular mechanics (MM) methods use simple, classical potential functions derived from vibrational spectroscopy to describe interatomic forces as a function of position.[2] The potential function is represented as a sum of individual potential energy bonding and non-bonding terms, and approximated with empirical and theoretical data. Well-parameterised MM calculations can produce useful, accurate, and rapid models of molecular potential energy surfaces, especially for large chemical systems.

The MM^+ force field[4] is utilised in this thesis to generate input structures for quantum mechanical calculations, and to analyse large supramolecular systems. This force field is an All-Atom model, explicitly calculating forces on each atom, for which the total potential energy is expressed as a sum of valence, nonbonding, and cross-term interactions:

$$E_{total} = E_{valence} + E_{cross\text{-}term} + E_{nonbond} \qquad \textbf{(Eq. 2. 1)}$$

2.1.1.1. Molecular Mechanics Bonding Potentials

The valence terms involves harmonic interactions between bound atoms:

$$E_{valence} = E_{bond} + E_{angle} + E_{torsion} + E_{inversion} \qquad \textbf{(Eq. 2. 2)}$$

where E_{bond} relates to bond stretching, E_{angle} to bond bending, $E_{torsion}$ to bond torsion, $E_{inversion}$ to bond inversion. The Morse function relates the bond energy to bond length:

$$E_{bond} = \sum D_e\left[1 - \exp\{-K_r(r - r_o)\}\right]^2 \qquad \textbf{(Eq. 2. 3)}$$

with a dissociation energy D_e and a spring constant K_r describing the bond stretching from the equilibrium r_o to a different bond length r. Near the equilibrium, the bond length behaves like a 1-D harmonic oscillator giving:

$$E_{bond} = \sum_{bonds} \tfrac{1}{2} K_r (r - r_o)^2 \qquad \textbf{(Eq. 2. 4)}$$

Angle-bending potentials in the MM^+ force field are also described by a quadratic harmonic equation:

$$E_{angle} = \sum_{angles} \tfrac{1}{2} K_\vartheta (\vartheta - \vartheta_o)^2 \qquad \textbf{(Eq. 2. 5)}$$

where K_ϑ is the bond angle bend constant for bond angles ϑ and equilibrium angles ϑ_o. The torsional angle potentials are parameterised to reflect the n-fold symmetry of dihedral angles, producing minima for *cis*-, *gauche*-, or *trans*-conformations, etc. The torsion potentials are expanded as a Fourier expansion in the dihedral angle ω:

$$E_{torsion} = \sum_{torsions} \frac{V_n}{2}\left[1 + \cos(n\omega - \omega_o)\right] \; ; \quad n = 1, 2, \text{ and } 3 \qquad \textbf{(Eq. 2. 6)}$$

where V_n is the parameterized energy of the n-fold barrier, with a $360°/n$ periodicity of dihedral rotation. Improper inversions between four bonded atoms, $E_{inversion}$, are modelled through Fourier expansions similar to Equation 2.6. Coupled motions between the various bond stretch and angle potentials, including stretch-stretch, stretch-bend, and bend-torsion-bend, produce cross-term interactions, $E_{cross\text{-}term}$, that improve the force field accuracy.

2.1.1.2. Molecular Mechanics Non-Bonding Potentials

The molecular mechanics non-bonded potentials are composed of van der Waals (E_{vdW}) and electrostatic (E_{elstat}) terms:

$$E_{nonbond} = E_{vdW} + E_{elstat} \qquad \textbf{(Eq. 2. 7)}$$

The van der Waals forces are described by a Lennard-Jones 6-12 potential:

$$E_{vdW} = \sum_{B>A}\left[\frac{a_{AB}}{r_{AB}^{12}} - \frac{b_{AB}}{r_{AB}^{6}}\right] \qquad \textbf{(Eq. 2. 8)}$$

where r_{AB} is the distance between atoms A and B, with parameterized van der Waals coefficients a_{AB} and b_{AB}. This potential described attractive interactions at $1/r^6$ intermolecular separations, and hard-sphere repulsions at $1/r^{12}$. Electrostatic contributions to the MM^+ force field arise from bond dipole moments interactions:

$$E_{elstat} = \varepsilon \sum_{B>A} \mu_A \mu_B \left[\frac{\cos\chi - 3\cos\alpha_A \cos\alpha_B}{r_{AB}^{3}}\right] \qquad \textbf{(Eq. 2. 9)}$$

where χ is the angle between the dipole vectors, and α_A / α_B are the angles the dipole vectors make with the distance vector $\mathbf{r}_{AB}$. MM^+ force field ignores non-bonded interactions between vicinal and geminal atoms (1,2 and 1,3 interactions).

2.1.2. Quantum Mechanical Methods

Quantum mechanical methods have been implemented to solve the time-independent Schrödinger equation (Eq. 2.1),[5] which is used to describe the wave character of particles.

$$\mathbf{H}\Psi = E\Psi \qquad \textbf{(Eq. 2. 10)}$$

where E is the total energy, Ψ is the total wavefunction, and **H** is the *Hamiltonian* operator for the system. The quantum mechanical Hamiltonian, which corresponds to the energy operator, consists of kinetic energy (T) and potential energy (V) linear operators:

$$\mathbf{H} = \{\mathbf{T} + \mathbf{V}\} \qquad \textbf{(Eq. 2. 11)}$$

For a molecular system, the kinetic energy **T** can be decomposed into two terms, corresponding to the kinetic energy of the nuclei and electrons, as shown in Equation 2. 12:

$$\mathbf{T} = \frac{-\hbar^2}{2}\sum_{\alpha}\frac{1}{m_\alpha}\nabla_\alpha^2 - \frac{\hbar^2}{2m_i}\sum_{i}\nabla_i^2 \qquad \textbf{(Eq. 2. 12)}$$

where $\hbar = h/2\pi$ involves the Planck constant h, m is the particle mass, and $\nabla^2 = (\partial^2/\partial_x{}^2 + \partial^2/\partial_y{}^2 + \partial^2/\partial_z{}^2)$. The potential energy **V** consists of three terms, nuclear-nuclear repulsions (term one), nuclear-electron attractions (term two) and electron-electron repulsions (term three).

$$\mathbf{V} = \sum_{\alpha}\sum_{\beta>\alpha}\frac{Z_\alpha Z_\beta e^2}{r_{\alpha\beta}} - \sum_{\alpha}\sum_{i}\frac{Z_\alpha e^2}{r_{i\alpha}} + \sum_{j}\sum_{i>j}\frac{e^2}{r_{ij}} \qquad \textbf{(Eq. 2. 13)}$$

where Ze is the nuclear charge, e is the electronic charge, r is the distance between two particles, the symbols $\alpha\beta$ refer to nuclei, and the symbols ij refer to electrons.

The resulting full multi-particle Hamiltonian operator $\mathbf{H}^{\text{total}}$ is:

$$\mathbf{H}^{\text{total}} = \frac{-\hbar^2}{2}\sum_{\alpha}\frac{1}{m_\alpha}\nabla_\alpha^2 - \frac{\hbar^2}{2m_i}\sum_{i}\nabla_i^2 + \sum_{\alpha}\sum_{\beta>\alpha}\frac{Z_\alpha Z_\beta e^2}{r_{\alpha\beta}} - \sum_{\alpha}\sum_{i}\frac{Z_\alpha e^2}{r_{i\alpha}} + \sum_{j}\sum_{i>j}\frac{e^2}{r_{ij}}$$

(Eq. 2. 14)

Applying $\mathbf{H}^{total}$ to the time-independent Schrödinger (Equation 2. 10) leads to a wavefunction solution, for the spatial motion of electrons and nuclei within the potential field defined in Equation 2.12, which can only adopt certain energy values.

Because of considerable mass differences between electrons and nuclei, nuclear motions can be neglected relative to electronic motions according to the Born-Oppenheimer approximation. Consequently, the Hamiltonian, $\mathbf{H}^{el}$ can be simplified as

$$\mathbf{H}^{el} = -\frac{\hbar^2}{2m_i}\sum_i \nabla_i^2 - \sum_\alpha \sum_i \frac{Z_\alpha e^2}{r_{i\alpha}} + \sum_j \sum_{i>j} \frac{e^2}{r_{ij}} \qquad \textbf{(Eq. 2. 15)}$$

which describes the motion of electrons in a potential field of fixed nuclei. In molecular multi-electron systems, the electron-electron repulsion term, $1/r_{ij}$, cannot be determined explicitly, and, therefore, must be approximated to solve the Schrödinger equation.

2.1.2.1. The molecular orbital approach[6]

The molecular orbital approximation expands the entire n-electron molecular wavefunction Ψ as a linear combination of n one-electron wavefunctions, ψ_i:

$$\Psi(1, 2, \ldots, n) = \psi_1(1)\ \psi_2(2)\ldots\ \psi_n(n) \qquad \textbf{(Eq. 2. 16)}$$

Electrons are antisymmetric with respect to exchange (i.e. $\Psi(i, j) = -\Psi(j, i)$); therefore, the approximate n-electron molecular wavefunction Ψ must take the form of an $n \times n$ Slater determinant:

$$\Psi = \sqrt{\frac{1}{N!}} \begin{vmatrix} \psi_1(1) & \cdots & \cdots & \psi_n(1) \\ \vdots & \ddots & & \vdots \\ \vdots & & \ddots & \vdots \\ \psi_1(n) & \cdots & \cdots & \psi_n(n) \end{vmatrix} \qquad \textbf{(Eq. 2. 17)}$$

where $(N!)^{1/2}$ is a normalization factor.

Each one-electron function ψ_i is a *molecular orbital* (MO), and may be written as a linear combination of atomic orbitals (LCAO),

$$\psi_i = \sum c^i_\mu \phi_\mu \qquad \textbf{(Eq. 2. 18)}$$

where c^i_μ is a coefficient which represents the contribution of the μ^{th} atomic orbital ϕ_μ within the i^{th} MO. In a spherical polar coordinate (r, θ, φ) system, the atomic wavefunctions ϕ_μ form a basis set for the molecular orbital ψ_i:[7]

$$\phi(r, \theta, \varphi) = R_{nl}(r)Y_{lm}(\theta, \varphi) \qquad \textbf{(Eq. 2. 19)}$$

where $R_{nl}(r)$ and $Y_{lm}(\theta, \varphi)$ are the radial and the angular components of ϕ_μ respectively. The angular part, $Y_{lm}(\theta, \varphi)$, arises from the spherical harmonics of the angular momentum quantum numbers $\boldsymbol{l}$ and $\boldsymbol{m}$. The radial part, $R_{nl}(r)$, results from the multiplication of a polynomial dependent on radial distance r, by an exponential decaying function $e^{-\zeta}$ (ζ is the orbital exponent) dependent on nuclear charge Z and principal quantum number $\boldsymbol{n}$.

Slater-type orbitals (STO) are simple forms of the radial contribution:[8]

$$R_{nl}(r) = (2\zeta)^{n+½} [(2n)!]^{-½} r^{n-1} \exp(-\zeta r) \qquad \textbf{(Eq. 2. 20)}$$

where the orbital exponent ζ is:

$$\zeta = (Z - s) / \boldsymbol{n}^* \qquad \textbf{(Eq. 2. 21)}$$

and $\boldsymbol{n}^*$ is an effective principal quantum number, screened through a constant s. In these Slater-type orbitals, the constant s and the effective principal quantum number $\boldsymbol{n}^*$ are parameterised by empirical data to decrease the computational cost relative to pure radial functions $R_{nl}(r)$, but they lack radial nodes and have to be orthogonalised. *Gaussian-type orbitals* (GTO) can also be used to approximate the radial descriptions:

$$R_{nl}(r) = (2\zeta)^{n+½} [(2n)!]^{-½} r^{n-1} \exp(-\zeta r^2) \qquad \textbf{(Eq. 2. 22)}$$

in which the exponential decay function is r^2-dependent.

Comparison of the radial distribution of a 3*s* hydrogen atom wavefunction with the STO and GTO descriptions reveals the absence of radial nodes in Slater-type orbitals, which are therefore not mutually orthogonal, in contrast with true H wavefunctions (Figure 2. 1). A linear combination of orthogonalized STO is consequently necessary to approximate the true H radial distribution. Worse than Slater type orbitals, Gaussian functions do not display any cusp or radial nodes. However, the product of two Gaussian functions results in another Gaussian, centred on a point halfway between the original functions, allowing the approximation of three- and four-centred integrals to equivalent two-centred integrals. Linear combinations of Gaussian functions can be used to reproduce STO distribution functions.

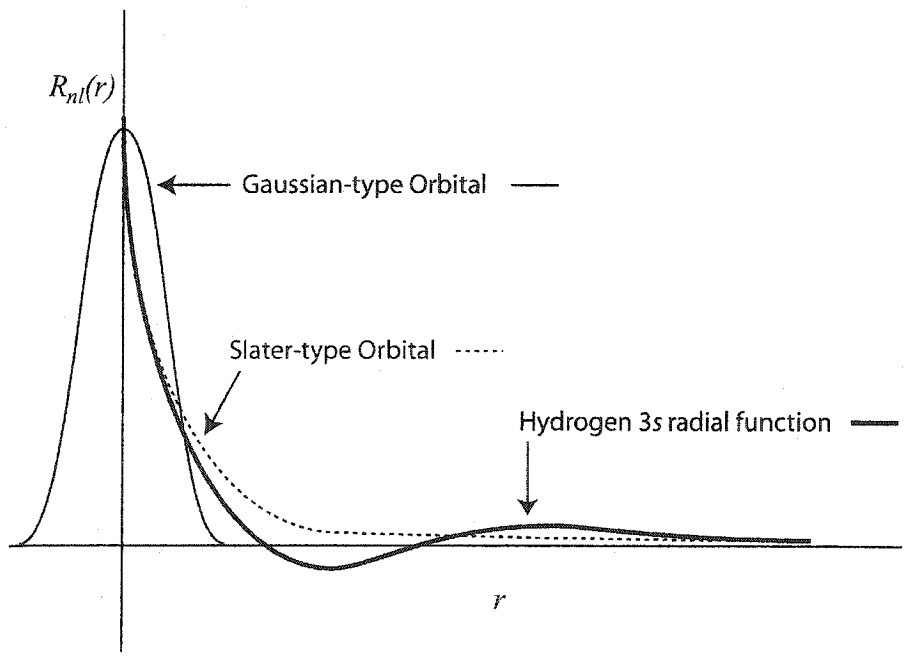


Figure 2. 1. Schematic radial distribution functions for a H 3*s* wavefunction, a Slater-type orbital, and a Gaussian-type orbital.

2.1.2.2. Hartree-Fock self-consistent field (HF-SCF) methods[9]

The self-consistent field molecular orbital theory (SCF-MO) systematically determines the total energy of a molecule using a Hartree-Fock wavefunction and a linear combination of one-electron atomic orbitals.[9] Because of inseparable $1/r_{ij}$ terms, the many-electron Hamiltonian operator is approximated by "effective" one-electron Hamiltonian operators, $\mathbf{F}(i)$, the Fock operators.

$$\mathbf{H}^{el} \approx \sum_p \mathbf{F}(p) = \sum_p \left(-\tfrac{1}{2}\nabla_p^2 + \mathbf{V}(p)\right) \qquad \textbf{(Eq. 2. 23)}$$

where $\mathbf{V}(p)$ is a one-electron potential functional, dependent on nuclei positions and the average fields presented by the remaining $n-1$ electrons. These one-electron Hamiltonian operators lead to orbital energies using:

$$\mathbf{F}_i(i)\psi_i(i) = \varepsilon_i\psi_i(i) \qquad \textbf{(Eq. 2. 24)}$$

where ε_i is the orbital energy. Because the potential $\mathbf{V}(p)$ is dependent on the average electron position, the spatial distribution of the electrons, the molecular orbitals ψ_i, must be solved to find $\mathbf{V}(p)$.

This apparent problem can be resolved recursively using the Variational Principle, which considers the true energy (E^{true}) as a minimum compared to any calculated energy (E^{calc}):

$$E^{true} \leq E^{calc} = \frac{\int \Psi^* \mathbf{H}^{total} \Psi d\tau}{\int \Psi^* \Psi d\tau} \qquad \textbf{(Eq. 2. 25)}$$

where $d\tau$ is the volume element for the electron, and Ψ^* is the complex conjugate of the wavefunction. Therefore, an initial set of one-electron wavefunctions are guessed using Equation 2. 24, to yield lower orbital energies. If the orbital ψ_i fits the energy minimum

criteria, the many-electron Hamiltonian will be minimised, and the obtained orbitals will be identical to those used to construct V(p). Such orbitals are defined as *self-consistent*, *Hartree-Fock* molecular orbitals (HF-MO), and satisfy orthonormal conditions:

$$S_{ij} = \int \psi_i(1)\psi_j(1)d\tau_1 = \delta_{ij} \qquad \textbf{(Eq. 2. 26)}$$

with

$\delta_{ij} = 0$ if $i \neq j$,

$\delta_{ij} = 1$ if $i = j$.

where S_{ij} is the overlap integral, and δ_{ij} is the Krönecker delta.

The one-electron Fock operator can be expanded as:

$$\begin{aligned} \mathbf{F}(i) &= -\frac{1}{2}\nabla_i^2 - \frac{Z}{r_i} + \sum_j \left(2\mathbf{J}_j - \mathbf{K}_j\right) \\ &= \mathbf{H}^{\text{core}} + \sum_j \left(2\mathbf{J}_j - \mathbf{K}_j\right) \end{aligned} \qquad \textbf{(Eq. 2. 27)}$$

where the two-electron, $1/r_{ij}$ term is replaced by the *Coulomb operator*, $\mathbf{J}_j$:

$$\mathbf{J}_j(1) = \int \psi_j^*(2)\frac{1}{r_{12}}\psi_j(2)d\tau_2 \qquad \textbf{(Eq. 2. 28)}$$

and the *exchange operator* $\mathbf{K}_j$:

$$\mathbf{K}_j(1)\psi_i(1) = \left[\int \psi_j^*(2)\frac{1}{r_{12}}\psi_i(2)d\tau_2\right]\psi_j(1) \qquad \textbf{(Eq. 2. 29)}$$

Equation 2. 24 becomes

$$\mathbf{H}^{\text{core}}\psi_i + \sum_j \left(2\mathbf{J}_j - \mathbf{K}_j\right)\psi_i = \sum_j \varepsilon_{ij}\psi_j \qquad \textbf{(Eq. 2. 30)}$$

A stationary point of the function G, corresponding to the minimum energy, can therefore be reached by solving

$$\delta G = 2\sum_i \int \delta\psi_i^* \left[\mathbf{H}^{\text{core}}\psi_i + \sum_j \left(2\mathbf{J}_j - \mathbf{K}_j\right)\psi_i - \sum_j \varepsilon_{ij}\psi_j \right] d\tau = 0$$

(Eq. 2. 31)

At the stationary point, $\mathbf{H}^{\text{core}}$ is the one-electron Hamiltonian for an electron moving in a field of fixed nuclei. The Coulomb operator $\mathbf{J}_j$ is the potential of another, indistinguishable electron occupying the same orbital, and corresponds to the potential energy of interaction between the smoothed-out charge distributions of the electrons. The exchange operator $\mathbf{K}_j$ minimises the interaction energy between electrons of parallel spins, and reflects the energy stabilisation caused by the partial correlation of electrons with parallel spins.

Expanding the one-electron, Hartree-Fock molecular orbitals with the LCAO approach (Equation 2. 16) yields:

$$\mathbf{F}_i \sum_\mu c_\mu^i \phi_\mu = \varepsilon_i \sum_\mu c_\mu^i \phi_\mu \qquad \textbf{(Eq. 2. 32)}$$

which can be expressed in matrix representation as the *Roothan equation*:[10]

$$\mathbf{Fc_i} = \varepsilon_i \mathbf{Sc_i} \qquad \textbf{(Eq. 2. 33)}$$

with a Fock matrix **F**, coefficient column vectors $\mathbf{c_i}$, and an overlap matrix **S**. Solutions to this equation will be non-trivial if the coefficients are non-zero, as the eigenvalues ε_i are determined from the *secular determinant* following the condition:

$$\det\left|F_{\mu\nu} - \varepsilon_i S_{\mu\nu}\right| = 0 \qquad \textbf{(Eq. 2. 34)}$$

where $F_{\mu\nu}$ and $S_{\mu\nu}$ are individual elements of the Fock and overlap matrices:

$$F_{\mu\nu} = h_{\mu\nu} + \sum_\sigma \sum_\lambda P_{\lambda\sigma}(J_{\lambda\sigma} - \tfrac{1}{2}K_{\sigma\lambda}) \qquad \textbf{(Eq. 2. 35)}$$

$$S_{\mu\nu} = \int \phi_\mu \phi_\nu d\tau \qquad \textbf{(Eq. 2. 36)}$$

and $P_{\mu\nu}$ are the elements of the *density matrix* $\mathbf{P}$:

$$P_{\mu\nu} = \sum_{i}^{occ} c_{\lambda}^{i} c_{\sigma}^{i} \qquad \textbf{(Eq. 2. 37)}$$

The Hartree-Fock / Roothan equations are solved by guessing an initial set of c^{i}_{μ} coefficients then generating a density matrix P used to calculate the initial Fock elements $F_{\mu\nu}$. Diagonalisation of the Fock matrix by standard matrix eigenvalue methods (allowable because of the orthonormal eigenvalue problem) produces a new matrix of linear expansion coefficients, and the problem is solved iteratively until self-consistency is obtained, the energy minimum reached.

2.1.2.3. Ab initio Calculation Methods[11]

Hartree-Fock *ab initio* calculations use only fundamental physical constants and atomic orbital basis sets to solve the approximate Schrödinger wavefunction equations. *Ab initio* calculations provide the most accurate theoretical descriptions of molecules, but are intrinsically dependent on basis set functions: the larger the basis set, the more accurate the result, but at the expense of increased computational time. A *minimal* basis set is composed of one Slater-type orbital (Equation 2. 11) for each atomic orbital of every atom within the molecule. A *double-zeta* basis set replaces every minimal basis STO by two new STO, with two different orbital exponents ζ. A *split-valence* basis set uses double-zeta descriptions of valence electrons, and a minimal basis description of core electrons. *Polarization functions* can further refine the atomic orbital descriptions by using STO with l quantum numbers one greater than original atomic orbital, for example, adding p functions to H, d functions to C and O, etc.

The basis sets employed in this thesis use linear combinations of Gaussian-type orbitals (Equation 2.13) to represent the STO, because of the natural computational efficiencies of Gaussian functions. The STO-3G basis set[12] is a minimal basis set description, with each STO approximated as a linear combination of 3 GTO. The 3-21G basis[13] is a split valence set, with each inner shell STO represented by a linear combination of three Gaussians. The valence electrons are treated in a double-zeta manner, with two GTO combining to form the first orbital description, and a single GTO as the second orbital function. The 6-31G basis[14] is a split valence set, with each inner shell STO represented by a linear combination of six Gaussians. The valence electrons are treated in a double-zeta manner, with three GTO combining to form the first orbital description, and a single GTO as the second orbital function. Polarized basis sets are also used, with the symbols * and ** representing first and second polarization functions.

2.1.2.4. Semi-Empirical Calculation Methods

Semi-empirical molecular orbital methods completely neglect or approximate some $1/r_{ij}$ electron repulsion integrals to solve the Schrödinger equation. To compensate for neglecting the integrals, the semi-empirical methods introduce parameters based on molecular data, such as ionisation potentials and electron affinities. Semi-empirical theories are therefore ideal for quantum analysis of moderately large organic and inorganic molecules by considerably reducing computational times, while retaining high accuracy.

The PM3[15] (Parametric Model 3) semi-empirical theory is used in this thesis because of their accurate prediction and characterisation of a wide range of chemical

systems.[16] Semi-empirical PM3 method use an STO-3G minimal basis set to describe the valence orbitals, and the Zero Differential Overlap (ZDO) approximation to simplify the Fock matrix. As a result, overlap between many atomic orbitals is small, and electron repulsion integrals will be negligible:

$$(\mu\nu \mid \lambda\sigma) = 0 \quad \text{unless } \mu=\nu \text{ and } \lambda=\sigma \qquad \textbf{(Eq. 2. 38)}$$

The PM3 theory also uses a Neglect of Diatomic Differential Overlap (NDDO) approximation, ignoring differential overlap between atomic orbitals located on different atoms, and does not compute three- and four-centred, two-electron integrals.

Overall, the semi-empirical Fock matrix is comprised of five terms.[11, 17, 18] The first term corresponds to one-centre, one-electron integrals, $H_{\mu\mu}$, that calculate the kinetic energy of an electron in an AO on atom A, and the potential energy V_{AB} that arises from attractions to other nuclei (atoms B):

$$F_{\mu\mu} = H_{\mu\mu} - \sum_{B \neq A} V_{AB} \qquad \textbf{(Eq. 2. 39)}$$

where $H_{\mu\mu}$ is the parametrically obtained, one-electron Hamiltonian and V_{AB} is a core-electron integral of the form:

$$V_{AB} = Z_B(\mu\mu \mid ss) \qquad \textbf{(Eq. 2. 40)}$$

Z_B is the core charge of nucleus B, with an approximate *s* orbital shape, meaning the $(\mu\mu \mid ss)$ term is identical to a two-electron repulsion integral. The second term contains one-centre, two-electron repulsion integrals which are parameterised from empirical atomic spectral data. For each atom, there are a maximum of five such integrals: (*ss* | *ss*), (*ss* | *pp*), (*sp* | *sp*), (*pp* | *pp*), and (*pp* | *p'p'*), where *p* and *p'* represent two different *p*-type atomic orbitals. The third term consists of two-centre, one-electron core resonance integrals , $H_{\mu\nu}$, proportional to the overlap integral, $S_{\mu\nu}$ between atomic orbitals:

$$H_{\mu\nu} = S_{\mu\nu} \tfrac{1}{2}(\beta_\mu + \beta_\nu) \qquad \textbf{(Eq. 2. 41)}$$

where β_μ and β_ν are adjustable parameters, specific to each atomic orbital type. The fourth term contains two-centre, two-electron integrals, which represent the energy of interaction between the charge distributions of atom A and atom B. Electron densities are approximated as point charges to reduce the computationally difficult evaluation of ($\nu\lambda$ | $\sigma\mu$)-type integrals, and adjustable parameters are introduced to compute the two-centre two-electron terms as summed multipolar interactions. Finally, the fifth term involves core-core repulsion integrals. The PM3 method only treats the valence electrons explicitly by creating an effective atomic core which combines inner shell electrons and nuclei. The net repulsion between two neutral molecules or atoms, E_N (A,B), can be estimated from simple electrostatics, across a interatomic core separation R_{AB}, as:

$$E_N(A,B) = \frac{Z_A Z_B}{R_{AB}} \qquad \textbf{(Eq. 2. 42)}$$

However, approximations must be introduced to account for attractive van der Waals forces, leading to the two-centre overlap integral:

$$E_N(A,B) = Z_A Z_B (s_A s_A \mid s_B s_B)\left[1 + \exp(-\alpha_A R_{AB}) \exp(-\alpha_B R_{AB})\right] \qquad \textbf{(Eq. 2. 43)}$$

where the exponential term accounts for decreased screening of the nucleus with decreasing interatomic separation. These approximations encompass van der Waals interactions, sterically crowded systems, and hydrogen-bonding forces in the PM3 method.

2.1.3. Theoretical Determination of Thermodynamic Properties

Vibrational analysis of geometry optimised structures was used to determine the theoretical thermodynamic properties of these systems in terms of entropy, energy, and heat capacity of these structures. Assuming an ideal gas behaviour and ground state electronic configurations from the studied species, the partition function $q(V,T)$, which describes the states available to the particles molecular distributed within the volume V at a temperature T, can be estimated to give the electronic, vibrational, translational, and rotational contributions to their thermochemistry.[19] Using a Boltzmann model, the entropy of the system is defined as:

$$S = k_B \ln W \qquad \textbf{(Eq. 2. 44)}$$

where k_B is Boltzmann's constant, and W is the probability of quantum states available to the particles. The most probable particle arrangement within the energy range is given by *Boltzmann's equation*:

$$\frac{N_i}{g_i} = \frac{N_A}{q} \exp\left(\frac{-\Delta\varepsilon_i}{k_B T}\right) \qquad \textbf{(Eq. 2. 45)}$$

where the partition summation q is defined as:

$$q = \sum g_i \exp\left(\frac{-\Delta\varepsilon_i}{k_B T}\right) \qquad \textbf{(Eq. 2. 46)}$$

and N_i is the number of particles of energy ε_i, g_i is the number of states of energy ε_i, N_A is Avogadro's number, $\Delta\varepsilon_i$ is the energy different between the ε_i and ε_0 energy levels. Using the partition function and $Nk_B = R$ (in molar units), the entropy contribution S can therefore be described as:

$$S = Nk_B[1 + \ln(q(V,T)/N) + T(\partial \ln q/\partial T)_V] = R[1 + \ln(q(V,T)) + T(\partial \ln q/\partial T)_V] \quad \textbf{(Eq. 2. 47)}$$

The thermal energy of the system E is defined in:

$$E = Nk_B T^2[T(\partial \ln q/\partial T)_V] \quad \textbf{(Eq. 2. 48)}$$

to give the heat capacity C_V using

$$C_V = (\partial E/\partial T)_{N,V} \quad \textbf{(Eq. 2. 49)}$$

The evaluation of the contribution of translational motions to the thermodynamics of the system requires the use of a translational partition function q_{trans} defined as:

$$q_{trans} = V(2\pi mk_B T/h^2)^{3/2} = \frac{k_B T}{P}(2\pi mk_B T/h^2)^{3/2} \quad \textbf{(Eq. 2. 50)}$$

for an ideal gas. The resulting translational entropy S_{trans} is described in:

$$S_{trans} = R(\ln q_{trans} + 5/2) \quad \textbf{(Eq. 2. 51)}$$

The translational internal thermal energy is:

$$E_{trans} = N_A k_B T^2[T(\partial \ln q_{trans}/\partial T)_V] = 3/2RT \quad \textbf{(Eq. 2. 52)}$$

and the constant volume heat capacity is deduced as:

$$C_{V,trans} = (\partial E/\partial T)_{N,V} = 3/2R \quad \textbf{(Eq. 2. 53)}$$

The contribution of electronic motions are determined using the electronic partition function q_{el}, which is described in:

$$q_{el} = \sum_{i \to n} \omega_i \exp(-\varepsilon_i/k_B T) \quad \textbf{(Eq. 2. 54)}$$

where ω is the degeneracy of the energy level. Assuming that excited states are not accessible, *i.e.* $\Delta\varepsilon_i >> k_B T$, the electronic partition function becomes:

$$q_{el} = \omega_0 \quad \textbf{(Eq. 2. 55)}$$

which cancels the electronic internal energy and heat capacity contributions, and gives the electronic entropy S_{el} in:

$$S_{el} = R[\ln q_{el} + T(\partial \ln q_{el} / \partial T)_V] = R \ln q_{el} \qquad \textbf{(Eq. 2. 56)}$$

Rotational contributions to the thermodynamic properties depend on whether the particle adopts a linear geometry or not. For a linear molecule, the rotational partition function q_{rot} is defined as:

$$q_{rot} = \frac{1}{\sigma_{rot}}\left(\frac{T}{\Theta_{rot}}\right) = \frac{1}{\sigma_{rot}}\left(\frac{8\pi^2 I k_B T}{h^2}\right) \qquad \textbf{(Eq. 2. 57)}$$

where I is the moment of inertia and σ_{rot} is the symmetry number. The resulting rotational entropy is:

$$S_{rot} = R[\ln q_{rot} + T(\partial \ln q_{rot} / \partial T)_V] = R(1 + \ln q_{rot}) \qquad \textbf{(Eq. 2. 58)}$$

The rotational contribution to the internal energy is defined as:

$$E_{rot} = RT^2(\partial \ln q_{rot} / \partial T)_V = RT \qquad \textbf{(Eq. 2. 59)}$$

to determine the rotational heat capacity C_V:

$$C_{V,rot} = (\partial E_{rot} / \partial T)_V = R \qquad \textbf{(Eq. 2. 60)}$$

In the case of a non-linear geometry, the spatial contributions of the rotation, in Cartesian space, must be taken into account to define the rotational partition function so that:

$$q_{rot} = \frac{1}{\sigma_{rot}}\left(\frac{T^{3/2}}{\Theta_{rot,x}\Theta_{rot,y}\Theta_{rot,z}}\right) \qquad \textbf{(Eq. 2. 61)}$$

Using $(\partial \ln q_{rot}/\partial T)_V = 3/2T$, the rotational entropy becomes:

$$S_{rot} = R[\ln q_{rot} + T(\partial \ln q_{rot} / \partial T)_V] = R(3/2 + \ln q_{rot}) \qquad \textbf{(Eq. 2. 62)}$$

while the rotational internal energy is described in:

$$E_{rot} = RT^2(\partial \ln q_{rot} / \partial T)_V = 3/2RT \qquad \textbf{(Eq. 2. 63)}$$

and the heat capacity C_V is defined:

$$C_{V,rot} = (\partial E_{rot} / \partial T)_V = 3/2R \qquad \textbf{(Eq. 2. 64)}$$

The vibrational contribution to the thermodynamic properties can be evaluated from the cumulated contributions of each individual vibrational mode K, which are characterised by their vibrational temperature $\Theta_{vib,K}$ ($\Theta_{vib,K} = h\nu_K / k_B$) while choosing the zero reference point as the potential energy minimum. For each vibrational mode K, the partition function $q_{vib,K}$ can be written as:

$$q_{vib,K} = \exp(-\Theta_{vib,K}/2T)/[1- \exp(-\Theta_{vib,K}/2T)] \qquad \textbf{(Eq. 2. 65)}$$

to give the total vibrational partition function q_{vib}:

$$q_{vib} = \prod_K q_{vib,K} \qquad \textbf{(Eq. 2. 66)}$$

The resulting vibrational entropy is:

$$S_{vib} = R\sum_K \left[\frac{\Theta_{vib,K}}{T\left[\exp(\Theta_{vib,K}/T) - 1\right]} - \ln(1 - \exp(-\Theta_{vib,K}/T)) \right] \textbf{(Eq. 2. 67)}$$

while the rotational internal energy is described in:

$$E_{vib} = R\sum_K \Theta_{vib,K} \left[\frac{1}{2} + \frac{1}{\exp(\Theta_{vib,K}/T) - 1} \right] \qquad \textbf{(Eq. 2. 68)}$$

and the heat capacity C_V is defined:

$$C_{V,vib} = R\sum_K \frac{\exp(\Theta_{vib,K}/T)}{T^2} \left[\frac{\Theta_{vib,K}}{\exp(\Theta_{vib,K}/T) - 1} \right]^2 \qquad \textbf{(Eq. 2. 69)}$$

The theoretical vibrational frequencies and zero-point energy are introduced to give the vibrational contributions to thermochemistry, then translational, electronic, and rotational

thermodynamic properties are determined and combined to give the temperature-corrected energy, enthalpy, and entropy for the studied system.

2.2. Experimental Methods

Measurements of supramolecular structure and properties requires specialized techniques and instruments, because the lack of X-ray single crystal analysis in many examples prevents the direct assessment of the formed aggregates in solution and in the solid state.[20] In this section, experimental methods for the characterisation of supramolecular structures are introduced. Electrospray ionisation mass spectrometry (ESI-MS) is the experimental method used to determine the size of supramolecular complexes in solution.[21] Fluorescence spectroscopy can be used to evaluate hydrogen-bonding and π-stacking in weakly bound systems. X-ray diffraction (XRD) uses powerful radiation beams to assess the crystallinity of supramolecular structures. Direct imaging of surface-deposited aggregates is available with transmission electron microscopy (TEM), a method that provides substantial insight into supramolecular structure and organisation. Dynamic light scattering (DLS) uses time-dependent electric interactions within macromolecular solutions to determine the diffusion constants of large aggregates, identifying the size and shape of these macromolecules.

2.2.1. Electrospray Ionisation Mass Spectrometry (ESI-MS)[21]

Electrospray ionisation mass spectrometry (ESI-MS) is the experimental method used to determine the composition of supramolecular complexes in solution.[22] Although

first dedicated to the characterisation of proteins, the use of ESI-MS has been extended to other polymers and biopolymers, supramolecular structures, and small polar molecules.

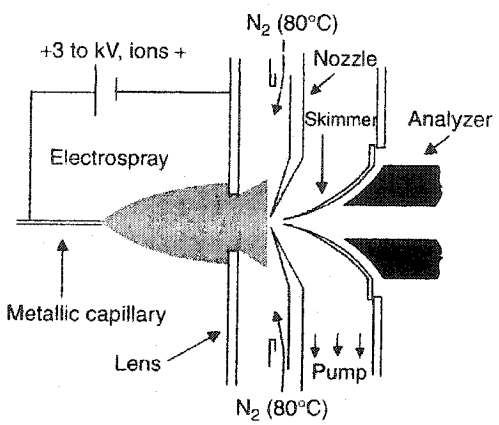


Figure 2. 2. Schematic representation of an electrospray ionisation source using a skimmer for ion focalisation and a N_2 heated flow for desolvation.

A diluted solution of the substrate in a polar solvent is introduced in the mass spectrometer through a small diameter capillary, and subjected to a high voltage. During the ionisation process, this positively charged capillary will attract the molecular anions while displacing the cationic species towards the capillary tip, causing positively charged droplets to be expelled into the mass spectrometer. Solvent evaporation increases the charge-to-volume ratio up to the Rayleigh limit in the ionised droplets, which disintegrate into smaller, nanometer size droplets. In contrast with conventional mass spectrometry techniques (*i. e.* EI-MS, CI-MS) which use drastic ionisation processes,[22] electrospray ionisation mass spectrometry involves a non-destructive ionisation technique during which the integrity of the measured macromolecular species is preserved. As a result, supramolecular structures held together by non-covalent interactions, can be detected as desolvated molecular species. The measured positively charged ions are usually multiply protonated or/and bound to metal alkali (Na^+, K^+, Li^+), or/and other cations.

2.2.2. Fluorescence Spectroscopy

Like UV-visible spectroscopy, fluorescence spectroscopy[23] can be used to evaluate binding in chemically labile systems. Fluorescence occurs as molecular species in their singlet excited state undergo a fast radiative process to return to their initial ground state energy. The resulting fluorescence intensity is linearly dependent on fluorophore concentration in very dilute solutions, but tends to decrease at high concentrations because of light scattering.[24] However, the concentration-dependence of fluorescence at low concentrations can be exploited for binding studies. The intensity of the absorbed light is related to the fluorescence intensity through the fluorescence quantum yield which represents the fraction of excited molecules that fluoresce.

The fluorescence intensity is more sensitive to subtle changes in the micro-environment of the solute than the absorbance. Strongly interacting solvents, such as hydrogen-bonding and polar solvents, can stabilise the ground state of the fluorophores and induce quenching. For example, inclusion of fluorophores into cyclodextrin macrocycle cavities enhanced the fluorescence as the excited state was protected from solvent-induced quenching.[25] On the other hand, the presence of lone pairs in host or guest molecules can cause fluorescence quenching.

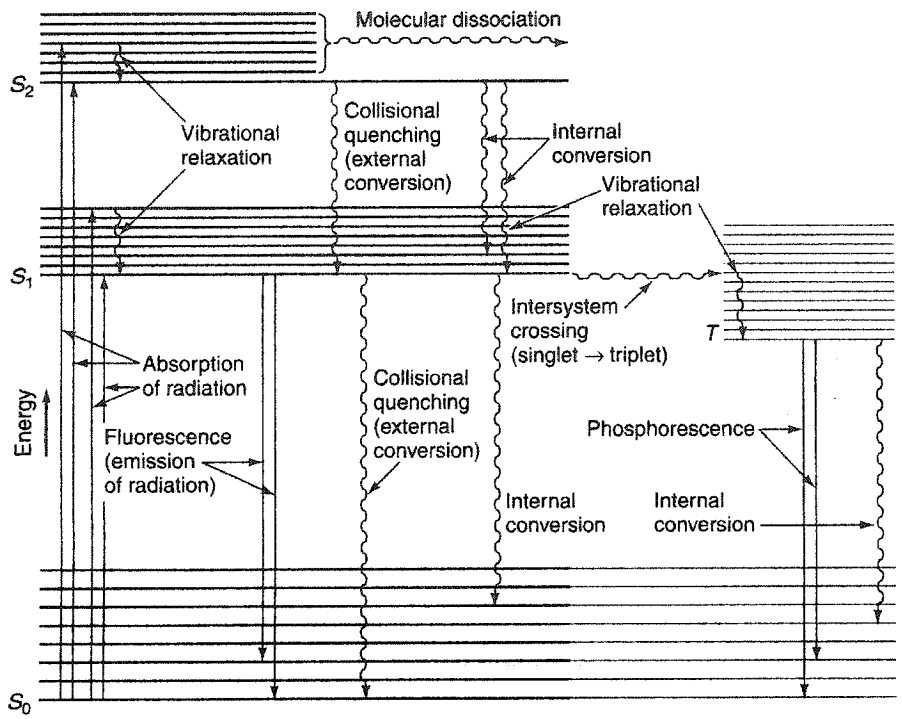


Figure 2. 3. Schematic representation of the various processes involved in the decay of excited systems.

Figure 2. 3 shows the various processes which are involved in the decay of excited molecular systems, and from which the Stern-Volmer equation[26] is derived:

$$I_f = I_0/(1+K_{SV}[Q]) \qquad \textbf{(Eq. 2. 70)}$$

where I_0 is the fluorescence intensity in the absence of quencher Q and K_{SV} is the Stern-Volmer constant.

In the absence of quencher, the decay of fluorescence is characterised by the lifetime τ_0 and involves fluorescence (k_F), non-radiative internal conversion (k_{IC}), and intersystem crossing processes (k_{ISC}). The addition of quencher results leads to a new lifetime τ which incorporates a supplementary bimolecular quenching step.

$$\tau_0 = 1/(k_{IC} + k_F + k_{ISC}) \qquad \textbf{(Eq. 2. 70a)}$$

$$\tau = 1/(k_{IC} + k_F + k_{ISC} + k_Q) \qquad \textbf{(Eq. 2. 70b)}$$

Stern-Volmer constants and lifetimes can be determined for free and bound guest fluorophores, then compared with the rate constants to determine the binding properties of the supramolecular system.[3]

2.2.3. X-ray Diffraction (XRD)

X-ray diffraction is the classic means to determine the structural properties in the solid state.[27, 28] High energy X-rays photons penetrate the inner shells of atoms and collide with the core electrons, giving rise to diffraction peaks due to the occupation of vacant core orbitals by higher-energy electrons. Regular spacings of densely packed atoms in crystalline materials lead to significant destructive and constructive interference of the diffracted waves, producing a X-ray diffraction pattern. The observed X-ray diffraction peaks are proportional to the spacings between lattice planes (*Bragg's law*):[29]

$$\lambda = 2d \sin\theta \qquad \textbf{(Eq. 2. 71)}$$

where λ is the X-ray wavelength, θ is the angle of reflection and d is the lattice spacing. The diffraction peaks can be related to the crystallographic unit cell (Figure 2. 4), which represents the fundamental repeat unit for the entire crystal structure. The XRD peaks are connected to the spacing of lattice points in the crystal by reciprocal indices. Each two-dimensional plane of lattice points intersects the unit cell axes at particular (a, b, c) distances, and the reciprocal distances ($1/a$, $1/b$, $1/c$) are the Miller indices (hkl); i.e. a Miller index of (120) corresponds to a lattice plane intersecting at the ($1a$, $\frac{1}{2}\, b$, $\infty\, c$) unit cell axes.

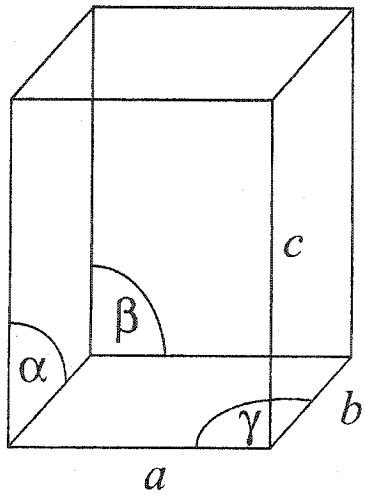


Figure 2. 4 Crystallographic unit cell with side lengths *a*, *b*, and *c*, and angles α (between *b* and *c*), β (between *c* and *a*), and γ (between *a* and *b*).

Examination of organic crystals by XRD can reveal information about supramolecular motifs and unit cell structure, provided the crystal faces can be assigned to the measured lattice peaks. [30]

2.2.4. Transmission Electron Microscopy (TEM)

Transmission electron microscopy uses a high-energy electron beam to investigate solid surfaces with high spatial resolution, providing a direct visualisation of positional order at the interface. The high-energy incident electron wave is scattered by elastic Coulomb interactions with the electron shell and the nuclei of the crystalline specimen.[31]

$$\Psi_0(\mathbf{r}) = \exp(-2\pi i \mathbf{k}_0 \mathbf{r}) \qquad \textbf{(Eq. 2. 72)}$$

where **r** relates to the position and $\mathbf{k}_0$ is the wave vector.

The scattered electron wavefunction in one single atom is defined as:

$$\Psi_S(\mathbf{r},\mathbf{u}) = \frac{\exp(-2\pi i k_0 r)}{r} f_e(\mathbf{u}) \qquad \textbf{(Eq. 2. 73)}$$

where $f_e(\mathbf{u})$ is the atomic scattering factor for electrons, or *scattering length*, given by:

$$f_e(\mathbf{u}) = \sigma \int_{\Omega} \exp(-2\pi i \mathbf{u} \cdot \mathbf{r}') \Phi(\mathbf{r}') d^3\mathbf{r}' \qquad \textbf{(Eq. 2. 74)}$$

with the scattering vector **u** (**u** = -(k_0-k')), the Coulomb potential of the scattering atom, $\Phi(\mathbf{r})$, and the interaction constant σ dependant on the relativistic mass of the incident electron and the elementary charge.

When considering a crystal unit cell containing N atoms of scattering lengths $f_e^{(i)}$, a *structure factor* can be deduced from:

$$F_S(\mathbf{u}) = \sum_{i=1}^{N} f_e^{(i)}(\mathbf{u}) \exp\{-2\pi i(\mathbf{u} \cdot \mathbf{r}_i')\} \qquad \textbf{(Eq. 2. 75)}$$

where $\mathbf{r}' = \mathbf{r}'' + \mathbf{r}_i$. The scattered waves, which evolve from the crystalline medium, interact with one another to induce electron diffraction. Similar to XRD peaks, the obtained electron diffraction peaks can be related to a reciprocal-lattice vector to give *h, k, l* Miller indices, and consequently to molecular structure.

In this thesis, transmission electron microscopy was used to generate high resolution images of self-assembled supramolecular structure. A high-energy electron beam is produced using a self-biasing electron gun equipped with a hot wire filament, and a cathodic Wehnelt shield. (Figure 2. 5) In this system, the pin-shaped cathode is heated by a small electric current to generate a thermionic electron cloud. Filament and shield are then submitted to a high voltage (50 –150 kV), while the rest of the system is maintained at ground potential, inducing motions within the electronic cloud. An increased beam current up to *ca.* 10 μA heats up the electron gun filament, accelerating the electron cloud towards the grounded anode or the bias shield. Surplus electrons collected onto the shield create a large negative charge on the shield, inhibiting additional

electron release. Self-biasing is achieved using the bias resistor, which regulates the filament heat and maintains filament and shield at equilibrium, below a saturation point. The condenser lens focuses the image of the electron beam, thereby controlling brightness. When reaching the specimen, the electron beam is partially deflected, depending on the electron density of the substrate, to create constrast. The greater the mass of the atoms, the greater is the degree of deflection. For example, biological and organic systems, which mainly contain light atoms, display weak contrasts and require staining treatments with heavy metal solutions or shadowing with an alloy. The Pt-C shadowing technique consists in successive evaporations of Pt-C at an angle then carbon at a 90°-angle on air-dried samples. This technique can be used to enhance contrast or to generate replicas of sensitive organic substrates.

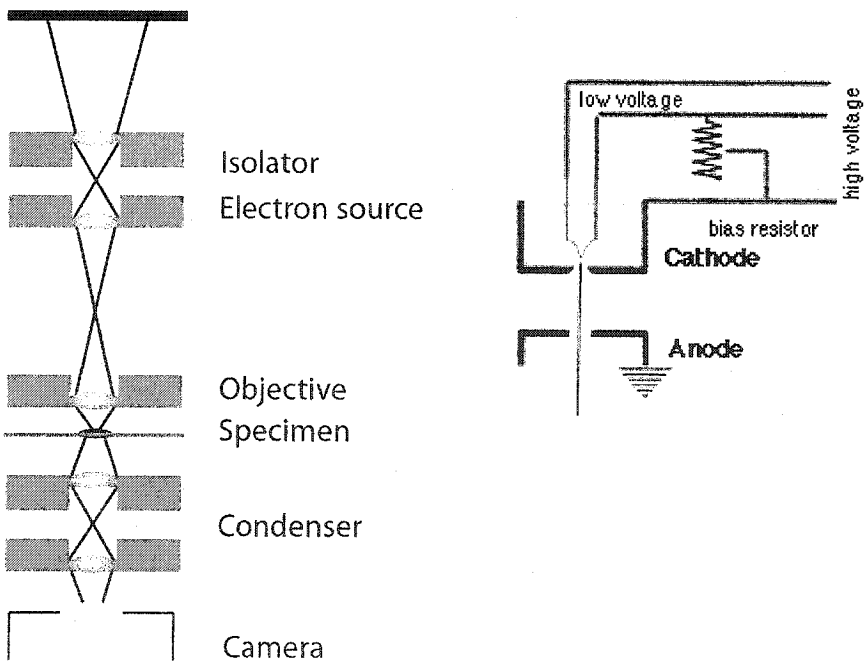


Figure 2. 5. Schematic representation of a transmission electron microscope. Inset: Electron source.

Once through the substrate, the scattered electrons are collected by an objective to form an image, that is subsequently enlarged by an additional projective lens-system. The resulting image can be seen on a fluorescent screen or photographed in black and white, where the contrast has been created by differences in electron density.

2.2.5. Dynamic Light Scattering (DLS)

Dynamic light scattering measures the time-dependence of scattered light intensity to produce an apparent diffusion coefficient D_{app}. This method is useful in explaining dynamic, relaxation processes which occur in macromolecular solutions or detecting the formation of higher-order supramolecular aggregates.[32]

Oscillating electric components of light can create distorsions of the charge distribution upon interaction with matter. The resulting scattered electric field is defined as:

$$E_s(\mathbf{R},t) = -\frac{\omega_0^2 n_0^2 E_0}{c^2 R}\exp(i\mathbf{K}_S^T \cdot \mathbf{R})\exp(-i\omega_0 t)\alpha(\mathbf{K},t') \qquad \textbf{(Eq. 2. 76)}$$

where ω_0 is the angular frequency, n_0 is the refractive index of the medium, E_0 is the magnitude of the incident electric field, c is the speed of light, $\mathbf{R}$ is the location of the detector in the laboratory frame ($R = |\mathbf{R}|$), $\mathbf{K}_s$ is the wave vector for the scattered electric field ($\mathbf{K} = \mathbf{K}_0 - \mathbf{K}_S$), and t is the time of detection of the light irradiated at the earlier time t'. The spatial Fourier transform of the polarizability from real space ($\mathbf{r}$) to momentum space ($\mathbf{K}$), $\alpha(\mathbf{K}, t')$, can be described as:

$$\alpha(\mathbf{K},t') = \int_s \alpha(r,t')\exp(i\mathbf{K}^T \cdot r)d^3r \qquad \textbf{(Eq. 2. 77)}$$

The intensity of scattered light, along with its polarizability, is largely dependent on the instantaneous position of the scattering centres. Permanent collision-induced motions give rise to fluctuations of the instantaneous light-scattered intensity in macromolecular systems. The decay rate of these fluctuations towards an average, equilibrium state is directly related to the dynamics of the molecules. To explain this time-dependence, an *autocorrelation function* $C(t)$ is defined as:

$$C(t) = \lim_{T\to\infty} \frac{1}{T} \int_{-T/2}^{T/2} x(t')x(t'+t)dt' = \langle x(0)x(t) \rangle \qquad \textbf{(Eq. 2. 78)}$$

where t is time and $x(t)$ is the time-dependent position with respect to the x-axis.

The scattered light is detected as a current using a photomultiplier tube, and an electric field correlation function can be generated:

$$\langle E_S^*(\mathbf{R},0)^T \cdot E_S(\mathbf{R},t) \rangle = B \langle \alpha^*(\mathbf{K},0)^T \cdot \alpha(\mathbf{K},t) \rangle \exp(-i\omega_0 t) \quad \textbf{(Eq. 2. 79)}$$

where B is a constant. The electric field correlation function can be normalised to give the the generalised Stokes-Einstein relationship for the mutual diffusion coefficient, D_m:

$$D_m = \frac{1}{N_A f_m} \left(\frac{\partial \pi}{\partial c_p} \right)_{T,\mu'} \qquad \textbf{(Eq. 2. 80)}$$

where $(\partial\pi/\partial c_p)_{T,\mu'}$ is the osmotic susceptibility, f_m is the friction factor, μ' is the chemical potential for all species except p, and N_A is Avogadro's number. The obtained mutual diffusion coefficient can then be used to determine the equivalent hydrodynamic radius.

2.3. References and Notes

[1] P. A. M. Dirac, *Proc. Roy. Soc. (London)*, **1929**, *123*, 714.

[2] D. B. Boyd, K. B. Lipkowski, *J. Chem. Ed.*, **1987**, *59*, 269.

[3] H. –J. Schneider, A. Yatsimirsky, *Principles and Methods in Supramolecular Chemistry*, John Wiley & Sons: Chicester, 2000.

[4] N.L. Allinger, *J. Am. Chem. Soc.*, **1977**, *99*, 8127.

[5] E. Schrödinger, *Ann. Physik*, **1926**, *79*, 361.

[6] J. A. Pople, D. L. Beveridge, *Approximate Molecular Orbital Theory*, McGraw-Hill Inc.: New York, 1970.

[7] E. Hückel, *Z. Physik*, **1931**, *70*, 204.

[8] J. C. Slater, *Phys. Rev.*, **1930**, *36*, 57.

[9] D. A. McQuarrie, *Quantum Chemistry*, University Science Books: Mill Valley, California, 1983.

[10] C. C. J. Roothan, *Rev. Mod. Phys.*, **1951**, *23*, 69.

[11] I. N. Levine, *Quantum Chemistry*, 3rd ed., Allyn and Bacon, Inc.: Boston, 1983.

[12] (a) W. J. Hehre, R. F. Stewart, J. A. Pople, *J. Chem. Phys.*, **1969**, *51*, 2657. (b) B. Collins, P. V. R. Schleyer, J. S. Binkley, J. A. Pople, *J. Chem. Phys.*, **1976**, *64*, 5142.

[13] (a) J. S. Binkley, J. A. Pople, W. J. Hehre, *J. Am. Chem. Soc.*, **1980**, *102*, 939. (b) M. S. Gordon, J. S. Binkley, J. A. Pople, W. J. Pietro, W. J. Hehre, *J. Am. Chem. Soc.*, **1982**, *104*, 2797. (c) W. J.Pietro, M. M. Francl, W. J. Hehre, D. J. Defrees, J. A.; Pople, J. S.Binkley, *J. Am. Chem. Soc.*, **1982**, *104*, 5039. (d) K. D. Dobbs, W. J. Hehre, *J. Comp.*

Chem., **1986**, *7*, 359. (e) K. D. Dobbs, W. J. Hehre, *J. Comp. Chem.* **1987**, *8*, 861. (f) K. D. Dobbs, W. J. Hehre, *J. Comp. Chem.* **1987**, *8*, 880.

[14] (a) W. J. Hehre, W. A. Lathan, R. Ditchfield, M. D. Newton, J. A. Pople, Gaussian 70 (Quantum Chemistry Program Exchange, Program No. 237, 1970). (b) W. J. Hehre, R. Ditchfield, J. A. Pople, *J. Chem. Phys.*, **1972**, *56*, 2257. (c) P. C. Hariharan, J. A. Pople, *Mol. Phys.*, **1974**, *27*, 209. (d) M. S. Gordon, *Chem. Phys. Lett.*, **1980**, 76, 163. (e) P. C. Hariharan, J. A. Pople, *Theo. Chim. Acta.*, **1973**, *28*, 213.

[15] (a) J. J. P. Stewart, *J. Comput. Chem.*, **1989**, *10*, 209. (b) J. J. P. Stewart, *J. Comput. Chem.* **1989**, *10*, 221. (c) J. J. P. Stewart, *J. Comput. Aided Mol. Design*, **1990**, *10*, 221.

[16] (a) A. C. Spivey, P. Charbonneau, T. Fekner, D. H. Hochmuth, A. Maddaford, C. Malardier-Jugroot, A. J. Redgrave, M. A. Whitehead, *J. Org. Chem.*, **2001,** *66*, 7394. (b) F. Rakotondradany, C. I. Williams, M. A. Whitehead, B. J. Jean-Claude, *J. Comput. Chem. (THEOCHEM)*, **2001**, *535*, 217. (c) C. I. Williams, M. A. Whitehead, B. J. Jean-Claude, *J. Org. Chem.*, **1997**, *62*, 7006.

[17] *HyperChem User Manual*, Hypercube Inc.: Gainesville, Florida, 1997.

[18] J. J. P. Stewart, *Mopac 2002 User Manual*; Fujitsu Limited: 2001. Available online at http://www.cachesoftware.com/mopac/Mopac2002manual/.

[19] J. W. Ochterski, *Thermochemistry in Gaussian*, Gaussian Inc., 2000.

[20] (a) J. W. Steed, J. L. Atwood, *Supramolecular Chemistry*, John Wiley & Sons: Chicester, 2000. (b) S. Leininger, B. Olenyuk, P. J. Stang, *Chem. Rev.*, **2000**, *100*, 853.

[21] E. de Hoffmann, V. Stroobant, *Mass Spectrometry: Principles and Applications*, 2nd ed., John-Wiley & Sons: Chichester, 2001.

[22] R. D. Smith, J. E. Bruce, Q. Wu, Q. L. Lei, *Chem. Soc. Rev.*, **26**, 191.

[23] A. Sharma, S. G. Schulman, *Introduction to Fluorescence Spectroscopy*, Wiley-Interscience: New York, 1999.

[24] D. A. Harris, C. L. Bashford, *Spectrophotometry and Spectrofluorometry: A Practical Approach* (Eds.), IRL Press: Oxford, 1987.

[25] R. P. Frankewich, K. N. Thimmaiah, W. L. Hinze, *Analyt. Chem.*, **63**, 2924.

[26] J. R. Lakowicz, *Principles of Fluorescence Spectroscopy*, Plenum Press: New York, 1983.

[27] P. W. Atkins, *Physical Chemistry*, 5th ed.; W. H. Freeman and Company: New York, 1994.

[28] G. H. Stout, L. H. Jensen, *X-Ray Structure Determination: A Practical Guide*, Macmillan Publishing: New York, 1968.

[29] W. H. Bragg, W. L. Bragg, *X-Rays and Crystal Structure*, G. Bell: London, 1915.

[30] (a) G. R. Desiraju, *Acc. Chem. Res.*, **1991**, *24*, 290. (b) G. R. Desiraju, *Acc. Chem. Res.*, **1996**, *29*, 441.

[31] A. Rosenauer, *Transmission Electron Microscopy of Semiconductor Nanostructures: An Analysis of Composition and Strain State*, Springer-Verlag: Berlin, 2003.

[32] K. S. Schmitz, *An Introduction to Dynamic Light Scattering by Macromolecules*, Academic Press, Inc.: San Diego, 1990.

Chapter 3.

Photoresponsive Supramolecular Systems: Self-Assembly of Azodibenzoic acid Linear Tapes and Cyclic Tetramers

Reproduced with permission from:

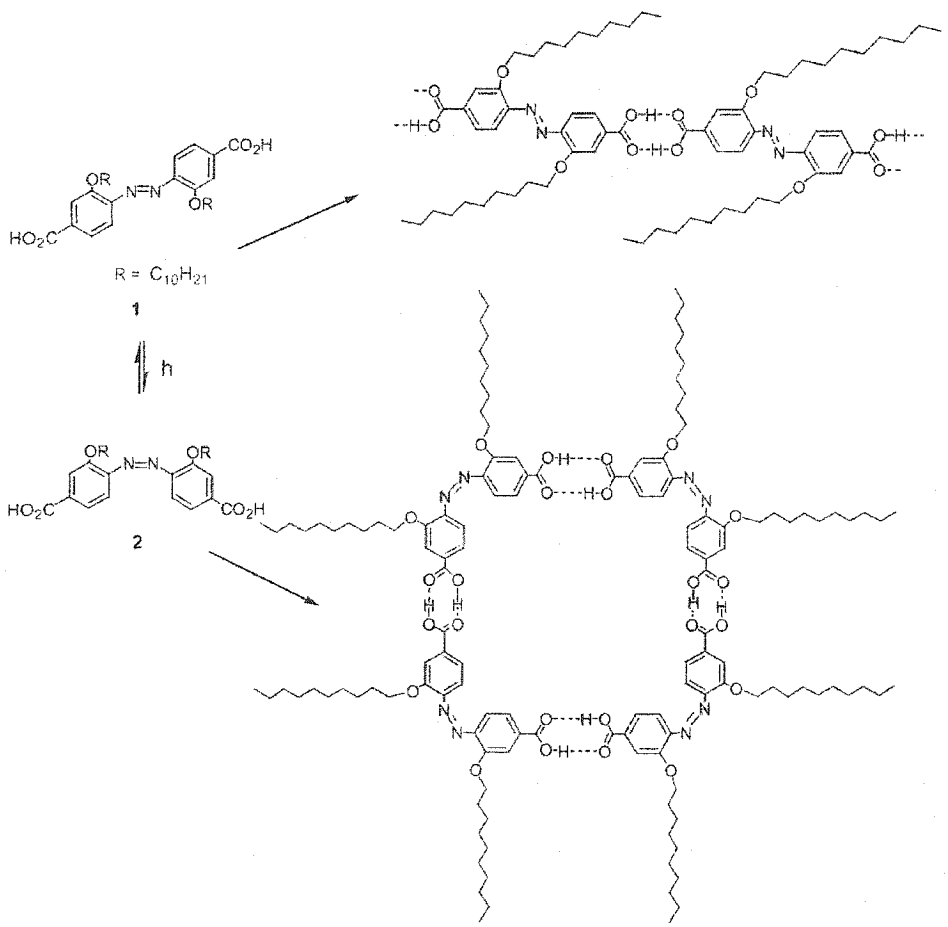
F. Rakotondradany, M. A. Whitehead, H. F. Sleiman, A.-M. Lebuis, *Chem. Eur. J.*, **2003**, *9*, 4771.

Copyright © 2003 WILEY-VCH Verlag GmbH & Co. KGaA, Weinheim.

3.1. Introduction

Molecular self-assembly has recently emerged as one of the most efficient methods to create new materials with controlled physical and chemical properties.[1] In particular, hydrogen bonded self-assembly has generated an impressive range of structures, such as helices,[1] linear tapes,[1,2] cyclic arrays[1,2d,3]and three-dimensional objects.[1,4]An especially attractive goal is to use external stimuli, such as electrical, chemical or optical signals to control the self-assembly process.[1-11] In particular, photoswitchable units have been incorporated in a variety of supramolecular systems,[5-11] such as peptides,[5] DNA,[6] dendrimers,[7] molecular hosts[8] as well as macromolecular and liquid crystalline structures.[9,10] These systems have almost exclusively relied on the photoswitching of a molecule between two distinct states,[5-8] or on using the reversible photoisomerization of a chromophore to pattern a surrounding polymer or liquid crystal matrix.[9,11]

We here report a new strategy to effect photochemical control over molecular self-assembly, by using photoresponsive azobenzene units **1** and **2** as *supramolecular building blocks*. (Scheme 3. 1) This results in the light-driven switching of a material between two dramatically different nanoscale morphologies.[11] The *trans*-azobenzene form of these molecules **1** associates into infinite hydrogen-bonded *linear tapes*, while the *cis*-azobenzene form **2** undergoes hydrogen bonded self-assembly into *cyclic tetramers*, which then further associate to form long, rod-like aggregates.



Scheme 3. 1. Hydrogen bond self-assembly of *trans*-**1** and *cis*-**2** azodibenzoic acid.

In the design of molecule **1**, the photoswitchable azobenzene unit is incorporated in the main chain, and two hydrogen bonding carboxylic acids are para to the N=N linkage. Dicarboxylic acids, such as isophthalic and terephthalic acid derivatives have been shown to associate into discrete hexameric rosettes and linear tapes respectively.[3a,b] The azobenzene units in molecule **1** can undergo a reversible *trans-cis* photoisomerization.[11,12] In the *trans* isomer **1**, the two carboxylic groups are expected to be aligned, and they can thus undergo hydrogen-bonding self-assembly into linear aggregates. On the other hand, in the photogenerated *cis*-form **2**, the carboxylic acids are expected to be oriented in a near perpendicular fashion, thus they can self-assemble into

cyclic structures. (Scheme 3. 1) Building block **1** also incorporates two long alkoxy chains ortho to the azo group, in order to sterically favor the formation of discrete, cyclic structures once converted to the *cis*-form **2**.[3]

3.2. Results and Discussion

3.2.1. Theoretical Calculations

To validate the above assumptions, we first investigated the geometry of *cis-p*-azodibenzoic acid as a model compound by semi-empirical PM3 molecular orbital calculations.[13] These consistently showed similar C-N=N bond angles for this building block, and an orientation of 82° between the carboxylic acid groups. We then proceeded to perform PM3 calculations, using the unsubstituted *p*-azodibenzoic acid, as well as *o-bis*(methoxy) azodibenzoic acid as model compounds, in order to estimate the most stable supramolecular structures from *trans*-**1** and *cis*-**2**. PM3 enthalpies and Gibbs free energies of reaction at 298 K were calculated for the formation of open and closed oligomers from monomeric *trans*- and *cis*-azodibenzoic acids (Table 3. 1).[14] These calculations indicated that the *trans*-azodibenzoic acid self-assembles most favorably into linear tapes (Figure 3. 1), while *cis*-azodibenzoic acid is most likely to form cyclic structures.[15] (Figure 3. 2) Comparison of the closed aggregates indicated that the cyclic tetramer shown in Figure 3. 2a is thermodynamically more stable than both the pentameric and hexameric rosettes.[16] (Table 3. 1) These calculations also suggested that the formation of closed structures from azodibenzoic acid trimers might be difficult. Consequently, as expected from our design, PM3 calculations predict that *trans*-azodibenzoic acid forms oligomeric linear tapes, whereas *cis*-azodibenzoic acid **2**

associates into cyclic structures, suggesting that the self-assembly of 1 can be reversibly photoinduced between dramatically different structures. It is of note that this study is one of a few examples of the use of semi-empirical calculations to fully optimize a supramolecular assembly.[17]



Figure 3. 1. PM3 optimized geometry of a linear hexameric tape formed from *trans*-azodibenzoic acid.

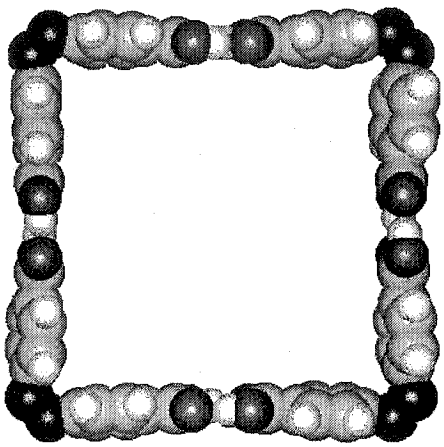
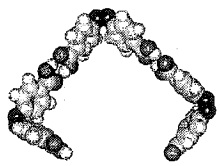


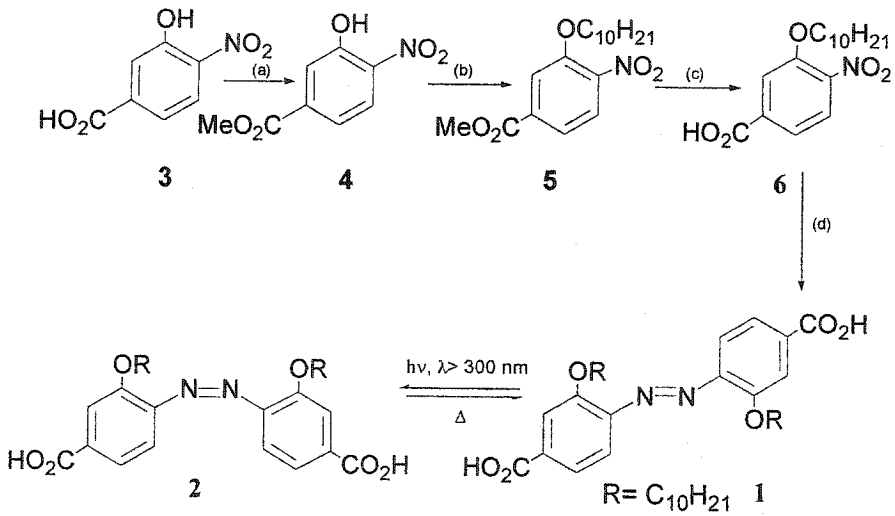
Figure 3. 2. PM3 optimized geometry of the square formed from *cis*-azodibenzoic acid.

Table 3. 1. PM3 standard enthalpies and Gibbs free energy of the self-assembly as a function of the hydrogen-bonded aggregate formed with the *trans*- and the *cis*-azodibenzoic acids at 298 K. These energies were obtained by substracting the cumulated energies of the n monomers involved in the self-asssembly of the compound from the energy of the formed complex.

Hydrogen-bonded aggregates		ΔH_r^0 kcalmol^{-1}	ΔG_r^0 kcalmol^{-1}
Trans-**1** Linear tape	 n = 6	-24.46	-11.24
Cis-**2** Linear tape	 n = 6	-39.55	31.25
Cis-**2** Trimer	 n = 3	-15.27	12.71
Cis-**2** Cyclic tetramer	 n = 4	-30.87	8.62
Cis-**2** Cyclic pentamer	 n = 5	-37.42	15.34
Cis-**2** Cyclic hexamer	 n = 6	-43.72	19.49

3.2.2. Synthesis and Self-Assembly of *trans*-Azodibenzoic Acid 1

Scheme 3. 2 outlines the synthesis of **1** from 3-hydroxy-4-nitrobenzoic acid **3**. Carboxylic acid **3** is first protected in acidic media to give ester **4**, which is then reacted with a stoichiometric amount of 1-bromodecane under mild basic conditions. The resulting ether **5** is deprotected under reflux in 1:1 KOH/MeOH, then reduced using zinc dust under basic conditions. The desired azodibenzoic acid **1** is isolated by chromatography of the corresponding methyl ester, followed by hydrolysis under basic conditions.[14]



Scheme 3. 2. Synthesis of 2,2'-*bis*(decyloxy)-4,4'-azodibenzoic acid **1**. (a) Conc. H_2SO_4, MeOH, reflux, 48 hrs, 96 %. (b) 1-$C_{10}H_{21}Br$, anhydrous K_2CO_3, DMF, N_2 atmosphere, 80°C, 24 hrs, 93 %. (c) KOH pellets, 1:1 MeOH/H_2O, reflux, 4 hrs, 96 %. (d) Zn dust (1.6 eq.), 30% aq. NaOH, 24 hrs; Zn dust (1.4 eq.), water, 3 days, 28 %.

We first studied the hydrogen-bond self-assembly behavior of *trans*-azodibenzoic acid **1**. Vapor pressure osmometry (VPO) measurements were carried out in CH_2Cl_2, using benzil (MW= 210) as the molecular weight standard.[18] The calculated *y*-intercept of the plot of VPO molecular weight versus concentration was found to match the origin,

and the calculated association constants of dimer, trimer, tetramer, etc. were nearly equal.[14] This indicates that **1** does not form discrete aggregates, but rather oligomeric linear chains. Single crystals of *trans*-**1** were grown by evaporation of a DMF solution, and the X-ray structure is shown in Figure 3. 3.[19] Diacid **1** does indeed form an extended hydrogen bonded network of linear tapes, confirming the PM3 calculations and the VPO results. In addition, these tapes pack together through their long alkyl substituents to form infinite parallel sheets. (Figures 3. 3b and 3. 3c) This high crystallinity of the *trans*-**1** monomer is also observed in its powder diffraction (XRD) pattern. (Figure 3. 5a)

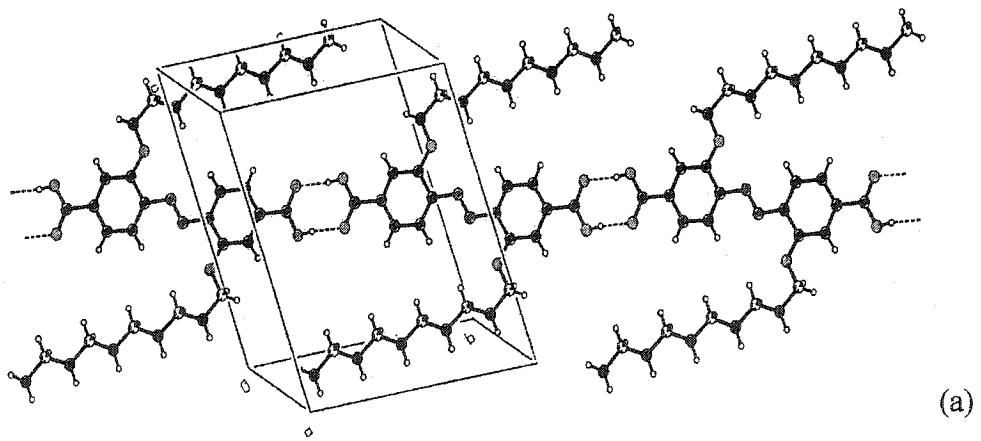


Figure 3. 3. (a) X-ray single crystal data showing the hydrogen-bonded tapes formed by *trans*-**1**.

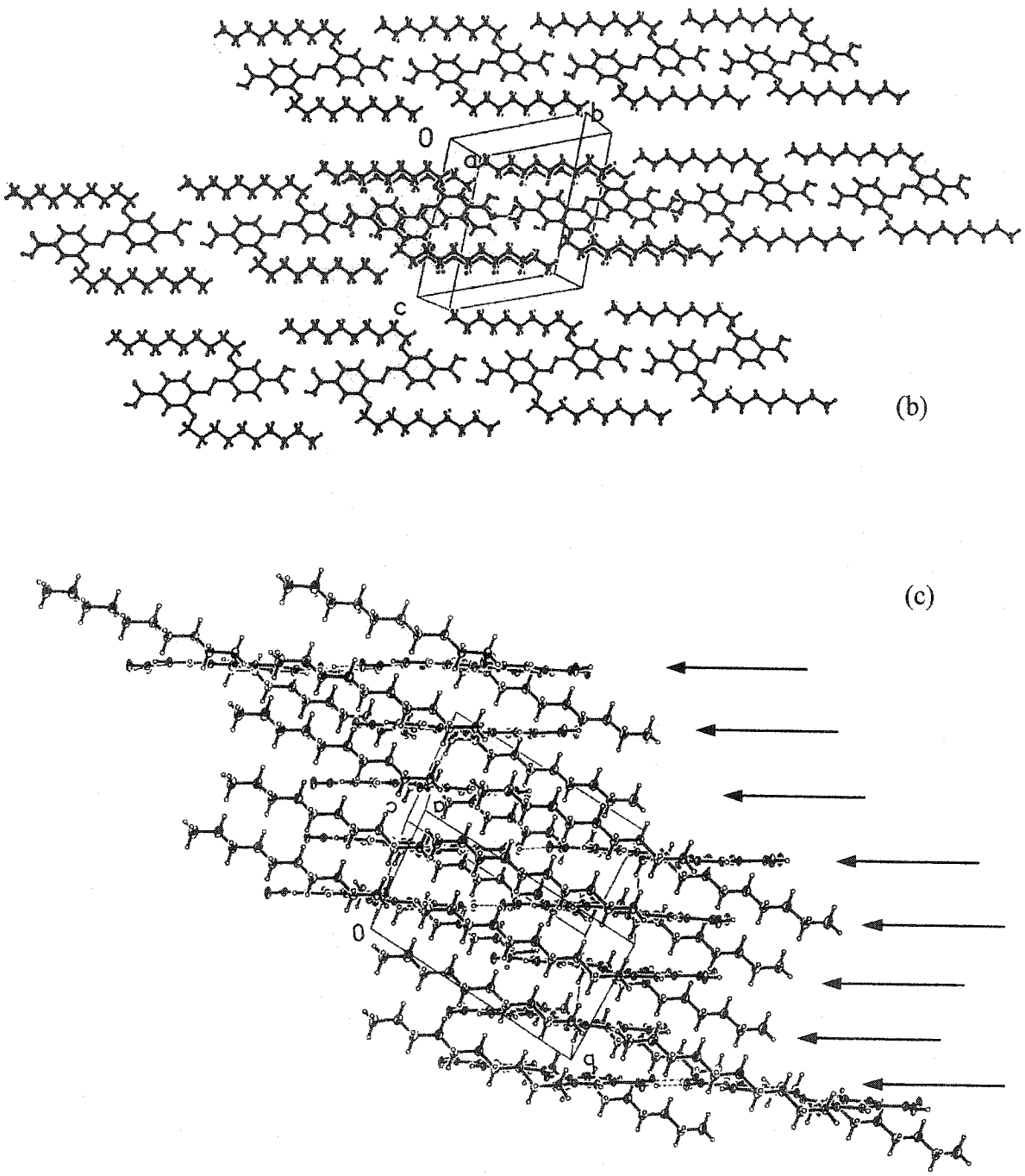


Figure 3. 3. (continued) (b) Sheets formed upon aggregation of these tapes (top view). (c) Sheets formed from these tapes (side view). The arrows indicate the planes defined by the sheets.

3.2.3. Reversible Photoisomerization of *trans*-Azodibenzoic Acid 1 to the *cis*-Form 2

The propensity of *trans*-**1** to undergo reversible photoisomerization was then examined by UV-vis and ^{1}H-NMR spectroscopy. Irradiation of samples of *trans*-**1** at λ>300 nm results in a decrease in the two UV-vis absorption maxima at 321 nm and 387 nm, with an isobestic point around 286 nm, and the appearance of a new peak at 250 nm corresponding to *cis*-**2**. (Figure 3. 4)

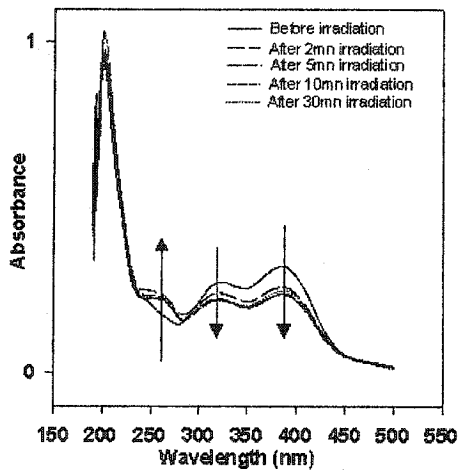
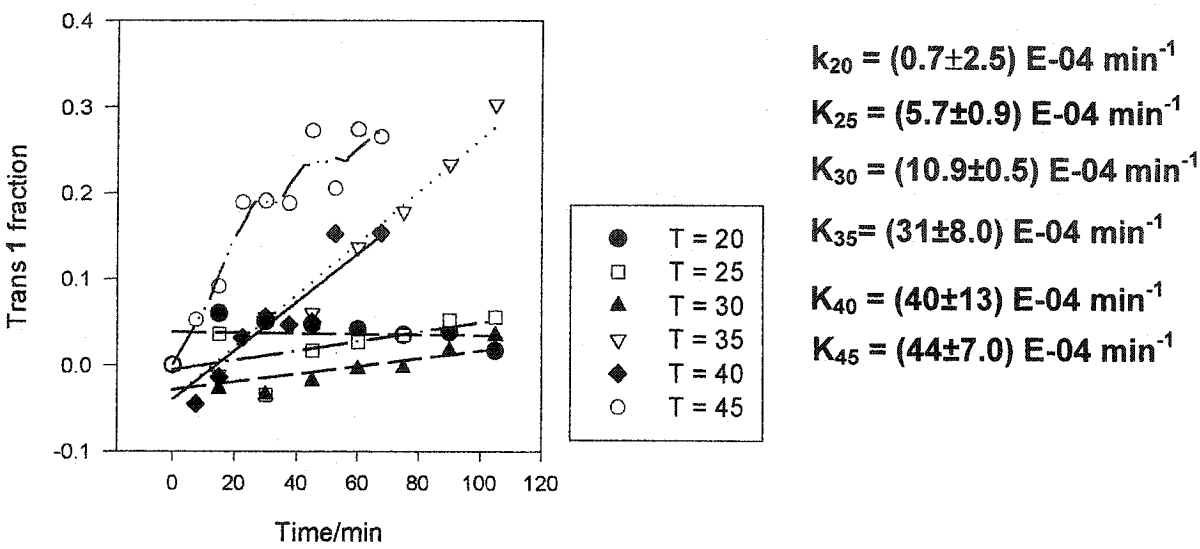


Figure 3. 4. UV-visible absorption spectrum recorded during the UV irradiation (λ> 300 nm) of a 3.44x10^{-5} M solution of *trans*-**1** in methanol.

In d_6-DMSO, this photoisomerization results in distinct ^{1}H-NMR signals for *trans*-**1** and *cis*-**2**, and a 1:1.3 *trans-cis* photostationary state can be reached after 2 hrs of irradiation. Kinetic studies were carried out on the thermal conversion of *cis*-azodibenzoic acid **2** to *trans*-**1**, using both UV-vis and ^{1}H-NMR in DMSO,[14] and an activation enthalpy $\Delta H^{\ddagger}$= 84.9 ± 2.5 kJmol^{-1} and entropy $\Delta S^{\ddagger}$= –72.8 ± 8.0 Jmol^{-1}K^{-1} were obtained. These results were similar to previously obtained parameters for *ortho*-alkyl

azobenzenes.[20] The conversion of *cis*-**2** to *trans*-**1** was complete in 1 hr at 70°C. These studies thus demonstrate the ready formation of *cis*-**2** via photochemical isomerization of **1**, and its facile thermal conversion to *trans*-**1**.

Figure 3. 5. Kinetics of the thermal cis-trans reisomerization monitored by ^{1}H-NMR in



$CDCl_3$. At 45°C, the concentration of *trans*-**1** increased stepwise as shown by the dash-dot-dot line.

In DMSO, *trans*-**1** and *cis*-**2** are expected to exist in their monomeric form, therefore the kinetics involve the isomerization of monomeric *cis*-**2** to monomeric *trans*-**1**. However, in a non-competitive solvent such as chloroform, *trans*-**1** and *cis*-**2** should associate into hydrogen-bonded structures. Thus, the kinetics in chloroform should reflect the interconversion between self-assembled supramolecular structures of *cis*-**2** and *trans*-**1**, and are expected to differ for this reaction from the results obtained in CH_3OH or DMSO. The photoisomerization behavior (λ> 300 nm) of *cis*-**2** to *trans*-**1** in $CDCl_3$ was

azobenzenes.[20] The conversion of *cis*-**2** to *trans*-**1** was complete in 1 hr at 70°C. These studies thus demonstrate the ready formation of *cis*-**2** via photochemical isomerization of **1**, and its facile thermal conversion to *trans*-**1**.

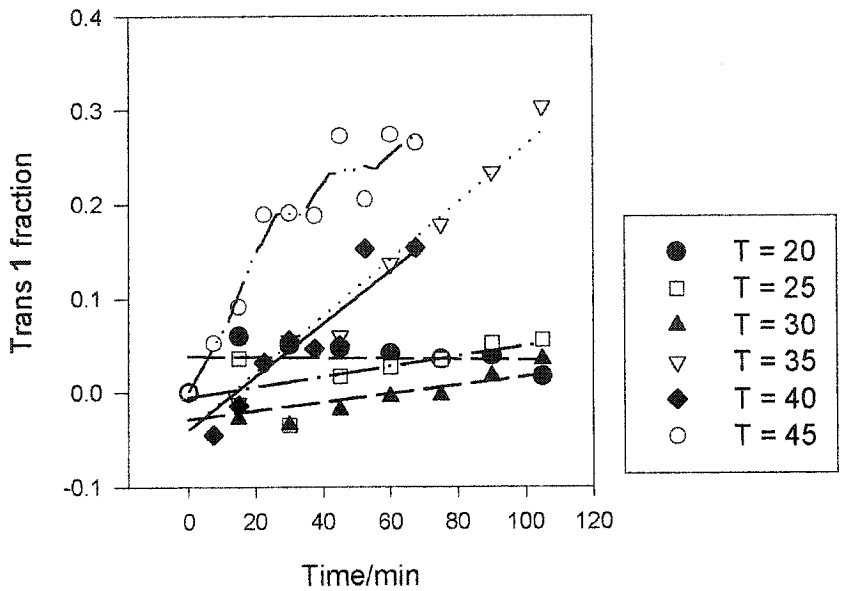


Figure 3. 5. Kinetics of the thermal cis-trans reisomerization monitored by ^{1}H-NMR in $CDCl_3$. At 45°C, the concentration of *trans*-**1** increased stepwise as shown by the dash-dot-dot line.

In DMSO, *trans*-**1** and *cis*-**2** are expected to exist in their monomeric form, therefore the kinetics involve the isomerization of monomeric *cis*-**2** to monomeric *trans*-**1**. However, in a non-competitive solvent such as chloroform, *trans*-**1** and *cis*-**2** should associate into hydrogen-bonded structures. Thus, the kinetics in chloroform should reflect the interconversion between self-assembled supramolecular structures of *cis*-**2** and *trans*-**1**, and are expected to differ for this reaction from the results obtained in CH_3OH or DMSO. The photoisomerization behavior (λ> 300 nm) of *cis*-**2** to *trans*-**1** in $CDCl_3$ was

compared to that in d_6-DMSO and CD_3OD, using ^{1}H-NMR spectroscopy at a range of temperatures (20°C to -30°C). While the photostationary state was rapidly reached upon photolysis of *cis*-**2** in all solvents even at low temperatures (ca. 5 min.), the *cis-trans* photoisomerization rate was nearly double in d_6-DMSO and d_4-methanol than in $CDCl_3$. This is consistent with the need for dissociation of the hydrogen-bonded supramolecular structure formed by *cis*-**2** in $CDCl_3$, prior to its reisomerization to *trans*-**1**.

Kinetic studies were carried out on the thermal conversion of *cis*-azodibenzoic acid **2** to *trans*-**1** in $CHCl_3$, using UV-vis and ^{1}H-NMR spectroscopy.[14] The obtained enthalpy of activation was higher in $CHCl_3$ ($\Delta H^{\ddagger} = 97.4 \pm 4.2$ kJmol^{-1}) than DMSO ($\Delta H^{\ddagger} = 84.9 \pm 2.5$ kJmol^{-1}), and the entropy of activation ($\Delta S^{\ddagger} = -15.9 \pm 13.7$ Jmol^{-1}K^{-1}) was more positive in $CHCl_3$ than DMSO ($\Delta S^{\ddagger} = -72.8 \pm 8.0$ Jmol^{-1}K^{-1}). This data is consistent with an additional contribution to the enthalpy of activation of the *cis-trans* isomerization, which involves dissociation of the *cis*-**2** hydrogen-bonded supramolecular structure. Furthermore, the larger entropy of activation is consistent with the presence of a higher degree of order in the supramolecular structure of *cis*-**2** in $CHCl_3$ than in the monomeric structure of **2** in DMSO. Consequently, the kinetic behaviour observed in chloroform for the *cis-trans* isomerization is consistent with the formation of higher-order supramolecular structures from *cis*-**2**, and their thermal and photochemical switching to the *trans*-**1** linear tapes (*vide supra*).

3.2.4. Self-Assembly of *cis*-Azodibenzoic Acid 2

Cis-azodibenzoic acid **2** can be isolated from photoirradiated samples of *trans*-**1** using reverse-phase HPLC,[14] and its stability (up to 2 days in the dark at 20°C and 2 weeks at 4°C) allowed its full characterization. As will be shown, the self-assembly

behavior of *cis*-**2** is radically different from *trans*-**1**. *Cis*-**2** is significantly more soluble in non-polar solvents (*i.e.*, CH_2Cl_2) than *trans*-**1**. ^{1}H-NMR spectra of **2** (CD_2Cl_2) taken at a range of concentrations, show symmetrical azobenzene peaks. These results are consistent with the formation of a discrete cyclic structure, rather than oligomeric aggregates from this molecule. Examination of the aromatic region upon dilution (from a saturated 3.0 mM solution to 0.2 mM), showed a small shift of ca. 0.01 ppm for these peaks. This shift was accompanied by a peak sharpening, suggesting the existence of π-π stacking interactions in solution.[21]

Vapor pressure osmometry (VPO) studies were carried out on solutions of **2** in CH_2Cl_2. In order to determine the molecular weight of the hydrogen-bonded structure formed by **2**, two molecular weight standards were used for this experiment, and the experiment was repeated using two different osmometers.[14] In all cases, the plots of VPO molecular weight versus concentration showed clear *y*-intercepts corresponding to M_n= 2210 using benzil (Δ= 1.2 %) and M_n= 2317 using polystyrene (Δ= 0.1 %), consistent with the formation of a tetramer (M_n= 2328) in solution.[14] In addition, ESI-MS of *cis*-**2** enabled the detection of a tetrameric structure at *m/z*= 2330.[14]

X-ray powder diffraction spectra were obtained for *cis*-**2**, and showed a dramatically different supramolecular structure for this isomer than for *trans*-**1**. (Figure 3. 5b) In contrast to the sharp peaks obtained for **1**, the spectrum of **2** features one main broad peak at 14.0°, followed by three less intense peaks at 24.0°, 25.7°, and 27.0°.[22a]

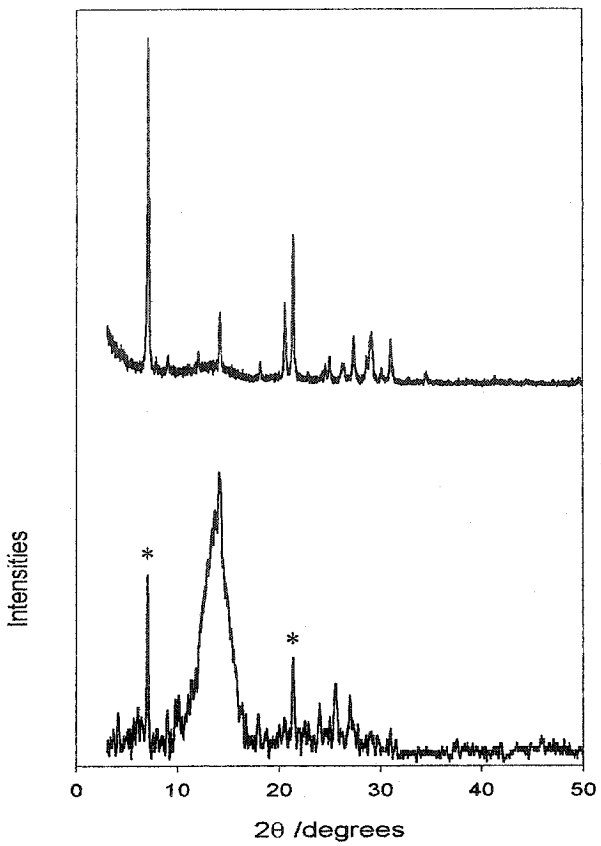


Figure 3. 6. (a) X-ray diffraction (XRD) pattern for *trans*-**1**. (b) XRD pattern for *cis*-**2**. The asterisks mark the presence of *trans*-**1** impurities.

Applying Scherrer's equation to the width at half-height of the main diffraction peak[22b, c] gave a crystal dimension of 3.6 ± 0.2 nm for this solid. This distance is in good agreement with the expected diameter for a *cis*-**2** cyclic tetramer (4.2 nm).[23] Thus ^{1}H-NMR, vapor pressure osmometry, ESI-MS, X-ray powder diffraction studies, as well as theoretical PM3 calculations are all consistent with the self-assembly of *cis*-**2** into discrete cyclic tetramers, in contrast with the oligomeric linear tapes obtained from *trans*-**1**.[24]

3.2.5. Transmission Electron Microscopy and Dynamic Light Scattering Studies

Transmission electron microscopy (TEM) studies of *trans*-**1** and *cis*-**2** allowed direct visualization of the large differences in their self-assembly behavior. Interestingly, these studies also revealed a second level of self-organization of these molecules. Figures 3. 6 and 3. 7 show transmission electron micrographs of replicas prepared from dispersions of *trans*-**1** and *cis*-**2** in 1,2-dichloroethane or by direct deposition onto a carbon-coated grid.[25] Large, sheet-like aggregates are observed for *trans*-**1** (Figure 3. 6), consistent with the ordered arrangement of stacked linear tapes from this molecule. (Figure 3. 3)

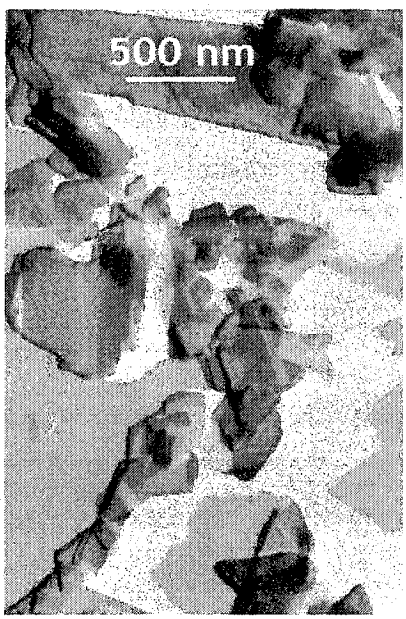
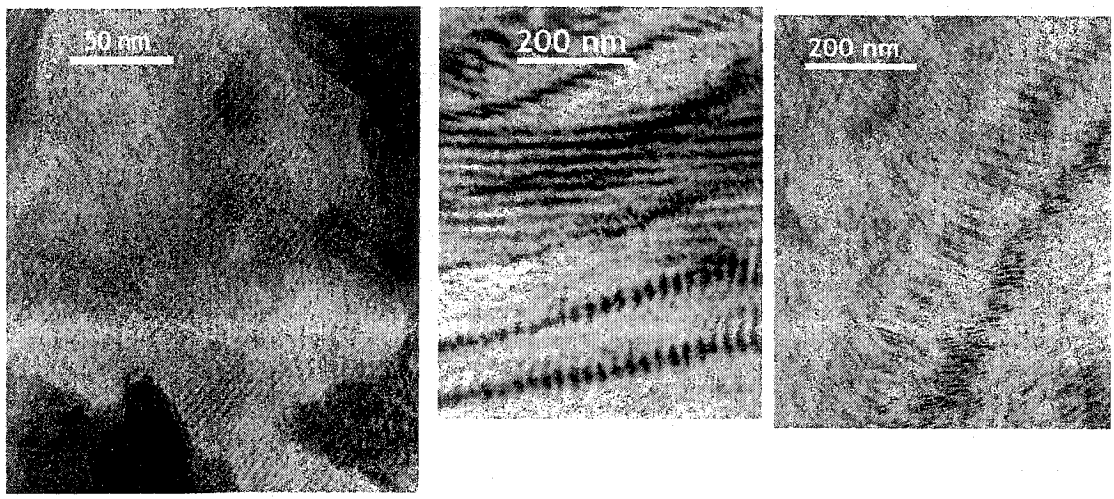


Figure 3. 7. TEM of a replica for *trans*-**1**.

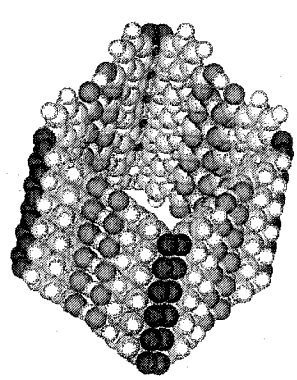
On the other hand, the TEM of samples of *cis*-**2** showed the formation of dramatically different supramolecular structures. In contrast with *trans*-**1**, periodic arrays of elongated aggregates, with length as great as 170 nm, arise from the *cis*-**2** isomer. (Figure 3. 7) In some cases, these structures aggregate into large bundles of 23 nm in diameter and 430 nm in length (Figure 3. 7d). The outer hydrodynamic diameter was measured as ca. 3.9 nm, in agreement with the estimated diameter of the self-assembled supramolecular cycles of *cis*-**2** (4.2 nm), and as already shown by our XRD, VPO and PM3 studies. (*vide supra*) This diameter was observed on more than 10 different, freshly purified samples of *cis*-**2**, and for various deposition conditions (direct deposition and replica methods, see experimental section).[25] This result suggests further organization of

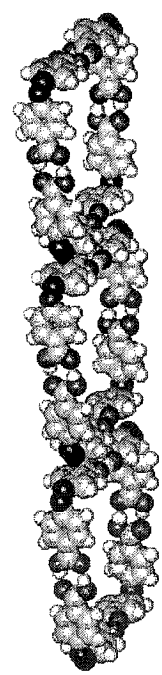
the supramolecular cycles from *cis*-**2** through π-π stacking and/or alkyl-alkyl interactions. Among the possible higher-order arrangements consistent with these observations, we have considered the two structures shown in Figures 3. 7e and 3. 7f. Rod-like structures would arise as a result of stacking interactions along the normal to the macrocycle plane. (Figure 3. 7e) Preliminary molecular mechanics MM^{+} and PM3 calculations showed that favorable π-π stacking of these *cis*-azodibenzoic acid supramolecular cycles can result into unidimensional, rod-like structures, when the aromatic rings are slightly rotated (ca. 30°) relative to the normal of the macrocycle plane, and the interplanar distances are shorter than ca. 4.5 Å.[14,26] On the other hand, side-by-side, lateral arrangement of these macrocycles with their rings parallel to the normal of the macrocycle plane can also lead to structures with high aspect ratio. (Figure 3. 7f) We are currently using both spectroscopic techniques (*e.g.*, solid-state NMR) and theoretical studies to determine whether the *cis*-**2** macrocycles pack into either of these modes, or into other intermediate higher-order arrangements.



(a) (b) (c)







(d) (e) (f)

Figure 3. 8. (a) TEM of directly deposited films of *cis*-**2**. (b), (c) and (d) TEM of replicas of *cis*-**2**. (e) and (f) Representations of possible packing modes (alkyl chains are omitted for clarity).

Dynamic light scattering (DLS) studies were carried out for *cis*-**2** in 1,2-dichloroethane at scattering angles of 45°, 90°, and 135°, and confirmed the presence of these elongated aggregates in solution.[27] The hydrodynamic diameters obtained for these angles were significantly different from one angle to the other, *e.g.*, 745 nm at 45° and 566 nm at 135°, clearly demonstrating the presence of elongated, rather than spherical *cis*-**2** aggregates in solution. In addition, changes in concentration led to diameters varying from 282-746 nm at 1.0 gL^{-1} and 565-746 nm at 2.5 gL^{-1}, consistent with the formation of longer structures at higher concentration.[14] Another set of DLS experiments was carried out for solutions of *cis*-**2**, which were cooled to 4°C for 2 days. These measurements indicate that much longer, non-spherical aggregates with hydrodynamic diameters ranging from 3090.0 nm to 4572.5 nm were formed. Thus, the photochemically formed *cis*-**2** undergoes self-assembly into elongated aggregates both in solution (DLS) and in the solid state (TEM).

3.3. Conclusion

We have shown that the self-assembly of azodibenzoic acids **1** and **2** can be reversibly photoswitched between two dramatically different supramolecular structures. On a first level, photoirradiation triggers the *trans* → *cis* azobenzene isomerization, which changes the self-assembly of these molecules from linear tapes in the *trans*-form, to discrete cyclic structures in the *cis*-form. On a second level, these *cis* azobenzene cyclic structures self-organize into elongated aggregates through stacking interactions. Overall, a primary photochemical event of the *trans-cis* isomerization has been

considerably amplified using supramolecular self-assembly. We are currently investigating the use of this novel strategy for the creation of reversibly photopatterned surfaces. In addition, efforts towards further stabilization of the *cis*-azobenzene form by increasing the number of hydrogen bonding interactions are currently underway.

3.4. Experimental Section

Materials. 3-hydroxy-4-nitrobenzoic acid was purchased from the Aldrich Chemical Co. Methyl-3-hydroxy-4-nitrobenzoate (3) was synthesized according to the reported procedure.[28] The structures of the intermediates and the final products were confirmed by FTIR and NMR spectroscopy, high-resolution and low-resolution MS, and elemental analysis.

Equipment. ^{1}H- and ^{13}C-NMR spectra were acquired on a Varian Mercury 400 and 500 MHz spectrometers. Infrared spectra were acquired on a Bruker IFS-48 FTIR spectrometer (solution, resolution: 2 cm^{-1}). UV-vis spectra were measured on a Varian CARY 1 UV-vis spectrophotometer equipped with a Peltier temperature controller. Preparative HPLC was carried out using a Hewlett-Packard model equipped with a semi-preparative Zorbax 300 SB- C18 9.4 mm x 25 cm reverse phase column. Transmission electron microscopy (TEM) was conducted on a JEOL-2000 FX instrument by using the replica and the direct deposition methods. Vapor pressure osmometry (VPO) measurements were carried out in dichloromethane using a Model 233 Molecular Weight Apparatus by Wescan Instruments, Inc. A second set of measurements was carried out in dichloromethane using Vapro 5520-model vapor pressure osmometer equipped with AC-

066 Head for 0-3200 mmol/kg range manufactured by Wescor. Electrospray ionization (ESI) was perfomed using a Finnigan SSQ7000 (ThermoFinnigan) or a Quattro II triple quadrupole (Micromass, Manchester, UK) mass spectrometer equipped with a syringe pump (Harvard Apparatus). X-Ray diffraction data were collected using a Siemens D-5000 diffractometer, consisting of a step scanner equipped with a 1.2 kW cobalt tube (λ= 1.78897 Å) coupled to a silicon detector.

Methyl-3-decyloxy-4-nitrobenzoate (4). 3-hydroxy-4-nitrobenzoic acid methyl ester (3) (2.00 g, 10.15 mmol), 1-bromodecane (2.1 mL, 10.15 mmol), anhydrous K_2CO_3 (4.20 g, 30.45 mmol), and dry DMF (26 mL) were purged with nitrogen. The reaction mixture was heated to 80°C under nitrogen for 24 hrs. After cooling to room temperature, the heterogenous mixture was poured into ice-cooled water, and the resulting precipitate (4) was filtered, washed with water and dried. (3.27 g, 96 %). ^{1}H-NMR ([D_6]acetone): δ 7.91 (d, 1H), 7.83 (s, 1H), 7.72 (d, 1H), 4.28 (t, 2H), 3.93 (s, 3H), 1.83 (m, 2H), 1.51-1.31 (m, 14H), 0.88 (t, 3H). ^{13}C-NMR ($CDCl_3$): δ 165.27, 151.94, 142.47, 134.63, 125.14, 121.02, 115.37, 69.90, 52.78, 31.84, 29.48, 29.47, 29.26, 29.19, 28.76, 25.74, 22.64, 14.08. EI-MS: *m/z* calc. for $C_{18}H_{27}NO_5$ 337.4, found 337.0.

3-Decyloxy-4-nitrobenzoic acid (5). Methyl-3-decyloxy-4-nitrobenzoate (4) (1.44 g, 4.27 mmol) and KOH pellets (287.5 g, 5.12 mmol) were heated to reflux in a 1:1 MeOH/ H_2O mixture (4 mL) for 4 hrs. The disappearance of the ester was checked by thin-layer chromatography (silica gel, dichloromethane). The reaction mixture was cooled using an ice-water bath, and concentrated HCl (~1.5 mL) was added dropwise. The resulting

precipitate was filtered, washed with water and air-dried (1.27 g, 93 %). ^{1}H-NMR ([D_6]DMSO): δ7.92 (d, 1H), 7.73 (d, 1H), 7.61 (dd, 1H), 4.20 (t, 2H), 1.70 (m, 2H), 1.38-1.23 (m, 14H), 0.84 (t, 3H). ^{13}C-NMR ($CDCl_3$): δ169.21, 151.94, 143.09, 133.70, 125.21, 121.72, 115.82, 69.98, 31.86, 29.75, 29.55, 29.47, 29.03, 26.02, 22.92, 22.59, 14.34. FTIR ($CHCl_3$) ν 2976 (C-H), 1717.4 (C=O), 1529.3 (N=O). EI-MS: *m/z* calc. for $C_{17}H_{25}NO_5$: 323.4, found 323.5. Elemental analysis calcd. (%) for $C_{17}H_{25}NO_5$ .2KCl : C 43.21, H 5.33, N 2.96; found: C 43.63, H 5.17, N 2.90.

***trans*-2,2'-Bis(decyloxy)-4,4'-azodibenzoic acid (1).** 3-decyloxy-4-nitrobenzoic acid (5) (1.073 g, 3.32 mmol) was heated to 80 °C in the presence of Zn dust (347.5 mg, 5.31 mmol), in 30% aqueous NaOH (15.55 mL). After 23 hrs, the reaction mixture was diluted with water (62 mL), and Zn dust was added (303.9 mg, 4.65 mmol). The reaction mixture was heated to 80-85°C for 3 days, and then cooled and filtered. The orange solution was acidified with glacial acetic acid. The obtained precipitate was filtered and washed with water (3x50 mL) and a minimum of ethanol (~20 mL). The solid was dissolved in dilute aqueous ammonia, the solution was acidified with dilute hydrochloric acid and heated to gentle reflux for 5 min. The resulting solid was filtered, washed repeatedly with water and ethanol, and dried. The crude (476 mg) contains a mixture of azoxy-, azo- and hydrazobenzene derivatives. These were methylated with diazomethane. The methyl esters were separated by silica gel chromatography with dichloromethane as the eluent. The isolated methyl azodibenzoate (284.7 mg, 0.47 mmol) was then hydrolyzed by refluxing for 4 hrs in a solution of KOH (pellets, 109.6 mg, 1.96 mmol) in 1:1 EtOH/H_2O (12 mL). Acidification with hydrochloric acid at 0°C,

filtration and drying gave (**1**) as yellow crystals (267.7 mg, 28 %). ^{1}H-NMR ([D_6]DMSO): δ 7.71 (d, 2H), 7.58 (dd, 2H), 7.47 (dd, 2H), 4.22 (t, 4H), 1.78 (m, 4H), 1.45-1.19 (m, 28H), 0.80 (t, 6H). ^{13}C-NMR ([D_4]methanol): δ 174.33, 157.45, 145.39, 142.94, 122.74, 117.42, 116.50, 70.66, 33.07, 30.80, 30.66, 30.46, 30.34, 27.25, 23.74, 14.47. FTIR (CH_2Cl_2) *v*: 3677, 3595 (O-H), 2976, 2915 (C-H), 1604 (C=O). FAB-MS (positive mode): *m/z* calc. 583.7 found 583.0 MALDI-TOF MS: *m/z* calc. for $C_{34}H_{50}N_2O_6.Li^+$ 589.7; found 589.0 Elemental analysis calcd. (%) for $C_{34}H_{50}N_2O_6$: C 70.07, H 8.65, N 4.81; found: C 69.67, H 8.94, N 4.45.

***cis*-2,2'-Bis(decyloxy)-4,4'-azodibenzoic acid (2).** An NMR tube filled with a solution of azodibenzoic acid (**1**) (7 mg, 0.012 mmol) in [D_6]DMSO (0.7 mL) was fitted inside a photochemical reactor equipped with a 450W Hanovia lamp, for which a Pyrex sleeve was used to cut-off the wavelengths below 300 nm. The disappearance of the *trans* isomer, and appearance of *cis*-isomer were monitored by ^{1}H-NMR. A 1:1.3 *trans/cis* photostationary state (^{1}H-NMR) was reached after 1hr. The reverse *cis-trans* thermal isomerisation in solution is quantitative after 2-3 days in the dark at room temperature, and upon heating at 70°C for 1 hr in [D_6]DMSO. The *cis*-isomer was isolated by reverse phase HPLC. A 30 min. gradient of 90:10 to 100:0 MeOH/H_2O (+ 0.06%TFA) was used as the mobile phase. The UV detector was set at 286 nm, which corresponds to the isobestic point observed when the *trans* isomer is irradiated in methanol. The collected fractions were immediately stored in the dark at low temperature (+4°C) before solvent evaporation in order to avoid thermal reisomerisation. ^{1}H-NMR ([D_6]DMSO): δ 7.42 (d,

2H), 7.35 (dd, 2H), 6.62 (d, 2H), 3.96 (t, 4H), 1.65 (m, 4H), 1.45-1.17 (m, 28H), 0.83 (t, 6H). FAB-MS (positive mode): *m/z* calc. 583.7, found 583.0.

Thermal *cis-trans* reisomerisation kinetics by ^{1}H-NMR. An NMR tube of irradiated azodibenzoic acid (5 mg, 0.008 mmol) in [D_6]DMSO (0.7 mL) was maintained at temperatures between 25°C and 60°C. The kinetics of the reaction were followed by monitoring the ^{1}H-NMR signal of the methylenic protons α to the ether oxygen (triplets between 3.5-4.5 ppm, where *trans*-**1** appears at 4.25 ppm and *cis*-**2** at 3.99 ppm).

Thermal *cis-trans* reisomerisation kinetics by UV-Vis. A solution of irradiated azodibenzoic acid (1 mg, 0.002 mmol) in DMSO (100 mL) was maintained at temperatures between 25°C and 60°C. The kinetics of the reaction were followed by monitoring the increase in absorbance at 315 nm. A solution of *cis*-**2** azodibenzoic acid (1 mg, 0.002 mmol) in $CHCl_3$ (100 mL) was maintained at temperatures between 20°C and 45°C. The kinetics of the reaction were followed by monitoring the increase in absorbance at 309 nm.

Vapor pressure osmometry (VPO) measurements. A total of 8 different stock solutions of *cis*- azodibenzoic acid at concentrations ranging from 2 gL^{-1} to 12 gL^{-1} were prepared in dichloromethane. 30 μL of solution were injected into the osmometer chamber. After temperature equilibration (5 min), the voltage was recorded in mV. 3 independent measurements were made at each concentration, and the experiments were duplicated. A calibration curve was generated using benzil (M= 210.23) and polystyrene

(M= 2100) as molecular weight standards under the same conditions. Average molecular weight of studied aggregates were calculated using Equation 3.1:

$$MW_{unknown} \times \lim_{C \to 0} \frac{VPO_{unknown}}{C_{unknown}} = MW_{s\,tan\,dard} \times \lim_{C \to 0} \frac{VPO_{s\,tan\,dard}}{C_{s\,tan\,dard}} \qquad \textbf{(Eq. 3. 1)}$$

Using a different instrument (see above), a total of 6 different stock solutions of *cis*- and *trans*-azodibenzoic acid were prepared in dichloromethane (higher solubility was observed for the *cis*-isomer than for the *trans*-isomer). 10 μL of solution were placed into the osmometer sample holder. After temperature equilibration (75 s), osmolality was recorded in $mmolkg^{-1}$. 5 independent measurements were made at each concentration, and the experiments were duplicated. A calibration curve was generated using benzil (M= 210.23) as the standard under the same conditions and the molecular weights were obtained.

Electrospray ionization mass spectrometry (ESI) measurements. A solution of *cis*-**2** in dichloromethane (or chloroform), to which were added a few μls of methanol, was infused at a flow rate of 5 μL min^{-1} for molecular weight determination. The spectrometer was programmed to scan for the negative product ions to give monomer, dimer, trimer and tetramer between *m/z* 100 and *m/z* 2500 with a spray voltage of 3.5 kV and capillary heater at 200°C, trimer with a spray voltage of 4.0 kV and capillary heater at 150°C and tetramer with a spray voltage of 3.5 kV and capillary heater at 150°C.

A solution of *cis*-**2** in chloroform onto which were added a few μLs of 5-30 mM Et_3N was directly infused into the mass spectrometer, which was configured for negative product ion analysis and used with the spray voltage set to 3.5 kV, source temperature

50°C, sample infusion rate 5 $\mu Lmin^{-1}$. The spectrometer was programmed to scan for the product ions from *m/z* 400 to *m/z* 2800 in multichannel acquisition mode (MCA) showing m/z for monomer, the dimer, the trimer and the tetramer-Et_3N complex.

Sample preparation for TEM measurements by the replica method. A solution of *cis*-**2** or *trans*-azodibenzoic acid **1** was prepared by dissolving the sample in 1,2-dichloroethane into a vial wrapped in aluminum foil at room temperature, and deposited on a freshly cleaved mica sheet. 7-9 μL of solution were transferred via pipet onto the mica leaf. After allowing the solvent to evaporate for 1-2 min, the mica sample was placed inside a high-vacuum Edwards Carbon coater equipped with Pt-C and C-guns. The replicas were prepared by successive evaporation of Pt-C at a 15°-angle then carbon at a 90°-angle on the air-dried sample. Each gun was consecutively turned on for about 10-15 s, starting with the Pt-C gun. The replica was detached from the mica surface by floating the thin Pt-C film on distilled water, transferred onto a 400 mesh TEM copper grid and dried overnight on filter paper, before observation under the microscope. On the micrographs, the Pt-C is seen as dark gray and the carbon as light gray. The size of the Pt-covered substrate agree with the size of the shadow. For the replicas, the error estimate on the measurements is ±1 nm.

Sample preparation for TEM measurements by the direct method. A solution of *cis*-**2** or *trans*-azodibenzoic acid **1** was prepared by dissolving the sample in 1,2-dichloroethane into a vial wrapped in aluminum foil at room temperature. A carbon-

coated 400 mesh copper grid, prewashed with chloroform for 12 hrs was dipped into the solution for approximately 5 min then dried on a filter paper.

X-ray powder diffraction (XRD) measurements. X-ray diffraction patterns were acquired for 2θ values ranging from 3 to 50 degrees for *trans*-**1** and *cis*-**2** azodibenzoic acid powders. Diffraction patterns for the *cis*-isomers were acquired on freshly chromatographed and vacuum-dried samples over 2-3 days. Despite these precautions, some thermal reisomerization to the *trans* isomer was observed by X-ray diffraction.

Dynamic light scattering (DLS) measurements. Dynamic light scattering measurements were carried out using a 532 nm laser equipped photo-multiplier detector. The autocorrelation functions were acquired for θ values of 45°, 90° and 135° for prefiltered solutions of *trans*-**1** and *cis*-**2** azodibenzoic acid in 1,2-dichloroethane. The wavelength of the laser source corresponds to an absorption minimum for the *cis*-azodibenzoic acid **2** in this solvent. Data acquisition was carried out at 20°C and within a few hours to prevent any thermal reisomerization of the *cis*-isomer. Inverse Laplace transforms of the data were performed using Provencher's FORTRAN program CONTIN,[29] and diffusion coefficients were determined from the slope of the relaxation frequencies (Γ) vs q^2. Assuming a spherical behaviour for the particles and using the translational coefficient D_T, and the Stokes-Einstein equation, the hydrodynamic diameters are calculated for each scattering angle.

Theoretical calculations. Optimizations of the azodibenzoic acid supramolecular assemblies were performed using the PM3 semi-empirical molecular orbital theory,[17b, c] which is less computationally expensive than *ab initio* or density functional methods. In addition, density-functional theory (DFT) B3LYP/6-31G* and *ab initio* HF/6-31G* calculations were performed on the *cis-p*-azodibenzoic acid monomer to confirm the geometry obtained using PM3.

The geometry of the *trans*- and *cis*-monomers were optimized using PM3 until an RMS gradient of 0.01 was reached. After this optimization, another monomer was added and the hydrogen-bonded structure energy was minimized. This monomer addition-optimization sequence was repeated up to the hexameric compound. The hydrogen-bonded geometry and the total heat of formation were extracted for each optimized species. Standard Gibbs free energies were obtained for each optimized structure by vibrational analysis.

Geometry optimizations used the PM3 method contained in the Gaussian98W[30] program package. PM3 frequencies were obtained from Gaussian98W. Frequencies were scaled using the default settings (Scaling factor = 0.8929).

Calculations for the packing of the *cis*-**2** azodibenzoic acid tetramers were performed using the molecular mechanics MM^+ applied to the Ring Packing Scan (RPS) method. This method consists in a rigid scan of the total energies of the stacked macrocycles while changing the distances between 3.5-6.0 Å along the *z*-axis and between 0.0-2.0 Å along the *x*-axis. The obtained minimum geometry was then optimized using PM3.

[1] (a) J. -M. Lehn, *Supramolecular Chemistry: Concepts and Perspectives*, VCH, Weinheim, **1995**. (b) G. M. Whitesides, E. E. Simanek, J. P. Mathias, C. T. Seto, D. N. Chin, M. Mammen, D. M. Gordon, *Acc. Chem. Res.*, **1995**, *28*, 37-44; c) J. S. Lindsey *New J. Chem.*, **1991**, *15*, 153. (d) D. S. Lawrence, T. Jiang, M. Levett, *Chem. Rev.* **1995**, *95*, 2229. (e) S. Leininger, B. Olenyuk, P. J. Stang, *Chem. Rev.*, **2000**, *100*, 853.

[2] (a) J. -M. Lehn, M. Mascal, A. DeCian, J. Fischer, *J. Chem. Soc., Chem. Commun.* **1990**, 479. (b) J. A. Zerkowski, C. T. Seto, D. A. Wierda, G. M. Whitesides, *J. Am. Chem. Soc.*, **1990**, *112*, 9025.

[3] (a) J. Yang, J. -L. Marendaz, S. J. Geib, A. D. Hamilton, *Tetrahedron Lett.* **1994**, *35*, 3665. (b) A. Zafar, J. Yang, S. J. Geib, A. D. Hamilton, *Tetrahedron Lett.* **1996**, *37*, 2327. (c) M. Mammen, E. E. Simanek, G. M. Whitesides, *J. Am. Chem. Soc.*, **1996**, *118*, 12614. (d) M. Mascal, N. M. Hext, R. Warmuth, J. R. Arnall-Culliford, M. H. Moore, J. P. Turkenburg, *J. Org. Chem.*, **1999**, *64*, 8479. (e) C. M. Drain, X. Shi, T. Milic, F. Nifiatis, *Chem. Commun.*, **2001**, 287. (f) S. V. Kolotuchin, S. C. Zimmerman, *J. Am. Chem. Soc.*, **1998**, *120*, 9092. (g) H. Fenniri, B. -L. Deng, A. E. Ribbe, K. Hallenga, J. Jacob, P. Thiyagarajan, *Proc. Natl. Acad. Sci. USA*, **2002**, *99*, 6487.

[4] (a) T. Kusukawa, M. Fujita, *J. Am. Chem. Soc.*, **1999**, *121*, 1397. (b) K. S. Kim, S. B. Suh, J. C. Kim, B. H. Hong, E. C. Lee, S. Yun, P. Tarakeshwar, J. Y. Lee, Y. Kim, H. Ihm, H. G. Kim, J.W. Lee, J. K. Kim, H. M. Lee, D. Kim, C. Cui, S. J. Youn, H. Y. Chung, H. S. Choi, C.-W. Lee, S. J. Cho, S. Jeong, J.-H. Cho, *J. Am. Chem. Soc.*, **2002**, *124*, 14268.

[5] (a) M. S. Vollmer, T. D. Clark, C. Steinem, and M. R. Ghadiri, *Angew. Chem. Int. Ed. Engl.*, **1999**, *38*, 1598. (b) D. T. Bong, T. D. Clark, J. R. Ganja, M. R. Ghadiri, *Angew. Chem. Int. Ed. Engl.*, **2001**, *40*, 988.

[6] H. Asanuma, T. Ito, T. Yoshida, X. Liang, M. Komiyama, *Angew. Chem. Int. Ed. Engl.*, **1999**, *38*, 2393.

[7] D. M. Junge, D. V. McGrath, *J. Am. Chem. Soc.*, **1999**, *121*, 4912.

[8] (a) S. Tsuchiya, *J. Am. Chem. Soc.*, **1999**, *121*, 48. (b) M. Takeuchi, S. Shinkai, *J. Chem. Soc., Perkin Trans. 2*, **1998**, *4*, 847.

[9] (a) K. Ichimura, *Chem. Rev.*, **2000**, *100*, 1847. (b) C. Ruslim, K. Ichimura, *Macromolecules*, **1999**, *32*, 4254. (c) H. -K. Lee, K. Doi, H. Harada, O. Tsutsumi, A. Kanazawa, T. Shiono, T. Ikeda, *J. Phys. Chem. B*, **2000**, *104,* 7023.

[10][10] (a) S. Kawata, Y. Kawata, *Chem. Rev.*, **2000**, *100*, 1777. (b) A. Nathanson, P. Rochon, *Can. J. Chem.*, **2001**, *79*, 1093. (c) *Holographic Data Storage*, H. J. Coufal, D. Psaltis, G.T. Sincerbox (Eds.), Springer-Verlag: Berlin, Heidelberg, 2000.

[11] (a) The control of gelation behavior has been reported with hydrogen bonding dithienylcyclopentenes. L. N. Lucas, J. van Esch, R. M. Kellogg, B. L. Feringa, *Chem. Commun.*, **2001**, 759. (b) T. Kawasaki, M. Tokuhiro, N. Kimizuka, T. Kunitake, *J. Am. Chem. Soc.*, **2001**, *123*, 6792.

[12] G. S. Hartley, *J. Chem. Soc.*, **1938**, 633.

[13] (a) J. J. P. Stewart, *J. Comp. Chem.*, **1989**, *10*, 209. (b) J. J. P. Stewart, *J. Comp. Chem.*, **1989**, *10*, 221. (c) A. D. Becke, *J. Chem. Phys.*, **1993**, 98, 5648. (d) The C-N=N angle obtained by our PM3 calculations for *cis-p*-azodibenzoic acid (126.9°), *cis-o-bis*-(methoxy)-*p*-azodibenzoic acid (127.2°), *cis-o-bis*-(decyloxy)-*p*-azodibenzoic acid

(127.8°) agrees with experimental X-ray results for *o*-substituted *cis*-azobenzene (126.4°). (see reference 20)

[14] See Appendix A.

[15] Similar PM3 calculations were performed on hydrogen-bonded isophthalic acid aggregates. These theoretical studies agree with experimental evidence, showing that the unsubstituted isophthalic acid form tapes instead of rosettes (see ref. 3a, 3b), thus validating our predictions.

[16] Attempts to form cyclic *cis*-azodibenzoic acid trimers by using PM3 only yielded the open aggregates. A triangle was obtained from HF/STO-3G monomers, which were then assembled to form the desired structure, then optimized using PM3. This optimization gave a triangle with bent hydrogen-bonds, which were weaker than in the larger macrocycles and in the open aggregates.

[17] Examples of supramolecular systems using semi-empirical methods: (a) R. Castro, M. J. Berardi, E. Cordova, M. O. de Olza, A. E. Kaifer, J. D. Evanseck, *J. Am. Chem. Soc.*, **1996**, *118*, 10257. (b) S. Sharma, T. P. Radhakrishnan, *J. Phys. Chem. B* **2000**, *104*, 10191. (c) D. Quinonero, A. Frontera, S. Tomas, G. A. Suner, J. Morey, A. Costa, P. Ballester, P. M. Deya, *Theor. Chem. Acc.* **2000**, 104, 50. (d) K. S. Kim, S. B. Suh, J. C. Kim, B. H. Hong, E. C. Lee, S. Yun, P. Tarakeshwar, J. Y. Lee, Y. Kim, H. Ihm, H. G. Kim, J. W. Lee, J. K. Kim, H. M. Lee, D. Kim, C. Cui, S. J. Youn, H. Y. Chung, H. S. Choi, C. -W. Lee, S. J. Cho, S. Jeong, J. -H. Cho, *J. Am. Chem. Soc.*, **2002**, *124*, 14268. (e) A. Lützen, M. M. Hapke, J. Griep-Raming, D. Haase, W. Saak, *Angew. Chem. Int. Ed. Engl.*, **2002**, *41*, 2086.

[18] E. E. Schrier, *J. Chem. Educ.*, **1968**, *45*, 176.

[19] (a) X-ray crystal data for *trans*-azo **1**: Crystal dimensions: 0.69 x 0.05 x 0.03, triclinic, P$\bar{1}$, a = 8.3795(2), b = 13.4914(3), c = 15.1038(4), α = 105.732(2), β = 94.757(2), γ = 91.273(2), V = 1636.10(7), $\rho calc.$ = 1.183, θ_{max} = 72.79, CuK\a, λ = 1.54178, collection method: phi scans, T = 293 K, 19813 measured reflections, 6258 independent reflections, 3029 observed reflections, maximum shift = 0.021, absorption correction type = multi scan, structure solution by direct method using SHELXS97, structure refinement using SHELXL96, 383 parameters, isotropic hydrogen atoms using defaults, *R1* = 0.0626, *wR2*= 0.1750, refinement against $|F2|$, CCDC 184609. (b) *International Tables for Crystallography.* Vol. C. Tables 4.2.6.8 and 6.1.1.4, Dordrecht: Kluwer Academic Publishers, **1992**. (c) SAINT Release 6.06; Integration Software for Single Crystal Data. Bruker AXS Inc., Madison, WI 53719-1173, **1999**. (d) G. M. Sheldrick. SADABS, Bruker Area Detector Absorption Corrections. Bruker AXS Inc., Madison, WI 53719-1173, **1996**. (e) SHELXTL Release 5.10; The Complete Software Package for Single Crystal Structure Determination. Bruker AXS Inc., Madison, WI 53719-1173, **1997**. (f) SMART Release 5.059; Bruker Molecular Analysis Research Tool. Bruker AXS Inc., Madison, WI 53719-1173, **1999**. (g) A. L. Spek, PLUTON Molecular Graphics Program, July 1995 version. University of Utrecht, Utrecht, Holland, **1995**. (h) A. L. Spek, PLATON, Molecular Geometry Program, July 1995 version. University of Utrecht, Utrecht, Holland. (version 190499 at McGill), **1995**. (i) XPREP Release 5.10; X-ray data Preparation and Reciprocal space.Exploration Program. Bruker AXS Inc., Madison, WI 53719-1173, **1997**.

[20] N. J. Bunce, G. Ferguson, C. L. Forber, G. J. Stachnyk, *J. Org. Chem.*, **1987**, *52*, 394.

[21] A. S. Shetty, J. Zhang, J. S. Moore, *J. Am. Chem. Soc.*, **1996**, *118*, 1019.

[22] (a) When the diffraction pattern of *trans*-**1** was substracted from the diffraction pattern of *cis*-**2**, the main diffraction peak appeared as one single peak. The peaks at 14.0, 24.0, 25.7 and 27.0° correspond to Bragg spacings of 0.73, 0.43, 0.40, and 0.38 nm, respectively. These dimensions may be related to the distance between two stacked cyclic tetramers of *cis*-**2**. (b) B. D. Cullity, *Elements of X-Ray Diffraction, Addison-Wesley*, Reading, MA, 1978. (c) B. -Z. Zhan, M. A. White, K. N. Robertson, T. S. Cameron, M. Gharghouri, *Chem. Comm.*, **2001**, *13*, 1176.

[23] This diameter was estimated from the PM3 optimized structure of the cis-azodibenzoic acid tetramer ($\varnothing$ = 2.31 nm) onto which were superimposed four optimized decyloxy-substituted monomers. The distance between two opposite chain-ends was measured directly.

[24] At very low concentrations (C < 3 gL^{-1}), the VPO data points lie slightly below the regression curves, suggesting the preponderance of monomeric species in such dilute solutions. (See Appendix A) However, at higher concentrations, the results are consistent with supramolecular tetramers.

[25] On the micrographs, the Pt-C is seen as dark gray and the carbon as light gray. For the replicas, the error estimate on the measurements is ±1 nm. However, the *cis*-**2** isomer is expected to form hydrogen-bonded macrocycles in the solid state as reflected by our XRD and TEM results.

[26] The total energy of stacked supramolecular structures was computed as a function of their inter-planar distance, the tilt of the aromatic rings with respect to the normal to the macrocycle plane, and the horizontal offset between the stacked macrocycles. The optimum structure obtained by using the MM^{+} force field was further optimized using

PM3, leading to a very similar structure. Moreover, PM3 calculations on *cis-o-bis*-(alkyl)azodibenzoic acid predict that the alkyl chains are able to adopt an orientation parallel to the azodibenzoic acid plane, thus enabling the hydrogen-bonding and stacking interactions to occur. As a result, PM3 and MM^+ calculations show that the orientation of the aromatic rings in the macrocycle and the position of the alkoxy chains can favor the efficient stacking of these tetrameric macrocycles into rod-like morphologies. See Chapter 5 for details.

[27] See experimental section for details.

[28] H. Zeng, R. S. Miller; R. A. II Flowers, B. Gong, *J. Am. Chem. Soc.*, 2000, *122*, 2635.

[29] (a) S. W. Provencher, *Comput. Phys.*, **1982**, *27*, 213. (b) S. W. Provencher, *Comput. Phys.*, **1982**, *27*, 229. (c) K. S. Schmitz, *An Introduction to Dynamic Light Scattering by Macromolecules*, Academic Press Inc., San Diego, CA, 1990.

[30] Gaussian 98W (Revision A.7), M. J. Frisch, G. W. Trucks, H. B. Schlegel, G. E. Scuseria, M. A. Robb, J. R. Cheeseman, V. G. Zakrzewski, J. A. Montgomery, Jr., R. E. Stratmann, J. C. Burant, S. Dapprich, J. M. Millam, A. D. Daniels, K. N. Kudin, M. C. Strain, O. Farkas, J. Tomasi, V. Barone, M. Cossi, R. Cammi, B. Mennucci, C. Pomelli, C. Adamo, S. Clifford, J. Ochterski, G. A. Petersson, P. Y. Ayala, Q. Cui, K. Morokuma, D. K. Malick, A. D. Rabuck, K. Raghavachari, J. B. Foresman, J. Cioslowski, J. V. Ortiz, A. G. Baboul, B. B. Stefanov, G. Liu, A. Liashenko, P. Piskorz, I. Komaromi, R. Gomperts, R. L. Martin, D. J. Fox, T. Keith, M. A. Al-Laham, C. Y. Peng, A. Nanayakkara, C. Gonzalez, M. Challacombe, P. M. W. Gill, B. G. Johnson, W. Chen, M. W. Wong, J. L. Andres, M. Head-Gordon, E. S. Replogle, J. A. Pople, Gaussian, Inc., Pittsburgh PA, 1998.

Chapter 4.

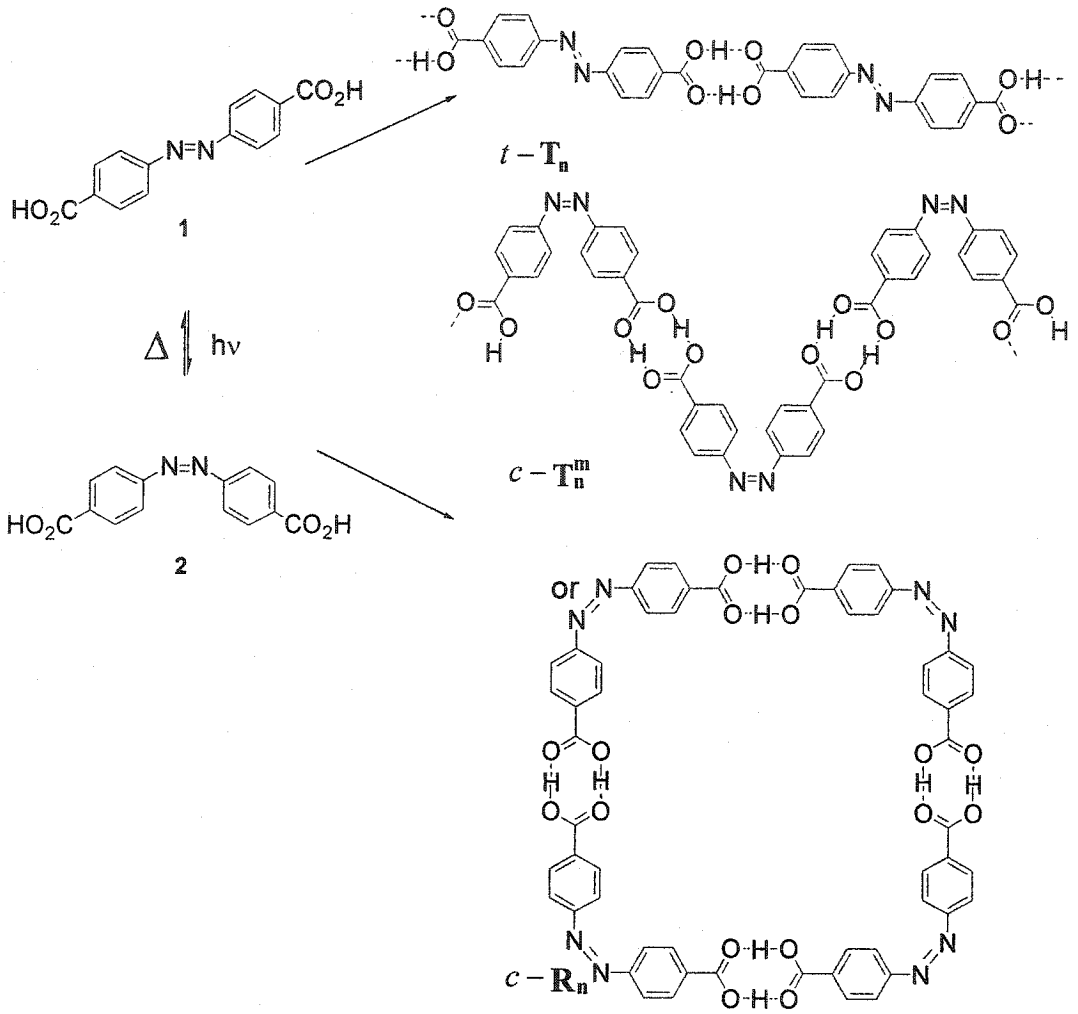
Photoresponsive Supramolecular Systems: Theoretical Study of Self-Assembled Azodibenzoic Acid Tapes and Rosettes

4.1. Introduction

Using weak additive non-covalent interactions, supramolecular self-assembly has been shown to efficiently control the physical and chemical properties of new materials.[1-5] In dicarboxylic acid-based self-assembly, the relative orientation of the carboxylic acid groups determines the hydrogen-bonded geometry. For example, terephthalic and isophthalic acids form linear tapes and cyclic hexameric rosettes respectively.[6-8] Similarly, molecular self-assembly has been successfully integrated into the fabrication of controllable materials with exciting potential applications in holographic and optical data storage,[9,10] including photoresponsive azobenzene-containing structures. Photochromic *trans*-azobenzene is conformationally more stable than *cis*-azobenzene, and isomerizes upon irradiation with UV-light (λ = 313 nm). The resulting *cis*-photoisomer reverts to the more stable *trans*-azobenzene when heated or irradiated with visible light.

A new strategy to control supramolecular architecture is to directly use dicarboxylic acid azobenzene derivatives as the building blocks, unlike previous work in which photoresponsive azobenzene units have been incorporated into supramolecular systems such as peptides,[11] DNA,[12] dendrimers[13] and molecular hosts,[14,15] and in macromolecular and liquid crystalline structures,[16,17] to induce structural change and give two-state photoswitches, patterned polymers and liquid crystals.

We have recently reported the self-assembly of hydrogen-bonded *trans*-**1** and *cis*-**2** derivatives.[18] In the design of building blocks **1** and **2** (Scheme 4. 1), the carboxylic acid groups are chosen para to the N=N linkage. The *trans-cis* isomerization of azodibenzoic acid dramatically changes the orientation of the carboxylic acid groups, to give different hydrogen-bonded architectures. In *trans p*-azodibenzoic acid **1**, the carboxylic acids are aligned with each other, resulting in the formation of linear tapes $t-\mathbf{T}_n$. In *cis p*-azodibenzoic acid **2**, the carboxylic acids have an angle between them which can lead to crinkled tapes $c-\mathbf{T}_n^m$ or closed aggregates $c-\mathbf{R}_n$.



Scheme 4. 1. Hydrogen-bond self-assembly of *trans*-**1** and *cis*-**2** *p*-azodibenzoic acids into linear tapes $t-\mathbf{T}_n$, crinkled tapes $c-\mathbf{T}_n^m$ and macrocycles $c-\mathbf{R}_n$.

For *trans*-**1** derivatives, X-Ray single crystal analysis showed the dicarboxylic acid monomers to form linear tapes $t-\mathbf{T}_n$ through hydrogen-bonding interactions. On the other hand, single crystals could not be isolated from the *cis*-**2** derivatives. Hydrogen-bonded *cis*- aggregates were characterized by mass spectrometry techniques, such as electrospray ionization mass spectrometry (ESI-MS) and vapor pressure osmometry

(VPO), as well as X-Ray powder diffraction, and showed the formation of distinct tetrameric structures. Because non-covalent interactions bring the building blocks together, the self-assembly process is thermodynamically controlled,[19-21] thereby leading to different conformations and multiple equilibria. Consequently, these experimental techniques could not determine the geometry of the hydrogen-bonded *cis*-**2** tetramers precisely. Computational studies have therefore emerged as an essential complementary tool to predict the self-assembly product or to validate molecular organization in cases where experimental techniques fail.[22] Molecular modeling,[23-27] semi-empirical AM1 and PM3 theories[28-31] as well as density functional theory[32-34] and *ab initio* calculations[35,36] have been previously used to determine hydrogen-bonded supramolecular geometries.

In this new approach, where vibrational and electronic properties of these supramolecular structures are calculated for the first time to explain the thermodynamics of self-assembly, is reported here. The semi-empirical PM3[37,38] treatment of the *trans*-**1** and *cis*-**2** monomers and their hydrogen-bonded oligomers, ranging from dimers to hexamers, allowed the calculations of the enthalpies and Gibbs free energies for the self-assembly at 298 K, to give the most thermodynamically favorable structures. The vibrational spectrum of each supramolecular conformation was evaluated to give a unique fingerprint and significant information about hydrogen-bond strength, uniquely confirming the products of the self-assembly. Molecular orbital diagrams and electron density maps give for each supramolecular structure significant results with which to assess the impact of electron delocalization on hydrogen-bonding.

4.2. Theoretical Procedures

The geometries of the *trans* and *cis* monomers and the azodibenzoic acid supramolecules were fully optimized using semi-empirical PM3 methods (RMS gradient = 0.01). The geometry of the *cis p*-azodibenzoic acid was also optimized using the density functional theory B3LYP[39]/6-31G* and *ab initio* HF/6-31G* methods to ascertain the orientation of the carboxylic acid groups. After the optimization of one monomer, another monomer was added and the hydrogen-bonded structure energy minimized. Once the optimum geometry of the dimer was reached, a third monomer was added for further energy minimization. This monomer addition-energy minimization sequence was repeated until a hexamer was obtained.

The total energies E_{tot} of the PM3 optimized aggregates were compared with the *ab initio* HF/STO-3G and density functional theory B3LYP/6-31G* single point calculations performed on the PM3 optimized aggregates. These single point calculations gave the same energies for the hydrogen-bonds. Standard enthalpies and Gibbs free energies at 298 K were calculated for each optimized structure by performing a vibrational analysis. The molecular orbital (MO) diagrams were computed for each optimized structure with a single point calculation.

To establish that PM3 calculations are able to investigate hydrogen-bonded supramolecular systems, calculations were performed on the experimentally well-known isophthalic acid.[40] The optimized PM3 hydrogen-bond lengths and angles of the isophthalic acid structures agreed with the isophthalic acid experimental hydrogen-bond lengths and angles. In addition, these calculations showed that hydrogen-bonded tapes of

unsubstituted isophthalic acid were thermodynamically more stable than hexameric isophthalic acid macrocycles, in good agreement with experiment. This confirms that the PM3 calculations do describe hydrogen-bonded architectures well.

The geometry optimizations and single point calculations used the semi-empirical PM3, *ab initio* HF/STO-3G or 6-31G* and density functional theory B3LYP/6-31G* methods within the Gaussian98W[41] program package. PM3 frequencies were obtained from Gaussian98W. Frequencies were used the default settings which are believed to give frequencies closer to experiment (Scaling factor = 0.8929). Density matrices were obtained from a population analysis within Gaussian98W and as usual symmetrized along the xy diagonal using the Microsoft Excel software.

4.3. Results and Discussion

4.3.1. *Trans*-1 and *cis*-2 *p*-Azodibenzoic Acid Monomers

In previously studied isophthalic acids, the 120°-angle between the carboxylic acids leads to the formation of crinkled tapes and cyclic hexameric rosettes, while in terephthalic acids, the 180°-orientation between the carboxylic acids creates linear tapes.[5-7] In the *trans*-azodibenzoic acid isomer **1**, the acid groups are in the same configuration as in terephthalic acid, as predicted from the PM3 optimized geometries. Therefore, the *trans*- isomer **1** is expected to form linear tapes (Scheme 4.1). This has indeed been shown experimentally.[18]

In the *cis p*-azodibenzoic acid **2**, the acid group orientation is less simple. The opening of the N=N bridge has previously been determined by *ab initio* and semi-empirical calculations[42-44] as well as X-ray diffraction[45-48] for the *trans*- and *cis*-azobenzene isomers and their ortho substituted derivatives. Both theory and experiment have shown that the N=N-C bond angles are greater than 120° (121.9° for *cis*-azobenzene[41]) and increase up to 126° in sterically encumbered *cis*-azobenzenes. The optimized *cis*- *p*-azodibenzoic acid N=N-C bond angle varied from 124° to 127° in agreement with previously calculated *cis*-azobenzene N=N-C bond angles.[47] The angle between the carboxylic acid groups obtained from semi-empirical PM3, *ab initio* HF/6-31G* and density functional theory B3LYP/6-31G* methods is thus expected to be *ca.* 80°. These calculations suggest that the geometry of the PM3 optimized *cis*- *p*-azodibenzoic acid is in agreement with other independent methods and that the *cis*-**2** isomer should form crinkled tapes $c-\mathbf{T}_n^m$ and macrocyclic structures $c-\mathbf{R}_n$ (n > 3).

4.3.2. Nomenclature of the hydrogen-bonded aggregates

Different conformations and multiple equilibria, characteristic of self-assembly, arise from the PM3 energy minimization because of the non-covalent nature of the hydrogen-bond. Dimers and trimers gave open structures exclusively, and consequently were not studied. Tetrameric, pentameric and hexameric aggregates range from linear and crinkled tapes to square and cyclic rosettes (Table 4. 1). A formalism is defined to describe the structure of the hydrogen-bonded species more clearly. Each hydrogen-bonded assembly is defined by $i-\mathbf{M}_n^m$, where *i* is either *t* for *trans* or *c* for *cis* depending

on the isomer used; **M** becomes **T** for the hydrogen-bonded linear tape or a crinkled tape, and **M** becomes **R** for the hydrogen-bonded macrocycle; **n** is the number of monomers in the aggregate, and **m** the number of kinks, which disrupt the linearity of a tape. For example, $c-\mathbf{T}_5^3$ is a pentameric tape formed using *cis*-**2** with 3 kinks (Figure 4. 1).

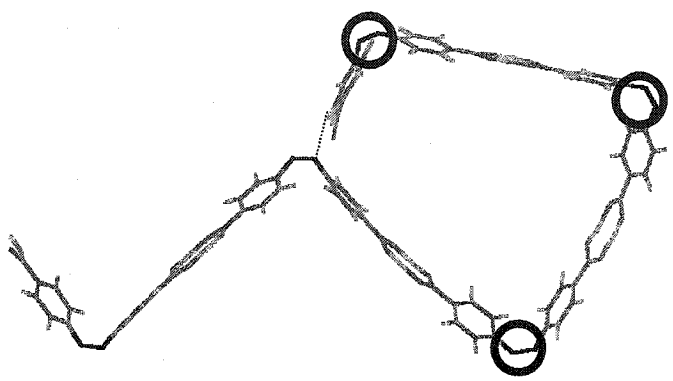


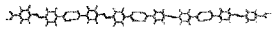
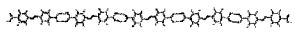
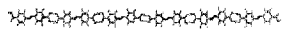
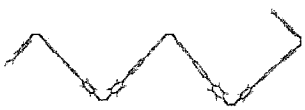
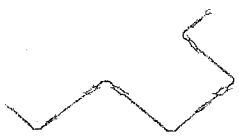
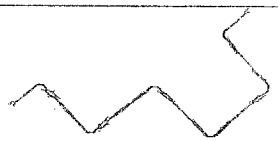
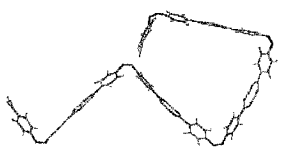
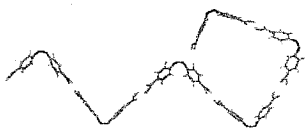
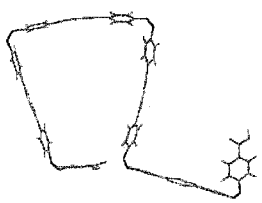
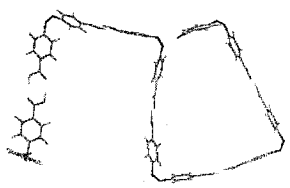
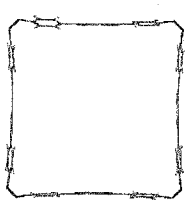
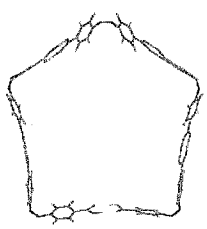
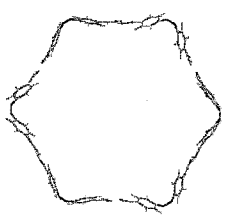
Figure 4. 1. Hydrogen-bonded *cis*-azodibenzoic acid pentameric tape $c-\mathbf{T}_5^3$ which contains 3 N=N kinks. (Each N=N kink is indicated by a dark circle.) The dashed line represents an additional, weak N···H hydrogen-bond (3.12 – 3.25 Å), between the *cis*-azobenzene nitrogen and the terminal carboxylic acid group.

4.3.3. PM3 Optimized Hydrogen-bond Geometries and Enthalpies

The aggregate structures indicate that the monomers retain their geometry from one oligomer to another, and the hydrogen-bond geometry does not change significantly from one degree of aggregation n to the next $n+1$, as expected for supramolecular assemblies (Table 4. 1). In all optimized azodibenzoic acid aggregates, the C=O bond lengthens slightly from 1.22 Å to 1.23 Å, the O–H bond from 0.95 Å to 0.96 Å when

bound. The C–O bond shortens from 1.35 Å to 1.34 Å, while the C–O–H angle opens from 109° to 112°, leading to the formation of the hydrogen-bond (O···H = 1.77 Å). The PM3 hydrogen-bond geometries agree with the X-ray data for carboxylic acid dimers.

Table 4. 1. PM3 optimized hydrogen-bonded linear, folded, or closed structures formed from *trans*-**1** and *cis*-**2** azodibenzoic acids.

Series	n = 4	n = 5	n = 6
$t-\mathbf{T}_n$			
$c-\mathbf{T}_n^0$			
$c-\mathbf{T}_n^1$			
$c-\mathbf{T}_n^2$			
$c-\mathbf{T}_n^3$			
$c-\mathbf{T}_n^4$			
$c-\mathbf{R}_n$			

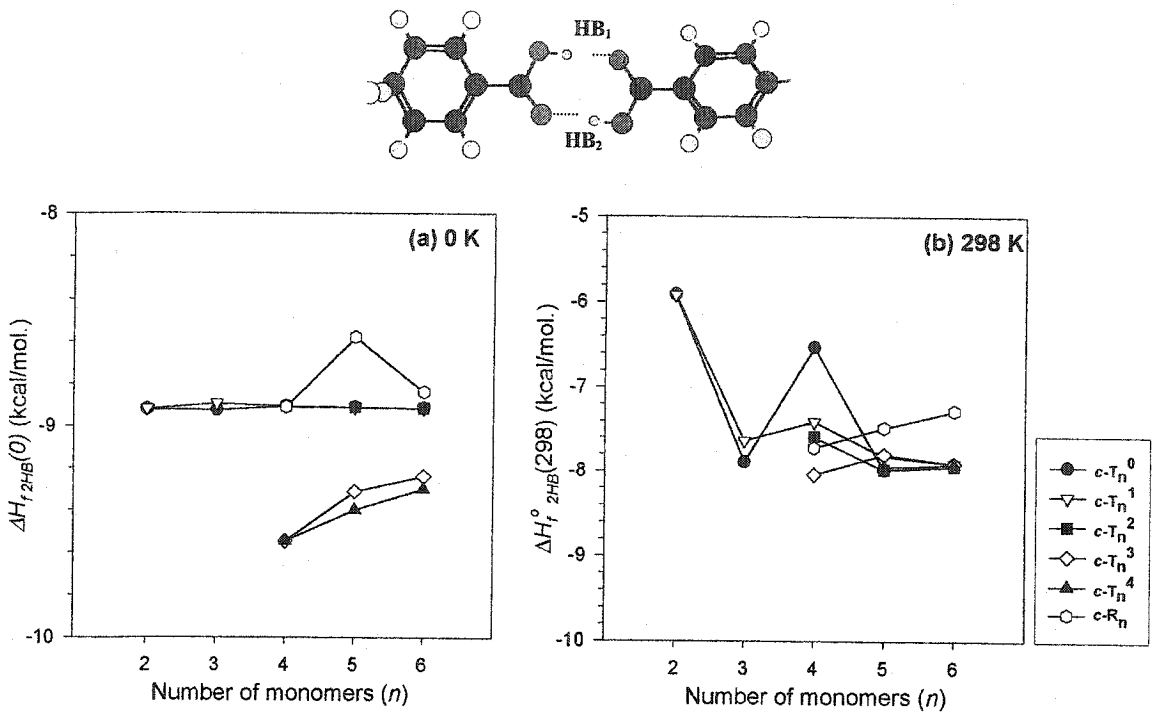


Figure 4. 2. Enthalpies of formation for two hydrogen-bonds HB_1 and HB_2 (inset) in the *cis*-azodibenzoic acid aggregates as a function of the number of monomers. (a) 0 K. (b) 298 K, 1 atm.

For each PM3 optimized structure, the enthalpy of formation at 0 K and at 298 K, 1 atm, for two hydrogen-bonds $\Delta H_{f\,2HB}(T)$ (Figure 4. 2) is calculated by:

$$\Delta H_{f\,2HB}(T) = \frac{H_f(M_n^m) - n \times H_f(M)}{n_{2HB}} \qquad \textbf{(Eq. 4. 1)}$$

where T is the temperature, $H_f(M)$ is the enthalpy of the monomer **M**, n_{2HB} the number of hydrogen-bond pairs, n the number of monomers involved, and $H_f(M_n^m)$ the enthalpy of $\mathbf{M_n^m}$. The hydrogen-bonding enthalpies are constant from one oligomer $\mathbf{M_n^m}$ to the next $\mathbf{M_{n+1}^m}$ through each series (Figure 4. 2), ranging between -8.7 and -9.6 kcal/mol at 0 K and between -5.9 and -8.1 kcal/mol at 298 K, consistent with the formation of weaker hydrogen-bonds at higher temperatures. The enthalpies of formation calculated for the

hydrogen-bonds of oligomers $c-\mathbf{T}_n^3$ and $c-\mathbf{T}_n^4$ are slightly lower (approx. -9.5 kcal/mol). This increased aggregate stability is consistent with the formation of an additional 3.12 – 3.25 Å, weak N···H hydrogen-bond between the azobenzene nitrogen of the fourth-monomer and the terminal carboxylic acid group (Figure 4. 1).

4.3.4. PM3 Enthalpies and Free Energies of the Optimized Hydrogen-bonded Structures

To compare with experiment,[49] the PM3 enthalpy for the self-assembly of *n* azodibenzoic monomers **M** into a hydrogen-bonded, supramolecular structure $\mathbf{M}_n^m$ at 298 K, $\Delta H_r^o(T)$, is calculated using:

$$\Delta H_r^o(T) = H_f^o(M_n^m, T) - n * H_f^o(M, T) \qquad \textbf{(Eq. 4. 2)}$$

where the temperature T is 298 K, $H_f^o(M_n^m, T)$ is the total enthalpy for $\mathbf{M}_n^m$, and $H_f^o(M,T)$ the total enthalpy for the monomer **M**. The enthalpies exhibit similar trends where the crinkled *cis*-tapes $c-\mathbf{T}_n^0$ are the most unstable structures, and the hydrogen-bonded macrocycles $c-\mathbf{R}_n$ are the most stable structures (Figure 4. 3a). The enthalpy difference between crinkled $c-\mathbf{T}_n^0$ and cyclic $c-\mathbf{R}_n$ structures (*ca.* 7.0 – 10.0 kcal/mol) originates from the formation of an additional hydrogen-bond dimer in the macrocyclic structures. Interestingly, the *cis*- $c-\mathbf{T}_n^1$ through $c-\mathbf{T}_n^4$ tapes have enthalpies decreasing with increased folding, suggesting the existence of a *folding parameter* in the self-assembly process in addition to the hydrogen-bonding terms. These trends present an

overall enthalpy decrease with increasing number of monomers, and therfore the *cis*-azodibenzoic acid self-assembly into hexameric macrocycles is the most favored reaction *enthalpically*, and the tetramer self-assembly the least favored.

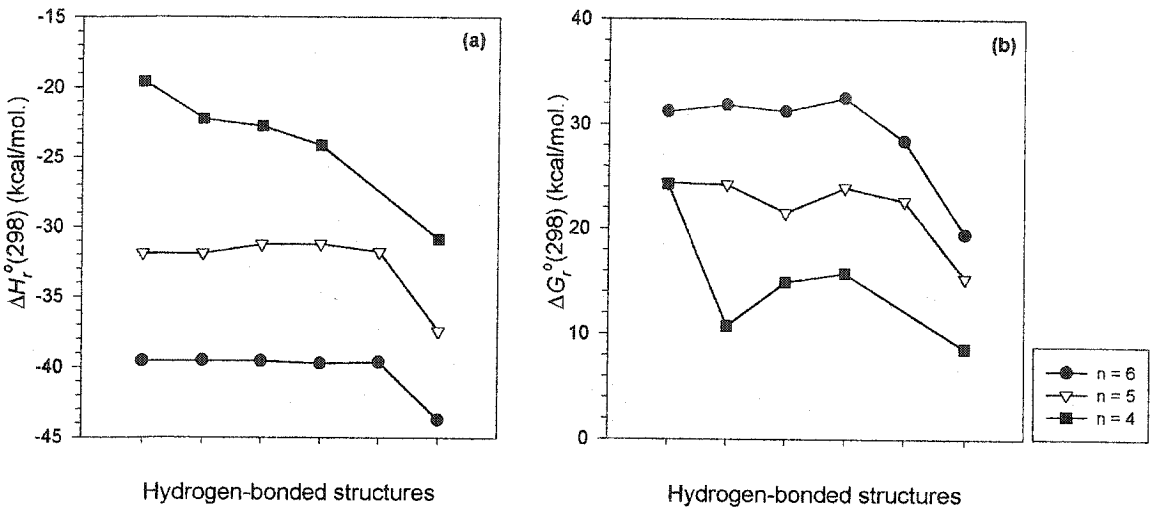


Figure 4. 3. (a) Enthalpies at 298 K for the hydrogen-bond self-assembly of *cis*-azodibenzoic acid as a function of the number of monomers. (b) Gibbs free energies at 298 K for the hydrogen-bond self-assembly of *cis*-azodibenzoic acid as a function of the number of monomers. (The geometry of the tetrameric $c-\mathbf{T}_n^3$ and $c-\mathbf{T}_n^4$ tapes are similar.)

Enthalpies have traditionally been used to evaluate the stability of covalently bound structures; however, they are not sufficient to describe the stability of thermodynamically controlled, hydrogen-bonded architectures. Standard PM3 Gibbs free energies for the self-assembly $\Delta G_r^o(298)$ have therefore been calculated in order to estimate the essential entropy contribution to the self-assembly of hydrogen-bonded $\mathbf{M}_n^m$ from n monomers **M** (Equation 4. 3):

$$\Delta G_r^o(298) = G_f^o(M_n^m,298) - n * G_f^o(M,298) \qquad \textbf{(Eq. 4. 3)}$$

where $G_f^o(M_n^m,298)$ is the temperature corrected Gibbs free energies at 298 K and 1 atm for the aggregate $\mathbf{M_n^m}$, and $G_f^o(M,298)$ the temperature corrected Gibbs free energies at 298 K and 1 atm for the monomer. The standard Gibbs free energies of formation $\Delta G_r^o(298)$ (Figure 4. 3b) suggest a conformational-dependence of the hydrogen-bond in the self-assembly process of *cis*-**2** aggregates. These energies show that *cis*-azodibenzoic acid units **2** are more likely to give hydrogen-bonded macrocycles $c-\mathbf{R_n}$, rather than tapes $c-\mathbf{T_n^m}$. Furthermore, these PM3 Gibbs free energies of reaction indicate that the self-assembly of cyclic hydrogen-bonded tetramers is more favourable than pentameric or hexameric structures when *cis*-**2** monomers are used. Consequently, the *cis*-**2** cyclic tetramer forms most favourably and its entropy cost of hydrogen-bond self-assembly is the lowest.

The detailed thermodynamic analysis of the hydrogen-bond self-assembly of *cis*-**2** underlines the critical importance of entropy in the prediction of supramolecular structure. In this example, hexameric macrocycles are shown to be the most stable *enthalpically*, whereas the smallest, tetrameric macrocycles are most favourable *thermodynamically*. This preferred macrocyclic structure formed by the *cis*-**2** monomers is consistent with the predicted monomer geometry, in which the carboxylic acid groups adopt a quasi-perpendicular orientation. Both enthalpy and energy trends show a *folding parameter* which contributes significantly to the stabilisation of the hydrogen-bonded supramolecular structures, favouring the formation of macrocycles over tapes.

4.3.5. PM3 Vibrational Properties of the Optimized Hydrogen-bonded Structures

The impact of conformational change on vibrational properties has been analysed to study the entropy costs for the hydrogen-bond self-assembly.[50,51] The vibrational spectrum for the hexameric macrocycle $c-\mathbf{R}_6$ is compared to the computed vibrational spectra of the hexameric crinkled tape $c-\mathbf{T}_6^0$ (Figure 4. 4) and the tetrameric macrocycle $c-\mathbf{R}_4$ (Figure 4. 5). The PM3 infrared spectra, of the *cis*-azodibenzoic acid aggregates, display broadly similar resonance frequencies, regardless of conformation (Figure 4. 4a) or size (Figure 4. 5a). Closer examination of the *cis*-rosette $c-\mathbf{R}_6$ spectra showed them to be slightly shifted towards higher frequencies than the *cis*-tape $c-\mathbf{T}_6^0$ spectra (Figure 4. 4). Each C-O-H bending, C-O, N=N and C=O stretching (ν = 1500 – 2000 cm^{-1}, Figure 4. 4b) and the C-H stretching motion (ν = 3000 – 3100 cm^{-1}, Figure 4. 4c) is 1– 2 cm^{-1} greater in the *cis*-rosette $c-\mathbf{R}_6$, suggesting stronger force constants and, consequently, greater stability in the *cis*-**2** macrocycles than in the crinkled tapes. Similarly, the C–O–H bending, N=N and C=O stretching (Figure 4. 5b) and C-H stretching (Figure 4. 5c) are slightly shifted towards higher frequencies in the hexameric *cis*-rosette $c-\mathbf{R}_6$ spectra than in the tetrameric *cis*-macrocycle $c-\mathbf{R}_4$ spectra.

More important, the *cis*-rosette $c-\mathbf{R}_6$ spectra display much smaller infrared intensities than the *cis*-tape $c-\mathbf{T}_6^0$ (Figure 4. 4a). This difference in infrared intensity shows the presence of stronger bond dipoles in the crinkled tape $c-\mathbf{T}_6^0$ than in the macrocyclic structure $c-\mathbf{R}_6$, suggesting that the crinkled tape $c-\mathbf{T}_6^0$ is more prone to

vibrational motions. The crinkled tape $c - T_6^0$ spectrum (Figure 4. 4b) displays coupled unsymmetrical modes between the C-N and N=N (*ca.* 1320 cm^{-1}) suggesting a favorable *cis* to *trans* isomerization of the *cis*-**2** monomer in the tape conformation and, consequently, a destabilization of the hydrogen- bonded structure.

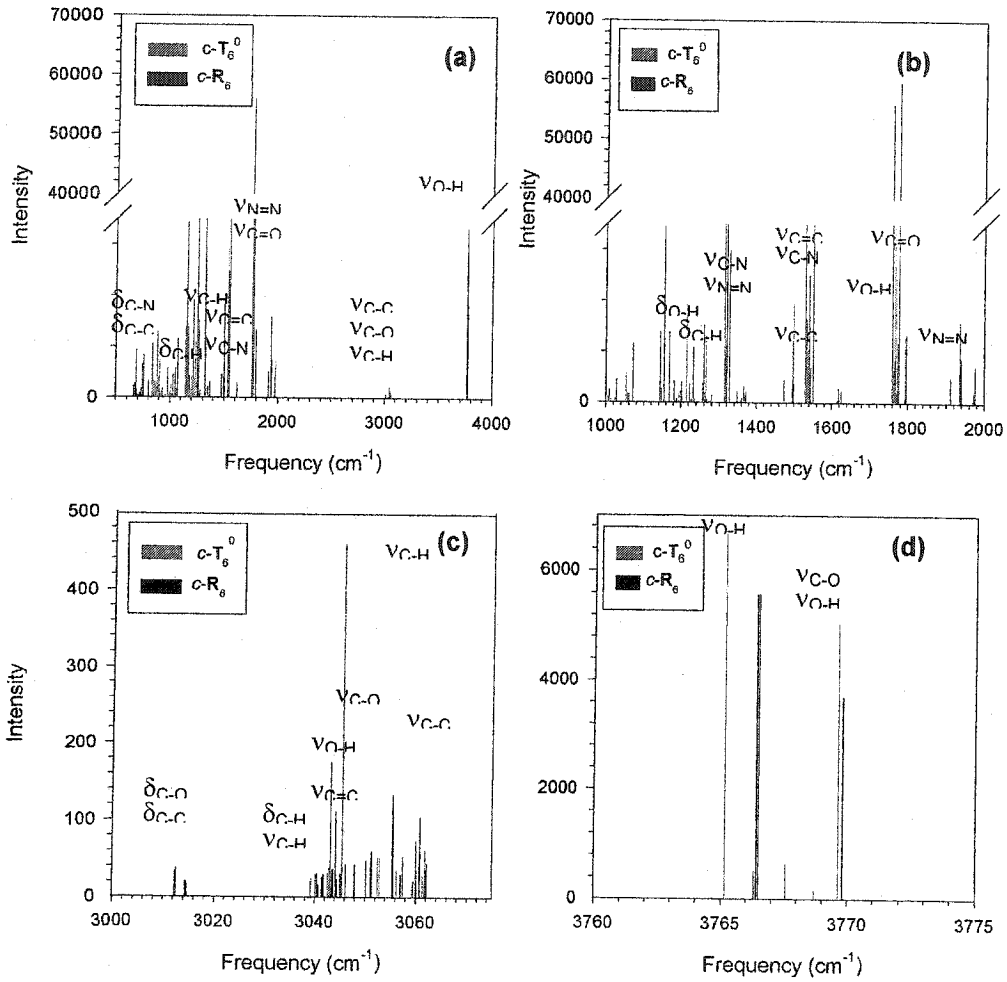


Figure 4. 4. Normal-mode frequencies for the *cis*-tape $c-\mathbf{T}_6^0$ and hexameric rosette $c-\mathbf{R}_6$. (a) Full spectrum. (b) 1000 – 2000 cm^{-1} region showing $\nu_{N=N}$ (1940 cm^{-1}) stretching, $\nu_{C=O}$ (1790 cm^{-1}) stretching, and $\delta_{C\text{-}O\text{-}H}$ (1100 cm^{-1}) in-plane bending frequencies. (c) 3000 – 3075 cm^{-1} region showing the aromatic $\nu_{sC\text{-}H}$ (3050 cm^{-1}) and $\nu_{asC\text{-}H}$ (3060 cm^{-1}) stretching frequencies. (d) 3760 – 3775 cm^{-1} region showing the bound and unbound $\nu_{O\text{-}H}$ stretching frequencies.

Examination of the C-H stretching region (3000-3100 cm^{-1}) (Figures 4. 4c and 4. 5c), shows normal modes around 3015 cm^{-1} corresponding to C-O and C-C bending motions which exist for the hexameric tape and macrocycle, but not for the tetrameric macrocycle $c-\mathbf{R_4}$. The presence of these frequencies in the vibrational spectrum for the hexameric macrocycle $c-\mathbf{R_6}$ (Figure 4. 5c) reflects the dissymmetry of the hexamer $c-\mathbf{R_6}$ compared with the tetrameric macrocycle $c-\mathbf{R_4}$, allowing more stretching and bending motions in hydrogen-bonded macrocycle $c-\mathbf{R_6}$. Further evidence for this dissymmetry is observed in the O-H stretching region (3760 – 3775 cm^{-1}) (Figures 4. 4d and 4. 5d). The crinkled tape $c-\mathbf{T_6^0}$ spectrum (Figure 4. 4d) displays two distinct, intense normal modes in this region which correspond to the bound (*ca.* 3765.5 cm^{-1}) and unbound (*ca.* 3769.5 cm^{-1}) hydroxyl groups. Similarly, the macrocyclic structure $c-\mathbf{R_6}$ displays two distinct, intense normal modes (*ca.* 3766.5 cm^{-1}) and (*ca.* 3769.5 cm^{-1}) for the hydroxyl groups, which not only show the asymmetry of this cyclic hexamer but also give bound and unbound character of the carboxylic acid groups (ν = 3760 – 3775 cm^{-1}) (Figures 4. 4d and 4. 5d). On the other hand, the O–H stretching region (Figure 4. 5d) of the tetrameric macrocycle shows a unique normal mode (3767.5 cm^{-1}), which corresponds to the bound O–H groups. This unique normal mode demonstrates the high symmetry of the hydrogen-bonded tetrameric macrocycle $c-\mathbf{R_4}$ and confirms its higher stability over the hydrogen-bonded hexameric macrocycle $c-\mathbf{R_6}$.

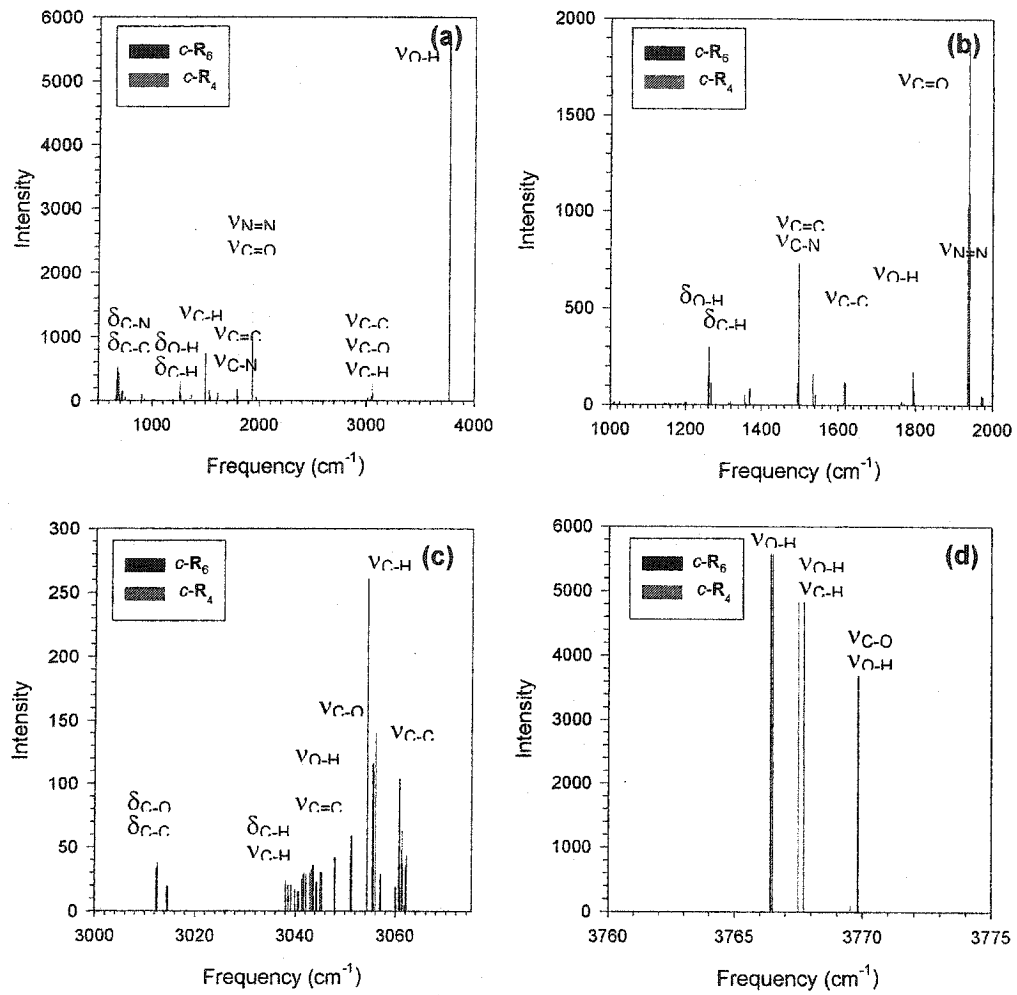


Figure 4. 5. Normal-mode frequencies for the tetrameric $c-\mathbf{R_4}$, pentameric $c-\mathbf{R_5}$ and hexameric *cis*-rosette $c-\mathbf{R_6}$. (a) Full spectrum. (b) 1500 – 2000 cm^{-1} region showing $\nu_{N=N}$ (1620 cm^{-1}) stretching, $\nu_{C=O}$ (1940 cm^{-1}) stretching, and $\delta_{C\text{-}O\text{-}H}$ (1795 cm^{-1}) in-plane bending frequencies. (c) 3000 – 3100 cm^{-1} region showing the aromatic $\nu_{sC\text{-}H}$ (3050 cm^{-1}) and $\nu_{asC\text{-}H}$ (3060 cm^{-1}) stretching frequencies. (d) 3760 – 3775 cm^{-1} region showing the bound $\nu_{O\text{-}H}$ (3766 cm^{-1}) and unbound $\nu_{O\text{-}H}$ (3769 cm^{-1}) stretching frequencies.

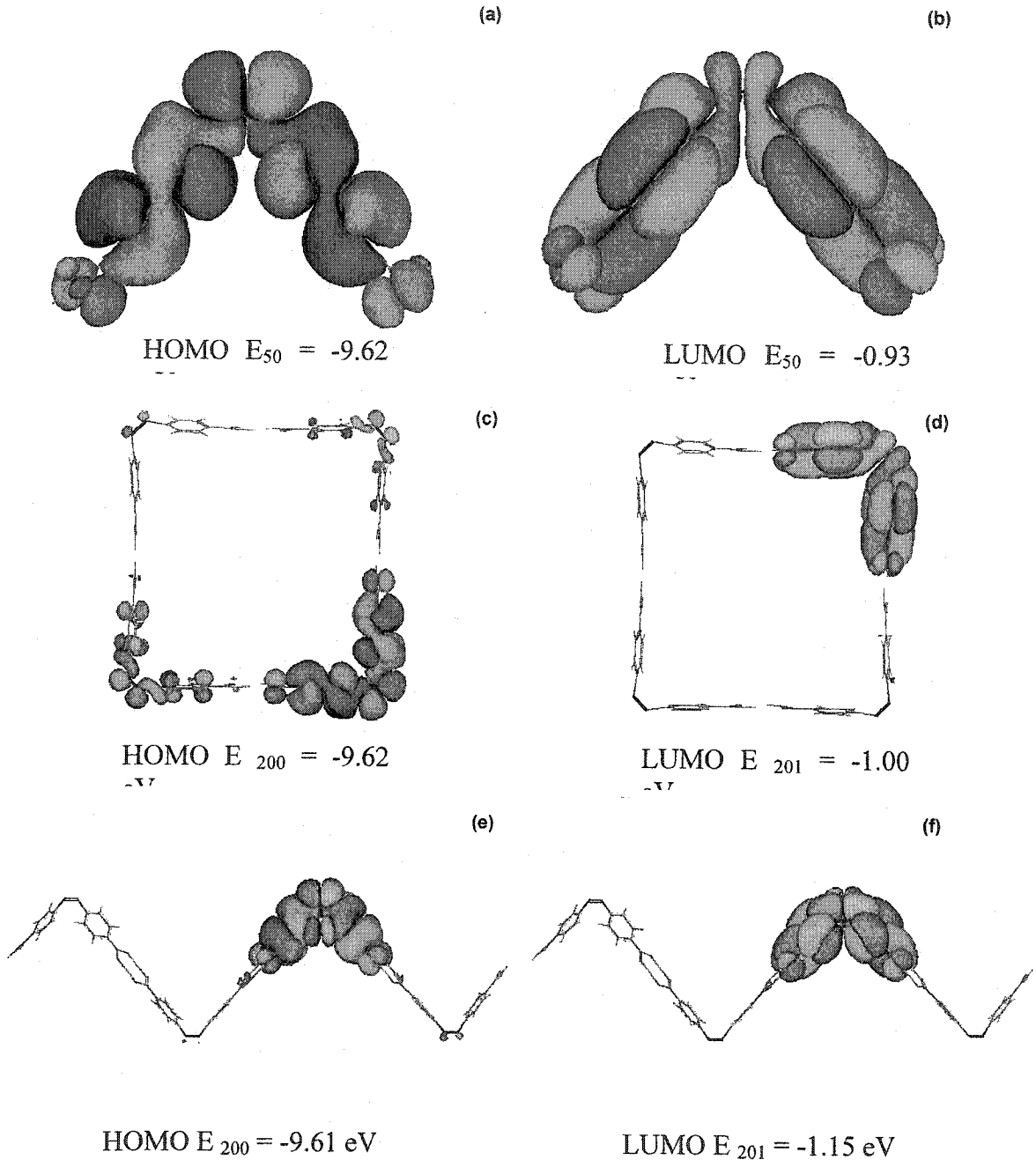


Figure 4. 6. Frontier molecular orbitals for the *cis*-**2** monomer and tetrameric structures. (a) Highest occupied (HOMO) and (b) lowest unoccupied (LUMO) molecular orbitals of *cis*-**2** monomer. (c) HOMO and (d) LUMO for macrocycle $c-\mathbf{R}_4$. (e) HOMO and (f) LUMO for tetrameric tape $c-\mathbf{T}_4^0$.

The molecular orbitals involved in hydrogen-bonding are much lower in energy than the HOMO (E ~ -9.61eV), confirming the strength of the hydrogen-bonds in the *cis*-**2** aggregates. Figure 4. 7 shows a typical example of these molecular orbitals in the tetrameric $c-\mathbf{R_4}$, pentameric $c-\mathbf{R_5}$ and hexameric *cis*-rosette $c-\mathbf{R_6}$. In these delocalized orbitals (E ~ -14.26 eV), the electron density is spread over the entire supramolecular structure and across the carboxylic acid dimers in a π-type interaction, indicative of hydrogen-bonding strength and directionality. The diagram for this bonding MO displays C_{2v} symmetry for the tetrameric macrocycle $c-\mathbf{R_4}$ (Fig. 7a) while it shows lower C_s and C_3 symmetry for the pentameric $c-\mathbf{R_5}$ (Fig. 7b) and hexameric macrocycles $c-\mathbf{R_6}$ respectively (Fig. 7c). This difference in MO symmetry, consistent with their energy differences, supports the results provided by the vibrational analysis and shows that hydrogen-bonding in the tetrameric macrocycle $c-\mathbf{R_4}$ is most favorable.

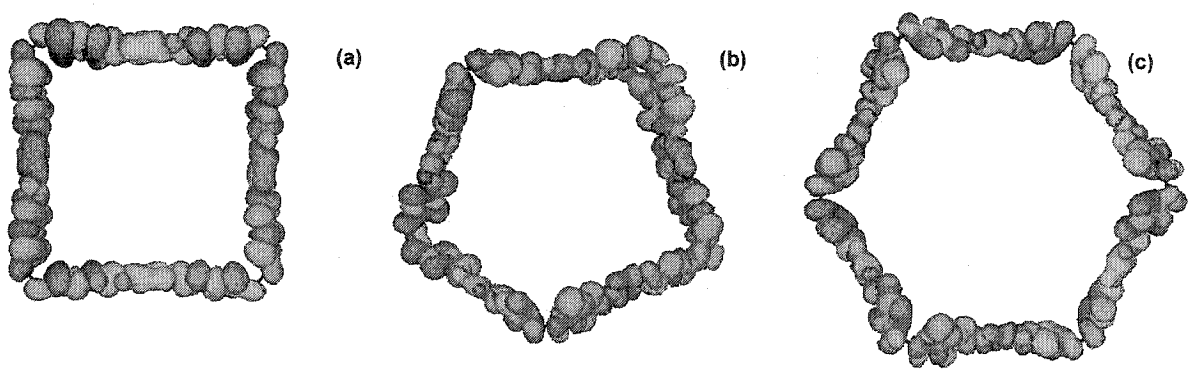


Figure 4. 7. Delocalized molecular orbitals of *cis*-2 macrocycles showing a π-type overlap across the hydrogen-bonds. (a) Tetramer $c-\mathbf{R_4}$. (b) Pentamer $c-\mathbf{R_5}$. (c) Hexamer $c-\mathbf{R_6}$.

Individual delocalized molecular orbital diagrams only provide a partial, qualitative depiction of the electronic properties for the supramolecular structure. The behavior of the entire electron cloud across the hydrogen-bonded structure is better described using electron density matrix maps. Hydrogen-bonding in the azodibenzoic acid aggregates is thus investigated using the density matrix. The elements of the density matrix derive from the Roothan-Hall equations,[53] which relate the Fock matrix F, representing the average effects of the entire electronic field on each orbital, to the overlap matrix S, and the diagonal matrix of orbital energies ε through the matrix of the molecular orbital coefficients C (Equation 4. 4):

$$FC = SC\varepsilon \qquad \textbf{(Eq. 4. 4)}$$

The Fock matrix elements are defined as:

$$F_{\mu\nu} = H_{\mu\nu}^{core} + \sum_{\lambda=1}^{N}\sum_{\sigma=1}^{N} P_{\lambda\sigma}\left[(\mu\nu|\lambda\sigma) - \frac{1}{2}(\mu\lambda|\nu\sigma)\right] \qquad \textbf{(Eq. 4. 5)}$$

where $H_{\mu\nu}^{core}$ is the matrix of the energy of a single electron in the bare nuclei and $P_{\lambda\sigma}$ the density matrix, which describes the contribution of atomic orbitals in the occupied molecular orbitals (Eq. 4. 6).

$$P_{\lambda\sigma} = 2\sum_{i=1}^{occupied} c_{\lambda i}^{*} c_{\sigma i} \qquad \textbf{(Eq. 4. 6)}$$

The diagonal elements of this matrix give the electron density on a particular atom in the molecular wavefunction, the off-diagonal elements the electron density shared by two atoms, reflecting their electronic interactions. Density matrices have been examined

previously to simulate the optical responses of conjugated and aggregated molecules such as very large carbon nanotubes,[54-59] bridged naphthalene dimers, stilbenoid derivatives, as well as polyacetylene oligomers and dendrimers.[60,61] In the case of the *trans*-**1** and *cis*-**2** derivatives, the density matrices are analyzed to obtain a quantitative insight into the electron density behavior across the aggregate and related to hydrogen-bonding and polymorphism.

The electron delocalization in these matrices can be described along two directions: L_d, the width along the main diagonal direction of the density matrix and L_c, the width along the antidiagonal direction. While L_d describes the extent of electron delocalization along the backbone of the observed species *i.e.* from one atom to its neighboring atom, L_c describes the extent of electron delocalization 'through space' *i.e.* from one atom to a remote atom. The x- and y-axis represent the orbital number on each atom. The electron density associated with the atomic orbitals of the carboxylic acid atoms, involved in the traditional valence bond concept is only part of the total molecular orbital, hence the highlighted regions of the density matrices.

The density plots of the *trans*-**1** and *cis*-**2** azodibenzoic acid tetramers are shown in Figures 4. 8 – 4. 10. These densities show symmetry with respect to the main diagonal, as well as high periodicity when the entire supramolecular structure is taken into account, confirming the additive nature of the hydrogen-bond assembly. Consequently, only two monomer units M1 and M2 are represented for the *trans*-**1** and *cis*-**2** tetramers for clarity (insets). In addition, orbital coefficients related to all the hydrogen atoms, except the carboxylic acid hydrogens, were discarded because of their negligible contribution to electron delocalization.

The *trans*-**1** tape $t-\mathbf{T}_4$ density matrix exhibits extensive electron delocalization along the backbone of the hydrogen-bonded structures. This is consistent with the linearity and the quasi-planarity of the aromatic species, which facilitate electron flow across the whole hydrogen-bonded structure. This electron delocalization is enhanced by significant, widespread electronic interactions between remote atoms.

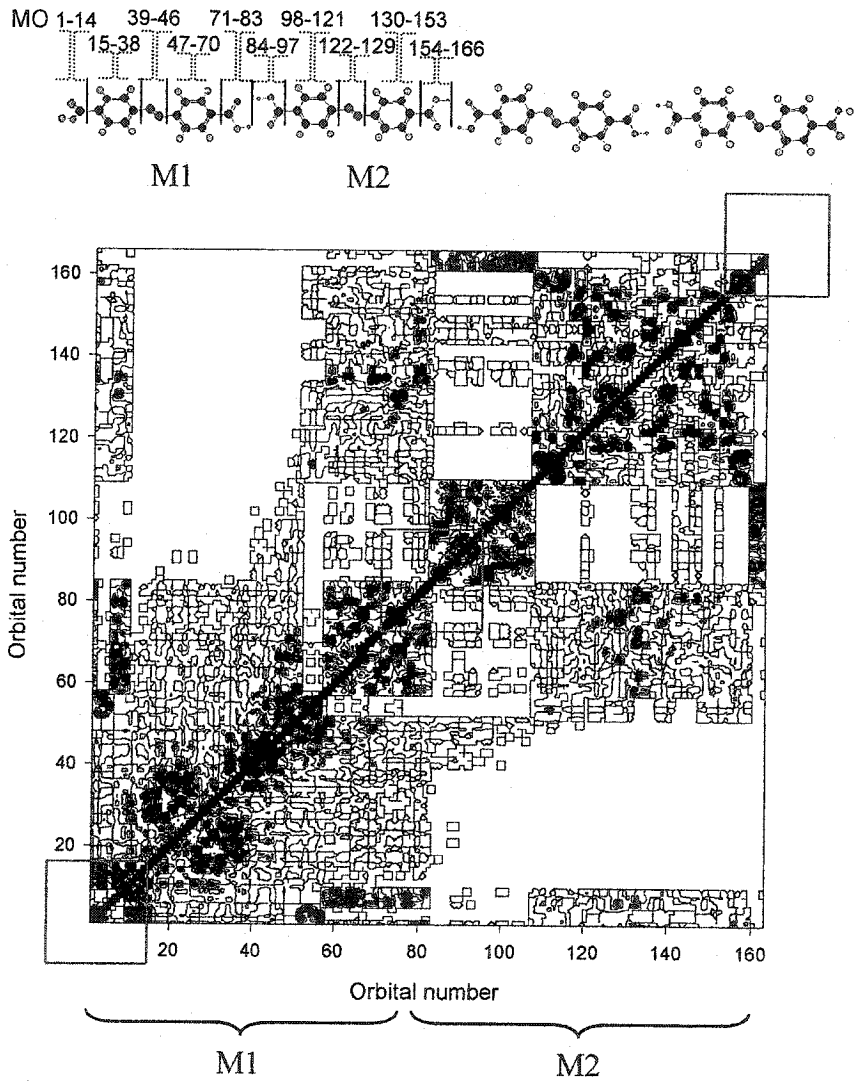


Figure 4. 8. Density matrix contour of the *trans*-azodibenzoic acid tetrameric tape $t-\mathbf{T}_4$. Bound and unbound carboxylic acid densities are highlighted using □. (Only the first two monomers M1 and M2 are shown for clarity)

The density matrix representations of the tetrameric $c-\mathbf{T}_4^0$ and $c-\mathbf{R}_4$ structures (Figures 4. 9 and 4. 10) differ dramatically from the density matrix representations of the *trans*-**1** aggregates $t-\mathbf{T}_4$. Unlike the *trans*-**1** tape $t-\mathbf{T}_4$ (Figure 4. 8), most of the electron density is concentrated along the main diagonal, indicating less electron delocalization in the *cis*-**2** aggregates than in the *trans*-**1** aggregates. This result is consistent with the U-shaped geometry of the *cis*-**2** isomer which confines the electron density.

Comparison of the carboxylic acid groups in the *cis*-**2** tape and in the *cis*-**2** macrocycle show that these atoms share electron density with both phenyl rings of the same azodibenzoic acid monomer (*e.g.* orbitals 1↔14 with orbitals 47↔70). However, in the case of the *cis*-**2** macrocycle, the phenyl rings of one monomer also share electron density with the phenyl ring of the next monomer (*e.g.* orbitals 15↔38 with orbitals 98↔121). Consequently, the electron delocalization is more restricted along the molecular backbone in the *cis*-**2** tapes than in the *cis*-**2** macrocycles. As a result of this reduced electron delocalization, the $c-\mathbf{T}_4^0$ tapes formed from the *cis-p*-azodibenzoic acid are more rigid than the macrocyclic aggregates, and are less favorable thermodynamically in agreement with the entropy calculations and frequency analysis.

The PM3 molecular orbital diagrams and density matrices show a more diffuse, consequently more mobile, electron cloud in the case of the $c-\mathbf{R}_4$ macrocycles than in the linear structures $c-\mathbf{T}_4^0$, which favors the formation of tetrameric macrocycles $c-\mathbf{R}_4$ from *cis*-azodibenzoic acid. In addition, the conformation-dependence of the density

matrices reveal the potential applications of these hydrogen-bonded azodibenzoic acid in the fabrication of new materials with tunable electronic properties.

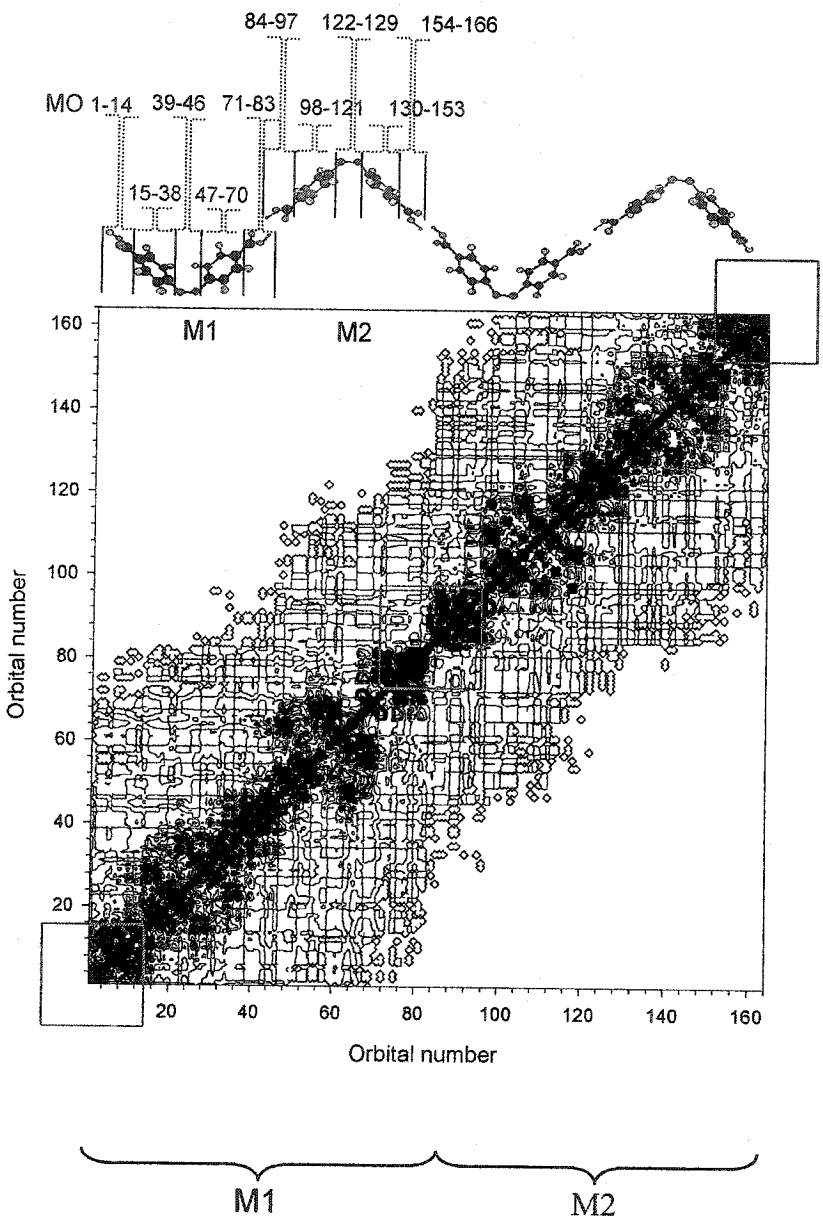


Figure 4. 9. Density matrix contour of the *cis*-azodibenzoic acid crinkled tetrameric tape $c-\mathbb{T}_4^0$. Bound and unbound carboxylic acid densities are highlighted using ⌊. (Only the first two monomers M1 and M2 are shown for clarity)

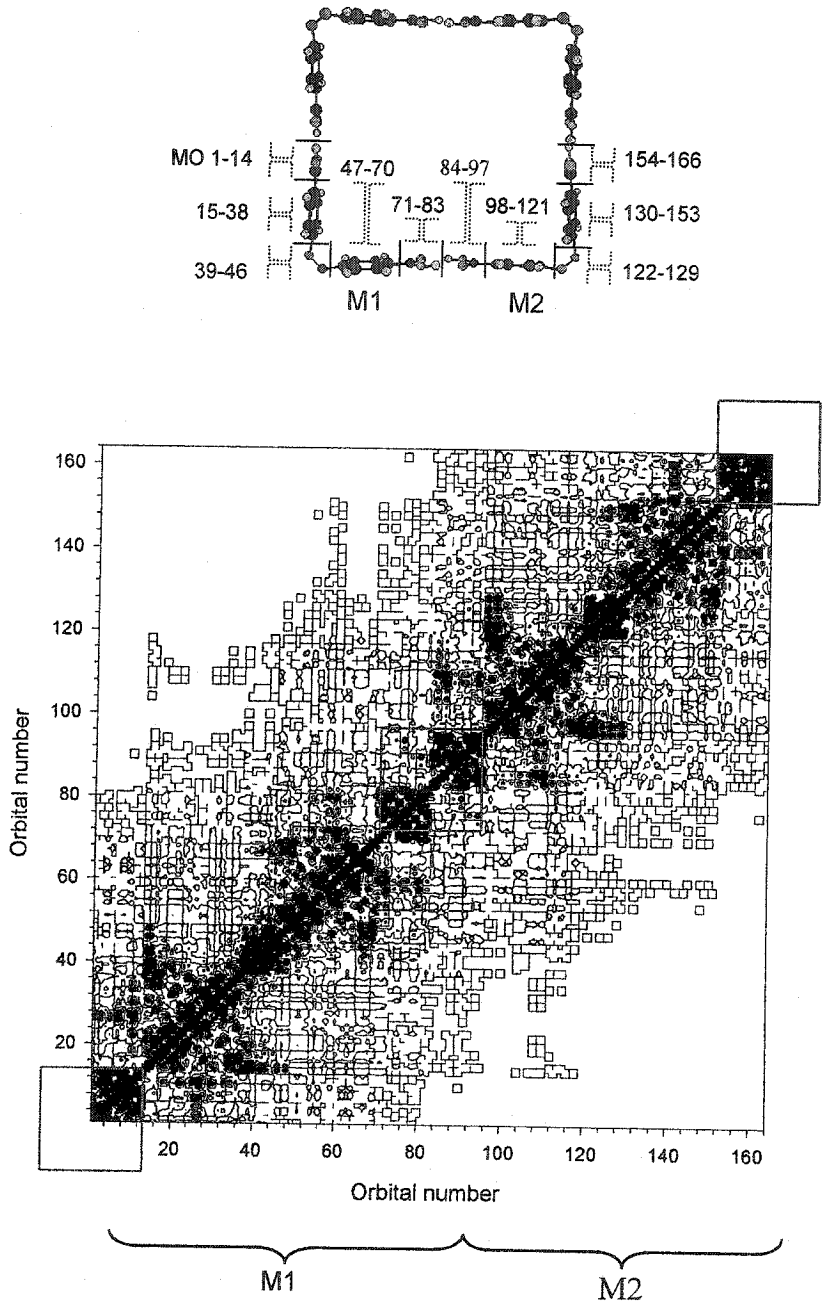


Figure 4. 10. Density matrix contour of the cis-azodibenzoic acid square $c - \mathbf{R}_4$. Bound and unbound carboxylic acid densities are highlighted using □. (Only the first two monomers M1 and M2 are shown for clarity)

4.4. Conclusion

In conclusion, we have used a new theoretical approach to evaluate hydrogen-bond self-assembly, and predict linear tapes from *trans*-**1** azodibenzoic acid and cyclic tetramers from *cis*-**2** monomers. The calculated energies show the crucial role of entropy in self-assembly processes and the need to consider the Gibbs free energy of the self-assembled molecules. The computed vibrational spectroscopy and electronic population analysis verify the caculations using the Gibbs free energy. Significant stretching and bending frequency shifts in the vibrational spectra are caused by conformational changes, affecting the relative flexibility and symmetry of the hydrogen-bonded structures, and supporting the preferred formation of macrocyclic tetramers from *cis*-**2**. The geometry of the macrocyclic structures also changes the symmetry of the molecular orbital wavefunctions and consequently their stability. The emergence of highly symmetrical patterns in the electron density maps provides a direct, quantitative visualization of through-bond and through-space electron delocalization in the supramolecular structures, emphasizing the stability of *trans*-**1** azodibenzoic acid linear tapes and *cis*-**2** cyclic tetramers. Further investigation of these vibrational and electronic properties are underway to better understand and improve the electronic properties of these supramolecular systems necessary for the design and implementation of novel functional materials.

4.5. References and Notes

[1] J. -M. Lehn, *Supramolecular chemistry: concepts and perspectives*, VCH: Weinheim, 1995.

[2] G. M. Whitesides, E. E. Simanek, J. P. Mathias, C. T. Seto, D. N. Chin, M. Mammen, D. M. Gordon, *Acc. Chem. Res.*, **1995**, *28*, 37.

[3] J. S. Lindsey, *New J. Chem.* **1991**, *15*, 153.

[4] D. S. Lawrence, T. Jiang, M. Levett, *Chem. Rev.*, **1995**, *95*, 2229.

[5] S. Leininger, B. Olenyuk, P. J. Stang, *Chem. Rev.*, **2000**, *100*, 853.

[6] J. Yang, J.-L. Marendaz, S. J. Geib, A. D. Hamilton, *Tet. Lett.*, **1994**, *35*, 3665.

[7] A. Zafar, J. Yang, S. J. Geib, A. D. Hamilton, *Tet. Lett.*, **1996**, *37*, 2327.

[8] S. Valiyaveetil, K. Müllen, *New J. Chem.*, **1998**, *2*, 89.

[9] D. W. Wise, G. E. Wnek, D. J. Trantolo, T. M. Cooper, J. D. Gresser (Eds.), *Photonic Polymer Systems: Fundamentals, Methods, and Applications*, Marcel Dekker: New York, 1998.

[10] H. J. Coufal, D. Psaltis, G. T. Sincerbox (Eds.), *Holographic Data Storage*, Springer-Verlag: Berlin, Heidelberg, 2000.

[11] M. S. Vollmer, T. D. Clark, C. Steinem, M. R. Ghadiri, *Angew. Chem. Int. Eng. Ed.*, **1999**, *38*, 11, 1598.

[12] H. Asanuma, T. Ito, T. Yoshida, X. Liang, M. Komiyama, *Angew. Chem. Int. Eng. Ed.* **1999**, *38*, 16, 2393.

[13] D. M. Junge, D. V. McGrath, *J. Am. Chem. Soc.*, **1999**, *121*, 4912.

[14] S. Tsuchiya, *J. Am. Chem. Soc.*, **1999**, *121*, 48.

[15] M. Takeuchi, S. Shinkai, *J. Chem. Soc., Perkin Trans. 2*, **1998**, *4*, 847.

[16] L. N. Lucas, J. van Esch, R. M. Kellogg, B. L. Feringa, *Chem. Commun.*, **2001**, 759.

[17] T. Kawasaki, M. Tokuhiro, N. Kimizuka, T. Kunitake, *J. Am. Chem. Soc.*, **2001**, *123*, 6792.

[18] F. Rakotondradany, M. A. Whitehead, A. -M. Lebuis, H. F. Sleiman, *Chem. Eur. J.*, **2003**, *9*, 4771.

[19] M. Mammen, E. E. Simanek, G. M. Whitesides, *J. Am. Chem. Soc.*, **1996**, *118*, 12614.

[20] M. Mammen, E. I. Shakhnovich, J. M. Deutch, G. M. Whitesides, *J. Org. Chem.*, **1998**, *63*, 3821.

[21] L. Jullien, H. Cottet, B. Hamelin, A. Jardy, *J. Phys.Chem. B*, **1999**, *103*, 10866.

[22] K. Müller-Dethlefs, P. Hobza, *Chem. Rev.*, **2000**, *100*, 143.

[23] E. E. Simanek, M. Mammen, D. M. Gordon, D. N. Chin, J. P. Mathias, C. T. Seto, G. M. Whitesides, *Tetrahedron*, **1995**, *51*, 607.

[24] R. Meissmer, X. Garcias, S. Mecozzi, J. Rebek, Jr. *J. Am. Chem. Soc.*, **1997**, *119*, 77.

[25] S. Ma, D. M. Rudkevich, J. Rebek, Jr., *J. Am. Chem. Soc.*, **1998**, *120*, 4977.

[26] P. Timmerman, J.-L. Weidmann, K. A. Jolliffe, L. J. Prins, D. N. Reinhoudt, S. Shinkai, L. Frish, Y. Cohen, *Perkin Trans. 2* **2000**, *10*, 2077.

[27] M. T. Huggins, A. K. Tipton, Q. Chen, D. A. Lightner, *Monatsh. Chem.*, **2000**, *131*, 825.

[28] R. Castro, M. J. Berardi, E. Cordova, M. O. de Olza, A. E. Kaifer, J. D. Evanseck, *J. Am. Chem. Soc.* **1996**, *118*, 10257.

[29] S. Sharma, T. P. Radhakrishnan, *J. Phys. Chem. B*, **2000**, *104*, 10191.

[30] D. Quinonero, A. Frontera, S. Tomas, G. A. Suner, J. Morey, A. Costa, P. Ballester, P. M. Deya, *Theor. Chem. Acc.*, **2000**, *104*, 50.

[31] K. S. Kim, S. B. Suh, J. C. Kim, B. H. Hong, E. C. Lee, S. Yun, P. Tarakeshwar, J. Y. Lee, Y. Kim, H. Ihm, H. G. Kim, J. W. Lee, J. K. Kim, H. M. Lee, D. Kim, C. Cui, S. J. Youn, H. Y. Chung, H. S. Choi, C.-W. Lee, S. J. Cho, S. Jeong, J.-H. Cho, *J. Am. Chem. Soc.*, **2002**, *124*, 14268.

[32] R.G. Hicks, M. T. Lemaire, L. Oehrstroem, J. F. Richardson, L. K. Thompson, Z. Xu, *J. Am. Chem. Soc.*, **2001**, *123*, 7154.

[33] R. Cini, C. Pifferi, *J. Chem. Soc., Dalton Trans.*, **1999**, *5*, 699.

[34] F. M. Raymo, M. D. Bartberger, K. N. Houk, J. F. Stoddart, *J. Am. Chem. Soc.*, **2001**, *123*, 9264.

[35] Y. -D. Wu, Y.-L. Zhao, *J. Am. Chem. Soc.*, **2001**, *123*, 5313.

[36] H. S. Son, B. H. Hong, C. -W. Lee, S. Yun, K. S. Kim, *J. Am. Chem. Soc.*, **2001**, *123*, 514.

[37] J. J. P. Stewart, *J. Comp. Chem.*, **1989**, *10*, 209.

[38] J. J. P. Stewart, *J. Comp. Chem.*, **1989**, *10*, 221.

[39] A. D. Becke, *J. Chem. Phys.*, **1993**, *98*, 5648.

[40] See supporting information.

[41] M. J. Frisch, G. W. Trucks, H. B. Schlegel, G. E. Scuseria, M. A. Robb, J. R. Cheeseman, V. G. Zakrzewski, J. A. Montgomery, Jr., R. E. Stratmann, J. C. Burant, S. Dapprich, J. M. Millam, A. D. Daniels, K. N. Kudin, M. C. Strain, O. Farkas, J. Tomasi, V. Barone, M. Cossi, R. Cammi, B. Mennucci, C. Pomelli, C. Adamo, S. Clifford, J. Ochterski, G. A. Petersson, P. Y. Ayala, Q. Cui, K. Morokuma, D. K. Malick, A. D. Rabuck, K. Raghavachari, J. B. Foresman, J. Cioslowski, J. V. Ortiz, A. G. Baboul, B. B. Stefanov, G. Liu, A. Liashenko, P. Piskorz, I. Komaromi, R. Gomperts, R. L. Martin, D. J. Fox, T. Keith, M. A. Al-Laham, C. Y. Peng, A. Nanayakkara, C. Gonzalez, M. Challacombe, P. M. W. Gill, B. G. Johnson, W. M. Chen, W. Wong, J. L. Andres, M. Head-Gordon, E. S. Replogle, J. A. Pople, *Gaussian 98W*, Revision A.7, Gaussian, Inc.: Pittsburgh, PA, 1998.

[42] C. L. Forber, E. C. Kelusky, N. J. Bunce, M. C. Zerner, *J. Am. Chem. Soc.*, **1985**, *107*, 5884.

[43] N. Kurita, S. Tanaka, S. Itoh, *J. Phys. Chem. A*, **2000**, *104*, 8114.

[44] H. Fliegl, A. Köhn, C. Hättig, R. Ahlrichs, *J. Am. Chem. Soc.*, **2003**, *125*, 9821.

[45] A. Mostad, C. Romming, *Acta Chem. Scand.* **1971**, *25*, 3561.

[46] J. M. Robertson, *J. Chem. Soc.*, **1939**, 232.

[47] A. D. Ryabov, L. G. Kuz'mina, N. V. Dvortsova, D. J. Stufkens, R. van Eldik, *Inorg. Chem.*, **1993**, *32*, 3166.

[48] N. J. Bunce, G. Ferguson, C. L. Forber, M. C. Zerner, *J. Org. Chem.* **1987**, *52*, 394.

[49] The relative stabilities between the different hydrogen-bonded structures were also examined using their total enthalpies and Gibbs free energies at 298 K, showing similar trends (See supporting information).

[50] D. C. Harris, M. D. Bertolucci, *Symmetry and Spectroscopy: An Introduction to Vibrational and Electronic Spectroscopy*, Oxford University Press: New York, 1978.

[51] In the case of trans- and cis- azobenzene, an error of about 200 cm^{-1} has been reported between PM3 and experiment for the 1500-2000 cm^{-1} range, which include N=N and C=O vibrational modes, and an error of ca. 300 cm^{-1} for the HF/6-31G* (See reference 42). Although, the same discrepancy is observed from the vibrational analysis of the cis-tapes $c-\mathbf{T}_n^m$ and macrocycles $c-\mathbf{R}_n$, it should not affect the comparative study of the PM3 normal-mode frequencies.

[52] The opposite is observed for isophthalic acid which displays less cost in entropy for self-assembly of tapes than for rosettes, reflecting the rigidity of the monomer.

[53] C. C. J. Roothan, *Rev. Mod. Phys.*, **1951**, *29*, 69.

[54] M. M. J. Treacy, T. W. Ebbesen, J. M. Gibson, *Nature*, **1996**, *381*, 678.

[55] M. S. Dresselhaus, G. Dresseihaus, P. C. Eklund, *Science of Fullerenes and Carbon Nanotubes*, Academic Press: San Diego, 1996.

[56] J. W. G. Wildoer, L. C. Venema, A. G. Rinzler, R. E. Smalley, C. Dekker, *Nature*, **1998**, *391*, 59.

[57] T. W. Odom, J. -L. Huang, P. Kim, C. M. Lieber, *Nature*, **1998**, *391*, 62.

[58] C. H. Olk, J. P. Heremans, *J. Mater. Res.*, **1994**, *9*, 259.

[59] R. Tamura, M. Tsukada, *Phys. Rev. B*, **1998**, *58*, 8120.

[60] W. Z. Liang, S. Yokojima, D. Zhou, G. H. Chen, *J. Phys. Chem. A*, **2000**, *104*, 2445.

[61] S. Tretiak, S. Mukamel, *Chem. Rev.* **2002**, *102*, 3171.

Chapter 5.

Photoresponsive Supramolecular Systems: Packing in Self-Assembled Azodibenzoic Acid Cyclic Tetramers

5.1. Introduction

Hydrogen-bonded *trans*- and *cis*-azobenzene dicarboxylic acid have been shown to self-assemble into two dramatically different supramolecular structures.[1] Theoretical prediction and experimental evidence in Chapter 3 clearly indicates that these two photoisomers self-assembled into two levels of self-organisation, where *trans*-isomers form linear tapes which pack into two dimensional sheets, and *cis*-isomers give cyclic tetramers which stack into rod-like nanostructures. In Chapter 4, theoretical investigations provided a strong basis for the formation of hydrogen-bonded linear tapes and cyclic tetramers from *trans*- and *cis*-azodibenzoic acid derivatives, through a comparison of the relative thermodynamic stabilities, vibrational and electronic properties between the different oligomer conformations. X-ray single crystal data of *trans*-**1** derivative (Scheme 3. 1, Chapter 3) clearly showed the formation of an extended two-dimensional network from van der Waals and π-stacking interactions between hydrogen-bonded linear tapes. In the case of the cyclic tetramers, transmission electron microscopy (TEM) and dynamic light scattering (DLS) studies revealed the presence of rod-like structures arising from *cis*-**2** solutions in 1,2-dichloroethane, consistent with a second level of self-organisation from the *cis* isomer. In the absence of X-ray single crystal evidence, theoretical investigations of the packing abilities of *cis*-**2** macrocylic tetramers are essential to elucidate the emergence of such higher-order of self-assembly.

Predicting the three-dimensional arrangement of molecular systems requires a full understanding of their behaviour along the potential energy surface. At the molecular level, such tasks require a conformational analysis of the geometry with respect to the

degrees of freedom for a given molecule to reach the global minimum. At the supramolecular level, the determination of all the degrees of freedom will quickly become cumbersome and time-consuming when following classical geometry optimisation procedures. As a result, a new strategy which relies on experimental knowledge about these cyclic tetramers and on simple single point calculations is developed to predict close-packing in these structures.

In this Chapter, empirical force field energy scans are initially performed to evaluate the preferred packing of the tetrameric macrocycles along the z-axis, defined by the normal to the macrocycle plane. Although empirical force fields usually provide accurate geometries, the electronic properties of the resulting close-packed arrangement can only be computed through quantum mechanical calculations. The preliminary structure estimated from the molecular mechanics energy scans is further optimised using the semi-empirical PM3 method, to generate interaction energies and molecular orbitals for the close-packed macrocycles.

π-π Intermolecular interactions have been shown to efficiently control DNA-duplex formation[2] and DNA-drug intercalation in biological systems,[3] and to ensure selective binding in polyaromatic supramolecular systems and supramolecular host-guest systems.[4,5] This Chapter will demonstrate that molecular and quantum mechanical methods can be efficiently combined to predict and characterise the π-π interactions and electronic properties of the three-dimensional nanostructure resulting from the macrocyclic tetramers. The computationally expensive quantum mechanical calculations of decyloxy-disubstituted *cis*-azodibenzoic acid **2** can be considerably reduced by the use of unsubstituted and methoxy-disubstituted *cis*-azodibenzoic acid as model monomers

without any loss of geometric and electronic information. The strategy developed to determine the optimal close-packing arrangement of the hydrogen-bonded azobenzene derivatives makes use of a very simple model in which three to five tetrameric macrocycles are stacked in either a face-to-face or a herringbone configuration along the z-axis.[6] In these macrocylic structures, the orientation of the aromatic rings relative to the z-axis can be fixed at an angle α. As shown in Figure 5. 1, the total energy E_{total} of each close-packed structure can be calculated as a function of (1) the orientation of the aromatic rings relative to the z-axis, α, (2) the interplanar distances along the z-axis, $d_{\pi\text{-}\pi}$, (3) the inter-macrocycle offset, $o_{\pi\text{-}\pi}$, and (4) the relative twist β between stacked tetrameric macrocycles. After mapping the potential energy of packing for the macrocycles through empirical methods, the geometries are optimised using quantum mechanics. To model infinite rod-like nanostructures, the size of the stacked macrocycles is extended from three to five components, allowing for the energy minimisation of the three central macrocycles while both end-macrocycles can serve as periodic boundaries. These semi-empirical calculations are used to confirm the preliminary molecular mechanics geometries and provide information on the electronic properties of the π-stacked azobenzene macrocycles.

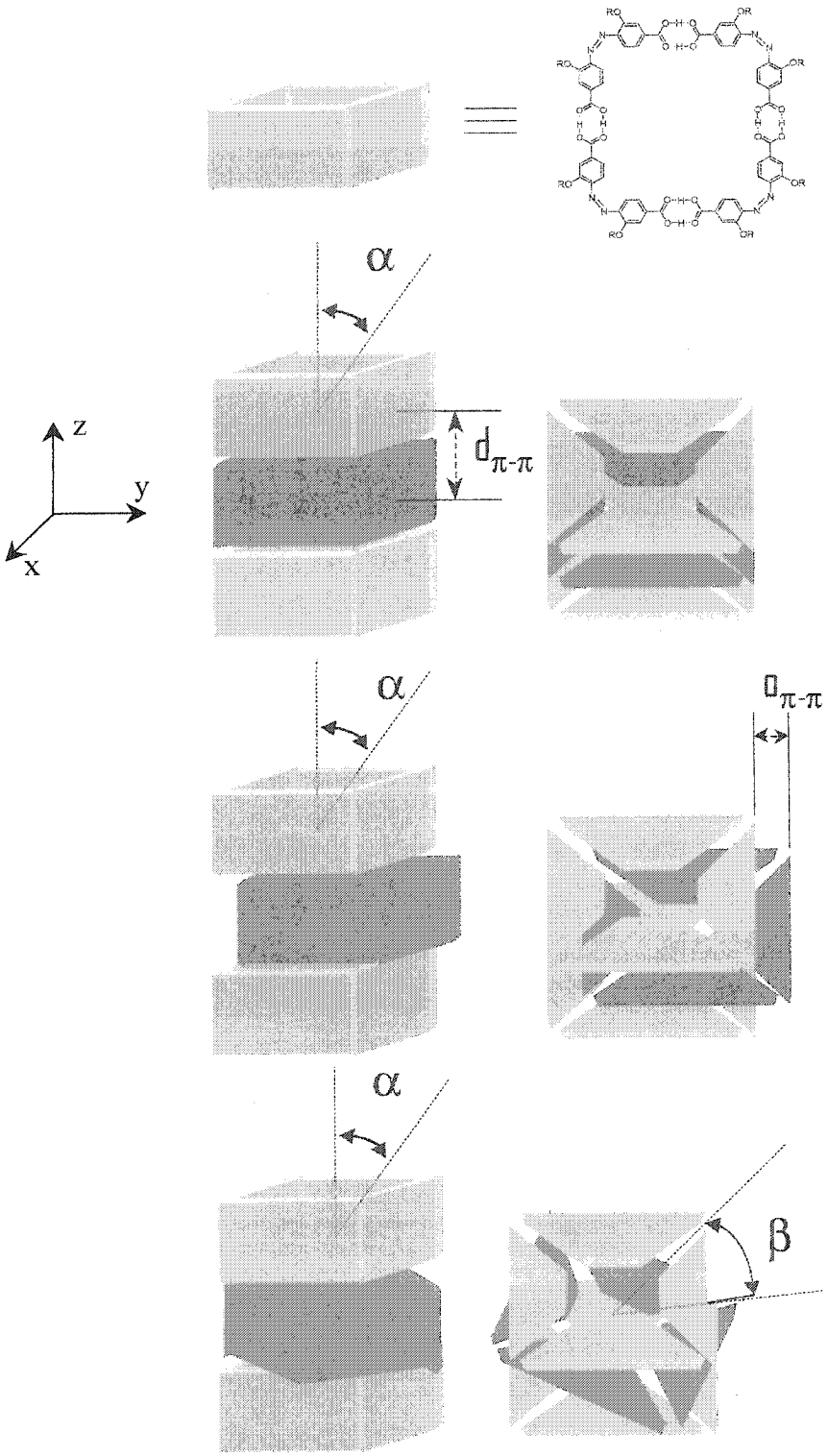


Figure 5. 1. Representation of α, the orientation of the aromatic rings relative to the z-axis, $d_{\pi-\pi}$, the interplanar distance along the z-axis, $o_{\pi-\pi}$, the horizontal offset, and β, the relative twist, between stacked tetrameric macrocycles.

5.2. Theoretical Methods

5.2.1. Initial Geometry of Monomers and Tetramers Through Quantum Mechanical Calculations

Quantum mechanical calculations were performed on the unsubstituted, methoxy-, ethoxy-, propyloxy-, and decyloxy-disubstituted *cis-p*-azodibenzoic acid monomers. Ethoxy- and decyloxy-disubstituted *cis-p*-azodibenzoic acid monomer geometries were obtained from progressive addition of methylene groups to *o*-bismethoxy-*cis-p*-azodibenzoic acid followed by energy minimisation. Quantum mechanical calculations were also carried out on the unsubstituted, methoxy-, ethoxy-, and propyloxy-disubstituted *cis-p*-azodibenzoic acid cyclic tetramers. Initial cyclic tetramer geometries containing methoxy-, ethoxy-, and propyloxy-disubstituted monomers were built from the PM3 optimised *p*-azodibenzoic acid macrocycle. A stepwise addition of methoxy and methylene groups to the energy minimised macrocycle was used to generate the input structures. Each addition was followed by energy minimisation of the disubstituted azodibenzoic acid. Quantum mechanics calculations were carried out using the semi-empirical PM3 method contained in the Gaussian98W[7] program package.

5.2.2. Scanning of Packing Structures Through Empirical Force Fields

One PM3 optimised cyclic tetramer was oriented so that the primary inertial axis of the hydrogen-bonded structure was aligned with the z-axis, the macrocycle plane was placed within the xy plane, and the macrocycle centre was at the origin. A one-dimensional array of identical macrocycle rings were then constructed along the z-axis with a starting intermolecular separation of 3.5 Å. The orientation of the aromatic rings

relative to the z-axis, α, was fixed at angles ranging between 0° and 90°. For each angle α, the total energy E_{tot} of the one-dimensional array was evaluated as a function of the interplanar distance $d_{\pi\text{-}\pi}$, the horizontal inter-ring offset $o_{\pi\text{-}\pi}$, and the rotational twist β to give low energy stacking configurations. The interplanar distance (3.5 Å < $d_{\pi\text{-}\pi}$ < 6.5 Å) was defined as the distance between each macrocycle with its direct neighbour along the z-axis; calculations were carried out at 0.1 Å increments. The horizontal offset (0 Å < $o_{\pi\text{-}\pi}$ < 2.0 Å) was the distance between the macrocylic tetramer centres relative to the z-axis; calculations were performed at 0.1 Å increments. The twist angle (0° < β < 45 °) arises from the relative rotation of the macrocyclic tetramers around the z-axis; calculations were carried out at 5° increments. Single point E_{tot} calculations were carried out using the empirical MM^+ force field contained in the HyperChem 5.1 program package.

5.2.3. Optimisation of Stacked Tetramers Through Quantum Mechanical Calculations

The spatial arrangement of these macrocycles established through empirical methods was further refined using quantum mechanics. To simulate long, infinite rod-like nanostructures, the size of the stacked macrocycles is extended from three to five components. The two end-macrocycles can serve as periodic boundaries for the infinite one-dimensional nanostructures, thus allowing for energy minimisation of the three central macrocycles. These quantum mechanical optimisations are used to confirm the preliminary molecular mechanics geometries, extract the π- interaction energies of the macrocycles and provide information on the molecular orbitals properties of the π-

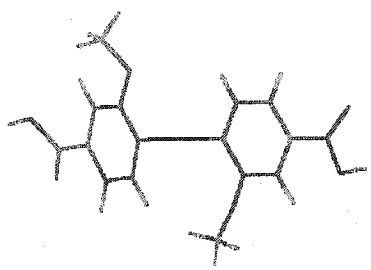
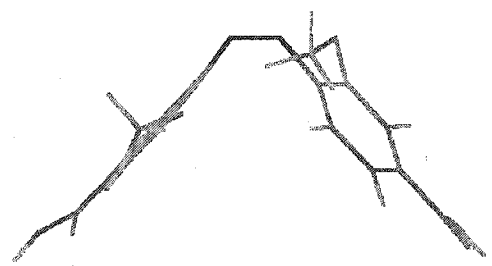
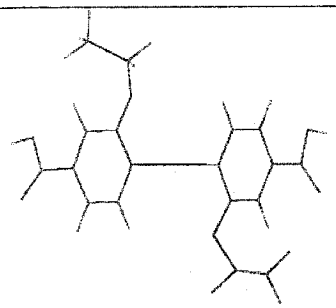
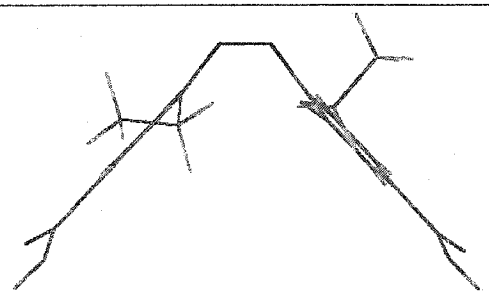
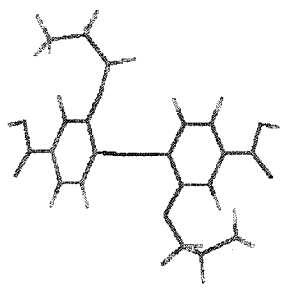
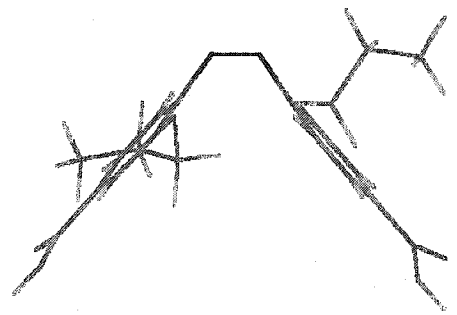
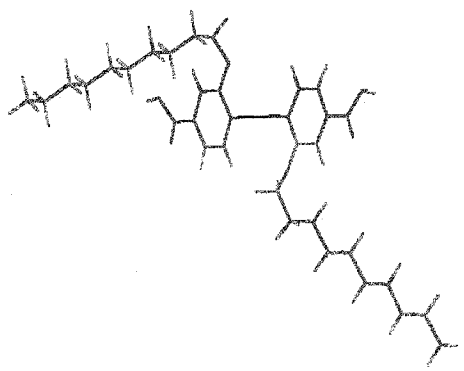
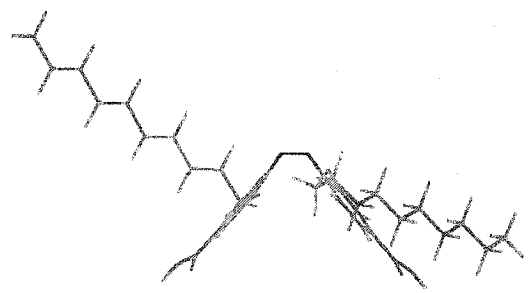
macrocycles and provide information on the molecular orbitals properties of the π-stacked azobenzene macrocycles. As for the monomers and tetramers, quantum mechanical calculations were carried out using the semi-empirical PM3 method contained in the Gaussian98W program package.

5.3. Results and Discussion

5.3.1. Quantum Mechanics Calculations of *cis*-Azodibenzoic Acid Cyclic Tetramers

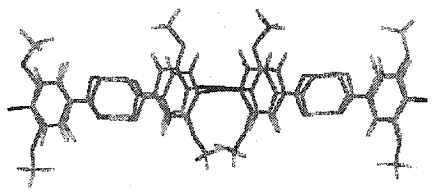
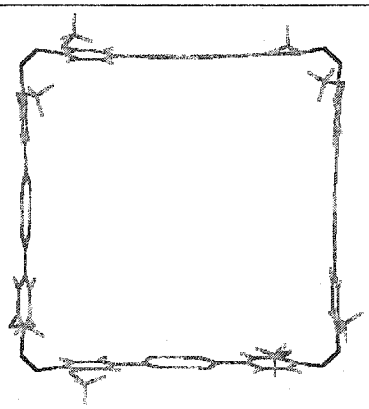
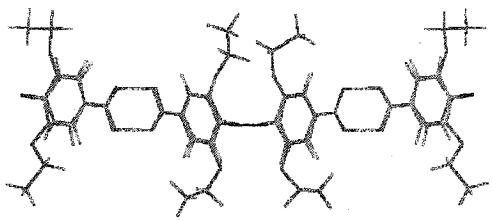
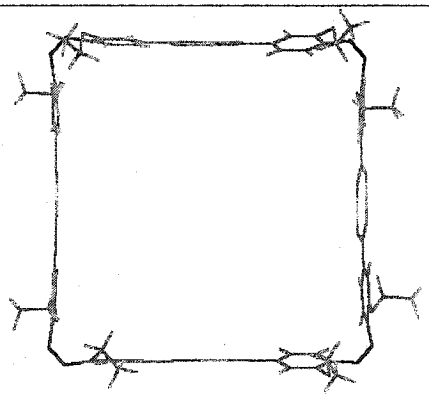
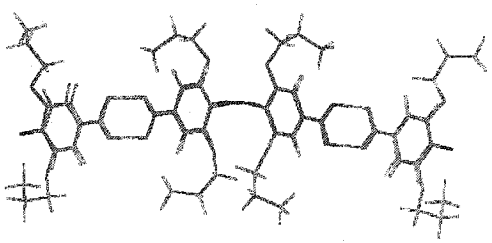
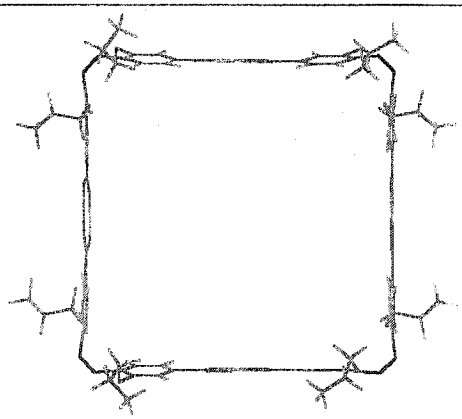
Alkoxy-disubstituted azobenzene monomers are optimised to generate good model geometries for the experimentally studied bisdecyloxy-*cis*-*p*-azodibenzoic acid system using the semi-empirical PM3. The unsubstituted *cis*-*p*-azodibenzoic acid model monomer adopts a geometry in which the carboxylic acid groups are oriented at a quasi-perpendicular, 82°-angle which results in tetramer cyclisation through hydrogen-bonding, as shown in Chapters 3 and 4.[8] Methoxy- (C_1), ethoxy- (C_2), propyloxy- (C_3), and decyloxy- (C_{10}) disubstituted monomer structures calculated with PM3 displayed similar geometries (Table 5. 1). In particular, the PM3 N=N-C bond angle was calculated to be 127.8°, giving a similar orientation as in the unsubstituted *cis*-azobenzene derivatives. Identical geometries were observed for the alkoxy disubstituted *cis*-*p*-azodibenzoic acids, in which the methoxy, ethoxy, propyloxy and decyloxy chains were lying in planes parallel to the C-N-C plane instead of pointing outwards, perpendicularly to the C-N-C plane.

Table 5. 1 . PM3 optimised alkoxy-substituted *cis-p*-azodibenzoic acid monomer geometries

	Side view	Top view
C_1		
C_2		
C_3		
C_{10}		

As shown in Table 5. 2, incorporation of methoxy-, ethoxy-, and propyloxy-azodibenzoic acid monomers into cyclic tetramers produced the same macrocycle geometries as for the unsubstituted *cis-p*-azodibenzoic acid model compound, as expected from the monomer geometries. The PM3 calculated hydrogen-bond parameters for the methoxy- and ethoxy- macrocycles were also identical to the unsubstituted supramolecular structure. Upon hydrogen-bond formation, the C=O bond lengthened slightly from 1.22 Å to 1.23 Å, the O–H bond from 0.95 Å to 0.96 Å. The C–O bond shortened from 1.35 Å to 1.34 Å, while the C–O–H angle opened from 109° to 112°, leading to hydrogen-bond formation (O···H = 1.77 Å), in agreement with X-ray data for carboxylic acid dimers.

Table 5. 2. PM3 optimised alkoxy-substituted *cis-p*-azodibenzoic acid macrocycle geometries

	Side view	Top view
C_1		
C_2		
C_3		

For each PM3 optimized structure, the enthalpy of formation at 0 K for two hydrogen-bonds $\Delta H_{f\,2HB}(T)$ is calculated by:

$$\Delta H_{f\,2HB}(T) = \frac{H_f(M_n^m) - n \times H_f(M)}{n_{2HB}} \qquad \textbf{(Eq. 5. 1)}$$

where T is the temperature (T = 0 K), $H_f(M)$ is the enthalpy of the monomer M, n_{2HB} the number of hydrogen-bond pairs, n the number of monomers involved, and $H_f(M_n)$ the enthalpy of the aggregates. Table 5. 3 lists the calculated macrocycle enthalpies. The hydrogen-bond enthalpies were not significantly affected by the successive addition of methylene groups to the alkoxy chain, and with values between –8.1 and –8.9 kcal/mol were consistent with the formation of strong hydrogen-bonds.

Table 5. 3. Macrocycle PM3 total enthalpies and hydrogen-bond enthalpies

	Total enthalpy (kcal/mol)	Hydrogen-bond enthalpy (kcal/mol)
C_1	- 158.5	- 8.88
C_2	- 170.6	- 8.13
C_3	- 179.1	- 8.69

5.3.2. Evaluation of Packing in *cis*-Azodibenzoic Acid Cyclic Tetramers

Theoretical calculations based on the empirical MM^+ force field were carried out to evaluate the spatial arrangement of *cis*-azodibenzoic acid cyclic tetramers. The

macrocycles containing unsubstituted and methoxy-substituted were chosen as model macrocycles because of their identical energetic and geometrical properties relative to macrocycles containing longer alkoxy chains. The methoxy-substituted monomers were specifically chosen to account for steric effects. Empirical MM^{+} force field calculations were used to determine the preliminary close-packed arrangement because the predicted MM geometries can provide an accurate theoretical visualisation of molecular materials.[9]

Experimental characterisation techniques of *cis*-azobenzene derivatives in Chapter 3 revealed the emergence of rod-like nanostructures, suggesting the presence of favourable alkyl-alkyl and π-stacking interactions between these azodibenzoic acid derivatives. Two packing modes could be envisaged for the spatial arrangement of the hydrogen-bonded cyclic tetramers (Figure 5. 2). The first proposed model shows the macrocycles positioned side by side, along the x-axis (Figure 5. 2a). In this first model, close-packed π-π interactions can occur only if the alkoxy chains are parallel to the z-axis and perpendicular to the macrocycles. However, the resulting nanostructures should have diameters approximately corresponding to one aromatic ring because of alkoxy chain interdigitation, and, therefore, should exhibit smaller diameters on surfaces than the ones measured by TEM (*ca.* 0.5 nm vs 3.9 nm).

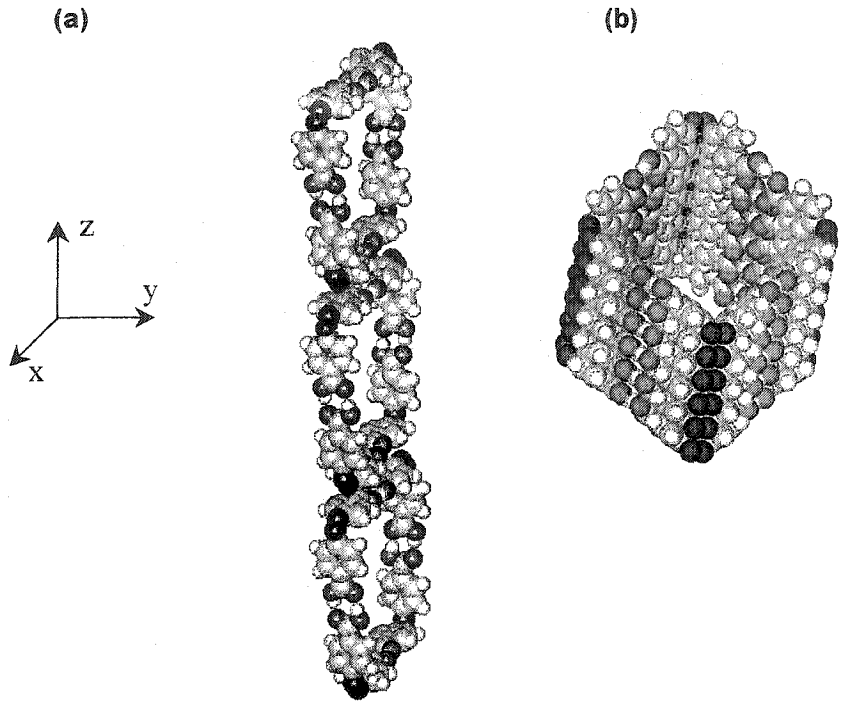


Figure 5. 2. (a) Representations of the possible packing mode between stacked tetrameric macrocycles according to the first model. (b) Representations of possible packing mode between stacked tetrameric macrocycles according to the second model.

In the second model, the cyclic azodibenzoic acid tetramers are stacked along the normal axis of the macrocycle (Figure 5. 2b). As a result, the diameter of the rod-like aggregates should correspond to the diameter of individual tetramers (4.2 nm), in agreement with direct TEM visualisation which gave *ca.* 3.9 nm diameters for the rod-like aggregates. However, the PM3 geometry optimisation of the cyclic tetramers leads to a perpendicular configuration of the aromatic rings relative to the normal of the macrocycle (Table 5. 1), which is unfavourable to direct π-stacking interactions in this first model. Theoretically calculated thermodynamic and vibrational properties of *cis*-

azodibenzoic acid tetramers, in Chapter 4, demonstrated the flexibility of the monomers, which should allow the aromatic rings to rotate about the N-C internal axis without affecting the supramolecular macrocyclic structure. As a result, a tilt of the aromatic rings with respect to the z-axis should be able to induce favourable π-π interactions between the macrocycles in the first model. Consequently, the first model should be the preferred mode of self-organisation of the *cis*-azodibenzoic acid macrocycles. A systematic sampling of the potential energy surface in terms of total energy E_{tot} is therefore essential for determining the close-packed face-to-face or herringbone arrangement of *cis*-azodibenzoic acid cyclic tetramers.

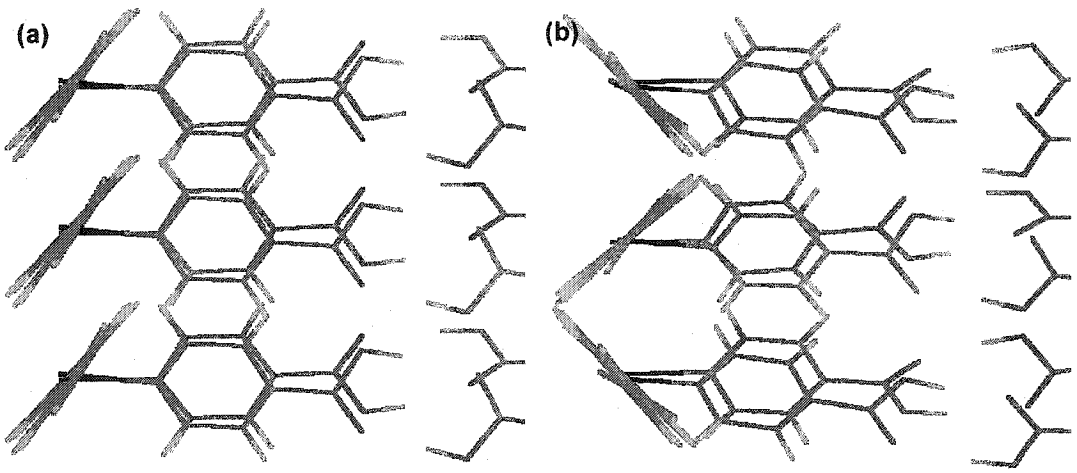


Figure 5. 3. (a) Representation of face-packed cyclic tetramers. (b) Representation of herringbone-packed cyclic tetramers.

5.3.2.1. Face-to-Face Packing Arrangement of Hydrogen-Bonded Cyclic Tetramers

Face-to-face arrangements which involve maximum overlap between the aromatic rings were first investigated to elucidate the packing of the *cis*-azodibenzoic acid cyclic

tetramers. To achieve this face-to-face configuration, the aromatic rings in all three stacked cyclic tetramers were simultaneously rotated by an angle α, defined as the aromatic tilt with respect to the z-axis (Figure 5. 1). The total energy E_{tot} of the stacked macrocyclic structures was calculated independently for the interplanar distance $d_{\pi\text{-}\pi}$, the aromatic ring rotation α, the inter-macrocycle offset $o_{\pi\text{-}\pi}$, and the relative twist around the z-axis β to determine the contribution of each geometrical parameter to face-to-face close-packing.

The influence of interplanar distance, $d_{\pi\text{-}\pi}$, was analysed between 3.5 Å and 6.5 Å for three cyclic tetramers stacked in a vertical configuration ($o_{\pi\text{-}\pi}$ = 0.0 Å, β = 0.0°) for different angles α (0° < α < 90°, Figures 5. 4 and 5. 5). The calculated energy plots for the macrocycle containing unsubstituted *cis*-azobenzene monomers, in Figures 5. 4a and 5. 4b, showed an overall energy decrease with increasing interplanar distances for all the aromatic ring conformations, which leveled off to a minimum beyond 4.5 – 5.0 Å, consistent with the presence of strong repulsive forces at short distances between the tetrameric macrocycles.

A decrease in energy with increasing interplanar distances was observed for the stacking of methoxy-disubstituted azobenzene macrocycles as for the unsubstituted *cis*-azobenzene macrocycles, (Figures 5. 5a and 5. 5b). This energy decrease led to a minimum around 5.0 Å and 6.0 Å in these disubstituted azobenzene tetramers (vs 4.5-5.0 Å in the unsubstituted azobenzene tetramers), indicating that the methoxy-substituent sterically hinders stacking between the macrocycles at small interplanar distances. As a result of these steric effects, a shift of the energy plots towards greater values was observed for the methoxy-disubstituted cis-azobenzene tetramers than for the

unsubstituted *cis*-azobenzene tetramers. The packing of both unsubstituted and disubtituted azobenzene macrocycles is therefore strongly dependent on distance, consistent with electrostatic interactions occurring between the negatively charged π-electron-clouds of the azobenzene chromophores.

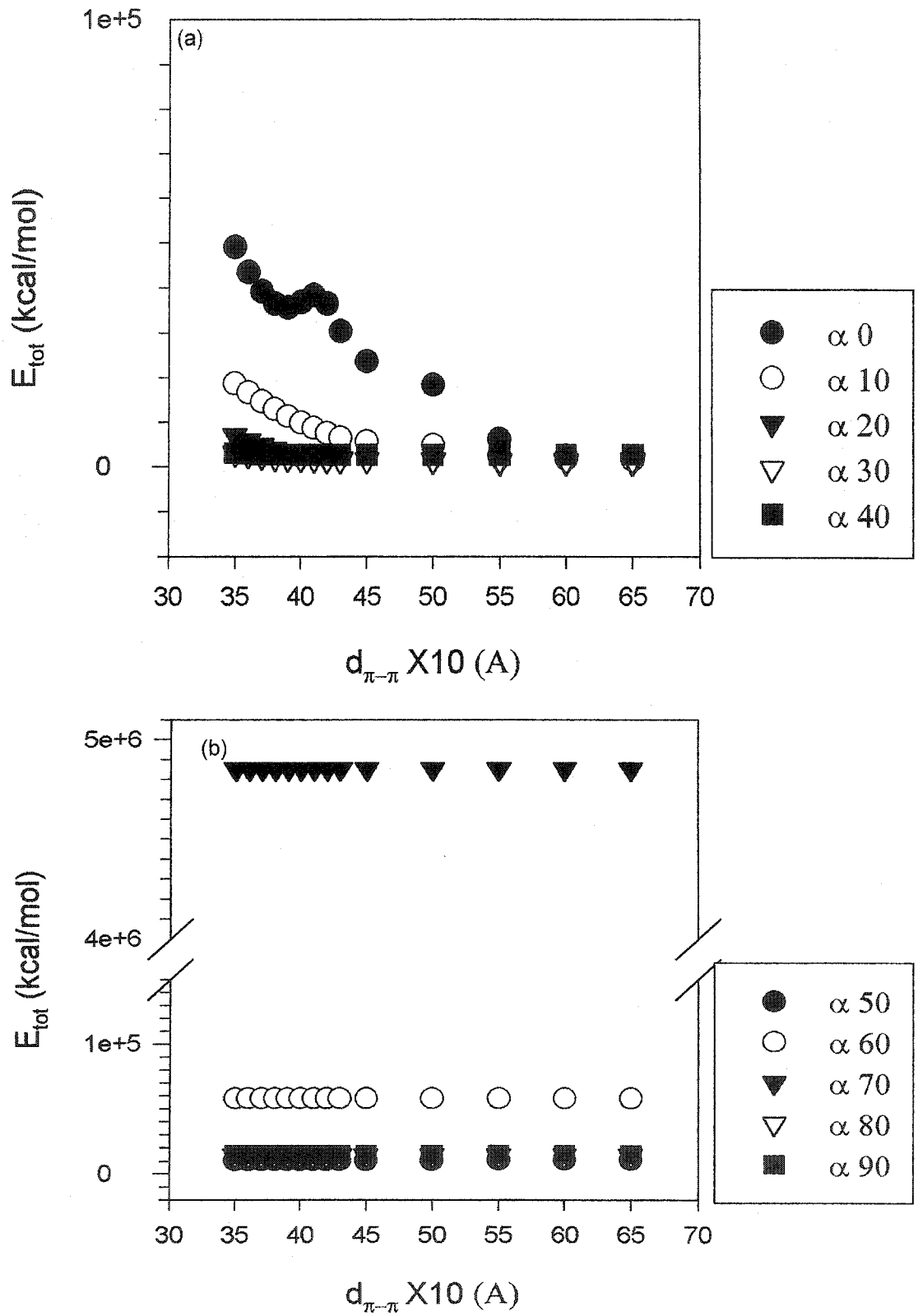


Figure 5. 4. Total energy plots as a function of interplanar distance $d_{\pi-\pi}$ for the unsubstituted *cis*-azobenzene derivatives. (a) For $0° < \alpha < 40°$ (b) $40° < \alpha < 90°$.

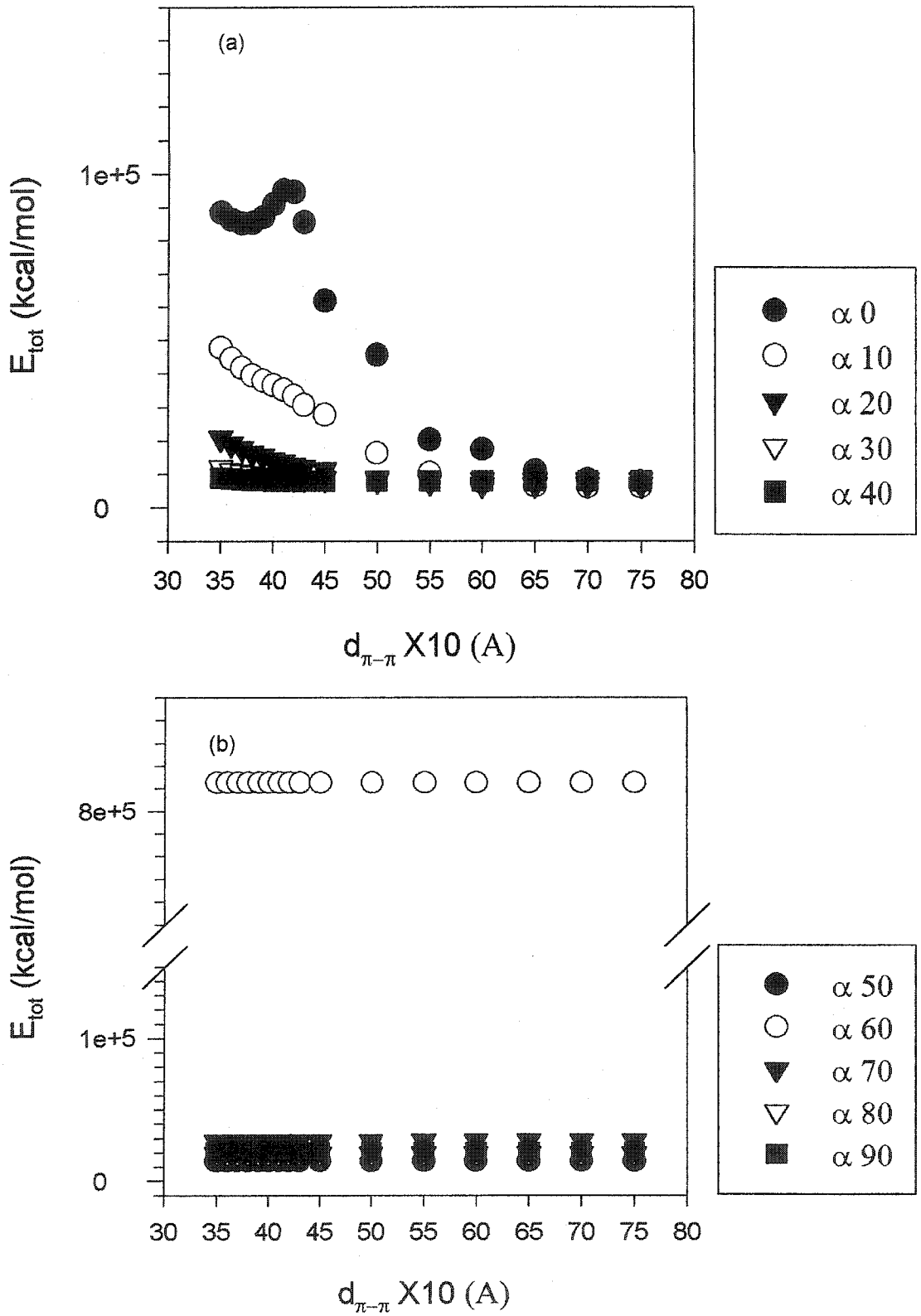


Figure 5. 5. Total energy plots as a function of interplanar distance $d_{\pi-\pi}$ for the methoxy-disubstituted *cis*-azobenzene derivatives. (a) For $0° < \alpha < 40°$ (b) $40° < \alpha < 90°$.

Energy plots shown in Figures 5. 4 and 5. 5 exhibited a strong angular dependence, which required further investigation. A noticeable decrease in energy lead to global minima at approximately 30° for close-packing distances lying between 3.5 Å and 5.0 Å in the unsubstituted azobenzene macrocycles. This total energy decrease, which occurs as the azobenzene aromatic rings tilt away from their perpendicular, equilibrium orientation, suggests a diminution of the repulsive, electrostatic interactions created by the negatively charged azobenzene π-electrons. Figure 5. 6 shows the spatial conformation of the three PM3 optimised cyclic tetramers ($\alpha = 0°$) stacked at an interplanar distance $d_{\pi\text{-}\pi}$, of 3.5 Å, without any horizontal offset ($o_{\pi\text{-}\pi} = 0.0$ Å). In this structure, the aromatic van der Waals radii of the hydrogen-bonded macrocycles are in close-contact, giving rise to repulsive forces between the stacked cyclic tetramers.

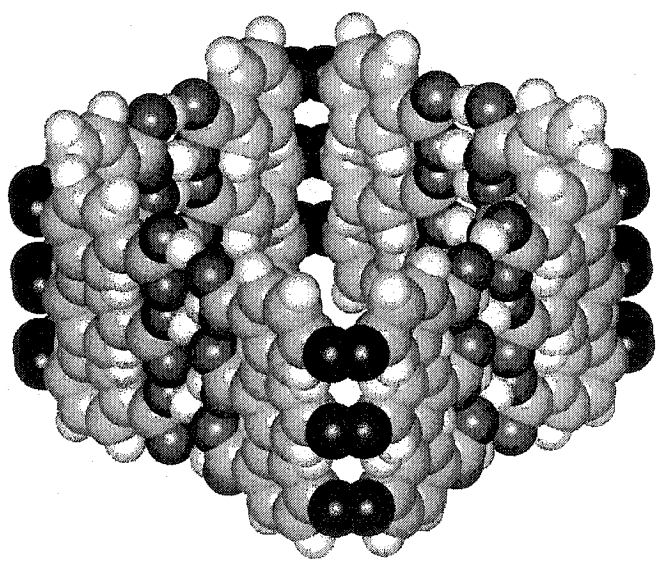


Figure 5. 6. PM3 optimised cyclic tetramers stacked at $d_{\pi\text{-}\pi} = 3.5$ Å, $\alpha = 0°$, $o_{\pi\text{-}\pi} = 0.0$ Å, $\beta = 0°$.

Similar to the total energy plot as function of interplanar distance, the plot of the total energy against the rotational angle α produced greater energy values in the methoxy-substituted than in the unsubstituted *cis*-azodibenzoic acid tetramers, consistent with the presence of steric hindrance between the close-packed macrocycles. A decrease in energy is also observed for the methoxy-subtituted macrocycle, leading to global minima at approximately 40° for close-packing distances lying between 3.5 Å and 5.0 Å. This total energy decrease suggests that the the repulsive, electrostatic interactions created by the negatively charged azobenzene π-electrons decrease as the aromatic rings tilt in the methoxy-substituted macrocycle. A shift of the energy minimum towards a larger α-angle of 40° was observed for the methoxy-substituted azobenzene derivative in comparison with the unsubstituted azobenzene macrocycle, suggesting increased electrostatic repulsive forces between the substituted structures because of steric effects. These repulsions between the cyclic tetramers may be caused by the electron-donating properties of methoxy groups, which increase the electron density in the azobenzene units.

The small angular tilt of the aromatic rings induced an energetic stabilisation of the cyclic tetramers stacked in a three-dimensional arrangement, in agreement with the second *cis*-azobenzene macrocycle packing model (Figure 5. 2b). Greater conformational changes towards planar *cis*-azodibenzoic acid monomer geometries resulted in dramatic energy increase, giving rise to a total energy maximum at $\alpha = 70°$-angle. Examination of the macrocycle geometry at $\alpha = 70°$ (Figure 5. 7) indicated that the aromatic hydrogen atoms were in direct contact in this quasi-planar ring

conformation. The contact observed between these hydrogens resulted in strong repulsive forces within the cyclic tetramers, leading to an energy maximum at $\alpha = 70°$.

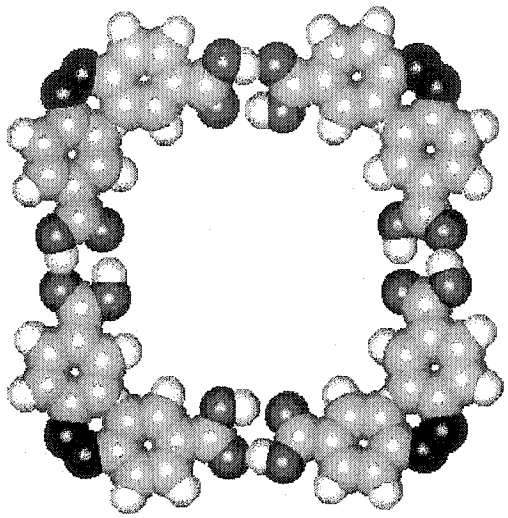


Figure 5. 7. Cyclic tetramers stacked at $d_{\pi\text{-}\pi} = 3.5$ Å, $\alpha = 70°$, $o_{\pi\text{-}\pi} = 0.0$ Å, $\beta = 0°$.

To further minimise the repulsive electrostatic intermolecular forces experienced by the stacked tetramers, the translation within the xy- plane $o_{\pi\text{-}\pi}$ was plotted against the total energy of three hydrogen-bonded macrocycles, placed at $d_{\pi\text{-}\pi} = 3.5$ Å and $\beta = 0°$ for different aromatic ring rotations α over a small distance interval.[10] (Figure 5. 8) The total energy plots against the horizontal translation $o_{\pi\text{-}\pi}$ displayed a decrease followed by a slight increase with increasing distances, yielding a wide energy well from 0.4 Å to 1.0 Å for both unsubstituted and methoxy-substituted azobenzene tetramers. However, small energy variations were observed for these energy plots, suggesting that only small translational motions in supramolecular stacks of *cis*-azodibenzoic acid macrocycles are required to compensate for electrostatic repulsion.

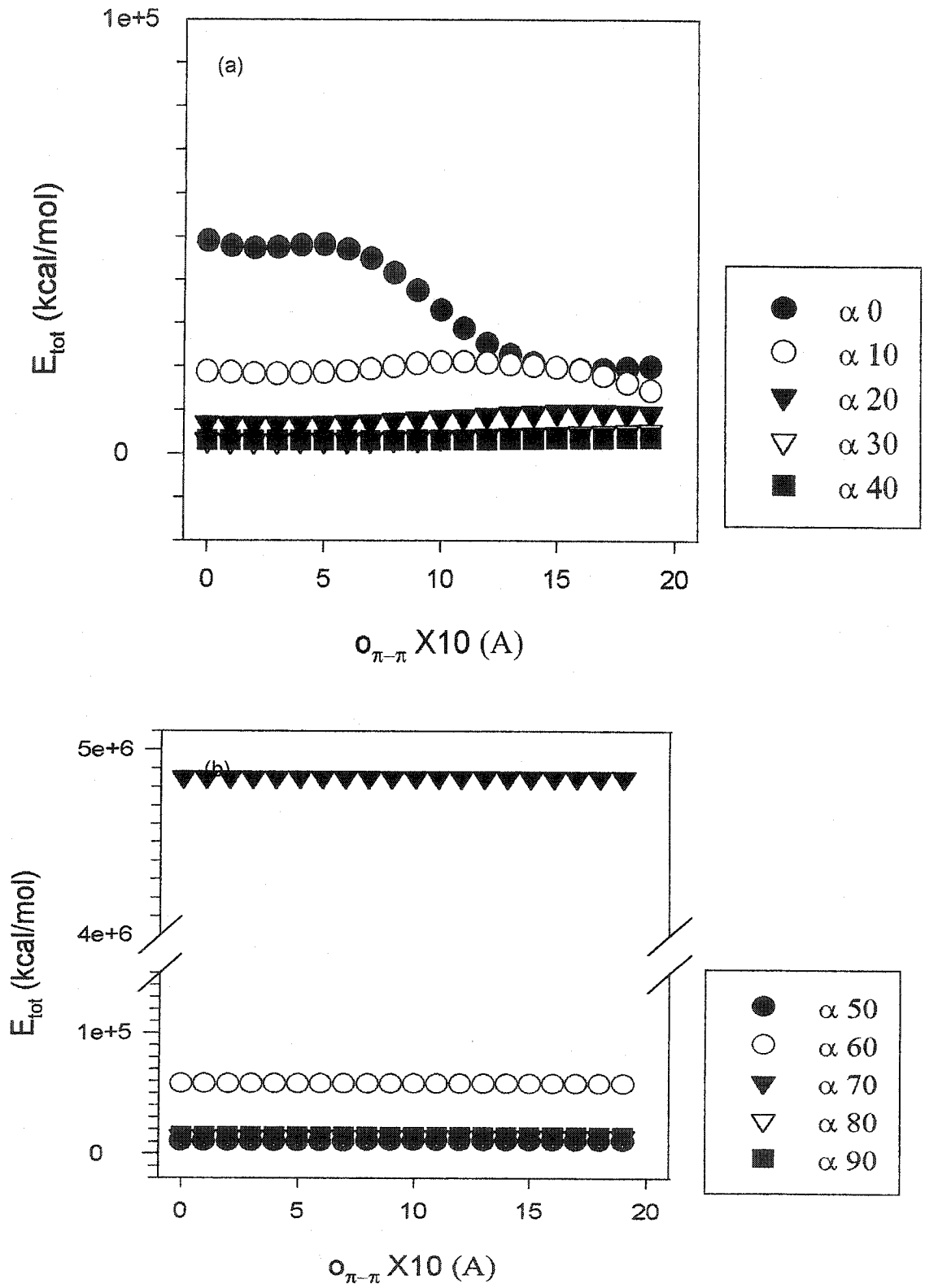


Figure 5. 8. Total energy plots as a function of horizontal offset $o_{\pi-\pi}$ for the unsubstituted *cis*-azobenzene derivatives. (a) For $0° < \alpha < 40°$. (b) $40° < \alpha < 90°$.

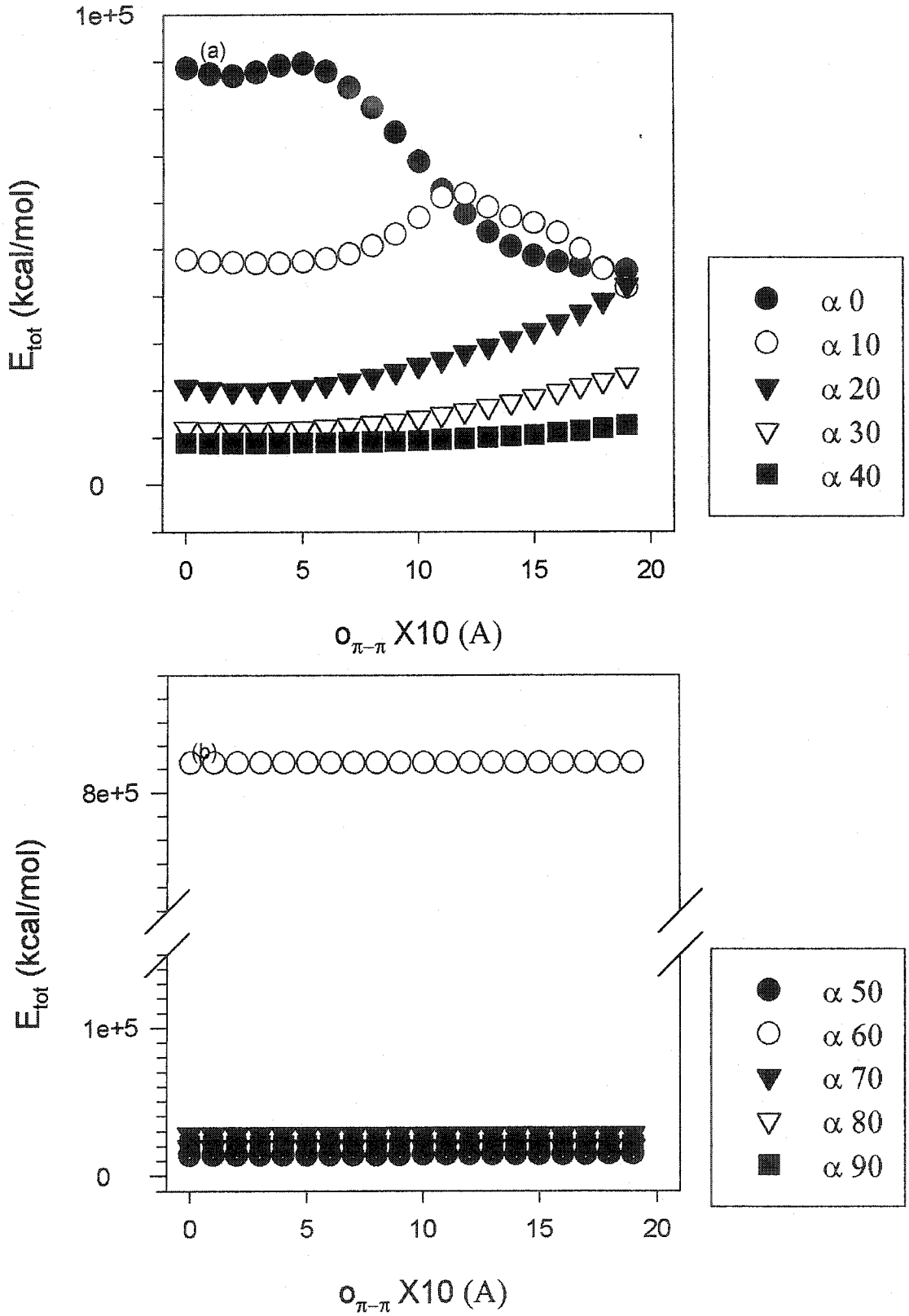


Figure 5. 9. Total energy plots as a function of horizontal offset $o_{\pi-\pi}$ for the methoxy-disubstituted *cis*-azobenzene derivatives. (a) For $0° < \alpha < 40°$. (b) $40° < \alpha < 90°$.

Rotational motions of the macrocyclic structures around the z-axis, β, were studied by sampling their effect of the total energies of cyclic tetramers vertically stacked along the z-axis ($o_{\pi\text{-}\pi} = 0.0$ Å, $\alpha = 0°$) at given interplanar distance $d_{\pi\text{-}\pi}$ (Figure 5. 10). The energy scan for angles β was performed by varying the position of the middle macrocycle between 0° and 45° while keeping the extreme macrocycles immobile, as a full 360°-rotation around the z-axis can produced through symmetry operations. The energy plots obtained from these rotational scans showed a sequence of local energy minima which were more pronounced in close-packed systems ($d_{\pi\text{-}\pi} = 3.5$ Å - 4.5 Å) than at greater interplanar distances. These local minima occur below 15° and above 25° which correspond to configurations in which the middle macrocycle N=N bonds are aligned with the N=N bonds of the neighbouring tetrameric macrocycles or the aromatic rings are in close proximity with the hydrogen-bonds.

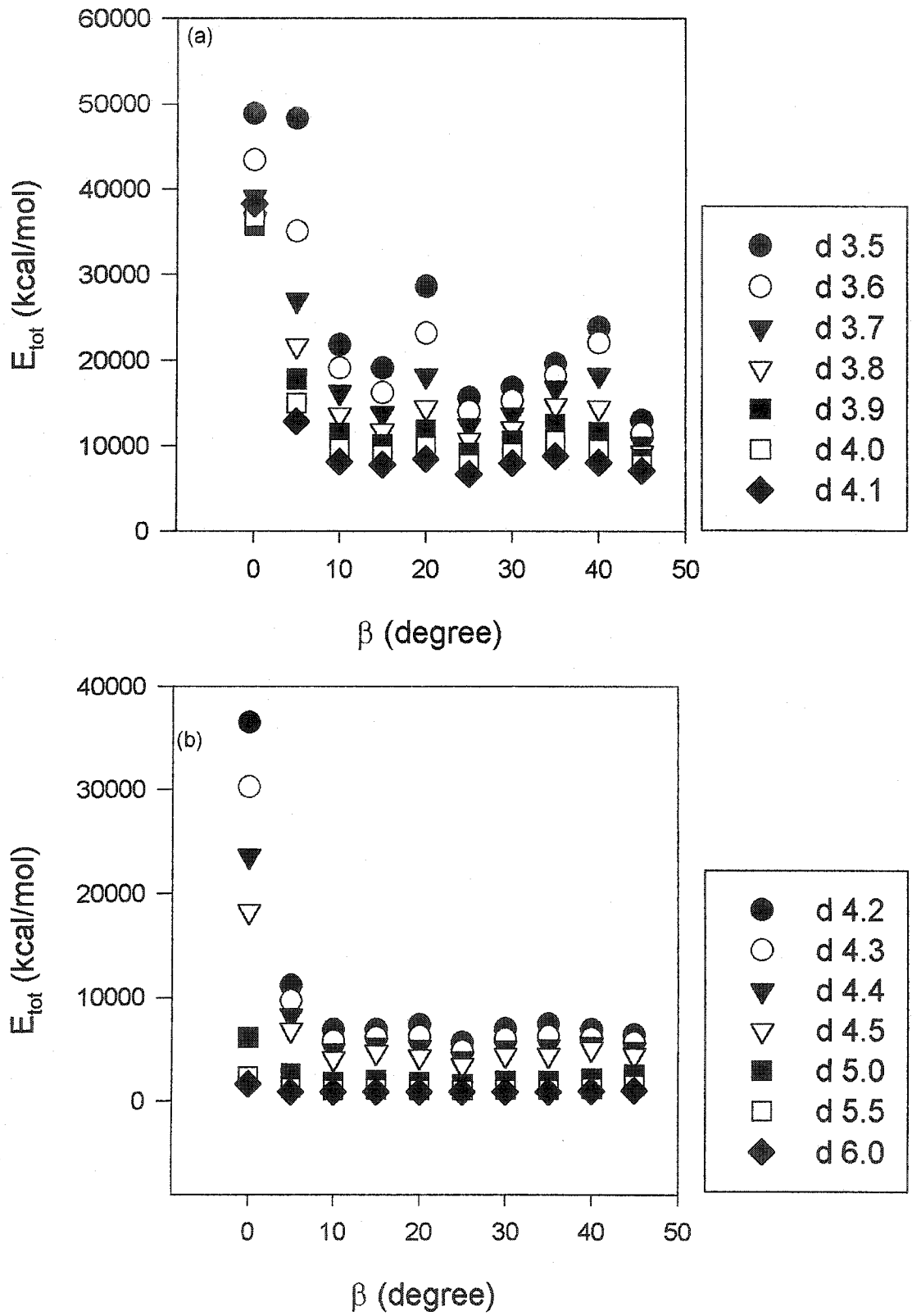


Figure 5. 10. Total energy plots as a function of macrocycle twist β for the unsubstituted *cis*-azobenzene derivatives. (a) For $0° < \alpha < 40°$. (b) $40° < \alpha < 90°$.

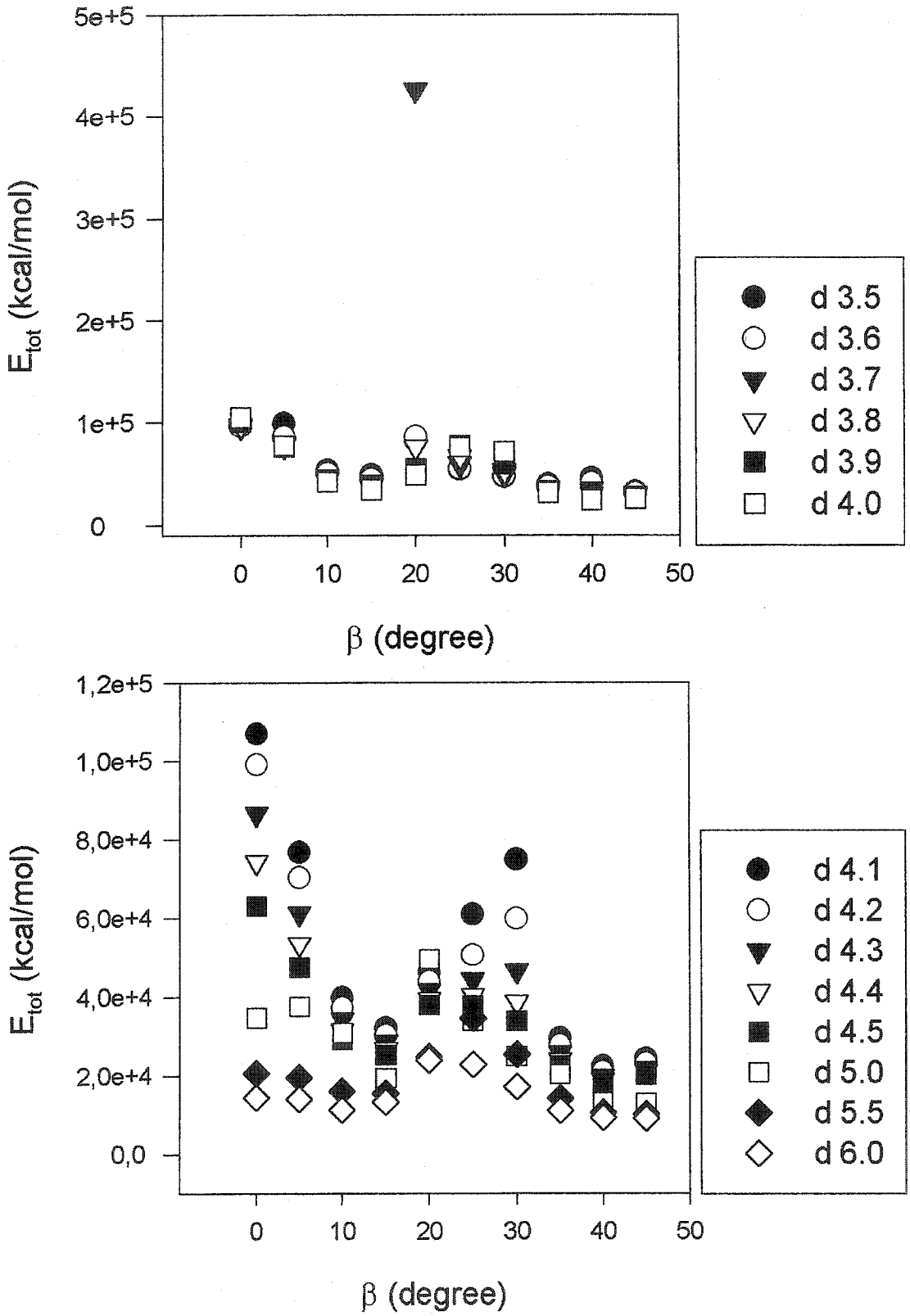


Figure 5. 11. Total energy plots as a function of macrocycle twist β for the methoxy-disubstituted *cis*-azobenzene derivatives. (a) For $0° < \alpha < 40°$. (b) $40° < \alpha < 90°$.

The resulting energy maxima at 20° correspond to structures in which the hydrogen-bonds point towards the carboxylic acid groups of the neighbouring macrocycles (Figure 5. 12), which could compete with the established hydrogen-bonding pattern, and therefore disrupt the tetramer geometries. However, like for the horizontal translation $o_{\pi\text{-}\pi}$, relatively small energy changes resulted from these rotational energy scans, suggesting the existence of free rotation within the face-packed cyclic tetramers.

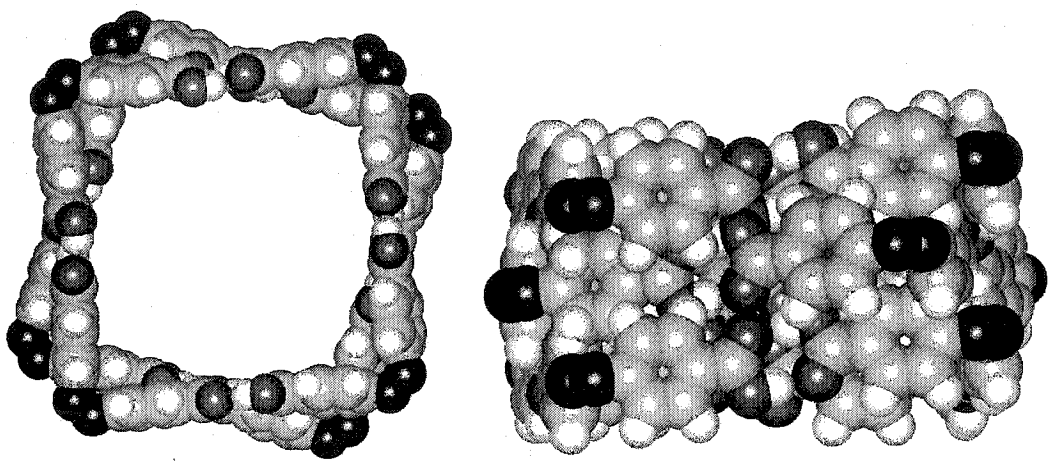


Figure 5. 12. PM3 optimised cyclic tetramers stacked at $d_{\pi\text{-}\pi}$= 3.5 Å, α = 0°, $o_{\pi\text{-}\pi}$= 0.0 Å, β = 20°. (a) Top view. (b) Side view.

As a result, empirical calculations of the total energy using the MM^+ force field show that the interplanar distance $d_{\pi\text{-}\pi}$ and the aromatic ring rotation α, contribute to the face-to-face packing of *cis*-azodibenzoic acid cyclic tetramers to a greater extent than the inter-macrocycle offset $o_{\pi\text{-}\pi}$ and the relative twist around the z-axis β. Close-packing should therefore be favourably achieved for interplanar distances greater than 4.0 - 4.5 Å and aromatic ring tilts ranging between 20° and 50° for face-packed unsubstituted *cis*-azodibenzoic acid cyclic tetramers. Optimal face-to-face arrangement should be

obtained for interplanar distances greater than 5.0 - 5.5 Å and aromatic ring tilts ranging between 20° and 50° in alkoxy- substituted macrocycles.

5.3.2.2. Herringbone Packing Arrangement of Hydrogen-Bonded Cyclic Tetramers

Close-packed herringbone-like structures in which aromatic tilt angles alternate from one macrocycle layer to the next were studied to further understand the three-dimensional arrangements of *cis*-azodibenzoic acid cyclic tetramers. Herringbone-type π-π interactions play an important stabilising role in crystals which involve alkynes, alkenes, and aromatic compounds.[11] Their stabilising effect is usually more pronounced in systems containing electron-rich donors, suggesting the presence of attractive electrostatic interactions between the hydrogen atom and the π-electron cloud in favour of hydrogen-bond formation in such systems.

Herringbone geometries of three stacked tetramers were generated from α-rotations of the outer macrocycle aromatic rings along with ($-\alpha$)-rotations of the middle macrocycle aromatic rings. Similar to face-packed *cis*-azodibenzoic acid tetramers, herringbone-packed geometries were investigated in terms of their total energy E_{total}, which could be determined independently for each geometrical parameter, $d_{\pi\text{-}\pi}$, α, and $o_{\pi\text{-}\pi}$. The relative positions of the three cyclic tetramers, $d_{\pi\text{-}\pi}$, was varied between 3.5 Å and 6.5 Å in a vertical configuration ($o_{\pi\text{-}\pi}$ = 0.0 Å, β = 0.0°) to give total energy plots for fixed angles α, within the [0° , 90°] interval, as shown in Figures 5. 13 and 5. 14. Higher energies were obtained from the herringbone (Figures 5. 13 and 5. 14), than from the face-packed macrocycle configurations (Figures 5. 4 and 5. 5), consistent with lower van

der Waals contributions in the herringbone arrangement than in the face-packed structures. These calculated energy plots displayed similar trends as the face-packed macrocycles, indicating an overall energy decrease with increasing interplanar distances for all the aromatic ring conformations. The minimum energy was reached at 4.5 – 5.0 Å interplanar distances in unsubstituted *cis*-azobenzene tetramers (Figure 5. 13), suggesting the presence of strong, repulsive electrostatic forces at short distances between the tetrameric macrocycles.

Smaller distance-dependent energy drops were observed in the herringbone than in the face-to-face structures, suggesting that the angled orientation of the aromatic rings in herringbone-stacked cyclic tetramers gives rise to weaker electrostatic repulsions than in the face-packing arrangements.

Steric repulsion between the alkoxy groups and the neighbouring rings of the methoxy-containing *cis*-azodibenzoic acid macrocycles resulted in a energy minimum at greater interplanar distances of 5.5 – 6.0 Å in methoxy-substituted structures (Figure 5. 14) compared to the energy minimum obtained for the unsubstituted structures. In addition, greater energy drops were obtained in the methoxy-substituted macrocycles compared to the unsubstituted structures.

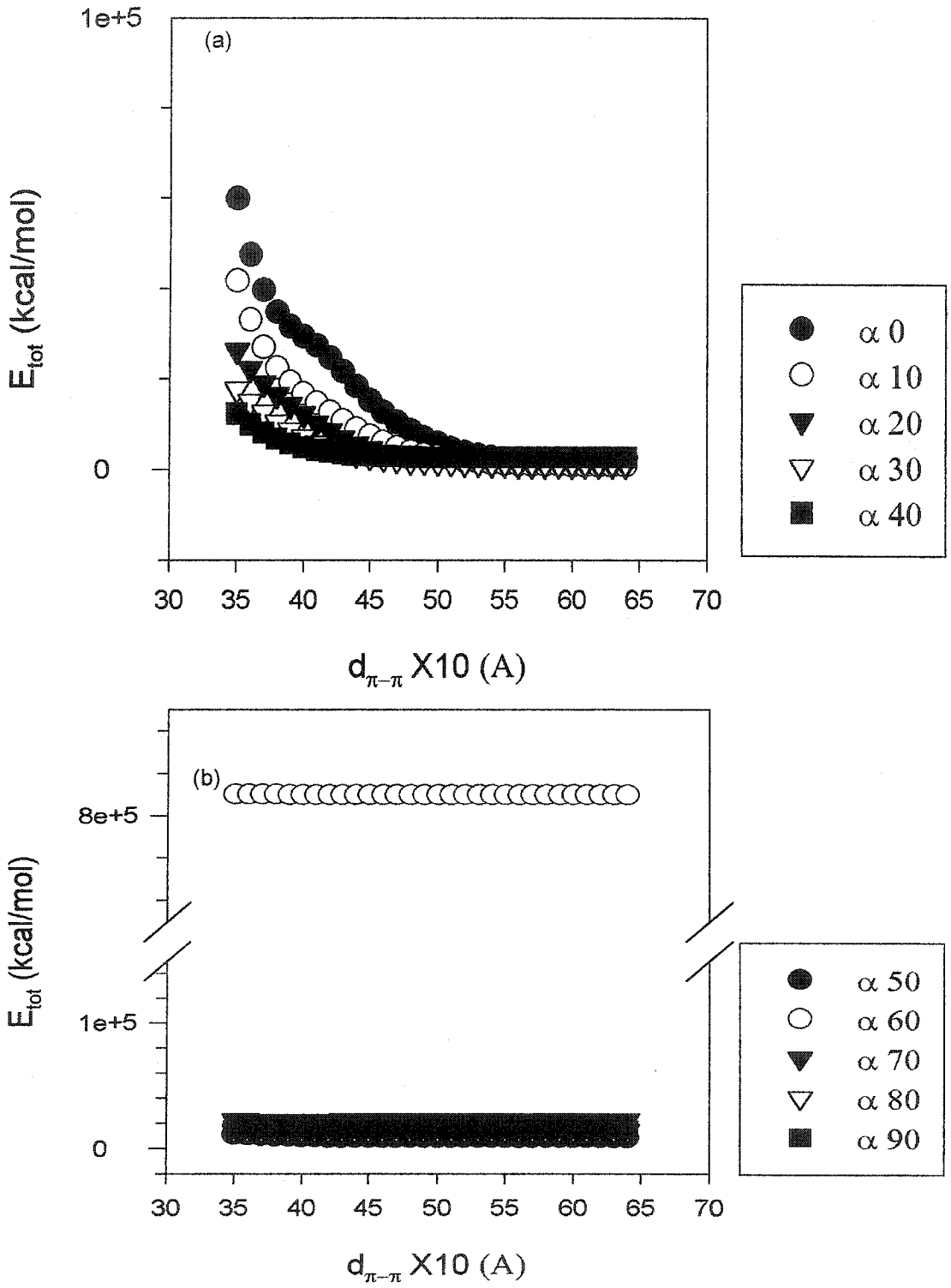


Figure 5. 13. Total energy plots as a function of interplanar distance $d_{\pi-\pi}$ for the unsubstituted *cis*-azobenzene derivatives.

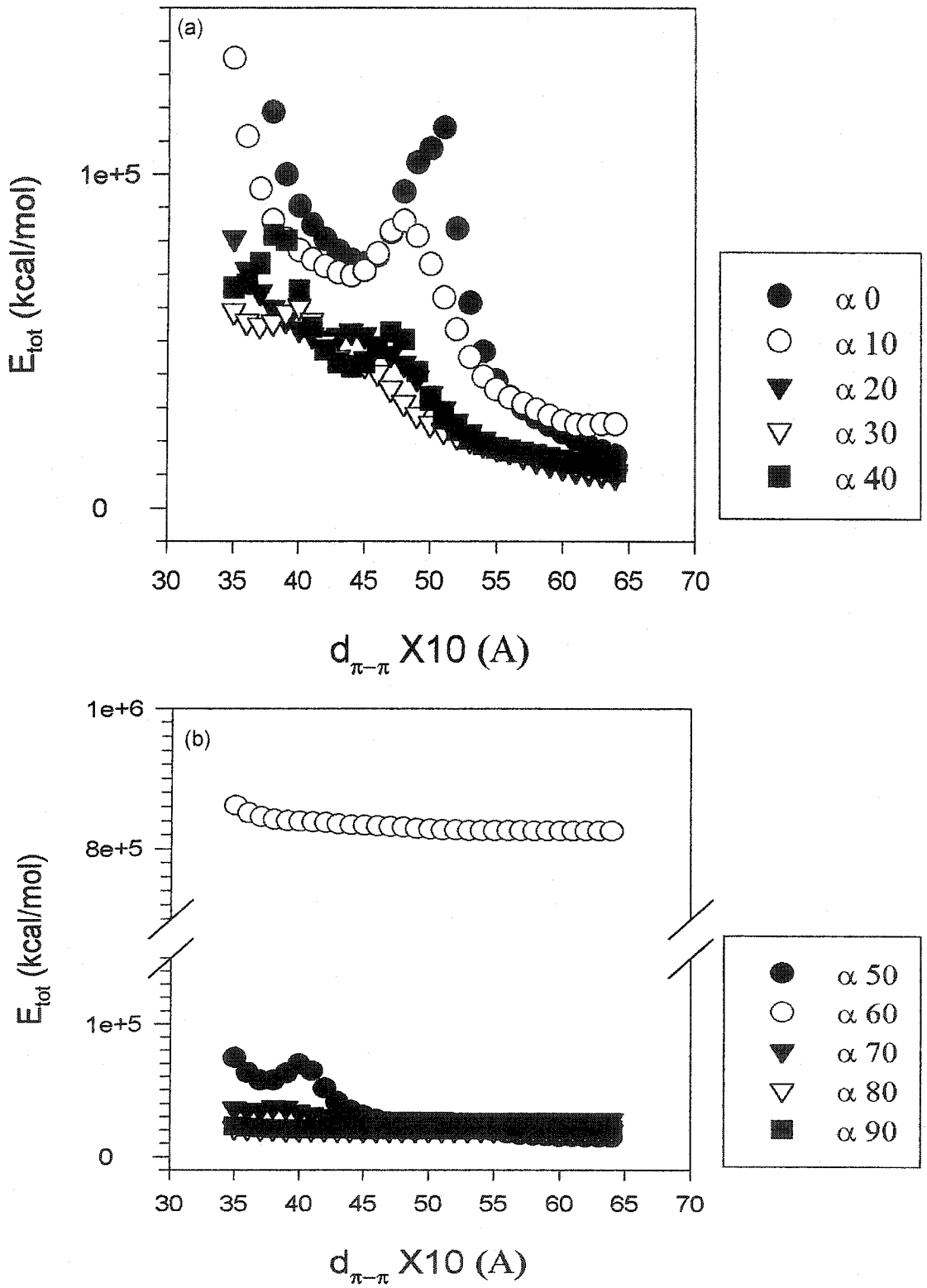


Figure 5. 14. Total energy plots as a function of interplanar distance $d_{\pi-\pi}$ for the methoxy-disubstituted *cis*-azobenzene derivatives. (a) For $0° < \alpha < 40°$. (b) $40° < \alpha < 90°$.

Figures 5. 13 and 5. 14 show the influence of conformational rotation on herringbone packing. The total energy plots of the herringbone stacked *cis*-azodibenzoic acid tetramers also showed a strong conformational dependence, as the total energy decreased to reach a global minima at approximately 45° for all interplanar distances. This result is consistent with the need of herringbone-packed structures to compensate for their weak van der Waals interactions by optimising attractive electrostatic interactions induced between the positively charged aromatic hydrogens and the negatively charged azobenzene π-electrons.[3] At 45°, the aromatic hydrogens of one macrocycle point towards the π-electron cloud of the neighbouring macrocycle to maximise electrostatic contact between the *cis*-azodibenzoic acid tetramers. As in the face-to-face packing, dramatic energy increase was observed in the herringbone structures because of unfavourable interactions between the aromatic rings of the quasi-planar tetramers. This increase in energy gave rise to a total energy maximum at $\alpha = 70°$-angle (Figures 5. 13b and 5. 14b).

As in the case of face-packed macrocycles, the total energy plots exhibited a significant steric sensitivity, which resulted in greater energies in the methoxy-substituted than in the unsubstituted *cis*-azodibenzoic acid tetramers (Figure 5. 14). However, in constrast with face-to-face packing, the methoxy group did not cause any energy minimum shift towards wider α-angles, confirming that optimal attractive electrostatic forces occur between electron-enriched cyclic tetramers and aromatic hydrogen atoms at 45°.

Total energy changes as a function of $o_{\pi\text{-}\pi}$, translation within the xy- plane, were determined for three herringbone-packed macrocycles, placed at $d_{\pi\text{-}\pi} = 3.5$ Å and $\beta = 0°$ for different aromatic ring rotations α. (Figures 5. 15 and 5. 16) Similar to the plots of energy vs. interplanar distance, the total energy curves decreased steadily with increasing distances, to give energy minima from 0.4 Å for both unsubstituted and methoxy-substituted azobenzene tetramers. As for the face-packed macrocycles, translational motions required to achieve maximal attraction between supramolecular stacks of *cis*-azodibenzoic acid macrocycles were relatively smaller than interplanar distances.

Rotational motions of the macrocyclic structures about the z-axis, β, determined for face-packed cyclic tetramers showed relatively small energy changes, suggesting the existence of free rotation within the stacked cyclic tetramers. Macrocycle rotation about the z-axis should result in minimal contact between the herringbone-packed *cis*-azodibenzoic acid macrocycles and, therefore, should destabilise the herringbone structure. Energy scans with respect to this macrocycle twist were consequently not required for the optimisation of herringbone-packing arrangement.

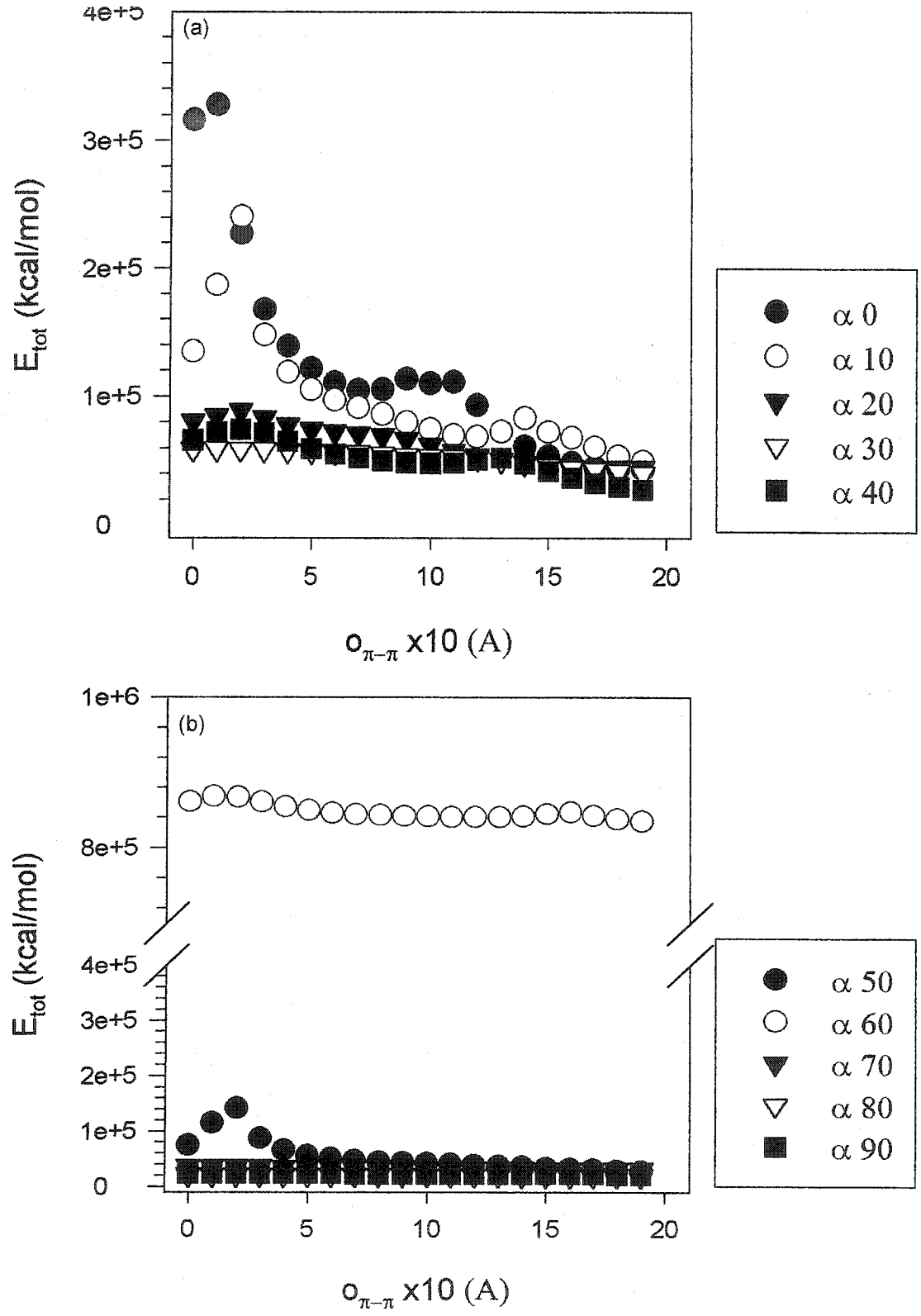


Figure 5. 15. Total energy plots as a function of horizontal offset $o_{\pi-\pi}$ for the unsubstituted *cis*-azobenzene derivatives. (a) For $0° < \alpha < 40°$. (b) $40° < \alpha < 90°$.

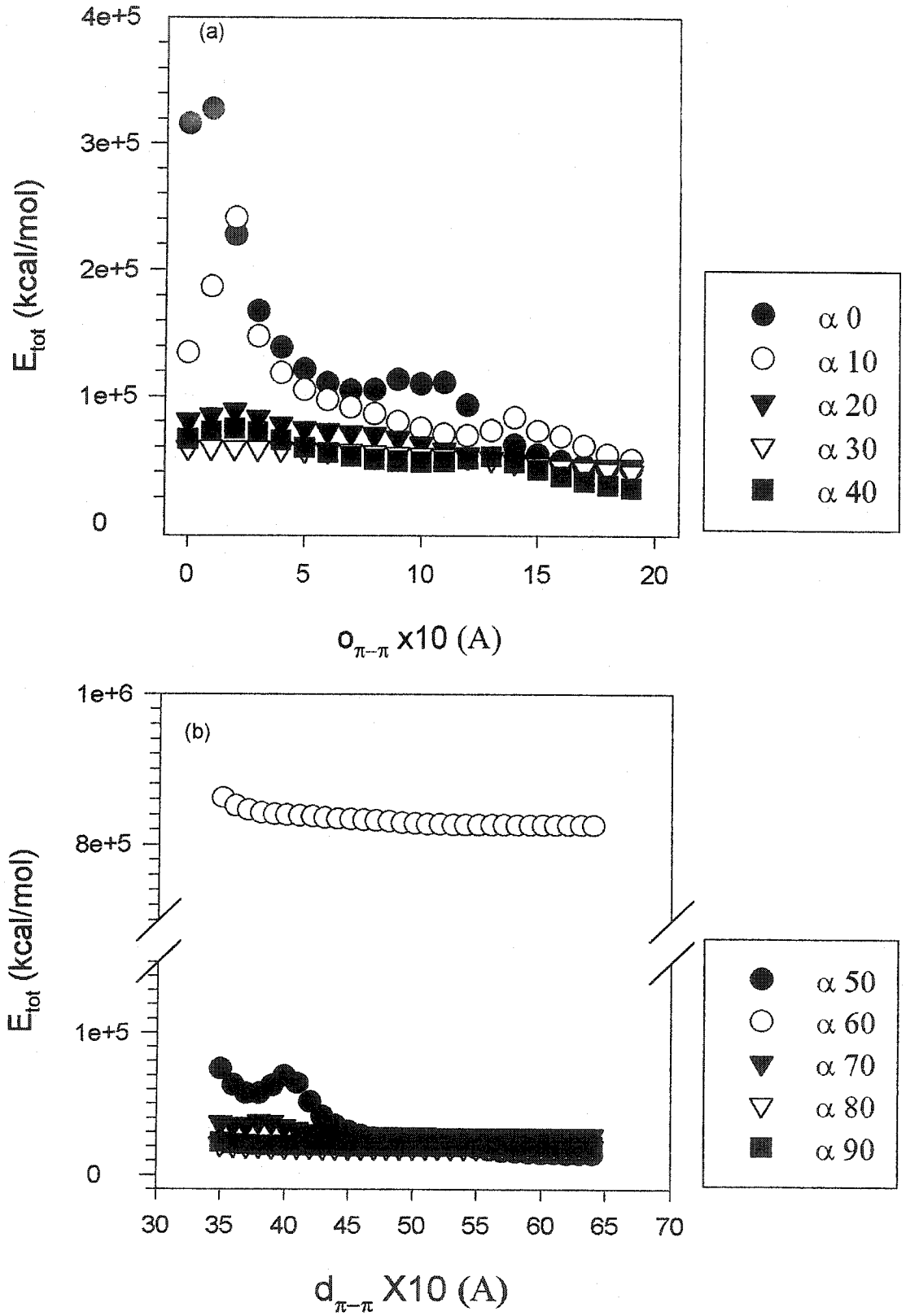


Figure 5. 16. Total energy plots as a function of horizontal offset $o_{\pi-\pi}$ for the methoxy-disubstituted *cis*-azobenzene derivatives. (a) For $0° < \alpha < 40°$. (b) $40° < \alpha < 90°$.

Herringbone-packing of *cis*-azodibenzoic acid cyclic tetramers was shown to be primarily affected by changes in interplanar distance $d_{\pi\text{-}\pi}$ and aromatic ring rotation α. Favourable close-packings are obtained for 4.0 - 4.5 Å and 5.0 - 5.5 Å interplanar distances, along with 45° aromatic ring tilts for herringbone-packed unsubstituted and methoxy-disubstituted *cis*-azodibenzoic acid cyclic tetramers respectively. Comparison of face-to-face and herringbone-packing energies clearly showed that the combined effects of van der Waals and electrostatic interactions in both spatial arrangements clearly suggest face-packing as the more favourable *cis*-azodibenzoic acid packing mode.

5.3.3. Quantum Mechanical Study of Packing in *cis*-Azodibenzoic Acid Cyclic Tetramers

5.3.3.1. Geometry Optimisation of Close-Packed Hydrogen-Bonded Cyclic Tetramers

Empirically determined total energy contour plots generated for herringbone and face-packing of unsubstituted and methoxy-disubstituted *cis*-azodibenzoic acid tetramers indicated face-packed structures as the preferred arrangements. To gain a better understanding of the experimentally observed rod-like nanostructures and improve the accuracy of the theoretical predictions, the MM^{+} geometries of the 1x3 and 1x5-arrays of stacked cyclic tetramers were optimised using the semi-empirical PM3 method (see theoretical methods).

Tables 5. 4 and 5. 5 show the optimal geometries for face-packed unsubstituted and methoxy-disubstituted *cis*-azodibenzoic acid structures. An optimal close-packing distance of 4.2 Å was reached for 30°-aromatic tilts and 0.5 Å-horizontal offset values in 1x3 arrays of face-packed unsubstituted *cis*-azodibenzoic acid cyclic tetramers, in agreement with the molecular mechanical prediction. Geometry optimisation of five cyclic tetramers from this optimal face-packed structure lead to different packing parameters. An interplanar distance of 6.0 Å was obtained between the three central tetramers, along with 20°-aromatic tilts and 0.5 Å-horizontal offsets. These tetramers were observed to move towards the macrocycles at the extremities, within an interplanar distance of 2.1 Å, consistent with increased translational abilities for the tetramers in the 1x5-array compared to the 1x3-array. This increased mobility allows the macrocycles to compensate for the repulsive electrostatic interactions.

The steric contribution of the methoxy-substituent was evident in the PM3 optimized disubstituted macrocycles, which consisted of 30°-aromatic tilts, interplanar distances of 6.3 Å, and 0.5 Å-horizontal offsets in the 1x3-array, again agreeing with the MM^+ packing scans. When placed in a 1x5- face-packed array, the three cyclic tetramers adopt a minimum energy configuration in which 20°-aromatic tilts were observed, in conjunction with interplanar distances of 5.9 Å and 0.5 Å-horizontal offset values, consistent with the empirical predictions. Although interplanar distances were kept homogenous throughout the five stacked cyclic tetramers, smaller aromatic tilts were observed in the PM3 optimised geometries than in the MM^+ energy scan results. These angular differences suggest that the *cis*-azodibenzoic acid tetramers adjust back to their individual minimum energy structures, while maintaining their close-packed face-to-face arrangement.

Interaction enthalpies, Table 5.6, were calculated from the enthalpies of formation of the geometry optimised architectures to quantify the intermolecular forces which are responsible for nanostructure formation. For each PM3 optimised structure, the interaction enthalpy at 0 K $\Delta H_f(T)$ was determined using:

$$\Delta H_f(T) = H_f(R_n) - n \times H_f(R) \qquad \textbf{(Eq. 5. 2)}$$

where T is the temperature (T = 0 K), $H_f(R)$ is the enthalpy of the cyclic tetramer,[12] n the number of tetramers involved, and $H_f(R_n)$ the enthalpy of the optimised face-packed structure. Face-packing interaction enthalpies increased proportionally with addition of hydrogen-bonded tetramers to the stacked structure, and ranged between –1.5 and +27.0 kcal/mol. Negative interaction enthalpies were calculated for the unsubstituted macrocycles, consistent with the formation of long-range, additive van der Waals interactions in these face-packed structures. Positive interaction enthalpies were obtained for the methoxy-disubstituted azobenzene tetramers, suggesting that steric effects destabilise the face-packed arrangement.

Table 5. 4. PM3 optimised geometries of stacked unsubstituted *cis-p*-azodibenzoic acid macrocycles

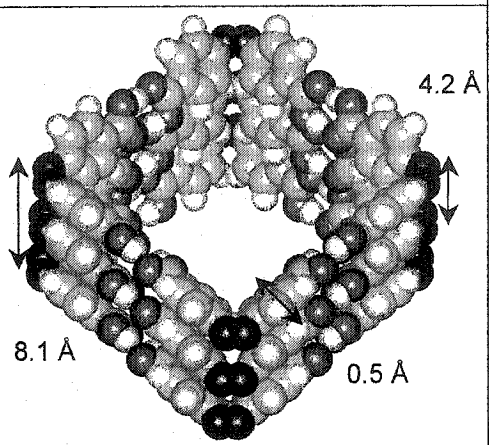
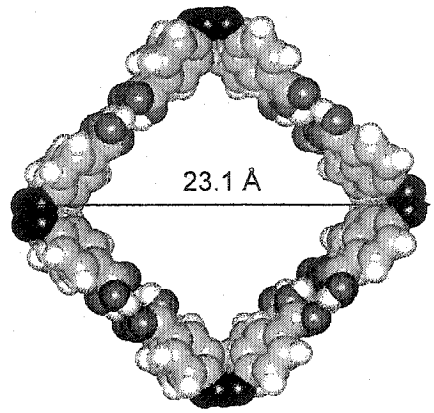
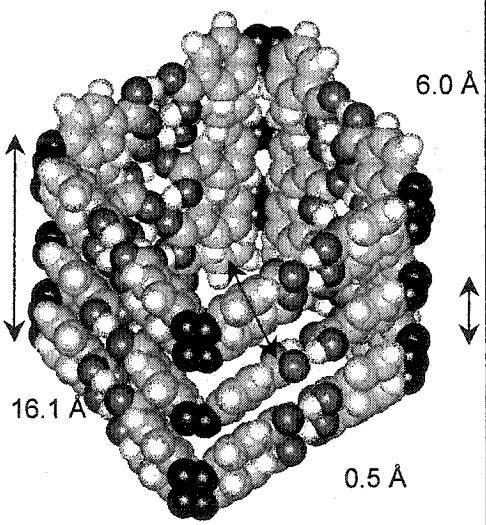
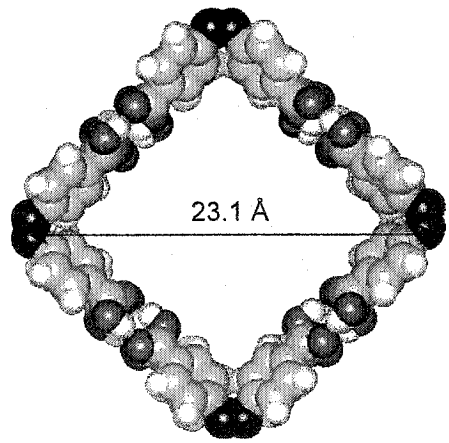
	Side view	Top view
1x3	 $\alpha = 30°; \beta = 0°$	
1x5	 $\alpha = 20°; \beta = 0°$	

Table 5. 5. PM3 optimised geometries of stacked methoxy-substituted *cis-p*-azodibenzoic acid macrocycles

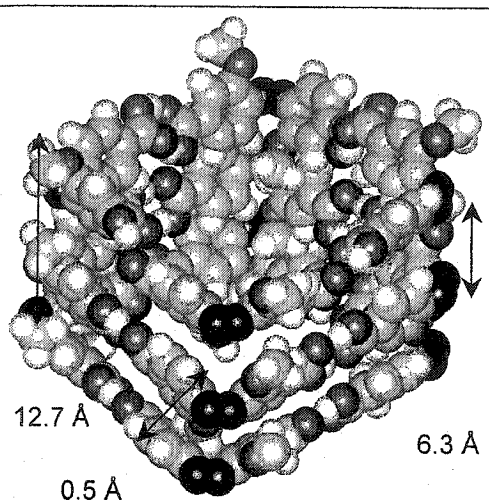
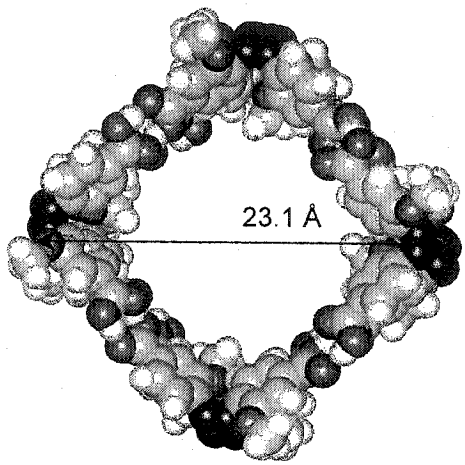
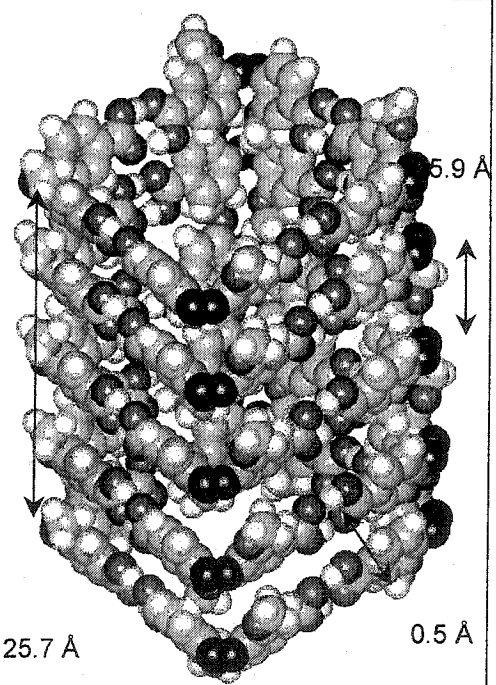
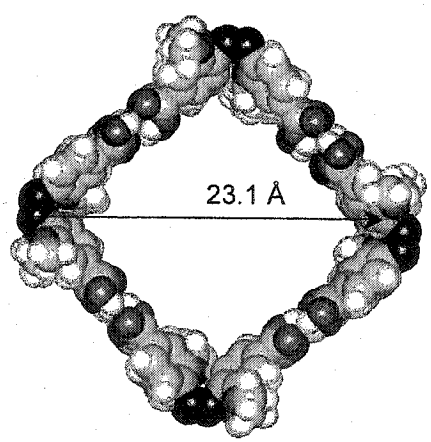
	Side view	Top view
1x3	 $\alpha = 30°; \beta = 0°$	
1x5	 $\alpha = 20°; \beta = 0°$	

Table 5. 6. Interaction energies for the face-packed cyclic tetramers.

		Total enthalpy (kcal/mol)	Interaction enthalpy (kcal/mol)
Unsubstituted tetramer	1x3	- 378.37	- 0.05
	1x5	- 1136.56	- 1.30
Methoxy-substituted tetramer	1x3	-659.43	9.99
	1x5	- 1981.46	26.82

5.3.3.2. Electronic Properties of Close-Packed Hydrogen-Bonded Cyclic Tetramers

Information on the electronic properties of the π-stacked azobenzene macrocycles was extracted from the PM3 optimised face-packed 1x3- and 1x5-arrays, to further characterise the second-order self-organisation of *cis*-azodibenzoic acid cyclic tetramers. The delocalised molecular orbitals of the face-packed 1x3 and 1x5-architectures are shown in Tables 5. 7 to 5. 10. The frontier molecular orbitals (HOMO and LUMO) of the stacked tetramers mainly covered the individual azobenzene monomers, displaying the same HOMO and LUMO properties as the hydrogen-bonded macrocycles. This similarity with single macrocycles was observed in the presence of molecular π-type orbital across the hydrogen-bonds, demonstrating the hierarchical self-assembly of these *cis*-azodibenzoic acid monomers into rod-like nanostructures. The lowest occupied

molecular orbitals (LOMO) were spread over the entire geometry optimised structure in all face-packed arrangements, indicating that π-stacking forces, along with hydrogen-bonding, effectively contribute to σ-type bonding interactions.

The HOMO and LUMO of the 1x3- face-packed array of unsubstituted macrocycles (Table 5. 7) were compared with the frontier molecular orbitals of the 1x5-face-packed array of unsubtituted macrocycles (Table 5. 8). The HOMO contour plot of the 1x3- face-packed array (Table 5. 7) covered the azobenzene part of the monomer which comprise the cyclic tetramers, similar to the HOMO diagram the 1x5-face-packed array (Table 5. 8). The LUMO contour plots of the 1x3- and 1x5-face-packed arrays (Table 5. 7) covered the azobenzene derivatives, indicating that the azobenzene units, rather than the carboxylic ends are the main reactive sections.

As in the case of the individual hydrogen-bonded azodibenzoic acid macrocycles, the hydrogen-bonding molecular orbitals involved in the formation of the face-packed 1x3- and 1x5 azodibenzoic acid were observed at much lower energies than the HOMOs (Tables 5. 7 and 5. 8). The hydrogen-bonding MO diagrams for the stacked macrocycles displayed in Table 5. 7 clearly showed a single lobe over the hydrogen-bond, consistent with the formation of strong hydrogen-bonded aggregates, suggesting that the tilt of the aromatic rings does not destabilise the cyclic tetramers. In the face-packed 1x3-array, the delocalised molecular orbital covering the hydrogen-bonds spread over the entire cyclic tetramer (Table 5. 7), indicating the macrocycle effectively forms a cohesive hydrogen-bonded complex within the array. In the 1x5 array, the hydrogen-bonding MO not only covers cyclic tetramers, but also is delocalised from one level of the geometry optimised stack to the next, providing evidence for favourable π-π interactions between the

hydrogen-bonded macrocycles. (Table 5. 8) The lowest occupied molecular orbital (LOMO) of the 1x3- and 1x5-arrays both covered the entire structure (Tables 5. 7 and 5. 8), suggesting the stability of the π-stacked assemblies.

Table 5. 7. PM3 Molecular orbital diagrams of 1x3 stacked unsubstituted *cis*-azobenzene tetramers

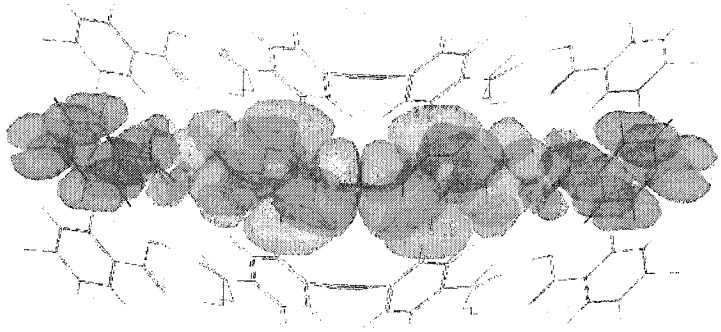
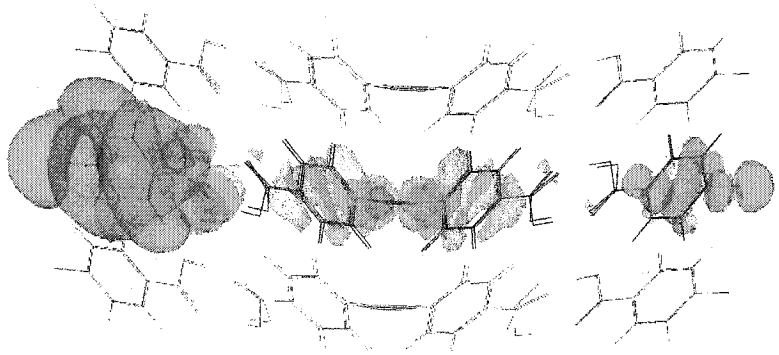
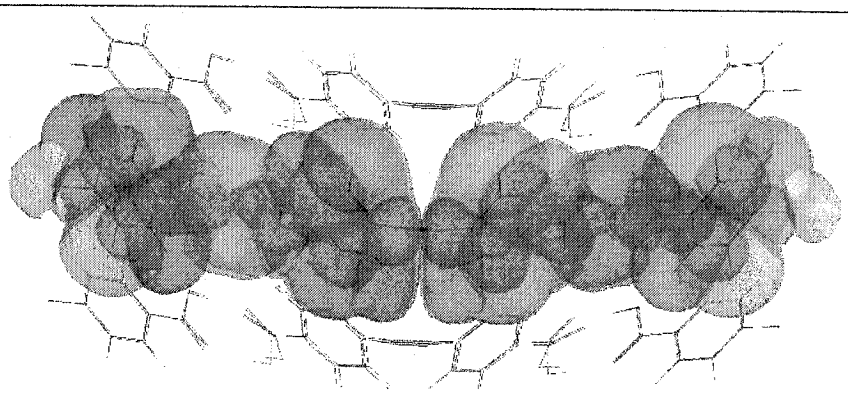
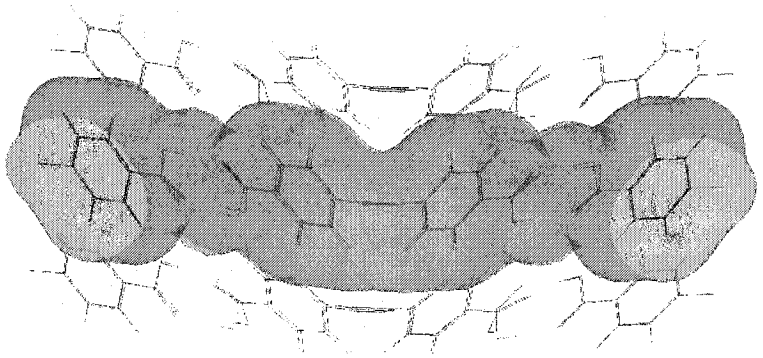
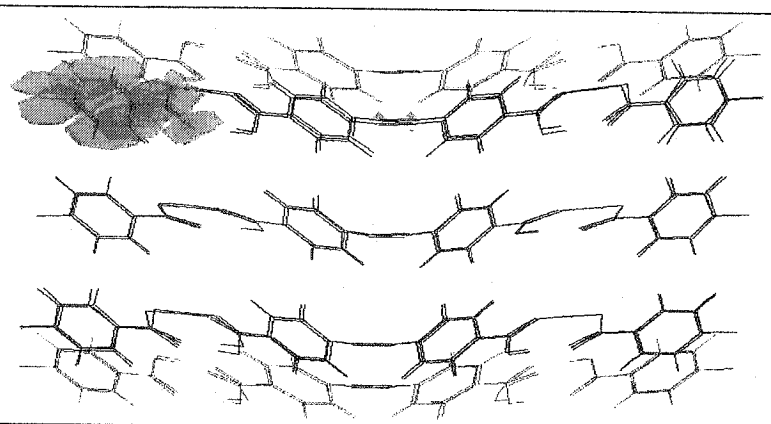
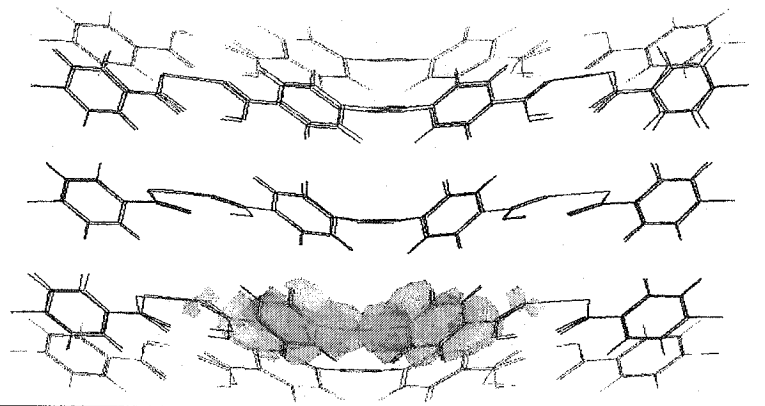
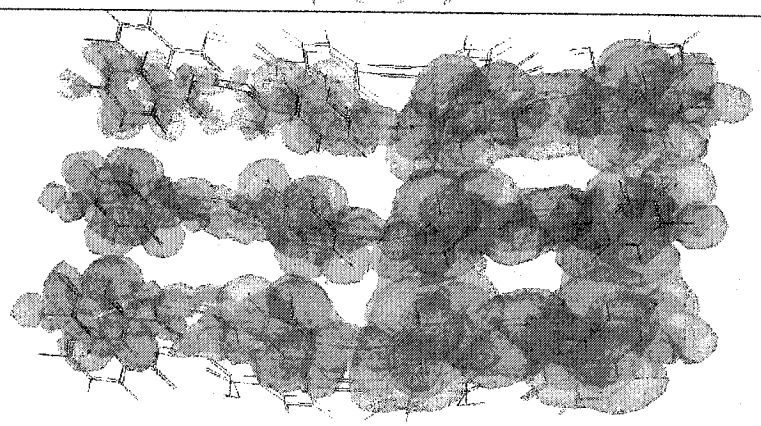
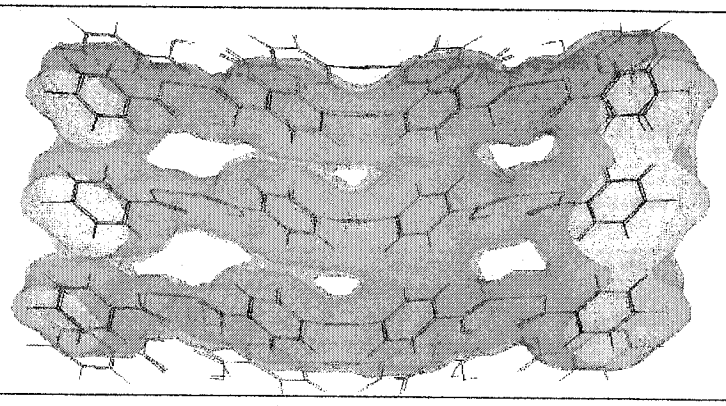
LUMO E = - 1.16 eV	
HOMO E = - 9.61 eV	
MO 137 E = - 14.28 eV	
LOMO E = - 41.74 eV	

Table 5. 8. PM3 Molecular orbital diagrams of 1x5 stacked unsubstituted *cis*-azobenzene tetramers

LUMO E = - 1.34 eV	
HOMO E = - 9.72 eV	
MO 413 E = - 14.40 eV	
LOMO E = - 42.08 eV	

The HOMO and LUMO of the 1x3- face-packed array of methoxy-subsituted macrocycles (Table 5. 9) were compared with the frontier molecular orbitals of the 1x5-face-packed array of f methoxy-subsituted macrocycles (Table 5. 10). Similar to HOMO diagram of the unsubstituted azobenzene arrays, the HOMO contour plots of the 1x3- and 1x5-face-packed array (Tables 5. 9 and 5. 10) covered the azobenzene part of the monomers. Likewise, the LUMOs of the 1x3- and 1x5-face-packed methoxy-disubstituted macrocycles (Table 5. 7) only covered the azobenzene derivatives, indicating that the azobenzene units, rather than the carboxylic ends are the main reactive sections.

The hydrogen-bonding molecular orbitals involved in the formation of the face-packed 1x3- and 1x5 azodibenzoic acid were observed at much lower energies than the HOMOs (Tables 5. 9 and 5. 10). These hydrogen-bonding displayed single lobe over the hydrogen-bond, consistent with the formation of strong hydrogen-bonded aggregates, suggesting that neither the tilt of the aromatic rings nor the presence of substituents at the periphery of the assembly weaken the cyclic tetramers (Table 5. 2) does not destabilise the cyclic tetramers. Both hydrogen-bonding MOs displayed extensive delocalisation over the macrocycles and over the 1x3 and 1x5 arrays, demonstrating the stabilisation of the molecules through hydrogen-bonding and π-π interactions.

Table 5. 9. PM3 Molecular orbital diagrams of 1x3 stacked methoxy-substituted *cis*-azobenzene tetramers

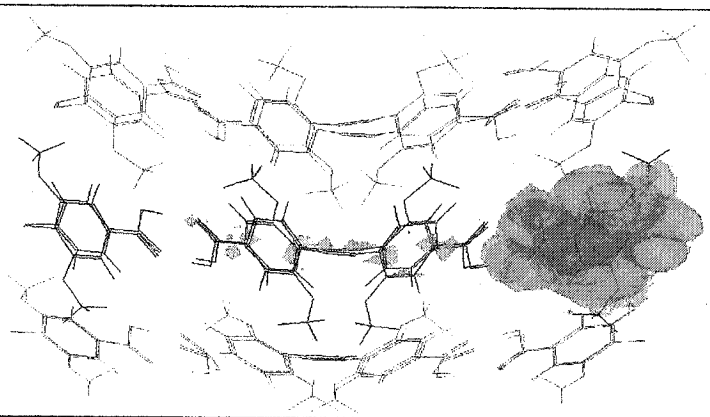
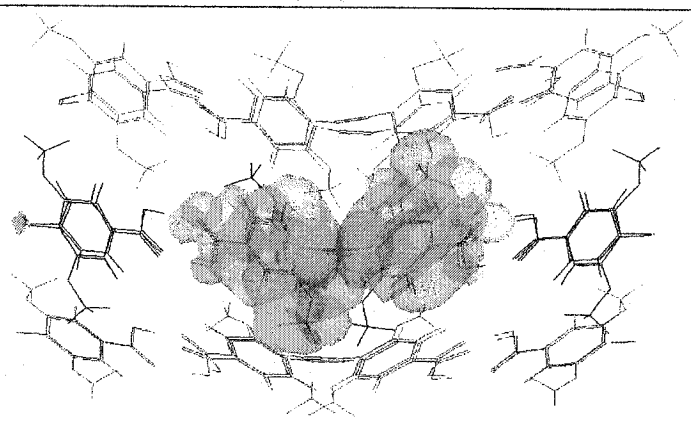
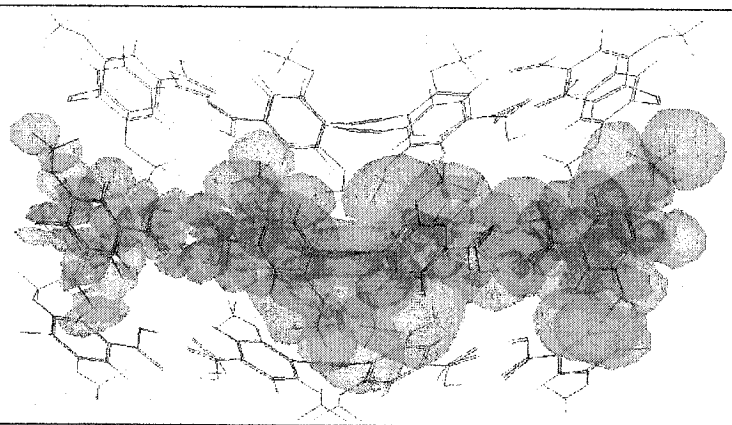
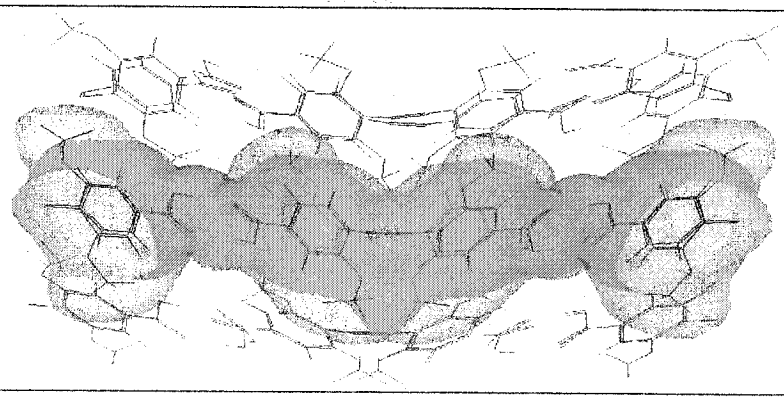
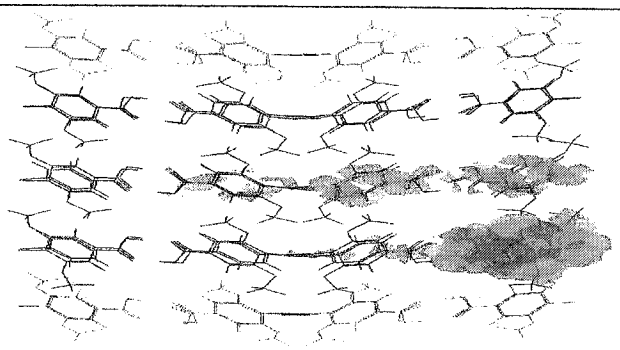
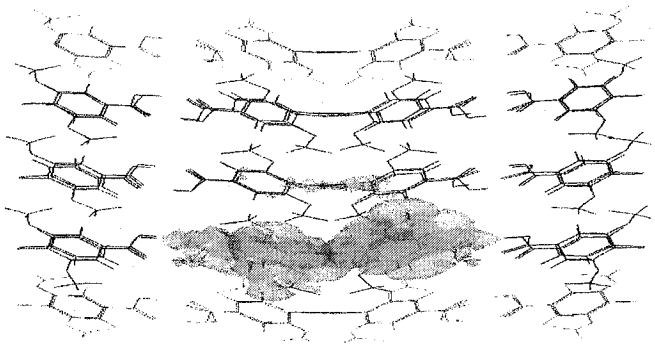
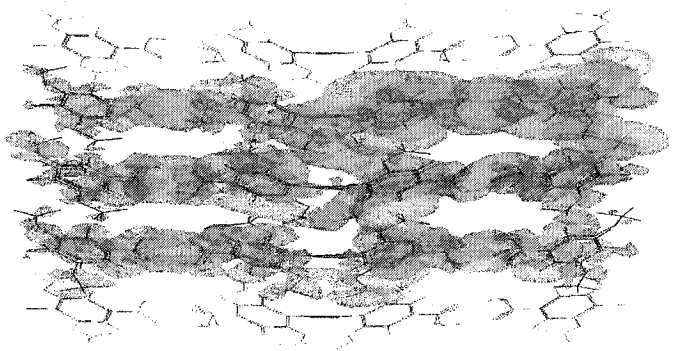
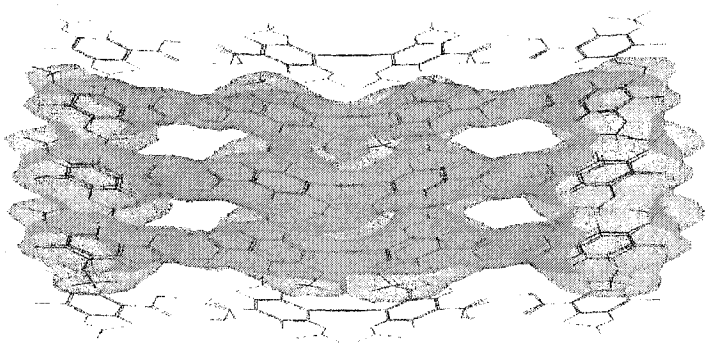
LUMO E = -1.07 eV	
HOMO E = -9.29 eV	
MO 179 E = -13.75 eV	
LOMO E = -42.09 eV	

Table 5. 10. PM3 Molecular orbital diagrams of 1x5 stacked methoxy-substituted *cis*-azobenzene tetramers

LUMO E = -1.15 eV	
HOMO E = -9.25 eV	
MO 433 E = -15.84 eV	
LOMO E = -42.29 eV	

The comparison of the calculated molecular orbital (MO) diagrams of the *cis*-azodibenzoic acid macrocycles (Figure 5. 17) clearly showed an evolution of the band structures from discrete energy levels to broad energy bands with increased number of hydrogen-bonded tetramers in the face-packed architecture, consistent with the additive character of π-π intermolecular interactions. In addition, this increased band structure is accompanied by HOMO-LUMO band gap decrease from 8.62 eV to 8.39 eV, and 8.38 eV to 8.09 eV in the unsubstituted and methoxy-disubstituted macrocycles respectively. This result suggest that the π-stacking interactions are additive and, more important, that the formation of rod-like nanostructures from *cis*-**2** azodibenzoic acid macrocycles results in increased electron conjugation towards a semi-conducting configuration.

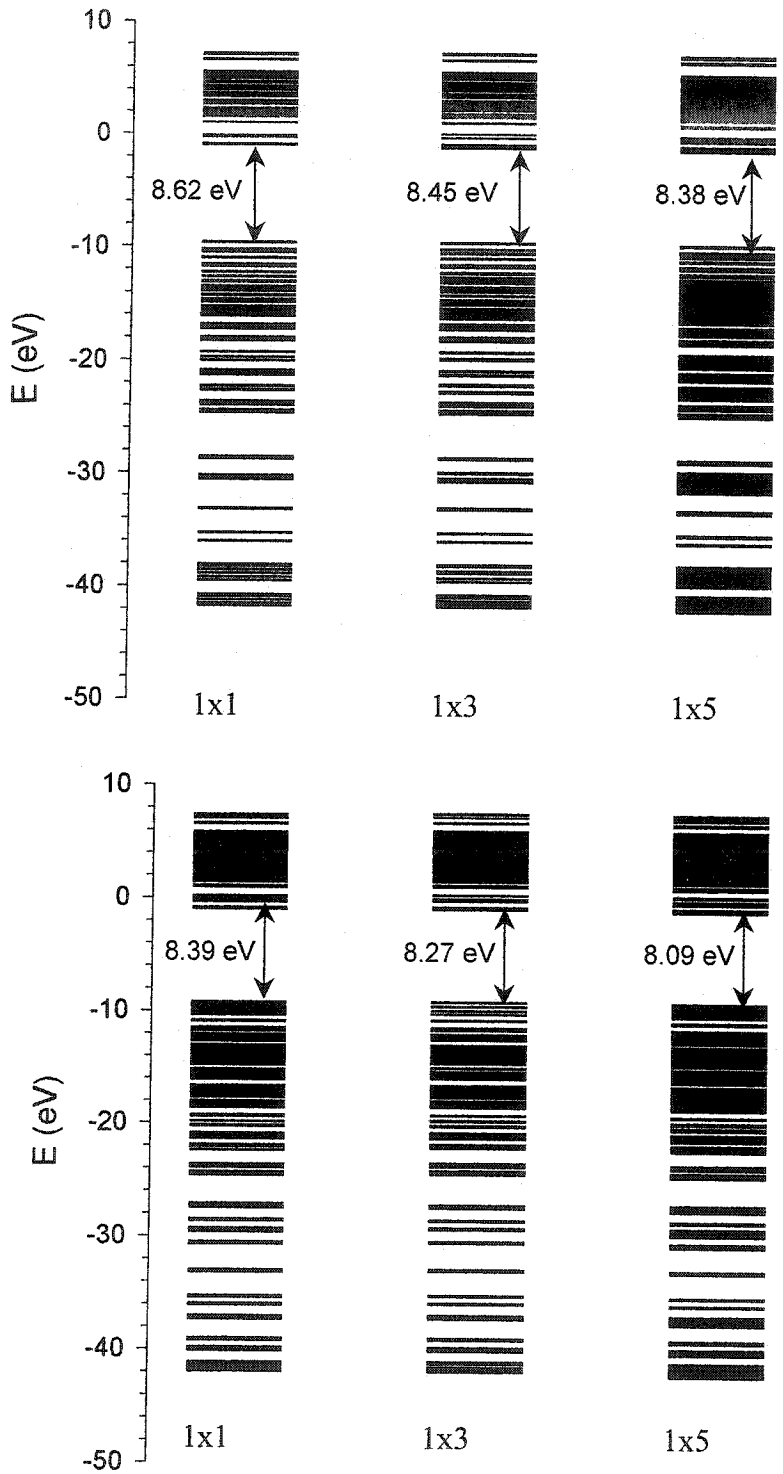


Figure 5. 17. Comparison of the molecular orbital diagrams of *cis*-azodibenzoic acid macrocycles alone (1x1), in a 1x3- and 1x5- face-packed arrays. (a) Unsubstituted *cis*-2 systems. (b) Methoxy-substituted *cis*-2 systems.

5.4. Conclusion

An effective, computationally inexpensive theoretical strategy based on empirical and quantum mechanical methods was developed to predict and characterise the π-π interactions of the three-dimensional nanostructure resulting from the macrocyclic tetramers, along with their electronic properties. This method significantly reduces the computational time of a calculation that might take years to a few days. Simple MM^{+} total energy scans performed in macrocycle arrays lead to a preliminary optimal close-packed arrangement of the hydrogen-bonded azobenzene derivatives. According to the geometrical requirements of competing van der Waals and electrostatic forces, these energy scans tend to favour a face-to-face configuration over a herringbone structure from the macrocycles. A geometrical refinement of the empirical distance and angular components was carried out using the semi-empirical PM3 method, giving rise to little conformational alterations as the cyclic tetramers adjusted towards geometries intermediate to meet the combined effects of van der Waals and electrostatic interactions. These quantum mechanical results therefore confirmed the strength of the geometrical arguments used in the molecular mechanics calculations. A quantum mechanical analysis revealed additive and conjugative electronic properties of these face-packed structures, showing the cohesive effects of the π-π intermolecular interactions and predicting increased electron delocalisation in larger rod-like *cis*-azodibenzoic acid nanostructures.

5.5. References and Notes

[1] F. Rakotondradany, M. A. Whitehead, A.-M. Lebuis, H. F. Sleiman, *Chem. Eur. J.*, **2003**, *9*, 4771.

[2] (a) R. E. Franklin, R. G. Gossling, *Nature*, **1953**, *171*, 740. (b) J. D. Watson, F. H. C. Crick, *Nature*, **1953**, *171*, *737*. (c) J. D. Watson, F. H. C. Crick, *Nature*, **1953**, *171*, 964.

[3] G. M. Blackburn, M. J. Gait (Eds.), *Nucleic Acids in Chemistry and Biology*, Oxford University Press: New York, 1990.

[4] (a) J. -M. Lehn, *Supramolecular Chemistry: Concepts and Perspectives*, VCH, Weinheim, 1995. (b) G. M. Whitesides, E. E. Simanek, J. P. Mathias, C. T. Seto, D. N. Chin, M. Mammen, D. M. Gordon, *Acc. Chem. Res.*, **1995**, *28*, 37. (c) J. S. Lindsey *New J. Chem.*, **1991**, *15*, 153. (d) D. S. Lawrence, T. Jiang, M. Levett, *Chem. Rev.*, **1995**, *95*, 2229.

[5] (a) G. R. Desiraju, A. J. Gavezzotti, *J. Chem. Soc., Chem. Commun.*, **1989**, 621. (b) B. Askew, P. Ballester, C. Buhr, K. S. Jeong, S. Jones, K. Parris, K. Williams, J. Rebek Jr., *J. Am. Chem. Soc.*, **1989**, *111*, 1082. (c) J. Jazwinski, A. J. Blacker, J. –M. Lehn, M. Cesario, J. Guilhem, C. Parscard, *Tetrahedron Lett.*, **1987**, *28*, 6057. (d) J. –M. Ortholand, A. M. Slawin, N. Spencer, J. F. Stoddart, D. J. Williams, *Angew. Chem. Int. Ed. Engl.*, **1989**, 1394. (e) M. S. Vollmer, T. D. Clark, C. Steinem, and M. R. Ghadiri, *Angew. Chem. Int. Ed. Engl.* **1999**, *38*, 1598. (f) D. T. Bong, T. D. Clark, J. R. Ganja, M. R. Ghadiri, *Angew. Chem. Int. Ed. Engl.*, **2001**, *40*, 988.

[6] (a) C. A. Hunter, J. K. M. Sanders, *J. Am.. Chem.. Soc.*, **1990**, *112*, 5525. (b) C. A. Hunter, *Chem. Soc. Rev.*, **1994**, *23*, 101. (c) H. Adams, F. J. Carver, C. A. Hunter, N. J. Osborne, *Chem. Commun.*, **1996**, 2529. (d) H. Adams, K. D. M. Harris, G. A. Hembury, C. A. Hunter, D. Livingstone, J. F. McCabe, *Chem. Commun.*, **1996**, 2531.

[7] Gaussian 98W (Revision A.7), M. J. Frisch, G. W. Trucks, H. B. Schlegel, G. E. Scuseria, M. A. Robb, J. R. Cheeseman, V. G. Zakrzewski, J. A. Montgomery, Jr., R. E. Stratmann, J. C. Burant, S. Dapprich, J. M. Millam, A. D. Daniels, K. N. Kudin, M. C. Strain, O. Farkas, J. Tomasi, V. Barone, M. Cossi, R. Cammi, B. Mennucci, C. Pomelli, C. Adamo, S. Clifford, J. Ochterski, G. A. Petersson, P. Y. Ayala, Q. Cui, K. Morokuma, D. K. Malick, A. D. Rabuck, K. Raghavachari, J. B. Foresman, J. Cioslowski, J. V. Ortiz, A. G. Baboul, B. B. Stefanov, G. Liu, A. Liashenko, P. Piskorz, I. Komaromi, R. Gomperts, R. L. Martin, D. J. Fox, T. Keith, M. A. Al-Laham, C. Y. Peng, A. Nanayakkara, C. Gonzalez, M. Challacombe, P. M. W. Gill, B. G. Johnson, W. Chen, M. W. Wong, J. L. Andres, M. Head-Gordon, E. S. Replogle, J. A. Pople, Gaussian, Inc., Pittsburgh PA, **1998**.

[8] This result was consistent with data published for *o*-substituted azobenzene derivatives. N. J. Bunce, G. Ferguson, C. L. Forber, G. J. Stachnyk, *J. Org. Chem.*, **1987**, *52*, 394.

[9] D. B. Boyd, K. B. Lipkowski, *J. Chem. Ed.*, **1987**, *59*, 269.

[10] A small distance interval equivalent to ½ phenyl group was chosen for evaluating the effect of the horizontal offset on total energies, because of the high symmetry of the cyclic tetramer.

[11] G. R. Desiraju, C. V. K. Sharma, *The Crystal as a Supramolecular Entity: Perspectives in Supramolecular Chemistry, Vol. 2,* John Wiley & Sons, Chicester, 1996.

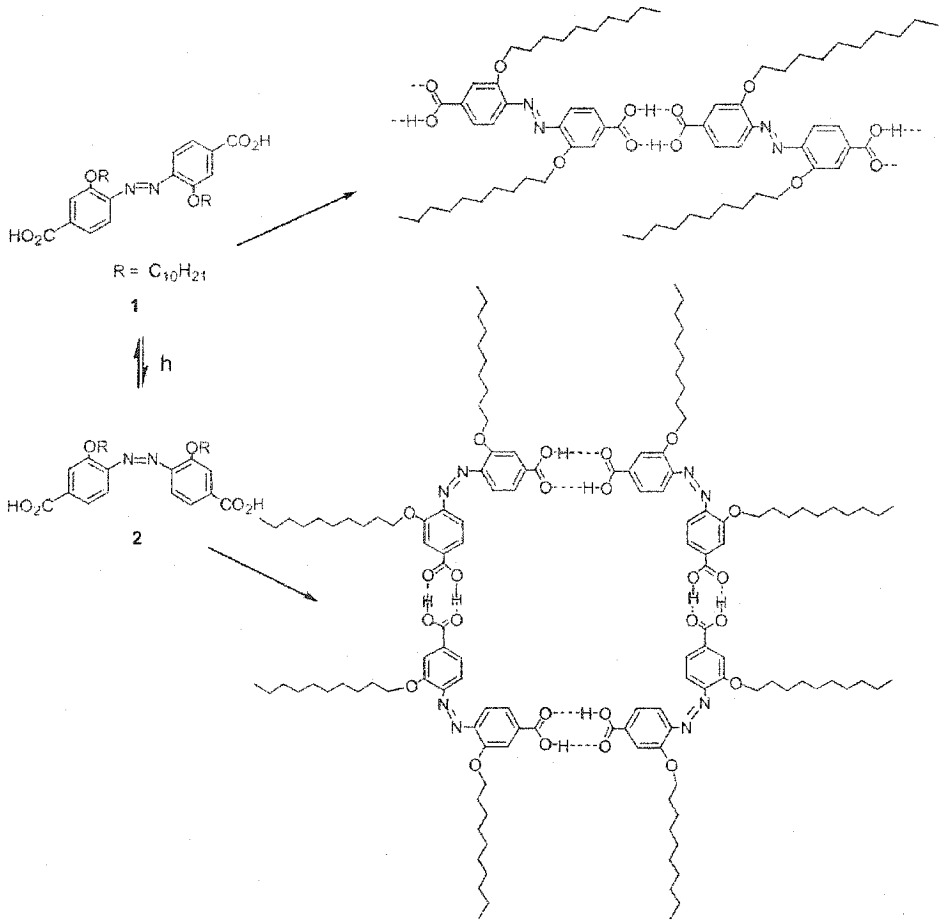
[12] The total enthalpy of the unsubstituted tetramer was calculated as – 378.42 kcal/mol.

Chapter 6.

New Photoresponsive Supramolecular Systems Using Metal Coordination and Multiple Hydrogen-Bonding

6.1. Introduction

Simple dicarboxylic acid derivatives form well-defined, supramolecular structures through hydrogen-bonding interactions.[1] As shown in Chapters 3-5, the self-assembly of photoresponsive azodibenzoic acid derivatives **1** and **2** results into two dramatically different, reversibly photoswitched supramolecular structures (Scheme 6. 1),[2] with interesting potential applications in fabricating of reversible, read-write-erase, optical data storage devices and photopatterned surfaces. Initially, photoirradiation triggers the *trans* → *cis* azobenzene isomerisation, which changes the self-assembly of these molecules from *trans*-linear tapes, to *cis*-discrete cyclic structures. Secondly, these *cis* azobenzene cyclic structures self-organize into elongated aggregates by stacking. Experimental techniques involving X-ray crystallography, X-ray powder diffraction, electron microscopy, dynamic light scattering, electrospray mass spectrometry and vapor pressure osmometry confirmed the theoretically predicted hydrogen-bonded systems.



Scheme 6. 1. Self-assembly of *trans*-**1** and *cis*-**2** azodibenzoic acid derivatives into hydrogen-bonded linear tapes and cyclic tetramers.

In particular, experimental photoisomerisation, and thermal recovery studies, of *trans*-azodibenzoic acid **1** demonstrated the competing effects of hydrogen-bonding and *cis-trans* reisomerisation in these dicarboxylic acid derivatives. Therefore, the design of *trans*-and *cis*-azobenzene monomers which can undergo self-assembly through stronger intermolecular interactions is required to counter the destabilizing thermal *cis-trans* reaction and to better control supramolecular architecture. Such tightly bound monomers

should favour the formation of *cis*-azobenzene supramolecular systems, which will allow for increased stability and higher photopatterning periodicity.

Three novel monomers have been designed to improve intermolecular cohesion between self-assembled azobenzene chromophores (Figure 6. 1). In the design of *trans*-**7** and *cis*-**8** monomers, two cyano groups para to the N=N linkage have replaced the carboxylic acid groups of **1** and **2**, allowing for stable coordination to late transition metals. In particular, silver (I) ions, which have been incorporated in crystal lattices involving nitrile substituted ligands, have generally exhibited a linear arrangement.[3] Consequently, the use of silver(I) ions to join *trans*-**7** and *cis*-**8** should preserve the geometry of the hydrogen-bonded azodibenzoic acid counterparts (Scheme 6. 1).

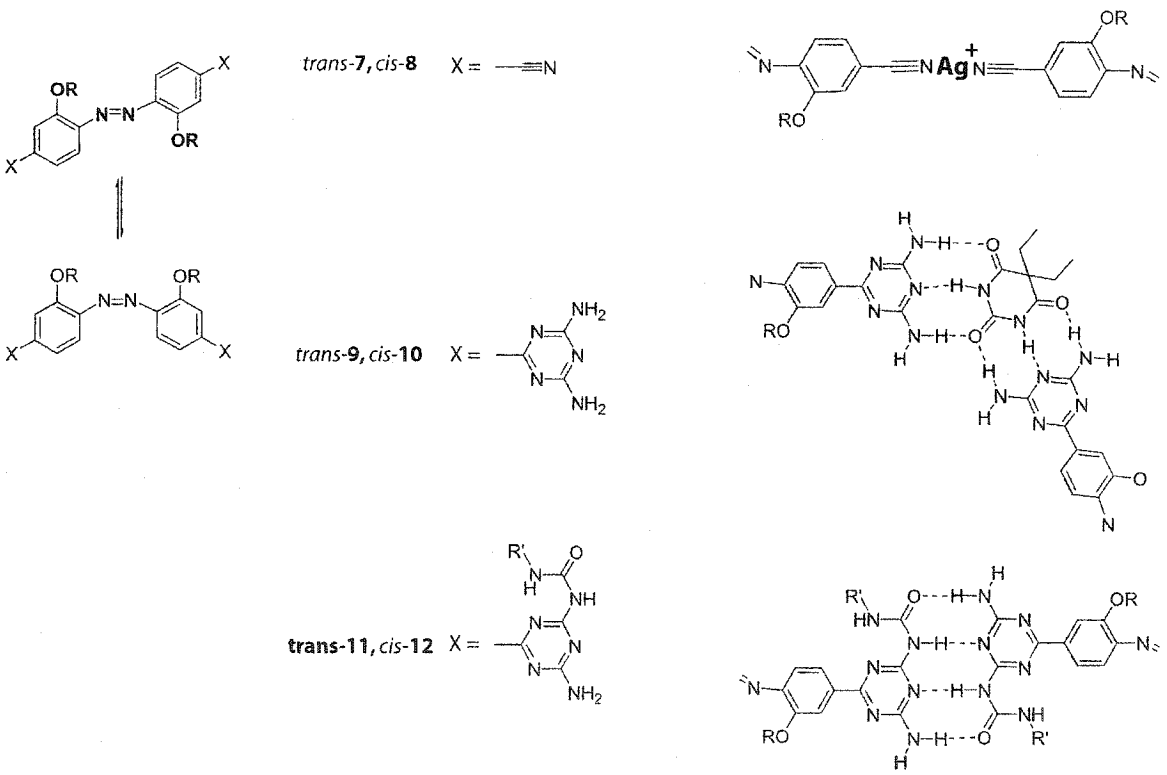
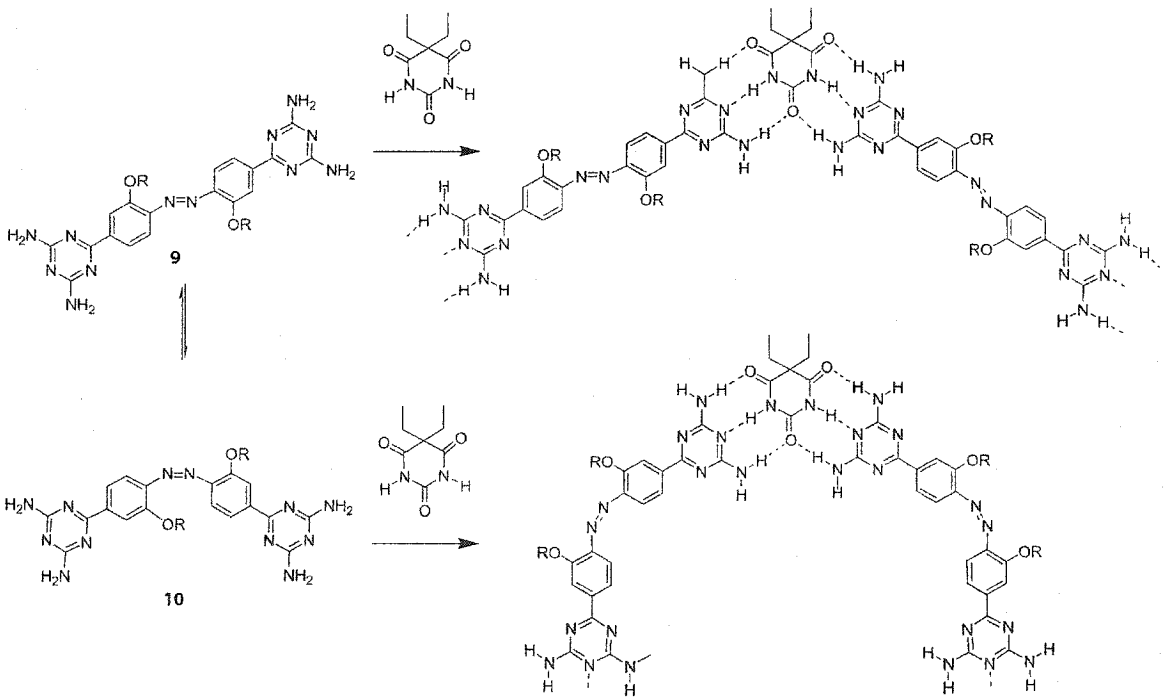


Figure 6. 1. Newly designed *trans*- and *cis*-azobenzene monomers for hydrogen-bonding and metal coordination

Trans-**9** and *cis*-**10** are azobenzene monomers are functionalised at each extremity with triazine units, to increase their hydrogen-bonding ability. These triazine substituents provide three DAD-type anchor points available for triple hydrogen-bond formation with ADA-type molecular guests, like barbituric acid and cyanuric acid derivatives. In the case of guests bearing linearly oriented ADA units, the self-assembly of *trans*-**9** and *cis*-**10** should give the same geometries as *trans*-**1** and *cis*-**2**. However, in the commonly used diethylbarbituric acid, the non-linear orientation of the ADA units (120° angles) should generate hydrogen-bonded structures different from the previously described linear tapes and cyclic tetramers (Scheme 6. 2).



Scheme 6. 2. Hydrogen-bond self-assembly of *trans*-**9** and *cis*-**10** azodibenzoic acid derivatives with diethylbarbituric acid.

Finally, *trans*-**11** and *cis*-**12** azobenzene monomers use the quadruple hydrogen-bonds offered by the ureidotriazine groups. In these self-complementary units, the ureido N-H proton forms a supplementary intramolecular hydrogen-bond with the triazine nitrogen, limiting the free rotation of the acetamide moiety and, consequently, orienting the carbonyl group towards the incoming guest molecule. Similar to the azobisbenzonitrile monomers **7** and **8**, the self-assembly of *trans*-**11** and *cis*-**12** should result in the formation of hydrogen-bonded linear tapes in the *trans*-form and discrete cyclic structures in the *cis*-form.

6.2. Results and discussion

6.2.1. Theoretical Evaluation of Monomer Geometries

The azobenzene monomer geometries were first optimised to establish the conservation of the N=N-C bond angles and, consequently, of the cyano, triazine, and ureidotriazine group orientations, upon modification of the para substitution. As shown in Chapter 4, a N=N-C bond angle of 119.7° was obtained for *trans*- *p*-azodibenzoic acid using the semi-empirical PM3 method, giving a 180°-angle between the carboxylic acid groups, while the *cis*- *p*-azodibenzoic acid PM3 N=N-C bond angle was calculated to be 127.0° in agreement with previously calculated *cis*-azobenzene N=N-C bond angles,[4] leading to a *ca.* 80°-angle between the carboxylic acid groups.

PM3 geometry optimisation of *trans*- and *cis*-*p*-azobisbenzonitrile model monomers gave 119.9° and 127.0° C-N=N angles for the *trans*- and *cis*- monomers respectively, indicating that the cyano groups adopt the same orientation as the carboxylic acid groups in *trans*- and *cis*-azodibenzoic acid. Similarly, these theoretical calculations

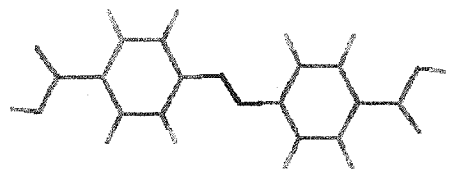
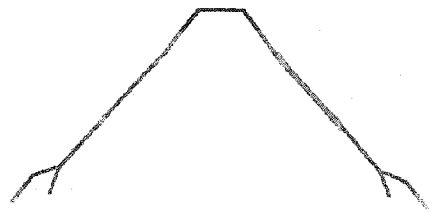
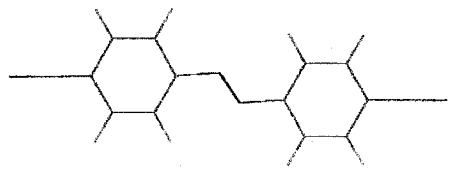
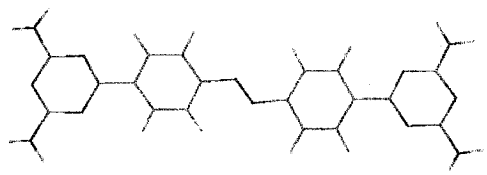
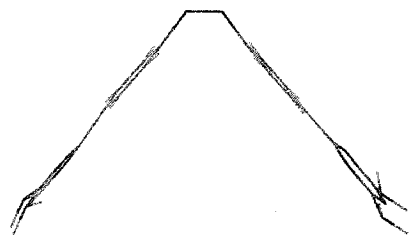
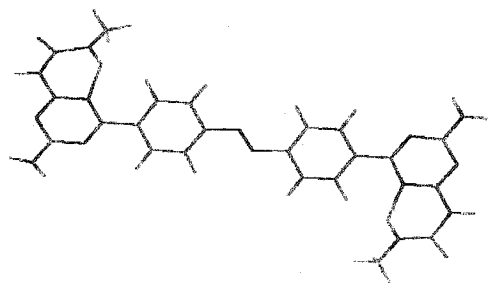
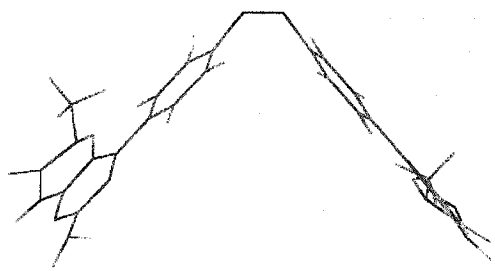
gave 119.9° C-N=N angles for *trans-p*-azobisbenzodiaminotriazine and *p*-azobisbenzoureidotriazine, indicating that the hydrogen-bonding extremities adopt the same 180°-orientation as in *trans-p*-azodibenzoic acid. As for the *cis-p*-azobisbenzodiaminotriazine and *p*-azobisbenzoureidotriazine monomers, a 127.0° C-N=N angle was obtained, giving a 80°-orientation between the binding units. Therefore, these theoretical studies suggest that the 180°-angle between the cyano groups in *trans*-**7** can lead to the formation of infinite linear tapes upon coordination with Ag(I) metal ions, while the 80°-orientation between the cyano groups in *cis*-**8** should preferably give macrocyclic tetramers when bound to Ag(I) ions.

The PM3 evaluated orientation of the diaminotriazine groups in *trans*- **9** and *cis*-**10** was identical to the calculated carboxylic acid groups in *trans*-**1** and *cis*-**2** and should result in the formation of linear tapes and tetrameric macrocycles. However, the 120°-orientation of the binding units in diethylbarbituric acid **14** cannot lead to the formation of infinite linear tapes from *trans*-azobisbenzodiaminotriazine **9**, nor to macrocyclic tetramers from *cis*-azobisbenzodiaminotriazine **10**. In the case of the *trans* isomer, the combination of linear azobenzene monomers with 120°-ditopic units can result in the formation of crinkled tapes or dodecameric rosettes. On the other hand, the molecular recognition of quasi-perpendicular *cis*-azobisbenzodiaminotriazine **10** by diethylbarbituric acid should give helical structures or octameric macrocycles (see description in 6. 2. 7.).

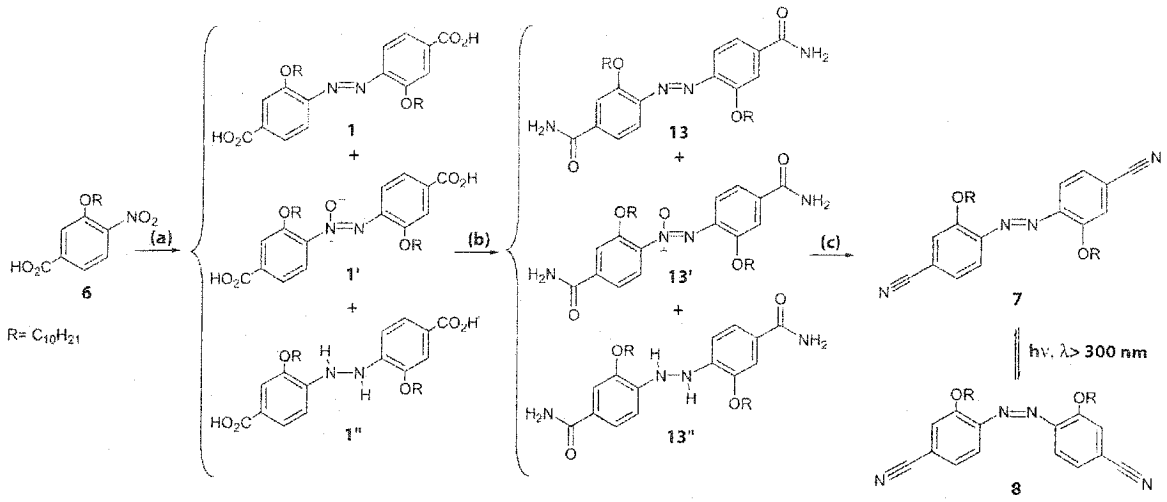
Trans- and *cis*- azobisbenzoureidotriazine **11** and **12** geometries were also optimised to adopt 180° and 80°-angles between the hydrogen-bonding units respectively, as for< the carboxylic acid groups in *trans*- and *cis*-azodibenzoic acid.

Consequently, the *trans*- ureidotriazine **11** should give ologomeric linear tapes, while *cis*-**12** should self-assemble into macrocyclic tetramers (see description in 6. 2. 8.).

Table 6. 1. *Trans*- and *cis*-azobenzene model monomers optimised using semi-empirical PM3 calculations.

PM3 geometry optimised *trans*- monomers	PM3 geometry optimised *cis*-monomers
 H_f = -87.67 kcal/mol	 H_f = -85.70 kcal/mol
 H_f = 161.70 kcal/mol	 H_f = 164.20 kcal/mol
 H_f = 158.67 kcal/mol	 H_f = 160.70 kcal/mol
 H_f = 78.10 kcal/mol	 H_f = 80.14 kcal/mol

6.2.2. Synthesis of *trans*-Azobisbenzonitrile 7



Scheme 6. 3. Synthesis of *trans*-azobisbenzontrile 7. (a) Zn dust (3 eqs.), aq. NaOH (30 %), 80-85 °C, 3 days, crude yield 60 %. (b) Neat $SOCl_2$, reflux, 4 hrs; aq. NH_3 (50 %), 0 °C → r. t., 12 hrs, *ca.* 90 %. (c) $POCl_3$, toluene, reflux, 5 hrs, 65 %.

The synthesis of *trans*-azobisbenzonitrile **7** from 3-decyloxy-4-nitrobenzoic acid **6** is shown in Scheme 6. 3. Reduction of 3-decyloxy-4-nitrobenzoic acid **6** with Zn dust in concentrated aqueous NaOH gave a mixture of azo-**1**, azoxy-**1'**, and hydrazo-**1''**-dibenzoic acids.[2] The crude mixture containing **1** was directly heated to reflux temperature in presence of neat thionyl chloride for 4 hrs, leading to a mixture of acyl chloride derivatives upon evaporation, which were treated with aqueous ammonia at room temperature. The obtained diamides **13**, **13'**, and **13"** were finally dehydrated at 80°C using $POCl_3$, to yield dicyano derivatives. The desired azobenzene derivative **7** was isolated by column chromatography.

6.2.3. Reversible Photoisomerization of *trans*-Azobisbenzonitrile 7 to the *cis*-Form 8

Similar to *trans*-azodibenzoic acid **1**, the ability of *trans*-azobisbenzonitrile **7** to reversibly isomerise upon irradiation with UV light to *cis*-azobenzonitrile **8** was monitored by UV-Vis and ^{1}H NMR. As for diacid **1**, the photoisomerisation of *trans*-azobisbenzonitrile **7** at $\lambda > 300$ nm in dichloromethane was reflected by the decrease of the two 315 and 390 nm absorbance maxima and the emergence of a new peak around 270 nm for the *cis*-**8**, leading to an isobestic point at 286 nm (Figure 6. 2). The formation of *cis* –azobisbenzonitrile **8** was clearly observed by the appearance of ^{1}H NMR peaks, distinct from *trans*-isomer **7** during photolysis.

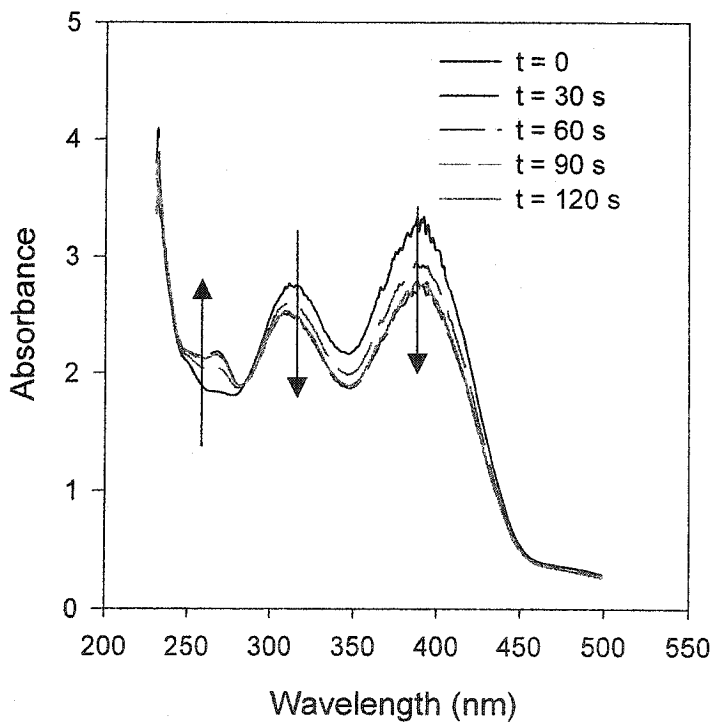


Figure 6. 2. UV-Vis spectrum of the photoirradiation of *trans*-**7** azobisbenzonitrile derivative in CH_2Cl_2 ($\lambda > 300$ nm).

Photoirradiation of *trans*-azobisbenzonitrile **7** at $\lambda > 300$ nm lead to a 1:0.3 trans/cis photostationary state,[5] which was reached more rapidly (15 min) than in the case of *trans*-**1** at room temperature. This result suggests a lower isomerisation energy barrier between the *trans*-**7** and *cis*-**8** azobisbenzonitrile isomers than between *trans*-**1** and *cis*-**2**, which shortens photoisomerisation time for the *trans*- isomer but, at the same time, affects isomerisation yields by allowing the thermal conversion of the *cis*-azobenzene derivative.

Preparative, thick layer chromatography of photoirradiated ($\lambda > 300$ nm) samples of azobisbenzonitrile **7** on alumina showed two separate orange bands, consistent with the presence of the two distinct, *trans* and *cis* isomers. The more polar coloured band, which corresponds to *cis*-azobisbenzonitrile **8,** could be isolated in a powder form. However, the isolated product was a *ca.* 1:1 mixture of *trans*-**7** and *cis*-azobisbenzonitrile **8** was observed by ^{1}H NMR, indicating that the *cis* isomer promptly isomerised thermally during the liquid extraction and evaporation steps.

Semi-empirical PM3 theoretical calculations were carried out to understand the discrepancies between the photochemical behaviour of the azodibenzoic acids, **1** and **2**, and the azobisbenzonitriles, **7** and **8**. Rotational energy scans were performed for the C-N=N-C torsion angle, which changes during isomerisation, using 2,2'-dimethoxy-azodibenzoic acid and 2,2'-dimethoxy-azobisbenzonitrile as model compounds (Figure 6. 3). The energy plotted as a function of the dihedral angle ω (Figure 6. 3a) showed two minima at 5.03° and 180.03 ° for *cis*- and *trans*-isomers respectively, separated by a 28.4 kcal.mol^{-1} energy barrier in the case of 2,2'-dimethoxy-azobisbenzonitrile. Rotational energy scans performed for 2,2'-dimethoxy-azodibenzoic acid gave dihedral angle

minima for *cis*- and *trans*-isomers at –0.56° and 176.0°, with a significantly greater isomerisation energy barrier (40.8 kcal.mol^{-1}, Figure 6. 3b). This difference in the theoretical PM3 isomerisation energy barriers is consistent with the UV-vis and ^{1}H NMR results, which showed a higher photoisomerisation yield for *trans*-azodibenzoic acid **1** than for *trans*-azobisbenzonitrile **7** and greater thermal stability for *cis*-azodibenzoic acid **2** than for *trans*-azobisbenzonitrile **8**.

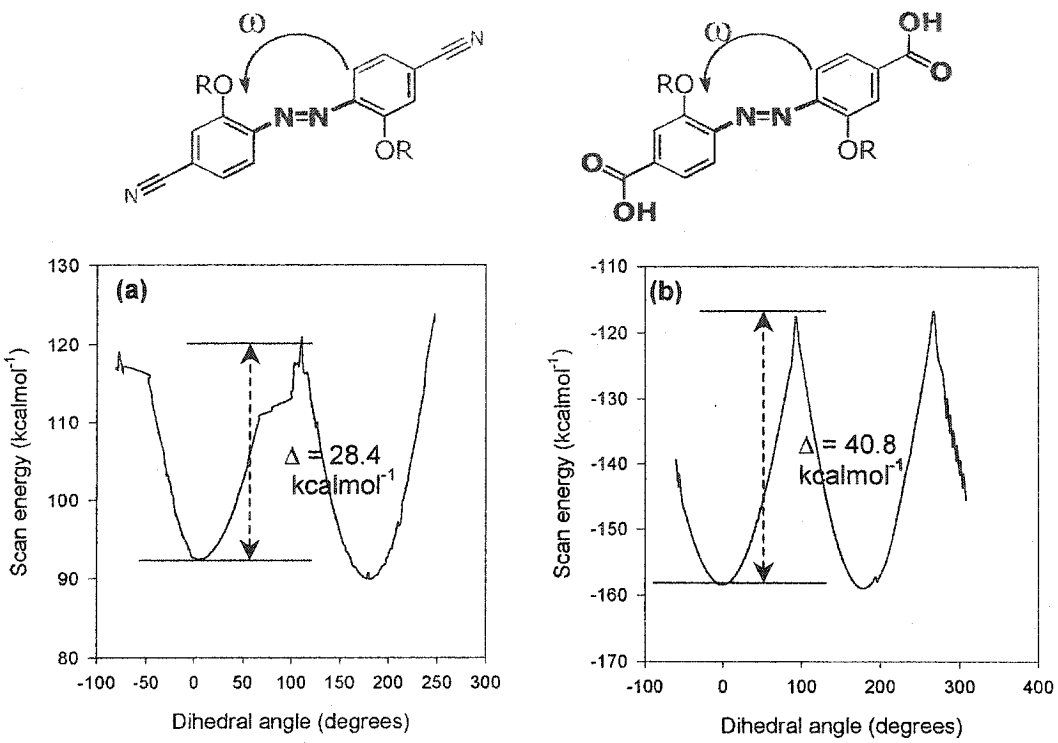
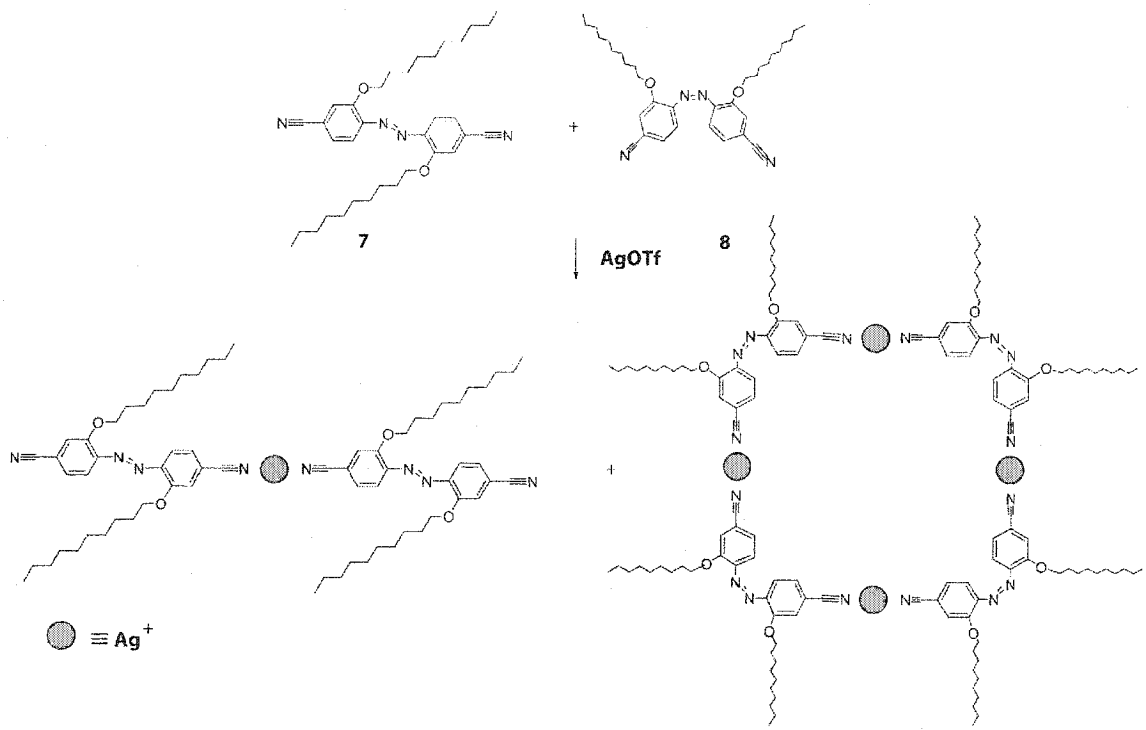


Figure 6. 3. (a) PM3 energy scan of ω, corresponding to the dihedral angle C-NN-C, in the 2,2'-dimethoxy-azobisbenzonitrile (inset). (b) PM3 energy scan of ω, corresponding to the dihedral angle C-NN-C, in the 2,2'-dimethoxy-azodibenzoic acid (inset).

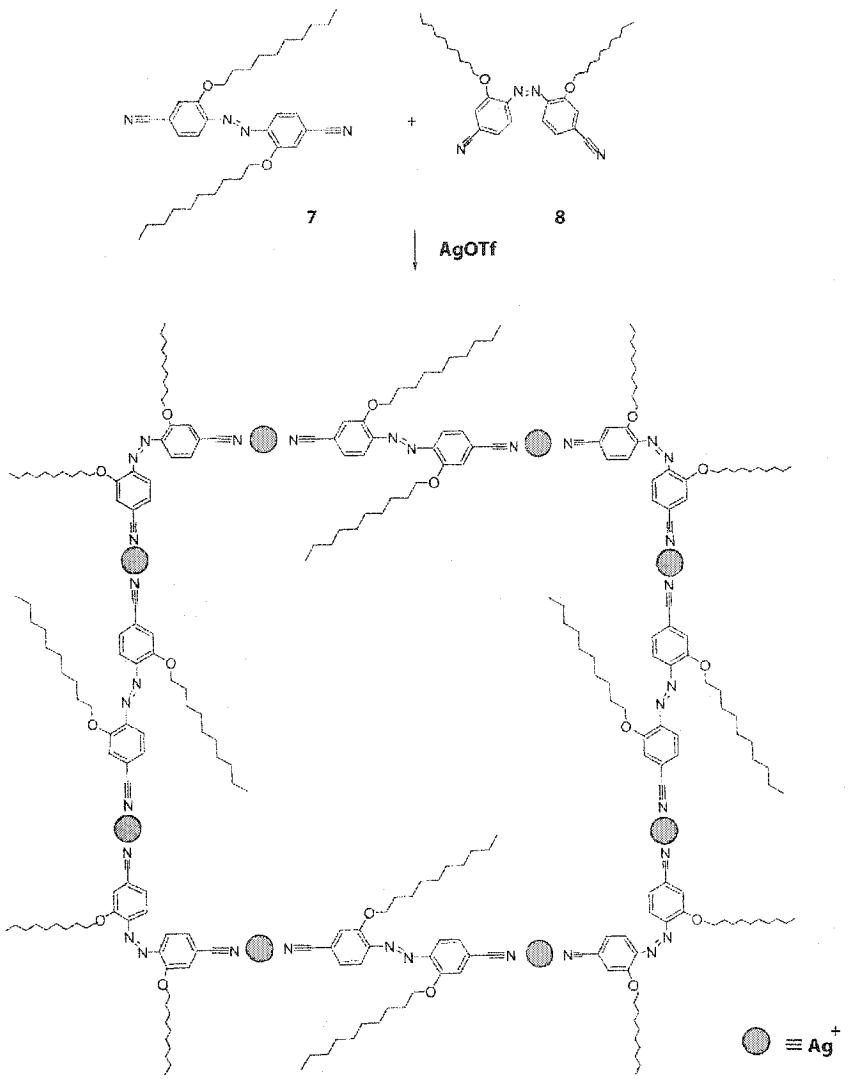
6.2.4. Self-Assembly of *trans*- 7 and *cis*- Azobisbenzonitrile 8

The formation of supramolecular structures from *trans*-**7** and *cis*-**8** in solution was investigated by ^{1}H NMR. Difficulties in isolating the *cis*-azobisbenzonitrile monomer required all the self-assembly studies to be carried out for 1:1 *trans/cis* mixtures, and not for the pure isomers. Among the many models for the metal coordination of silver(I) to an equimolar mixture of *trans*-**7** and *cis*-**8** azobisbenzonitrile, two models shown in Schemes 6. 4 and 6. 5 can be envisaged. The first model corresponds to the simultaneous

formation of linear tapes from *trans*-**7** and Ag(I) and cyclic tetramer from *cis*-**8** and Ag(I) (Scheme 6. 4). The second model involves the assembly of all three components into a unique supramolecular structure (Scheme 6. 5). In this supramolecular square, the corners consist of four *cis*-**8** monomers which are joined to *trans*-**7** linear linkers through metal coordination with Ag(I).



Scheme 6. 4. Self-assembly of *trans*-**7** and *cis*-**8** azobisbenzonitrile derivatives into metal-coordinated linear tapes and cyclic tetramers.



Scheme 6. 5. Proposed model for the self-assembly of *trans*-**7** and *cis*-**8** azobisbenzonitrile derivatives into a metal-coordinated cyclic octamer.

^{1}H NMR spectra of the *trans-cis* equimolar mixture in $CDCl_3$ (Figure 6. 4a) and in C_6D_6 (Figure 6. 4b) were found to display significant differences in the aromatic (6-8 ppm) and in the α-methylenic ether regions (4-3 ppm). While the symmetry of the aromatic peaks was preserved with solvent change, four triplets were seen in deuterated benzene for the methylenic protons, instead of two in deuterated chloroform. This result

suggests that intermolecular interactions may occur between the monomers, *trans*-**7** and *cis*-**8** and benzene molecules.

The titration of the *trans*-**7**/*cis*-**8** 1:1 mixture in C_6D_6 with a solution of silver triflate in C_6D_6 was monitored by ^1H NMR as in Figures 4b-d. For *trans*-**7**, one equivalent of added AgOTf induced downfield shifts for the aromatic proton H_b (+ 0.10 ppm) and for the α-methylenic protons (+ 0.06 ppm), consistent with metal coordination between *trans*-azobisbenzonitrile monomers and silver(I) ions. Larger downfield shifts were observed for the aromatic proton $H_{a'}$ (+ 0.15 ppm) and for the α-methylenic protons (+ 0.1 ppm) of the *cis*-**8** isomer upon addition of 1 equivalent of silver(I) ions, resulting in the coalescence of the α-methylenic protons. Addition of 1 equivalent of silver(I) ions resulted in the emergence of a single set of symmetrical peaks from both *trans*- and *cis*-isomers (Figure 6. 4c). This observation suggests that discrete metal-coordinated supramolecular species may form in solution, following the model displayed in Scheme 6. 5. However, the formation of a single silver(I)/azobenzonitrile complex in solution can also result in symmetrical ^1H NMR spectra. Further addition of silver(I) ions does not affect the symmetry of the ^1H NMR spectrum of the *trans*/*cis* 1:1 mixture (Figure 6. 4d), showing the stability of the formed supramolecular structure.[6] This result is consistent with possible peripheral coordination of silver(I) ions to small, electron-rich binding pockets provided by the ether oxygen atoms and the *cis*-azobenzene nitrogen atoms (Figure 6. 5).

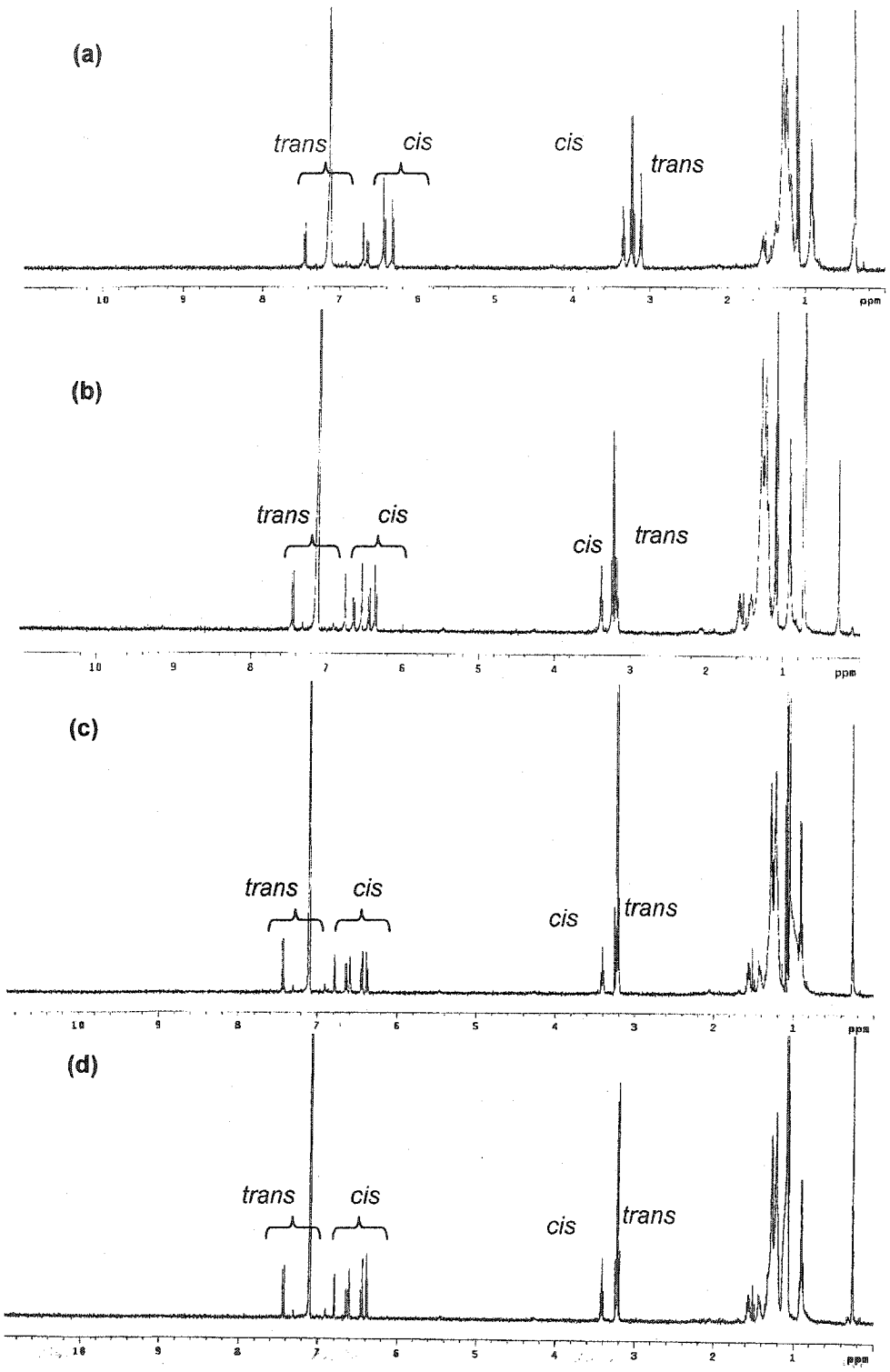


Figure 6. 4. ^{1}H NMR titration of equimolar mixture of *trans*-**7**/*cis*-**8** azobisbenzonitrile using AgOTf. (a) Before titration. (b) After adding 0.5 eq of AgOTf. (c) After adding 1.0 eq. of AgOTf. (d) After adding 2.0 eq. of AgOTf.

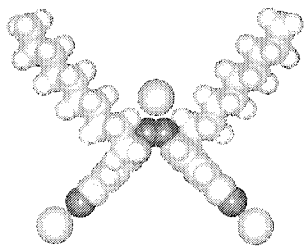


Figure 6. 5. Representation of peripheral coordination of silver(I) ions to the ether oxygen atoms and the nitrogen atoms of *cis*-**8**.

The titration of the *trans*-**7**/*cis*-**8** 1:1 mixture in benzene with a solution of silver triflate in benzene was monitored by UV-vis as in Figure 6. 6. The addition of silver(I) solution to an equimolar mixture of *trans*-**7** and *cis*- azobisbenzonitrile **8** in benzene was reflected by the decrease of the two 315 and 390 nm absorbance maxima and the emergence of a new peak around 500 nm, leading to an isobestic point at 426 nm (Figure 6. 6a). The absorbance of the 1:1 *trans/cis* mixture was also monitored as a function of the concentration of silver(I) ions at λ = 500 nm. The absorbance plot displayed a first linear increase followed by a plateau, which intersected at 1 eq. AgOTf (Figure 6. 6b). This result indicates that aggregation may occur between *trans*-**7** and *cis*-azobisbenzonitrile **8** and silver(I) ions. This behaviour is consistent with the absence of change in the ^{1}H NMR spectra after this concentration (Figure 6. 4b-d).

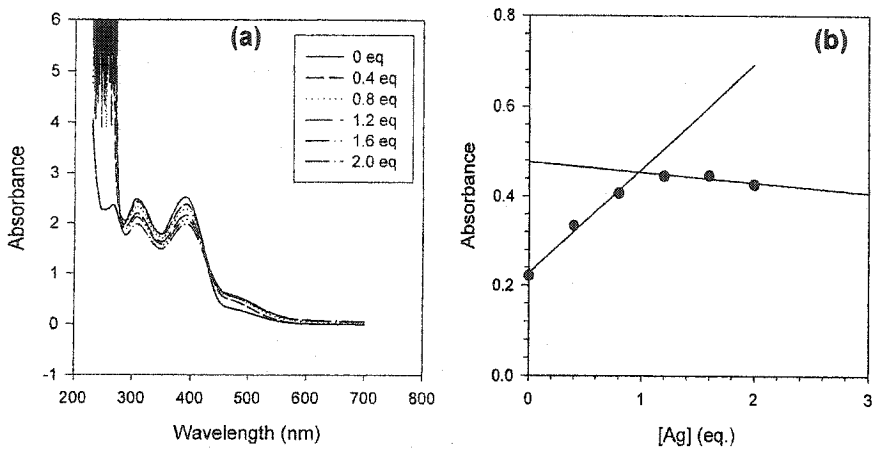


Figure 6. 6. (a) UV-Vis titration of the equimolar *trans*-**7**/*cis*-**8** mixture by AgOTf. (b) Absorbance of the equimolar *trans*-**7**/*cis*-**8** mixture by AgOTf at $\lambda = 500$ nm.

6.2.5. Transmission Electron Microscopy of *trans*- 7 and *cis*-Azobisbenzonitrile 8 in presence of Ag(I)

Transmission electron microscopy (TEM) studies of *trans*-**1** and *cis*-azodibenzoic acid **2** allowed direct visualisation of the dramatic differences between their self-assembled structures at the microscopic level. In the case of *trans*-**7** and *cis*-azobisbenzonitrile **8**, transmission electron microscopy should reflect the metal coordination of both monomers, present as a mixture. By analogy to our previous dicarboxylic acid system,[2] linear tapes built from *trans*-**7** can appear as large, sheet-like aggregates, while periodic arrays of elongated aggregates can arise from the formation of cyclic tetramers *cis*-**8** isomer as observed for *trans*-**1** and *cis*-azodibenzoic acid **2** according to the first model (Scheme 6. 3). Figure 6. 7 shows a typical example of transmission electron micrograph prepared from equimolar mixtures of *trans*-**7** and *cis*-**8** in benzene in presence of silver triflate. The TEMs of samples of *trans*-**7** and *cis*-

azobisbenzonitrile **8** mixtures show periodic arrays of elongated aggregates (Figure 6. 7a) with length as great as 100 nm. The outer diameter of these elongated aggregates was determined to be 4.5 nm from the intensity profile of the electron micrograph (Figure 6. 7c), which measures the contrast across the rod-like structures, hence the topography. Many interpretations can be given to the presence of these higher-order. One explanation is that self-assembled macrocyclic structures may result from the complexation of silver(I) ions with *trans*-**7** and *cis*-**8** in benzene, as proposed in Scheme 6. 3, and that these macrocycles may self-organise into higher-order arrays. The outer diameter measured for these aggregates (Figure 6. 7b) , in agreement with the estimated diameter of the self-assembled supramolecular cycles which incorporate both *trans*-**7** and *cis*-**8** monomers (4.4 nm).[7]

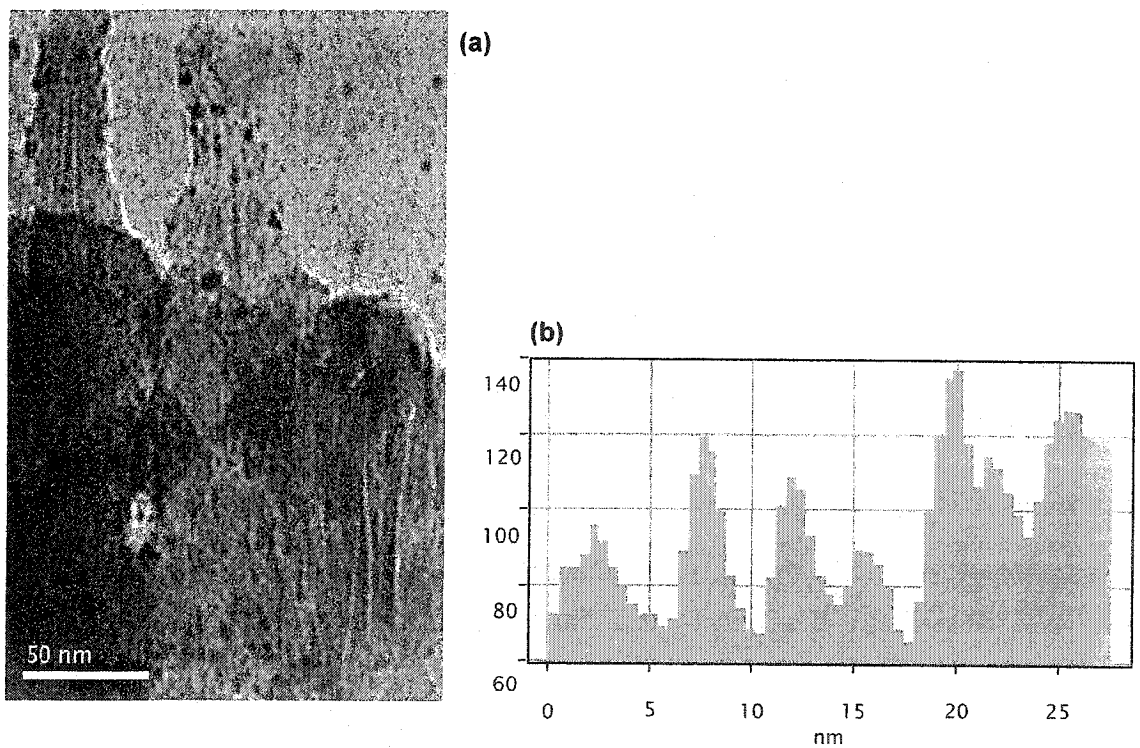
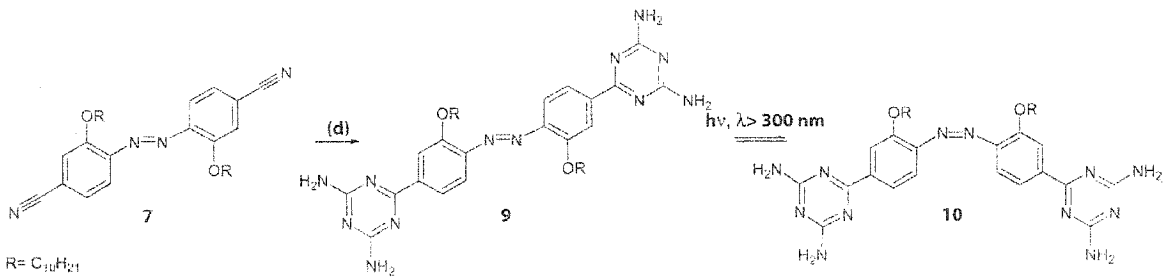


Figure 6. 7. (a) Electron micrograph of the equimolar mixture of *trans*-**7**/*cis*-**8**/AgOTf . (b) Profile analysis of electron micrograph (a).

Preliminary investigations of the metal-coordination of *trans*-**7** and *cis*-**8** were carried out using silver(I) as binding ions. ^{1}H NMR and UV-vis spectroscopy showed the favourable complexation between the metal ions and the organic ligands, and the possible formation of self-assembled species in solution. Preliminary visualisation of the formed complex by TEM indicated that higher-order aggregates can arise from the three-component mixture. Further investigations are underway to characterise the nature of these aggregates and to incorporate different late transition metals to azobisbenzonitrile mixtures.

Synthesis of *trans*-Azobisbenzodiaminotriazine 9



Scheme 6. 6. Synthesis of *trans*-azobisbenzodiaminotriazine **9** from *trans*-azobisbenzonitrile derivative **7**. (d) Dicyandiamide, KOH, *i*-PrOH, reflux, 1 day, 28 %.

Various attempts involving the one-step reaction fom the methyl ester derivative of **1** with biguanidium sulfate in basic media were unsuccessful.[8] A synthetic route of *trans*-azobisbenzodiaminotriazine **9**, exploiting *trans*-azobisbenzonitrile **7** as key intermediate, was followed instead (Scheme 6. 6). In this reaction, dicyano derivative **7** was coupled with dicyandiamide under basic conditions to yield the desired compound, which was purified by chromatography.

6.2.7. Self-Assembly of *trans*-9 and *cis*-Azobisbenzodiaminotriazine 10

6.2.7.1. Design of Theoretical Models for the Self-Assembly of *trans*-9 and *cis*-Azobisbenzodiaminotriazine 10

The diaminotriazine azobenzene derivatives *trans*-**9** and *cis*-**10** adopt similar geometries as *trans*- and *cis*-azobenzene dicarboxylic acid derivatives as predicted by PM3 calculations. However, the use of non-linear diethylbarbituric acid guest to form hydrogen-bonded supramolecular structures will strongly affect the self-assembly of linear tapes from *trans*-**9** and cyclic tetramers from *cis*-**10**. Theoretical calculations were thus necessary to measure the extent of such a change over hydrogen-bonding as well as to predict and evaluate the geometries of the resulting hydrogen-bonded *trans*-**9** and *cis*-azobisbenzodiaminotriazine **10** with diethylbarbituric acid systems. Two types of supramolecular model systems were used to perform the geometry optimisations. The first model system consists of unsubstituted *trans*- and *cis*-*p*-azobisbenzodiaminotriazine hydrogen-bonded to diethylbarbituric acid monomers. The choice of a second model system became essential to reduce computational time, inherent to the number of atoms involved in the calculation, without losing any valuable geometrical or electronic information. In this second model system, the diaminotriazine derivatives **9** and **10** were replaced by *trans*- and *cis*-*p*-azodibenzoic acid, while the diethylbarbituric acid by its equivalent, the isophthalic acid using a geometry argument.

PM3 optimised dimeric structures obtained from hydrogen-bonding between *trans*- and *cis*-diaminotriazine azobenzene monomers and diethylbarbituric acid were first compared with PM3 optimised hydrogen-bonded dimers of *trans*- and *cis*-azodibenzoic

acid with isophthalic acid. In Chapter 4, the calculated aggregate structures indicated that the monomers retained their geometry from one oligomer to another, and the hydrogen-bond geometry did not change significantly from one degree of aggregation n to the next $n+1$, as expected for supramolecular assemblies. As shown in Tables 6. 2 through 6. 4, the calculated dimer geometries, in particular the orientation of the recognition units which is essential in determining the geometry of the self-assembly product, were identical in both sets of building blocks. As for the monomers, the azobenzene binding sites were approximately 80° apart. As expected from model design, the recognition sites in diethylbarbituric and isophthalic acids were both found to be oriented at a 120° angle.

The PM3 hydrogen-bond geometries involving the azodibenzoic acid/isophthalic acid pair indicated that the C=O bond lengthened slightly from 1.22 Å to 1.23 Å, the O–H bond from 0.95 Å to 0.97 Å upon hydrogen-bond formation. The C–O bond shortened from 1.36 Å to 1.34 Å, while the C–O–H angle opened from 109° to 112°, giving rise to the hydrogen-bond (O···H = 1.77 Å). These results agreed with the optimized azodibenzoic acid aggregates[9] as well as X-ray data for carboxylic acid dimers. In contrast with hydrogen-bond formation in *trans*- and *cis*- azodibenzoic acids, hydrogen-bond formation in *trans*- and *cis*- azobisbenzodiaminotriazine derivatives does not require bond angle opening because of the proper alignment of the triazine donor-acceptor-donor units relative to the barbituric acid acceptor-donor-acceptor units. Nevertheless, a 0.99 Å to 1.01 Å NH bond lengthening was observed from the triazine amino groups along with a longer C=O (1.22 Å to 1.24 Å) and NH bonds (1.00 Å to 1.63 Å) in the barbituric acid amido group, resulting in strong hydrogen bonds (N···H = 1.07 Å and O···H = 1.77 Å) .

The frontier molecular orbitals (MO) of the hydrogen-bonded dimers formed by the diaminotriazine derivatives were compared with the frontier molecular orbitals of the dicarboxylic acid dimers (Tables 6. 2 - 6. 5). The HOMO and LUMO contour plots and energies of the *trans*- and *cis*-diaminotriazine dimers (Tables 6. 2 and 6. 4) were found similar to the HOMO and LUMO contour plot and energy of the dicarboxylic acid dimers (Tables 6. 3 and 6. 5). In the *trans*- diaminotriazine and diacid dimers, the highest occupied (HOMO) and lowest occupied molecular orbitals (LUMO) covered the azobenzene derivatives exclusively (Table 6. 2), indicating that the azobenzene units, rather than the diaminotriazine or the carboxylic ends are the main reactive sections. Likewise, the HOMO and LUMO of the *cis*-aggregates mainly covered the azobenzene part of the molecules, in agreement with previously calculated hydrogen-bonded azobenzene derivatives. The HOMO-LUMO gap of the *trans*-azodibenzoic acid-isophthalic acid dimer ($\Delta E_{HOMO\text{-}LUMO}$ = 8.31 eV) is significantly larger than the HOMO-LUMO gap of the *trans*-azobisbenzodiaminotriazine/ diethylbarbituric acid dimer ($\Delta E_{HOMO\text{-}LUMO}$ = 7.95 eV), consistent with increased number of π-symmetry molecular orbitals due to the presence of additional aromatic rings in the diaminotriazines. Similarly, the HOMO-LUMO gap of the *cis*-azodibenzoic acid/ isophthalic acid dimer ($\Delta E_{HOMO\text{-}LUMO}$ = 8.65 eV) is greater than the HOMO-LUMO gap of the *cis*-azobisbenzodiaminotriazine-diethylbarbituric acid dimer ($\Delta E_{HOMO\text{-}LUMO}$ = 7.78 eV).

Table 6. 2. *Trans*-azobisbenzotriazine/diethylbarbituric acid model dimers optimised using semi-empirical PM3 calculations, along with their frontier and hydrogen-bonding molecular orbitals

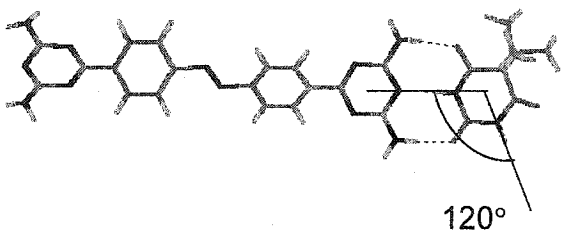
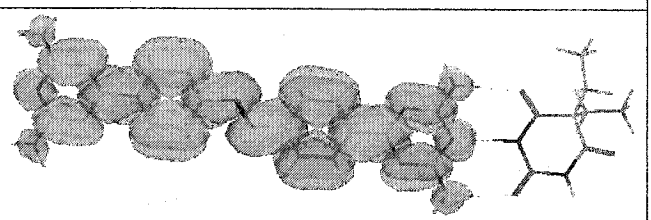
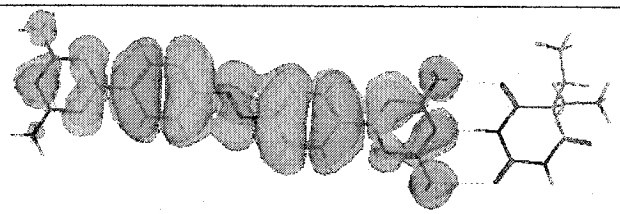
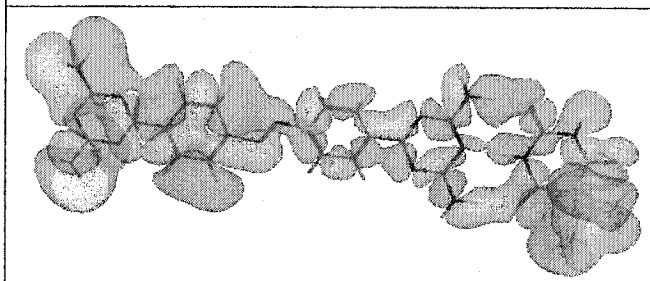
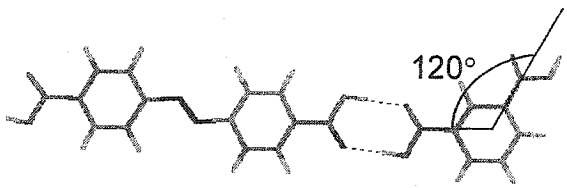
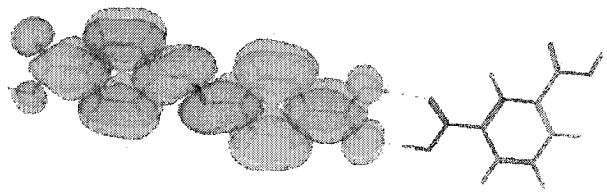
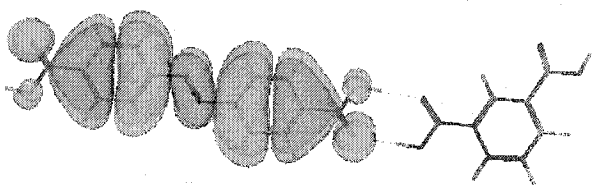
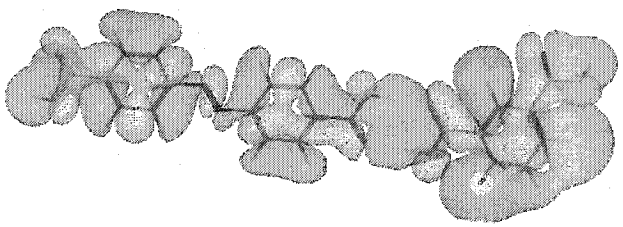
PM3 optimised *trans*- dimer geometries	PM3 frontier molecular orbitals
	 LUMO E = -1.12 eV
	 HOMO E = -9.07 eV
	 MO 54 E = -16.16 eV

Table 6. 3. *Trans*-azodibenzoic acid/isophthalic acid model dimers optimised using semi-empirical PM3 calculations, along with their frontier and hydrogen-bonding molecular orbitals.

PM3 optimised *trans*- dimer geometries	PM3 molecular orbitals
	 LUMO E = -1.51 eV
	 HOMO E = -9.82 eV
	 MO 40 E = -16.87 eV

As in the case of the hydrogen-bonded azodibenzoic acid aggregates (see Chapter 4), several molecular orbitals involved in hydrogen-bonding formation were observed at much lower energies than the HOMO (Tables 6.2 - 6.5). Unlike the MOs in weakly bound PEO/corilagin systems which showed a pinch in the lobe overlapping the O···H bond,[10] the hydrogen-bonding MO diagrams for the dimers displayed in Tables 6.2 - 6.5 clearly showed a single lobe over the hydrogen-bond, consistent with the formation of strong hydrogen-bonded aggregates. The MO contour plots and energies of the *trans*-

and *cis*-diaminotriazine dimers (Tables 6. 2 and 6. 4) were found similar to the MO contour plot and energy of the dicarboxylic acid dimers (Tables 6. 3 and 6. 5). In the *trans*- diaminotriazine and diacid dimers, the delocalised molecular orbitals covering the hydrogen-bonds spread over the entire complex (Tables 6. 2 and 6. 3), indicating that the azobenzene units and the acid do effectively form a stable hydrogen-bonded complex. Likewise, hydrogen-bonding MO of the *cis*-aggregates covered the entire dimers (Tables 6. 4 and 6. 5), suggesting the stability of the hydrogen-bonded *cis*- complexes. The geometrical features and electronic properties of azobisbenzodiaminotriazine/ diethylbarbituric acid dimer were calculated to be the same as for the azodibenzoic acid/isophthalic acid pair. As a result, the use of the *trans*- and *cis*-azodibenzoic acid/isophthalic acid should yield suitable geometrical and electronic analogues for the hydrogen-bonded structures generated by the synthesized *trans*-**9** and *cis*-**10** azobenzene derivatives (Figure 6. 1).

Table 6. 4. *Cis*-azobisbenzotriazine/diethylbarbituric acid model dimers optimised using semi-empirical PM3 calculations, along with their frontier molecular orbitals.

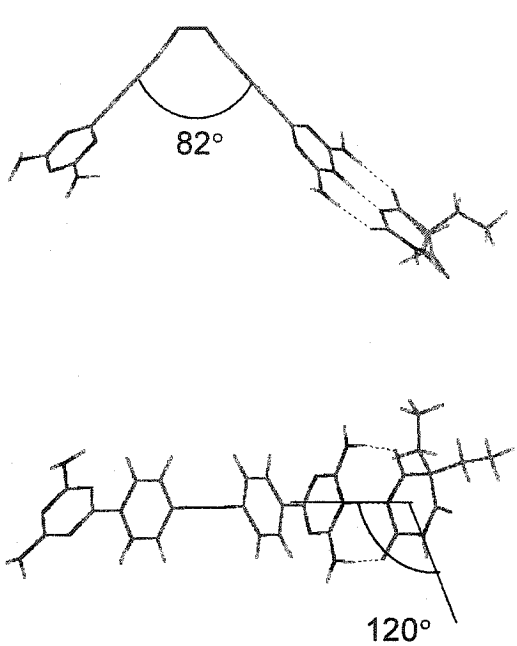
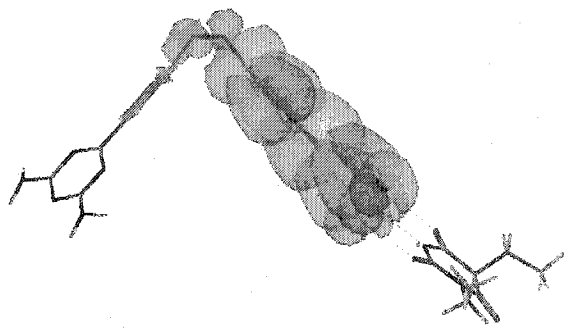
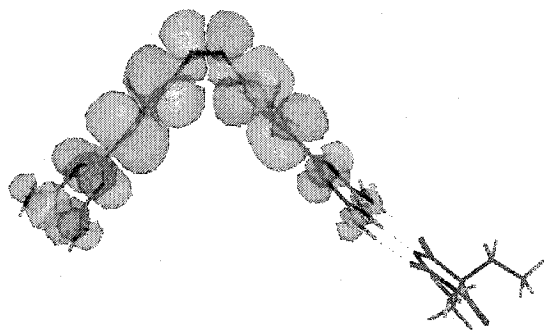
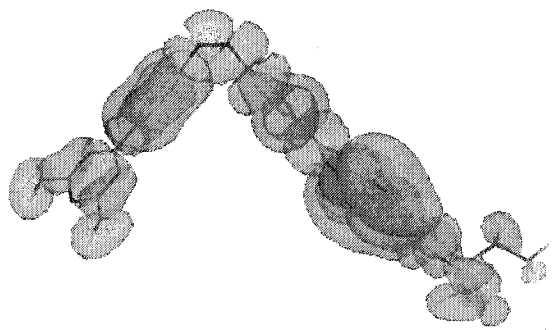
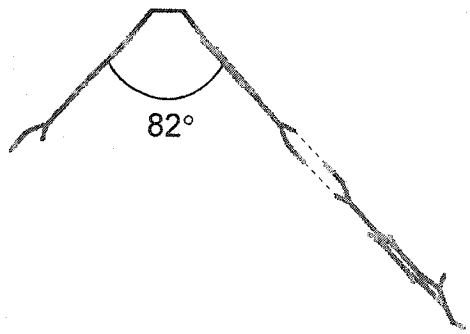
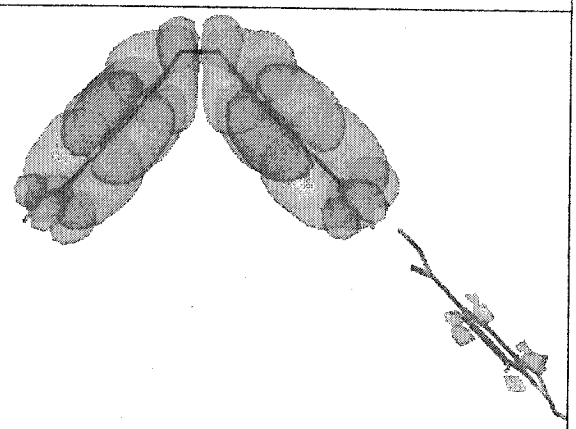
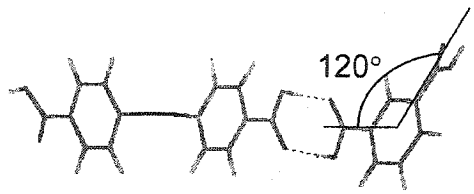
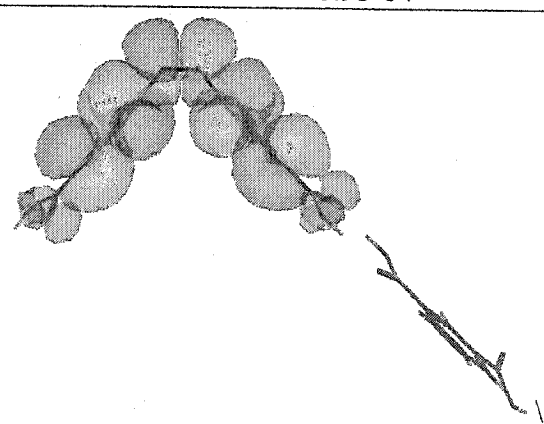
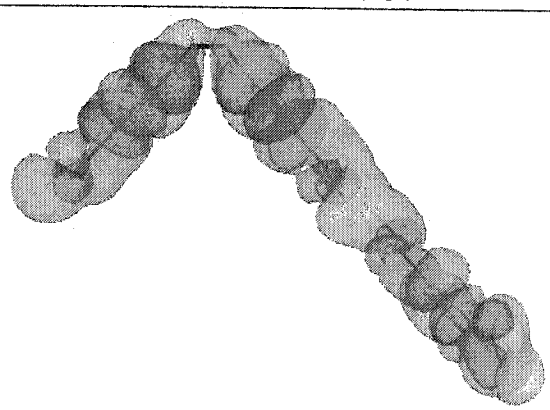
PM3 optimised *cis*-dimer geometries	PM3 molecular orbitals
	 LUMO E = - 1.51 eV  HOMO E = - 9.29 eV  MO 42 E = -19.16 eV

Table 6. 5. *Cis*-azodibenzoic acid/isophthalic acid model dimers optimised using semi-empirical PM3 calculations, along with their frontier and hydrogen-bonding molecular orbitals.

PM3 optimised *cis*- dimer geometries	PM3 molecular orbitals
	 LUMO E = - 0.95 eV
	 HOMO E = -9.60 eV
	 MO 40 E = -17.00 eV

6.2.7.2. Theoretical Evaluation of the Self-Assembly of *trans*-**9** and *cis*-Azobisbenzodiaminotriazine **10**

Hydrogen-bonded supramolecular structures displayed in Figures 6. 8 and 6. 9 represent the possible oligomeric systems that could be formed by *trans*-**9** and *cis*-**10** isomers. *Trans*-azobisbenzodiaminotriazine **9** can pair with diethylbarbituric acid to give linear tapes (Figure 6. 8a) or cyclic dodecamers (Figure 6. 8b), acting as a rigid-rod spacer between triple hydrogen-bonded recognition units. Like previously studied triazine-barbituric acid based-building blocks,[11] closing of the hydrogen-bonded structures into rings should be mainly influenced by the steric factor of the substituents on the monomers and the resulting packing properties of the supramolecular systems. The apparent lack of steric hinderance in the linear tape model (Figure 6. 8a) is expected to lead to the formation of oligomeric species from *trans*-**9**. Further theoretical investigations of the *trans*-azobisbenzotriazine structures were consequently considered unnecessary.

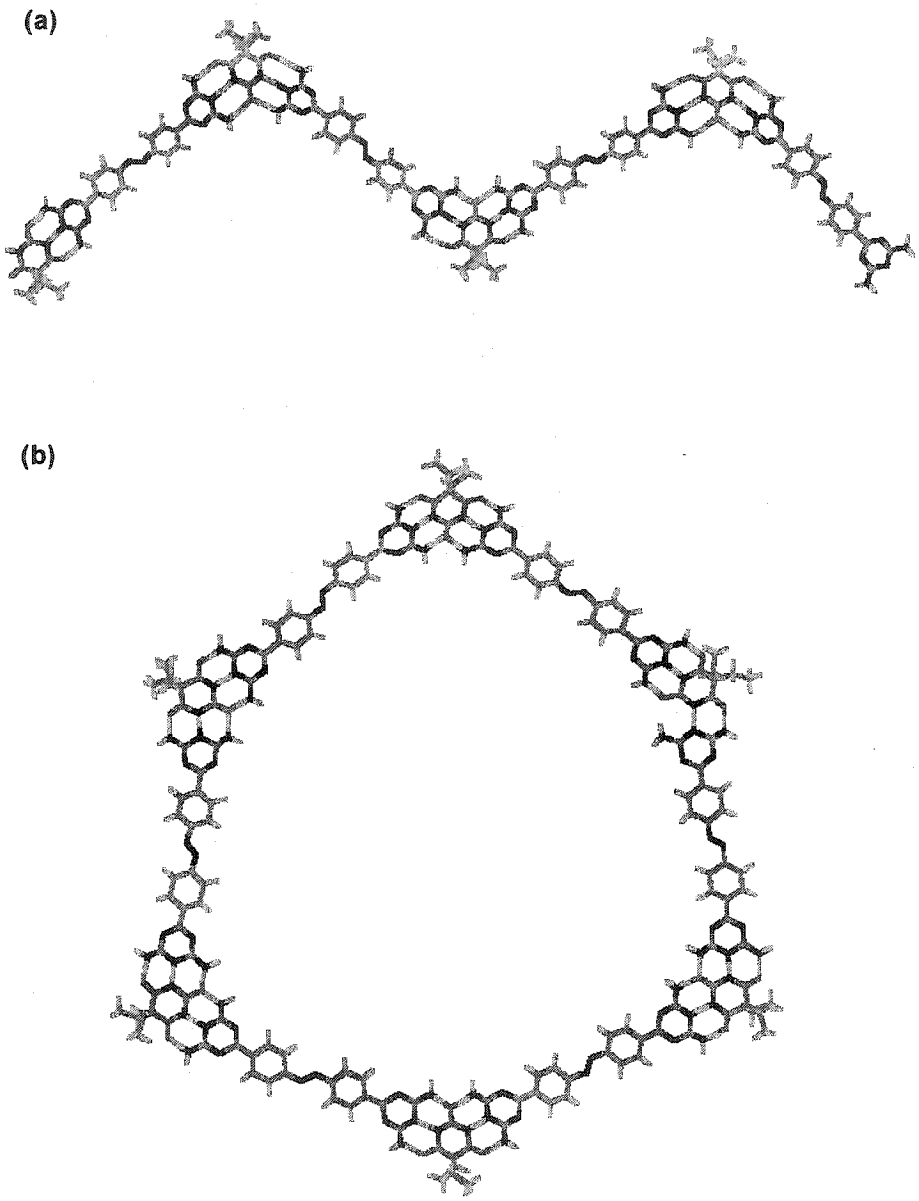


Figure 6. 8. (a) Representation of hydrogen-bonded linear tapes from *trans*-azobisbenzodiaminotriazine with diethylbarbituric acid. (b) Representation of hydrogen-bonded cyclic dodecamers from *trans*-azobisbenzodiaminotriazine with diethylbarbituric acid.

Because of the almost perpendicular orientation of its binding sites, the prediction of *cis*-**10** hydrogen-bond self-assembly with diethylbarbituric acid is more complex and, consequently, merits more attention. As demonstrated in Figure 6. 9, unusual supramolecular geometries can emerge from the 120°/90° diethylbarbituric acid/*cis*-azobisbenzodiaminotriazine combination, as open hydrogen-bonded helices (Figure 6. 9a) and closed boat-shape macrocycles can be created (Figure 6. 9b and c). Quantum mechanical methods were thus applied to get a better understanding of these hydrogen-bonded systems.

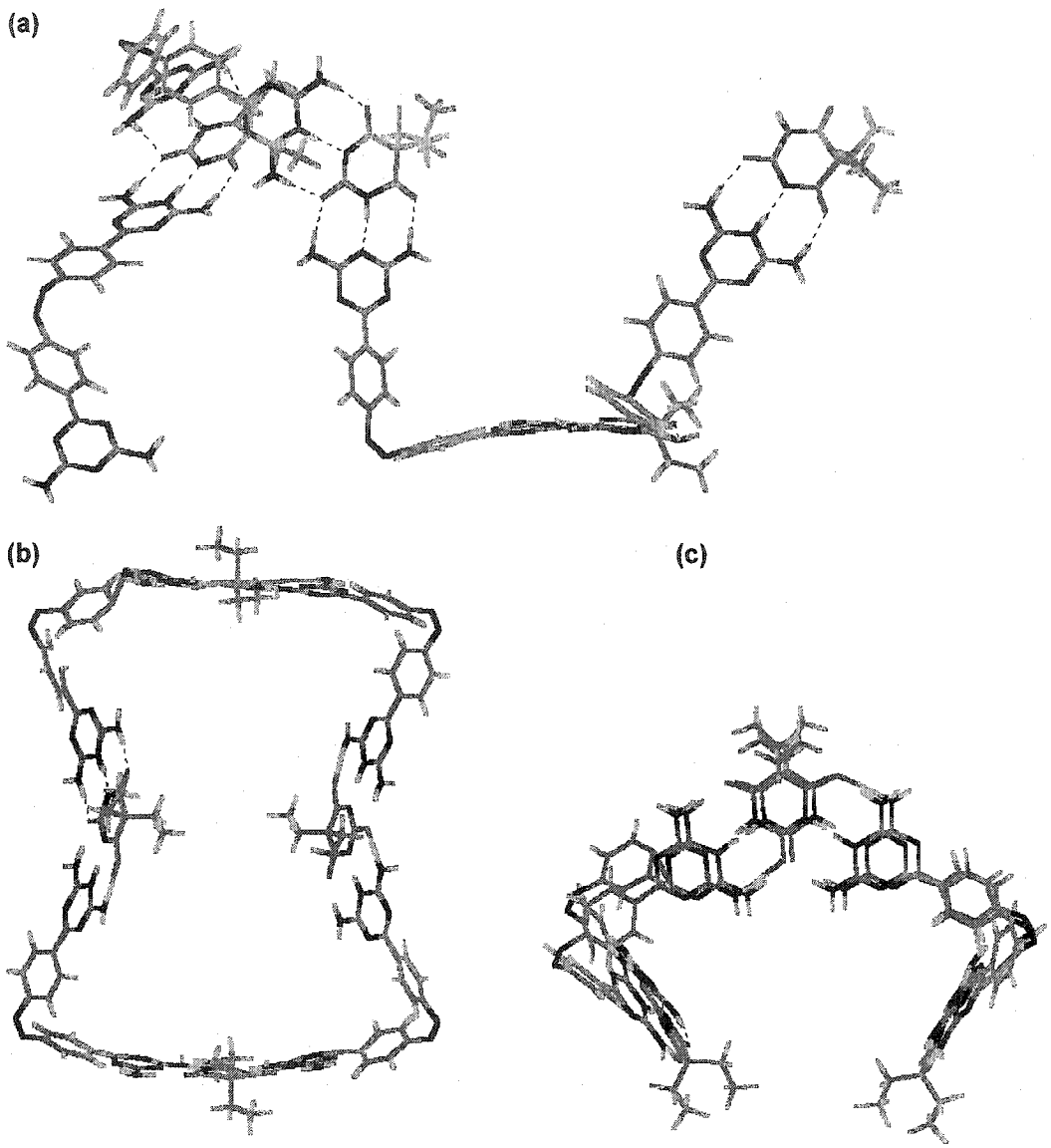


Figure 6. 9. (a) Representation of hydrogen-bonded helical octamers from *cis*-azobisbenzodiaminotriazine with diethylbarbituric acid. (b) and (c) Representation of hydrogen-bonded boat-like octamers from *cis*-azobisbenzodiaminotriazine with diethylbarbituric acid. (b) Top view. (c) Side view.

The computation study of these hydrogen-bonded structures was carried out using the *cis*-azodibenzoic acid/isophthalic acid model. The hydrogen-bonded analogues of these helical and boat-like structures were designed from *cis*-azodibenzoic and isophthalic acids and semi-empirical PM3 calculations were carried out to predict the self-assembly of *cis*-azobisbenzotriazine with diethylbarbituric acid, resulting in the octameric structures shown in Figure 6. 10.

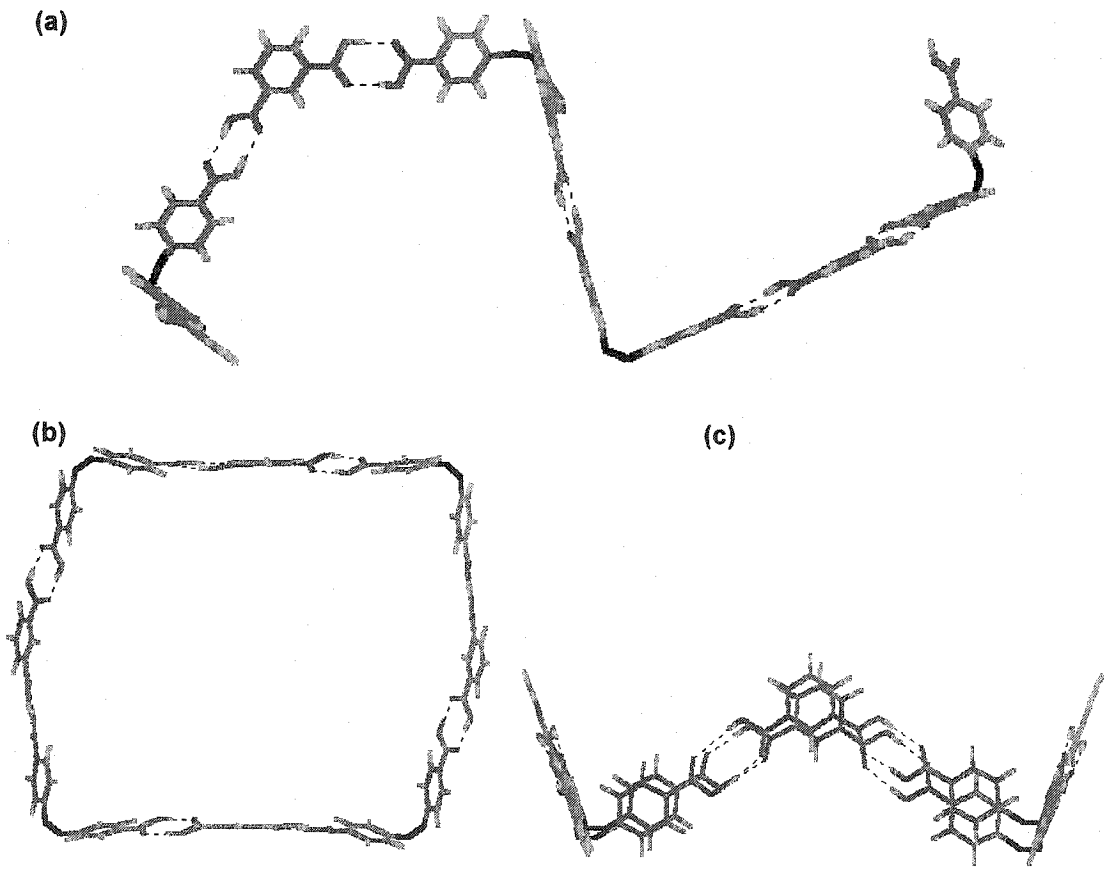


Figure 6. 10. (a) Representation of hydrogen-bonded helical octamers from *cis*-azodibenzoic acid with isophthalic acid. (b) and (c) Representation of hydrogen-bonded cyclic octamers from *cis*-azodibenzoic acid with isophthalic acid. (b) Top view. (c) Side view.

The PM3 optimised hydrogen-bonds in the octameric systems displayed geometries which were similar to the hydrogen-bonds formed in the *cis*-azodibenzoic acid/isophthalic acid dimers. Hydrogen-bond strengths were evaluated from the total enthalpies of these structures to identify which of the open or closed aggregate should be more favorably obtained by self-assembly. These hydrogen-bond enthalpies were calculated using:

$$\Delta H_{f\,2HB}(T) = \frac{H_f(M_{n+m}) - (n \times H_f(M_n) + m \times H_f(M_m))}{n_{2HB}} \quad \textbf{(Eq. 6. 1)}$$

where T is the temperature (T = 0 K), $H_f(M_n)$ is the enthalpy of the azodibenzoic acid monomer M_n, $H_f(M_m)$ is the enthalpy of the isophthalic acid monomer M_m, n_{2HB} the number of hydrogen-bond pairs, n the number of azodibenzoic acid monomers involved, m the number of isophthalic acid monomers involved, and $H_f(M_{n+m})$ the enthalpy of the hydrogen-bonded aggregate. Like in the single-component *cis*-azodibenzoic acid aggregates, the hydrogen-bonding enthalpies differed from one oligomer to the other. The enthalpies of formation calculated for the hydrogen-bonds amounted to - 8.9 kcal/mol in the helical structure versus – 8.2 kcal/mol in the boat-like macrocycle. The presence of weaker hydrogen-bonds in the macrocyclic octamer suggests that the *cis*-azodibenzoic acid self-assembly with isophthalic acid into open hydrogen-bonded oligomers is the preferred mode of aggregation.

Electronic evidence is necessary to gain insight into the formation of open, helical structures from *cis*-azodibenzoic and isophthalic acids. The HOMO and LUMO of the hydrogen-bonded helix (Table 6. 6) formed by the cis-azodibenzoic acid/isophthtalic acid

pair were compared with the frontier molecular orbitals of the cis-azodibenzoic acid/isophthtalic acid macrocycle (Table 6. 7). The HOMO contour plot of the cis-azodibenzoic acid/isophthtalic acid helix (Table 6. 7) were found similar to the HOMO diagram the azodibenzoic acid/isophthtalic acid macrocyle (Table 6. 6). The LUMO contour plot of the cis-azodibenzoic acid/isophthtalic acid helix (Table 6. 7) covered the azobenzene derivatives, indicating that the azobenzene units, rather than the carboxylic ends are the main reactive sections. However, the LUMO of the azodibenzoic acid/isophthtalic acid macrocyle also spread over the neighbouring isophthalic monomer (Table 6. 6), indicating that the hydrogen-bonded azobenzene/isophthalic section are reactive.

As in the case of the hydrogen-bonded azodibenzoic acid/isophthalic acid dimers (Table 6. 5), the hydrogen-bonding molecular orbitals involved in the formation of the azodibenzoic acid/isophthalic acid octamers were observed at much lower energies than the HOMO (Tables 6. 6 and 6. 7). Like the hydrogen-bonding MO diagrams for the dimers, the hydrogen-bonding MO diagrams for the helical octamers displayed in Table 6. 6 clearly showed a single lobe over the hydrogen-bond, consistent with the formation of strong hydrogen-bonded aggregates. In the *cis*-azodibenzoic acid/isophthalic acid helix, the delocalised molecular orbitals covering the hydrogen-bonds spread over the entire complex (Table 6. 6), indicating the *cis*-azodibenzoic acid and the isophthalic acid effectively form a cohesive hydrogen-bonded complex. Likewise, lowest occupied molecular orbital (LOMO) of the *cis*-azodibenzoic acid/isophthalic acid helix covered the entire structure (Tables 6. 6), suggesting the stability of the hydrogen-bonded *cis*-helical octamers. In contrast with the *cis*-azodibenzoic acid/isophthalic acid macrocycle, the

delocalised hydrogen-bonding molecular orbital only covered a section of the octamer (Table 6. 7), indicating the *cis*-azodibenzoic acid and the isophthalic acid effectively form an unstable hydrogen-bonded complex. The LOMO of the *cis*-azodibenzoic acid/isophthalic acid macrocycle displayed a pinch, consistent with the lower stability of the hydrogen-bonded macrocycle compared to helical structure. As a result, the *cis*-azodibenzoic acid/isophthalic acid pair should yield hydrogen-bonded helical aggregates rather than macrocyclic structures, in agreement with the calculated enthalpies.

Table 6. 6. Frontier and hydrogen-bonding molecular orbitals calculated for the *cis*-azodibenzoic acid/isophthalic acid helix using semi-empirical PM3 calculations.

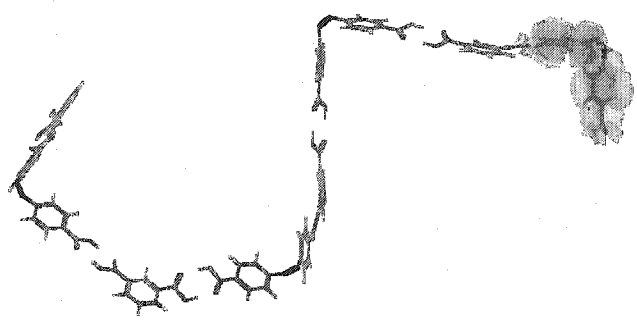
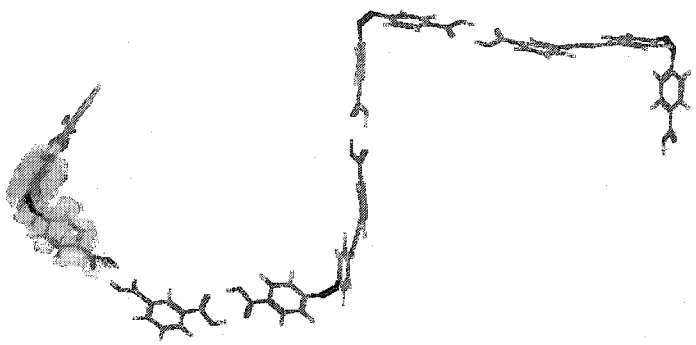
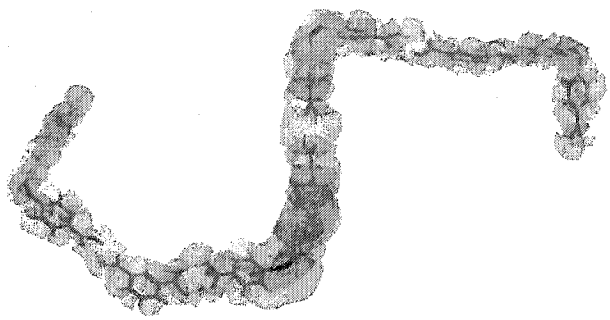
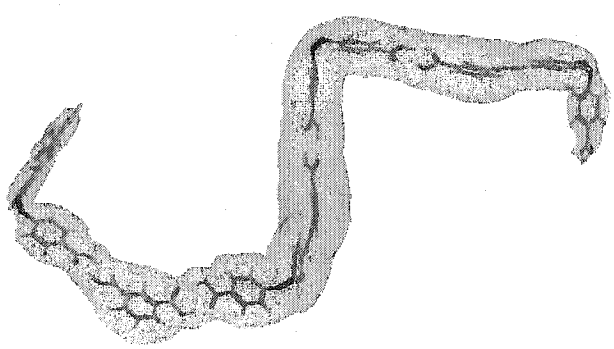
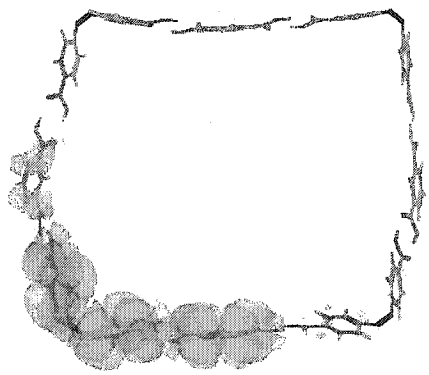
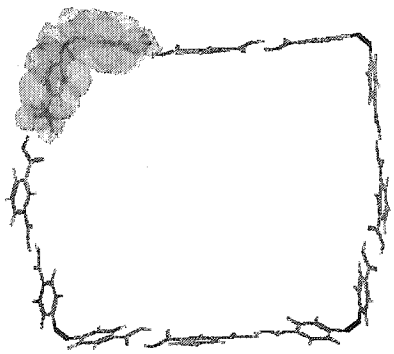
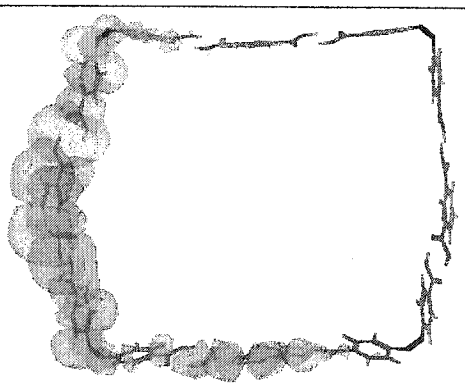
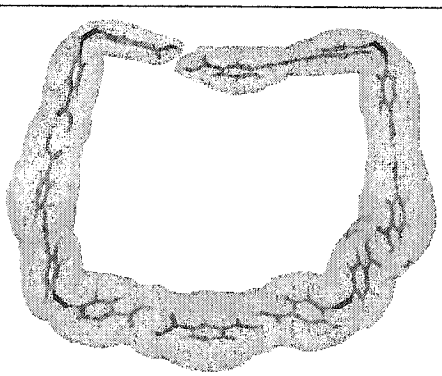
LUMO E = -0.96 eV	
HOMO E = -9.59 eV	
MO 151 E = -17.23 eV	
LOMO E = -41.87 eV	

Table 6. 7. Frontier and hydrogen-bonding molecular orbitals calculated for the *cis*-azodibenzoic acid/isophthalic acid macrocycle using semi-empirical PM3 calculations.

LUMO E = -0.96 eV	
HOMO E = -9.58 eV	
MO 151 E = -17.23 eV	
LOMO E = -41.86 eV	

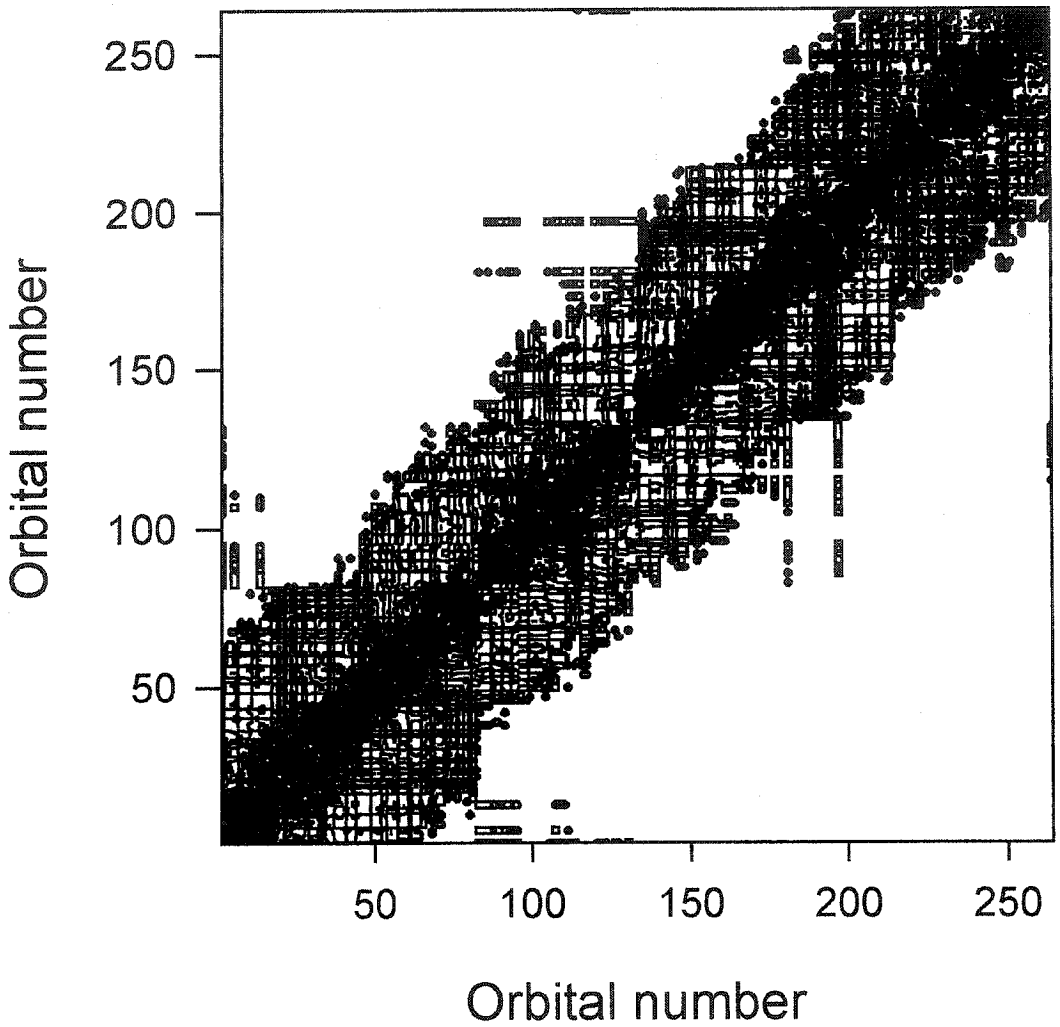


Figure 6. 11. Electron density contour map of the hydrogen-bonded helical octamer formed by *cis*-azodibenzoic acid/isophthalic acid.

The density matrix representation of the closed octameric macrocycles (Figure 6. 12) is similar to the density matrix representation of the open structures (Figure 6. 11), as most of the electron density is concentrated along the main diagonal. However, the density map does not show off-diagonal electronic interactions between remote atoms. Consequently, the electron delocalization is more restricted along the molecular backbone

in the *cis*-azodibenzoic acid/isophthalic acid macrocycle than in the *cis*-azodibenzoic acid/isophthalic acid helix. As a result of this reduced electron delocalization, the octameric macrocycle formed from *cis-p*-azodibenzoic acid and isophthalic acid are less favorable thermodynamically, in agreement with the calculated hydrogen-bond enthalpies and delocalised molecular orbitals.

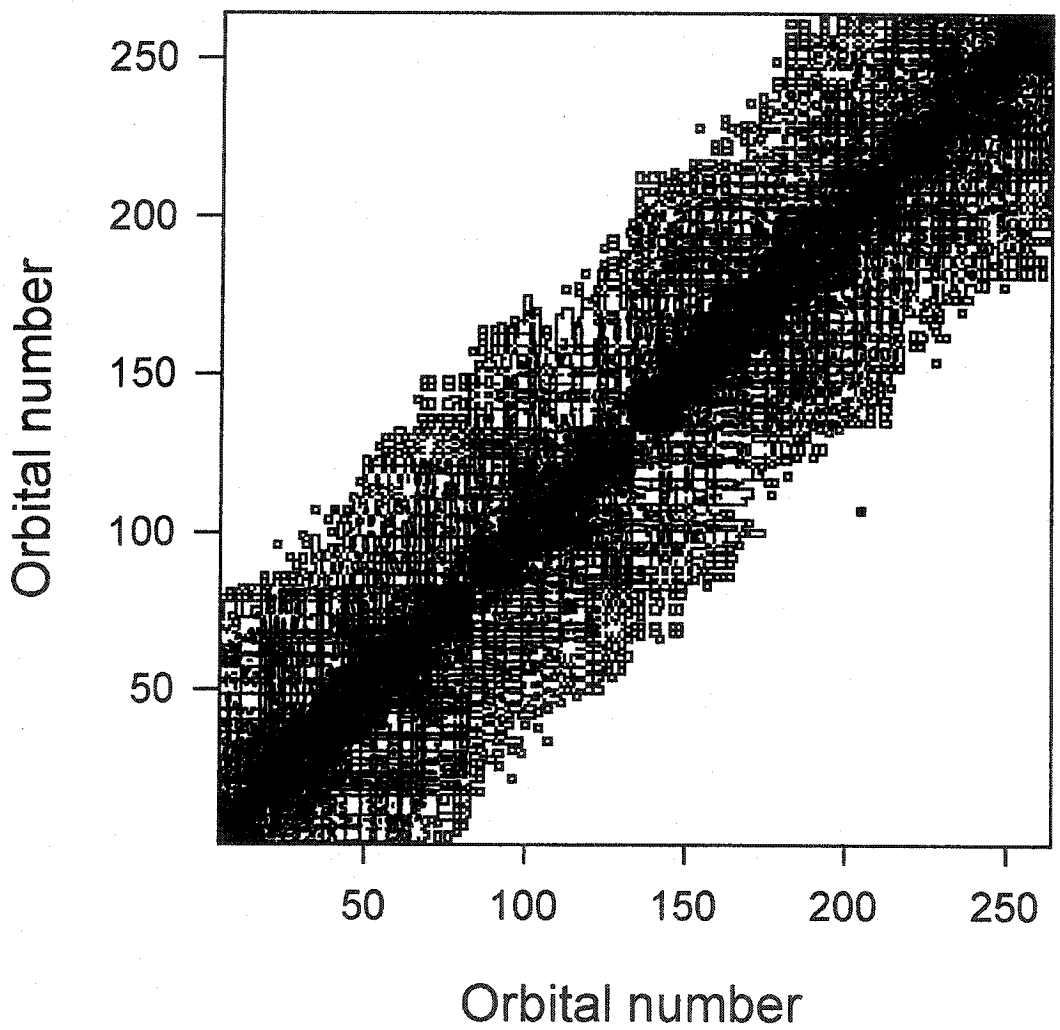


Figure 6. 12. Electron density contour map of the hydrogen-bonded cyclic octamer formed by *cis*-azodibenzoic acid/isophthalic acid.

Theoretically determined hydrogen-bond enthalpies and electron density matrices indicate that the *cis*-azodibenzoic acid and isophthalic acid model pair most favourably self-assemble to form open, helical structures through hydrogen-bonds. These calculations therefore suggest that the self-association of *cis*-azobisbenzotriazine **10** with diethylbarbituric acid may lead to hydrogen-bonded oligomeric species as depicted in Figure 6. 9a.

6.2.8. Self-Assembly of *trans*-11 and *cis*-Azobisbenzoureidotriazine 12

To determine the self-assembly products of azobisbenzoureidotriazine **11** and **12**, geometry optimization of *trans*- and *cis-p*-azobisbenzoureidotriazine as model monomers was carried out using the semi-empirical PM3 method. As mentioned in section 6. 2. 1, theoretical calculations gave 119.9° and 127.0° C-N=N angles for the *trans*- and *cis*-monomers respectively, indicating that the ureidotriazine groups adopt the same orientations as the carboxylic acid groups in *trans*- and *cis*-azodibenzoic acid. As a result, the ureidotriazine groups are 180° apart in *trans*-**11**, and may lead to the formation of infinite linear tapes upon hydrogen-bonding, while the ureidotriazine groups have an approximately 80°-orientation, and may preferably give macrocyclic tetramers when self-associated.

Figure 6. 13 shows the PM3 optimised macrocyclic structure arising from the hydrogen-bonding of *cis-p*-azobisbenzoureidotriazine derivatives, featuring a larger internal cavity (Ø = 2.9 nm) than in the original *cis-p*-azodibenzoic acid macrocycle (Ø = 2.3 nm).

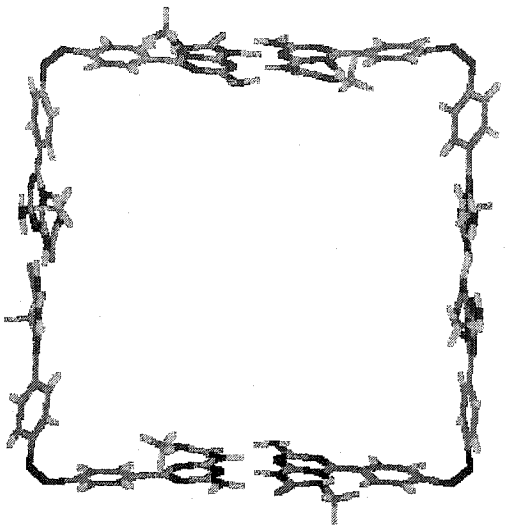


Figure 6. 13. PM3 optimised geometry of *cis*-azobisbenzoureidotriazine

In this tetrameric macrocycle, four hydrogen-bonds for which bond lengths range between 1.80-1.81 Å, and ensure cohesive interactions between the monomers, instead of three in the *cis*-azobisbenzodiaminotriazine/ diethylbarbituric acid supramolecular structures. Hydrogen-bond enthalpies were evaluated from the total enthalpies of these structures to determine the stabilisation of the cyclic tetramer. These hydrogen-bond enthalpies were calculated using:

$$\Delta H_{f\,4HB}(T) = \frac{H_f(M_n) - n \times H_f(M)}{n_{4HB}} \qquad \text{(Eq. 6.2)}$$

where T is the temperature, $H_f(M)$ is the enthalpy of the monomer M, n_{4HB} the number of quadruple hydrogen-bonds, n the number of monomers involved, and $H_f(M_n)$ the enthalpy of the aggregate. The enthalpy for quadruple hydrogen-bond formation was

calculated to be -6.2 kcal/mol in the *cis*-azobisbenzoureidotriazine macrocyclic tetramer, while the enthalpy for hydrogen-bond dimers amounted to – 8.5 kcal/mol in the *cis*-azodibenzoic acid macrocyclic tetramer, suggesting weaker hydrogen-bonds in the quadruply hydrogen-bonded macrocycle than in the *cis*-azodibenzoic acid macrocycle.

As for the hydrogen-bonded systems involving *cis*-azodibenzoic acid monomers, the electron density map of the *cis*-azobisbenzoureidotriazine macrocycle was built and compared with the dicarboxylic acid system to explain this discrepancy (Figure 6. 14). Similar to densities shown in Figures 6.11 and 6.12, the density matrix of the *cis*-**12** model macrocycle is symmetrical with respect to the main diagonal, as well as highly periodic for the entire supramolecular structure. Therefore, only two of each monomers M1 and M2 were represented for the *cis*-azobisbenzoureidotriazine tetramer for clarity (insets) and orbital coefficients corresponding to all the hydrogen atoms were neglected, except for the carboxylic acid hydrogens.

The density matrix of the *cis*-azobisbenzoureidotriazine macrocycle exhibited extensive electron delocalization along the backbone of the hydrogen-bonded structures (Figure 6. 11). In particular, greater electron densities were detected for this supramolecular system, reflecting the presence of additional aromatic rings in the macrocycle. In contrast with the *cis*-azodibenzoic acid, the presence of off-diagonal terms was reduced to closely positioned atoms in the *cis*-azobisbenzoureidotriazine density matrix, consistent with the lower hydrogen-bond enthalpy.

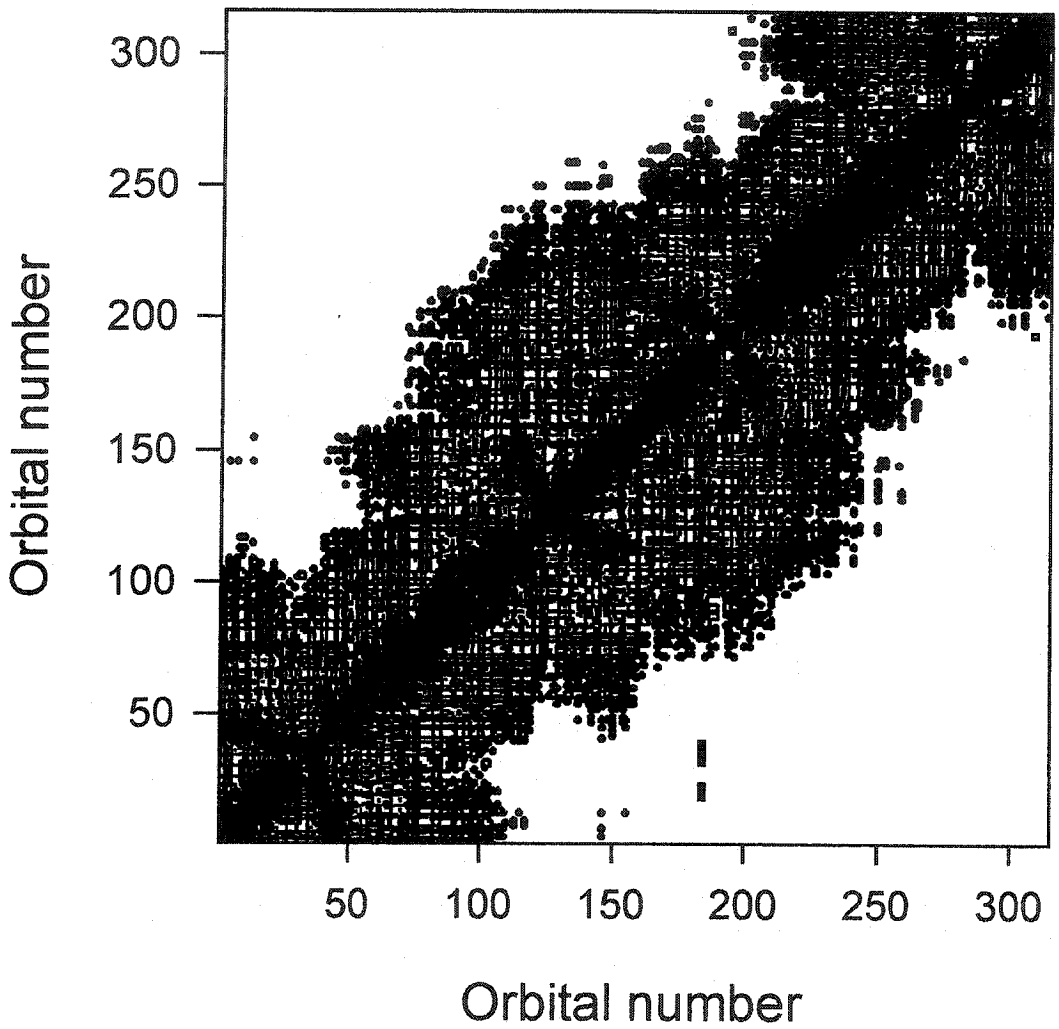


Figure 6. 14. Electron density contour map of the hydrogen-bonded cyclic tetramer formed by *cis*-azobisbenzoureidotriazine

6.3. Conclusion

Theoretical and experimental methods have been applied to the formation of metal-coordinated and multiply hydrogen-bonded supramolecular structures from novel photoresponsive *trans*- and *cis*-azobenzene monomers in this chapter. Theoretical

investigations of geometry in the *trans*- and *cis*-isomers demonstrated the conservation of angular orientations from recognition sites in comparison with the azodibenzoic acid derivatives, allowing the prediction of linear and cyclic supramolecular structures from these monomers. As a result, supramolecular linear tapes and cyclic tetramers should arise from the coordination of *trans*- and *cis*-azobisbenzonitrile derivatives with silver(I) ions, and from the hydrogen-bonding of self-complementary *trans*- and *cis*-azobisureidotriazine monomers.

Preliminary experimental spectroscopic and microscopic evidence revealed the successful complex formation between the *cis*- and *trans*-azobisbenzonitrile monomers and the silver(I) ions, despite the rapid formation of unseparable equimolar mixtures of *cis*- and *trans*-azobisbenzonitrile isomers. The detection of elongated aggregates from these mixtures suggests the formation of higher-order structures from these complexes.

Implementation of a new theoretical supramolecular model was required for the prediction of hydrogen-bonded *trans*- and *cis*-azobisbenzotriazine structures. Triple hydrogen-bonding of *trans*- and *cis*-azobisbenzotriazine monomers with non-linear, barbituric acid guests should introduce 120°-bends in the supramolecular structures, and thereby distort the linear tapes and in the cyclic tetramers. Delocalised molecular orbitals and density matrix analysis of geometry optimised hydrogen-bonded *trans*- and *cis*-azodibenzoic acid/isophthalic acid model structures suggested the preferred formation of crinkled tapes from the *trans*- azodibenzoic acid/isophthalic acid mixture, and helical oligomers from the *cis*- azodibenzoic acid/isophthalic acid pair. Further investigations of the self-assembly behaviour of these azobenzene monomers are currently underway, to generate stable photoresponsive architectures.

6.4. Experimental and Theoretical Methods

6.4.1. Generalities

Materials. 3-hydroxy-4-nitrobenzoic acid was purchased from the Aldrich Chemical Co. 3-Decyloxy-4-nitrobenzoic acid (**6**) was synthesized according to the procedure shown in Chapter 3.[1] The structures of the intermediates and the final products were confirmed by NMR spectroscopy and mass spectrometry.

Equipment. ^{1}H and ^{13}C-NMR spectra were acquired on a Varian Mercury 400 and 500 MHz spectrometers. UV-vis spectra were measured on a Varian CARY 1 UV-vis spectrophotometer equipped with a Peltier temperature controller and a Hewlett-Packard 8453 UV-vis spectrophotometer. Transmission electron microscopy (TEM) was conducted on a JEOL-2000 FX instrument by using the direct method.

6.4.2. Synthesis and Experimental Characterisation

***trans*-2,2'-Bis(decyloxy)-4,4'-azobisbenzonitrile (7).**[8] 3-decyloxy-4-nitrobenzoic acid **6** (1.073 g, 3.32 mmol) was heated to 80 °C in the presence of Zn dust (347.5 g, 5.31 mmol), in aqueous NaOH (30 %, 15.55 mL). After 23 hrs, the reaction mixture was diluted with water (62 mL), and Zn dust was added (303.9 mg, 4.65 mmol.). The reaction mixture was heated to 80-85°C for 3 days, and then cooled and filtered. The orange solution was acidified with glacial acetic acid (20 mL). The obtained precipitate was filtered and washed with water (3 x 50 mL) and a minimum of ethanol (20 mL). The solid was dissolved in dilute aqueous ammonia (2 mL), the solution was acidified with

dilute hydrochloric acid (10 mL) and heated to gentle reflux for 5 min. The resulting solid was filtered, washed repeatedly with water and ethanol, and dried. The crude (476 mg) contains a mixture of azo-**1**, azoxy-**1'**, and hydrazobenzene **1"** derivatives. ^{1}H NMR of **1** ([D$_6$]DMSO): δ 7.71 (d, 2H), 7.58 (dd, 2H), 7.47 (dd, 2H), 4.22 (t, 4H), 1.78 (m, 4H), 1.45-1.19 (m, 28H), 0.80 (t, 6H). ^{13}C NMR ([D$_4$]methanol): δ 174.33, 157.45, 145.39, 142.94, 122.74, 117.42, 116.50, 70.66, 33.07, 30.80, 30.66, 30.46, 30.34, 27.25, 23.74, 14.47. A portion of the crude mixture (200.0 mg, *ca.* 0.34 mmol.) was dissolved in neat $SOCl_2$ (10 mL) and heated to reflux for 4 hrs. The solvent was evaporated under reduced pressure. The residue was dissolved with freshly distilled diethylether (10 mL) and cooled to 0°C. Concentrated NH_3 (50 %, 5 mL) was added dropwise and ice (1 g) was added to the reaction mixture. The reaction was proceeded overnight at room temperature after which diethylether was added. The yellow orange solution was washed with water (2 x 15 mL) and brine (15 mL) then dried using $MgSO_4$. The solvent was evaporated on the rotovap giving a mixture of diamides **13**, **13'**, **13"** (*ca.* 200 mg). ^{1}H NMR of **13** ([D$_6$]DMSO): δ 7.71 (d, 2H), 7.58 (dd, 2H), 7.47 (dd, 2H), 4.22 (t, 4H), 1.78 (m, 4H), 1.45-1.19 (m, 28H), 0.80 (t, 6H). The amide mixture was directly dissolved in freshly distilled toluene (6 mL) and an excess of $POCl_3$ (0.2 mL) was added under N_2 atmosphere. The reaction proceeded for 5 hrs at reflux temperature. After cooling, the solvents were evaporated under reduced pressure. The residue was dissolved in dichloromethane (20 mL), washed with water (2 x 15 mL), then dried over $MgSO_4$. The solvents were evaporated on the rotovap giving an orange solid. The desired compound 7 was isolated by column chromatography on silica gel using dichloromethane as eluent. (121.1 mg, from **13**, 65 %). ^{1}H NMR of 7 ($CDCl_3$): δ 7.65 (d, 2H), 7.33 (dd, 2H), 7.29

(dd, 2H), 4.19 (t, 4H), 1.92 (m, 4H), 1.50-1.28 (m, 28H), 0.89 (t, 6H). CI-MS: m/z: calcd for $C_{34}H_{48}N_4O_2$: 544; found: 544.

***cis*-2,2'-Bis(decyloxy)-4,4'- azobisbenzonitrile (8).** An NMR tube filled with a solution of azobisbenzonitrile 7 (7 mg) in chloroform (0.7 mL) was fitted inside a photochemical reactor equipped with a 450W Hanovia lamp, for which a Pyrex sleeve cuts-off the wavelengths below 300 nm. The disappearance of the *trans* isomer, and appearance of *cis* isomer were monitored by ^{1}H NMR. The 1:0.3 *trans/cis* photostationary state was reached after 15 min. The *cis* isomer **8** could be isolated by preparative thick layer chromatography on alumina using CH_2Cl_2/Hexanes (1:9) as eluent or by column chromatography on silica gel using CH_2Cl_2/Hexanes (1:9) as eluent. The reverse *cis-trans* thermal isomerisation gives a 1:1 *trans/cis* photostationary state after *ca.* 15 min in the dark and is quantitative after a few hours in the dark at room temperature. The isolated product was a 1:1 mixture of *trans*-**7** and cis-**8**. ^{1}H NMR of **8** ($CDCl_3$): δ 7.08 (dd, 2H), 7.04 (d, 2H), 6.66 (dd, 2H), 3.96 (t, 4H), 1.80 (m, 4H), 1.30-1.19 (m, 28H), 0.90 (t, 6H).

***trans*-2,2'-Bis(decyloxy)-4,4'-azobisphenyl-7,9-diamino- 6,8,10-triazine- (9).**[8] Azobisbenzonitrile **8** (121 mg, 0.22 mmol) was dissolved in a KOH/*i*-PrOH solution (0.6 %, 1 mL) and dicyanodiamide (41 mg, 0.49 mmol) was added to the basic mixture. The reaction was proceeded for 36 hrs under N_2 atmosphere at reflux temperature. The reaction mixture was dissolved with diethyl ether (20 mL), the organic layer was washed with water (2 x 10 mL) and brine (10 mL), dried over $MgSO_4$, and the solvent was

evaporated under reduced pressure. The desired compound was isolated by column chromatography on silica gel using MeOH/CH_2Cl_2 (5:95) (32.1 mg, 20 %). ^{1}H NMR of **9** ($CDCl_3$): δ 7.84 (dd, 2H), 7.79 (d, 2H), 6.72 (dd, 2H), 5.13 (s, 4), 4.14 (t, 4H), 1.85 (m, 4H), 1.49-1.28 (m, 28H), 0.90 (t, 6H). ESI-MS: m/z: (negative mode) 714 (M), 357 (M/2); (positive mode) 359.4 ((M+2)/2), 739.2 (M^++Na^++H^+).

^{1}H NMR titration of *trans*- 7 and *cis*-2,2'-bis(decyloxy)-4,4'- azobisbenzonitrile 8 with AgOTf. Azobisbenzonitriles **7** and **8** (3 mg) were solubilized in C_6D_6 (0.5 mL) and placed in an NMR tube in the dark. A stock solution of AgOTf (12 mg) in C_6D_6 (0.8 mL) was also prepared and stored in the dark. 40 μL-increments of this stock solution were added to the azobisbenzonitrile solution and ^{1}H NMR spectra were acquired for each addition.

Sample preparation for TEM measurements by the direct method. A solution of *cis*- or *trans*- azobisbenzonitrile **7** and **8** was prepared by dissolving the sample in benzene into a vial wrapped in aluminium foil at room temperature. A carbon-coated 400 mesh copper grid, prewashed with chloroform for 12 hrs was dipped into the solution for approximately 5 min then dried on a filter paper.

6.4.3. Theoretical calculations

Optimisations of the supramolecules formed by azobenzene derivatives were performed using the PM3 semi-empirical molecular orbital theory,[12] which is less computationally expensive than *ab initio* or density functional methods. The geometry of

the *trans* and *cis* monomers were optimized using PM3 until an RMS gradient of 0.01 was reached. After this optimization, another monomer was added and the hydrogen-bonded structure energy was minimized. This monomer addition-optimization sequence was repeated up to the hexameric compound. The hydrogen-bonded geometry and the total heat of formation were extracted for each optimized species.

Geometry optimisations used the PM3 method contained in the Gaussian98W[13] program package. Density matrices were obtained from a population analysis within Gaussian98W and as usual symmetrized along the xy diagonal using the Microsoft Excel software.

6.5. References and Notes

[1] (a) M. –J. Brienne, J. Gabard, M. Leclerq, J. –M. Lehn, M. Cesario, C. Pascard, M. Cheve, G. Dutruc-Rosset, *Tetrahedron Lett.*, **1994**, *35*, 8157. (b) M. Bailey, C. J. Brown, *Acta Crystallogr*, **1967**, *22*, 387. (c) R. Alcala, S. Martínez-Carrera, *Acta Crystallogr*, **1972**, *B28*, 1671. (d) J. Yang, J. -L. Marendaz, S. J. Geib, A. D. Hamilton, *Tetrahedron Lett.*, **1994**, *35*, 3665. (e) A. Zafar, J. Yang, S. J. Geib, A. D. Hamilton, *Tetrahedron Lett.*, **1996**, *37*, 2327. (f) S. C. Zimmerman, F. Zeng, D. E. C. Reichert, S. V. Kolotuchin, *Science*, **1996**, *271*, 1095 (g) P. Thiyagarajan, F. Zeng, C. Y. Ku, S. C. Zimmerman, *J. Mater. Chem.*, **1997**, *7*, 1221. (h) F. Zeng, S. C. Zimmerman, S. V. Kolotuchin, D. E. C. Reichert, Y. Ma, *Tetrahedron*, **2002**, *58*, 825.

[2] F. Rakotondradany, M. A. Whitehead, A.-M. Lebuis, H. F. Sleiman, *Chem. Eur. J.*, **2003**, *9*, 4771.

[33] (a) W. Choe, Y.-H. Kiang, Z. Xu, S. Lee, *Chem. Mater.*, **1999**, *11*, 1776. (b) D. Venkataraman, G. B. Gardner, A. C. Covey, S. Lee, J. S. Moore, *Acta Crystallogr.* **1996**, *52*, 2416. (c) N. Schultheiss, R. P. Douglas, E. Bosch, *Inorg. Chem.*, **2003**, *42*, 8886.

[4] (a) A. D. Ryabov, L. G. Kuz'mina, N. V. Dvortsova, D. J. Stufkens, R. van Eldik, *Inorg. Chem.*, **1993**, *32*, 3166. (b) N. J. Bunce, G. Ferguson, C. L. Forber, M. C. Zerner, *J. Org. Chem.*, **1987**, *52*, 394.

[5] The photostationary state was determined by integration of the ^{1}H NMR peaks.

[6] The relative stability of the formed metal-coordinated structure was also observed by the conservation of the 1:1 *trans/cis* ratio once AgOTf was added. Removal of the silver (I) ions using ion exchange resins gave the *trans*-**9** monomer.

[7] The diameter of the three-component self-assembled structure of *trans*-**7** and *cis*-**8** with silver(I) ions was estimated from the QM/MM optimized structure of hydrogen-bonded *trans*-**1** *cis*-azodibenzoic acid **2**.

[8] J. H. K. K. Hirschberg, L. Brunsveld, A. Ramzi, J. A. J. M. Vekemans, R. P. Sijbesma, E. W. Meijer, *Nature*, **2000**, *407*, 167.

[9] See Chapter 4.

[10] R. Gaudreault, PhD Thesis, McGill University, 2004.

[11] (a) J. –M. Lehn, *Supramolecular chemistry: concepts and perspectives*, VCH: Weinheim, 1995. (b) G. M. Whitesides, E. E. Simanek, J. P. Mathias, C. T. Seto, D. N. Chin, M. Mammen, D. M. Gordon, *Acc. Chem. Res.*, **1995**, *28*, 37. (c) D. S. Lawrence, T. Jiang, M. Levett, *Chem. Rev.*, **1995**, *95*, 2229. (d) S. Leininger, B. Olenyuk, P. J. Stang, *Chem. Rev.*, **2000**, *100*, 853.

[12] (a) S. Sharma, T. P. Radhakrishnan, *J. Phys. Chem. B*, **2000**, 104, 10191. (b) D. Quinonero, A. Frontera, S. Tomas, G. A. Suner, J. Morey, A. Costa, P. Ballester, P. M. Deya, *Theor. Chem. Acc.*, **2000**, 104, 50.

[13] Gaussian 98W (Revision A.7), M. J. Frisch, G. W. Trucks, H. B. Schlegel, G. E. Scuseria, M. A. Robb, J. R. Cheeseman, V. G. Zakrzewski, J. A. Montgomery, Jr., R. E. Stratmann, J. C. Burant, S. Dapprich, J. M. Millam, A. D. Daniels, K. N. Kudin, M. C. Strain, O. Farkas, J. Tomasi, V. Barone, M. Cossi, R. Cammi, B. Mennucci, C. Pomelli, C. Adamo, S. Clifford, J. Ochterski, G. A. Petersson, P. Y. Ayala, Q. Cui, K. Morokuma, D. K. Malick, A. D. Rabuck, K. Raghavachari, J. B. Foresman, J. Cioslowski, J. V. Ortiz, A. G. Baboul, B. B. Stefanov, G. Liu, A. Liashenko, P. Piskorz, I. Komaromi, R. Gomperts, R. L. Martin, D. J. Fox, T. Keith, M. A. Al-Laham, C. Y. Peng, A. Nanayakkara, C. Gonzalez, M. Challacombe, P. M. W. Gill, B. G. Johnson, W. Chen, M. W. Wong, J. L. Andres, M. Head-Gordon, E. S. Replogle , J. A. Pople, Gaussian, Inc., Pittsburgh PA, 1998.

Chapter 7.

Hydrogen-Bond Self-Assembly of DNA-Base Analogues: Theory and Experiment

7.1. Introduction

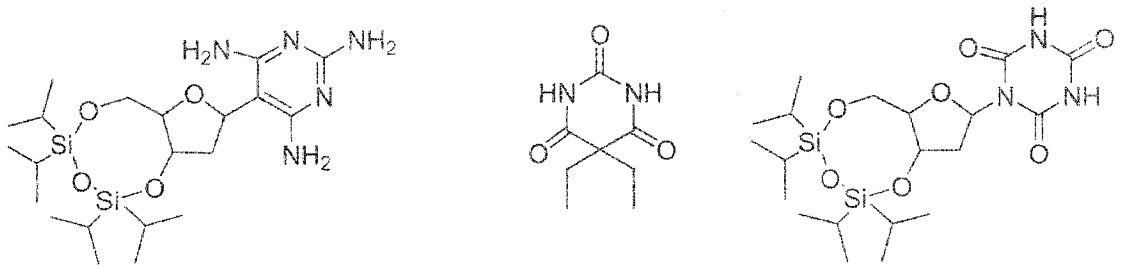
The hierarchical assembly of low-molecular weight building blocks has successfully generated functional supramolecular architectures with high predictability.[1] In this thesis, Chapters 3 through 6 showed that molecularly self-assembled photoresponsive systems could be constructed from the combination of strong, directional, hydrogen-bonding or metal coordinating forces, with weak isotropic, intramolecular π-stacking and van der Waals interactions. These supramolecular structures have been thoroughly investigated using theoretical methods and experimental characterization techniques, stressing the impact of light-induced isomerisation on self-organisation. From a methodology perspective, theory and experiment were intimately connected to characterize these hierarchical assemblies and, consequently, to improve their binding selectivity and strength. On the one hand, theoretical calculations were essential in the prediction of non-covalently bound oligomeric geometries along with their thermodynamic properties from experimentally designed, and synthesized, monomeric species. The molecular diagrams and density matrix contour plots computed for the geometry optimized structures were able to replace the computationally costly Gibbs free energy calculations, providing quantitative information on the self-assembly. On the other hand, the combination of molecular as well as bulk material characterisation techniques were essential for identification of these monomers and their self-assembly behaviour, and for correlation with theoretical results. This Chapter extends these principles to novel, biologically interesting systems based on deoxyribonucleoside analogues.

Engineering materials with controlled physical and chemical properties at the nanoscale has attracted considerable attention from researchers. Supramolecular chemistry has emerged as a powerful method to achieve this goal because of its ability to efficiently generate well-defined, functional architectures.[1] In particular, hydrogen-bond self-assembly has successfully exploited the specificity of Watson-Crick pairing between complementary DNA-bases to create cages,[2] helical,[3] linear,[4] and macrocyclic structures[5,6] with controlled functionality from DNA inspired building blocks.

At the same time, the incorporation novel nucleosides into DNA[7] has been actively pursued to develop new artificial hydrogen-bonded[7a-e], π-stacked, [7f,g] or metal-coordinated[7h-l] DNA base pairs, which can be enzymatically replicated and perform new biological tasks. DNA[8] itself is prone to form higher-order aggregates *in vitro* using hydrogen-bond interactions. Among these unusual DNA aggregates, triple helices[9] and G-quadruplexes,[10] are especially attractive because of their well-defined morphologies and their biological properties and therapeutic implications.[11, 12] A DNA *iso*-guanosine pentaplex with potential biological properties has been generated recently using metal-assisted hydrogen-bonding.[13] Here we report the design and self-assembly of artificial nucleosides to create new DNA motifs, and to expand the repertoire of DNA assemblies from pentaplexes to hexameric architectures.

The work described here differs from previous studies on self-assembled DNA and integrates knowledge from chemical biology with organosupramolecular chemistry. Our main strategy is to use newly synthesised DNA-base analogues to generate a new family of hydrogen-bonded supramolecular structures. The synthesis and characterisation of a DNA-base analogue **15** (Figure 7. 1), which can undergo hydrogen-

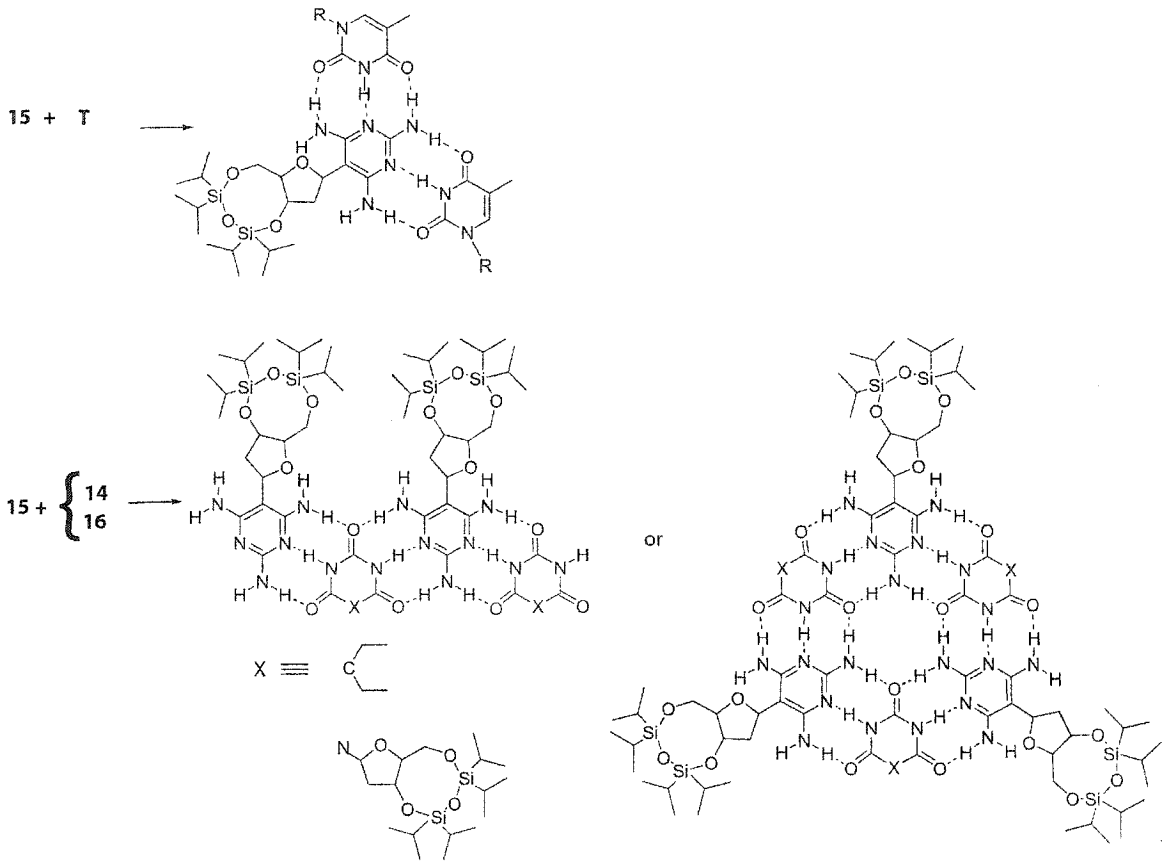
bond self-assembly with natural and artificial DNA-bases as well as with small molecules, is described with a theoretical and experimental study of its hydrogen-bonding and π-stacking ability. Self-assembly of building block **15** through hydrogen-bonding and π-stacking is shown to lead to rod-like nanostructures.



15 **14** **16**

Figure 7. 1. Diethylbarbituric acid **14**, and triaminopyridine **15** and cyanuric acid nucleosides **16**

DNA-base analogue **15** consists of a triaminopyrimidine-base attached to a 3',5'-disiloxane protected ribofuranose (Figure 7. 1), providing two DAD-type hydrogen-bonding sites. The spatial orientation of these hydrogen-bonding groups is similar to the relative position of the carboxylic acid groups in isophthalic acid; therefore, a 120°-angle is expected between the DAD-faces. Nucleoside **15** can thus be associated with two complementary thymine residues to form DNA-based triple helices, and with barbituric acid derivatives like **14** and cyanuric acid derivatives like **16** to give linear tapes or hexameric rosettes (Figure 7. 1 and Scheme 7. 1).



Scheme 7. 1. Hydrogen-bond self-assembly of nucleoside **15** with thymine **T**, barbituric acid **14** and cyanuric acid **16**

7.2. Results and discussion

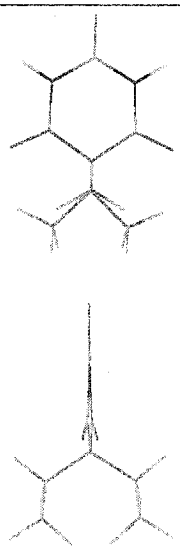
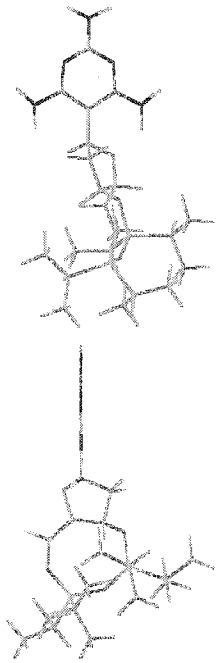
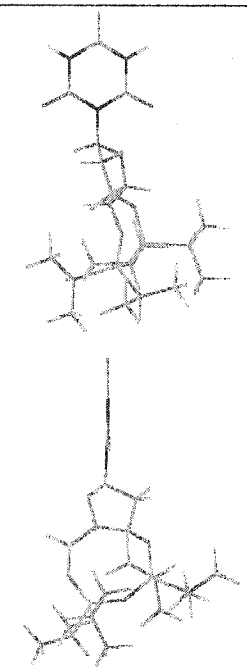
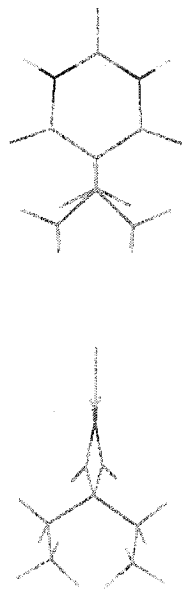
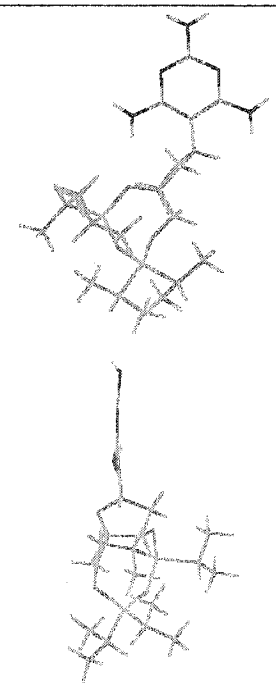
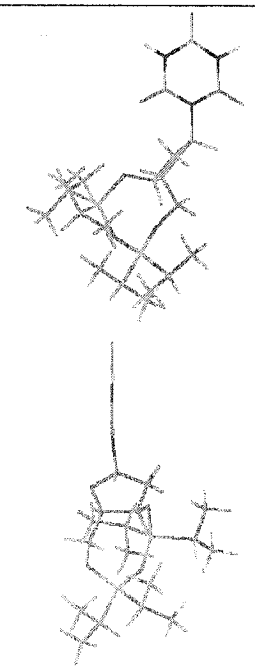
7.2.1. Theoretical Predictions

7.2.1.1. Theoretical Calculations of Hydrogen-bond Geometries

The geometry of the diethylbarbituric acid, triaminopyrimidine **15** and cyanuric acid **16** monomers was first investigated by semi-empirical PM3 molecular orbital calculations to determine the theoretical supramolecular geometries.[14] These monomers consistently showed 120°-orientations between the triple hydrogen-bonding sites, suggesting that the geometry of the PM3 optimized triaminopyrimidine **15** would give

linear tapes and macrocyclic structures with diethylbarbituric acid **14** and cyanuric acid **16**.

Table 7. 1. Theoretical monomer structures determined using MM^+ and PM3 geometry optimisations.

	Diethylbarbituric acid **14**	Triaminopyrimidine **15**	Cyanuric acid **16**
MM^+			
PM3			

7.2.1.2. Theoretical Evaluation of Hydrogen-bond Geometry

Molecular mechanics MM^+ calculations were carried out to evaluate the hydrogen-bond geometry of the supramolecular structures arising from the self-assembly of triaminopyrimidine **15** and diethylbarbituric acid **14,** as well as triaminopyrimidine **15** and cyanuric acid **16**. The aggregate structures indicate that the monomers retain their geometry from one oligomer to another, and the hydrogen-bond geometry does not change significantly, as expected for supramolecular assemblies (Table 1).[15] In all optimized DNA-analogue aggregates, the barbituric acid and cyanuric acid C=O bond lengthens slightly from 1.21 Å to 1.23 Å, the N–H bond from 0.99 Å to 1.02 Å when bound. The triaminopyrimidine N-H bond also lengthens from 1.00 Å to 1.02 Å, leading to the formation of strong, ionic N···H and O···H hydrogen-bonds (N···H = 1.00 Å, O···H = 0.95 Å).[16] PM3 calculations performed on similar triaminopyrimidine/barbituric acid complexes resulted in lengths of 1.66 Å and 1.78 Å for the N···H and O···H hydrogen-bonds, along with significant N-H and C=O bond lengthening in both monomers. These geometric differences arise from the input MM^+ structure, in which the hydrogen-bonds were given a ionic character.

7.2.1.3. Molecular Modelling of Hydrogen-bonded Aggregates

The MM^+ optimised hydrogen-bonded structures obtained from triaminopyrimidine **15** and diethylbarbituric acid **14,** as well as triaminopyrimidine **15** and cyanuric acid **16** were analysed to determine the most favourable supramolecular geometry. The influence of the sterically encumbered nucleoside on the self-assembly behaviour was also assessed from the computational results (Table 7. 2).

Table 7. 2. Theoretical hydrogen-bonded **14 + 15** complexes determined using MM^+ geometry optimisations

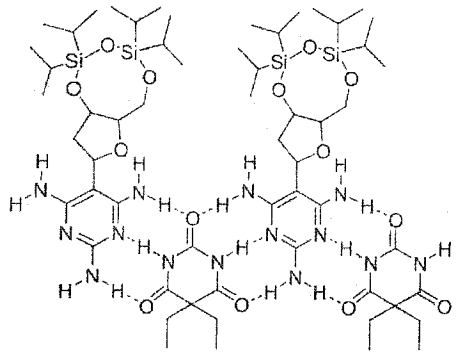
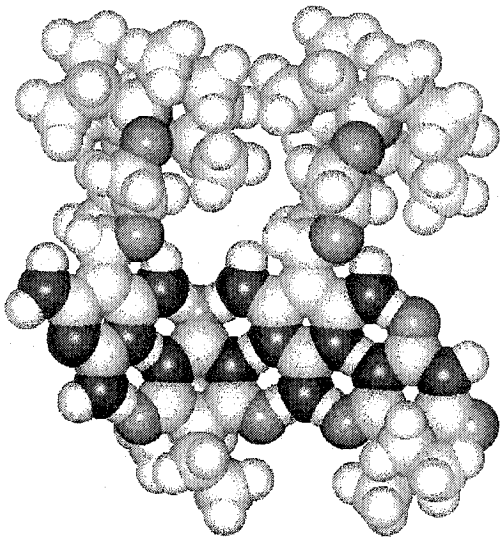
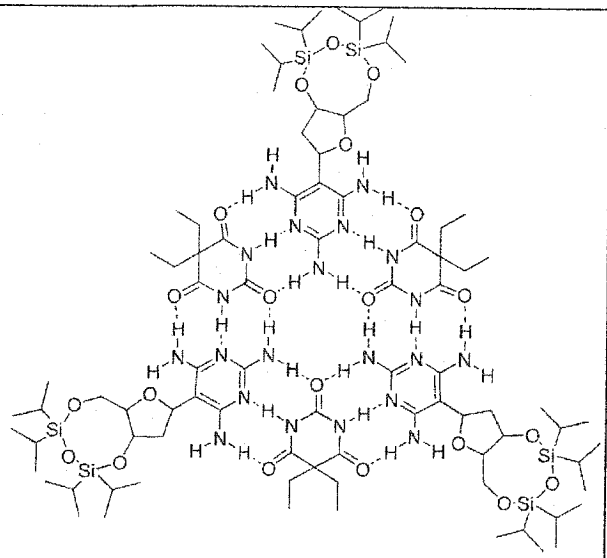
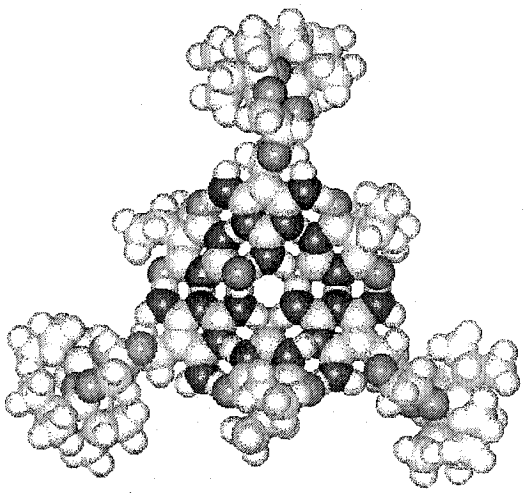
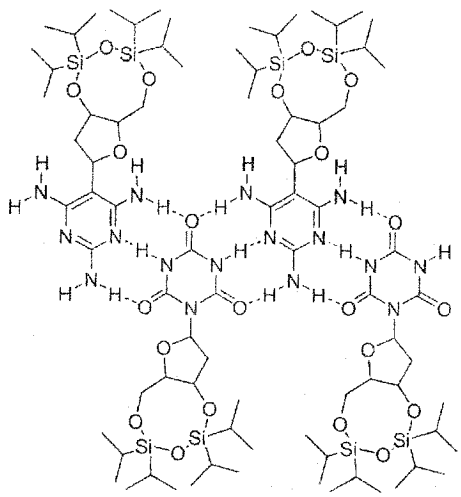
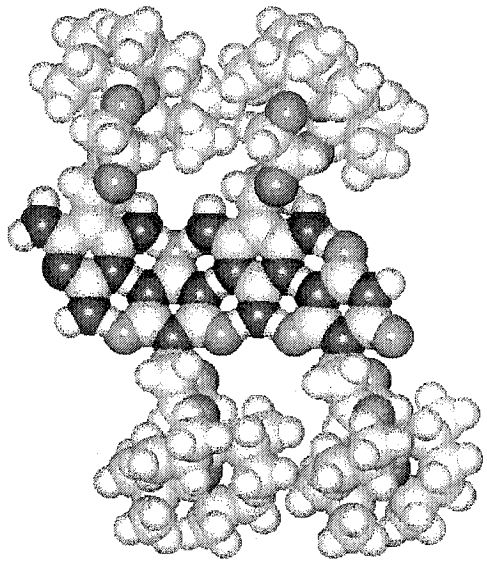
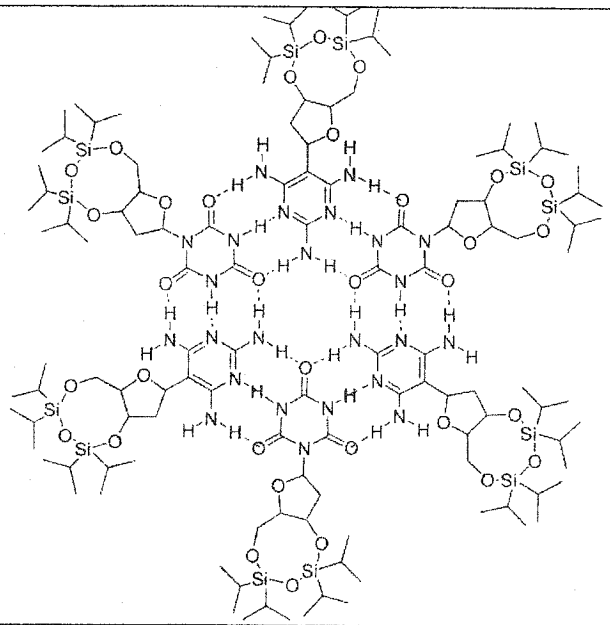
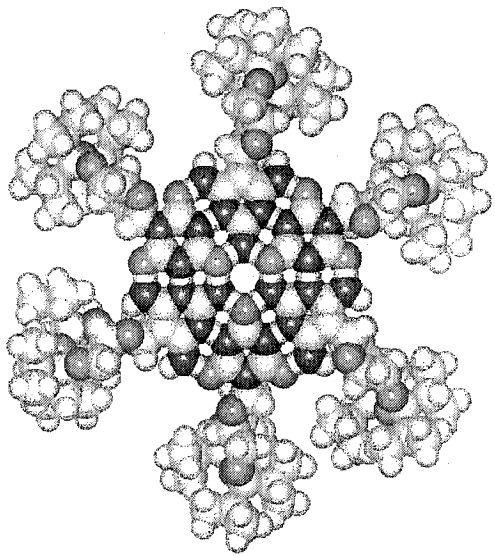
14 + 15 complexes	MM^+ optimised structures
	 MM^+ energy = 81.5 kcal/mol
	 MM^+ energy = 177.1 kcal/mol

Table 7. 3. Theoretical hydrogen-bonded **15** + **16** complexes determined using MM^+ geometry optimisations

15 + **16** complexes	MM^+ optimised structures
	 MM^+ energy = 107.9 kcal/mol
	 MM^+ energy = 195.5 kcal/mol

These preliminary molecular mechanics MM^+ calculations allowed a direct visualisation of steric interactions between the substituents in these hydrogen-bonded structures. Both hydrogen-bonded linear tapes formed with triaminopyrimidine **15** and diethylbarbituric acid **14,** and with triaminopyrimidine **15** and cyanuric acid **16** showed the protected sugar groups at close alkyl-alkyl packing distances of 3.7 Å.[17] The overlaid structures in Figure 7. 2 show that, while the cyanuric acid nitrogen atom enables the triaminopyrimidine **15**/cyanuric acid **16** tape to remain within the same plane, the barbituric acid tetrahedral carbon atom allows the triaminopyrimidine **15**/ diethylbarbituric acid **14** tape to deviate from planarity. This absence of planarity tape suggested that the triaminopyrimidine **15**/ diethylbarbituric acid **14** tape might be able to compensate for unfavourable steric repulsions between bulky disiloxane substituents by adopting a distorted geometry. In constrast, steric hindrance can only be overcome through the formation of hexameric rosettes in the case of the triaminopyrimidine **15**/cyanuric acid **16** pair.

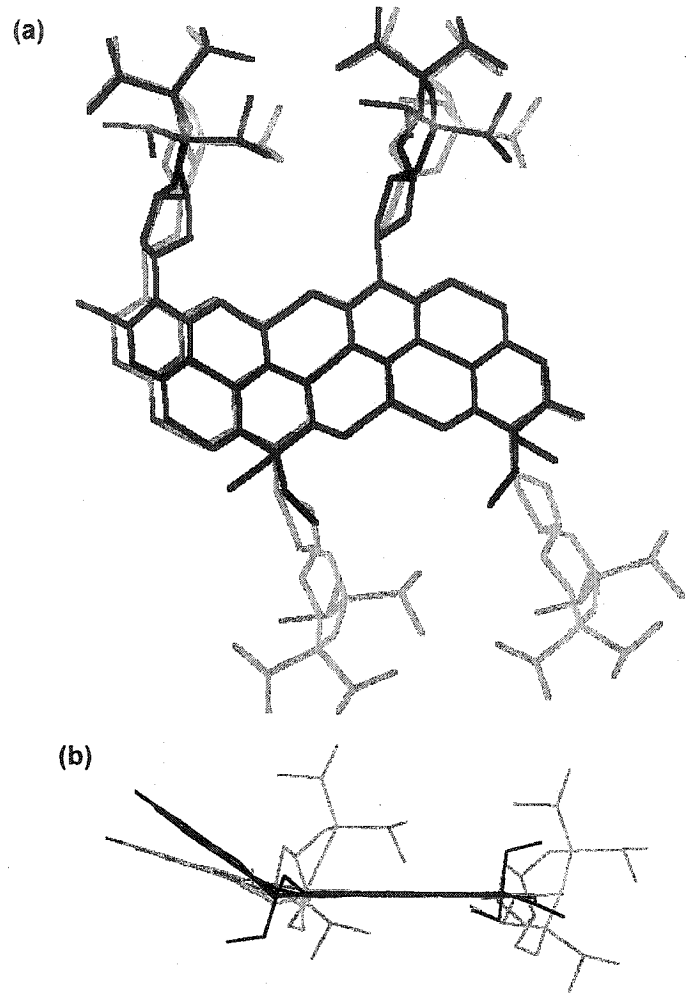


Figure 7. 2. Overlay of triaminopyrimidine **15**/ diethylbarbituric acid **14** (black) and triaminopyrimidine **15**/ and cyanuric acid **16** linear tapes. (a) Top view. (b) Side view.

As a result, geometrical arguments based on empirical force field calculations suggest that the triaminopyrimidine **15** and diethylbarbituric acid **14** can favourably self-assemble into oligomeric linear tapes (Table 7. 1), while triaminopyrimidine **15** and cyanuric acid **16** are more likely to form discrete hexameric macrocycles. (Table 7. 2)

7.2.1.4. Electronic Population Analysis of the PM3 Optimized Hydrogen-bonded Structures

The emergence of highly symmetrical patterns in the electron density maps provided a direct, quantitative visualization of through-bond and through-space electron delocalization in the hydrogen-bonded photoresponsive structures in Chapters 4 and 6, highlighting the relative stabilities of the supramolecular conformers. Likewise, density matrix plots were mapped for the triaminopyrimidine **15**/diethylbarbituric acid **14** linear tape (Figure 7. 3) and hexameric rosette (Figure 7. 4), along with electron density matrices for the triaminopyrimidine **15**/cyanuric acid **16** complexes (Figures 7. 5 and 7.6). These densities show symmetry with respect to the antidiagonal, as well as high periodicity when the entire hexameric structure is taken into account, as was observed for the hydrogen-bonded azobenzene derivatives. Because of this high symmetry, only four each monomer units are needed to describe the electron density of the entire supramolecule. Therefore, two of each components are represented for clarity. Although electronically dense, the disiloxane and ethyl substituents were taken into account for the population analysis, but were discarded in the contour plots because they obscured the influence of electron density on hydrogen-bonding (see theoretical methods). All the hydrogen atoms, except the amino and amido hydrogens participating in hydrogen-bonds, were neglected because of their poor contribution to electron delocalisation.

The density matrices obtained for the linear tape (Figure 7. 3) and hexameric rosette (Figure 7. 4) formed by the triaminopyrimidine **15**/diethylbarbituric acid **14** pair broadly showed similar electron delocalisation patterns. However, the linear tape exhibited an extensive electron delocalisation along the hydrogen-bonded backbone

(Figure 7. 3). This result is consistent with the linearity and the quasi-planarity of the aromatic species (see above), which facilitate electron flow across the whole hydrogen-bonded structure. However, the density map of the hexameric rosette (Figure 7. 4) showed less continuity along the main diagonal than the density map of the linear tape (Figure 7. 3), suggesting that electron density is more confined in the hydrogen-bonded macrocycle than in the linear aggregate. Consequently, the triaminopyrimidine **15** and diethylbarbituric acid **14** are more stable in a linear conformation than cyclised, in agreement with the MM^{+}-based geometrical arguments.

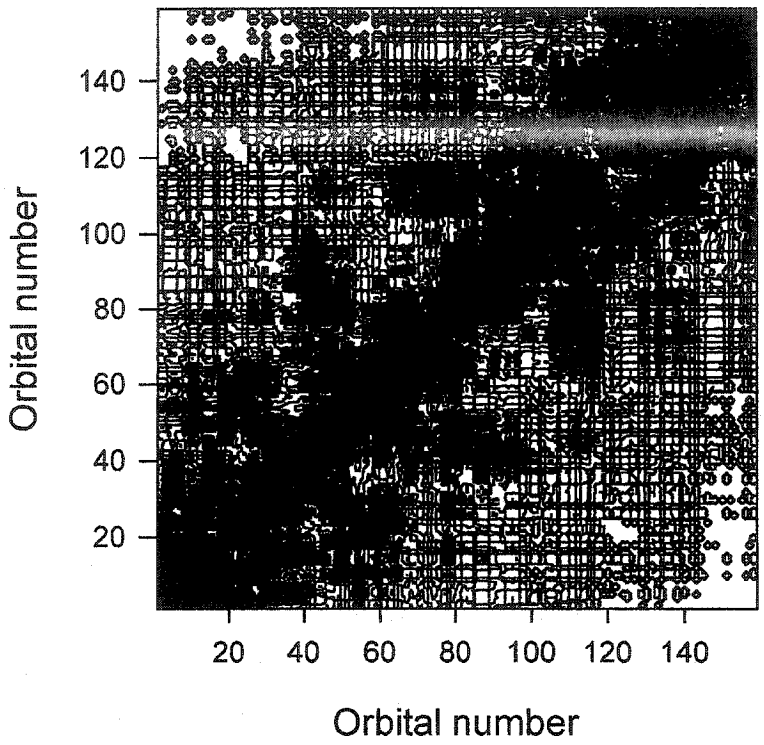


Figure 7. 3. Density matrix of the triaminopyrimidine **15**/diethylbarbituric acid **14** linear tape. The substituents were omitted for clarity.

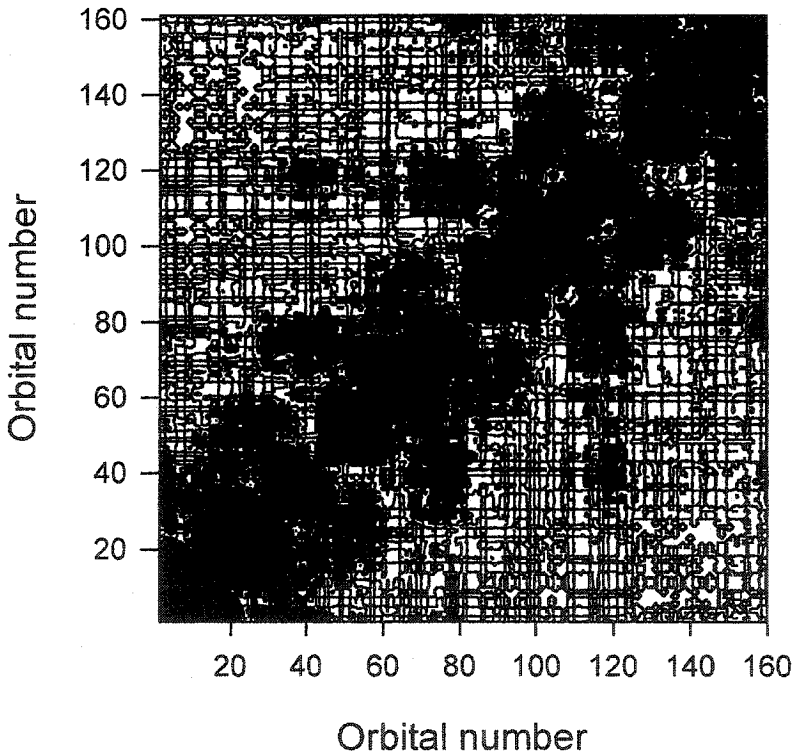


Figure 7. 4. Density matrix representation of the triaminopyrimidine **15**/diethylbarbituric acid **14** rosette. The substituents were omitted for clarity.

The density matrix representations of the hydrogen-bonded triaminopyrimidine **15**/cyanuric acid **16** structures (Figures 7. 5 and 7. 6) differ dramatically from the density matrix representations of the triaminopyrimidine **15**/diethylbarbituric acid **14** aggregates. Unlike the triaminopyrimidine **15**/diethylbarbituric acid **14** (Figures 7. 3 and 7. 4), most of the electron density is concentrated along the main diagonal. Comparison of the density matrices obtained for the linear tape (Figure 7. 5) and hexameric rosette (Figure 7. 6) formed by the triaminopyrimidine **15**/cyanuric acid **16** pair revealed similar electron delocalisation patterns. The relative stability of the hydrogen-bonded triaminopyrimidine **15**/cyanuric acid **16** structures is therefore mainly dependent on steric factors rather than electronic effects. These steric factors were determined from the MM^{+} optimised geometries and suggested that the triaminopyrimidine **15** and cyanuric acid **16** should form macrocyclic aggregates instead of linear structures.

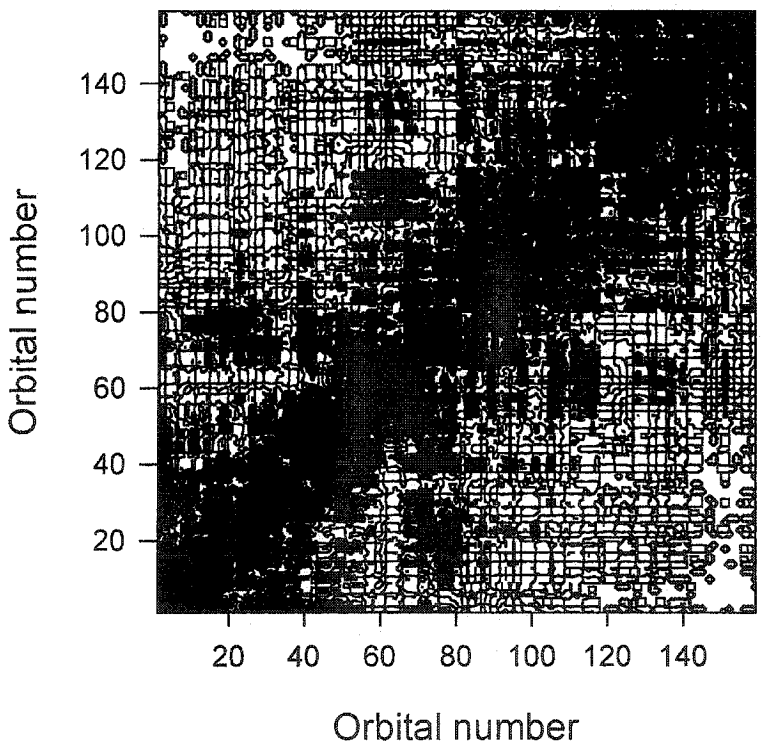


Figure 7. 5. Density matrix of the triaminopyrimidine **15**/cyanuric acid **16** linear tape. The substituents were omitted for clarity.

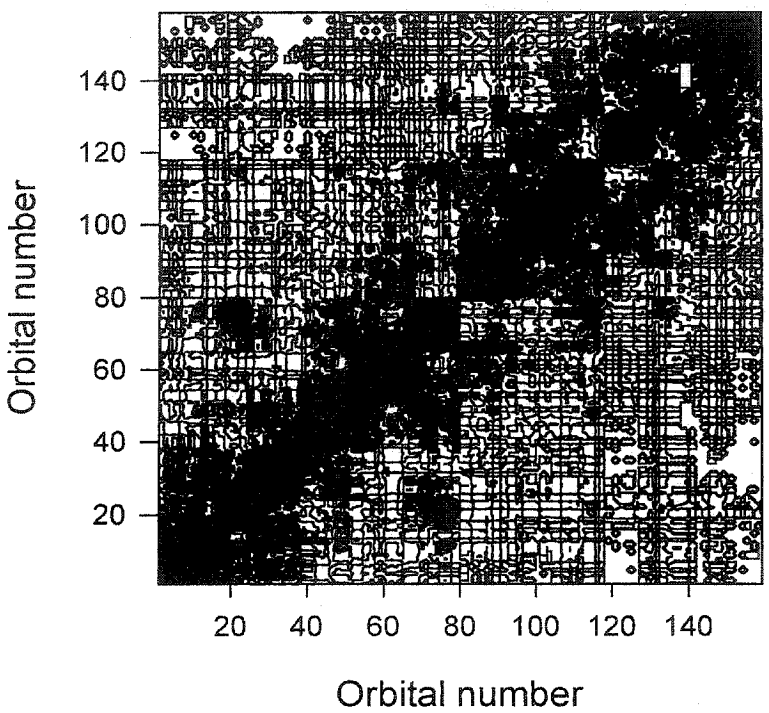
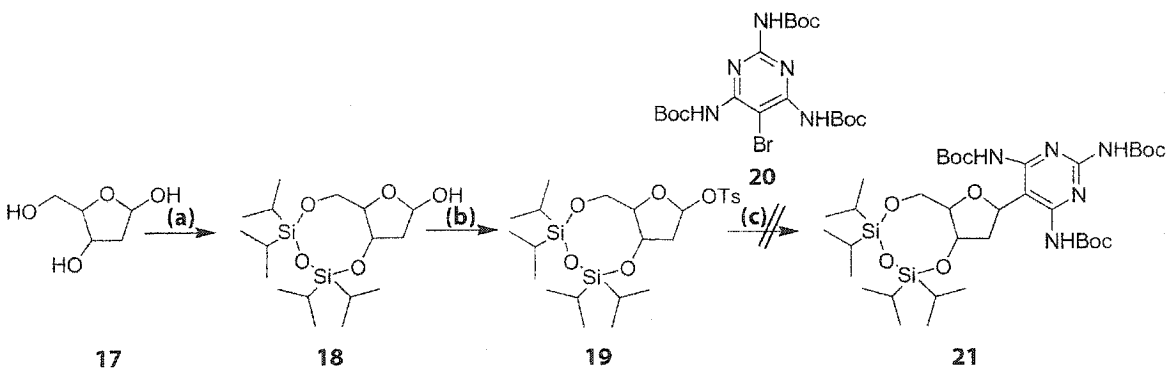


Figure 7. 6. Density matrix of the triaminopyrimidine **15**/cyanuric acid **16** rosette. The substituents were omitted for clarity.

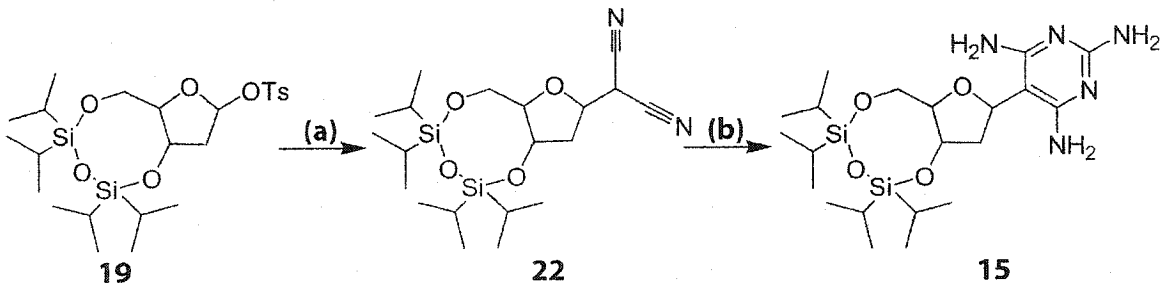
7.2.2. Synthesis of DNA-base Analogues 15 and 16

7.2.2.1. Synthesis of Triaminopyrimidine DNA-base Analogue **15**



Scheme 7. 2. Attempted synthesis of protected nucleoside **21**. (a) 1,1',3,3'-tetraisopropyldisiloxane, pyridine, 40 °C, 2 hrs, 69 %. (b) *p*-toluenesulfonyl chloride, Et_3N, CH_2Cl_2, 97 %. (c) **20**, *n*-BuLi (1.2 eq), -78 °C → r.t., 4hrs then 20 hrs.

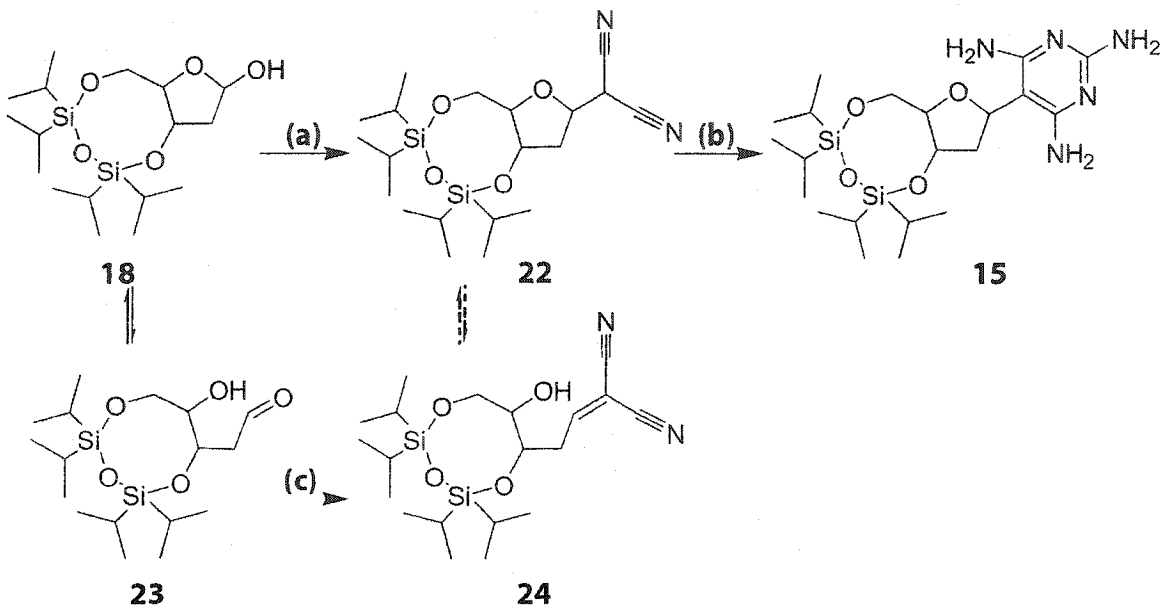
Several approaches were considered for the synthesis of triaminopyrimidine DNA-base analogue **15**. The first synthetic route involved the coupling of the tosyl-activated 2-deoxy-D-ribose **19** with the lithiated *t*-BOC-protected 1,3,5-triaminopyrimidine, generated through trans-metallation of the brominated triaminopyrimidine **20** using *n*-BuLi (Scheme 7.2). However, instead of producing the desired protected nucleoside **21**, this simple synthetic method lead to a mixture of *t*-BOC-protected 1,3,5-triaminopyrimidine and 3',5'-protected sugar **18**, suggesting unfavourable steric hindrance between the disiloxane and *t*-butoxycarbonyl protecting groups.



Scheme 7. 3. Attempted synthesis of triaminopyrimidine **15**. (a) Malononitrile (3 eq.), 95 % NaH (3 eq.), THF, 0 °C → r.t., 12 hrs, 5-10 %. (b) Guanidine hydrochloride, Na, EtOH, reflux, 8 hrs, 29 %.

A second synthetic method consisted of two main coupling steps (Scheme 7.3). First, the tosylated sugar **19** was allowed to undergo a nucleophilic attack of malononitrile under basic conditions to give the dicyano derivative, which was then reacted with guanidine to obtain the desired triaminopyrimidine **15**. Although the first coupling reaction successfully lead to malonate **22**, the isolated yield was disappointingly low (<10 %). Mass spectrometry analysis of the reaction products revealed the formation of dimeric species and deprotected sugar derivatives, suggesting the lack of stability of

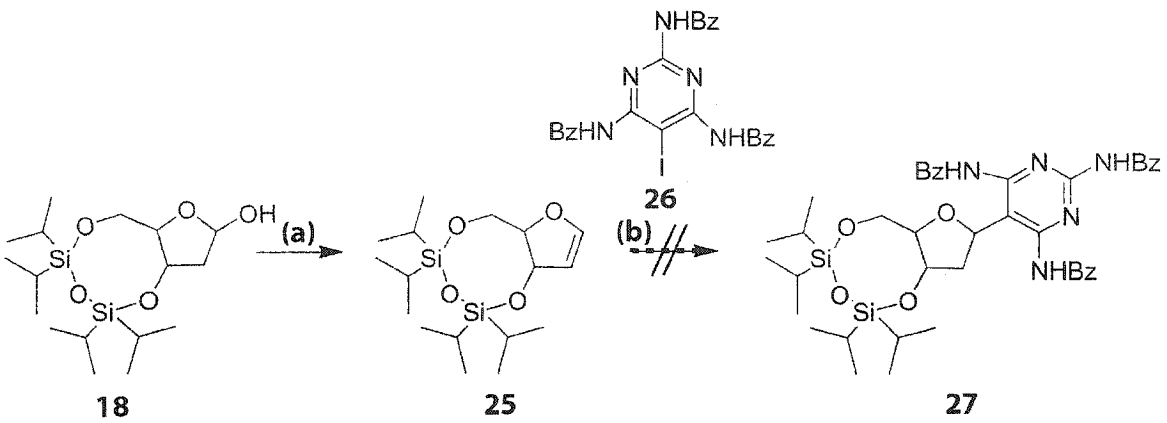
the tosylated sugar to the basic reaction conditions, possibly as a result of the labile tosyl leaving group or a base-sensitivty of the protecting group.



Scheme 7. 4. Synthesis of triaminopyrimidine **15**. (a) Malononitrile (3 eq.), 95 % NaH (3 eq.), THF, 0 °C → r.t., 2 hrs, 33 %. (b) Guanidine hydrochloride, Na, EtOH, reflux, 5 hrs, 29 %. (c) Malononitrile (3 eq.), 95 % NaH (1 eq.), THF, 0 °C → r.t., 24 hrs or malononitrile (1 eq.), K_2CO_3 (0.1 eq.), MeOH, 24 hrs, 13 %.

Alternatively, direct reaction of malononitrile with the 3',5'-protected sugar under similar conditions (Scheme 7. 4),[18] through the nucleophilic attack of the *keto* form of the 2-deoxyribofuranose derivative **23**, improved the coupling yield, thus allowing for the synthesis of **15** with neutralised guanidinium hydrochloride. Reduction of the basicity of the reaction mixture by decreasing the NaH/malononitrile ratio or even by using catalytic amounts of K_2CO_3 resulted in isomer **24**, detected by mass spectrometry and ^{1}H NMR (Scheme 7. 4). ^{1}H NMR spectroscopy suggested the presence of both α- and β-anomeric sugars in solutions of the triaminopyrimidine nucleoside **15**, which as used as is in the self-assembly studies.

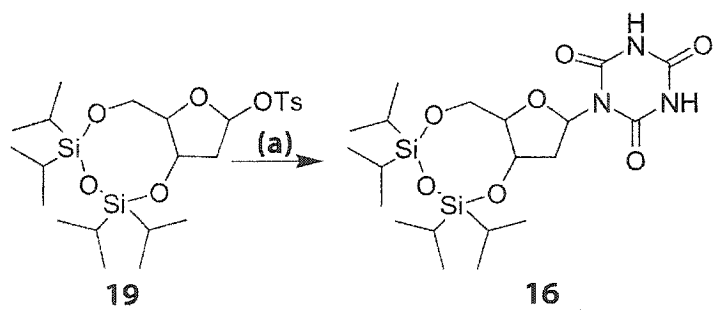
sugars in solutions of the triaminopyrimidine nucleoside **15**, which as used as is in the self-assembly studies.



Scheme 7. 5. Attempted synthesis of triaminopyrimidine **15** from glycals. (a) Methanesulfonyl chloride, Et_3N, CH_2Cl_2, -40 °C/- 50 °C → 50°C, 3hrs → 15 hrs, 10 %. (b) PdOAc, $AsPh_3$, MeCN, reflux, 4 hrs.

A third approach utilising the palladium-mediated cross-coupling reaction[19] of 3',5'-diprotected ribofuranoid glycal **25** with iodinated benzoyl-protected triaminopyrimidine was also explored to improve the overall yield (Scheme 7. 5). However, preliminary synthetic attempts at the first elimination step gave the glycal in low yields (*ca.* 10 %).

7.2.2.2. Synthesis of Cyanuric Acid DNA-base Analogue **16**



Scheme 7. 6. Synthesis of cyanuric acid **16**. (a) Cyanuric acid, potassium nonafluorobutanesulfonate, hexamethyldisilazane, $(CH_3)_3SiCl$, reflux, 16 hrs, 37 %.

Scheme 7. 6 outlines the synthesis of DNA-base analogue **16**, derived from a previously published procedure where a toluyl-protected 2-deoxyribofuranosylchloride is used as a starting material.[20] The tosyl derivative of the 3',5'-disiloxane protected sugar was first formed and coupled with *in situ* protected cyanuric acid under basic conditions to yield the cyanuric acid DNA-base analogue **16**. Similar to the triaminopyrimidine analogue **15**, nucleoside **16** was obtained as a mixture of α- and β-sugar anomers from ^{1}H NMR data, but was not purified further for the self-assembly studies.

7.2.3. Self-Assembly of Triaminopyrimidine 15 with Diethylbarbituric Acid 14

7.2.3.1. ^{1}H NMR Titration of DNA-base Analogue **15** by Diethylbarbituric Acid **14**

The hydrogen-bonded self-assembly of DNA-base analogue **15** with diethylbarbituric acid **14** was investigated by performing a ^{1}H NMR titration experiment (Figure 7. 7). The ^{1}H NMR of the triaminopyrimidine **15** in CD_2Cl_2 showed broad peaks in the three main regions corresponding to the amino groups (*ca.* 6.9 ppm), to the sugar protons (3.0-5.0 ppm) and to the disiloxane protecting groups (*ca.* 1.1 ppm). These broad peaks suggests the presence of oligomeric aggregates which arise from the self-association of individual triaminopyrimidine units in solution. Progressive addition of a diethylbarbituric acid solution in deuterated dichloromethane induced a downfield shift of the NH_2 protons from 6.96 ppm to 8.71 ppm, characteristic of hydrogen-bond formation. However, the ^{1}H NMR of the triaminopyrimidine/ diethylbarbituric acid equimolar mixture did not display improved peak widths, even after 2 days of ultrasonication. This

result suggests the formation of hydrogen-bonded polydisperse, oligomeric structures from DNA-base analogue **15** and diethylbarbituric acid **14**.[5, 6]

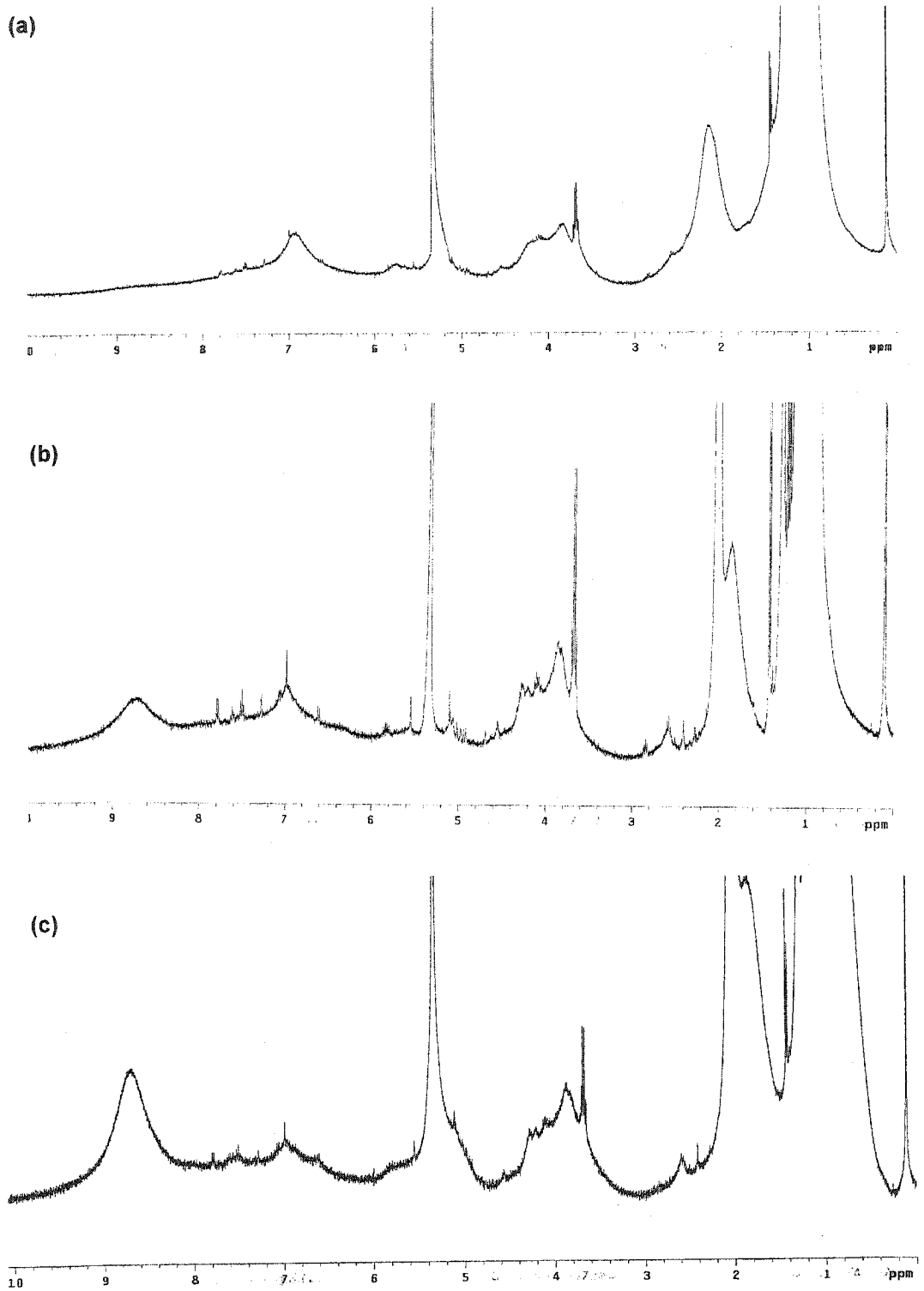


Figure 7. 7. ^{1}H NMR titration of DNA-base analogue **15** using diethylbarbituric acid **14** in CD_2Cl_2. (a) Before titration. (b) After adding 0.5 eq of diethylbarbituric acid **14**. (c) After adding 1.0 eq. of diethylbarbituric acid **14**.

7.2.3.2. Electrospray Ionisation Mass Spectrometry of DNA-base Analogue **15** and Diethylbarbituric Acid **14** Mixture

The ^{1}H NMR titration experiment suggested that the self-assembly of triaminopyrimidine nucleoside **15** with diethylbarbituric acid **14** resulted in hydrogen-bonded oligomers. However, these ^{1}H NMR experiments do not provide quantitative information about the size of these hydrogen-bonded aggregates. Electrospray ionisation mass spectrometry (ESI-MS) analysis was therefore necessary to quantify the number of monomers involved in the hydrogen-bonding of triaminopyrimidine nucleoside **15** with diethylbarbituric acid **14**.

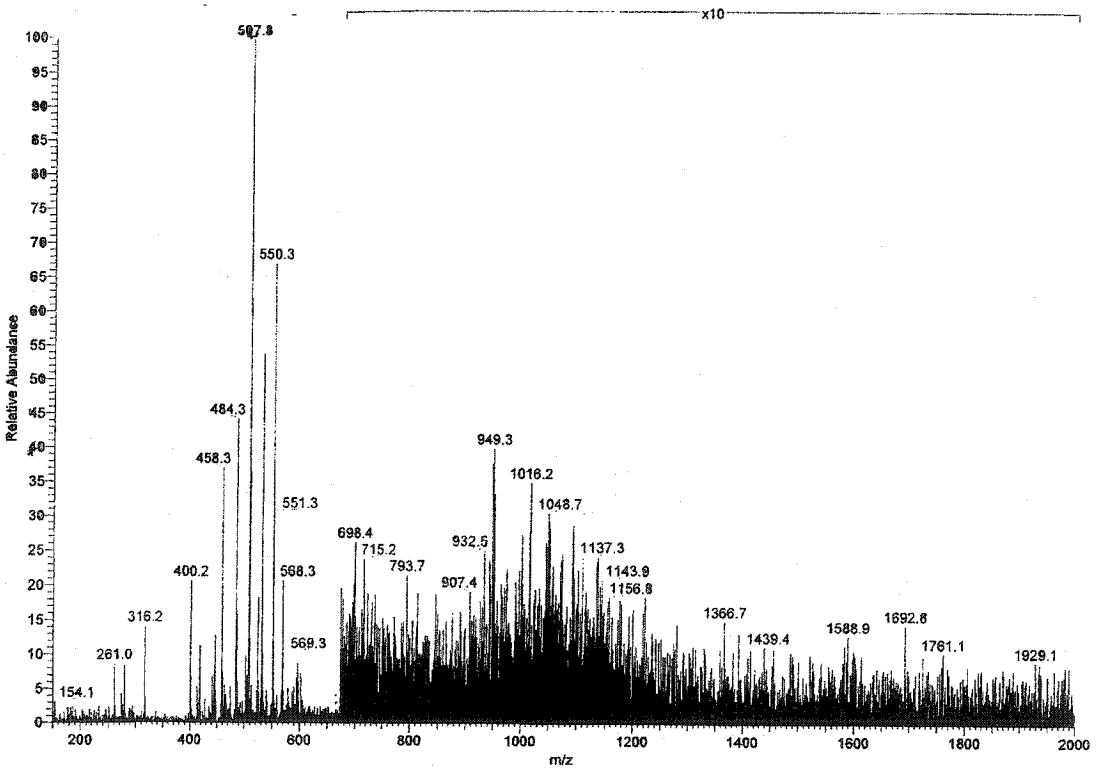


Figure 7. 8. Electrospray ionisation mass spectrum of equimolar triaminopyrimidine nucleoside **15** and diethylbarbituric acid **14** mixture.

Figure 7. 8 shows the ESI mass spectrum obtained for equimolar mixtures of triaminopyrimidine nucleoside **15** and diethylbarbituric acid **14**. Using M_1 and M_2 for the monomer molecular weights (M_1 for **15** = 483, M_2 for **14** = 184), m/z molecular ions detected can be listed as $(M_1+M_2+Na^+ +Li^+)$, $2(M_1+M_2+Na^+ +Li^+)$, $(2M_1+M_2+2H^+)$, $2(M_1+Na^+ +H^+)$. However, no peak corresponding to the hexameric rosette expected molecular weight (M = 2004) was detected, consistent with the absence of discrete supramolecular structures from triaminopyrimidine **15** and diethylbarbituric acid **14**.

7.2.4. Self-Assembly of Triaminopyrimidine 15 with DNA-base Analogue 16

7.2.4.1. ^{1}H NMR Titration of DNA-base Analogue **15** by Cyanuric Acid **16**

As shown by similar ^{1}H NMR titration experiments, the hydrogen-bonded self-assembly of triaminopyrimidine DNA-analogue **15** (Figure 7. 9a) with cyanuric acid DNA-analogue **16** (Figure 7. 9b) differs dramatically from its assembly with diethylbarbituric acid **14** (Figure 7. 10). Addition of cyanuric acid **16** caused the same 1.75 ppm downfield shift of the NH_2 protons, as in the case of diethylbarbituric acid guest molecules, due to intermolecular hydrogen-bonding between the two DNA-base analogues. On the other hand, addition of 1 equivalent of a CD_2Cl_2 solution of cyanuric acid **16** resulted in the immediate emergence of a finer structure for both complementary molecules (Figure 7. 10), suggesting the creation of discrete, macrocyclic structures from **15** and **16** in solution. Despite a significant gain in peak resolution, the NMR peaks were still slightly broad. This is likely due to the presence of two anomers for each of the

triaminopyrimidine **15** and cyanuric acid **16**, which can possibly result in a less selective self-assembly for this system.

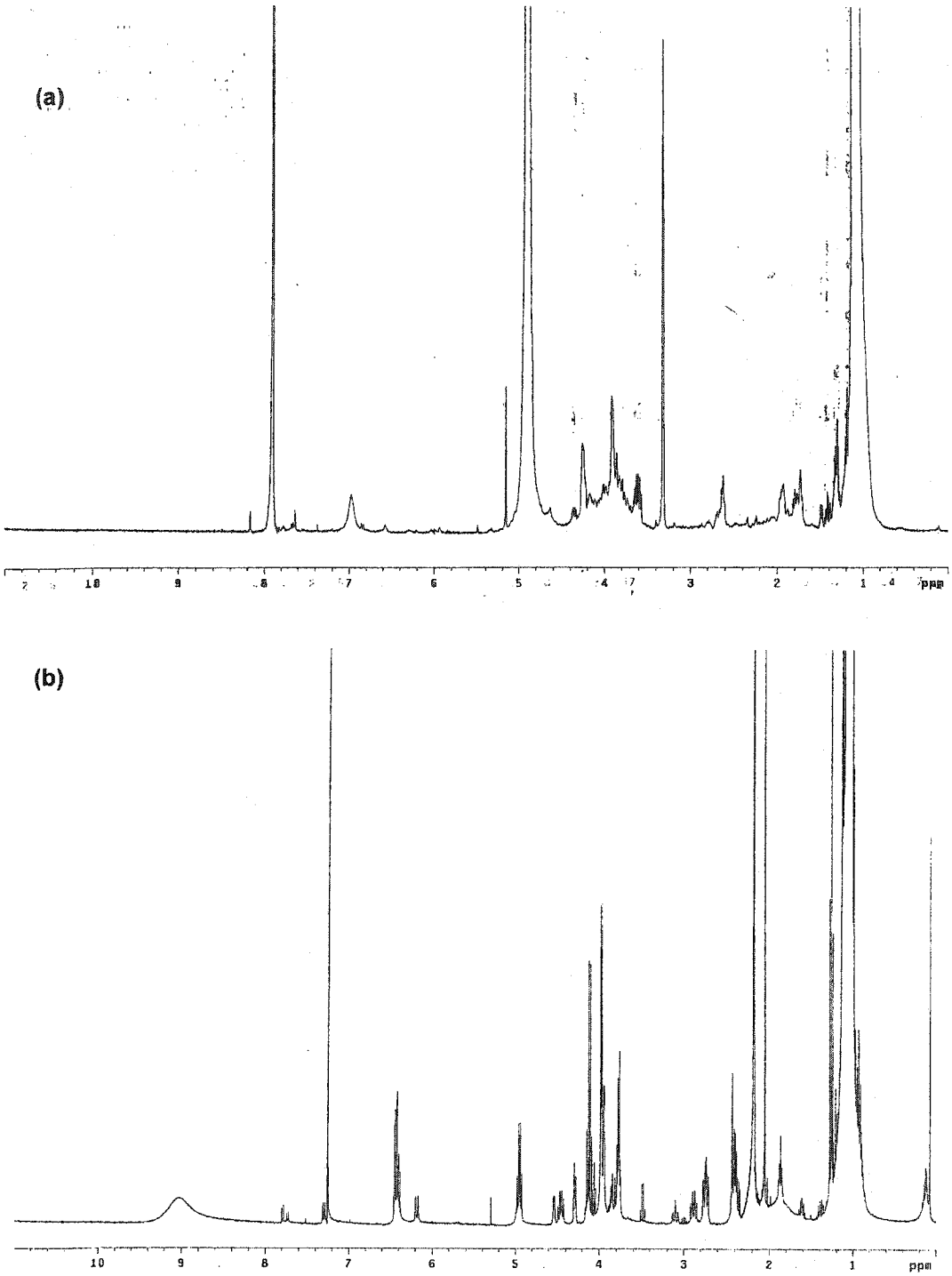


Figure 7. 9. (a) ^{1}H NMR spectrum of DNA-base analogue **15** in MeOD. (b) ^{1}H NMR spectrum of DNA-base analogue **16** in $CDCl_3$.

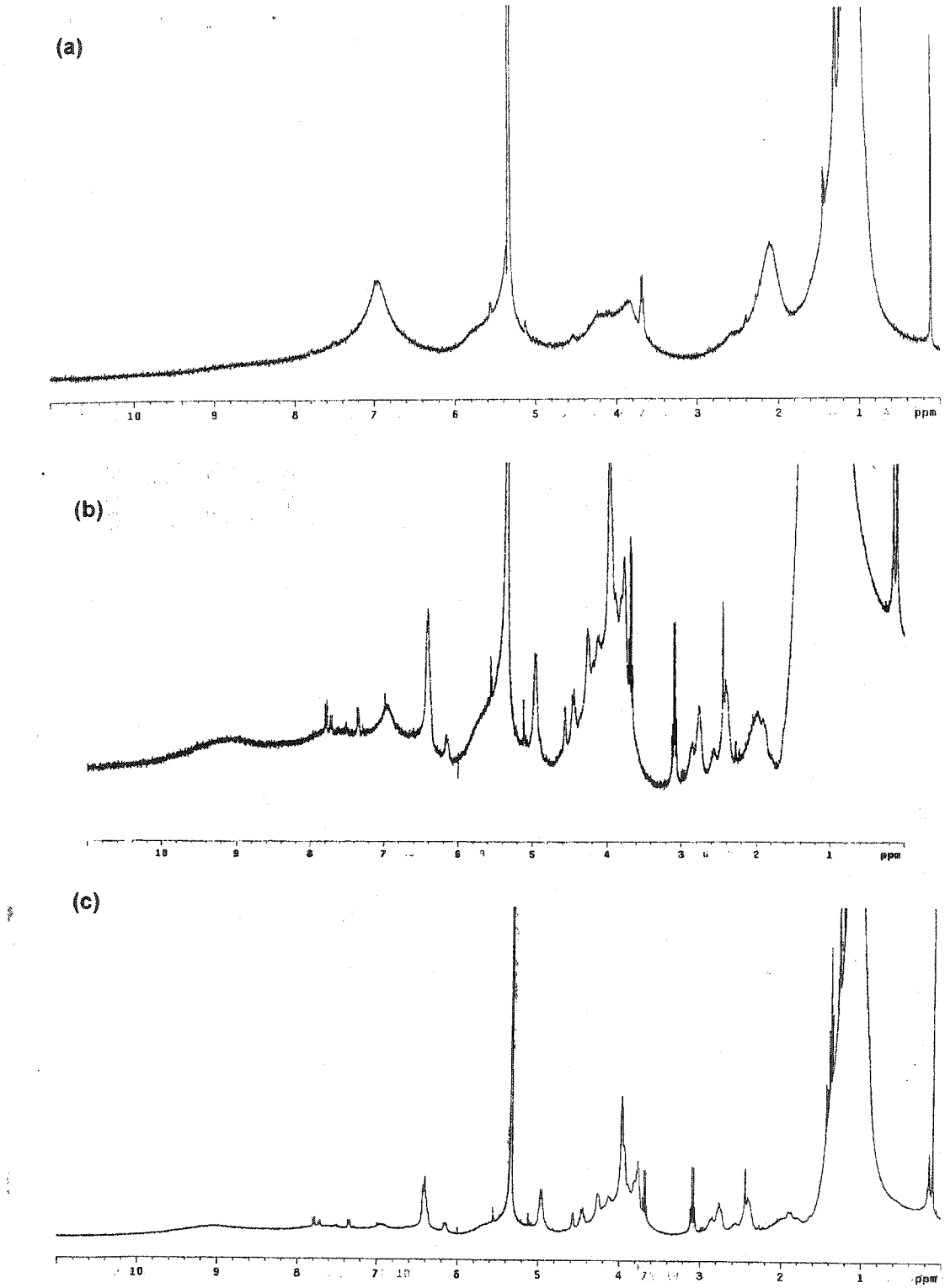


Figure 7. 10. ^{1}H NMR titration of DNA-base analogue **15** using cyanuric acid **16** in CD_2Cl_2. (a) Before titration. (b) After adding 0. 5 eq. of cyanuric acid **16**. (c)After adding 1.0 eq. of cyanuric acid **16**.

7.2.4.2. Electrospray Ionisation Mass Spectrometry of DNA-base Analogue **15** and Cyanuric Acid **16** Mixtures

As for the triaminopyrimidine nucleoside **15**/diethylbarbituric acid **14** system, ESI-MS analysis was required to evaluate the size of the discrete supramolecular structures formed from DNA-base analogues **15** and **16**.

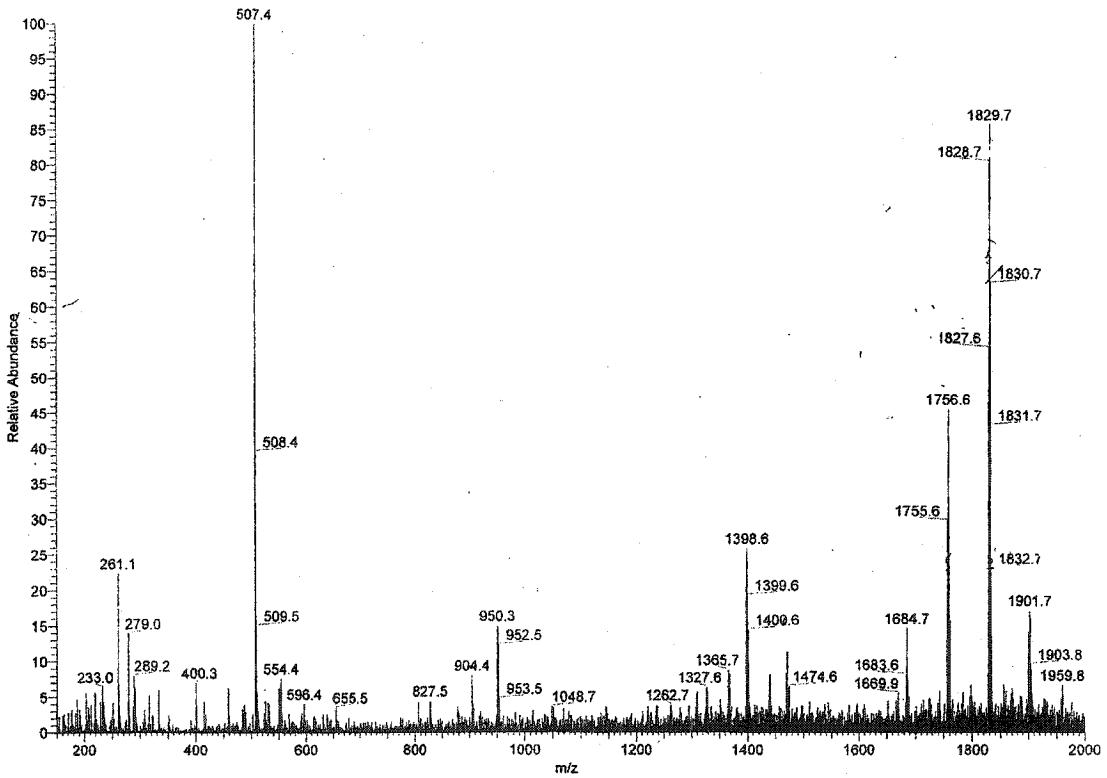


Figure 7. 11. Electrospray ionisation mass spectrum of equimolar triaminopyrimidine **15** and cyanuric acid **16** mixture.

The hydrogen-bonded aggregates observed for the equimolar mixture of nucleosides **15** and **16** corresponded to highly charged hexameric rosettes containing sodium or

potassium ions in the 1700-2000 Da mass range (Figure 7. 11). Using M_1 and M_2 for the monomer molecular weights (M_1 for **15** = 483, M_2 for **16** = 486), R_6 for the hexameric rosette expected molecular weights (R_6 = 2907), m/z molecular ions detected can be listed as $[3(R_6\text{-}6H^+\text{+}6Na^+)\text{+}5H^+]/5$, $[3R_6\text{+}2Na^+\text{+}Li^+\text{+}2H^+]/5$, $[R_6\text{+}2H^+\text{+MeOH}]/2$, $[3R_6\text{+}2H^+]/6$, $M_1\text{+}M_2$, and $M_1 + Na^+$.[21] These molecular ions suggest the possible presence of monomeric, dimeric, and hexameric hydrogen-bonded species in this equimolar mixture of **15** and **16**. As a result, our preliminary 1H NMR spectroscopy and ESI-MS studies, as well as theoretical MM+ and PM3 calculations are all consistent with the probable self-assembly of triaminopyrimidine DNA-analogue **15** with cyanuric acid DNA-analogue **16** into cyclic hexamers by hydrogen-bonding.. On the other hand, these data suggested that oligomeric linear tapes were obtained from triaminopyrimidine nucleoside **15** and diethylbarbituric acid **14**.

7.2.5. Absorbance and Fluorescence Properties of DNA-base Analogue 15

DNA-strand hybridisation has mostly been assayed by absorbance. Fluorescence spectroscopy has been used to evaluate DNA-hybridisation using fluorophore labelled-oligonucleotides which can be attached to microarrays.[22] Substituted pyrimidines, including a few 2, 4, 6-triaminopyrimidine derivatives,[23] have been shown to exhibit fluorescence properties. Triaminopyrimidine nucleoside **15** was discovered to be strongly fluorescent under exposure to UV-Visible light.[24] The fluorescence of triaminopyrimidine **15** solutions in chloroform was measured in conjunction with its UV-Vis absorbance spectra (Figures 7. 12 and 7. 13).

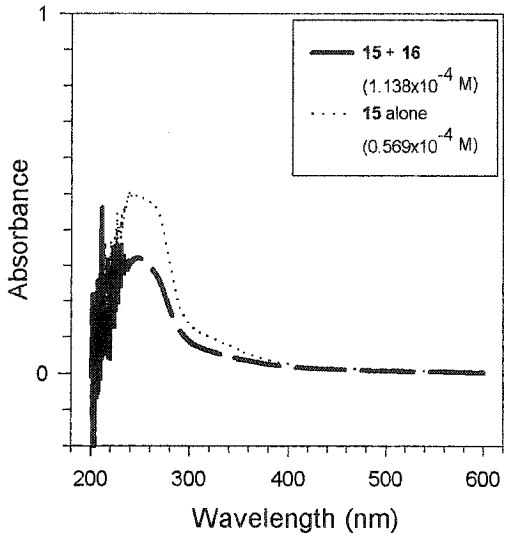


Figure 7. 12. UV-Vis absorbance spectra of triaminopyrimidine **15** alone and in equimolar mixtures of cyanuric acid **16** in chloroform.

The UV-Vis absorbance spectra indicated a principal absorbance at λ_{max} = 254 nm, corresponding to a $\pi \rightarrow \pi^*$ transition of the triaminopyrimidine **15**, along with a shoulder around 350 nm (Figure 7. 12).[25] Preliminary fluorescence measurements were used to monitor the self-assembly between triaminopyrimidine **15** and its complementary cyanuric acid building block **16**, and probe the potential abilities of nucleoside analogue **15** to detect hybridisation which relies on the combined effects of hydrogen-bonding and π-stacking interaction (Figure 7. 13). Addition of 1 equivalent of cyanuric acid **16** solution in chloroform induced a 1.4-fold fluorescence quenching, along with a 3 nm-bathochromic shift. These fluorescence experiments consequently suggest that π-stacking might be involved during the hydrogen-bond assembly of triaminopyrimidine **15** and cyanuric acid **16** and the presence of higher-order structures from these complementary units.[26]

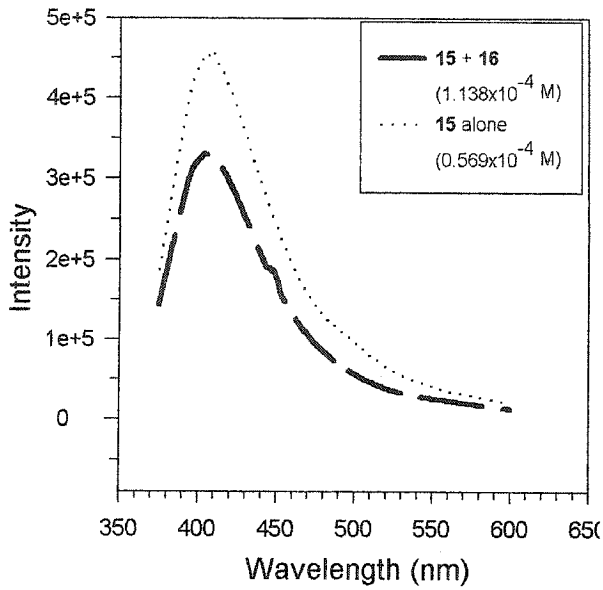


Figure 7. 13. Steady-state emission fluorescence spectra of triaminopyrimidine **15** alone and in equimolar mixtures of cyanuric acid **16** at λ_{exc} = 365 nm in chloroform.

7.2.6. Transmission Electron Microscopy and Dynamic Light Scattering Studies of Triaminopyrimidine 15/ Diethylbarbituric acid 14 and Triaminopyrimidine 15 / Cyanuric Acid 16 Mixtures

Transmission electron microscopy (TEM) studies of triaminopyrimidine **15**/ diethylbarbituric acid **14** and triaminopyrimidine **15** /cyanuric acid **16** mixtures allowed direct visualisation of second level of self-organisation of these molecules, as well as their different self-assembly behaviour. Figures 7. 14 and 7.15 show transmission electron micrographs of carbon-coated grids prepared from deposited solutions of triaminopyrimidine **15**/diethylbarbituric acid **14** and triaminopyrimidine **15**/cyanuric acid **16** mixtures in dichloromethane.[27] Large, sheet-like aggregates are observed for triaminopyrimidine **15**/diethylbarbituric acid **14** (Figure 7. 14).[28]

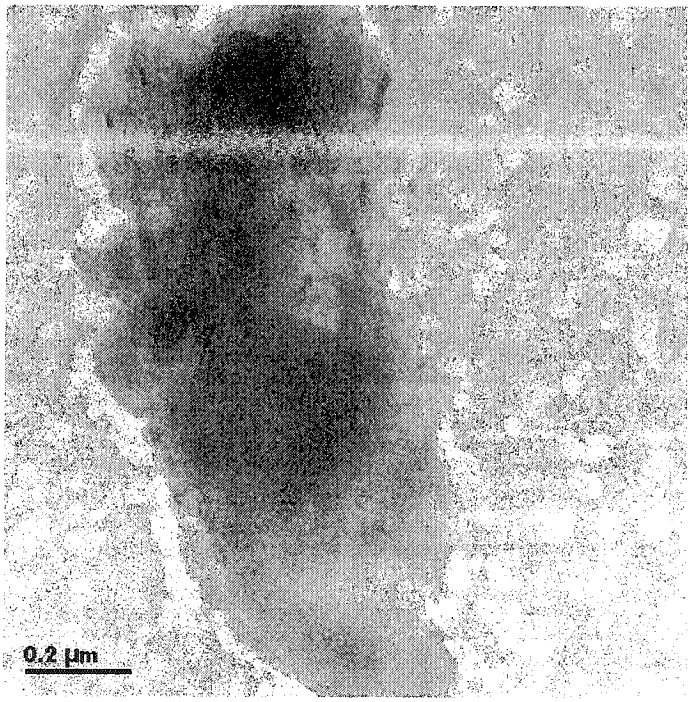


Figure 7. 14. Electron micrographs prepared from deposited solutions of triaminopyrimidine **15**/diethylbarbituric acid **14**.

On the other hand, the TEM of samples of triaminopyrimidine **15**/cyanuric acid **16** mixtures showed the formation of significantly different supramolecular structures. In contrast with triaminopyrimidine **15**/diethylbarbituric acid **14** mixtures, elongated aggregates, with length as great as 170 nm, arise from the triaminopyrimidine **15**/cyanuric acid **16** pair. (Figure 7. 15) The outer hydrodynamic diameter of these elongated aggregates was determined from the intensity profile of the electron micrograph (Figures 7.15c-d), which measures the contrast across the rod-like structures, hence the topography. The outer hydrodynamic diameter of these rod-like structures was measured as *ca.* 4.2 ± 1.0 nm, in close agreement with the estimated diameter of the self-assembled hexameric macrocycles of triaminopyrimidine **15** and cyanuric acid **16** (3.2 nm). This diameter was observed on freshly purified samples of triaminopyrimidine **15** and cyanuric acid **16** mixtures, and for various direct deposition conditions (with and

without staining) (see experimental section).[29] As suggested by the fluorescence measurements, this result also confirms further organisation of the supramolecular cycles from triaminopyrimidine **15** and cyanuric acid **16** equimolar mixtures through π-π stacking and/or alkyl-alkyl interactions.

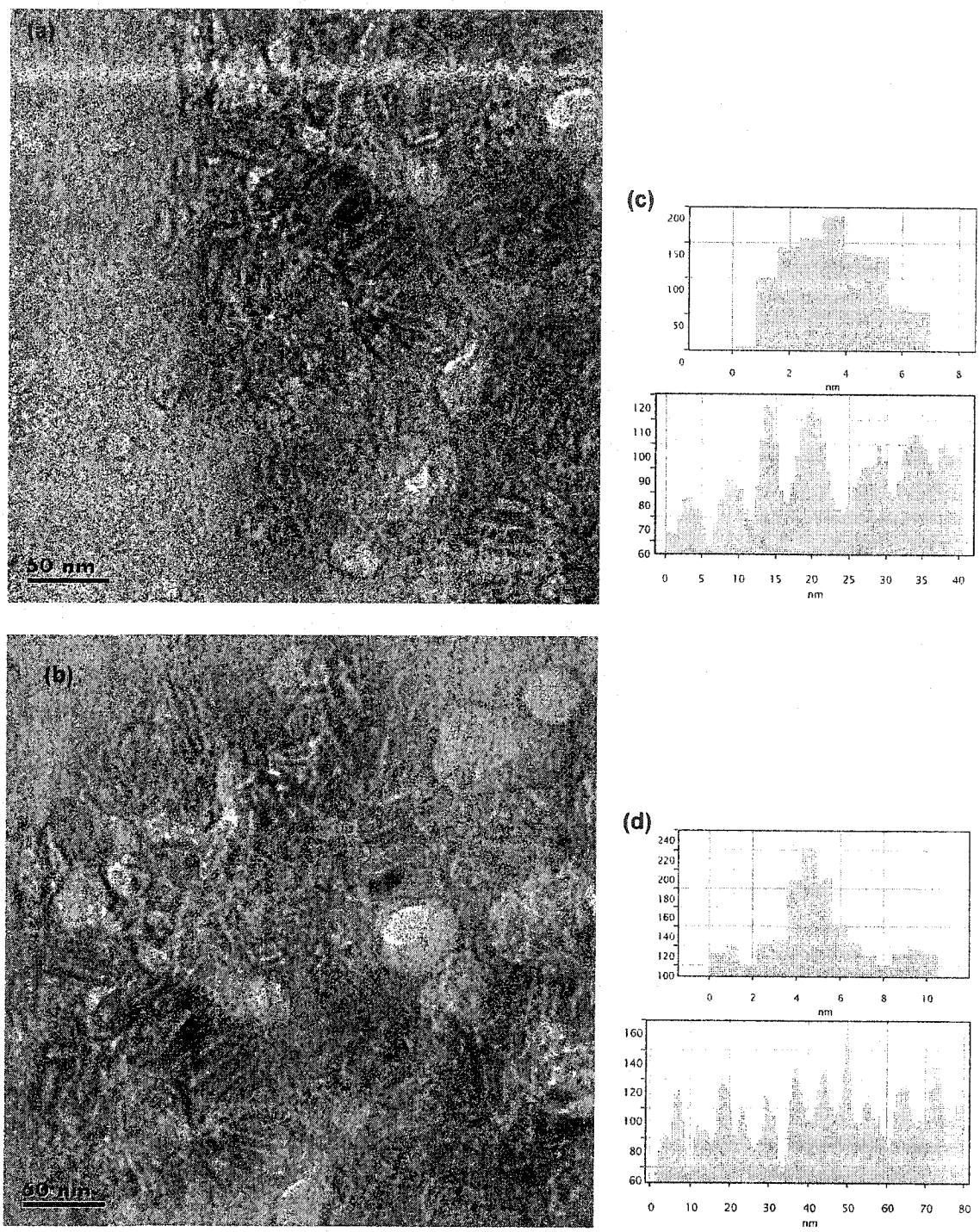


Figure 7. 15. (a) and (b) Electron micrographs prepared from deposited solutions of triaminopyrimidine **15**/ cyanuric acid **16** using uranyl acetate as a staining agent. (c) and (d) Profile analysis of the TEM images. Insets: magnified profile analysis to single rod-like structures (see text).

Dynamic light scattering (DLS) studies were carried out for equimolar mixtures of triaminopyrimidine **15** and cyanuric acid **16** in dichloromethane at scattering angles of 45°, 90°, and 135°, and confirmed the presence of these elongated aggregates in solution.[30] The hydrodynamic diameters obtained for these angles were significantly different from one angle to the other, *e.g.,* 165.1 nm at 45° and 93.8 nm at 135°, consistent with the presence of elongated, rather than spherical aggregates in solution. Thus, the undergoes self-assembly into elongated aggregates both in solution (DLS) and in the solid state (TEM).

7.2.7. Theoretical Evaluation of the Packing Properties

Similar studies of hydrogen-bonded rosettes showed that tube-like structures would arise as a result of stacking interactions along the normal to the hexameric rosette plane.[6d,e] Semi-empirical PM3 calculations were carried out to determine the π-stacking properties of these hexameric DNA-rosettes. A DNA-triple helical system composed of triaminopyrimidine and thymine dinucleotides was used as a starting geometry to reduce the computational time required by such quantum mechanical method. The optimised structures displayed favourable interactions between the hydrogen-bonded base-pairs, suggesting the formation of rod-like nanostructures from hexameric rosettes. (Figure 7. 16)

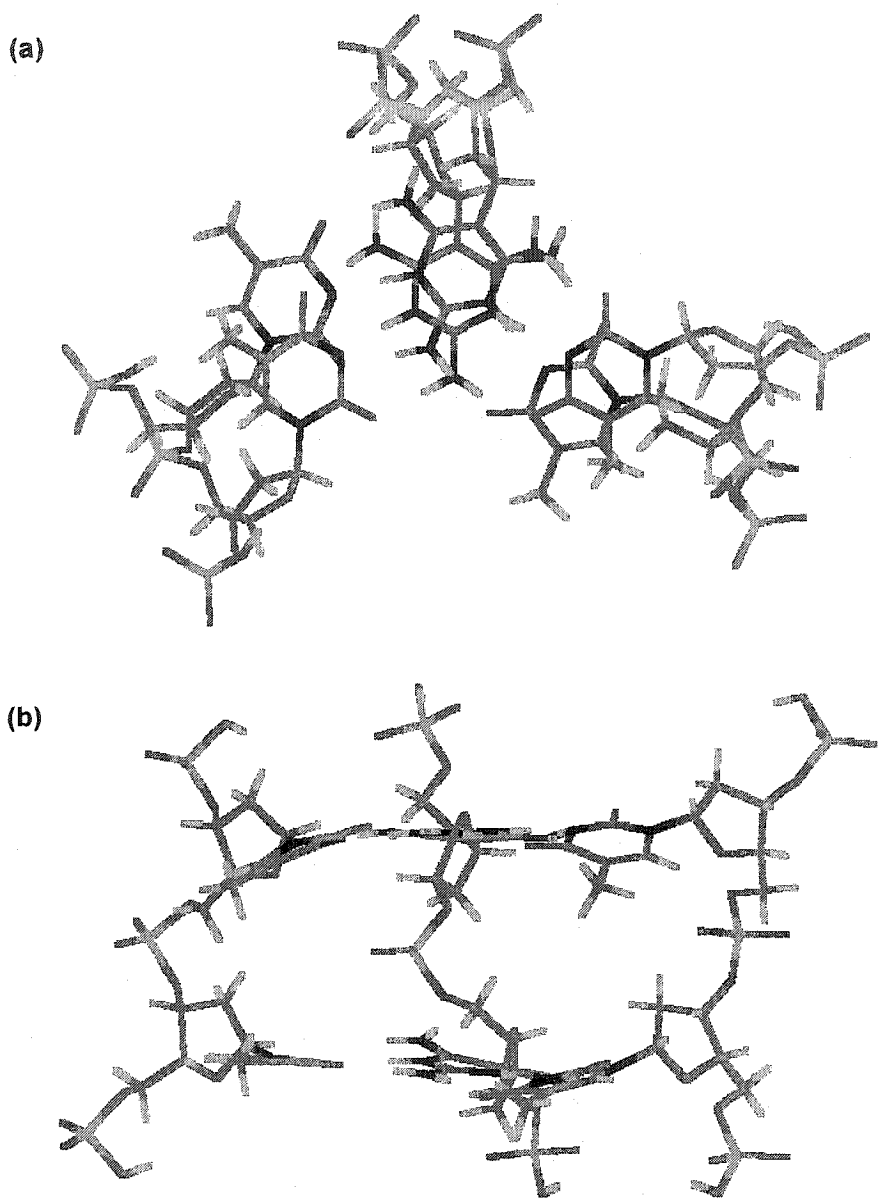
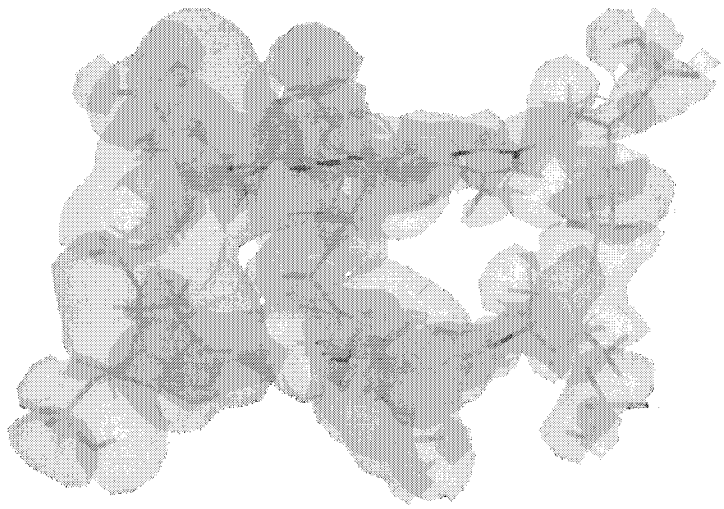
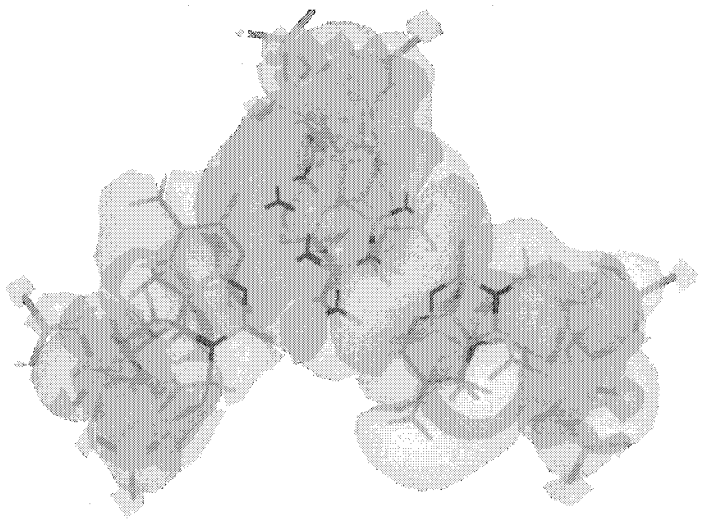


Figure 7. 16. PM3 optimised geometry for the triaminopyrimidine/thymine dinucleotide triplex. (a) Top view. (b) Side view.

Electronic evidence is necessary to gain insight into the formation of open, helical structures from *cis*-azodibenzoic and isophthalic acids. The hydrogen-bonding molecular orbitals involved in the formation of the triaminopyrimidine/thymine dinucleotide triplex were observed at low energies (Table 7. 4). The hydrogen-bonding MO diagram for the helical triplex displayed in Table 7. 4 clearly showed a single lobe over the hydrogen-bond, consistent with the formation of strong hydrogen-bonded aggregates. Molecular orbital 176 (Table 7. 4) covered the entire hydrogen-bonded structure and displayed a positive lobe of π- symmetry between the stacked bases, providing evidence for favourable π-π stacking interactions in the dinucleotide triplex. As a result, triaminopyrimidine 15 and thymine should yield stable hydrogen-bonded helical aggregates.

Table 7. 4. MO diagram of hydrogen-bonded **T + 15** complexes determined using PM3 geometry optimisations

MO Energy	MO diagram
MO 176 E = -3.77eV	
MO 97 E = -10.34eV	

These preliminary PM3 results showed the possible incorporation of these monomers into new artificial DNA strands, but also the favourable triplex formation with natural, complementary thymine-containing DNA strands, which find considerable interest in antisense/antigene technology. These PM3 optimised structures displayed

favourable π-π intermolecular interactions between the base-pairs, demonstrating the formation of rod-like nanostructures from hexameric rosettes. (Figure 7. 16) Figure 7. 17 shows the proposed model for π-stacked triaminopyrimidine **15**/ cyanuric acid **16** hexameric rosettes, generated from the MM^+ optimised macrocycle geometries. In this proposed model, favourable π-π stacking of such supramolecular cycles can lead to helical structures with high aspect ratio where the hexameric rosettes would be slightly twisted relative to the normal of the macrocycle plane at interplanar distances ranging between ca. 4.5 Å and 6 Å.

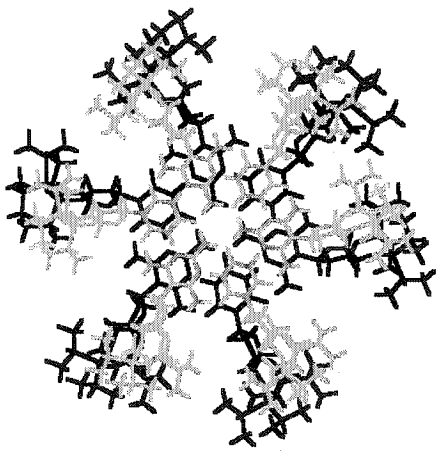


Figure 7. 17. Proposed model for the stacking geometry of the triaminopyrimidine **15**/ cyanuric acid **16** hexameric rosette, generated from the MM^+ optimised macrocycles fitted on top of each other. Top view.

7.3. Conclusion

In conclusion, a novel biomimetic DNA analogue with interesting fluorescence properties has been successfully synthesised to generate functional supramolecular architectures. Preliminary experimental studies suggest that triaminopyrimidine nucleoside **15** might undergo a sterically controlled self-assembly into hydrogen-bonded

linear tapes and hexameric rosettes. Further self-association of the hydrogen-bonded triaminopyrimidine/cyanuric acid complex into elongated, rod-like nanostructures was detected through dynamic light scattering and transmission electron microscopy, suggesting the hierarchical formation of higher-order, π-stacked assemblies. Interestingly, the hydrogen-bond self-assembly of the DNA analogue significantly decreased the fluorescence of the nucleosides, and this guest-induced fluorescence quenching can be used for the development of DNA- hybridisation probes. In addition, preliminary theoretical results not only indicated the possible incorporation of the triaminopyrimidine nucleoside into new types of artificial DNA strands but also triplex formation with natural, complementary DNA strands containing thymine, thereby extending the applications of this monomer to DNA analogue to antisense/antigene technology.

7.4. Experimental section

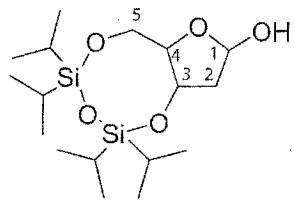
7.4.1. Generalities

Materials. All reagents were purchased from the Aldrich Chemical Co. The structures of the intermediates and the final products were confirmed by NMR spectroscopy and mass spectrometry.

Equipment. ^{1}H and ^{13}C-NMR spectra were acquired on a Varian Mercury 400 and Varian Unity 500 spectrometers, 2D-COSY NMR spectra were acquired on a Varian Unity 500 spectrometer. Electrospray ionization (ESI) and atmospheric pressure chemical ionization (APCI) mass spectra were acquired by direct infusion into a Quattro

II triple quadrupole (Micromass, Manchester, UK) with the spray voltage set to 3.5 kV, the source temperature 150-200°C, sample infusion rate 5 µl/min using a syringe pump (Harvard Apparatus). UV-vis spectra were measured on a Varian CARY 1 UV-vis spectrophotometer equipped with a Peltier temperature controller. Fluorescence data was acquired using a PTI (Photon Technology International) TimeMaster model C-720F spectrofluorimeter. Transmission electron microscopy (TEM) was conducted on a JEOL-2000 FX instrument by using the direct method with and without uranyl staining.

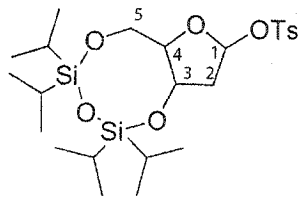
7.4.2. Synthesis



18

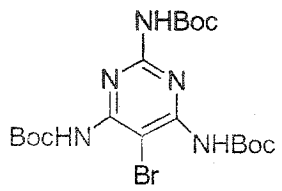
2-deoxy-3,5-*bis*-O-(tetraisopropylsiloxyl)-D-ribofuranose (18). 2-deoxy-D-ribose (1 g, 7.41 mmol) in freshly distilled pyridine (9.26 mL) was stirred under N_2 atmosphere at 40°C in presence of 1,3-dichloro-1,1',3,3'-tetraisopropyldisiloxane (2.6 mL, 8.89 mmol). After 2 hrs, the reaction mixture was neutralized using 1M HCl (3 mL) and diluted with diethyl ether (50 mL). The organic layer was washed with saturated $NaHCO_3$ (50 mL) and water (2 x 50 mL), then dried over $MgSO_4$. The solvent was evaporated under reduced pressure to give a colorless oil. The desired compound **18** was isolated by column chromatography on silica gel using an ethylacetate/hexanes (20:90) as the eluent. **18** (1.922 g, 69 %). ^{1}H-NMR (400 MHz, $CDCl_3$) δ 5.46 (dd, H_1, 4.8 Hz), 4.45 (m, H_4),

H_3), 3.85 (dd, H_5), 3.68 (dd, H_5), 2.31 (m, H_2), 2.02-2.12 (m, H_2), 1.07 (s, 28 H). ESI-MS (neg): 376.



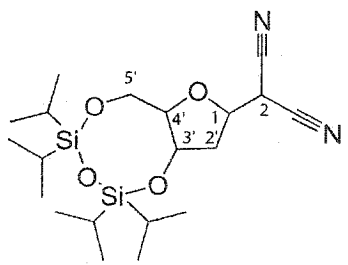
19

1-O-(*p*-toluenesulfonyl)-2-deoxy-3,5- *bis*-O-(tetraisopropylsiloxyl)- ribofuranose (19). A solution of compound **18** (250 mg, 0.66 mmol) in dry CH_2Cl_2 (5 mL) was stirred with *p*-toluenesulfonyl chloride (150.0 mg, 0.66 mmol) under N_2 atmosphere in presence of Et_3N (0.1 μL) for 2 hrs. The reaction was diluted with CH_2Cl_2 (10 mL) and quenched by adding water (10 mL). The organic layer was washed with saturated $NaHCO_3$ (2 x 10 mL) and water (10 mL), then dried over $MgSO_4$. The solvents are evaporated under reduced pressure. The formation of the *p*-toluenesulfonyl derivative **19** was verified by ^{1}H-NMR in $CDCl_3$ which showed 2 sets of doublets of doublets in the aromatic region and 2 singlets corresponding to the methyl protons, consistent with the presence of 2 anomers α and β. The formed compound was used without further purification (341.7 mg, crude yield 97 %) ^{1}H-NMR (400 MHz, $CDCl_3$) δ 7.92 (d, Ar-H_1), 7.78 (d, Ar-H_1'), 7.40 (d, Ar-H_2), 7.12 (d, Ar-H_2'), 5.56 (t, H_1), 4.57 (dd, H_4), 4.12-3.84 (m, H_3, $2H_5$), 3.17 (dd, H_2), 3.00 (dd, H_2), 2.50 (s, $1CH_3$), 2.50 (s, $1CH_3$), 2.33 (s, $1CH_3$), 1.04 (s, 28 H).



20

(Tri-N-*tert*-butoxycarbonyl)-2,4,6-triamine-5-bromopyrimidine (20). 2,4,6-Triamino-5-bromopyrimidine was synthesized from 2,4,6-triaminopyrimidine using a reported protocol.[31] The brominated pyrimidine (721.9 mg, 3.52 mmol), di(*tert*-butoxy)carbonate (5.096 g, 24.79 mmol), and dimethylaminopyridine (310.4 mg, 2.48 mmol) were dissolved in presence of Et_3N (4.04 mL, 28.34 mmol) in freshly distilled THF (45 mL). The reaction mixture was stirred under N_2 atmosphere at room temperature for 15 hrs resulting in an orange brown suspension. The reaction was quenched using aqueous 5 % $NaHCO_3$ (1.5 mL), and the solvents were evaporated under reduced pressure. The obtained residue was dissolved in diethyl ether (25 mL), and the organic layer was washed with aqueous 5 % $NaHCO_3$ (2 x 25 mL), water (25 mL) and brine (25 mL). The organic layer was dried over anhydrous $MgSO_4$, filtered, and the solvents were evaporated under reduced pressure. The desired compound **20** (972.7 mg, 54 %) was isolated by column chromatography on silica gel using ethyl acetate/hexanes (40:60) as the eluent. $R_f \sim 0.75$. ^{1}H-NMR (400 MHz, $CDCl_3$) δ (ppm): 1.10-1.90 (27 H).

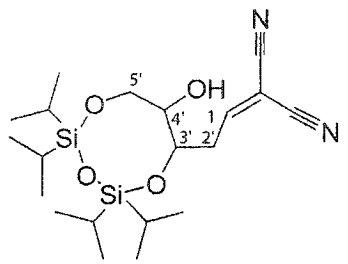


22

1-(2'-deoxy-5',3'- *bis*-O-(tetraisopropylsiloxyl)- ribofuranosyl) propanedinitrile (22). Method A. Malononitrile (149.0 mg, 2.26 mmol) in freshly distilled THF (1 mL) was added dropwise to a suspension of 95% NaH (54 mg, 2.26 mmol) in THF (0.25 mL) at 0°C. Tosylate **19** (400 mg, 0.75 mmol) in THF (0.5 mL) was added dropwise, and the reaction mixture was stirred at room temperature overnight under N_2 atmosphere. The reaction was quenched with 5% aqueous NH_4Cl (6 mL). The reaction mixture was diluted with ethylacetate or dichloromethane (25 mL) and washed with water (2 x 25 mL) and brine (25 mL). The organic layer was dried over anhydrous $MgSO_4$, filtered, and the solvents were evaporated under reduced pressure. Compound **22** (20 mg, 5%) was obtained as an off-white oil after silica gel chromatography using ether/hexanes (60:40) as eluent.

Method B. Malononitrile (52.7 mg, 0.80 mmol) in freshly distilled THF (0.5 mL) was added dropwise to a suspension of 95% NaH (19.2 mg, 0.80 mmol) in THF (0.25 mL) at 0°C. Protected sugar **18** (100 mg, 0.26 mmol) in THF (0.5 mL) was added dropwise, and the reaction mixture was stirred at room temperature under N_2 atmosphere. The reaction was monitored by TLC until disappearance of the starting material (1 hr), then quenched with saturated NH_4Cl (6 mL). The reaction mixture was diluted with dichloromethane (25 mL) and washed with water (2 x 25 mL) and brine (25 mL). The organic layer was dried over anhydrous $MgSO_4$, filtered, and the solvents were evaporated under reduced pressure. Compound **22** (37.7 mg, 33 %) was obtained as an off-white oil after silica gel chromatography using ether/hexanes (60:40) as eluent. $R_f \sim 0.25$. ^{1}H-NMR (400 MHz, $CDCl_3$) δ 4.38 (dd, H_4'), 4.13-3.98 (m, H_1', H_3', H_5'), 3.77

(dd, H_5'), 3.13-3.18 (m, H_2'), 2.55-2.22 (m, H_2'), 1.06 (s, 28 H). APCI-MS: m/z: Calc. 425.0 (M+1), 849.0 (2M+1); found: 425.4 (M+1), 849.1 (2M+1) .

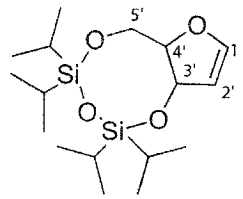


24

1-(2'-deoxy-5',3'- *bis*-O-(tetraisopropylsiloxyl)- ribofuranosyl) propylidene dinitrile (24). Method A: Malononitrile (17.6 mg, 0.26 mmol) in freshly distilled MeOH (1 mL) was added to a suspension of K_2CO_3 (3.7 mg, 0.026 mmol) in MeOH (0.5 mL) at room temperature. Protected sugar **18** (50 mg, 0.13 mmol) in THF (0.5 mL) was added dropwise, and the reaction mixture was stirred at room temperature overnight under N_2 atmosphere. The reaction was then quenched with saturated NH_4Cl (6 mL). The reaction mixture was diluted with dichloromethane (25 mL) and washed with water (2 x 25 mL) and brine (25 mL). The organic layer was dried over anhydrous $MgSO_4$, filtered, and the solvents were evaporated under reduced pressure. Compound **24** (8.3 mg, 15 %) was obtained as an off-white oil after silica gel chromatography using ether/hexanes (60:40) as eluent. $R_f \sim 0.5$.

Method B: Malononitrile (17.8 mg, 0.27 mmol) in freshly distilled THF (0.5 mL) was added dropwise to a suspension of 95% NaH (12.2 mg, 0.53 mmol) in THF (0.25 mL) at 0°C. Protected sugar **18** (200 mg, 0.53 mmol) in THF (0.5 mL) was added dropwise, and the reaction mixture was stirred at room temperature under N_2 atmosphere. The reaction was monitored by TLC until disappearance of the starting material (1 hr),

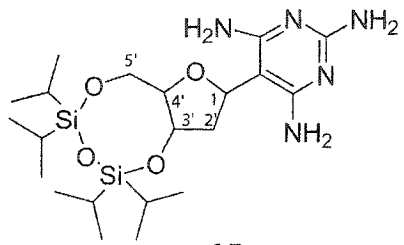
then quenched with saturated NH_4Cl (6 mL). The reaction mixture was diluted with dichloromethane (25 mL) and washed with water (2 x 25 mL) and brine (25 mL). The organic layer was dried over anhydrous $MgSO_4$, filtered, and the solvents were evaporated under reduced pressure. Compound **24** (29.1 mg, 13 %) was obtained as an off-white oil after silica gel chromatography using ether/hexanes (60:40) as eluent. $R_f \sim$ 0.5. ^{1}H-NMR (400 MHz, $CDCl_3$) δ 4.53 (d, H_1), 4.14 (dd, H_4'), 4.04 (dd, H_5'), 3.97 (dd, H_3'), 3.82 (dd, H_1'), 3.77 (dd, H_5'), 3.04 (m, H_2'), 2.40-2.19 (m, H_2'), 1.06 (s, 28 H).



25

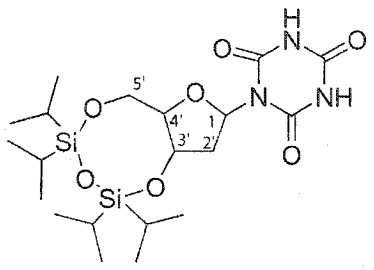
1,4-Anhydro-(5',3'-*bis*-O-(tetraisopropylsiloxyl))- 2'-deoxy-D-*erythro*-pent-1-enitol (25). The 3,5-diprotected sugar **18** (100 mg, 0.265 mmol) was placed under vacuum in a flame-dried three-neck flask equipped with a condenser. Dichloromethane (2 mL) was added under N_2 atmosphere with Et_3N (139 µL, 1.006 mmol). The resulting solution was cooled to -40°C/-50°C, then mesyl chloride (25.5 µL, 0.331 mmol) was added dropwise. The reaction mixture was maintained at -40°C/-50°C for 3 hrs, then warmed up to room temperature and heated to reflux (50°C-60°C) for 15 hrs. The obtained solution was cooled to room temperature and filtered through a short silica gel column. The filtrate was evaporated under reduced pressure and the obtained clear oil was purified by silica gel chromatography using diethyl ether/petroleum ether (2:98) as eluent, to give **25** (9.5 mg, 10 %). ^{1}H-NMR (400 MHz, $CDCl_3$) δ 6.40 (dd, H_1'), 4.84 (t, H_2'), 4.44 (t, H_3'), 4.12

(dt, H_4'), 3.89 (dd, H_5'), 3.78 (m, H_5'), 1.07 (s, 28 H). ^{13}C-NMR (100 MHz, $CDCl_3$) δ 146.16, 100.90, 70.56, 64.75, 64.63, 18.14, 17.99, 17.95, 17.90, 17.83, 17.65, 17.56, 17.54, 14.60, 13.70, 13.63, 13.05.



15

1-(2'-deoxy-3',5'-*bis*-O-(tetraisopropylsiloxyl)-ribofuranosyl)pyrimidine-2,4,6-triamine (15). Sodium (15.05 mg, 0.65 mmol) and guanidine hydrochloride (62.5 mg 0.65 mmol) were stirred in freshly distilled EtOH (1.5 mL) under N_2 atmosphere until a solution was obtained. A solution of **22** (185.0 mg, 0.44 mmol) in freshly distilled EtOH was added dropwise to the mixture which was heated to reflux for 5 hrs. The reaction mixture was cooled to room temperature and the solvents were evaporated under reduced pressure. The desired compound (60.9 mg, 29%) was isolated as a mixture of α and β anomers by column chromatography on silica gel using dichloromethane/ethanol (0:100 to 40:60 gradient). R_f ~ 0.1 (10:90 dichloromethane/ethanol). ^{1}H-NMR (400 MHz, CD_3OD) δ 6.98 (s, NH_2), 4.25 (m, H_1'), 3.82-4.01 (dd, H_3', H_4'), 3.61 (m, H_5'), 2.63 (m, H_5'), 2.01-1.71 (m, $2H_2$'), 1.06 (s, 28 H). ^{13}C-NMR (100 MHz, CD_3OD) δ 159.34, 158.65, 118.69, 77.52, 77.16, 76.41, 69.27, 68.85, 44.85, 38.29, 36.06, 24.43, 23.82, 16.98, 13.00. ESI-MS: m/z : Calc. 484 (M+1), 507 (M+Na+1), found 484.3 (M+1), 507.3 (M+Na+1).



16

1-(2-deoxy-3,5-*bis*-O-(tetraisopropylsiloxyl)- ribofuranosyl)cyanuric acid (16). A mixture of the tosyl derivative **19** (353 mg, 0.67 mmol), cyanuric acid (85.2 mg, 0.67 mmol), potassium nonafluorobutanesulfonate (539.6 mg, 1.75 mmol), hexamethyldisilazane (98 μL, 0.54 mmol), and trimethylsilyl chloride (261 μL, 2.08 mmol) was heated to reflux in freshly distilled acetonitrile (6.66 mL) under N_2 atmophere. The reaction was allowed to proceed for 16 hrs, then cooled to room temperature. The solvents were evaporated under reduced pressure and the residue was dissolved with $CHCl_3$ (25 mL), washed with saturated $NaHCO_3$ (25 mL) and water (25 mL), then dried over $MgSO_4$. After solvent evaporation, the desired compound (119.2 mg, 37%) was isolated by two consecutive column chromatographies on silica gel using dichloromethane then ethylacetate/hexanes 1:1 as the eluent. ^{1}H-NMR (400 MHz, $CDCl_3$) δ 6.44 (m, H_1'), 4.96 (dd, H_4'), 4.55-4.28 (m, H_3'), 3.98 (dd, H_5'), 3.78 (dd, H_5'), 2.75 (m, H_2'), 2.40 (m, H_2'), 1.07 (s, 28 H). ^{13}C-NMR (100 MHz, $CDCl_3$) δ 148.53, 148.16, 147.91, 85.79, 83.60, 81.75, 72.74, 70.42, 63.58, 38.87, 17.86, 13.69.

7.4.3. Characterisation of the Self-Assembly of Nucleoside 15 with Barbituric Acid 14 and Cyanuric Acid 16

Electrospray Ionisation Mass Spectrometry (ESI) measurements. An equimolar solution of triaminopyrimidine **15** with diethylbarbituric acid **14** or cyanuric acid **16** in a 10 % MeOH/CH_2Cl_2 mixture was directly infused into a Quattro II triple quadrupole (Micromass, Manchester, UK) configured for positive product ion analysis and used with the spray voltage set to 3.5 kV, source temperature 100-200°C, sample infusion rate 5 µl/min using a syringe pump (Harvard Apparatus). For molecular weight determination, the spectrometer was programmed to scan for the product ions from *m/z* 150 to *m/z* 2000 in multichannel acquisition mode (MCA) showing m/z for the monomers and the hexamer.

Sample preparation for TEM measurements by the direct method. A solution of cyanuric acid and 2,4,6-triaminopyrimidine (1:1) was prepared by dissolving the sample in dichloromethane. A carbon-coated 400 mesh copper grid prewashed with chloroform for 12 hrs was dipped into the solution for approximately 1 min then dried on filter paper.

Sample preparation for TEM measurements by staining. A solution of cyanuric acid and 2,4,6-triaminopyrimidine (1:1) was prepared by dissolving the sample in dichloromethane. The solution (10 µL) was deposited on a carbon-coated 400 mesh copper grid, prewashed with chloroform for 12 hrs, then blotted. A drop of aqueous 2 % uranyl acetate was deposited on the air-dried copper grid, blotted, rinsed with a drop of water after 30 s, then dried on paper filter.

Dynamic light scattering (DLS) measurements. Dynamic light scattering measurements were carried out using a 532 nm laser equipped photo-multiplier detector. The autocorrelation functions were acquired for θ values of 45°, 90° and 135° for prefiltered equimolar solutions of triaminopyrimidine **15** and cyanuric acid **16** in dichloromethane. Data acquisition was carried out at 20°C and within a few hours to get a better particle size distribution. Inverse Laplace transforms of the data were performed using Provencher's FORTRAN program CONTIN,[32] and diffusion coefficients were determined from the slope of the relaxation frequencies (Γ) vs q^2. Assuming a spherical behaviour for the particles and using the translational coefficient D_{Tr} and the Stokes-Einstein equation, the hydrodynamic diameters are calculated for each scattering angle.

7.4.4. Theoretical Calculations

The geometries of the triaminopyrimidine, cyanuric acid, and barbituric acid monomers were optimised using PM3 until an RMS gradient of 0.01 was reached. Optimisation of the medium-size supramolecular structures were performed using the PM3 semi-empirical molecular orbital theory. After this optimisation, another monomer was added and the hydrogen-bonded structure energy was minimised. This monomer addition-optimisation sequence was repeated up to the hexameric compound. The hydrogen-bonded geometry and the total heat of formation were extracted for each optimised species. Geometry optimisations used the PM3 method contained in the Gaussian98W[33] program package.

Optimisation of the large-size supramolecular structures were performed using the MM^+ molecular mechanics method. The hydrogen-bonded geometry and the heats of formation were extracted for each MM^+ optimised species by performing a single point calculation using the semi-empirical PM3 method. The PM3 density matrices were obtained from a population analysis within Gaussian98W and as usual symmetrised along the xy diagonal using the Microsoft Excel software.

7.5. References and Notes

[1] (a) J.-M. Lehn, *Supramolecular Chemistry: Concepts and Perspectives*, VCH: Weinheim, 1995. (b) J. L. Atwood, J. E. D. Davies, D. D. MacNicol, F. Vögtle, J. –M. Lehn (eds), *Comprehensive Supramolecular Chemistry*, Pergamon: Oxford, 1996. (c) Whitesides, G. M.; Simanek, E. E.; Mathias, J. P.; Seto, C. T.; Chin, D. N.; Mammen, M.; Gordon, D. M. *Acc. Chem. Res.* **1995**, *28*, 37-44. (d) Lawrence, D. S.; Jiang, T.; Levett, M. *Chem. Rev.* **1995**, *95*, 2229-2260. (e) M. M. Conn, J. Rebek, Jr., *Chem. Rev.* **1997**, *97*, 1647. (f) L. J. Prins, D. N. Reinhoudt, P. Timmerman, *Angew. Chem., Int. Ed.* **2001**, *40*, 2382. (h) E. A. Archer, H. Gong, M. J. Krische, *Tetrahedron*, **2001**, *57*, 1139-1159. (g) R. E. Meléndez, A. D. Hamilton, *Top. Curr. Chem.*, **1998**, *198*, 97.

[2] C. M. Drain, R. Fischer, E. G. Nolen, J. –M. Lehn, *J. Chem. Soc., Chem. Commun.*, **1993**, 243.

[3] (a) S. L. Forman, J. C. Fettinger, S. Pieraccini, G. Gottarelli, J. T. Davis, *J. Am. Chem. Soc.*, **2000**, *122*, 406. (b) T. Giorgi, S. Lena, P. Mariani, M. A. Cremoni, S. Masiero, S.

Pieraccini, J. P. Rabe, P. Samori, G. Piero, G. P. Spada, G. Gottarelli, *J. Am. Chem. Soc.*, **2003**, *125*, 14741.

[44] (a) J. L. Sessler, M. Sathiosatham, K. Doerr, V. Lynch, K. A. Abboud, *Angew. Chem., Int. Ed.*, **2000**, *19*, 1300. (b) J. L. Sessler, R. Wang, *Angew. Chem., Int. Ed.*, **1998**, *37*, 1726. (c) J. L. Sessler, R. Wang, *J. Org. Chem.*, **1998**, *63*, 4079. (d) E. Mezzina, P. Mariani, R. Itri, S. Masiero, S. Pieraccini, G. S. Spada, F. Spinozzi, J. T. Davis, G. Gottarelli, *Chem. Eur. J.*, **2001**, *7*, 389.

[5] (a) Trimers: S. C. Zimmerman, B. F. Duerr, *J. Org. Chem.*, **1992**, *57*, 2215. (b) E. Boucher, M. Simard, J. D. Wuest, *J. Org. Chem.* **1995**, *60*, 1408. (c) J. L. Sessler, J. Jayawickramarajah, M. Sathiosatham, C. L. Sherman, J. S. Brodbelt, *Org. Lett.*, **2003**, *5*, 2627. (d) 2 + 2 Tetramer: J. Yang, E. Fan, S. J. Geib, A. D. Hamilton, *J. Am. Chem. Soc.*, **1993**, *115*, 5314. (e) Isoguanine tetramers: S. Tirumala, J. T. Davis, *J. Am. Chem. Soc.*, **1997**, *119*, 2769. (f) Isoguanine pentamer-cesium complex: X. Shi, J. C. Fettinger, M. Cai, J. T. Davis, *Angew. Chem., Int. Ed.*, **2000**, *39*, 3124. (g) 3 + 3 Hexamer: J. A. Zerkowski, C. T. Seto, G. M. Whitesides, *J. Am. Chem. Soc.*, **1992**, *114*, 5473. (h) R. H. Vreekamp, J. P. M. van Duynhoven, M. Hubert, W. Verboom, D. N. Reinhoudt, *Angew. Chem., Int. Ed. Engl.*, **1996**, *35*, 1215.

[6] For hexamers using GC-like hydrogen-bonding: (a) A. Marsh, M. Silvestri, J. -M. Lehn, *Chem. Commun.*, **1996**, 1527. (b) M. Mascal, N. M. Hext, R. Warmuth, J. R. Arnall-Culliford, M. H. Moore, J. P. Turkenburg, *J. Org. Chem.*, **1999**, *64*, 8479. (c) Y. Ma, S. V. Kolotuchin, S. C. Zimmerman, *J.* Am. Chem. Soc., **2002**, *124*, 13757. (d) H. Fenniri, P. Mathivanan, K. L. Vidale, D. M. Sherman, K. Hallenga, K. V. Wood, J. G. Stowell, J.

Am. Chem. Soc., **2001**, *123*, 3854. (e) H. Fenniri, B. Deng, A. E. Ribbe, J. Am. Chem. Soc. **2002**, 124, 11064.

[7] (a) A. Piccirilli, T. Krauch, S. E. Moroney, S. A. Benner, *Nature*, **1990**, ***343***, 33. (b) C. Y. Switzer, S. E. Moroney, S. A. Benner, *Biochemistry*, **1993**, *32*, 10489. (c) D. L. McMinn, A. K. Ogawa, Y. Wu, J. Liu, P. G. Schultz, F. E. Romesberg, *J. Am. Chem. Soc.*, **1999** , *121* , 11585. (d) E. L. Tae, Y. Wu, G. Xia, P. G. Schultz, F. E. Romesberg, *J. Am. Chem. Soc.*, **2001**, *123*, 7439. (e) Y. Wu, A. K. Ogawa, M. Berger, D. L. McMinn, P. G. Schultz, F. E. Romesberg, *J. Am. Chem. Soc.*, **2000**, *122*, 7621. (f) E. T. Kool, *J. Am. Chem. Soc.*, **1991**, *113*, 6265. (g) T. Vo, S. Wang, E. T. Kool, *Nucleic Acids Res.*, **1995**, *23*, 2937. (h) H. Weizman ,Y. Tor , *J. Am. Chem. Soc.*, **2001**, *123*, 3375. (i) K. Tanaka, A. Tengeiji, T. Kato, N. Toyama, M. Shiro, M. Shionoya, *J. Am. Chem. Soc.*, **2002**, *124*, 12494. (j) N. Zimmermann, E. Meggers, P. G. Schultz, *J. Am. Chem. Soc.*, **2002**, *124* , 13684. (k) S. Atwell, E. Meggers, G. Spraggon, P. G. Schultz, *J. Am. Chem. Soc.*, **2001**, *123*, 12364. (l) O. Thum, S. Jäger, M. Famulok , *Angew. Chem. Int. Ed.*, **2001**, *40*, 3990.

[8] (a) R. E. Franklin, R. G. Gossling, *Nature*, **1953**, *171*, 740. (b) J. D. Watson, F. H. C. Crick, *Nature*, **1953**, *171*, *737.*

[9] (a) C. Giovannangeli, C. Hélène, *Curr. Opin. Mol. Ther.*, **2000**, *2*, 288. (b) D. Praseuth, A. L. Guieysse, C. Hélène, *Biochim. Biophys. Acta.*, **1999**, *1489*, 181. (c) K. M. Vasquez, J. H. Wilson, *Trends Biochem. Sci.*, **1998**, *23*, 4. (d) M. P. Knauert, P. M. Glazer, *Hum. Mol. Genet.*, **2001**, *10*, 2243. (e) R. V. Guntaka, B. R. Varma, K. T. Weber, *Int. J. Biochem. Cell. Biol.*, **2003**, *35*, 22.

[10] (a) M. A. Keniry, *Biopolymers*, **2001**, *56*, 123. (b) D. Rhodes, R. Giraldo, *Curr. Opin. Struct. Biol.*, **1995**, *5*, 311. (c) D. S. Pilch, G. E. Plum, K. J. Breslauer, *Curr. Opin. Struct. Biol.*, **1995**, *5*, 334. (d) J. Feigon, K. M. Koshlap, F. W. Smith, *Methods Enzymol.*, **1995**, *261*, 225.

[11] For DNA-triple helices : (a) J. Sun, T. Garestier, C. Hélène, *Curr. Opin. Struct. Biol.*, **1996**, *6*, 327. (b) N. T. Thong, C. Hélène, *Angew. Chem. Intl. Ed. Engl.*, **1993**, *32*, 666.

[12] For G-quartets: (a) E. H. Blackburn, *Cell*, **1994**, *77*, 621. (b) D. Sen, W. Gilbert, *Nature*, **1988**, *334*, 364. (c) W. I. Sundquist, A. Klug, *Nature*, **1989**, *342*, 825. (c) J. R. Williamson, M. K. Raghuraman, T. R. Cech, *Cell*, **1989**, *59*, 871. (d) S. Neidle, G. Parkinson, *Nat. Rev. Drug. Res.*, **2002**, *1*, 383.

[13] J. C. Chaput, C. Switzer, *Proc. Natl. Acad. Sci.*, **1999**, *96*, 10614. (b) X. Shi, J. C. Fettinger, M. Cai, J. T. Davis, *Angew. Chem., Int. Ed.*, **2000**, *39*, 3124.

[14] (a) J. J. P. Stewart, *J. Comp. Chem.* **1989**, *10*, 209. (b) J. J. P. Stewart, *J. Comp. Chem.* **1989**, *10*, 221.

[15] See Chapters 3, 4, and 5.

[16] The aggregates were designed by deliberately adding hydrogen-bonds between the hydrogen atoms and the heteroatoms to give strong, directional ionic character to the calculated MM^+ hydrogen-bonds.

[17] A. J. Dickie, A. K. Kakkar, M. A. Whitehead, *Langmuir*, **2002**, *18*, 5657.

[18] (a) F. Germain, Y. Chapleur, B. Castro, *Tetrahedron*, **1982**, *38*, 3593. (b) F. Germain, Y. Chapleur, B. Castro, *Synthesis*, **1983**, 121.

[19] (a) G. D. Daves Jr., *Acc. Chem. Res.* **1990**, *23*, 201. (b) M. Kassou, S. Castillón, *Tet. Lett.*, **1994**, *30*, 5513. (c) H. – C. Zhang, M. Brakta, G. D. Daves Jr., *Nucleosides and*

Nucleotides, **1995**, *14*, 105. (d) J. J. Chen, J. A. Walker II, W. Lu, D. S. Wise, L. B. Townsend, *Tet. Lett.*, **1995**, *46*, 8363. (e) J. A. Walker II, J. J. Chen, D. S. Wise, L. B. Townsend, *J. Org. Chem.*, **1996**, *61*, 2219. (f) P. Raboisson, A. Baurand, J. – P. Cazenave, C. Gachet, D. Schultz, B. Spiess, J. –J. Bourguignon, *J. Org. Chem.*, **2002**, *67*, 8063.

[20] D. Gasparutto, S. Da Cruz, A. – G. Bourdat, M. Jaquinod, J. Cadet, *Chem. Res. Toxicol.*, **1999**, *12*, 630.

[21] Many other possible structures were tried and were inconsistent with the observed peaks.

[22] (a) S. L. Beaucage, *Current Med. Chem.*, **2001**, *8*, 1213. (b) A. H. Uddin, P. A. Piunno, R. H. E. Hudson, M. J. Damha, U. J. Krull, *Nucl. Acids Res.*, **1997**, *25*, 4139. (c) A. Geiger, A. Lester, Ane, J. Kleiber, H. Orum, *Nucleosides & Nucleotides*, **1998**, *17*, 1717. (d) C. Dueymes, J. L. Decout, P. Peltie, M. Fontecave, *Angew. Chem. Int. Ed.*, **2002**, *41*, 486. (e) A. Mees, C. Behrens, A. Schwögler, M. Ober, T. Carell, *Eur. J. Org. Chem.*, **2003**, *14*, 2670. (f) M. Schena, D. Shalon, R. W. Davis, P. O. Brown, *Science*, **1995**, *270*, 467.

[23] (a) S. Narita, T. Kitagawa, E. Hirai, *Chem. Pharm. Bull.*, **1985**, *33*, 4928. (b) E. B. Knott, *J. Soc. Chem. Ind.*, **1941**, *60*, 313.

[24] Blue fluorescence could be qualitatively observed on TLC plates or in solutions of nucleoside **15** using a hand-held UV-lamp ($\lambda_1 = 254$ nm, $\lambda_2 = 365$ nm).

[25] The excitation spectrum at $\lambda = 410$ nm showed a low intensity maximum at 280 nm along with a sharper, high intensity peak at $\lambda = 365$ nm. Therefore, the emission spectra of triaminopyrimidine were acquired at $\lambda = 365$ nm.

[26] An example of supramolecular system using fluorescence to probe binding can be found in P. Tecilla, R. P. Dixon, G. Slobodkin, D. S. Alavi, D. H. Waldeck, A. D. Hamilton, *J. Am. Chem. Soc.*, **1990**, *112*, 9408.

[27] On the micrographs, the uranyl acetate appears dark gray and the carbon light gray. The error on the measurements is estimated to be ±1 nm.

[28] Similar electron micrographs were generated from hydrogen-bonded linear tapes of *trans*-azodibenzoic acid derivatives. No fine structure was detected at higher magnifications, consistent with the absence of rod-like nanostructures from the triaminopyrimidine 15/diethylbarbituric acid 14 mixture. See Chapter 3 for details.

[29] Unstained samples of equimolar triaminopyrimidine **15**/cyanuric acid **16** mixtures showed rod-like nanostructures by electron microscopy, but staining was necessary to get a better contrast.

[30] See experimental section for details.

[31] J. P. Jonak, S. F. Zakrezewski, L. H. Mead, M. T. Hakala, *J. Med. Chem.*, **1970**, *6*, 1170.

[32] (a) S. W. Provencher, *Comput. Phys.* **1982**, *27*, 213. (b) S. W. Provencher, *Comput. Phys.* **1982**, *27*, 229. (c) K. S. Schmitz, *An Introduction to Dynamic Light Scattering by Macromolecules*, Academic Press Inc., San Diego, CA, **1990**.

[33] Gaussian 98W (Revision A.7), M. J. Frisch, G. W. Trucks, H. B. Schlegel, G. E. Scuseria, M. A. Robb, J. R. Cheeseman, V. G. Zakrzewski, J. A. Montgomery, Jr., R. E. Stratmann, J. C. Burant, S. Dapprich, J. M. Millam, A. D. Daniels, K. N. Kudin, M. C. Strain, O. Farkas, J. Tomasi, V. Barone, M. Cossi, R. Cammi, B. Mennucci, C. Pomelli, C. Adamo, S. Clifford, J. Ochterski, G. A. Petersson, P. Y. Ayala, Q. Cui, K. Morokuma,

D. K. Malick, A. D. Rabuck, K. Raghavachari, J. B. Foresman, J. Cioslowski, J. V. Ortiz, A. G. Baboul, B. B. Stefanov, G. Liu, A. Liashenko, P. Piskorz, I. Komaromi, R. Gomperts, R. L. Martin, D. J. Fox, T. Keith, M. A. Al-Laham, C. Y. Peng, A. Nanayakkara, C. Gonzalez, M. Challacombe, P. M. W. Gill, B. G. Johnson, W. Chen, M. W. Wong, J. L. Andres, M. Head-Gordon, E. S. Replogle, J. A. Pople, Gaussian, Inc., Pittsburgh PA, 1998.

Chapter 8.

Conclusions, Contributions to Original Knowledge, and Suggestions for Future Work

8.1. Conclusions

This thesis has explored the self-assembly of photoresponsive and biomimetic organic molecules into well-defined supramolecular structures with significant potential to develop new optoelectronic and functional materials. The combined theoretical-experimental approach developed in the thesis has led to a detailed understanding of non-covalent synthesis, and the conclusions may be summarized into two categories.

8.1.1. Theoretical and Experimental Investigations of Self-Assembled Photoresponsive Materials

The self-assembly of photoresponsive azobenzene derivatives results in the formation of reversibly photoswitched supramolecular structures between two significantly different morphologies. X-Ray single crystal analysis showed the *trans*-azobenzene monomers to form linear tapes through hydrogen-bonding interactions, and these linear tapes organise into sheets through π-π stacking and alkyl-alkyl interactions. Photoirradiation of *trans*-azobenzene monomers to their *cis*-isomer geometries dramatically affects the self-assembly of these molecules, changing the linear tapes formed from the *trans*-isomer into discrete cyclic structures from the *cis*-form. Additional favourable π-π stacking and alkyl-alkyl interactions produce long, rod-like nanostructures from *cis*-azodibenzoic acid cyclic structures, indicative of a second level of self-organisation in these monomers. Experimental mass spectrometry, diffraction, and microscopy techniques were extensively used to investigate *cis*-azodibenzoic acid self-assembly, demonstrating the formation of distinct *cis*- tetrameric structures.

However, none of these methods could determine the geometry of the hydrogen-bonded *cis*- tetramers precisely. In the absence of single X-ray crystals, a direct approach was needed to evaluate supramolecular architecture. Computational studies therefore emerged as an essential complementary tool to characterise the self-assembly product and to validate molecular organisation.

Semi-empirical PM3 calculations were used to generate hydrogen-bonded geometries, and to evaluate the entropy and the Gibbs free energy of the possible self-assembled molecules. Vibrational spectra, molecular orbital wavefunctions, and electron density matrices were calculated to analyse and explain the thermodynamics of self-assembly. Vibrational analysis determined that significant changes in stretching and bending frequencies occurred because of conformational change, demonstrating the relative flexibility and symmetry of the hydrogen-bonded structures. A direct, quantitative visualisation of electron delocalisation was provided by highly symmetrical electron density maps, emphasizing the preferred formation of linear tapes and macrocyclic structures from *trans*- and *cis*-azodibenzoic acid derivatives.

A molecular modelling method was implemented to investigate and to describe the self-organisation of *cis*-azobenzene macrocycles into higher-order, three-dimensional assemblies. Theoretical close-packing arrangements were produced by examining the intrinsic geometry and symmetry of the constituent macrocycles. Optimal macrocycle arrangements were determined theoretically by examining the conformational energy of the formed molecular assemblies along the potential energy surface. The resulting close-packed structures are physically valid, and meet the van der Waals and electrostatic interaction requirements for the formation of stacked macrocycles. The PM3 optimisation of these empirically generated π-stacking models confirmed the optimal

close-packing configurations determined by the molecular modelling predictions. Analysis of the molecular orbital wavefunctions revealed an increased electron delocalisation in large rod-like *cis*-azobenzene nanostructures, consistent with the additive and conjugative nature of π-π intermolecular interactions in these face-packed structures. The theoretical π-stacked models therefore correctly represent infinite rod-like nanostructures, with no loss of information, and demonstrate semi-conducting properties.

Theory and experiment were also applied to the self-assembly of novel supramolecular structures from metal-coordinated and multiply hydrogen-bonded photoresponsive *trans*- and *cis*-azobenzene monomers. The PM3 geometry optimisation of the *trans*- and *cis*-isomers demonstrated that the angular orientations of the recognition sites were the same as in the *trans*- and *cis*-azodibenzoic acid derivatives, allowing prediction of linear and cyclic supramolecular structures from these monomers upon self-assembly with linear ditopic guests. Preliminary experimental evidence gathered on these new azobenzene derivatives showed the hierarchical formation of rod-like nanostructures, confirming the semi-empirically predicted systems. In this thesis, a new theoretical model was required to predict self-assembled architectures from *trans*- and *cis*-azobenzene derivatives and non-linear ditopic guests. PM3 optimisations of two-component supramolecular models gave rise to crinkled tapes and helical geometries, as a result of distorsions of the previously determined linear tapes and cyclic tetramers.

8.1.2. Theoretical and Experimental Investigations of Self-assembled Biomimetic Materials

The self-assembly of artificial, fluorescent DNA-bases with potential DNA-detection properties results in the formation of dramatically different supramolecular structures depending on the steric environment of the monomers. Theoretical and experimental methods were used to determine the propensity of these nucleosides to form hydrogen-bonding and π-stacking interactions, and to characterise the resulting supramolecular structures.

Experimental characterisation techniques showed that the triaminopyrimidine monomers form linear oligomers through hydrogen-bonding interactions with small barbiturates, and consequently, self-organise into sheet-like aggregates from these linear tapes through π-π stacking and alkyl-alkyl interactions. The use of sterically encumbered cyanuric acid nucleosides dramatically altered the hydrogen-bond self-assembly of these molecules, giving rise to discrete hexameric macrocycles which further associate to form elongated nanostructures.

Computational studies were carried out to further validate the hydrogen-bonded supramolecular structures, and to provide geometric and electronic explanations to the self-assembly behaviour of the triaminopyrimidine nucleoside. Molecular modelling techniques were used to generate optimised hydrogen-bonded linear and cyclic aggregates, allowing direct visualisation of steric interactions between substituents. Geometric requirements distorted the barbiturates from planarity resulted in the formation of supramolecular oligomers from the triaminopyrimidine/barbituric acid complex, while they lead to ring-closing in the cyanurates, and consequently, to the formation hexameric

macrocycles from the triaminopyrimidine/cyanuric acid pair. A PM3 quantum mechanical analysis of the electron densities gave highly periodic patterns indicative of extended electron delocalisation across the hydrogen-bonded structures.

Hydrogen-bonded DNA-triplexes between the triaminopyrimidine dinucleotides and thymine dinucleotides were optimised using PM3 quantum mechanical calculations to investigate the π-stacking capabilities of these DNA-bases, and to envisage their introduction into DNA-strands. The optimised structures displayed favourable π-π intermolecular interactions between the base-pairs, confirming the formation of rod-like nanostructures from hexameric rosettes. These preliminary PM3 results clearly showed the incorporation of these monomers into new artificial DNA strands, but also the favourable triplex formation with natural, complementary thymine-containing DNA strands. These theoretical calculations demonstrated potential applications of this triaminopyrimidine DNA analogue to antisense/antigene technology.

8.2. Contributions to Original Knowledge

8.2.1. An Integrated Theoretical and Experimental Approach

A unique interplay of theory and experiment was essential to ensure the success of this research. In this thesis, theoretical predictions initiated the study of functional supramolecular materials, while experimental techniques allowed the synthesis and the charaterisation of the predicted self-assembled structures. Theoretical calculations were essential in predicting the hydrogen-bonded linear and cyclic geometries formed by the photoresponsive azobenzene derivatives and by the biomimetic nucleosides, which were

characterised experimentally. These experimental studies not only validated the theoretical results, but also detected higher-order assemblies for the hydrogen-bonded structures thereby offering new challenges for theory. Theoretical methods were used as a characterisation tool to understand the packing properties of these higher order assemblies. It is this symbiotic relationship between theory and experiment that produced a thorough description of these supramolecular systems and provided a detailed understanding of non-covalent synthesis.

8.2.2. Self-Assembly of Reversibly Photoswitched Supramolecular Structures

This thesis describes a new method whereby light is used to control the self-assembly of supramolecular structures. A novel azobenzene system, which undergoes reversible trans-cis photoisomerization, was designed such that its *trans*- and *cis*-forms self-assemble into dramatically different higher-order structures. The *trans*-azobenzene form of this molecule associates into infinite hydrogen-bonded linear tapes, while the *cis*-azobenzene form undergoes hydrogen bonded self-assembly into cyclic tetramers, which then further aggregate to form rod-like nanostructures.

There has been tremendous interest in the incorporation of photoresponsive units such as azobenzene in macromolecular systems. These systems have almost exclusively used the reversible *trans-cis* photoisomerization of azobenzene, in order to photopattern the surrounding polymer or liquid crystalline matrix. The approach described in this thesis is a significant departure from previous methods, in that it uses photoresponsive

azobenzene units as *supramolecular building blocks*, to construct photoswitchable self-assembled structures. As such, this represents a novel and complementary strategy to the previously established methods, and will likely find important applications in optical data storage and patterning.

8.2.3. Self-Assembly of Artificial DNA-Bases into Hexameric Rosettes and Triple Helices

For the first time, new artificial nucleosides were synthesised to generate hydrogen-bonded supramolecular structures in this thesis. These artificial deoxyribonucleoside monomers incorporate complementary triaminopyrimidine and cyanuric acid recognition units as aromatic bases, integrating design features proper to biological chemistry and organosupramolecular chemistry. In addition, bulky disiloxane protecting groups are used as substituents in order to sterically induce macrocycle formation in organic solvents.

Previous studies on DNA self-assembly exploited the pre-existing complementarity of natural DNA-bases to build supramolecular assemblies. The strategy described in this thesis differs dramatically from these previous methods, because typical supramolecular building blocks are introduced into DNA. Consequently, these complementary triaminopyridimine and cyanuric acid nucleosides form the hydrogen-bonded aggregates, consistent with hexameric macrocycles which self-organise into rod-like nanostructures through π-π interactions.

The potential use of the biological properties of the triaminopyrimidine nucleoside was explored in thesis for the first time, through preliminary quantum mechanical calculations. The triaminopyrimidine nucleosides offer two binding sites available for hydrogen-bonding with acceptor-donor-acceptor type guest molecules like thymine nucleosides. A dinucleotide bearing two triaminopyrimidine bases was therefore hybridised with two complementary thymine dinucleotides to give rise to a DNA triple helix. The double-deckered trimer was successfully optimised using quantum mechanical PM3 calculations, demonstrating the favourable incorporation of this artificial nucleoside into biologically interesting assemblies.

8.2.4. Quantum Mechanical Investigations of Thermodynamic Properties in Supramolecular Structures

For the first time, a systematic analysis of unsubstituted and bisalkoxy-substituted azodibenzoic acid derivatives was performed by semi-empirical PM3, *ab initio*, and density functional theory (DFT). Semi-empirical monomer geometries correlate well with high-level *ab initio* and DFT results, establishing a theoretical basis for structural analysis by PM3 calculations.

The first detailed thermodynamic analysis of hydrogen-bonded supramolecular structures was performed in this thesis using quantum mechanical analysis. Hydrogen-bonded azodibenzoic acid geometries were systematically optimised using the semi-empirical PM3 method, then validated by comparison with similarly optimised supramolecular structures from experimentally well-known isophthalic acid. The calculated PM3 Enthalpies and Gibbs free energies revealed the significant contribution

of a *folding parameter* to the stabilisation of the hydrogen-bonded supramolecular structures, favouring the formation of macrocycles over tapes from *cis*-isomers. This thermodynamic analysis determined that hexameric macrocycles are most stable enthalpically, while smaller, tetrameric macrocycles are most favourable thermodynamically, highlighting the need for entropy calculations to predict supramolecular structure.

8.2.5. Vibrational Analysis of Hydrogen-Bonded Supramolecular Aggregates

Theoretical vibrational spectra were computed, for the first time, to explain the thermodynamic behaviour of the self-assembled azodibenzoic acid tapes and macrocycles. Analysis of the generated vibrational spectra pointed to stretching and bending frequency shifts, along with intensity variations, providing specific fingerprints to each supramolecular conformation. In addition, these vibrational changes with conformation demonstrated the relative flexibility and symmetry of the hydrogen-bonded supramolecular structures, to support the preferred formation of macrocyclic tetramers from *cis*-azodibenzoic acid derivatives.

8.2.6. Density Matrix Analysis of Hydrogen-Bonded Supramolecular Structures

For the first time, electronic properties were determined for supramolecular systems involving hydrogen-bonded azodibenzoic acid derivatives, and hydrogen-bonded

structures containing triaminopyrimidine DNA-base analogues. While individual molecular orbital diagrams only show single-electron wavefunctions, electron density matrices provide a full quantitative depiction of the entire electron cloud across the supramolecular structure. Therefore, electron density maps were generated to measure short-range and long-range interatomic electronic interactions within hydrogen-bonded assemblies.

Electron density matrices have been used to characterise conjugated and aggregated molecules such as very large carbon nanotubes, bridged naphthalene dimers, stilbenoid derivatives, as well as polyacetylene oligomers and dendrimers, but it is the first time that such an analysis is applied to hydrogen-bonded supramolecular systems.

The generated contour plots in both photoresponsive and biomimetic supramolecular systems clearly displayed high periodicity and symmetry from both diagonal and off-diagonal matrix elements, reflecting the geometric arrangement of repeating monomeric units within the hydrogen-bonded structures. Analysis of the electron density maps indicated that the electron density associated with the atomic orbitals of the recognition units only represented a small section of the total molecular orbital. The extent of electron delocalisation or confinement could consequently be directly visualised to assess the relative stabilities of the supramolecular assemblies, and to correlate and predict their thermodynamic properties.

8.2.7. Directed Energy Scan of Close-Packed Supramolecular Macrocycles

In this thesis, a new computational technique was developed to provide a detailed theoretical description of packing within rod-like nanostructures of *cis*-azodibenzoic acid

derivatives. A series of close-packed arrangements were generated from hydrogen-bonded macrocycles, and total energies were systematically calculated for each spatial macrocycle orientation using molecular modelling techniques, to give a preliminary close-packed configuration that correctly accounts for the packing interactions of experimental cyclic tetramers.

This theoretical work is the first study where the effects of aromatic ring orientation and interplanar distances on hydrogen-bonded macrocycle packing are systematically determined, along with the study of offset and twist between π-stacked tetrameric macrocycles. This directed energy scan constitutes an economical method to predict close-packed macrocycle arrangements, which is able to generate reasonable, experimentally fit input structures for quantum mechanical optimisation and analysis.

8.2.8. Molecular Orbital Analysis of Close-Packed Supramolecular Macrocycles

PM3 semi-empirical calculations were used to optimise the preliminary molecular mechanics geometries generated from the method outlined in Section 8. 2. 6, and to confirm the predicted close-packed arrangements. The molecular orbitals of these geometry optimised π-stacked azobenzene macrocycles were examined to provide, for the first time, insight into the electronic properties of these rod-like nanostructures.

The quantum mechanical analysis clearly showed a significant π-electron delocalisation through the entire geometry optimised structures, demonstrating that additive and conjugative π-stacking forces effectively hold these face-packed structures

together. The analysis of these electronic properties also indicated more pronounced electron delocalisation in larger macrocycle arrays, in conjunction with a transition from discrete MO energy levels to conductive band structure. This observed electronic behaviour was accompanied by a HOMO-LUMO band gap narrowing towards values typical of non-doped, organic semi-conducting materials, revealing a potential to develop optoelectronic devices from rod-like *cis*-azobenzene nanostructures.

8.3. Suggestions for Future Work

8.3.1. Characterisation of Metal-Coordinated and Multiply Hydrogen-Bonded Photoresponsive Structures

Much work remains to completely characterise the self-assembly of metal-coordinated and multiply hydrogen-bonded photoresponsive *trans*- and *cis*-azobenzene supramolecular structures, starting from the experimental techniques used to identify the *trans*- and *cis*-azodibenzoic acid systems. X-ray powder diffraction, electrospray ionisation mass spectrometry, vapour pressure osmometry, dynamic light scattering, single crystal diffraction X-ray should therefore be used to determine the structural properties of azobisbenzonitrile and azobisbenzotriazine self-assembly.

Although a model was proposed for the discrete supramolecular structures generated by equimolar *cis-trans* mixtures of azobisbenzonitrile, further understanding of these structures should be obtained from the use of different metal ions which would display higher affinities. Low temperature isolation of the *cis*-isomer from the photolysed azobenzene mixture should be implemented to prevent the thermal isomerisation of the

cis-azobisbenzonitrile monomer. *Ab initio* and density functional theory calculations of supramolecular models which incorporate both silver(I) and azobisbenzonitrile are necessary to provide a better theoretical description of these metal-coordinates systems.

Photoirradiation of *trans*-azobisbenzotriazine needs to be investigated to efficiently generate the *cis*-isomer. The hydrogen-bonded self-assembly of *trans*- and *cis*-monomers with barbituric acid derivatives was predicted to give open systems in both cases, instead of the linear and macrocyclic structures shown for the dicarboxylic acid derivatives. Linear guests with triple hydrogen-bonding abilities should consequently be designed to preserve these hydrogen-bonded geometries.

The synthesis of the azobisbenzoureidotriazine derivatives with quadruple hydrogen-bonding abilities needs to be completed, along with their full experimental characterisation. Due to their self-complementarity and their geometric similarity with the azodibenzoic acid monomers, the azobisbenzoureidotriazine derivatives should generate quadruply hydrogen-bonded linear tapes and macrocycles. Theoretical investigation of the cyclic tetramers showed a significant π-electron delocalisation across the four hydrogen-bonds, increasing intermolecular binding in these structures. As a result, experimental investigations of this system should show an increased stability of the hydrogen-bonded macrocycles, which would be more convenient for the practical creation of reversibly photopatterned surfaces.

8.3.2. Theoretical Investigations of Self-Assembly in Solvated Environments

The theoretical investigation of the hydrogen-bonded structures described in this thesis were carried out in the gas phase. The non-covalent self-assembly of low molecular weight building blocks has displayed a significant solvent-dependent behaviour, as protic, polar solvents like water and alcohols can compete with hydrogen-bonds but at the same time favour π-stacking interaction.

Several implicit and explicit solvent models can be implemented to account for direct and indirect solvent-monomer interactions. Implicit solvent models, which use a spherical or elliptical dielectric continuum around the studied molecular system, would provide an average depiction of medium effects. Although more time-consuming, explicit solvent models should give a more accurate description of direct interactions with the solvent. Even better, a mixed explicit-implicit solvent model should account for medium effects with no loss of information.

8.3.3. Theoretical Investigation of Macrocycle Networks

Further understanding of these supramolecular materials can be gained through incorporation of the close-packed macrocycle into three-dimensional networks. Such theoretical calculations would use a molecular modelling technique similar to the one developed in Section 8. 2. 6, applying systematic energy scans to hexagonal and cubic networks of rods.

These complementary studies would provide understanding of bundle formation, and would be useful to improve the alignment and the periodicity of the rod-like

nanostructures in novel functional materials. In addition, quantum mechanical methods would be used to investigate the electronics of these networks, and to probe enhanced electron delocalisation in these three-dimensional semi-conducting materials.

8.3.4. Incorporation of Triaminopyrimidine Nucleosides into DNA

The formation of hexameric macrocycles from triaminopyrimidine and cyanuric acid monomers opens the door to a wide range of biological and materials applications. Incorporation of the triaminopyrimidine DNA analogues should give rise to a new family of supramolecular assemblies. As demonstrated by semi-empirical PM3 optimisation, DNA-triple helix formation should be achieved easily from the association of triaminopyrimidine and thymine nucleotides. Consequently, experimental protocols should be developed to generate oligonucleotides containing one to several triaminopyrimidine bases at different positions, which would be hydridised with natural oligonucleotides bearing thymine residues. Effective hybridisation and enhanced binding properties, compared with triple helical structures of adenine and thymine, would be probed using fluorescence measurements, gel electrophoresis techniques, as well as melting temperature measurements.

8.3.5. Improvements of Triaminopyrimidine/Cyanuric Acid DNA-Rosettes

The cyanuric acid/triaminopyrimidine hexameric rosettes displayed a higher-order self-organisation into rod-like nanostructures into π-stacking abilities, which need to be investigated in more details and improved. Several options can be envisaged to improve

nanostructure formation in these hexameric rosettes. One way is to separate the α- and β-anomers present in each nucleoside. Such a separation should result in monodisperse assemblies with interesting chiroptical properties from equimolar mixtures cyanuric acid/triaminopyrimidine. Another way to improve nanostructure formation would be to preorganise the nucleosides by creating covalent, phosphate linkages between the sugar units. This method should lead to multi-deckered hexameric rosettes of DNA analogues, with potential biological applications.

Appendix A.

Photoresponsive Supramolecular Systems : Self-Assembly of Azodibenzoic acid Linear Tapes and Cyclic Tetramers

Supplementary information of : F. Rakotondradany, M. A. Whitehead, A.-M. Lebuis, H. F. Sleiman, *Chem. Eur. J.*, **2003**, *9*, 4771.

I.	Reverse phase HPLC trace of the *trans-cis* mixture	S2
II.	Thermal *cis-trans* reisomerisation kinetics by ^{1}H-NMR	S2
III.	Thermal *cis-trans* reisomerisation kinetics by UV-Vis	S3
IV.	Comparison of ^{1}H-NMR and UV-Vis kinetic data	S4
V.	Vapor pressure osmometry (VPO) measurements	S5
VI.	Electrospray ionization mass spectrometry (ESI-MS) measurements	S9
VII.	Sample preparation for TEM measurements by the replica method	S11
VIII.	Space-filling model of a *cis*-**2** square.	S11
IX.	Dynamic light scattering (DLS) measurements	S12
X.	Theoretical calculations	S13

Reverse phase HPLC trace of the *trans-cis* mixture.

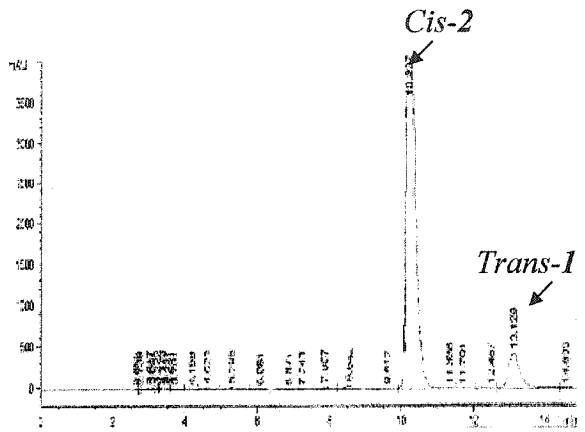
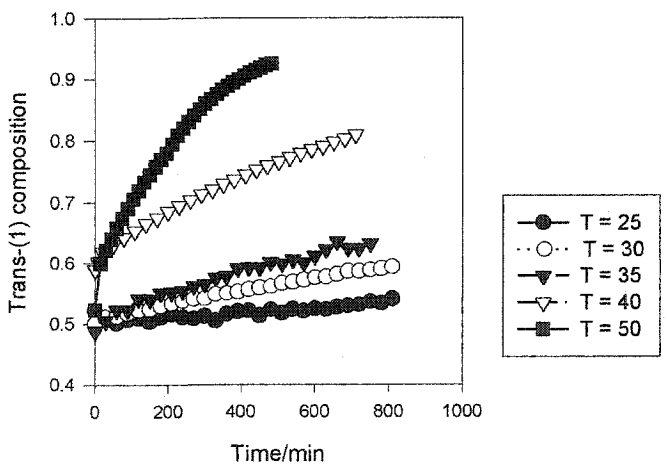


Figure 1. Reverse phase HPLC Trace of a mixture of cis-**1** and trans-**2** azodibenzoic acids. Retention times for cis and trans isomers are ~10 min and ~13 min using a 90:10→100:0 MeOH/H_2O (+ 0.06%Trifluoroacetic acid) gradient over 30 min.

Thermal *cis-trans* reisomerisation kinetics by ^{1}H-NMR.



k_{25} = (0.7±0.2)E-04 min^{-1}

k_{30} = (2.0±0.9) E-04 min^{-1}

k_{35} = (3.0±0.3) E-04 min^{-1}

k_{40} = (4.1±0.3) E-04 min^{-1}

k_{50} = (9.6±1.1) E-04 min^{-1}

Figure 2. Kinetics of the thermal cis-trans reisomerization monitored by ^{1}H-NMR in d_6-DMSO.

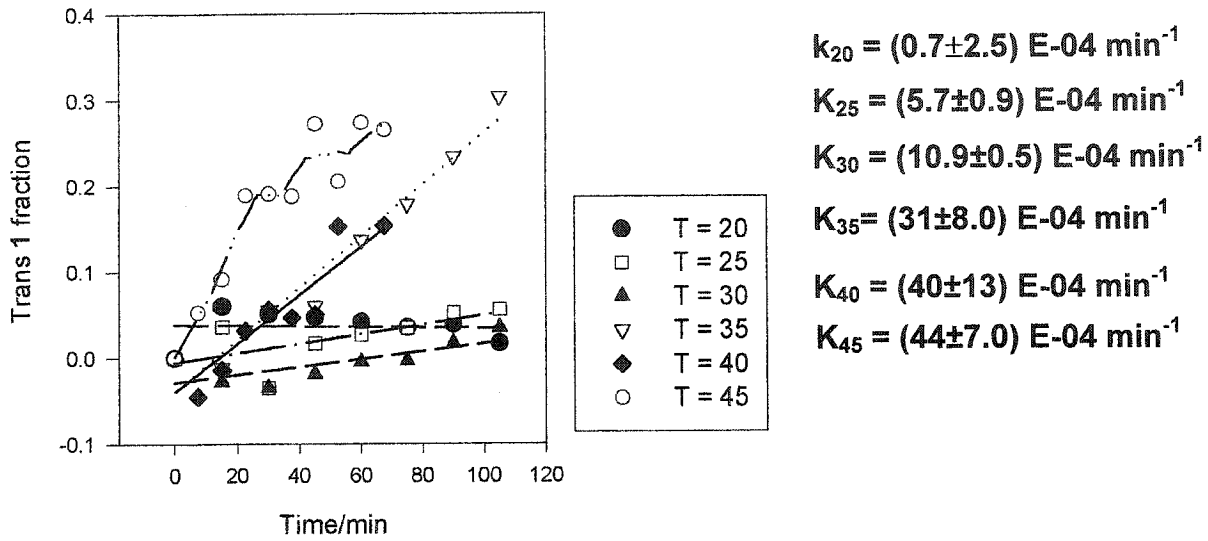


Figure 3. Kinetics of the thermal cis-trans reisomerization monitored by ^{1}H-NMR in $CDCl_3$. At 45°C, the concentration of *trans*-**1** increased stepwise as shown by the dash-dot-dot line.

Thermal *cis-trans* reisomerisation kinetics by UV-Vis.

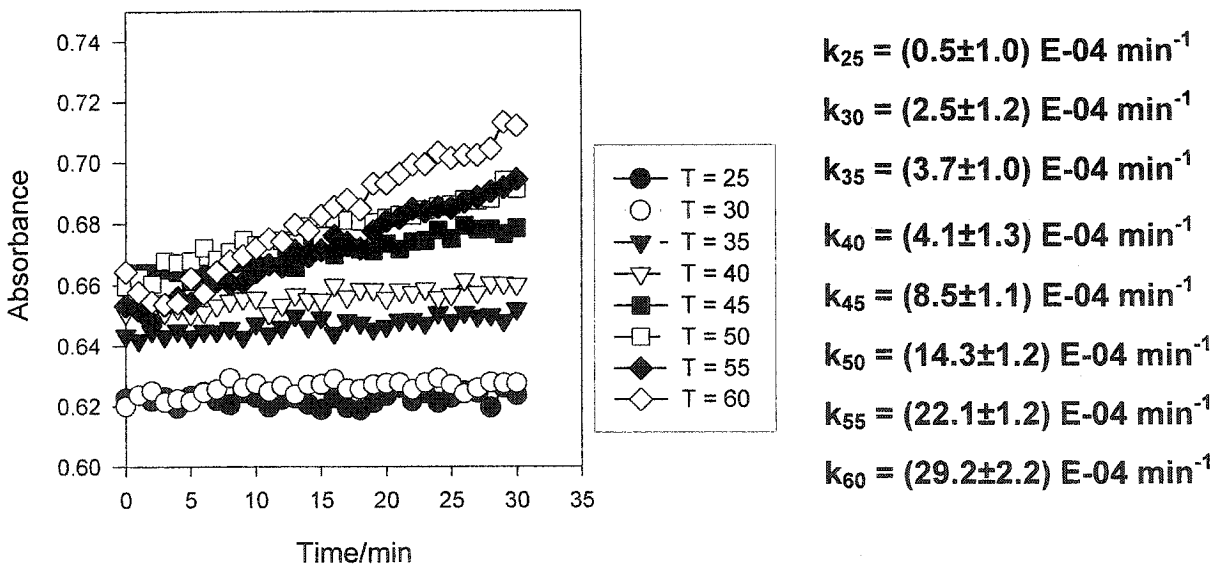
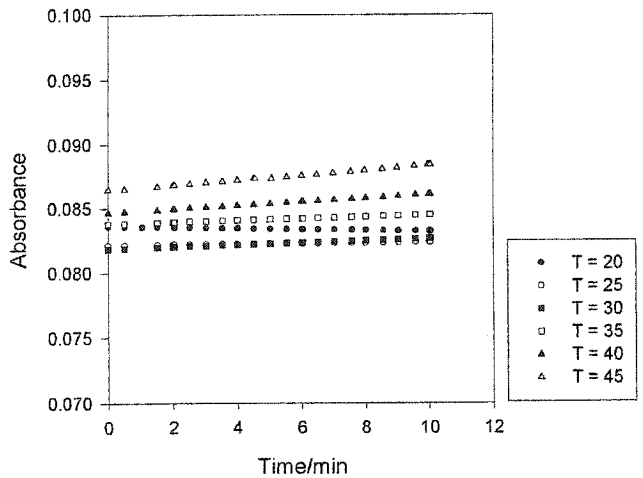


Figure 4. Kinetics of the thermal cis-trans reisomerization monitored by UV-Vis in DMSO.



k_{20} = (0.5±1.0) E-04 min^{-1}

K_{25} = (3.2±1.1) E-04 min^{-1}

k_{30} = (9.7±1.1) E-04 min^{-1}

K_{35} = (8.1±1.1) E-04 min^{-1}

K_{40} = (17.1±1.1) E-04 min^{-1}

K_{45} = (24.1±1.0) E-04 min^{-1}

Figure 5. Kinetics of the thermal cis-trans reisomerization monitored by UV-Vis in chloroform.

Table 1. Comparison of the kinetics of the thermal cis-trans reisomerization monitored by UV- Vis and ^{1}H-NMR in DMSO and chloroform.

Solvent		**DMSO**	**Chloroform**
$\Delta H^{\neq}$	**kJ mol^{-1}**	84.9 ± 2.5 [a]	109.4 ± 4.9 [a]
		90.6 ± 4.9 [b]	97.4 ± 4.2 [b]
$\Delta S^{\neq}$	**J mol^{-1} K^{-1}**	-72.8 ± 8.0 [a]	15.3 ± 21.9 [a]
		-77.8 ± 14.8 [b]	-15.9 ± 13.7 [b]
Ea	**kJ mol^{-1} K^{-1}**	105.1 ±2.5 [a]	134.6 ± 6.7 [a]
		93.0 ± 4.9 [b]	99.8 ± 4.2 [b]

[a] UV-Vis [b] ^{1}H-NMR

Vapor pressure osmometry (VPO) measurements.

In the Model 233, vapor pressure is not measured directly due to difficulties in sensitivity, but is measured indirectly by using two thermistors to measure voltage changes caused by changes in temperature. The Model 233 aluminum chamber is opened and 20 mL of dichloromethane is poured into the center cylinder over the thermistors to ensure a solvent saturated atmosphere inside the chamber. The injection syringes are cleaned with solvent. The temperature control was set to 30°C and the chamber was allowed to equilibrate for at least one hour. The reference syringe was loaded with pure solvent and the measuring syringe with the appropriate solution, and returned to the apparatus.

Calibration with materials of known molecular weight was first carried out to determine the calibration constants. Benzil (M= 210) and polystyrene standard PS2100 (M= 2100) were the two molecular weight standards used in this experiment.

Four or five solutions of the standards were prepared at concentrations ranging from 2 gL^{-1} to 20 gL^{-1} in the case of benzil and from 14 gL^{-1} to 40 gL^{-1} in the case of polystyrene. 30 μL of solvent and solutions were simultaneously added to both thermistors by using the marked screw drives that inject the needles (3 turns). The voltage was read after stabilization of the signal (approx. 5 min). Three or more trials for the same sample were run to ensure reproducibility of the reading. Finally, the pure solvent voltage was subtracted from these readings to give the true ΔV for the various concentrations. The data was plotted as ΔV/C versus C (gL^{-1}) and a best fit straight line is extrapolated to zero concentration.

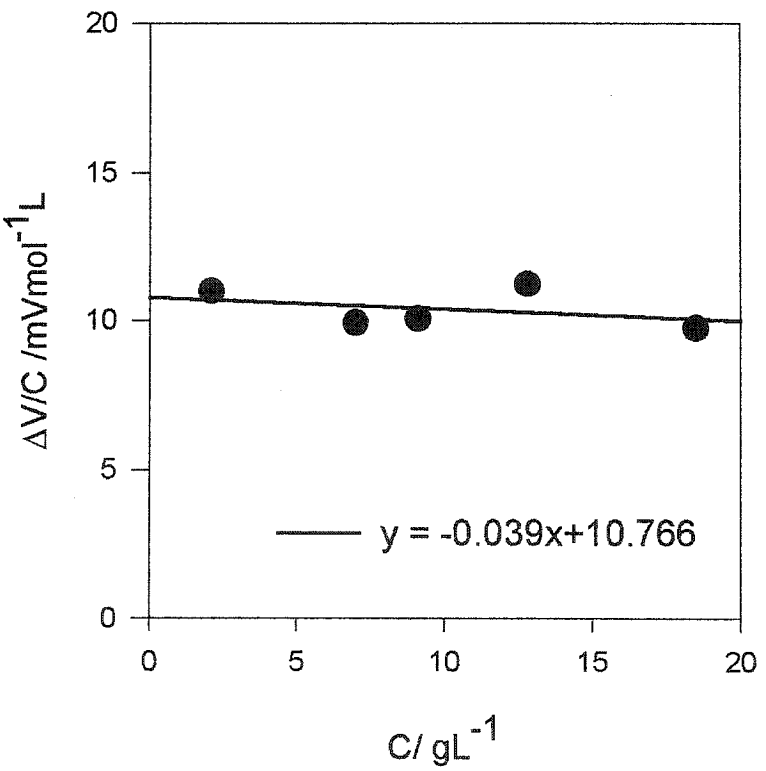


Figure 6. VPO Calibration curve using benzil in dichloromethane.

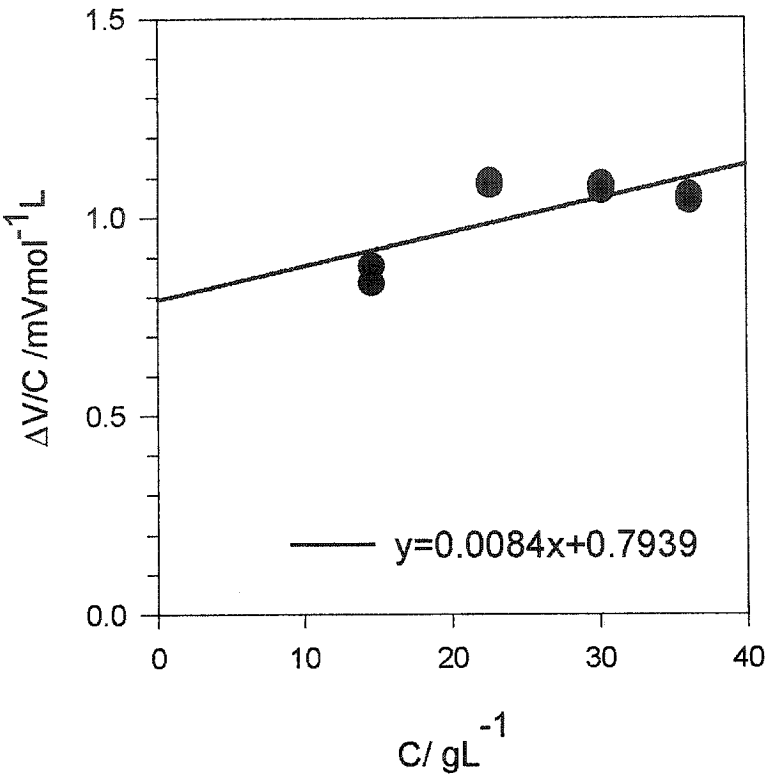


Figure 7. VPO Calibration curve using the polystyrene standard in dichloromethane.

A total of 8 different stock solutions of *cis*-azodibenzoic acid ranging in concentration from 2 gL^{-1} to 12 gL^{-1} were prepared in dichloromethane. As in the case for the molecular weight standards, 30 μL of solution and solvent were injected simultaneously into the osmometer chamber. After temperature equilibration (5 min), the voltage was read. 3 independent measurements were made at each concentration, and the experiments were duplicated. Average molecular weights of studied aggregates were calculated using equation 1:

$$MW_{unknown} \times \lim_{C \to 0} \frac{\Delta V_{unknown}}{C_{unknown}} = MW_{s\,\tan\,dard} \times \lim_{C \to 0} \frac{\Delta V_{s\,\tan\,dard}}{C_{s\,\tan\,dard}} = K \qquad (1)$$

where K = 210x10.766 = 2261 for benzil and K = 2100x0.7939 = 1667 for polystyrene.

The data was plotted as Mn ($gmol^{-1}$) versus C (gL^{-1}) and a best fit straight line is extrapolated to zero concentration using both molecular weight standards to give *Mn*. (Figure 8)

The graph shows the emergence of a second regime at C<3 gL^{-1} which is likely due the preponderance of monomeric species of *cis*-**2** in solution.

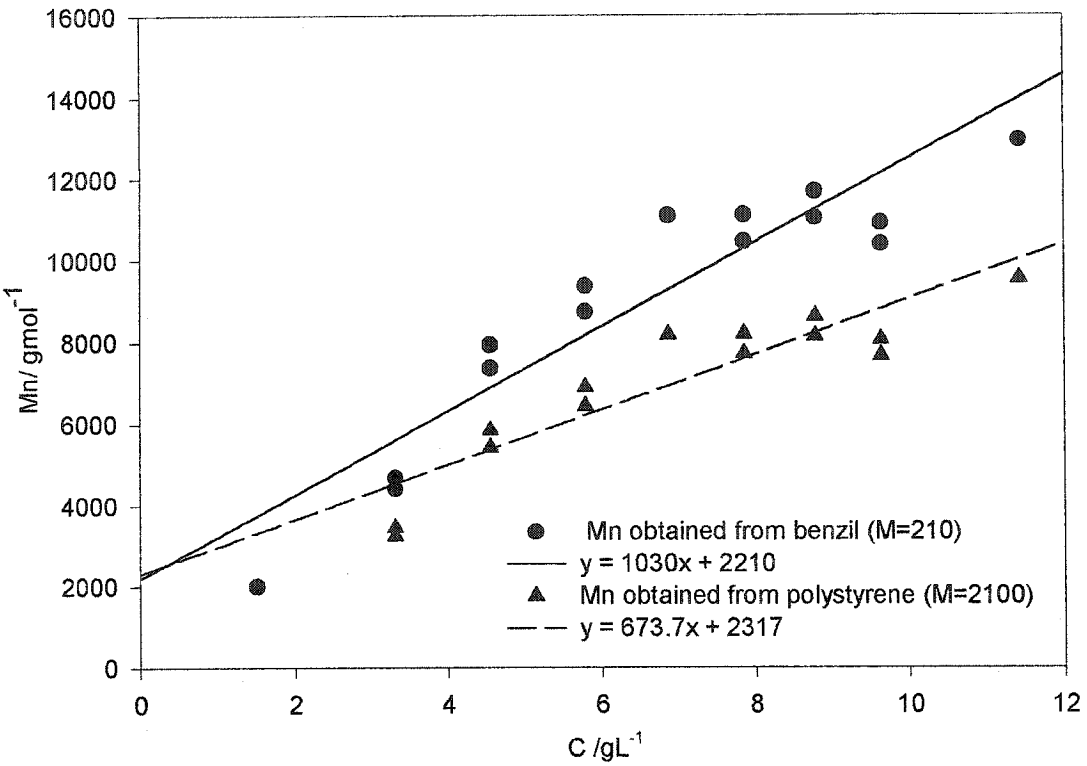


Figure 8. VPO molecular weights vs. C plots for *cis*-**2** using benzil (–) and polystyrene (--) in dichloromethane.

A similar experiment giving the same *Mn* value for *cis*-azodibenzoic acid **2** was performed using a Vapro 5520-model vapor pressure osmometer equipped with AC-066 Head for 0-3200 $mmolkg^{-1}$ range manufactured by Wescor. Using this different instrument, a total of 6 different stock solutions of *cis*- and *trans*-azodibenzoic acid were prepared in dichloromethane (higher solubility was observed for the *cis*-isomer than for the *trans*-isomer). 10 μL of solution were placed into the osmometer sample holder. After temperature equilibration (75 s), osmolality was recorded in $mmolkg^{-1}$. 5 independent measurements were made at each concentration, and the experiments were duplicated. A calibration curve was generated using benzil (MW= 210.23) as the standard under the same conditions. A K value of 5040 was obtained from benzil. Average molecular weights for the studied aggregates were calculated using equation 1 and plotted against the concentration. (Figure 9)

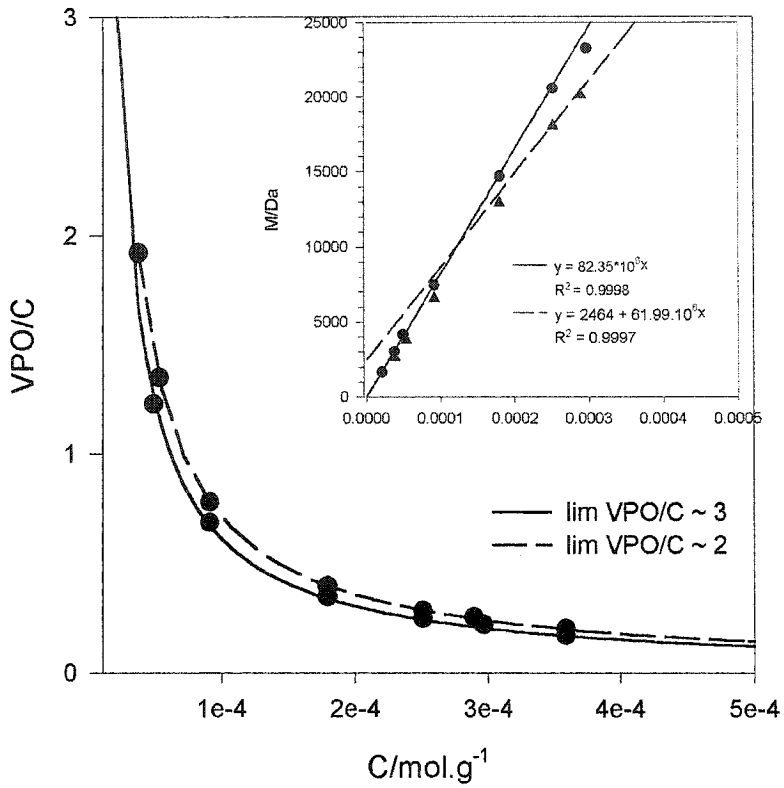


Figure 9. Plot of VPO/C as a function of concentration for *trans*-**1** (—) and *cis*-**2** (--) in dichloromethane. The limit is taken ca. 1e-5 molg^{-1}. Insets: VPO molecular weights vs. C.

Electrospray ionization mass spectrometry (ESI-MS) measurements.

- Solvent: Dichloromethane/Chloroform/Dichloroethane plus a little bit of MeOH
- Conditions: Negative mode
  - spray voltage: 3.5 kV, capillary heater:200°C m/z 100-2500
  - spray voltage: 4.0 kV, capillary heater:150°C m/z 1700-1800
  - spray voltage: 3.5 kV, capillary heater:150°C m/z 2300-2500
- Results: m/z observed monomer, dimer, trimer and tetramer only when MeOH was used. M signals are weaker for higher aggregates. Chlorinated solvents do not show any M.

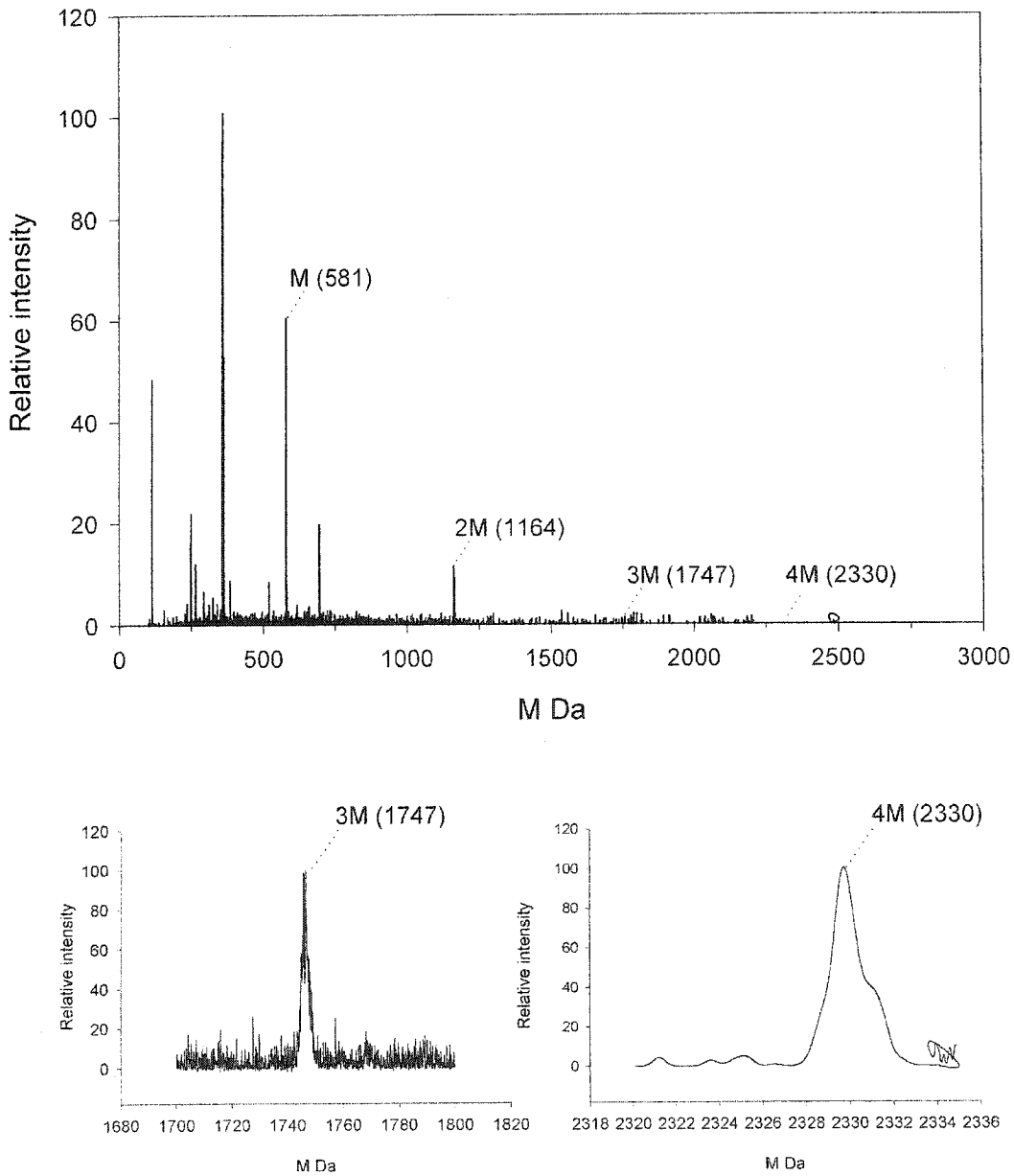


Figure 10. ESI-MS spectrograms of *cis*-**2** in chloroform (with traces methanol).

- Solvent: 5-30 mM Et_3N +Chloroform
- Conditions: spray voltage: 3.5 kV, capillary heater: 50°C

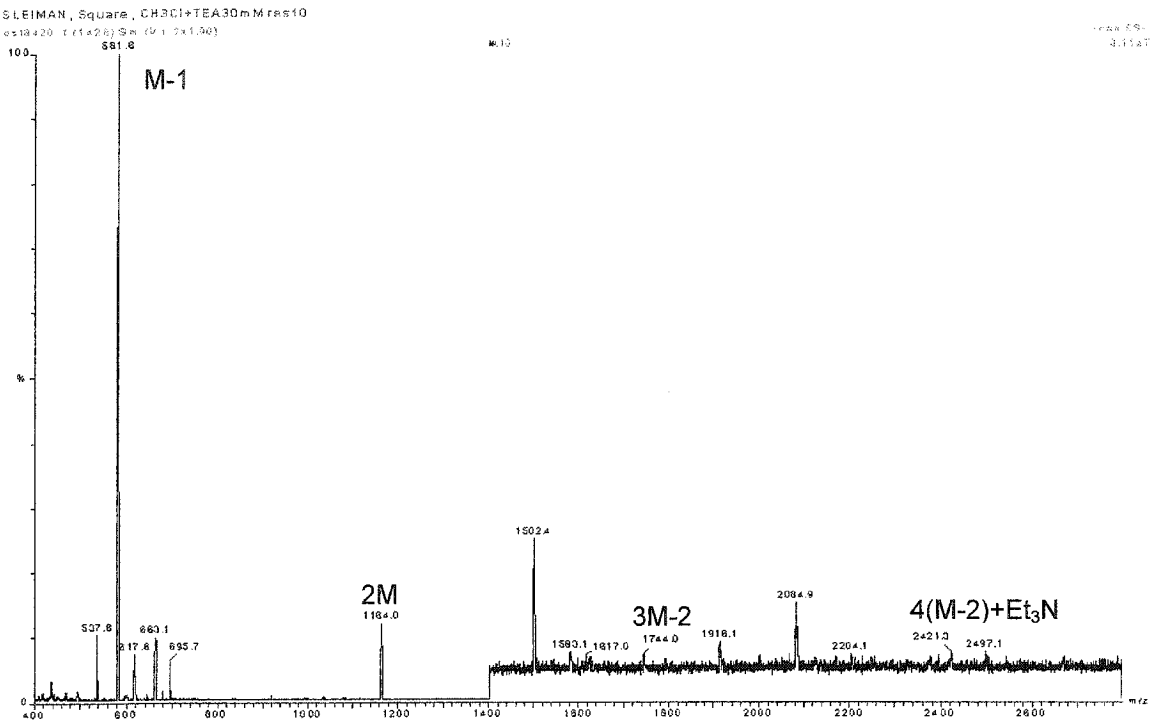


Figure 11. ESI-MS spectrograms of *cis*-**2** in chloroform (in presence of triethylamine).

Sample preparation for TEM measurements by the replica method.

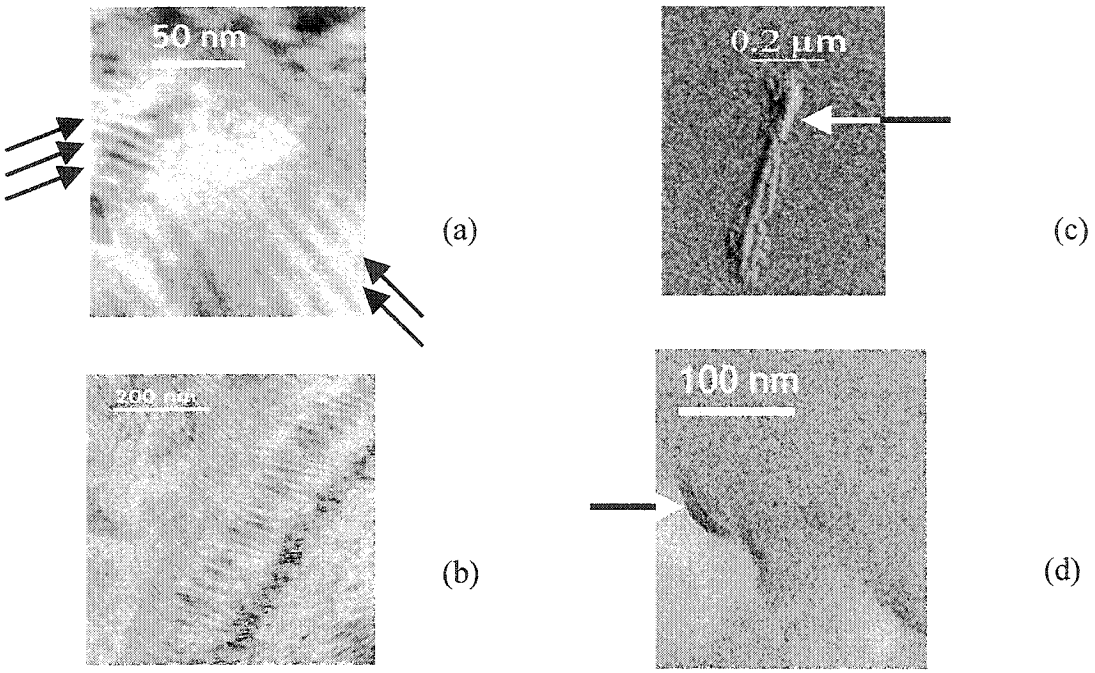


Figure 12. Transmission electron micrographs of a replica of *cis*-**2** in 1,2-dichloroethane showing nanorods (~4 nm) layered side-by-side (a) and (b), aggregated into bundles (c), or isolated (d).

Space-filling model of a *cis*-2 square.

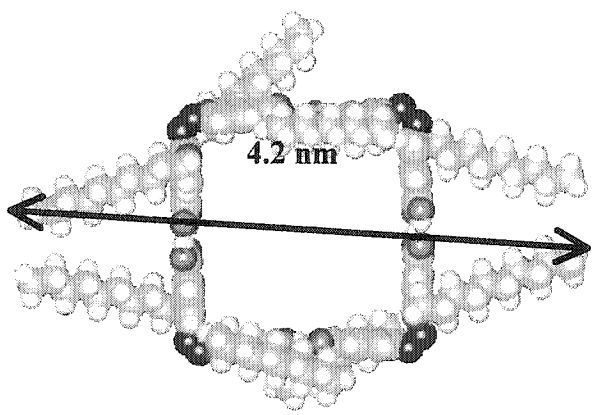


Figure 13. Space-filling model showing the geometry of four PM3 optimized *cis*-**2** monomers forming a square.

Dynamic light scattering (DLS) measurements.

Table 3. Calculated hydrodynamic diameters d_H at different scattering angles θ for *trans*-azo **1** and *cis*-azo **2**.

	C gL^{-1}	Average $d_{H(\theta = 45°)}$ nm	Average $d_{H(\theta = 90°)}$ nm	Average $d_{H(\theta = 135°)}$ nm
Trans- azo **1** (d_H in nm)	1[a]	827.5	1315.0	1613.6
Cis- azo **2** (d_H in nm)	2.5[a]	745.3	708.5	565.7
	2[b]	3090	4492.5	4572.5
	1.43[b]	3287.5	3172.5	2105
	1.11[b]	2915	2785	2645
	0.9[b]	2222.5	2332.5	3350
	1[a]	282.3	639.3	746.9
	~0.2[a]	178	178	178

[a] Freshly prefiltered with a .45 μ filter [b] After 48 hrs storage at 4°C.

Theoretical calculations.

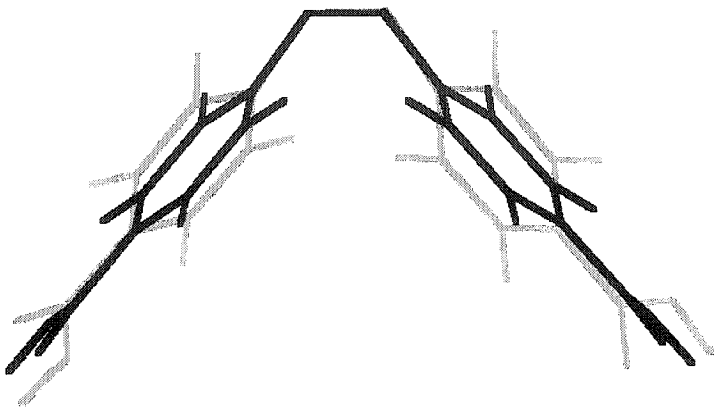


Figure 14. Overlay of PM3 (in black) and B3LYP/6-31G* (in grey) optimized *cis*-azodibenzoic acid monomers showing that the carboxylic acid groups are ca. 80° apart.

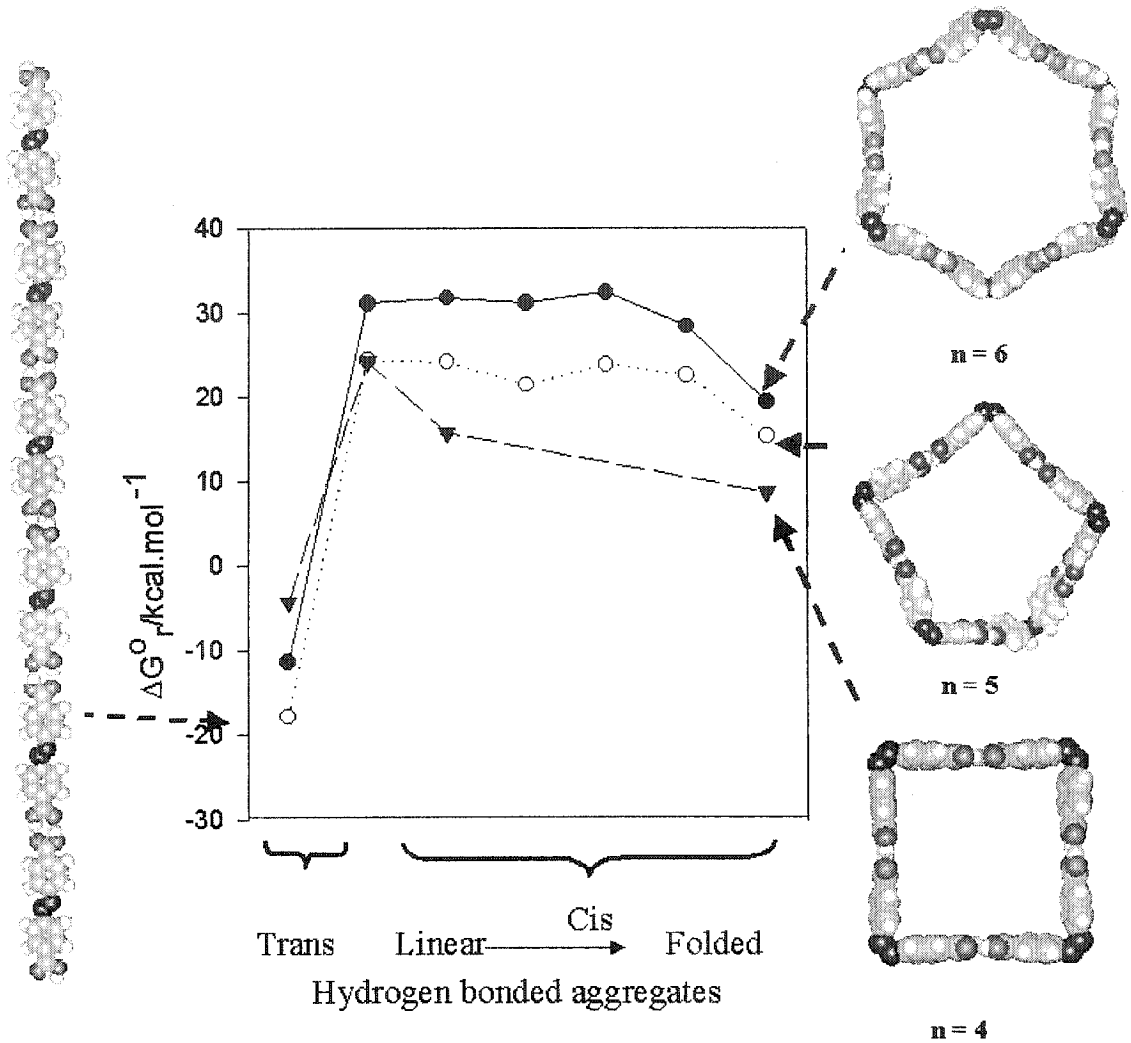


Figure 15. Evolution of the standard Gibbs free energy of the self-assembly as a function of the hydrogen-bonded aggregate formed with the *trans* and the *cis* azodibenzoic acids at 298 K.